



Multilayer solar cells based on CdTe grown from nitrate precursor.

SALIM, Hussein Ismail

Available from the Sheffield Hallam University Research Archive (SHURA) at:

<http://shura.shu.ac.uk/20315/>

A Sheffield Hallam University thesis

This thesis is protected by copyright which belongs to the author.

The content must not be changed in any way or sold commercially in any format or medium without the formal permission of the author.

When referring to this work, full bibliographic details including the author, title, awarding institution and date of the thesis must be given.

Please visit <http://shura.shu.ac.uk/20315/> and <http://shura.shu.ac.uk/information.html> for further details about copyright and re-use permissions.

102 113 366 3



REFERENCE

ProQuest Number: 10700961

All rights reserved

INFORMATION TO ALL USERS

The quality of this reproduction is dependent upon the quality of the copy submitted.

In the unlikely event that the author did not send a complete manuscript and there are missing pages, these will be noted. Also, if material had to be removed, a note will indicate the deletion.



ProQuest 10700961

Published by ProQuest LLC (2017). Copyright of the Dissertation is held by the Author.

All rights reserved.

This work is protected against unauthorized copying under Title 17, United States Code
Microform Edition © ProQuest LLC.

ProQuest LLC.
789 East Eisenhower Parkway
P.O. Box 1346
Ann Arbor, MI 48106 – 1346

Multilayer Solar Cells Based on CdTe Grown From Nitrate Precursor

Hussein Ismail Salim

A thesis submitted in partial fulfilment of the requirements of
Sheffield Hallam University for the degree of
Doctor of Philosophy

March 2016

Declaration

I hereby declare that the work described in this thesis is my own work, done by me and has not been submitted for any other degree anywhere.

Hussein Ismail Salim

Acknowledgement

First and foremost, I would like to express my profound gratitude to my advisor, Prof. I.M. Dharmadasa for the continuous support of my PhD study and research, for his patience, motivation, enthusiasm, and immense knowledge. His guidance helped me in all the time of research and writing of this thesis. I would also like to thank my second supervisor, Prof. Alexei Nabok, for his assistance.

I remain indebted to the staff of Materials and Engineering Research Institute (MERI) especially Prof. Douglas Cleaver, Deborah Durmus, Deeba Zahoor, Bob Burton, Corrie Houton, Gillian Hill, Rachael Toogood, Gary Robinson and others due to their sincerity of helping me in completing this research programme.

I appreciate the encouragement and useful discussions of my colleagues in the Electrodeposition group of MERI, Dr. O.K. Echendu, Dr. A.R. Weerasinghe, Dr. F. Fauzi, Dr. N.A. Abdulmanaf, M.L. Madugu., O.I. Olusola, A.A. Ojo during the research. The L. Bowen of Physics department, Durham University, S. Creasy and V. Patel of MERI, Sheffield Hallam University, are also thanked for assisting with SEM measurements. Also, Professor M.B. Dergacheva and Dr. K.A. Urazov from Institute of Organic Catalyst & Electrochemistry, Kazakhstan and Prof. M. Walls, Dr. A. Abbas and research group from CREST, Loughborough University are thanked for the AFM and TEM measurements. Lastly Prof. T. Druffel, Dr. R. Dharmadasa and their research group from University of Louisville, USA should be acknowledged for their efforts to perform UPS and PL measurements. Thanks to A. Mohammed and B. Kadhem and M. Salim for useful contributions during the research.

To my parents, Ismail Salim and Asia Abdulqhadir, I thank them for their efforts and sacrifices in raising me up and giving me love, care, support, prayer and much more. To my parent's in-law, Gindal Salim and Khadija Asmikhan, I really appreciate their support and prayer to me and my family.

For my lovely wife Mohabad Gindal, I would like to thank her for taking care of my son, Bahman Hussein. I sincerely appreciate her efforts and sacrifices in supporting me going through difficult times.

Last but not least, I would like to express my gratitude to the Ministry of Higher Education and Scientific Research at the Kurdistan Region of Iraq and also University of Zakho and Duhok for their assistance and financial support.

Dedication

To my late beloved brother "*Mohammed Ismail Salim*" and all those who bravely sacrifice their lives for the liberation of humanity wherever they maybe.

List of Publications

Journal publications

1. I.M. Dharmadasa, P.A. Bingham, O.K. Echendu, **H.I. Salim**, T. Druffel, R. Dharmadasa, G.U. Sumanasekera, R.R. Dharmasena, M.B. Dergacheva, K.A. Mit, and K.A. Urazov, Fabrication of CdS/CdTe-based thin film solar cells using an electrochemical technique, *Coatings*, **4**(3) (2014) 380-415. (doi: 10.3390/coatings4030380).
2. Imyhamy M. Dharmadasa, Ayotunde A. Ojo, **Hussein I. Salim**, and Ruvini Dharmadasa. "Next Generation Solar Cells Based on Graded Bandgap Device Structures Utilising Rod-Type Nano-Materials" *Energies*, **8**(6) (2015) 5440-5458. (doi:10.3390/en8065440).
3. N.A. bdul-Manaf,, **H.I. Salim**, M.L. Madugu,, O.I. Olusola, and I.M. Dharmadasa, Electro-Plating and Characterisation of CdTe Thin Films Using CdCl₂ as the Cadmium Source, *Energies*, **8**(10) (2015) 10883-10903. (doi: 10.3390/en81010883).
4. I.M. Dharmadasa, O.K. Echendu, F. Fauzi, N.A. Abdul-Manaf, **H.I. Salim**, T. Druffel, R. Dharmadasa, and B. Lavery, Effects of CdCl₂ treatment on deep levels in CdTe and their implications on thin film solar cells: A comprehensive photoluminescence study, *Journal of Materials Science: Materials in Electronics*, **26**(7) (2015) 4571-4583. (doi: 10.1007/s10854-015-3090-4).
5. **H.I. Salim**, V. Patel, A. Abbas, J.M. Walls, and I.M. Dharmadasa, Electrodeposition of CdTe thin films using nitrate precursor for applications in solar cells, *Journal of Materials Science: Materials in Electronics*, **26**(5) (2015) 3119-3128. (doi: 10.1007/s10854-015-2805-x).
6. I.M. Dharmadasa, O.K. Echendu, F. Fauzi, **H.I. Salim**, N.A. Abdul-Manaf, J.B. Jasinski, A. Sherehiy, and G. Sumanasekera, Study of Fermi level position before and after CdCl₂ treatment of CdTe thin films using ultraviolet photoelectron spectroscopy, *Journal of Materials Science: Materials in Electronics*, (2016) 1-8. (doi: 10.1007/s10854-016-4391-y).
7. **H.I. Salim**, O.I. Olusola, A.A. Ojo, K.A. Urasov, M.B. Dergacheva and I.M. Dharmadasa, Electrodeposition and characterisation of CdS thin films using thiourea precursor for application in solar cells, *Journal of Materials Science: Materials in Electronics*, (2016). (doi: 0.1007/s10854-016-4629-8).

Conference publications

1. O.K. Echendu, A.R. Weerasinghe, F. Fauzi, **H.I. Salim**, N.A. Abdul Manaf and I. M. Dharmadasa, Electroplating of semiconductor materials for photovoltaic and optoelectronic device applications, 4th Association of Professional Sri Lankans Convention, APSL - Research Symposium (APSL-RS), 17 November 2012, Sheffield, United Kingdom. (Oral Presentation).
2. I.M. Dharmadasa, D.G. Diso, O.K. Echendu, **H.I. Salim**, N.A. Abdul Manaf, M. B. Dergacheva, K.A. Mit and K.A. Urazov, Thin film photovoltaic solar cells with nano- and micro-rod type II-VI semiconducting materials grown by electroplating, Proceedings of the 9th Photovoltaic Science, Applications and Technology Conference C95 (PVSAT 9), Swansea, United Kingdom, (2013) 79-82.
3. I.M. Dharmadasa, D.G. Diso, O.K. Echendu, **H.I. Salim**, N.A. Abdul Manaf, M.B. Dergacheva, K.A. Mit and K.A. Urazov, Thin film photovoltaic solar cells with nano- and micro-rod type II-VI semiconducting materials grown by electroplating, 9th Photovoltaic Science, Applications and Technology Conference C95 (PVSAT 9), 10-12 April 2013, Swansea, United Kingdom. (Oral Presentation).
4. I. M. Dharmadasa, D.G. Diso, O.K. Echendu, **H.I. Salim**, N.A. Abdul Manaf, M.B. Dergacheva, K.A. Mit and K.A. Urazov, Thin film photovoltaic solar cells with nano- and micro-rod type II-VI semiconducting materials grown by electroplating, 39th IEEE Photovoltaic Specialist Conference, 16-21 June 2013, Florida, USA. (Poster).
5. N.A. Abdul-manaf, O.K. Echendu, **H.I. Salim**, L. Bowen and I.M. Dharmadasa, Electrodeposition and characterization of polyaniline for development of organic/inorganic hybrid solar cells, 2nd International Conference on Solar Energy Materials, Solar Cells and Solar Energy Applications (SOLAR ASIA), 22-24 August 2013, Willayah Persekutuan, Malaysia, 105-110 (Oral Presentation).
6. N.A. Abdul-Manaf, O.K. Echendu, F. Fauzi, **H.I. Salim**, I.M. Dharmadasa, Development of Polyaniline as a pinhole plugging layer in CdS/CdTe solar cells, UK Semiconductors & UK Nitrides Consortium Summer Meeting, 3-4 July, 2013, Sheffield, United Kingdom. (Poster).

7. **H.I. Salim**, A. Abdul Manaf and I.M. Dharmadasa, Electrodeposition of CdTe Thin Film Solar Cells Using Cadmium Nitrate Precursor, Proceeding of the 10th Photovoltaic Science, Application and Technology (PVSAT-10), Loughborough University, Loughborough, UK, (2014) 149-152 (Poster).
8. **H.I. Salim**, A. Abdul-Manaf, I.M. Dharmadasa, Growth of CdTe thin film by electrodeposition method using cadmium nitrate precursor, UK Semiconductors & UK Nitrides Consortium Summer Meeting, 9-10 July, 2014, Sheffield, United Kingdom. (Poster).
9. M.L. Madugu, P.A. Bingham, **H.I. Salim**, O.I. Olusola, and I.M. Dharmadasa, Development of InxSe_y Buffer Layers for Application in CdTe Based Thin Film Solar Cells, Conference: 29th European Photovoltaic Solar Energy Conference and Exhibition, Amsterdam, Netherlands (EU PVSEC 2014) 1847-1851(Poster).
10. I.M. Dharmadasa, A. Ojo, **H.I. Salim** and R. Dharmadasa, Next Generation Solar Cells Based on Graded Bandgap Devices Utilising Rod-type Electroplated Nano-Materials, Conference: Photovoltaic Science Applications and Technology (PVSAT-11), Conference C97 of the SOLAR ENERGY SOCIETY, University of Leeds, Leeds, UK, (2015) 169 (Oral Presentation).
11. **H.I. Salim**, O.I. Olusola and I.M. Dharmadasa, Cathodic electrodeposition of CdS thin films from thiourea precursor for solar cell applications, Conference: Photovoltaic Science Applications and Technology, PVSAT-11, Conference proceeding C97 of the SOLAR ENERGY SOCIETY, University of Leeds, Leeds, UK, (2015) 149-150 (Poster).
12. **H.I. Salim**, A. Ojo, I.M. Dharmadasa, Effect of CdCl₂ and CdCl₂+CdF₂ treatment on the structural, morphological and optical properties of electrodeposited CdTe thin films, UK Semiconductors & UK Nitrides Consortium Summer Meeting, 1-2 July, 2015, Sheffield, United Kingdom. (Poster).
13. N.A. Abdul-Manaf, **H.I. Salim**, M.L. Madugu and I.M. Dharmadasa, Electrodeposition of CdTe thin films using chloride precursor for the application in solar cells, Conference: Photovoltaic Science Applications and Technology (PVSAT-11), Conference proceeding C97 of the SOLAR ENERGY SOCIETY, University of Leeds, Leeds, UK, (2015) 137-140 (Poster).

This thesis presents the research and development of low-cost multilayer graded-bandgap solar cells based on electrodeposited CdTe. The electronic quality layers used in this research are electrodeposited CdS and CdTe and chemical bath deposited (CBD) CdS. In the literature, the electrodeposition of CdS layers has been mainly reported using sodium thiosulphate ($\text{Na}_2\text{S}_2\text{O}_3$), ammonium thiosulphate $(\text{NH}_4)_2\text{S}_2\text{O}_3$ and thioacetamide ($\text{C}_2\text{H}_5\text{NS}$) as the precursor for sulphur ions. The major disadvantages of these precursors are the precipitation of elemental S and CdS particles in the solution during growth which can affect the quality of the deposited thin films. Electrodeposition of the CdS from acidic and aqueous solutions using thiourea ($\text{SC}(\text{NH}_2)_2$) precursor has been able to overcome this disadvantage. No visible precipitations of elemental S or CdS particles were observed in the deposition electrolyte showing a stable bath during the growth.

Also, in the literature, the CdTe thin films have been mainly electrodeposited using CdSO_4 as the precursor for Cd ions whereas in this thesis the electrodeposition of the CdTe thin films were carried out comprehensively using cadmium nitrate $\text{Cd}(\text{NO}_3)_2$ as the precursor for Cd ions. Reports are scarce on the electrodeposition of CdS and CdTe thin films history using thiourea and nitrate precursors. Using these precursors, the CdS and CdTe have been successfully electrodeposited from aqueous solution on glass/fluorine-doped tin oxide (FTO) substrates, using simplified two-electrode system instead of the conventional three-electrode system. Also, the CBD-CdS thin films have been successfully grown from aqueous solution on glass/FTO substrates.

The electrodeposited and chemical bath deposited materials were characterised for their structural, compositional, morphological, optical, electrical and defect properties using X-ray diffraction (XRD), Raman spectroscopy, energy dispersive X-ray diffraction (EDX), scanning electron microscopy (SEM), atomic force microscopy (AFM), transmission electron microscopy (TEM), optical absorption (UV-Vis spectroscopy), photoelectrochemical (PEC) cell, current-voltage (I-V), capacitance-voltage (C-V), DC electrical measurements, ultraviolet photoelectron spectroscopy (UPS) and photoluminescence (PL) techniques. Most of the properties of CdTe grown using nitrate precursor are comparable to CdTe grown using sulphate precursor. However, PL studies indicate the presence of low defect in the material.

Using CdTe as the main absorber material, fully fabricated solar cell structures of the n-n hetero-junction plus large Schottky barrier type and multilayer graded-bandgap solar cells were fabricated instead of the conventional p-n junction type structures. Also, the electrodeposited ZnS and ZnTe layers grown by PhD researchers within the same group at Sheffield Hallam University (SHU) were incorporated in the multilayer graded-bandgap structure. Improved $\text{CdCl}_2 + \text{CdF}_2$ treatment of CdTe at 450°C shows further enhancements over the conventional CdCl_2 treatment parameters. The fully fabricated devices were characterized using I-V and C-V measurement techniques. The highest device parameters obtained in this research work are the open-circuit voltage of 663 mV, short-circuit current density of 26.2 mAcm^{-2} and fill factor of

0.65. The best efficiency achieved in this research work was 7.1% for the glass/FTO/n-CdS(CBD)/n-CdTe/Au solar cell structure. The best devices with the efficiencies in the range (5.1-7.1)% presented in this thesis have shown the doping concentrations in the range $\sim(1.30 \times 10^{16}$ to $6.50 \times 10^{15}) \text{ cm}^{-3}$.

Table of contents

Declaration	i
Acknowledgement.....	ii
Dedication	iii
List of Publications	iv
Abstract	vii
Table of contents	ix
Chapter 1: Introduction	1
1.1 Global energy demand and energy crisis	1
1.2 None-renewable energy sources and environmental impacts	4
1.3 Alternative renewable energy sources	4
1.3.1 Wind energy	5
1.3.2 Geothermal energy	6
1.3.3 Hydroelectric energy	7
1.3.4 Biomass energy	8
1.3.5 Tidal energy	9
1.3.6 Solar energy	9
1.3.6.1 Solar radiation	10
1.3.6.2 Solar thermal	11
1.3.6.3 Solar Photovoltaic	12
1.4 Aim and objectives of this work	13
1.5 Conclusion	15
1.6 References	17
Chapter 2: Photovoltaic Solar Energy Conversion.....	21
2.1 Introduction	21
2.2 Inorganic solar cells	22
2.2.1 Silicon based solar cells	22
2.2.1.1 Monocrystalline silicon solar cells.....	23
2.2.1.2 Polycrystalline silicon solar cells	25
2.2.1.3 Amorphous silicon solar cells	26

2.2.2	III-V compound semiconductor solar cells	26
2.2.3	Chalcogenide semiconductor based solar cells	28
2.3	Organic solar cells.....	29
2.4	Dye-sensitised solar cells	32
2.5	Hybrid solar cells	34
2.6	Conclusion	35
2.7	References	36
Chapter 3: Thin films deposition techniques.....		42
3.1	Introduction	42
3.2	Physical deposition techniques	42
3.2.1	Sputtering	43
3.2.2	Molecular beam epitaxy (MBE).....	44
3.2.3	Closed space sublimation (CSS)	46
3.3	Chemical deposition techniques.....	47
3.3.1	Gas phase deposition.....	47
3.3.1.1	Metalorganic chemical vapour deposition (MOCVD).47	
3.3.1.2	Plasma enhanced chemical vapour deposition (PECVD)	48
3.3.1.3	Photo-enhanced chemical vapour deposition (PHCVD)	49
3.3.2	Liquid phase deposition	49
3.3.2.1	Electrodeposition (ED).....	50
3.3.2.2	Chemical bath deposition (CBD)	51
3.3.2.3	Spin-coating	53
3.3.2.4	Spray pyrolysis.....	54
3.4	Conclusion	55
3.5	References	56
Chapter 4: Materials characterisation techniques.....		63
4.1	Introduction	63
4.2	X-ray techniques	63
4.2.1	X-Ray diffraction (XRD)	63
4.2.2	Energy dispersive X-ray spectroscopy (EDX)	65
4.2.3	X-ray fluorescence (XRF).....	66
4.3	Optical spectroscopy techniques	67

4.3.1	Spectrophotometry	67
4.3.2	Photoluminescence spectroscopy (PL)	70
4.3.3	Ultraviolet photoelectron spectroscopy (UPS).....	71
4.3.4	Raman spectroscopy.....	73
4.4	Electron beam microscopy techniques.....	74
4.4.1	Scanning electron microscopy (SEM)	74
4.4.2	Transmission electron microscopy (TEM)	76
4.4.3	Atomic force microscopy (AFM).....	77
4.5	Electrical characterisation techniques.....	80
4.5.1	Direct current (DC) conductivity measurements	80
4.5.2	Photoelectrochemical (PEC) cell measurements	81
4.5.3	Hall Effect Measurements.....	83
4.6	Conclusions.....	86
4.7	References	87
Chapter 5: Devices characterisation techniques		89
5.1	Introduction.....	89
5.2	Current-Voltage (I-V) Characterisation	89
5.2.1	I-V Characteristics under dark conditions.....	90
5.2.2	I-V Characteristics under illuminated conditions	94
5.2.3	Capacitance-Voltage characteristics	99
5.2.4	Spectral response characterisation	102
5.2.5	Conclusions.....	104
5.3	References	105
Chapter 6: Deposition and characterisation of ED-CdS window material		106
6.1	Introduction.....	106
6.2	Preparation of ED-CdS deposition system.....	107
6.3	Results and discussions.....	108
6.3.1	Voltammogram	108
6.3.2	Visual appearance of ED-CdS layers with growth voltage.....	110
6.3.3	X-ray diffraction.....	111
6.3.3.1	Effect of annealing temperature on the XRD patterns of ED-CdS layers.....	116
6.3.3.2	Effect of annealing time on the XRD patterns of ED-CdS layers	117

6.3.4	Variation of thickness with growth time for the ED-CdS layers	119
6.3.5	Optical absorption spectrophotometry	121
6.3.5.1	Effect of growth voltage on the optical properties of ED-CdS layers.....	121
6.3.5.2	Effect of annealing temperature on the optical properties of ED-CdS layers	124
6.3.5.3	Effect of annealing time on the optical properties of ED-CdS layers	126
6.3.6	Scanning electron microscopy (SEM)	127
6.3.6.1	Variation of ED-CdS surface morphology with growth voltage.....	127
6.3.6.2	Effect of annealing temperature on the surface morphology of ED-CdS layers.....	131
6.3.6.3	Effect of annealing time on the surface morphology of ED-CdS layers.....	134
6.3.7	Energy Dispersive X-ray (EDX) Analysis.....	136
6.3.8	Atomic force microscopy (AFM).....	139
6.3.9	Raman spectroscopy.....	142
6.3.10	Photoelectrochemical (PEC) cell measurement.....	143
6.3.11	Electrical resistivity measurements.....	144
6.4	Conclusions.....	146
6.5	References	148
Chapter 7:	Deposition and characterisation of CBD-CdS window material	152
7.1	Introduction	152
7.2	Preparation of CBD-CdS aqueous solution	152
7.3	Reaction mechanism	153
7.4	Results and discussions.....	154
7.4.1	X-ray diffraction.....	154
7.4.1.1	Effect of films thickness on the XRD patterns of CBD-CdS layers	154
7.4.1.2	Effect of annealing temperature on the XRD patterns of CBD-CdS layers.....	157

7.4.1.3	Effect of annealing time on the XRD patterns of CBD-CdS layers	158
7.4.2	Optical absorption spectroscopy	160
7.4.2.1	Effect of film thickness on the optical properties of CBD-CdS layers.....	160
7.4.2.2	Effect of annealing temperatures on the optical properties of CBD-CdS layers	162
7.4.2.3	Effect of annealing time on the optical properties of CBD-CdS layers.....	164
7.4.3	Scanning electron microscopy (SEM)	165
7.4.3.1.	Effect of annealing temperature on the surface morphology of CBD-CdS layers.....	166
7.4.3.2.	Effect of annealing time on the surface morphology of CBD-CdS layers.....	169
7.4.4	Energy dispersive x-ray (EDX) analysis.....	171
7.4.5	Raman spectroscopy.....	173
7.4.6	Hall Effect measurements	173
7.5	Conclusions	175
7.6	References	177
Chapter 8: Deposition and characterisation of CdTe absorber material		180
8.1	Introduction	180
8.2	Preparation of CdTe deposition electrolyte.....	183
8.3	Results and discussion	184
8.3.1	Voltammogram	184
8.3.2	X-ray diffraction.....	186
8.3.2.1	Optimisation of growth voltage	186
8.3.2.2	Effect of the growth time on the structural properties of CdTe layers	189
8.3.2.3	Effect of growth time on the thickness of CdTe layers	192
8.3.2.4	Effect of CdCl ₂ and CdCl ₂ +CdF ₂ treatments on the XRD patterns of CdTe layer at different temperatures	194

8.3.2.5	Effect of CdCl_2 treatment on XRD patterns of Te-rich CdTe layers	197
8.3.3	Photoelectrochemical (PEC) cell measurements	199
8.3.4	Optical absorption spectrophotometry	201
8.3.4.1	Effect of growth voltage on the optical properties of CdTe layer.....	201
8.3.4.2	Effect of the growth time on the optical properties of CdTe layers	203
8.3.4.3	Effect of temperature on the optical properties of CdCl_2 and $\text{CdCl}_2+\text{CdF}_2$ treated CdTe layers	205
8.3.5	Scanning electron microscopy (SEM)	207
8.3.5.1	Effects of CdCl_2 and $\text{CdCl}_2+\text{CdF}_2$ treatment on the morphological properties of CdTe layers at different temperatures	207
8.3.6	Energy Dispersive X-ray (EDX).....	212
8.3.7	Transmission electron microscopy (TEM)	214
8.3.8	Raman spectroscopy.....	216
8.3.9	Ultraviolet photoelectron spectroscopy (UPS).....	217
8.3.10	Photoluminescence studies (PL)	222
8.4	Conclusions	225
8.5	References	228
Chapter 9: Solar cell fabrication and characterisation		234
9.1	Introduction	234
9.2	Fabrication of glass/FTO/n-CdS/n-CdTe/Au solar cells.....	234
9.2.1	Energy band diagram of glass/FTO/n-CdS/n-CdTe/Au solar cell	237
9.2.2	Effect of CdTe surface etching on the performance of glass/FTO/n-CdS/n-CdTe/Au solar cells	239
9.2.3	Effect of CdCl_2 and $\text{CdCl}_2+\text{CdF}_2$ treatment on the performance of the glass/FTO/n-CdS/n-CdTe/Au solar cells at different temperatures	243
9.2.4	Assessment of the fabricated glass/FTO/n-CdS/n-CdTe/Au solar cells using ED-CdS and CBD-CdS layers for comparison	249

9.2.5	Assessment of glass/FTO/n-CdS/n-CdTe/Au solar cells under dark and illumination conditions.....	251
9.2.6	The C-V measurements for glass/FTO/n-CdS/n-CdTe/Au solar cells	256
9.2.7	Stability of fabricated glass/FTO/n-CdS (CBD)/n-CdTe/Au solar cells	259
9.3	Fabrication of glass/FTO/n-ZnS/n-CdTe/Au solar cells	262
9.4	Fabrication of glass/FTO/n-CdS/n-CdTe/p-ZnTe/Au solar cells.....	265
9.5	Fabrication of multi-layer graded-bandgap solar cells.....	268
9.5.1	Fabrication of glass/FTO/n-CdS(ED)/n-CdTe/p-CdTe/Au multi-layer graded-bandgap solar cells	270
9.5.2	Fabrication of glass/FTO/n-CdS(CBD)/n-CdTe/p-CdTe/Au multi-layer graded-bandgap solar cells	274
9.6	Fabrication of glass/FTO/n-ZnS/n-CdS(ED)/n-CdTe/Au multi-layer graded-bandgap solar cells.....	277
9.7	Conclusions	280
9.8	References	282
Chapter 10:	Next generation solar cells	287
10.1	Introduction	287
10.2	Intermediate band (IB) solar cells	288
10.3	Quantum dot/quantum well solar cells	289
10.4	Solar cells with down conversion.....	290
10.5	Solar cells with up-conversion	291
10.6	Plasmonic solar cells	293
10.7	Hot-carrier solar cells	293
10.8	Tandem solar cells with tunnel junctions	294
10.9	Organic solar cells (OSCs)	295
10.10	Dye-sensitised solar cells (DSSCs) and Perovskite solar cells (PSCs) ..	295
10.11	Graded-bandgap solar cells	297
10.12	Conclusions	299
10.13	References	300
Chapter 11:	Conclusions and recommendations for future work	304
11.1	Conclusions	304
11.2	Recommendations for future work	305

11.2.1	Preparation of deposition electrolyte using high-purity chemicals	305
11.2.2	Effective addition of Te and Cd ions into the deposition electrolyte during the growth	306
11.2.3	Reducing the resistivity of ED-CdS, CBD-CdS and CdTe layers	307
11.2.4	The use of low-resistivity transparent conducting oxide (TCO) layer	308
11.2.5	Improvement of the solar cell stability using pinhole plugin layer (PPL) and MIS-type structure	308
11.2.6	Multi-layer graded-bandgap solar cells	309
11.3	References	310

1.1 Global energy demand and energy crisis

All over the globe, the economy, healthcare, lifestyle, and individual humans' need are essentially dependent on the energy resources. Energy sources are everyday need of human activities, technological development and industrial evolution toward both benefits and crisis of the entire globe and its inhabitant; nevertheless it has been the fact how to indicate a reliable energy source. Day by day globalization is increasing the communication and transportation through the whole world and humans are more relying on the energy [1]. Understanding the global energy consumption and development has been the focus of many scientists and scientific studies in the last decade. The world's energy consumption is more related to the oil intake as it has been the focus of many industries and factories, as well as many technological products are intended to be adoptable with oil and its resources. Based on the British Petroleum Statistical Review in 2015, in the last two decades oil consumption has reached to 32% of the whole world's energy consumption alongside with coal and natural gasses that comes to the second and third most energy use with 30% and 24% of the world's energy use respectively. This shows the percentage of fossil fuel is 86% which is the combination of oil, coal and natural gasses energy sources [2,3]. In addition, there are other energy sources that are being used like nuclear energy, hydroelectricity, and renewable energy sources including wind, solar, geothermal, biomass and biofuels as shown in the Figures 1.1 (a) and (b).

Global energy demand leans toward the increase with the increase of population. It's been estimated that by the next 3 decades the global energy demand will increase up to 30% as the population reaches to 9 billion. This increase will cause the energy supply to increase as well in order to overcome the need of the entire world's population, as well as to have a "safe, secure, affordable, and environmentally responsible" energy source. As a result, scientists, leaders and investors are concentrating to rely more on renewable energy to achieve these goals. The demand on energy will be for lighting, heating and cooling, and home equipment and devices which will be dependent on electricity. In addition, to achieve electricity, the demand for oil, coal and natural gasses will still be the top energy sources [4]. However, the need for energy will be increasingly high all around the world to achieve the human need; this will cause to

increase the emission of carbon dioxide (CO₂), toxic material that pollutes the environment, air and water, and increasing global warming. This is the subject for many scientists nowadays and how they can create affordable energy to cover the needs and not to harm the globe.

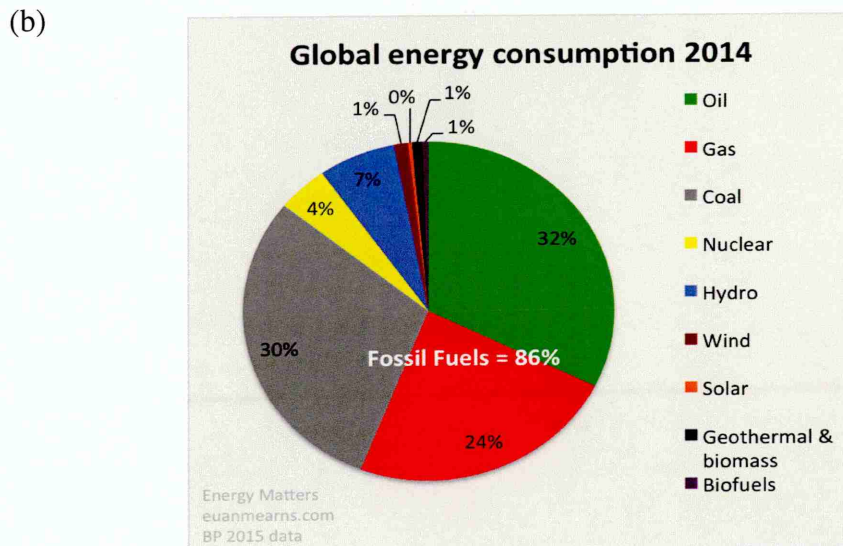
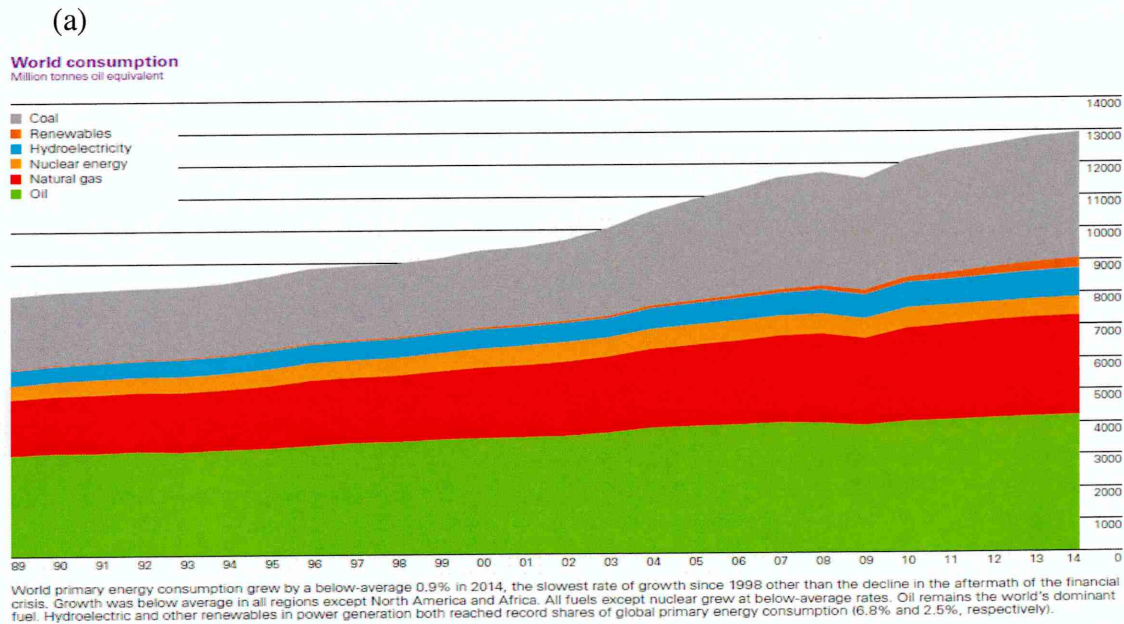


Figure 1.1: BP Statistical Review of World Energy 2014 [2,3].

The extensive burning of fossil fuel in transportation and human activities causes emission of CO₂ alongside with the increase of greenhouse gasses (GHG) causing the increase of temperature all over the world leading to the crisis. Not just that but to decrease the rate of natural resources as well. The concentrated level of CO₂ in

the atmosphere can be called stable at the rate of 280 parts per million (ppm). It's been mentioned that the rate of CO₂ around the world has reached to 450 ppm causing an increase in the atmospheric temperature. It's been expected that doubling the CO₂ rate in the atmosphere to 560 ppm will increase the temperature up to 2.2°C around the world. This increase may result in climate change with harmful human, social, and economic impacts. In the last 70 years, the rate of carbon dioxide has increased more than 70% as shown in Figure 1.2 [5].

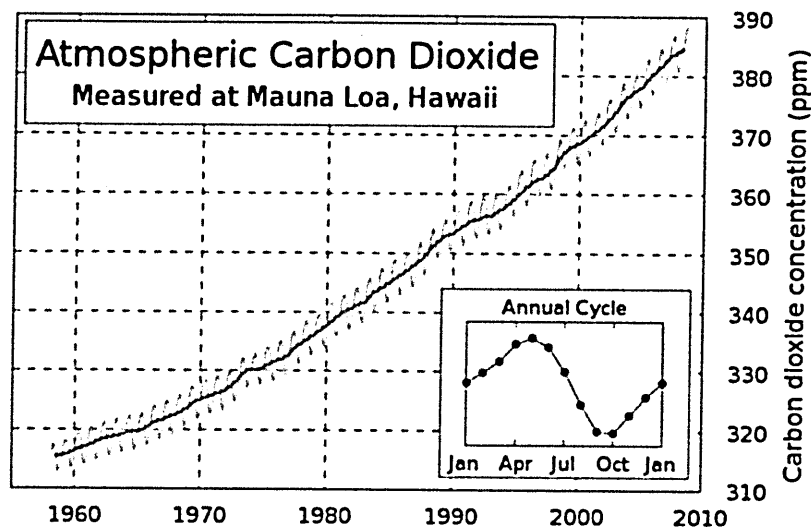


Figure 1.2: Keeling curve of atmospheric CO₂ concentrations, measured at Mauna Loa observatory [5].

The global energy crisis has made many organizations to seek the solution and some technological and non-technological development solutions have been presented by the Intergovernmental Panel on Climate Change (IPCC) report. With the increase in energy demands, the natural resources are diminishing and society is facing the usage of more of the natural resources that are limited. Though, the causes of energy crisis are so many, they are mainly concentrated in over consumption of fossil fuel and this is respectively related to overpopulation that increases the demand of consuming energy, too much waste in energy that creates pollution in the environment, undefined sources of energy that are yet to be found, and not relying on the renewable energy sources due to poor infrastructure in technological development [6]. In brief, all the above causes of the global energy crisis must be studied in a scientific manner in order to create a natural and clean future for the next generation and this is being presented recently through energy conservation and energy efficiency [7].

1.2 None-renewable energy sources and environmental impacts

Non-renewable energy sources are the natural energy sources from earth that cannot be replenished and replaced if it is used up at the same time that is consumed, for example, oil, coal and natural gasses [8]. In the entire world, the uniqueness of minerals is to be non-renewable. These resources are finite in their sense of consumption of economical and physical and they are the major concern that they will be unavailable for the future generation. Conservation and sustainability of non-renewable energy are the keys to protect next generation for using energy. One of the main natural resources that is being consumed by the whole world is the oil which is limited in some places and is not available in the most consuming countries of the western hemisphere. It has been found in many places and yet to be found more and more in different regions, but at the same time, it is a non-renewable source that is limited [9]. The more the rate of finding oil and other non-renewable energy sources increase the more demand is coming to the field and more consumption is being processed that leave harmful impacts to the globe. In addition, these footages are serious impacts on the whole environment and living being.

Observing the environmental impacts, non-renewable energy use has created the limiting environmental condition. Harmful to all, deforestation and fossil fuel combustion are the very reasons of environmental destruction and impacts [9]. Atmospheric effects, acid rain, land pollution, and oil spills are the causes of non-renewable energy sources consumption. The usage of fossil fuels emits dangerous greenhouse gasses such as CO₂ that pollute air and damages ozone layer and leaving us no cover from sun's radiation and causing diseases all over the world. Furthermore, the emission of sulphur and some other chemicals to atmosphere creates acid rain that harms human body and organisms, materials, and buildings in the environment. Also, harmful ashes inside solid waste create pollution to the land. Oil spills are dangerous to shores and ecosystem that will create damage to the aquatic creatures, and has a negative effect on economy and human health [10–12].

1.3 Alternative renewable energy sources

In contrast to non-renewable energy sources, any sources that are not resulting from fossil or nuclear fuel, and are from natural happening inexhaustible are called

renewable energy sources like wind, geothermal, hydroelectric, biomass, tidal and solar energies [13]. Renewable energy sources are beneficial in their principle of being available more than the world's energy demand. This can be count as an alternative to the fossil fuel, which is environmentally friendly and more reliable for future generation as their limit is not restricted to provide the sustainable energy services. In the last 3 decades, renewable energy sources specially wind and solar energies have been serving social and economic improvements in general as example electricity. It is getting more and more reliable to focus on renewable energy sources for future uses instead of natural gas, coal and oil, as renewable energy cost is getting lower unlike fossil fuel and they are getting more dependable for advanced technologies. Currently, the renewable energy sources supply from 15% to 20% of the world's energy demand and they are less dangerous to the environment as they are not contributing to air pollution, acid rain and global climate change [14].

1.3.1 Wind energy

Wind energy is considered to be one of the cleanest and widely available renewable energy sources all around the world, and it has no pollution during power generation. Wind energy is mainly used to create electricity which can be used for heating, cooling, cooking, lighting and other devices that humans use in everyday life. Using oil has made most developed countries change their industry toward providing oil and after the oil crisis of the 70's, they have been interested in renewable energy sources such as the wind [14]. Using wind energy to generate electricity is a phenomenon that is in the interest of the industry, as well as the economy. For this purpose, the wind turbines are usually used and are mostly installed in places with decent wind sources. Figure 1.3 shows the schematic diagram of the energy transformation in wind turbines.

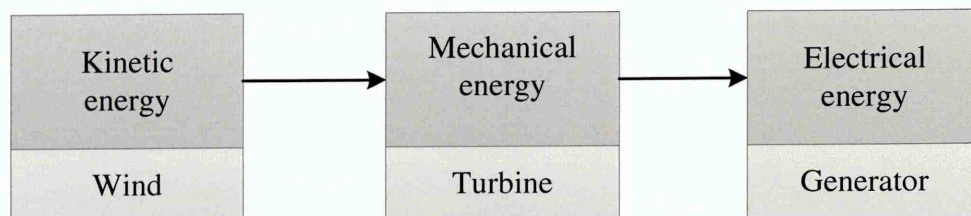


Figure 1.3: Schematic diagram of the energy transformation in wind turbine [15].

There are different types of turbines that are being used to generate electricity including horizontal axis and vertical axis turbines. Horizontal axis turbines are more efficient than vertical axis turbines to provide power. These types of turbines are manufactured with the ability to provide tens of watts to several megawatts and diameter of blades ranging from 1 m to 100 m [16]. From the 1990s to 2010 wind energy production has reached up to 160 GWs of energy [16]. The power generated by the wind (P_{wind}) is given by Equation (1.1) [15]:

$$P_{wind} = \frac{1}{2} \rho A V_{wind}^3 \quad (1.1)$$

where, ρ is air density, A is area swept by blades, and V_{wind} is wind speed.

1.3.2 Geothermal energy

Geothermal energy is a type of renewable energy that is existing in the core of earth and comes out in the form of heat. It is widely used for providing energy as electricity. The use of geothermal energy has no impacts on the environment and in contrast, it mitigates the climate change and reduces the greenhouse gasses (GHG) emission. It has been estimated that the geothermal energy has the potential to generate electricity at a range of 118 to 146 EJ/yr (Exajoules/year) in 3 km depth, and 318 to 1,109 EJ/yr in 10 km depth [16]. Nevertheless, the geothermal technical potential limits are directly related to the enhanced geothermal system (EGS). In EGS, an injection well is drilled into dry rock. Afterward, the water is forced into the injection well, which widens the ground fractures below. This process is known as ‘hydraulic stimulation’. The water travels through fractures in the rock and become hot. The hot water then travels up a production well to create steam for a turbine and thus produce electricity [16]. The use of geothermal energy is unlimited; United States, produces geothermal electricity on average of 15 billion kilowatt hours of power/year, compared to 25 million barrels of oil and 6 million tons of coal/year. The only emission from the geothermal power plant is water vapour as water is the “carrier medium” for geothermal electricity [17].

There are many types of geothermal power plants to create electricity such as dry-steam, flash steam, and binary power plants [18]. The simplest and mostly used

geothermal power plant is dry-steam that has been used for over hundred years. In a dry-steam power plant, steam produced from the geothermal reservoir and it runs the turbines to power the generators. Dry-steam power plant is easy to build as they only need steam, injection piping and the steam cleaning device. Recently, steam plants generate up to 40% of United States' geothermal electricity production [19]. Figure 1.4 shows the schematic of dry-steam power plants.

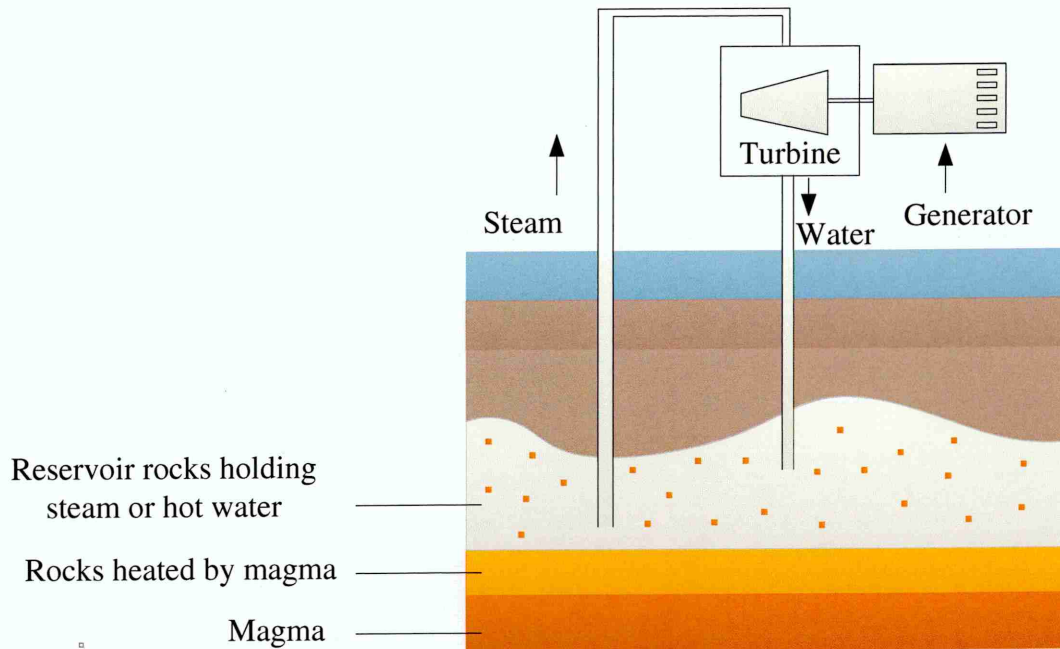


Figure 1.4: Schematic diagram of geothermal power plants (dry-steam). Redrawn from [20].

1.3.3 Hydroelectric energy

Hydroelectric energy is a source of renewable energy that comes from using water in motion to create power (electricity). It is a form of energy that does not expend resources to generate electricity and they are environmentally friendly in which there is no air, land or water pollution. A hydroelectric power plant has created an enormous power supply in developed countries. As mentioned earlier, heating, cooling, cooking, lighting and using house devices needs electricity. Developed countries have shaped scientific focus on generating electricity from hydroelectric systems. Recently, many countries are using water that reaches ponds, lakes, reservoirs, or oceans for creating electricity. In generating electricity using hydroelectric systems, the flowing water turns

the turbines and changes the pressure source of water to mechanical energy and then to electricity [21]. Hydroelectric power provided 16.4% of the world's electricity in 2015 and it can be count as a great alternative toward using fossil fuels and it's environmentally friendly as well as slowing down the crisis with energy supplies [22].

The hydroelectric energy schematic view is very easy to understand. It uses water from reservoir created by the dam with high pressure from gravity and channels of flowing water to pass through turbines. The amount of the water flow can be controlled through the intake and the system has been made in a way that the flowing water reaches the blades of the turbine to create motion and generate the power leading toward creating electricity as shown in Figure 1.5.

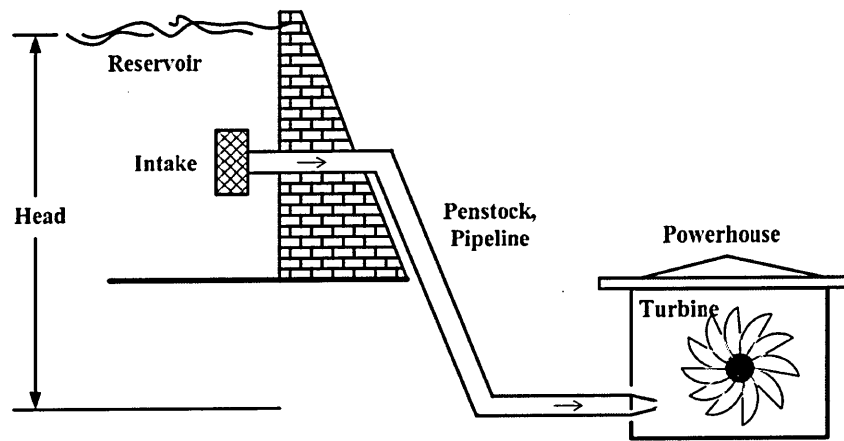


Figure 1.5: Schematic diagram of the hydroelectric power generation [23].

1.3.4 Biomass energy

Biomass is a form of renewable energy that can be defined as “the plant material derived from the reaction between CO_2 in air, water and sunlight, via photosynthesis, to produce carbohydrates that form the building blocks of biomass” [24]. Biomass considered being one of the major sources of energy all over the world, and it has been estimated to subsidize (10-14)% of the world's energy source. As mentioned, biomass is produced by plants converting sunlight to plant material by photosynthesis and it includes water plants, land plants, and organic waste as well as animal waste. Biomass is the sun energy stored in plant's chemical molecules including carbon, hydrogen and oxygen, and these molecules can be broken to create energy and release their stored

energy through digestion, combustion, or decomposition to be used as supplementary fuel for generating power using landfill gas fuel, and stimulate ignition gas machines [24]. Biomass has the variety of benefits as it can be converted to thermal energy, liquid, solid, gas fuels, and other chemical products by different type of conversion. As an example, United States provides 10 GW of electricity generation based on mature and direct combustion technology, through using Biomass energy [25].

1.3.5 Tidal energy

Tidal energy is a renewable energy source that stands for the power inherent in the flow and motion of water at sea or ocean created by tides. The tides can be defined as the increase and decrease in water levels due to the motion of water from one place to other. Scientific understanding of water motion comes from the vast energy by the movement of sun, moon, and earth relative to each other and their rotational movement [26]. The energy in the water motion can be used to generate other types of energy useful to mankind and industry which is electricity. Electricity can be generated by tidal energy using barrage or a dam where tides can reach different levels. Barrage or dams can trap tidal water and create potential energy. This potential energy can be used by either kinetic energy of current in ebbing and surging or potential energy from the difference in tides of being high and low, to generate the flows, rotating the turbines generating electricity [27]. Tidal energy like many other sources of renewable energy has become the focus of many scientists, investors, and politicians for providing electricity, and it has been estimated that the tidal range deployment in 2012 was around 514 MW all around the world [28].

1.3.6 Solar energy

Solar energy refers to the energy that comes directly from the sun in the forms of electromagnetic radiation and heat. Every second, sun converts millions of tons of hydrogen to helium, which is called thermonuclear process and that is how the sun creates its energy. Through all the radiation that comes from the sun, only a small fraction of it reach the earth and this radiation is being used for providing heating, cooling, transportation, and electricity [29]. Solar energy is a clean energy and environmentally friendly power supply and comparing to other types of renewable

energy it has more life span. Everyday sun provides the earth with thousand times more energy that is demanded by the whole world. However, the proportion use of solar energy is still low. Solar energy makes an important contribution in providing power and with the development of technology the cost of using such power is getting low and the demand of using it is getting high. For example, in Germany, they have been able to produce 17 gigawatts (GW) of solar power in 2010 using photovoltaic plants covering the need of around four million three-person households. In 2015, Germany again set a world record producing 25.8 GW of power using photovoltaic plants. This has been done through different types of solar energy storages including small and middle scale rooftops photovoltaic plants, solar carports, off-grid system or free-field solar power systems [30,31].

1.3.6.1 Solar radiation

The sun's output is known as solar radiation which comes in the form of electromagnetic radiation of a wide spectrum. The electromagnetic radiation ranges from high-energy (short-wavelength) to low-energy (long-wavelength). The solar spectrum covers ultraviolet (UV) radiation ranging from (100-400) nm, the visible (VIS) radiation ranging from (400-700) nm and the infrared (IR) radiation (700 nm and above). The ultraviolet, visible and infrared radiations are significant parts of the solar spectrum which play an important role in terrestrial solar energy application including solar thermal and photovoltaic. The amount of solar radiation incident on a square meter of Earth's atmosphere or Earth's surface is known as irradiance and is measured in watts per square meter (Wm^{-2}). The solar irradiance before entering Earth's atmosphere is about $1,366 \text{ Wm}^{-2}$ which is known as air mass zero (AM0) [32]. When solar radiation passes through the Earth's atmosphere, the intensity of solar radiation is attenuated by ozone layer (O_3), water molecules, nitrogen molecules, CO_2 , and dust. By the time the incoming solar radiation reaches the Earth's surface (sea level), the solar irradiance is reduced to 1000 Wm^{-2} or 100 mWcm^{-2} which is known as air mass 1.5 (AM1.5) [32]. Figure 1.6 shows the solar spectrum comprising electromagnetic radiation of various wavelengths or frequencies.

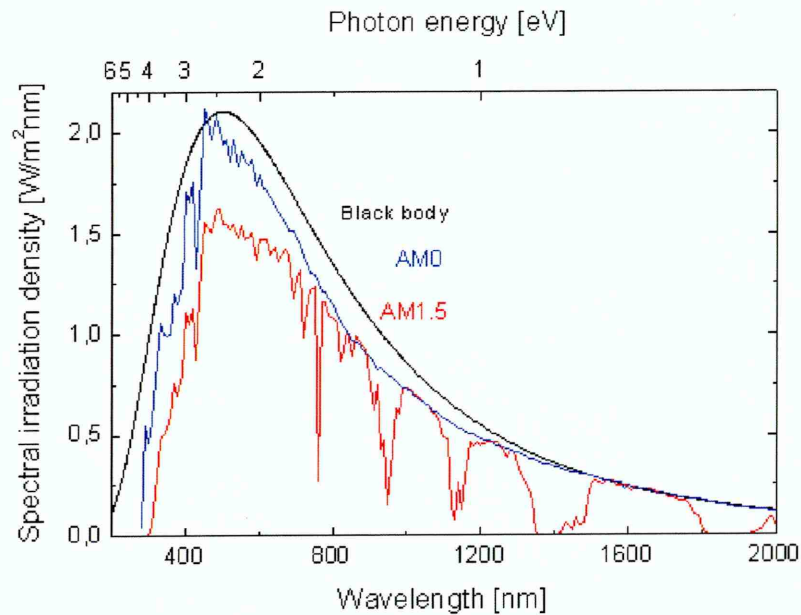


Figure 1.5: The solar spectrum showing the spectral irradiance as a function of photon wavelength at outer Earth's atmosphere (black body), at the top of the atmosphere (AM0) and at the sea level (AM1.5) [33].

When solar radiation or photons reach the surface of the Earth, it can be converted to the useful forms of the energy. It can be directly converted into heat energy or electric energy. Based on these types of solar energy conversions, the solar energy can be mainly classified into two categories including solar thermal and solar photovoltaic which are presented in the following sections.

1.3.6.2 Solar thermal

Solar thermal is basically using the sun's heat to generate energy as heat or electricity. Sun has the power of generating an enormous amount of heat by fusing hydrogen to helium through thermonuclear reaction, and passes that heat to the earth that can cover the whole world's energy supply. The outer layer of sun generates an equivalent black body temperature of about 5778 K [34]. Solar thermal energy is mainly using the sunlight to generate heat and that heat can be used to power the engine (heat engine) to generate electricity, or through heating devices to be used directly to heat the water for houses, buildings, schools, and hospitals. Also, in solar thermal energy fluids are being used to be heated for example water, oil, salts, air, nitrogen,

helium, etc [35,36]. In addition, there are different types of engines like steam engines, gas turbines, and Stirling engines that can be used to generate power. Solar thermal energy is very useful for mankind and it's been used through thermal conversion processes, which is to absorb solar radiation at the surface of the receiver. When the receiver is heated, the liquid inside the receiver can transfer heat to the needed engine. The heat energy that can be received from the receiver is mainly dependent on the insolation, which is the degree to which the sunlight is concentrated, and the reduction of heat losses through the working fluid. Using heat is very reliable to generate electricity and the sun is a major source of it. The energy from sun absorbed by the earth and its atmosphere are approximately 120,000 terawatts. In brief, it can be mentioned that solar thermal energy is environmentally friendly and economically competitive electric source for any part of the world [37].

1.3.6.3 Solar photovoltaic

Solar photovoltaic (PV) captures the solar energy using photovoltaic cell and convert this energy directly into electricity. This physical phenomenon was first observed in 1839 by Edmond Becquerel, a French Scientist. Solar PV has many advantages, which is environmentally friendly, has no noise, no moving parts, no GHG emissions, no use of fossil fuel or water, low maintenance is needed, up to about 30 years lifetime, even operates in cloudy weather condition, and can be used for multi-energy supply. In PV cells, there are mainly four basic steps that must be brought together in order to effectively convert sunlight energy into electricity [38]. These include (i) effective absorption of photons using suitable semiconducting materials, (ii) breaking up the bonds between the atoms to create charge carriers (electron-hole, or e-h pairs), (iii) effective separation of photogenerated charge carriers before their recombination, and (iv) the collection of the photogenerated charge carrier at opposite contacts to create useful electric current. The PV cells can be fabricated using different PV materials and growth techniques which are presented in chapters 2 and 3 of this thesis. Some examples of the PV cells are silicon (Si) based solar cells (first generation), thin film solar cells (second generation) and the next generation solar cells (third generation). The details of these three solar cell generations are presented in chapter 10. The silicon-based solar cells have relatively higher efficiency than other solar cells; however, their manufacturing costs are also higher [39]. The thin film solar cells have

comparatively lower efficiency than Si-based solar cells. However, thin film solar cells are much cheaper than those of Si-based solar cells. The main absorber materials used in thin film solar cells include cadmium telluride (CdTe), Copper indium gallium diselenide (CIGS) and amorphous silicon (a:Si) [40–42]. The next generation PV cells focused on the high-efficiency solar cell through full spectrum utilisation. These include concentrator solar cell [43], multijunction tandem solar cells [44] and multi-layer graded-bandgap solar cells [38,45,46].

1.4 Aim and objectives for this work

The CdS/CdTe thin film solar cells have long been considered as one of promising choice for the development of low-cost and reliable solar cells. A lot of researches have been carried out so far to increase the efficiency of CdS/CdTe solar cells and reduce the cost of production. The majority of these research groups work on conventional n-p heterojunction structure between n-CdS and p-CdTe. The first high-efficiency (15.8%) n-CdS/p-CdTe solar cell was reported by Britt and Ferekides in 1993 [47]. The efficiency of thin film n-CdS/p-CdTe solar cells was stagnated for about a decade until 2000 when Wu *et al* reported an increase of 0.7% to the efficiency of 16.5% [48]. For another decade, the efficiency was again stagnated at this value based on the n-CdS/p-CdTe heterojunction structure, but during the past three years (2013-2015) First Solar Company announced a rapid progress in producing a new world record efficiency of 21.5% [49].

In 2002, Dharmadasa *et al* has proposed the new model to develop and improve the efficiency of the CdS/CdTe thin film solar cells. This model explains the device behaviour in terms of the combination of n-n-heterojunction (n-CdS/n-CdTe) and large Schottky barrier formation at n-CdTe/Metal interface [50]. Based on the new model, they reported the efficiency of ~18% using electrodeposited n-CdTe from non-aqueous solution (ethylene glycol) at the temperature of 160°C. The details of the n-n+Schottky junction for the glass/FTO/n-CdS/n-CdTe/Au solar cells are presented and discussed in chapter 9. It should be noted that the flammability and toxicity of non-aqueous solutions raise a concern about health and safety during growth of semiconductor layers. Therefore, it is much safer to use aqueous solution for the growth of CdS and CdTe semiconductor thin films. The reliability, scalability and manufacturability of CdS/CdTe thin film solar cells grown by the simple and low-cost electrodeposition technique using

aqueous solution has been proven by British Petroleum (BP) Solar in 1991 with reported efficiency of 14.2% [51].

The main aim of this research project is to develop low-cost high efficiency multilayer graded bandgap solar cells based on CdTe absorber material. In this thesis, CdS layers were grown by two different aqueous solution growth methods. These include low-cost electrodeposition (ED) and chemical bath deposition (CBD) growth techniques. The CdTe layers were grown only by the electrodeposition technique from aqueous solutions using the 2-electrode system. The previous PhD researchers at the SHU solar energy research group have deposited the CdS layers using sodium thiosulphate ($\text{Na}_2\text{S}_2\text{O}_3$) and ammonium thiosulphate $(\text{NH}_4)_2\text{S}_2\text{O}_3$ as the precursor for sulphur (S) ions [52–58]. Also, these researchers have grown the CdTe layers using cadmium sulphate (CdSO_4) and cadmium chloride (CdCl_2) as the precursor for cadmium (Cd) ions.

In this work, the electrodeposited CdS and CdTe layers were deposited using two new precursors. The CdS layers were grown using thiourea [$\text{SC}(\text{NH}_2)_2$] as the precursor for sulphur (S) ions and the CdTe layers were grown using cadmium nitrate tetrahydrate ($\text{Cd}(\text{NO}_3)_2 \cdot 4\text{H}_2\text{O}$) as the precursor for Cd ions [59,60]. These two precursors were new within our research group and also the reports are scarce on the electrodeposition of CdS and CdTe history using thiourea and nitrate precursors respectively [61–63].

The research objectives of this work are as follow:

- i. Growth and optimisation of CBD-CdS as window layer using aqueous solution.
- ii. Growth and optimisation of the ED-CdS window layer using thiourea and ED-CdTe absorber layer using $\text{Cd}(\text{NO}_3)_2 \cdot 4\text{H}_2\text{O}$ precursor the 2-electrode system in aqueous solution.
- iii. To study the structural, compositional, optical, morphological, and electrical properties of the CBD-CdS, ED-CdS and ED-CdTe layers using available facilities in the Material and Engineering Research Institute at Sheffield Hallam University (SHU) and with our external collaborators.

- iv. To study the effect of the CdCl_2 and $\text{CdCl}_2+\text{CdF}_2$ treatment on the structural, optical, morphological properties and device performance of the fabricated solar cells.
- v. To fabricate the n-CdS/n-CdTe heterojunction plus large Schottky barrier at n-CdTe/metal interface using n-CdS(CBD) and n-CdS(ED) as window layers for comparison. The fabricated structures include glass/FTO/n-CdS(CBD)/n-CdTe/Au and glass/FTO/n-CdS(ED)/n-CdTe/Au solar cells.
- vi. Incorporation of p-ZnTe(ED) as the pinhole plugging layer and to increase the potential barrier height and improve the device performance of the CdS/CdTe solar cells. The solar cells were fabricated with the structure of glass/FTO/n-CdS(ED)/n-CdTe/p-ZnTe/Au. The ZnTe layers were grown by PhD researchers at SHU solar energy group.
- vii. To fabricate the multi-layer graded-bandgap solar cells using the n-CdS (CBD), n-CdS(ED), n-CdTe(ED) and n-ZnS (ED) layers. The n-ZnS layers were also grown by PhD researchers at SHU. The fabricated multi-layer graded-bandgap solar cells include glass/FTO/n-CdS(CBD)/n-CdTe/p-CdTe/Au, glass/FTO/n-CdS(ED)/n-CdTe/p-CdTe/Au, glass/FTO/n-ZnS/n-CdS(ED)/n-CdTe/Au structures.
- viii. Assessment of the efficiency of the fabricated thin film solar cells using current-voltage (I-V) measurement and developing these devices by optimisation of all processing steps to achieve highest possible efficiency

1.5 Conclusions

In brief, this chapter presents the human needs for energy all over the world and the issues in the supply and demand of energy sources as well as the impacts of using energies to the environment through emission and consumption. Different types of energy sources have been summarised and the urge to seek for sustainable renewal energy sources, which is more affordable and friendlier to the environment, has been the focus of many scientist, activists and politicians. Using fossil fuel in the past has made many changes in increasing CO_2 emission and greenhouse gasses toward global warming causing damage to the environment as it has been mentioned earlier. Renewable energy sources were identified to comprehend which energy source can be a better option for the current and future need of mankind economically, environmentally,

and socially. Among all the renewable energy sources mentioned earlier in this chapter, the solar energy seems to be one of the best choices for terrestrial renewable energy applications.

The last section of this chapter presents the aims and objectives of this research programme.

1.6 References

- [1] R. Dell, *J. Power Sources*, **100** (2001) 2–17.
- [2] <https://www.bp.com/content/dam/bp/pdf/energy-economics/statistical-review-2015/bp-statistical-review-of-world-energy-2015-full-report.pdf>, Last accessed January (2016).
- [3] <http://euanmearns.com/global-energy-trends-bp-statistical-review-2015/>, Last accessed January (2016).
- [4] I. Sabir, *Energy Updat.*, **5** (2013) 3–5.
- [5] R.A. Coyle, E.D. Simmons, *Understanding the Global Energy Crisis*, Purdue University Press, West Lafayette, Indiana, 2014.
- [6] M.S. Sthel, J.G.R. Tostes, J.R. Tavares, *Nat. Sci.*, **05** (2013) 244–252.
- [7] <https://education.nationalgeographic.org/assets/file/energy-teacher-guide-ch6.pdf>, Last accessed January (2016).
- [8] M. Dale, *Energy Policy*, **43** (2012) 102–122.
- [9] <http://www.eolss.net/sample-chapters/c12/E1-01-02-11.pdf>, Last accessed January (2016).
- [10] <https://blog.udemy.com/disadvantages-of-fossil-fuels/>, Last accessed January (2016).
- [11] P. Shrivastava, *Organ. Stud.*, **15** (1994) 705–726.
- [12] <http://www.livestrong.com/article/157263-what-are-the-effects-of-non-renewable-resources-on-living-organisms/>, Last accessed January (2016).
- [13] N.L. Panwar, S.C. Kaushik, S. Kothari, *Renew. Sustain. Energy Rev.*, **15** (2011) 1513–1524.
- [14] G.N. Tiwari, R.K. Mishra, *Advanced Renewable Energy Sources*, Cambridge : Royal Society of Chemistry, (2012).
- [15] M. Singh, S. Santoso, *Dynamic Models for Wind Turbines and Wind Power Plants*, National Renewable Energy Laboratory, Austin, Texas, (2011).
- [16] W.E. Glassley, *Geothermal Energy: Renewable Energy and the Environment*, 2nd Ed., CRC Press, (2014).
- [17] <http://www.geo-energy.org/reports/Environmental%20Guide.pdf>, Last accessed January (2016).
- [18] M. Yari, *Renew. Energy*, **35** (2010) 112–121.
- [19] <http://geo-energy.org/reports/Geothermal%20Technology%20->

- [%20Part%20II%20\(Surface\).pdf](#), Last accessed January (2016).
- [20] <http://www.tutorvista.com/content/science/science-ii/sources-energy/geothermal-energy.php>, Last accessed January (2016).
- [21] G.P. Sims, *Energy Policy*, **19** (1991) 776–786.
- [22] <https://www.worldenergy.org/wp-content/uploads/2015/05/World-Energy-Resources-Charting-the-Upsurge-in-Hydropower-Development-2015-Infographic1.pdf>, Last accessed January (2016).
- [23] http://www.uprm.edu/aret/docs/Ch_8_Micro_hydro.pdf, Last accessed January (2016).
- [24] P. McKendry, *Bioresour. Technol.*, **83** (2002) 37–46.
- [25] <http://www.iitmicrogrid.net/microgrid/pdf/papers/renewables/BiomassEnergy.pdf>, Last accessed January (2016).
- [26] S.P. Neill, M.R. Hashemi, M.J. Lewis, *Renew. Energy*, **85** (2016) 580–587.
- [27] F. O Rourke, F. Boyle, A. Reynolds, *Appl. Energy*, **87** (2010) 398–409.
- [28] <http://www.greenfacts.org/en/tidal-energy/l-2/1.htm>, Last accessed January (2016).
- [29] M. Kaltschmitt, W. Streicher, A. Wiese, *Renewable Energy*, Springer Berlin Heidelberg, Berlin, Heidelberg, (2007).
- [30] <http://www.renewablesinternational.net/germanys-new-solar-record-25-or-27-gw/150/452/86973/>, Last accessed January (2016).
- [31] http://www.enviropaedia.com/topic/default.php?topic_id=316, (2016).
- [32] D. Chiras, *Solar Electricity Basics: A Green Energy Guide*, New Society Publishers, Gabriola Island, Canada, (2010).
- [33] <http://www.superstrate.net/pv/illumination/am.gif>, Last accessed January (2016).
- [34] <http://77facts.com/the-average-temperature-on-the-surface-of-the-sun-is-5778-kelvin/>, Last accessed January (2016).
- [35] Z. Yang, S. V. Garimella, *Sol. Energy*, **84** (2010) 974–985.
- [36] A. Mawire, A. Phori, S. Taole, *Appl. Therm. Eng.*, **73** (2014) 1323–1331.
- [37] <http://www.nrel.gov/docs/legosti/old/1846.pdf>, Last accessed January (2016).
- [38] I.M. Dharmadasa, *Advances in Thin-Films Solar Cells*, Pan Stanford Publishing Pte. Ltd, Boulevard, Singapore, (2012).
- [39] G.W. Crabtree, N.S. Lewis, *Phys. Today*, **60** (2007) 37–42.
- [40] B.M. Basol, S.S. Ou, O.M. Stafsuud, *J. Appl. Phys.*, **58** (1985) 3809–3813.
- [41] N.B. Chaure, A.P. Samantilleke, R.P. Burton, J. Young, I.M. Dharmadasa, *Thin*

- Solid Films*, **472** (2005) 212–216.
- [42] I.M. Dharmadasa, *Curr. Appl. Phys.*, **9** (2009) e2–e6.
 - [43] M.A. Green, K. Emery, Y. Hishikawa, W. Warta, E.D. Dunlop, *Prog. Photovoltaics Res. Appl.*, **24** (2016) 3–11.
 - [44] I.M. Dharmadasa, *Sol. Energy Mater. Sol. Cells*, **85** (2005) 293–300.
 - [45] I.M. Dharmadasa, J.S. Roberts, G. Hill, *Sol. Energy Mater. Sol. Cells*, **88** (2005) 413–422.
 - [46] I. Dharmadasa, A. Ojo, H. Salim, R. Dharmadasa, *Energies*, **8** (2015) 5440–5458.
 - [47] J. Britt, C. Ferekides, *Appl. Phys. Lett.*, **62** (1993) 2851–2852.
 - [48] X. Wu, R. Ribelin, R.G. Dhere, D.S. Albin, T.A. Gessert, S. Asher, D.H. Levi, A. Mason, H.R. Moutinho, P. Sheldon, in: Conf. Rec. Twenty-Eighth IEEE Photovolt. Spec. Conf. - 2000 (Cat. No.00CH37036), IEEE, 2000, pp. 470–474.
 - [49] <http://investor.firstsolar.com/releasedetail.cfm?ReleaseID=895118>, Last accessed January (2016).
 - [50] I.M. Dharmadasa, A.P. Samantilleke, N.B. Chaure, J. Young, *Semicond. Sci. Technol.*, **17** (2002) 1238–1248.
 - [51] J. Woodcock, A. Turner, M. Ozsan, J. Summers, in: Photovolt. Spec. Conf. 1991., Conf. Rec. Twenty Second IEEE, New York, 1991, pp. 842–847.
 - [52] D.G. Diso, Research and Development of CdTe Based Thin Film PV Solar Cells, (PhD Thesis) Sheffield Hallam University, (2011).
 - [53] D.G. Diso, G.E.A. Muftah, V. Patel, I.M. Dharmadasa, *J. Electrochem. Soc.*, **157** (2010) H647.
 - [54] O.K. Echendu, F. Fauzi, A.R. Weerasinghe, I.M. Dharmadasa, *Thin Solid Films*, **556** (2014) 529–534.
 - [55] O.K. Echendu, Thin Film Solar Cells Using All-Electrodeposited ZnS, CdS and CdTe Materials, (PhD Thesis) Sheffield Hallam University, (2014).
 - [56] F. Fauzi, Research and Development of CdS/CdTe Solar Cells Incorporating ZnTe Layers, (PhD Thesis) Sheffield Hallam University, 2015.
 - [57] N.A. Abdul-Manaf, A.R. Weerasinghe, O.K. Echendu, I.M. Dharmadasa, *J. Mater. Sci. Mater. Electron.*, **26** (2015) 2418–2429.
 - [58] N.A. Abdul-Manaf, Organic/Inorganic Hybrid Solar Cells Based on Electroplated CdTe, (PhD Thesis) Sheffield Hallam University, 2015.
 - [59] H.I. Salim, V. Patel, A. Abbas, J.M. Walls, I.M. Dharmadasa, *J. Mater. Sci. Mater. Electron.*, **26** (2015) 3119–3128.

- [60] H.I. Salim, O.I. Olusola, A.A. Ojo, K.A. Urasov, M.B. Dergacheva, I.M. Dharmadasa, *J. Mater. Sci. Mater. Electron.*, (2016).
- [61] T. Nishio, M. Takahashi, S. Wada, T. Miyauchi, K. Akita, H. Goto, S. Sato, O. Sakurada, *Electr. Eng. Japan (English Transl. Denki Gakkai Ronbunshi)*, **164** (2008) 12–18.
- [62] P. V. Braun, P. Osenar, M. Twardowski, G.N. Tew, S.I. Stupp, *Adv. Funct. Mater.*, **15** (2005) 1745–1750.
- [63] K. Yamaguchi, P. Mukherjee, T. Yoshida, H. Minoura, *Chem. Lett.*, (2001) 864–865.

2.1 Introduction

The time line of the photovoltaic solar energy conversion goes back to 1839 when 19 years old Edmund Becquerel, a French scientist, discovered the photovoltaic effect while experimenting with a solid electrode submerged in an electrolyte solution [1]. Afterwards, Adams and Day in 1876 observed that the electric current could be generated in the solid layer of selenium solely when it is exposed to light [2]. Soon after, in 1883, Charles Fritts coated the selenium layer with an extremely thin layer of gold, so that it was transparent to light, and produced a solar cell with conversion efficiency between 1 and 2% [3]. In 1887, German physicist James Moser discovered the effect of a dye-sensitised photoelectrochemical (PEC) cell by adding dye to a solar cell [4]. Later, in 1904 another German physicist, Wilhelm Hallwach made a semiconductor-junction solar cell by combination of copper and copper oxide [5]. In 1905, Albert Einstein explained the photoelectric effect which he was later awarded with the Nobel Prize. In 1918, Jan Czochralski a Polish scientist invented a method called after his name “Czochralski method” for growth of single crystal silicon [6]. In 1954, the Bell laboratory announced the first practical silicon solar cells with conversion efficiency of ~4.5% for space application [7]. Later, Hofmann Electronics achieved 14% efficiency using silicon solar cells. In 1970, the first high efficiency GaAs heterojunction solar cell was produced by Zhores Alferov and his team in USSR. The world oil crisis in 1973 triggered the widespread public awareness for early research on solar photovoltaic energy conversion. In 1991, Brian O'Regan and Michael Grätzel developed the dye-sensitised solar cell with power conversion efficiency of more than 10% [8]. In 1994, the National Renewable Energy Laboratory (NREL) for the first time developed GaInP/GaAs solar cell exceeding 30% power conversion efficiency. Later, organic solar cells have attracted great interests due to its low-cost solution process capability. Today, hybrid solar cells combine advantages of both organic and inorganic materials to utilise the low-cost cell production.

2.2 Inorganic solar cells

Inorganic materials are the most established semiconductors and dominate the photovoltaic market from the beginning. So far, the highest efficiency solar cells have been fabricated using inorganic materials [9]. The inorganic semiconductor materials used to produce photovoltaic solar cells comprises mono crystalline silicon, poly crystalline silicon, amorphous silicon, the group III-V compounds and chalcogenide semiconductors.

2.2.1 Silicon based solar cells

The first silicon solar cell was reported by American engineer Russell Ohl in 1941 and had the energy conversion efficiency of less than 1% [10]. Thirteen years later, the efficiency of silicon solar cells had reached 6%, as reported by Chapin *et al* at Bell Laboratory [11]. However, due to high costs of such cells (\$300 per W) commercial applications were limited to novelty items. A major breakthrough in silicon photovoltaic cells was reported in 1983 when University of New South Wales (UNSW) demonstrated 18% efficiency for metal-insulator n/p (MINP) solar cells [12]. In 1990, M.A. Green [13] reported the efficiency of above 23% by the passivated emitter rear locally (PERL) diffused silicon solar cells. In 1998, the energy conversion efficiency for mono crystalline silicon solar cells was increased to 24.4% and this value was later revised to 25% for a 4 cm² solar cell area as reported by M.A. Green [14]. So far, the highest efficiency reported for monocrystalline silicon is 25.6% for cell area of 143 cm². This efficiency record was announced by Panasonic HIT[®] Solar Cell in 2014 and the structure of this solar cell is shown in Figure 2.1 [15]. The world record efficiency for polycrystalline and amorphous silicon solar cells so far are 20.8% and 10.2% with the cell areas of 243.9 cm² and 1.0 cm² respectively [16].

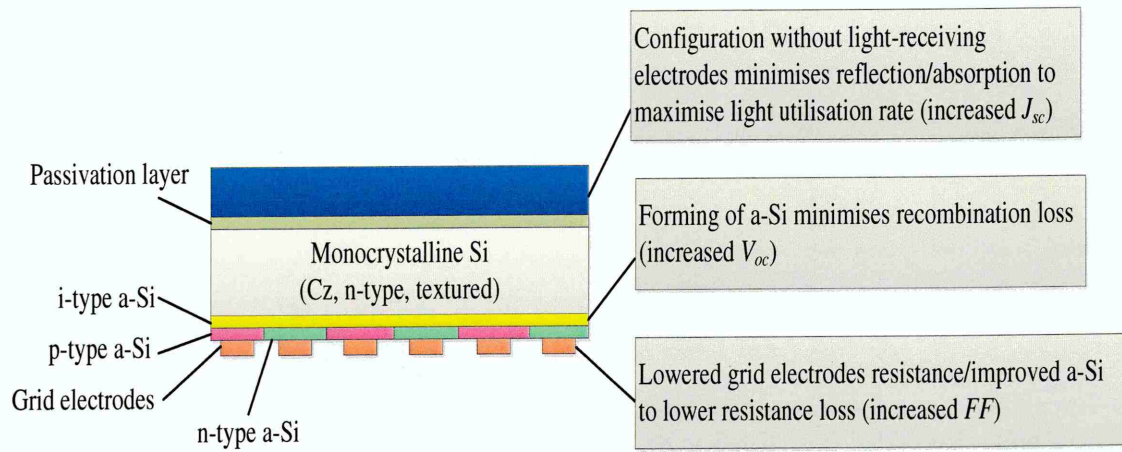


Figure 2.1: Typical structure of 25.6% efficiency for monocrystalline silicon based solar cells. Redrawn from [15].

2.2.1.1 Monocrystalline silicon solar cells

More than 90% of the earth's crust contains Silica (SiO_2) which makes silicon, the second most abundant element on earth [17]. The process of transforming raw silicon into usable monocrystalline and polycrystalline silicon is shown in Figure 2.2.

The process starts with the reduction of SiO_2 with Carbon at high temperature of 1500 to 2000°C using electric furnace as shown in Equation (2.1) [18].



The result is the brown Metallurgical Grade Silicon (MG-Si) with 97% purity. In order to bring the impurity below the parts-per-billion level, MG-Si is reacted with HCl to form the trichlorosilane (TCS) in a fluidized-bed reactor at 300°C according to the following chemical reaction [18]:



During transforming of MG-Si into TCS, Fe, Al and B impurities are removed. Afterwards, TCS is heated in the hydrogen environment at 1100°C for duration between 200 to 300 hours to obtain high purity (9N) silicon. The chemical reaction of TCS with hydrogen is shown in Equation (2.3) [18]:

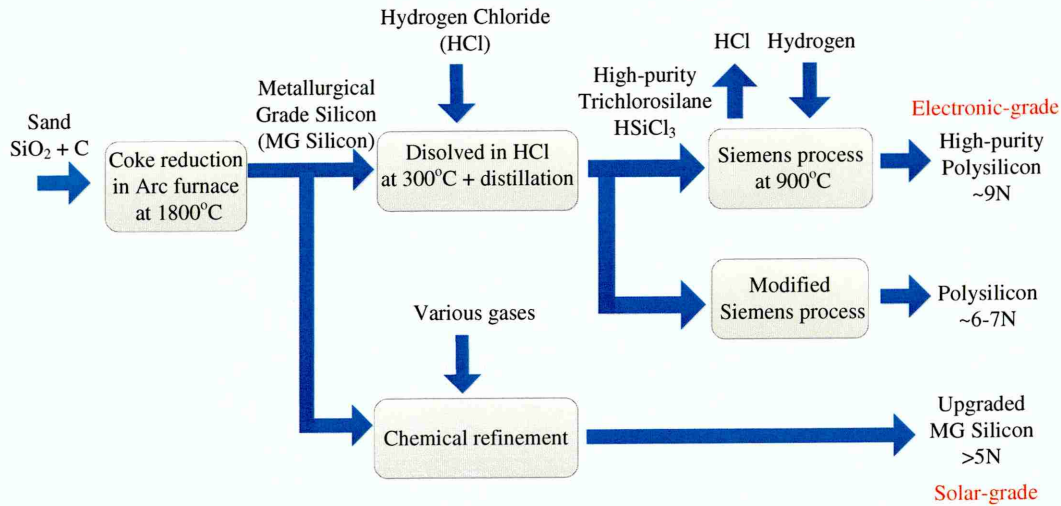


Figure 2.2: The process of making polycrystalline silicon starting from raw materials. Redrawn from [19].

In the process of growing single crystal silicon, the Czochralski method is used as shown in Figure 2.3. In Czochralski process high purity silicon is encouraged to be used as molten to form single crystal silicon. Then the substance will be heated to its melting point (~1400°C) inside a crucible made out of quartz. Afterward, small piece of single crystal silicon known as “seed crystal” is dipped into the saturated molten silicon solution. Seed crystal is the tool used to grow a large crystal of the material. The large crystal will grow when the seed crystal is dipped into the molten silicon and slowly pulled out with rotational motion. During this time the rod and the crucible rotate in opposite direction to minimise the effect of convection in the melt. In the manufacturing of silicon single crystal, the temperature gradient, pulling rate and rotation speed influences the size of single crystal. As the seed crystal slowly pulled upward, the

molten silicon is solidified as same as the seed. The result is the large cylindrical single crystal silicon which is called ingot or boule. The ingot can be grown to (300-400) mm in diameter with a length of about 1 m [20]. Using diamond wire saw, the ingot is then sliced into cylindrical disc shape silicon wafers with the thickness of about 200 to 500 μm and a resistivity of about 1 Ωcm [21,22].

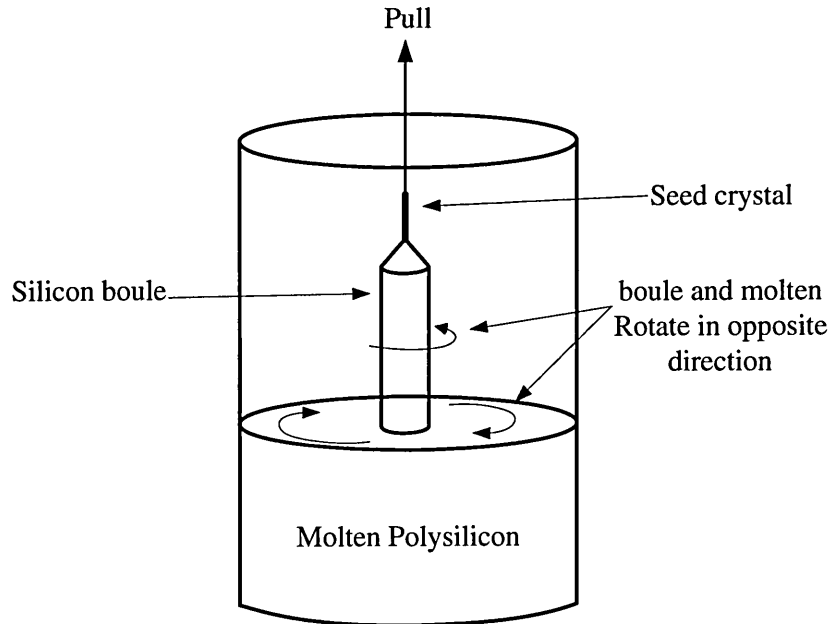


Figure 2.3: The Czochralski process. The seed crystal is dipped into molten polysilicon and then pulled upwards while rotating to produce silicon boule. Redrawn from [23].

It should be noted that silicon has indirect bandgap of 1.12 eV at room temperature with a low absorption coefficient (α) $< 50 \text{ cm}^{-1}$ [24,25]. For these reasons, in silicon solar applications the thickness of the silicon layers should be thick enough in order to effectively absorb the photons.

According to the reported data, the manufacturing cost of crystalline silicon modules has dropped from \$4 per W in 2007 to \$0.50 per W in 2014 [26].

2.2.1.2 Polycrystalline silicon solar cells

Polycrystalline silicon can be obtained by pouring the molten silicon into a cast and then slowly cooled down until it solidifies. Then, the rectangular block of the polycrystalline silicon were cut into small wafer with the area of 156 mm^2 [27].

Therefore, it is easier to arrange these rectangular shape wafers on a rectangular piece of glass. In terms of manufacturing cost polycrystalline solar cells are less expensive and less efficient than those of monocrystalline solar cells. The lower efficiency of the polycrystalline silicon solar cells is due to the presence of grain boundaries which can act as recombination or scattering centres for photogenerated charge carriers in the device [28]. Polycrystalline solar cells can be recognised by its light or dark blue colour. Also, visible grains of polycrystalline silicon create metal flake effect while monocrystalline silicon solar cells have dark black colour [29]. In terms of temperature tolerance, polycrystalline silicon solar panels are better than monocrystalline solar panels.

2.2.1.3 Amorphous silicon solar cells

Amorphous silicon (a-Si) or disordered silicon has been extensively used in solar cell applications. Generally, a-Si suffers from poorer quality due to the presence of large number of dangling bonds and defect states (10^{19} - 10^{20}) cm^{-3} in the material [30]. Also, in a-Si the density of defect states increase when it is exposed to light and it is known as Staebler-Wronski effect [31]. The dangling bond can be passivated by adding hydrogen into the a-Si. This process is called hydrogenation and it effectively reduces the density of states in the bandgap of a-Si. The hydrogenated amorphous silicon (a-Si:H) have some advantages over the crystalline silicon (c-Si). The technology of processing a-Si:H is relatively simple and inexpensive. The a-Si:H has a direct energy bandgap in the range 1.7-1.9 eV and absorption coefficient of 10^4 cm^{-1} near its bandgap [32,33]. For this reason, for a given thickness, a-Si:H absorb much more photons than c-Si. In addition, much less materials are required for a-Si:H and also this material can be deposited on a wide range of substrates including flexible, curved and roll-away type substrates. Other advantages of a-Si:H is that it can be easily grown and doped by some conventional semiconductor growth techniques such as sputtering, glow discharge plasma process [34], reactive evaporation [35] and plasma enhanced chemical vapour deposition (PECVD) [36] etc. The high efficiency monocrystalline silicon solar cell has been achieved by incorporation of a-Si in the device as previously shown in Figure 2.1.

2.2.2 III-V compound semiconductor solar cells

III-V semiconductor solar cells consist of the layers with elements from group III and V of the periodic table. The main III-V semiconductor compounds include InP, GaAs, InSb, InAs, GaP and GaSb. These materials play an important role in the development of optoelectronic devices and high efficiency solar cells [37]. The energy bandgap of the InP and GaAs are 1.35 eV and 1.42 eV respectively [38,39]. The direct bandgap and high absorption coefficient of the InP and GaAs compounds make them suitable for solar cell applications. So far, the highest efficiency reported for GaAs and InP thin film solar cells under AM1.5 at ~ 300 K are 28.8% and 22.1% for the cell areas of 0.99 cm^2 and 4.0 cm^2 respectively [40]. Also, the highest module efficiency achieved for GaAs is 24.1% for a module area of 858.5 cm^2 [40]. Also, GaAs and InP have high electron mobility values within their crystals which make these materials suitable in high efficiency solar cells application. The reported electron mobility values for GaAs and InP are $\sim 7000\text{ cm}^2\text{V}^{-1}\text{s}^{-1}$ and $\sim 5400\text{ cm}^2\text{V}^{-1}\text{s}^{-1}$ respectively [41,42].

Other III-V semiconductor compounds such as GaP can be used as window material in multijunction solar cells due to their wide direct bandgap in the range $\sim (2.87\text{--}2.96)$ eV [43]. Also, GaP can have indirect energy bandgap in the range $(2.26\text{--}2.66)$ eV [43] which makes this material suitable in the manufacture of low-cost red, yellow and green light-emitting diodes (LEDs) [44].

Also ternary and quaternary semiconductor compounds can be formed by combination of three or four elements of the III-V semiconductors. The ternary compounds (InGaP, InGaAs, AlGaAs and InAlP) and quaternary compounds (GaInAsP and GaInNP) have been used in multijunction solar cells. The efficiency value reported in 2013 for InGaP based solar cells is about $\sim 21\%$ [40]. Also, the efficiency of 37.9% has been reported for InGaP/GaAs/InGaAs multijunction solar cells with the cell area of $\sim 1.05\text{ cm}^2$ under AM1.5 and ~ 300 K [40]. Under concentrated sunlight, the efficiencies of 46.0% and 29.1% have been reported for the GaInP/GaAs multijunction cells and GaAs single cells with same cell area of 0.05 cm^2 respectively [40]. These efficiency values have been reported between the years 2013 and 2014.

There are various growth techniques which have been used to grow group III-V semiconductor compounds. These growth techniques include molecular beam epitaxy (MBE) [45], magnetron sputtering [46], metalorganic chemical vapour deposition (MOCVD) [47] and etc.

2.2.3 Chalcogenide semiconductor based solar cells

Chalcogenides are compounds that consist of the chemical elements in group VI (chalcogen) of the periodic table. This group is known as oxygen family and consists of the elements, oxygen (O), sulphur (S), selenium (Se), and tellurium (Te). The Chalcogenide semiconductors can be formed by combination of at least one metallic element and one chalcogen. The chalcogenide semiconductors can be divided into different categories such as I-VI (e.g. CuO and Cu₂S), II-VI (e.g. CdS, CdTe, ZnTe and ZnS), III-VI (e.g. InSe and In₂S₃), IV-VI (e.g. SnS), I-III-VI (e.g. CuInSe₂ (CIS), CuInGaSe₂ (CIGS) and I-II-IV-VI (Cu₂ZnSnS₄ (CZTS)). In these categories of semiconductors, CdS and ZnS are mainly used as buffer/window materials while CdTe, Cu₂S, CIS, CIGS and CZTS have been used as absorber materials.

There are currently many research groups in the field of solar cells which are working on CdTe, CIGS and CZTS based thin film semiconductors. The main aims of these research groups are to make the solar cells cheaper or more efficient in order to be a viable alternative energy resource. CdTe has a direct energy bandgap of 1.45 eV at room temperature [48]. The energy bandgap of the CIGS can be tuned from 1.00 to 1.70 eV depending on the amount of Ga in the CIGS layer [49]. Recently, First Solar announced the new world record efficiency of 21.5% for CdTe based thin film solar cells with the cell area of 0.34 cm² [40,50]. So far, the world record efficiency for CIGS based thin film solar cell is 21.7% for a 0.49 cm² solar cell area as reported by Stuttgart's Centre for Solar Energy and Hydrogen Research on 2014 [40,51]. The highest module efficiency reported for CdTe and CIGS thin films are 17.5% and 15.7% respectively [40]. Also, there are lots of interests on CZTS solar cells because it is composed of abundant and inexpensive copper, zinc, tin and sulphur materials. The best efficiency for CZTS solar cells is 12.6% for a 0.42 cm² cell area which has been announced by Solar Frontier, a Japan-based thin-film solar technology company on 2013 [40].

There are many methods to grow chalcogenide semiconductor materials. For example the low cost growth techniques used to grow CdTe and CdS thin films includes electrodeposition (ED) [52,53] and chemical bath deposition (CBD) [54]. Some of other methods used to grow these materials are sputtering [55], vacuum evaporation [56], closed space sublimation (CSS) [57] etc.

2.3 Organic solar cells

Organic solar cells (OSCs) are promising devices in the solar photovoltaic energy conversion and have shown potential to harness solar energy in a cost-effective way. OSCs are fabricated from organic compounds usually polymers and also known as polymer solar cells. The history of the organic solar cells dates back to 1958 when Kearns and Calvin reported a photovoltage of 200 mV for magnesium phthalocyanine (MgPh) disks coated with a thin film of air-oxidized tetramethyl p-phenylenediamine (TM ϕ D) [58]. In 1974, Ghosh *et al* observed a maximum power conversion efficiency of 0.01% using Al/MgPh/Au cell structure [59]. In 1986, a power conversion efficiency of 1.0% has been achieved by Tang using copper phthalocyanine and a perylene tetracarboxylic derivative and under simulated illumination of AM2 [60]. Since then, significant improvement in OSCs has been achieved by development of the bulk heterojunctions (BHJ), better junction engineering and better materials purity and control. In 2005, Yang *et al* [61] achieved power conversion efficiency of 4.4% for a OSCs based on a bulk heterojunction of polymer poly (3-hexylthiophene) (P3HT) and methanofullerene. Afterward, P3HT system became a standard in OSCs and acting as a basis for most attempts to commercialise OSCs. There are lots of reports on OSCs showing promising results in power conversion efficiency [62,63]. In 2013, Hosoya *et al* has reported an efficiency of 11.0% for OSCs with a cell area of 0.99 cm² [64].

It is worth mentioning that the mechanism of OSCs and inorganic solar cells are different. In inorganic solar cells, electron-hole pairs are generated in the bulk of the absorber material. These electron-hole pairs are not strongly bound together and will be separated due to the existence of built-in electric field within the device. In OSCs, the coulomb attraction force between the electron and hole is stronger than inorganic materials due to their lower relative permittivity. For this reason, the absorbed photon in OSCs does not directly create an electron-hole pair but it creates an exciton. The binding energy of the exciton (200-400 meV) is much larger than the thermal energy kT at room temperature (~ 25 meV) [65,66]. In order to overcome the binding energy of this exciton, the heterojunction structure has been used as shown in Figure 2.4. In this structure, the HOMO (highest occupied molecular orbital) and LUMO (lowest unoccupied molecular orbital) have discontinuity at their energy band diagram. The terms HOMO and LUMO are respectively equivalent to the valence band (VB) and conduction band (CB) in the inorganic solar cells. Due to the comparatively higher

energy levels of left molecule (donor) are always higher than that of the right molecule (acceptor), therefore, it is energetically favourable for the electron to hop from donor molecule (left) to the acceptor molecule (right) as shown in Figure 2.4. It is important to note that due to the band discontinuity at the interface it is very unlikely that electron overcomes the potential barrier to return to the donor molecule (left). Also, the holes will stay on the left side (donor) due to the presence of potential barrier at the donor-acceptor interface. However, if the interface is very defective, then there will be a chance for a fraction of electrons to be trapped in these defects. In order to overcome this problem, two different metal contacts with two different work functions are used in the device (e.g Al and ITO). It is also important to note that the diffusion length of the exciton is typically ~ 10 nm whereas the thickness of the absorber material needs to be at least 100 nm to effectively absorb the light [67]. This means that a very thin or very thick layer of donor and acceptor molecule on top of each other would not be sufficient in effective absorption of light.

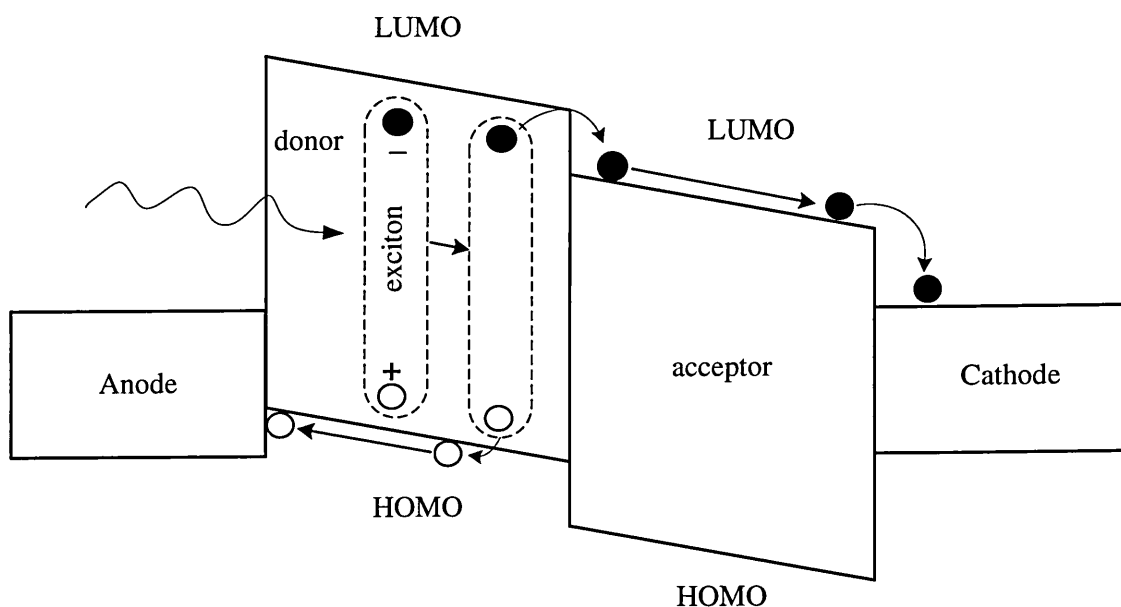


Figure 2.4: The energy band diagram of organic semiconductors. Redrawn from [68].

This is because, when two layers are thin, the solar cell will be transparent and when the layer is thick, then the solar cell will absorb only a fraction of light within an exciton diffusion length of the interface. Therefore, only a few electrons and holes will be generated. In both cases, the photocurrent will be very small. The solution for that is the

bulk heterojunction (BHJ) structure as shown in Figure 2.5. In this structure, the two molecules are mixed such that the distance between each point in the volume to the next interface is within about 10 nm. In order to transport the electron and hole to their respective contact, hole transport layer (HTL) and electron transport layer (ETL) need to be used (see Figure 2.5). In the standard BHJ structure, the ITO is coated with a hole transport layer (HTL) while the electron transport layer (ETL) is coated on top of the photoactive layer (a blend of donor and acceptor materials). Usually, thin films of doped conjugated polymer like PEDOT:PSS [poly(3,4-ethylenedioxythiophene) poly(styrenesulfonate)] or a thin oxide layer (e.g. MoO_3) have been used as HTLs whereas oxide layers such as ZnO or titanium oxide (TiO_2) have been used as the ETLs [69-71].

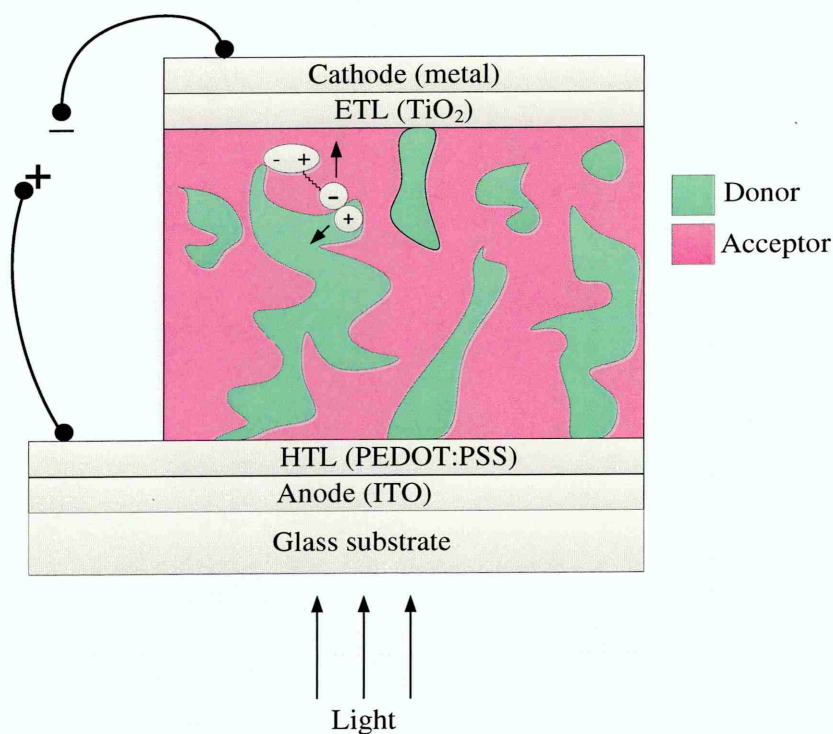


Figure 2.5: Architecture of bulk heterojunction (BHJ) organic solar cells. Redrawn from [70].

Some advantages of organic solar cells include; (i) low-cost (ii) ability to utilise large area solar panel, (iii) contains flexible solar module, and (iv) can be fabricated using roll-to-roll production. The major disadvantages of organic solar cells are their operational life-time is not as long and their power conversion efficiency are still lower

than inorganic and Si-based solar cells. In photovoltaic application, most of the organic thin films have been deposited by low-cost and non-vacuum growth technique such as spin coating [72], sol-gel [73] and screen printing [74]. Also, organic thin films have been grown using vacuum systems including organic vapour phase deposition (OVPD) [75], thermal evaporation [76] etc.

2.4 Dye-sensitised solar cells

Dye-sensitised solar cell (DSSC) is a class of low-cost solar cells which have been co-invented by Michael Grätzel and Brian O'Regan in 1988 [77]. This name is given, because it mimics the photosynthesis process by absorbing natural light using a light-sensitive dye. In 1991, Grätzel and co-workers achieved a conversion efficiency of ~7% using DSSC [78]. In 2012, the efficiency of DSSC was increased to 11.9% for a cell with active area of 1 cm² [40]. Two years later, Grätzel *et al* increased the efficiency to 13% by molecular engineering of the DSSC [79].

The DSSC consists of a wide bandgap mesoporous n-type semiconductor (TiO₂) which serves as electron transport medium, a dye which is the main light absorbing material, a Redox electrolyte couple (I/I₃⁻) for the regeneration of the dye and two electrodes (anode and cathode) [80]. The mechanism of the DSSC is based on the photoelectrochemical (PEC) process. Figure 2.6 represents the energy band diagram and step by step operating principle of DSSC.

Step 1: The dye molecule is initially in its ground state (S), when photons strike the cell; the dye molecule gets excited from its ground state (S) into excited state (S*). The excited dye molecule has now enough energy to overcome the energy bandgap of the semiconductor.

Step 2: The excited dye molecule (S*) is oxidised and an electron is injected into the conduction band of the semiconductor and leaves the dye in an oxidised state S⁺. The injected electron moves freely towards the anode (TCO) due to the slope produced in the energy band diagram of the semiconductor and transported to the external load.

Step 3: The iodide (I⁻) in the electrolyte donates an electron to the oxidised dye molecule (S⁺) and return it to its original state, S. At the same time, when iodide (I⁻) donates its electron, the tri-iodide (I₃⁻) is generated.

Step 4: When electron moves from anode to cathode through external load, the tri-iodide (I₃⁻) gain an electron (reduces) at the cathode and iodide (I⁻) is regenerated

again. Therefore, the electric current is generated continuously as long as photons hit the dye molecules.

The open-circuit voltage (V_{oc}) of the DSSC corresponds to the differences between the redox potential of the electrolyte and the Fermi level of the semiconductor as shown in figure 2.6.

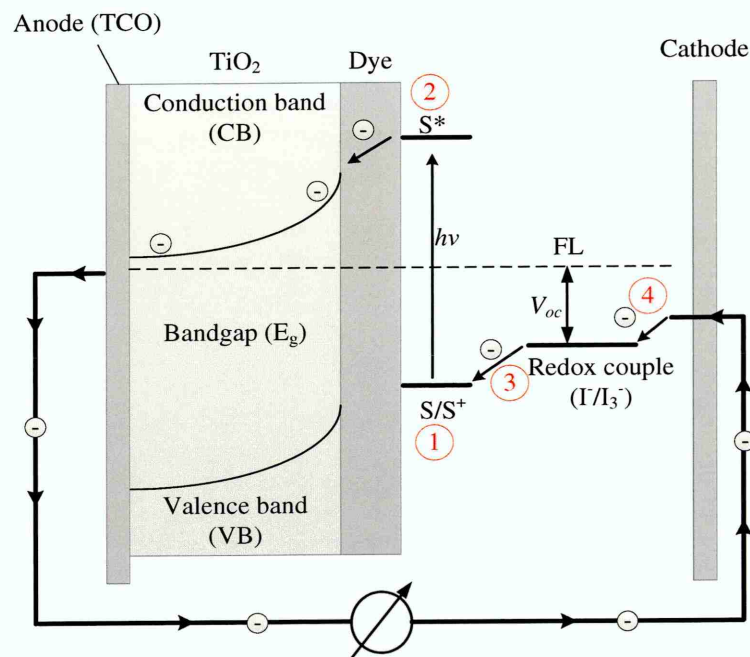


Figure 2.6: Principle of operation and energy band diagram of dye-sensitised solar cells. Redrawn from [78].

In DSSC, the wide bandgap semiconductor oxide layers are usually used as photoanode. Some examples of these oxide layers are TiO₂ [80], ZnO and Nb₂O₅ [81]. This oxide layers can be deposited using different methods such as mechanical compression [82], spin-coating [83], sol-gel [84], screen printing [74] and etc. Also, platinum and carbon electrodes have been used as counter electrodes (cathode) in DSSC. The most common dye materials that have been investigated and used in the DSSC include ruthenium (II)-polypyridine complexes and Triphenylamine-based dyes [85]. The main advantages of DSSC are; (i) the DSSC are cost-effective, (ii) thin film deposition is carried out in a normal atmospheric condition and DSSC is manufactured using low-energy consumption, (iii) it is a fast deposition process and can be easily scaled up. The major disadvantage of DSSC is that the liquid electrolyte used in DSSC

is temperature sensitive, i.e. at low temperature the electrolyte can freeze and at high temperature the electrolyte can expand which makes the sealing of the solar panel a major problem and can seriously reduce the performance of the solar cells.

2.5 Hybrid solar cells

Hybrid solar cells focus on innovative concepts towards more efficient solar cells using both organic and inorganic materials. The aim of using hybrid solar cell is to combine the unique properties of low-cost organic materials with highly efficient, well-characterized inorganic materials [86]. Currently, the hybrid solar cells have attracted great attention from the PV community. Although, hybrid photovoltaic has the potential to achieve high power conversion efficiency, yet the observed efficiencies are lower than inorganic solar cells.

The main materials which are currently used in the fabrication of hybrid solar cells are Si, cadmium compounds, metal oxide nanoparticules and low bandgap nano particles and carbon nanotubes (CNTs) [87]. Also, the DSSC which is presented in the previous section are typically hybrid solar cells. Another class of hybrid solar cells is similar to DSSC because it uses the nanoporous metal-oxide inorganic matrixes (e.g. TiO_2 and ZnO). However, instead of dye or electrolyte, conjugated polymer such as polythiophene derivative has been incorporated in the device architecture [88]. Also, hybrid solar cells based on heterojunction of CNTs and n-type Si has been reported with power conversion efficiency of more than 7% [89,90]. The efficiency of 11.3% has also been reported for c-Si/PEDOT:PSS (poly(3,4-ethylenedioxythiophene) polystyrene sulfonate) devices in 2012 [91]. Zielke *et al* in 2014 has achieved the efficiency of 17.4% for c-Si/PEDOT:PSS hybrid solar cells using backPEDOT cell structure [92]. Also, there are many reports on the inorganic/polymer hybrid solar cells fabricated using semiconductors such as CdSe nano rod [93], CdSe quantum dot [94], and ZnO nano wires [95]. However, the power conversion efficiencies of these hybrid solar cells are still low. The perovskite solar cells, a new generation of DSSC solar cells, are also hybrid solar cells which have raised high hope for a future of high efficiency solar cells [96]. More details about the perovskite solar cells are presented in chapter 10.

2.6 Conclusions

Different classes of photovoltaic solar cells including inorganic, organic, dye-sensitised and hybrid solar cells were presented in this chapter. The importance and efficiencies of each class of solar cells were discussed. So far, the winner in the worldwide PV markets is inorganic solar cells. In the inorganic group, the GaAs-based solar cells lead the efficiency record while Si-based solar cells are in the second place. The multijunction cells and single cells GaAs-based solar cells have reached the efficiency of 46.0% and 29.1% respectively under concentrated sunlight with the module efficiency of 24.1% for GaAs thin films. Si solar cells as second winner of this group, has the efficiency of 25.6% for monocrystalline module and 20.8% efficiency for polycrystalline laboratory-scale cells. The CdTe and CIGS thin films also in the inorganic solar cells group have reached the lab-cell efficiencies of 21.5% and 21.7% respectively. The best module efficiency obtained for CdTe and CIGS thin films are 17.5% and 15.7% respectively. Also, the cost-effective organic and hybrid solar cells follow the inorganic solar cells with the promising results in the near future.

2.7 References

- [1] http://solarcellcentral.com/history_page.html, Last accessed January (2016).
- [2] <http://www.gosolarcalifornia.ca.gov/about/gosolar/california.php>, Last accessed January (2016).
- [3] <https://www.pvlighthouse.com.au/resources/courses/altermatt/The%20PV%20Principle/The%20first%20solar%20cells.aspx>, Last accessed January (2016).
- [4] <http://usaalternativeenergynow.blogspot.co.uk/2011/10/timeline-of-solar-cells.html>, Last accessed January (2016).
- [5] L.M. Fraas, *Low-Cost Solar Electric Power*, Springer, New York, (2014) pp.2.
- [6] J.N. Lalena, D.A. Cleary, E. Carpenter, N.F. Dean, *Inorganic Materials Synthesis and Fabrication*, A John Wiley & Sons, INC., Publication, New Jersey, (2008).
- [7] I.M. Dharmadasa, *Advances in Thin-Films Solar Cells*, Pan Stanford Publishing Pte. Ltd, Boulevard, Singapore, (2012) pp.26.
- [8] Brian O'regan & Michael Grätzel, *Nature*, **353** (1991) 737-740.
- [9] R.W. Miles, G. Zoppi and I. Forbes, *Materialstoday*, **10**(11) (2007) 20-27.
- [10] J. Pandey, R. Khare, S. Khare and D. Singh, *International Journal of Advanced Research in Engineering and Applied Sciences*, **4**(11) (2015) 93-103.
- [11] D.M. Chapin, C.S. Fuller and G.L. Pearson, *J. Appl. Phys.*, **25** (1954) 676-677.
- [12] A. McEvoy, T. Markvart, L. Castaner, T. Markvart and L. Castaner, *Practical Handbook of Photovoltaics: Fundamentals and Applications* (2nd Edition), Elsevier, (2003) pp. 106.
- [13] M.A. Green, *Semicond. Sci. Technol.*, **8** (1993) 1-12.
- [14] M.A. Green, *Progress in Photovoltaics: Research and Applications*, **17** (2009) 183-189.
- [15] <http://news.panasonic.com/press/news/official.data/data.dir/2014/04/en140410-4/en140410-4.html>, Last accessed January (2016).
- [16] M.A. Green, *Prog. Photovolt: Res. Appl.*, **23** (2015): 805-812.
- [17] http://www.cleanroom.byu.edu/EW_formation.phtml, Last accessed January (2016).
- [18] <http://www.pveducation.org/pvcdrom/manufacturing/refining-silicon>, Last accessed January (2016).

- [19] http://www.greenrhinoenergy.com/solar/technologies/pv_manufacturing.php, Last accessed January (2015).
- [20] M.A. Green, *Energ policy*, **28** (2000) 989-998.
- [21] S. Ranjan, S. Balaji, R.A. Panella, B.E. Ydstie, *Computers and Chemical Engineering*, **35**(8) (2011)1439-1453.
- [22] <http://www.pveducation.org/pvcdrom/design/solar-cell-parameters>, Last accessed January (2016).
- [23] http://matschmi.de/intr_phys_semi_dev/crystal_growth/production_of_silicon.html, Last accessed January (2016).
- [24] S.M. Sze and K.K. Ng, *Physics of Semiconductor Devices*, 3rd edition, John Wiley & Sons, Inc., New Jersey, United States of America (2007).
- [25] H. A. Weakliem and D. Redfield, *J. Appl. Phys.*, **50**(3) (1979) 1491-1493.
- [26] <http://www.theweek.co.uk/63407/solar-power-will-be-as-cheap-as-coal-amid-new-advances>, Last accessed January (2016).
- [27] <http://www.tindosolar.com.au/poly-vs-mono-crystalline/>, Last accessed January (2016).
- [28] I. Sanyal, K.K. Chattopadhyay, S. Chaudhuri, and A. K. Pal, *J. Appl. Phys.*, **70** (2) (1991) 841-845.
- [29] <http://www.solarchoice.net.au/blog/monocrystalline-vs-polycrystalline-solar-panels-busting-myths/>, Last accessed January (2016).
- [30] D.E. Carlson, *Prog. Crystal Growth Charact.*, **4**(3) (1981) 173-193.
- [31] D.L. Staebler and C.R. Wronski, *Applied Physics Letters*, **31** (1977) 292-294.
- [32] O. Vetterl, F. Finger, R. Carius, P. Hapke, L. Houben, O. Kluth, A. Lambertz, A. Mueck, B. Rech and H. Wagner, *Solar Energy Materials & Solar Cells*, **62** (2000) 97-108.
- [33] A.V. Shah, H. Schade, M. Vanecek, J. Meier, E. Vallat-Sauvain, N. Wyrsch, U. Kroll, C. Droz and J. Bailat, *Prog. Photovolt: Res. Appl.*, **12** (2004) 113-142.
- [34] B.G. Budagyan, A.A. Sherchenkov, A.E. Berdnikov, and V.D. Chernomordik, *Russian Microelectronics*, **29**(6) (2000) 391-396.
- [35] J.C. Anderson and S. Biwas, *J. Non-Cryst. Solids*, **77&78** (1985) 817-820.
- [36] C. Koch, M. Ito and M. Schubert, *Sol. Ener. Mat. Sol. Cells*, **68** (2001) 227-236.
- [37] S. Mokkaapati and C. Jagadish, *Materialstoday*, **12**(4) (2009) 22-32.
- [38] R. Gurwitz, A. Tavor, L. Karpeles, I. Shalish, W. Yi, G. Seryogin and V. Narayanamurti, *Appl. Phys. Lett.*, **100** (2012) 191602-1.

- [39] R. Ahuja, S. Auluck, O. Eriksson, J.M. Wills and B. Johansson, *Solid State Communications.*, **104**(5) (1997) 249-252.
- [40] M.A. Green, K. Emery, Y. Hishikawa, W. Warta, E.D. Dunlop, *Prog. Photovolt: Res. Appl.*, **23** (2015) 805-812.
- [41] S.M. Sze and J.C. Irvin, *Solid-State Electronics*, **11** (1968) 599-602.
- [42] W. Walukiewicz, J. Lagowski, L. Jastrzebski, P. Rava, M. Lichtensteiger, C.H. Gatos, and H.C. Gatos, *J. of Appl. Phys.*, **51** (1980) 2659-2668.
- [43] P.J. Dean, *Journal of Luminescence*, **1,2** (1970) 398-419.
- [44] P.B. Hart, *Proceedings of the IEEE*, **61**(7) (1973) 880-884.
- [45] Y. Rajakarunanayake, B.H. Cole, J.O. McCaldin, D.H. Chow, J.R. Söderström, T.C. McGill and C.M. Jones, *Appl. Phys. Lett.*, **55**(12) (1989) 1217-1219.
- [46] G.de M. Azevedo, J.H. Dias da Silva, E. Avendaño, *Nuclear Instruments and Methods in Physics, Research B*, **238** (2005) 329-333.
- [47] J. Fang, P.H. Holloway, J.E. Yu, K.S. Jones, B. Pathangey, E. Brettschneider and T.J. Anderson, *Applied Surface Science*, **70/71** (1993) 701-706.
- [48] J.J. Loferski, *J. Appl. Phys.*, **27** (1956) 777.
- [49] M. Venkatachalam, M.D. Kannan, S. Jayakumar, R. Balasundaraprabhu, N. Muthukumarasamy, *Thin Solid Films*, **516** (2008) 6848-6852.
- [50] <http://renewables.seenews.com/news/first-solar-hits-21-5-efficiency-with-cdte-pv-cell-462095>, Last accessed September (2016).
- [51] http://www.pv-magazine.com/news/details/beitrag/zsw-sets-217-thin-film-efficiency-record_100016505/#axzz3yxLRoddB, Last accessed February (2016).
- [52] B.M. Basol, *Journal of Applied Physics*, **55** (1984) 601-603.
- [53] O.K. Echendu, F. Fauzi, A.R. weerasinghe and I.M. Dharmadasa, *Thin Solid Films*, **556** (2014) 529-534.
- [54] P.K. Nair, M.T.S. Nair, V.M. Garcia, O.L. Arenas, Y. Pena, A. Castillo, I.T. Ayala, O. Gomezdaza, A. Sanchez, J. Campos, H. Hu, R. Suarez, M.E. Rincon. *Solar Energy Materials and Solar Cells*, **52** (1998) 313-344.
- [55] E.M. Feldmeier, A. Fuchs, J. Schaffner, H.-J. Schimper, A. Klein, and W. Jaegermann, *Thin Solid Films*, **519** (2011) 7596-7599.
- [56] Z. He, G. Zhao, W. Weng, P. Du, G. Shen, and G. Han, *Vacuum*, **79** (2005) 14-18.
- [57] J. Britt and C. Ferekides, *Appl. Phys. Lett.*, **62**(22) (1993) 2851-2852.
- [58] D. Kearns and M. Calvin, *J. Chem. Phys.*, **29** (1958) 950-951.

- [59] M.D. Archer and M.A. Green, *Clean Electricity from Photovoltaics*, 2nd Ed., Imperial College Press, London, United Kingdom, (2015) pp. 17.
- [60] C.W. Tang, *Applied Physics Letters*, **48** (1986) 183-185.
- [61] G. Li, V. Shrotriya, J. Huang, Y. Yao, T. Moriarty, K. Emery, and Y. Yang, *Nature Materials*, **4** (2005) 864-868.
- [62] Z. He, C. Zhong, S. Su, M. Xu, H. Wu and Y. Cao, *Nature Photonics*, **6** (2012) 591-595.
- [63] B. Kadem, W. Cranton and A. Hassan, *Organic Electronics*, **24** (2015) 73-79.
- [64] M. Hosoya, H. Oooka, H. Nakao, T. Gotanda, S. Mori , N. Shida , R. Hayase, Y. Nakano, M. Saito, *Proceedings of the 93rd Annual Meeting of the Chemical Society of Japan*, (2013) 21-37.
- [65] R.N. Marks, J.J.M. Halls, D.D.C. Bradley, R.H. Friend and A.B. Holmes, *J. Phys. Condens. Matter*, **6** (1994) 1379-394.
- [66] S. Barth, H. Basler, *Phys. Rev. Lett.*, **79** (1997) 4445-4448.
- [67] D.R. Kozub, K. Vakhshouri, S.V. Kesava, C. Wang, A. Hexemer and E.D. Gomez, *Chem. Commun.*, **48** (2012) 5859-5861.
- [68] P. Kumar and S. Chand, *Prog. Photovolt: Res. Appl.*, **20** (2012) 377-415.
- [69] Y. H. Kim, C. Sachse, M.L. Machala, C. May, L. Müller-Meskamp and K. Leo, *Adv. Funct. Mater.*, **21** (2011) 1076-1081.
- [70] <http://www-ssrl.slac.stanford.edu/content/science/highlight/2011-01-31/effects-thermal-annealing-morphology-polymer%E2%80%9393fullerene-blends-organic>, Last accessed February (2016).
- [71] M. Thambidurai, J.Y. Kim, Y. Ko, H.J. Song, H. Shin, J. Song, Y. Lee, N. Muthukumarasamy, D. Velauthapillaic and C. Lee, *Nanoscale*, **6** (2014) 8585-8589.
- [72] D.M. DeLongchamp, B. M. Vogel, Y. Jung, M. C. Gurau, C. A. Richter, O. A. Kirillov, J. Obrzut, D. A. Fischer, S. Sambasivan, L. J. Richter, and E. K. Lin, *Chem. Mater.*, **17** (2005) 5610 – 5612.
- [73] A. Goktas, F. Aslan, E. Yasar and I. H. Mutlu, *J. Mater. Sci: Mater. Electron*, **23** (2012) 1361 – 1366.
- [74] S. Ito, P. Chen, P. Comte, M. K. Nazeeruddin, P. Liska, P. Pechy and M. Gratzel, *Prog. Photovolt: Res. Appl.*, **15** (2007) 603 – 612.
- [75] M. Baldo, M. Deutsch, P. Burrows, H. Gossenberger, M. Gerstenberg, V. Ban, and S. Forrest, *Advanced Materials*, **10**(18) (1998) 1505-1514.

- [76] A.A.M. Farag, W.G. Osiris, and A.H. Ammar, *Applied Surface Science*, **259** (2012) 600-609.
- [77] <https://workspace.imperial.ac.uk/people/public/chemistry/Brian%20ORegan/EarlyHistory.html>, Last accessed February (2016).
- [78] B. Oregan, and M. Grätzel, *Nature*, **353** (6346) (1991) 737-740.
- [79] S. Mathew, A. Yella, P. Gao, R. H. Baker, B.F.E. Curchod, N.A. Astani, I. Tavernelli, U. Rothlisberger, Md. K. Nazeeruddin and M. Grätzel, *Nature*, **6**(3) (2014) 242-247.
- [80] M. Grätzel, *Journal of Photochemistry and Photobiology C: Photochemistry Reviews*, **4** (2003) 145-153.
- [81] A. Le Viet, R. Reddy, M.V. Chowdari, B.V.R. Ramakrishna, S. Jose, *Journal of Physical Chemistry C*, **114**(49) (2010) 21795-21800.
- [82] T.H. Meen, J.K.Tsai, Y.S. Tu, T.C. Wu, W.D. Hsu and S.J. Chang, *Nanoscale Research Letters*, **9**(1) (2014)1-8.
- [83] C.Y.W. Lin, D. Channei, P. Koshy, A. Nakaruk and C.C. Sorrell, *Ceramics International*, **38** (2012) 3943-3946.
- [84] M. Kumar, M. Kumar and D. Kumar, *Microelectronic Engineering*, **87** (2010) 447-450.
- [85] N. Robertson, *Angew. Chem. Int. Ed.*, **45** (2006) 2338-2345.
- [86] M. Wright, A. Uddin, *Solar Energy Materials & Solar Cells*, **107** (2012) 87-111.
- [87] P.L. Ong and I.A. Levitsky, *Energies*, **3** (2010) 313-334.
- [88] H. J. Snaith, *The Journal of Physical Chemistry Letters*, **4** (21) (2013) 3623-3630.
- [89] J. Boucle, P. Ravirajan and J. Nelson, *J. Mater. Chem.*, **17** (2007) 3141-3153.
- [90] Z. Li, V.P. Kunets, V. Saini, Y. Xu, E. Dervishi, G.J. Salamo, A.R. Biris, A.S. Biris, *Appl. Phys. Lett.*, **93** (2008) 243117.
- [91] Y. Jia, J. Wei, K. Wang, A. Cao, Q. Shu, X. Gui, Y. Zhu, D. Zhuang, G. Zhang, B. Ma, L. Wang, W. Liu, Z. Wang, J. Luo, D. Wu, *Adv. Mater.*, **20** (2008) 4594-4598.
- [92] D. Zielke, A. Pazidis, F. Werner, and J. Schmidt, *Solar Energy Materials and Solar Cells*, **131** (2014) 110-116.
- [93] W.U. Huynh, J.D. Janke, A.P. Alivisatos, *Science*, **295**(5564) (2002) 2425-2427.

- [94] J. Albero, Y. Zhou, M. Eck, F. Rauscher, P. Niyamakom, I. Dumsch, S. Allard, U. Scherf, M. Krüger and E. Palomares, *Chemical Science*, **2**(12) (2011) 2396-2401.
- [95] S. AbdulMohsin and J.B. Cui, *J. Phys. Chem. C*, **116** (17) (2012) 9433-9438.
- [96] Q. Liu, M. Ono, Z. Tang, R. Ishikawa, K. Ueno, and H. Shira, *Appl. Phys. Lett.*, **100** (2012) 183901-1.

3.1 Introduction

Thin film deposition can be defined as a process of adding a thin layer (few nanometer (monolayer) to several micrometers) of one material on another (substrate). The study and development of thin film deposition techniques have played an important role in the development of optoelectronic devices, semiconductors and solar cells. There are large numbers of deposition techniques used to grow thin films for different applications. Most of these growth techniques are capable of producing high quality thin films using complex systems at a very high manufacturing cost. However, there are other growth techniques that can deposit good quality thin films at lower cost. New researches aim to reduce the cost of production and improve the performance of the devices. To date, the cost of many devices including solar cells has been reduced by using thin films [1,2]. The efficiency can also be increased by understanding the science behind the thin films and deposition techniques. Generally, the thin films deposition techniques can be mainly classified in two categories; the physical deposition techniques and chemical deposition techniques [3]. This chapter presents the various deposition techniques used for the growth of semiconductor thin films.

3.2 Physical deposition techniques

Physical deposition techniques refer to the different vacuum deposition methods used to deposit thin films by the transportation and condensation of a vapourised form of desired film material onto the substrate surface [4]. The coating method includes purely physical processes such as high temperature vacuum evaporation with subsequent condensation or plasma sputtered bombardment rather than involving a chemical reaction at the surface to be coated as in chemical vapour deposition [5]. The main physical deposition techniques include sputtering, molecular beam epitaxy (MBE) and closed space sublimation (CSS) which will be presented in the following sections.

3.2.1 Sputtering

The word sputtering refers to the ejection of atoms from the surface of the target material when it is bombarded by the energetic particles (ions) [6]. The sputtering is principally based on the momentum transfer concept. The basic operating principle of sputtering deposition is shown in Figure 3.1. In sputtering process, target material (the material desired to be deposited) is bombarded with energetic ions, usually inert gas such as argon ions (Ar^+). When argon ions collide with atoms on the surface of target, then, the surface atoms are ejected and move towards the substrate and start to condense into film. The whole process takes place in a vacuum chamber.

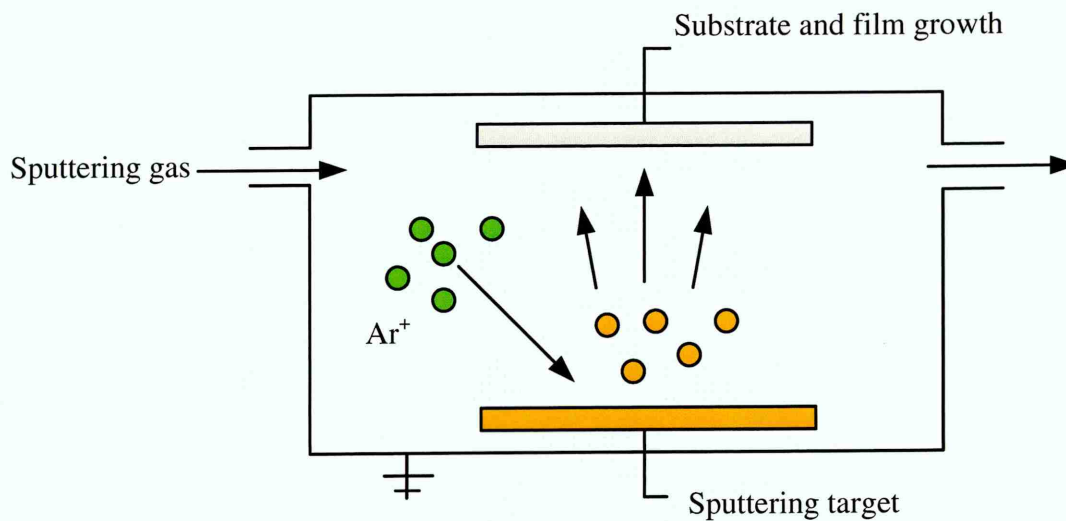


Figure 3.1: Basic operating principle of sputtering deposition technique. Redrawn from [7].

There are basically four methods to sputter the material onto a substrate. The method is known as Direct current (DC) sputtering and the second one is called as radio frequency (RF) sputtering. The third and fourth methods are referred to as magnetron sputtering and reactive sputtering [8]. The DC sputtering is the simplest sputtering process which is mostly used in the deposition of metallic materials. However, in DC sputtering method, an electrically conductive target is required and the dielectric and inorganic materials such as oxides cannot be deposited using this method. DC sputtering has been widely used to deposit thin films such as indium tin oxide (ITO) [9], ZnO [10], and CdS [11].

The RF sputtering technique is more flexible than DC sputtering method and non-conducting (insulating) targets such as silicon oxide and polymers can also be used in sputtering process. In RF sputtering the alternating current (AC) is used instead of DC current in order to avoid the accumulation of positive charge on the surface of the target. In this method, the insulating target can be sputtered by applying a radio frequency (RF) at 13.5 MHz [12].

In the magnetron sputtering method, a strong magnetic field is generated near the target area. The strong magnetic field prevents the electrons being attracted towards the substrates and results in better sputtering process. Many semiconductor thin films have been deposited using magnetron sputtering. These semiconductor thin films include CdTe [13], CdS [14], ZnS [15], ZnO [16] and GaAs [17].

The most complex sputtering method is the reactive sputtering process. In this method, a reactive gas and argon ions are used together to form a plasma. During this process, the reactive gas is activated and chemically combines with the target atoms to form a compound. The oxygen and nitrogen gases have been widely used as reactive gases in the deposition of dielectrics, resistors and semiconductors [18-20].

3.2.2 Molecular beam epitaxy (MBE)

MBE is a physical evaporation process with no chemical reaction involved in the deposition process. In this technique, thin epitaxial films of wide variety of materials such as oxides, semiconductors and metals can be deposited. Also, in MBE growth technique, high purity materials (>99.99999% purity) can be grown with high precision (<0.01 nm) in a ultra-high vacuum facility (basic pressure 10^{-10} mbar) [21]. Generally, in MBE the growth temperature is lower than other physical evaporation techniques (PVD). The advantage of low temperature processing is that it minimises the “autodoping or intermixing effect” during growth. The autodoping is basically due to the out diffusion from substrate into the epitaxial layer and vice versa or evaporation from the substrate and reintroduction from the gas stream [22].

In order to grow crystalline materials using MBE system, a substrate or base materials such as Si, Ge or Ga is placed on the heater block such that it can be brought close to the source ovens (effusion cell or effusion gun) containing the constituent atoms or molecules in the form of gas. Each effusion cell has its independent heating coil so that the source material can be separately heated up to its evaporation

temperature. Then, a precise beam of atoms or molecules are fired from effusion guns onto substrate. During this process, the hot substrate is continuously rotated in order to obtain a uniform deposition. Each effusion guns contain a shutter so that firing of different atoms onto substrate can be controlled by opening or closing each individual shutter. The fired atoms or molecules from the effusion cells eventually land on the surface of the substrate and condense on to systematic ultra-thin films as shown in Figure 3.2.

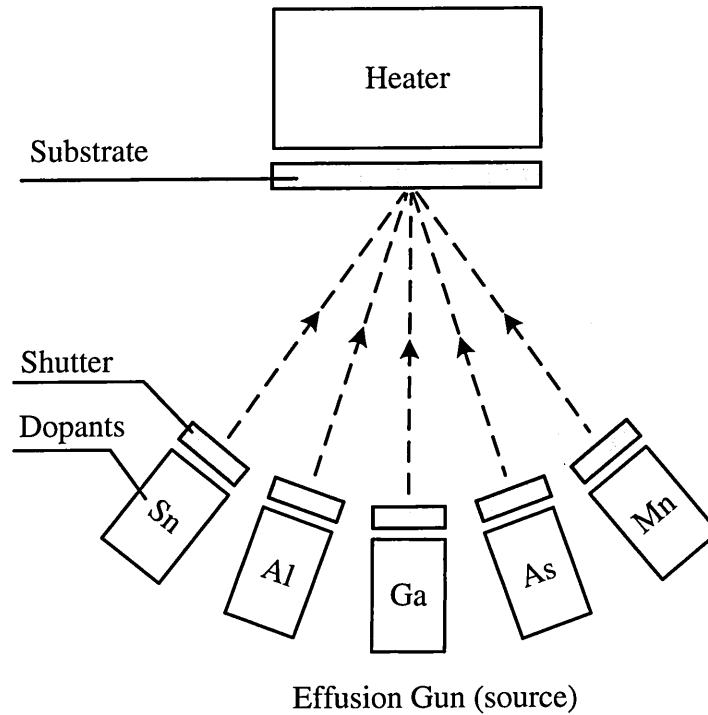


Figure 3.2: Molecular beam epitaxy (MBE) growth system. Redrawn from [23].

The advantages of MBE technique are the growth of high-quality and low defect layers. Also, in MBE highly-uniform thin films can be precisely doped at carefully controlled way. However, this method has some disadvantages such as low crystal growth rate (few microns per hour) which means that it is more suitable for laboratory-scale scientific research. Also, MBE is a very costly and sophisticated system and it requires high vacuum condition and expert attention. Lots of thin-film semiconductors have been grown using this technique including HgCdTe [24], ZnTe on GaAs [25], Si on Si [26] and GaN on GaAs [27].

3.2.3 Closed space sublimation (CSS)

Closed space sublimation (CSS) also known as closed space vapour transport (CSVT) is a dry vapour deposition technique. Figure 3.3 shows the schematic diagram of CSS deposition system. In this technique, the source material (e.g. 5N CdTe powder) is placed on high purity graphite crucible. The substrate which is also supported by high purity graphite plate is heated to the desired temperature (e.g. 500°C for CdTe [28]) using tungsten or quartz halogen lamps. Then, the high purity graphite crucible containing source material is heated at high temperature (e.g. 600°C for CdTe) [28]. In this process, the source material is sublimed and condensed on the substrate. During the deposition, the distance between source material and substrate is kept at constant distance ranging between few millimetres to 1 cm maximum in order to obtain a uniformly deposited thin film [29]. The entire CSS process takes place in a vacuum chamber at a pressure of about 10^{-3} mbar [30]. Also, a gas or mixture of gases (Cl, F, Ar, N) can be added to the vacuum chamber during the growth. For example, Cl and F gases are incorporated into CdTe layer during the growth deposition in order to enhance the layer properties. The deposition rate in the CSS process is high as compared to other growth techniques. For example, the deposition rate for CdTe thin film grown by CSS method is reported as 2 $\mu\text{m}/\text{min}$ [31].

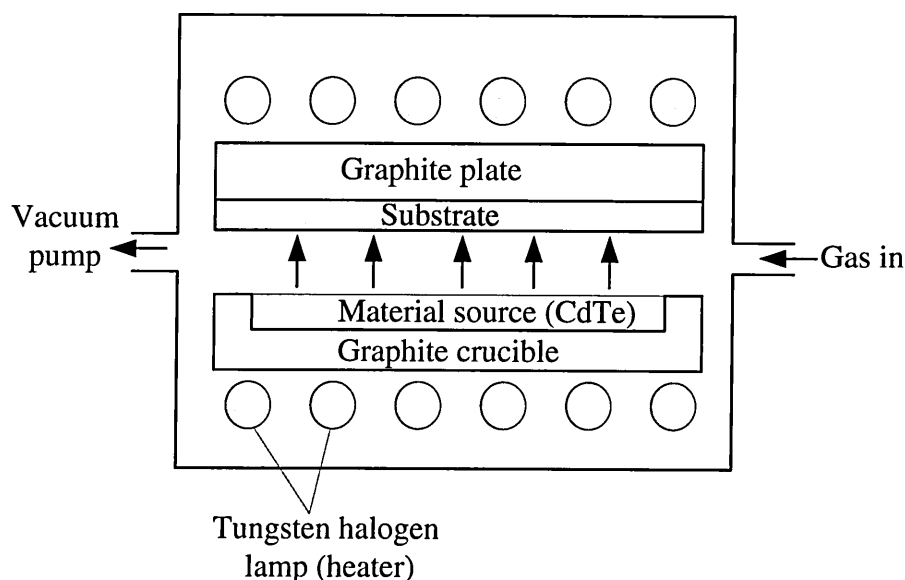


Figure 3.3: Schematic diagram of CSS deposition system made for growth of CdTe layers.

The CSS is one of the various growth techniques which can be used in large area manufacturing process and has been widely used in solar cell applications due to its efficient material utilisation. Also, high quality semiconductor material such as CdTe layer has been grown by this technique [32-34]. Other semiconductor materials grown by CSS technique include CdS [35], ZnTe [36], ZnS and CdSe [37] etc.

3.3 Chemical deposition techniques

The chemical deposition is a chemical process technique which has been used to grow high-quality and high performance solid materials. This process has also been used in manufacturing of thin film semiconductors. The chemical deposition technique can be mainly classified into two categories; the gas phase and liquid phase deposition process.

3.3.1 Gas phase deposition

The gas phase deposition includes a wide variety of thin film growth techniques such as metalorganic chemical vapour deposition (MOCVD), plasma enhanced vapour deposition and photo-chemical vapour deposition etc. These techniques are presented and discussed in the following sections.

3.3.1.1 Metalorganic chemical vapour deposition (MOCVD)

Metalorganic chemical vapour deposition (MOCVD) sometimes called metalorganic vapour phase epitaxy (MOVPE) is used to grow epitaxial, polycrystalline compound semiconductors, and amorphous as well as dielectric thin films [38]. In this technique the source material which are in the form of gas are transported and then deposited onto the substrate. The source materials usually used in MOCVD are the various mixtures of organometallic compounds and hydrides. In MOCVD process, the metal alkyl such as dimethyl cadmium $(\text{CH}_3)_2\text{Cd}$ or trimethyl gallium $(\text{CH}_3)_3\text{Ga}$ are used as the metal (group II or group III) source and the non-metal (group V or group VI) source are usually AsH_3 , PH_3 , H_2Se or dimethyl tellurium (DMTe) [39]. In the reaction chamber and at elevated temperature the source materials decompose and the desired

film such as III-V and II-VI compound semiconductors and alloys are deposited on the substrate.

In MOCVD, the pressure used in the reaction chamber is typically in the range (25-1000) mbar which is much different than MBE [40]. The main advantages of MOCVD method are that it is capable of producing high quality pure and dense materials. Also, a uniform film with good adhesion and reproducibility can be deposited at high deposition rate. Also, complex-shape can be easily coated with this technique. The major disadvantages of MOCVD are that the source materials used are expensive and highly toxic, flammable, explosive and corrosive. In addition, it is not easy to grow stoichiometric multicomponent material using this method [40].

MOCVD is increasingly being applied in fabrication of multijunction solar cells used in space application [40]. Also high quality LEDs based on InGaAlP and III-nitride has been grown by MOCVD techniques [41,42]. Also, large number of semiconductor have been grown using this technique. Some of these semiconductors include GaAs [43], AlGaAs [44], CdTe [45], CdS [46], ZnS [47] and ZnSe [48] etc.

3.3.1.2 Plasma enhanced chemical vapour deposition (PECVD)

Plasma enhanced chemical vapour deposition (PECVD) is an excellent technique for growth of thin films at lower temperature without losing film quality. For example silicon dioxide (SiO_2) can be deposited by PECVD at 300 to 350°C while CVD requires temperatures in the range 600 to 850°C for depositing thin films with the same quality [49]. In PECVD, plasma is generated by electrical energy at a pressure in the range (0.01-1.0) mbar and this energy is transferred into a gas mixture. As a result, the gas mixture is transformed into reactive radical such as ions, neutral atoms and molecules or other excited particles. These ions, atoms and molecules eventually interact with the substrate and as a result of this interaction, thin film deposition takes place on the substrate. In PECVD, because the interaction of these energetic particles occurs by collision in the gas form, therefore, the substrate can be kept at low temperature during deposition process. Hence, the thin film can be deposited at lower temperature as compared to conventional CVD process which is the major advantage of PECVD [50]. Other advantages of PECVD are uniformity of the layer, good adhesion to substrate, low pinhole density and also chamber can be easily cleaned after deposition [51]. The disadvantages of PECVD are that the equipment is expensive and only wafer

with small size can be placed in the deposition chamber. In addition, only one side of the wafer can be coated with the thin film. Also, it is difficult to deposit pure and stoichiometric material by PECVD method [51].

The PECVD has been widely used in manufacturing cost-effective materials in the electronics, industrial and medical applications. This technique is also capable of depositing thin films such as dielectrics or insulator (SiO , SiO_2 , SiON) [52], amorphous Si (a-Si) [53], polycrystalline Si [54], CdTe [55], CdS [56], ZnS [57] and ZnO [58].

3.3.1.3 Photo-enhanced chemical vapour deposition (PHCVD)

In photo-enhanced chemical vapour deposition (PHCVD), the reactants which are in the gas or vapour phase are activated by electromagnetic radiation (usually short wavelength such as ultraviolet) [59]. In this process, the reactant molecules or atoms absorb the photon energy and transform into free radical (ions) species. Then, the free radical species interact to form the desired films. The formation of free radicals can be enhanced by addition of mercury gas into the reactant gas mixture [59]. The mercury vapour act as photosensitiser and is activated by the electromagnetic radiation from a high intensity quartz mercury resonance lamp with a typical wavelength of 253.7 nm. The excited mercury atoms then transfer their kinetic energy to the reactant by the collisions process and then free radicals are formed. The main advantage of this process is that the thin films such as SiO_2 [60] and a-Si:H [61] can be deposited at low temperature (typically 150°C) and also reduces the radiation damage as compared to PECVD [59].

3.3.2 Liquid phase deposition

Liquid phase deposition (LPD) refers to wet thin film growth techniques at low temperatures. In LPD, the thin film deposition can be carried out using electrochemical or non-electrochemical methods. These techniques have been widely used to grow thin films such as metal, semiconductor and insulators for commercial applications including optoelectronic devices and solar cells. The main LPD techniques include electrodeposition (ED), chemical bath deposition (CBD), spin coating and spray pyrolysis.

3.3.2.1 Electrodeposition (ED)

Electrodeposition is the process of coating of an electrically conducting object (substrate) with a layer of metal or compounds (semiconductors) using electrical current [62]. This technique has been widely used in industry to suppress or prevent the corrosion of a metal [63]. The electrodeposition can be carried out using conventional three or two electrode system as shown in Figures 3.4 (a) and 3.4 (b) respectively. The three electrode system as presented in Figure 3.4 (a) is consisted of counter electrode (anode), working electrode (cathode), reference electrode, power supply, electrolyte, stirrer and hot plate. In two electrode set up, the reference electrode is omitted in order to simplify the system, reduce the cost of set up and prevent the leakage of unwanted impurity ions from reference electrode into deposition electrolyte (see chapter 8, section 8.1 for full details). The three electrode system is usually used in most analytical electrochemical experiments which are interested in the potential at only the working electrode. By addition of a reference electrode (an electrode in which the potential is constant) the current between the working and counter electrode, as well as the voltage between the reference and working electrode can be monitored [64]. The electrodeposition of thin films can be carried out either anodically or cathodically. In anodic deposition, the negatively charged ions are oxidized (donate electrons) and are attracted to the anode (conducting substrate) while in cathodic deposition, the positively charged ions are reduced (gain electrons) and are attracted to the cathode (conducting substrate). In semiconducting thin film growth process, cathodic deposition is more favourable than anodic deposition. The reason is that in cathodic deposition, the stoichiometry of the semiconductor thin films (e.g. CdS, CdTe) can be controlled easily. Also, in cathodic deposition method, the deposited films have fewer defects and shows better adhesion to the substrates [65]. The anodic deposition is usually used for the growth of polymer materials since it offers better polymerization process and produces a layer with better quality [66].

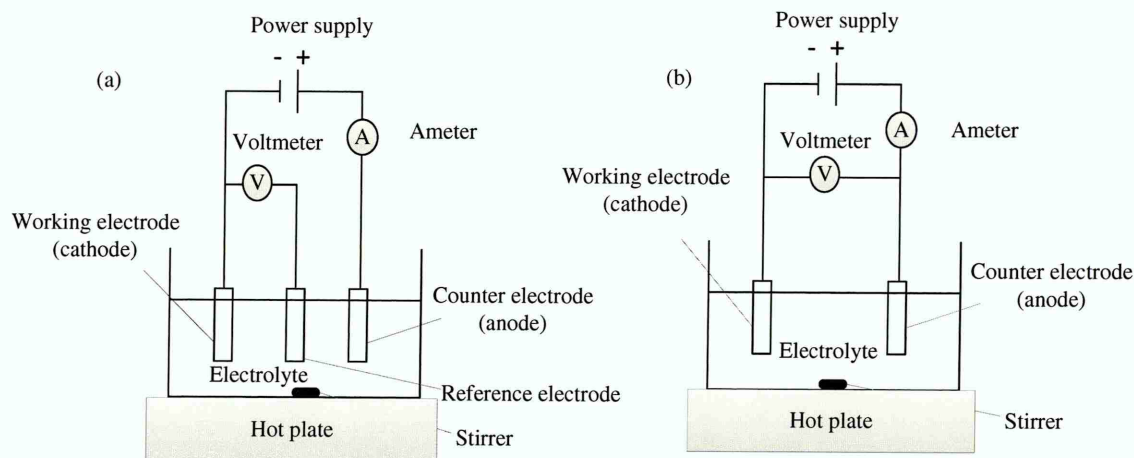


Figure 3.4: Schematic diagram of (a) three-electrode system and (b) two-electrode system used for electrodeposition of semiconductors. Redrawn from [67, 68].

The main advantages of electrodeposition technique are: (i) low deposition temperature at atmospheric conditions, avoiding expensive vacuum system, (ii) p-type, i-type and n-type semiconductors (CdTe) can be easily deposited just by varying deposition potential [69-71], (iii) the bandgap can be engineered [69, 70], (iv) self-purification and built-in hydrogen passivation [69,70], (v) deposition electrolyte has prolonged life time [69,70], (vi) extrinsic dopants can be easily added to the electrolyte during deposition [72], (vii) it is simple, material waste is minimum and low-cost [69,70] and (viii) its proven scalability and manufacturability.

Electrodeposition has been used to grow both single crystal and polycrystalline materials [73-75]. There are varieties of high quality materials which have been grown by electrodeposition technique for different applications. These materials include CdTe [76-81], CdS [82,83], ZnS [84], ZnTe [85], CdSe [86], ZnSe [72,87], GaAs [88], InP [89], CuInSe₂ [71,87,90], CIGS [91], Polyaniline [92-94] etc. This technique is a continuous process and therefore attractive in an industrial production line.

3.3.2.2 Chemical bath deposition (CBD)

In chemical bath deposition (CBD) method, precipitation of solid phase takes place as a result of the super saturation or chemical reaction in the deposition bath. The precipitation occurs at certain temperature when ionic product of the reactant exceeds the solubility product [95]. When the ionic product is less than solubility product, no precipitation takes place. This is because the produced solid phase dissolves back into

the solution. In other words, CBD is the way of controlling chemical reaction so that thin film can be deposited by the process of precipitation.

The CBD method is usually used for the deposition of chalcogenide thin films. In a typical CBD method, the substrate is dipped in a solution having the chalcogenide source, metal ions and an added base. A complexing agent is also added into solution in order to control the hydrolysis and amount of free metal ions [96]. The CBD process depends on the slow release of chalcogenide ions into an alkaline solution in which metal ions are buffered at low concentration. The concentration of free metal ions is controlled by the formation of complex species in the solution according to the following chemical reaction [97]:



The concentration of free ions at certain temperature can be obtained by the relation [97]:

$$\frac{[M^{2+}][A]}{[M(A)^{2+}]} = K_i \quad (3.2)$$

Here, the K_i is the instability constant of the complex ions. It should be noted that each different complexing agent has different instability constant. Increase in the instability constant means that more ions are released in the solution. The stability of the complex depends on the temperature and pH of the solution. When the temperature of the solution increases, the complex becomes less stable while an increase in pH makes the complex more stable [97]. The concentration of metal ions can be controlled by controlling the concentration of complexing agent and the temperature of the solution. There are large numbers of complexing agents used in CBD growth technique in order to stabilise the solution bath and deposit the uniform layer with better quality. For example, the complexing agent used to grow CBD-CdS thin films are ammonium hydroxide (NH_4OH), citrate ($\text{C}_6\text{H}_5\text{O}_7^{3-}$) and tartrate ($\text{C}_4\text{H}_4\text{O}_6^{2-}$) [97] ions.

The CBD method has been widely used to grow a range of I-VI, II-VI, IV-VI and V-VI compound semiconductor thin films for different applications such as solar cells and photodetectors. These compound semiconductor thin films include CdS, CdSe, ZnS, ZnSe, SnS, SnSe, Ag_2S , CuS, CuSe, PbS, PbSe, Sb_2S_3 , Bi_2S_3 , Bi_2Se_3 , etc. [98-100]. Although the method looks simple, this is a batch process, and creates large volume of

waste solution. Specially, when used for Cd-containing compounds, toxic waste management could be expensive in a production line.

3.3.2.3 Spin-coating technique

Spin-coating is another type of wet chemical deposition technique which has been used for several decades in thin films fabrication. A typical process involves the dispensing of small puddle of prepared solution onto the center of a substrate which is attached to the spinner. The substrate spins at high speed (typically around 1000-6000 rpm) and the centripetal acceleration will cause the solution to spread all over the substrate. At the end of this process, a thin film of desired material with the thickness in the range of few nanometers up to few micrometers is formed on the surface of the substrate. The thickness of the film depends on the viscosity, spin speed and spin time, drying rate, surface tension and concentration of the solution [101]. Multilayer structures can also be produced using spin-coating technique. Figure 3.5 show the schematic of the spin-coating process.

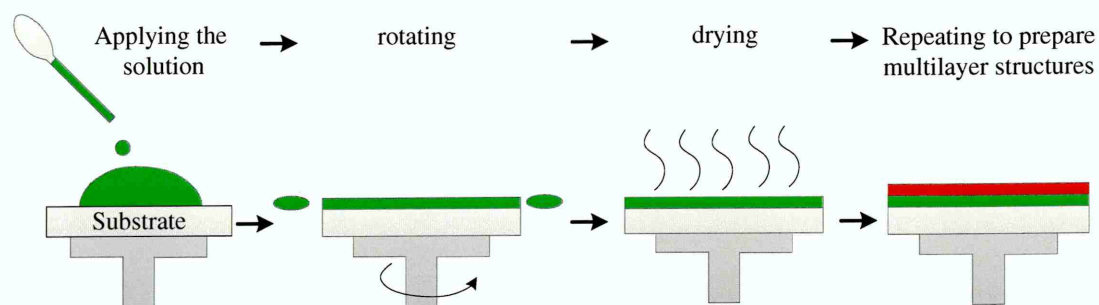


Figure 3.5: Schematic of the spin-coating process. Redrawn from [102].

Some advantages of spin-coating technique are; (i) simplicity, (ii) ability to deposit on conducting and non-conducting substrates, (iii) uniform coating and repeatability, (iv) possibility of making well-defined film thicknesses. The disadvantages of these techniques are; (i) the difficulty of spinning and coating of large area samples, and (ii) only one side of the sample can be coated during spin-coating process [103].

The spin-coting has been extensively used in industry for production of optical mirror and photolithography [104]. Also, this technique has been used to grow thin film

semiconductors such as TiO_2 [105], ZnO [106], SnO_2 [107] and organic semiconductors [108-111] and single wall carbon nano tubes [112].

3.3.2.4 Spray pyrolysis

Spray pyrolysis is considered as a simple, scalable and cost-effective technique to prepare thin and thick films. This technique has been extensively used to grow films for various applications such as solar cells [113], sensors [114] and solid oxide fuel cells [115]. Also this technique has been used for several decades in glass industry [116].

Typical spray pyrolysis equipment involves an atomiser, precursor solution, substrate heater and temperature controller. The types of atomiser used in spray pyrolysis includes: (i) air blast atomiser in which the liquid is exposed to the stream of air [117], (ii) ultrasonic atomiser where ultrasonic frequencies produce the short wavelengths necessary for fine atomisation [118], and (iii) electrostatic atomiser in which the liquid is exposed to a high electric field [119].

In spray pyrolysis process, a solution containing the desired compound to be deposited is prepared. This solution is then reduced to fine particles (droplet) by means of atomiser. Then, the carrier gases which are usually non-reacting gases (e.g. N_2 , Ar, He) moves (spray) the fine particles onto the heated substrate. In this process, the solute precipitates on the substrate and the solvent evaporates and eventually thin films crystallise on the surface of substrate. The schematic of spray pyrolysis system is shown in Figure 3.6.

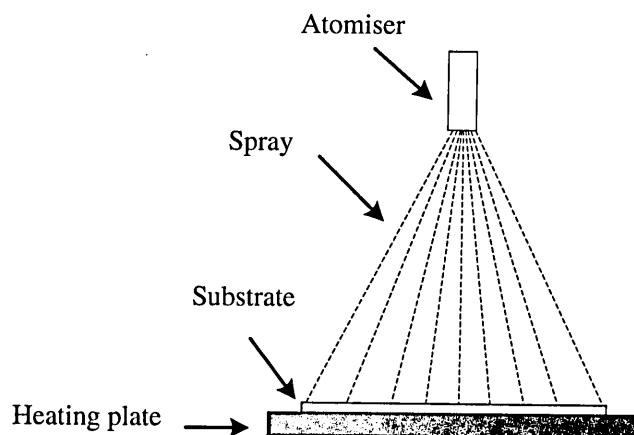


Figure 3.6: Schematic diagram of spray pyrolysis system. Redrawn from [115].

The nature of deposited films using spray pyrolysis technique depends on the type of atomiser used, concentration of precursors in the solution, type of solvent used and temperature of the substrate [120]. The semiconductor thin films which have been grown using this technique include CdTe [121], CdS [122], CdSe [123], ZnS [124] and ZnO [125].

3.4 Conclusions

The main thin film deposition techniques were summarised in this chapter. In general, the thin films deposition techniques are mainly classified in two categories; the physical and chemical deposition techniques.

Each of these deposition techniques has its own advantages and disadvantages depending on area of interest. Generally, in physical deposition techniques which need vacuum system, the deposition process is carried in three steps; (i) formation of an evaporant from the source material, (ii) transport of the evaporant from the source to the substrate, and (iii) condensation of the evaporant onto the substrate to form the thin film deposit.

The deposition techniques which are carried out under vacuum condition produce high quality thin films, however, they are also more expensive than non-vacuum system due to the establishment of a vacuum, and significant amount of heat required for evaporation of source material which requires expensive and complex equipment. Material wastage is high in those techniques.

For large area, low-cost thin film productions, liquid phase growth techniques (electrodeposition, spray pyrolysis) are more favourable than the gas phase deposition techniques. Overall, in photovoltaic applications, the most important factors which should be considered are low-cost, reproducibility, scalability and manufacturability.

3.5 References

- [1] R.A. Street, *Adv. Mater.*, **21** (2009) 2007-2022.
- [2] K.L. Chopra, P.D. Paulson and V. Dutta, *Prog. Photovolt: Res. Appl.*, **12** (2004) 69-92.
- [3] K. Seshan, *Handbook of thin-film deposition processes and techniques*, 2nd edition, Noyes publications, New York, USA (2002).
- [4] http://www.appropedia.org/Vapor_Deposition_of_thin_Films, Last accessed February (2016).
- [5] http://everything.explained.today/Physical_vapor_deposition/, Last accessed February (2016).
- [6] <http://www.semicore.com/what-is-sputtering>, Last accessed February (2016).
- [7] <https://en.wikipedia.org/wiki/Sputtering>, Last accessed February (2016).
- [8] R. Behrisch, *Sputtering by Particle Bombardment*, Springer, Berlin (1981).
- [9] J. Bhattacharya, S. Chaudhuri, D. De and A.K. Pal, *Thin Solid Films*, **128** (1985) 231-239.
- [10] A.N. Banerjee, C.K. Ghosh, K.K. Chattopadhyay, H. Minoura, A.K. Sarkar, A. Akiba, A. Kamiya and T. Endo, *Thin Solid Films*, **496** (2006) 112-116.
- [11] P.K. Ghosh, U.N. Maiti and K.K. Chattopadhyay, *Materials Letters*, **60** (2006) 2881-2885.
- [12] J.S. Logan, *Thin Solid Films*, **188** (1990) 307-321.
- [13] E.M. Feldmeier, A. Fuchs, J. Schaffner, H.-J. Schimper, A. Klein, W. Jaegermann, *Thin Solid Films*, **519** (2011) 7596-7599.
- [14] J.H. Lee and D.J. Lee, *Thin Solid Films*, **515** (2007) 6055-6059.
- [15] D.H. Hwang, J.H. Ahn, K.N. Hui, K.S. Hui and Y.G. Son, *Nanoscale Research Letters*, **7**(1) (2012) 1-7.
- [16] C. Besleaga, G.E. Stan, A.C. Galca, L. Ion and S. Antohe, *Applied Surface Science*, **258** (2012) 8819-8824.
- [17] G.de M. Azevedo, J.H. Dias da Silva, E. Avendaño, *Nuclear Instruments and Methods in Physics, Research B*, **238** (2005) 329-333.
- [18] E.C. Knox-Davies, J.M. Shannon and S.R.P. Silva, *Journal of Applied Physics*, **99** (2006) 073503-1.
- [19] D. Rademacher, T. Zickenrott, M. Vergöhl, *Thin Solid Films*, **532** (2013) 98-105.

- [20] T. Riekkinen, J. Molarius, T. Laurila, A. Nurmela, I. Suni, J.K. Kivilahti, *Microelectronic Engineering*, **64** (2002) 289-297.
- [21] <https://www.ee.ucl.ac.uk/about/MBE>, Last accessed February (2016).
- [22] <http://www.semi1source.com/glossary/default.asp?searchterm=autodoping>, Last accessed February (2016).
- [23] <http://eng.thesaurus.rusnano.com/wiki/article2035>, Last accessed February (2016).
- [24] T. Aoki, Dj, Smith, Y. Chang, J. Zhao, G. Badano, C. Grein, S. Sivananthan, *Applied Physics Letters*, **82**(14) (2003) 2275-2277.
- [25] Y. Rajakarunanayake, B.H. Cole, J.O. McCaldin, D.H. Chow, J.R. Söderström, T.C. McGill and C.M. Jones, *Appl. Phys. Lett.*, **55**(12) (1989) 1217-1219.
- [26] D.J. Eaglesham, H.-J. Gossmann, and M. Cerullo, *Phys. Rev. Lett.*, **65**(10) (1990) 1227-1230.
- [27] Z.Q. He, X.M. Ding, X.Y. Hou and X. Wang, *Appl. Phys. Lett.*, **64** (1994) 315-317.
- [28] A. Bosio, N. Romeo, S. Mazzamuto and V. Canaveri, *Prog. in Crystal Growth.*, **52** (2006) 247-279.
- [29] C.S. Solanki, *Solar Photovoltaics: Fundamentals, Technologies and Applications*, 3rd edition, PHI Learning Private Limited, Delhi-110092, (2015) p.217.
- [30] A. Rios-Flores, J.L. Peña, V. Castro-Pena, O. Ares, R. Castro-Rodriguez, A. Bosio, *Solar Energy*, **84** (2010) 1020-1026.
- [31] R. Castro-Rodriguez, A. Bosio N. Romeo, A. Bosio, V. Canevari, M. Terheggen and L.V. Roca, *Thin Solid Films*, **431-432** (2003) 364-368.
- [32] J. Britt and C. Ferekides, *Appl. Phys. Lett.*, **62**(22) (1993) 2851-2852.
- [33] X. Wu, *Sol. Energy*, **77** (2004) 803-814.
- [34] C.S. Ferekides, D. Marinskiy, V. Viswanathan, B. Tetali, V. Palekis, P. Selvaraj and D.L. Morel, *Thin Solid Films*, **361-362** (2000) 520-526.
- [35] J. Schaffner, E. Feldmeier, A. Swirschuk, H.-J. Schimper, A. Klein and W. Jaegermann, *Thin Solid Films*, **519** (2011) 7556-7559.
- [36] D. Kurbatov, V. Kosyak, M. Kolesnyk, A. Opanasyuk, and S. Danilchenko, *Integrated Ferroelectrics*, **103** (2009) 32-40.
- [37] O. de Melo, E. SaÂnchez, H. RodrÃ³guez, S. De Roux, F. RaÂbago-Bernal and J. Ruiz-Garcia, *Mater. Chem. Phys.*, **59** (1999) 120-124.

- [38] H. Juergensen, *Materials Science in Semiconductor Processing*, **4** (2001) 467-474.
- [39] A.G. Thompson, *Materials Letters*, **30** (1997) 255-263.
- [40] H.S. Nalwa, *Handbook of Nanostructured Materials and Nanotechnology*, Vol. 1, Synthesis and Processing, Academic Press, (1996) USA.
- [41] C. Karl, J. Ebbecke, T. Lutz, C. Kauss, and R. Zeisel, *J. Appl. Phys.*, **114** (2013) 033108-1.
- [42] H. Wang, Y. Zhao, C. Wu, X. Dong, B. Zhang, G. Wu, Y. Ma and G. Du, *Journal of Luminescence*, **158** (2015) 6-10.
- [43] R. Pena-Sierra, J. G. Castro-Zavala and A. Escobosa, *J. Cryst. Growth*, **107** (1991) 337-341.
- [44] T. Soga, Y. Takahash, S. Sakai and M. Umeno, *J. Cryst. Growth*, **68** (1984) 169-175.
- [45] I. Mora-Sero, R. Tena-Zaera, J. Gonzalez and V. Munoz-Sanjose, *J. Cryst. Growth*, **262** (2004) 19-27.
- [46] A.C. Jones, S.A. Rushworth, P.J. Wright, B. Cockayne, P. O'Brien and J.R. Walsh, *J. Cryst. Growth*, **97** (1989) 537-541.
- [47] J. Fang, P.H. Holloway, J.E. Yu, K.S. Jones, B. Pathangey, E. Brettschneider and T.J. Anderson, *Applied Surface Science*, **70/71** (1993) 701-706.
- [48] J. Sollner, M. Deschler, H. Jiirgensenf, H. Kalisch, W. Taudt, H. Hamadeh, M. Heuken, U. Blieske, M. Saad, A. Bauknecht, T. Kampschulte, J. Albert and M.Ch. Lux-Steiner, *J. Cryst. Growth*, **184/185** (1998) 158-162.
- [49] M. Lu, *Silicon Heterojunction Solar Cell and Crystallization of Amorphous Silicon*, UMI[®], USA (2008) p.17.
- [50] <http://www.plasmaequip.com/WHAT%20IS%20PECVD.pdf>, Last accessed February (2016).
- [51] M.J. Madou, *Fundamentals of Microfabrication: The Science of Miniaturization*, 2nd Edition, CRC Press, London (2002) p.148.
- [52] Y.T. Kim, D.S. Kim and D.H. Yoon, *Thin Solid Films*, **475** (2005) 271-274.
- [53] B. Swatowska, T. Stapiński and S. Zimowski, *Opto-Electron. Rev.*, **20**(2) (2012) 168-173.
- [54] M. Matsumoto, Y. Inayoshi, M. Suemitsu, T. Yara , S. Nakajima, T. Uehara , Y. Toyoshima, *Thin Solid Films*, **516** (2008) 6673-6676.

- [55] L.M. Williams, P.-Y. Lu, and S.N.G. Chu, *Appl. Phys. Lett.*, **54**(14) (1989) 1329-1331.
- [56] N.I. Fainer, M.L. Kosinova, Y.M. Rumyantsev, E.G. Salman and F.A. Kuznetsov, *Thin Solid Films*, **280** (1996) 16-19.
- [57] J.S. Jie, W.J. Zhang, Y. Jiang, X.M. Meng, J.A. Zapien, M.W. Shao and S.T. Lee, *Nanotechnology*, **17** (2006) 2913-2917.
- [58] X. Liu, X. Wu, H. Cao, and R.P.H. Chang, *J. Appl. Phys.*, **95**(6) (2004) 3141-3147.
- [59] R.A. Levy, *Microelectronic Materials and Processes*, Kluwer Academic Publishers, Netherland, (1986) p.216.
- [60] K.H. Lee, P.C. Chang and S.J. Chang, *Microelectronic Engineering*, **104** (2013) 105-109.
- [61] F. Boulitrop and D.J. Dunstan, *Journal of Non-Crystalline Solids*, **77 & 78** (1985) 663-666.
- [62] M. Schlesinger and M. Paunovic, *Modern Electroplating*, 5th Edition, A John Wiley & Sons, INC, New Jersey, USA, (2010).
- [63] P. Niranatlumpong and H. Koiprasert, *Surface & Coatings Technology*, **201** (2006) 737-743.
- [64] <https://www.quora.com/Why-do-we-use-a-three-electrode-system-for-analytical-electrochemistry>, Last accessed February (2016).
- [65] G.F. Fulop, and R.M. Taylor, *Annual Review of Materials Science*, **15**(1) (1985) 197-210.
- [66] A. Kitani, J. Izumi, J. Yano, Y. Hiromoto and K. Sasaki, *Bulletin of the Chemical Society of Japan*, **57**(8) (1984) 2254-2257.
- [67] <http://www.intechopen.com/books/state-of-the-art-in-biosensors-general-aspects/bioelectronics-for-amperometric-biosensors%3A>, Last accessed February (2016).
- [68] <http://knowledge.electrochem.org/encycl/art-e01-electroplat.htm>, Last accessed February (2016).
- [69] I.M. Dharmadasa and J. Haigh, *J. Electrochem. Soc.*, **153** (1) (2006) G47-G52.
- [70] I.M. Dharmadasa, *Advances in Thin-Films Solar Cells*, Pan Stanford Publishing Pte. Ltd, Boulevard, Singapore, (2012) pp.40-44.
- [71] I.M. Dharmadasa, R.P. Burton and M. Simmonds, *Solar Energy Materials & Solar Cells*, **90** (2006) 2191-2200.

- [72] I.M. Dharmadasa, A.P. Samantilleke, J. Young, M.H. Boyle, R. Bacewicz and A. Wolska, *J. Mater. Sci: Mater. Electron*, **10** (1999) 441-445.
- [73] I.V. Zubeck, R.S. Feigelson, R.A. Huggins and P.A. Pettit, *J. Cryst. Growth*, **34** (1976) 85-91.
- [74] F. Xiao, B. Yoo, K.N. Bozhilov, K.H. Lee and N.V. Myung, *J. Phys. Chem. C*, **111** (2007) 11397-11402.
- [75] I.M. Dharmadasa and O.K. Echendu, *Encyclopedia of Applied Electrochemistry*, (2014) 680-691.
- [76] B.M. Basol, *Journal of Applied Physics*, **55** (1984) 601-603.
- [77] A.K. Turner, J.M. woodcock, M.E. Ozsan, J.G. Summers and J. Barker, S. Binns, K. Buchanan, C. Chai, S. Dennison, R. Hart, D. Johnson, R. Marshall, S. Oktik, M. Patterson, R. Perks, S. Roberts, M. Sadeghi, J. Sherborne, J. Szubert and S. Webster, *Solar Energy Materials*, **23** (1991) 388-393.
- [78] N.B. Chaure, A.P. Samantilleke, I.M. Dharmadasa, *Solar Energy Materials & Solar Cells*, **77** (2003) 303-317.
- [79] O.K. Echendu, F. Fauzi, A.R. weerasinghe and I.M. Dharmadasa, *Thin Solid Films*, **556** (2014) 529-534.
- [80] H.I. Salim, V. Patel, A. Abbas, J.M. Walls and I.M. Dharmadasa, *J. Mater. Sci: Mater Electron.*, **26** (2015) 3119-3128.
- [81] N.A. Abdul-Manaf, H.I. Salim, M.L. Madugu, O. I. Olusola and I.M. Dharmadasa, *Energies*, **8** (2015) 10883-10903.
- [82] D.G. Diso, G.E.A. Muftah, V. Patel and I.M. Dharmadasa, *J. Electrochem. Soc.*, **157**(6) (2010) H647-H651.
- [83] N.A. Abdul-Manaf, A.R. Weerasinghe, O.K. Echendu, I.M. Dharmadasa, *J. Mater. Sci: Mater. Electron.*, **26** (2015) 2418-2429.
- [84] O.K. Echendu, A.R. Weerasinghe, D.G. Diso, F. Fauzi, and I.M. Dharmadasa, *J. Elect. Mater.*, **42**(4) (2013) 692-700.
- [85] F. Fauzi, D.G. Diso, O.K. Echendu, V. Patel, Y. Purandare, R. Burton and I.M. Dharmadasa, *Semiconductor Science and Technology*, **28**(4) (2013) 045005.
- [86] O.I. Olusola, O.K. Echendu and I.M. Dharmadasa, *J. Mater. Sci: Mater. Electron.*, **26**(2) (2015) 1066-1076.
- [87] D. Lincot, *Thin Solid Films*, **487** (2005) 40-48.
- [88] R.C. De Mattei, D. Elwell and R.S. Feigelson, *J. Cryst. Growth*, **43** (1978) 643-644.

- [89] D. Elwell, *J. Cryst. Growth*, **52** (1981) 741-752.
- [90] A. Bouraiou, M.S. Aida, E. Tomasella and N. Attaf, *J. Mater. Sci.*, **44** (2009) 1241.
- [91] I.M. Dharmadasa, N.B. Chaure, G.J. Tolan, and A.P. Samantilleke, *Journal of The Electrochemical Society*, **154**(6) (2007) H466-H471.
- [92] A. Aykanat and J.O. Iroh, *The Journal of Adhesion*, **78** (2002) 629-643.
- [93] H. Zhang, J. Wang, Z. Wang, F. Zhang and S. Wang, *Synthetic Metals*, **159** (2009) 277-281.
- [94] N.A. Abdul-Manaf, O.K. Echendu, F. Fauzi, L. Bowen and I.M. Dharmadasa, *Journal of Electronic Materials*, **43**(11) (2014) 4003-4010.
- [95] T.L. Chu and S.S. Chu, *Solid-State Electronics*, **38**(3) (1995) 533-549.
- [96] P.K. Nair, M.T.S. Nair, V.M. Garcia, O.L. Arenas, Y. Pena, A. Castillo, I.T. Ayala, O. Gomezdaza, A. Sanchez, J. Campos, H. Hu, R. Suarez, M.E. Rincon. *Solar Energy Materials and Solar Cells*, **52** (1998) 313-344.
- [97] M. Lakshmi, *Studies on chemical bath deposited semiconducting copper selenide and iron sulfide thin films useful for photovoltaic applications*, Doctoral thesis, Cochin University of Science and Technology, India (2001).
- [98] K.L. Chopra, R.C. Kainthla, D.K. Pandya and A.P. Thakoor, *Physics of Thin Films*, Vol. 12, ed G Hass *et al*, New York:Academic, (1982) p. 201.
- [99] C.D. Lokhande, *Mater. Chem. Phys.* **27** (1991) 1-43.
- [100] R.S. Mane and C.D. Lokhande, *Mater. Chem. Phys.* **65** (2000) 1-31.
- [101] <https://louisville.edu/micronano/files/documents/standard-operating-procedures/SpinCoatingInfo.pdf>, Last accessed February (2016).
- [102] <http://www.intechopen.com/books/solar-cells-new-approaches-and-reviews/inorganic-organic-perovskite-solar-cells>, Last accessed February (2016).
- [103] M.N. Rahaman, *Ceramic Processing and Sintering*, 2nd edition, Marcel Dekker, Inc., New York, USA, (2003).
- [104] N. Sahu, B. Parija and S. Panigrahi, *Indian J. Phys.*, **83**(4) (2009) 493-502.
- [105] C.Y.W. Lin, D. Channei, P. Koshy, A. Nakaruk and C.C. Sorrell, *Ceramics International*, **38** (2012) 3943-3946.
- [106] A. Nalbant, Ö. Ertek and I. Okur, *Arab J. Sci. Eng.*, **38** (2013) 1909-1915.
- [107] F. Gu, S.F. Wang, M.K. Lu, X.F. Cheng, S.W. Liu, G.J. Zhou, D. Xu and D.R. Yuan, *J. Cryst. Growth*, **262** (2004) 182-185.

- [108] D.M. DeLongchamp, B.M. Vogel, Y. Jung, M.C. Gurau, C.A. Richter, O.A. Kirillov, J. Obrzut, D.A. Fischer, S. Sambasivan, L.J. Richter, and E.K. Lin, *Chem. Mater.*, **17** (2005) 5610-5612.
- [109] F. Zhang, C. Di, N. Berdunov, Y. Hu, Y. Hu, X. Gao, Q. Meng, H. Sirringhaus and D. Zhu, *Adv. Mater.*, **25** (2013) 1401-1407.
- [110] K. Oku, S. Inasawa, Y. Tsuji and Y. Yamaguchi, *Drying Technology*, **30** (2012) 832-838.
- [111] A.K. Hassan, C. Goy, A.V. Nabok, *Thin Solid Films*, **516** (2008) 9006-9011.
- [112] A. Hassan, H. Banimuslem, T. Basova, A.D. Gülmeze, M. Durmuş, Ayşe Gül Gürek and V. Ahsen, *Sensors and Actuators B: Chemical*, **224** (2016) 780-788.
- [113] B.R. Pamplin, *Progress in Crystal Growth and Characterization of Materials*, **1**(4) (1979) 395-403.
- [114] G. Korotcenkov, V. Brinzari, J. Schwank, M. DiBattista, A. Vasiliev, *Sensors & Actuators: B. Chemical*, **77**(1) (2001) 244-252.
- [115] D. Perednis and L.J. Gauckle, *Solid State Ionics*, **166** (2004) 229-239.
- [116] J.M. Mochel, US Patent 2,564,707 (1951).
- [117] A.R. Balkenende, A. Bogaerts, J.J. Scholtz, R.R.M. Tjiburg, and H.X. Willems, *Philips Journal of Research*, **50**(3-4) (1996) 365.
- [118] S.P.S. Arya and H.E. Hintermann, *Thin Solid Films*, **193**(1-2), (1990) 841.
- [119] C.H. Chen, E.M. Kelder, P.J.J.M. van der Put, and J. Schoonman, *J. Mater. Chem.*, **6**(5) (1996) 765.
- [120] P.S. Patil, *Mater. Chem. Phys.*, **59** (1999) 185-198.
- [121] V.V. Ison, A.R. Rao and V. Dutta, *Solid State Sciences*, **11** (2009) 2003-2007.
- [122] A.A. Yadav, M.A. Barote and E.U. Masumdar, *Solid State Sciences*, **12** (2010) 1173-1177.
- [123] A.A. Yadav, M.A. Barote and E.U. Masumdar, *Mater. Chem. Phys.*, **121** (2010) 53-57.
- [124] T. Dedova, M. Krunk, O. Volobujeva, and I. Oja, *Phys. Stat. Sol., (c)*, **2**(3) (2005) 1161-1166.
- [125] A. Ashour, M.A. Kaid, N.Z. El-Sayed and A.A. Ibrahim, *Applied Surface Science*, **252** (2006) 7844-7848.

4.1 Introduction

Thin films are very important in many fields of modern science (e.g. solar cells technology). For this reason, a large number of techniques have been developed for their characterisation. These characterisation techniques provide the required information to determine the suitability or otherwise of a particular material for specific application. The in-depth characterisation of properties of the materials may not be achieved by using only one technique. The effective way to extract more information about thin films is to use the combination of techniques. These techniques are usually employed to study the structural, compositional, morphological, electrical and optical properties of the thin film semiconductors. This chapter presents and discusses the widely available techniques used to characterise semiconductor thin films for solar cells application.

4.2 X-ray techniques

The use of X-ray technique in the field of material analysis has now entered its eighth decade. The X-ray technique covers many methods based on the scattering, emission and absorption properties of X-radiation. The most commonly used X-ray methods involve X-ray diffraction (XRD), Energy dispersive X-ray spectroscopy (EDX) and X-ray fluorescence (XRF). These techniques are used to reveal the information about the crystal structure, chemical composition and physical properties of materials and thin films. The following sections present the principles of X-ray techniques (XRD, EDX, XRF) used to analyse the thin films for solar cells application.

4.2.1 X-Ray diffraction (XRD)

An X-ray is a form of electromagnetic radiation with wavelengths in the same order of typical atomic distance which is about $(0.1-10) \text{ \AA}$ [1]. The energy of the electromagnetic radiation can be calculated using Equation (4.1) [2]:

$$E = h\nu = \frac{hc}{\lambda} \quad (4.1)$$

where E is the energy of the photon, λ is the wavelength, ν is the frequency, c is the velocity of light ($3 \times 10^8 \text{ ms}^{-1}$) and h is Planck's constant ($6.626 \times 10^{-34} \text{ Js}$). Therefore, the energy equivalent of a 1 \AA (10^{-10} m) X-ray photon is:

$$E = \frac{hc}{\lambda} = \frac{(6.626 \times 10^{-34} \text{ Js}) (3 \times 10^8 \text{ ms}^{-1})}{(1.602 \times 10^{-19} \text{ JeV}^{-1}) (10^{-10} \text{ m})} = 12.4 \text{ keV}$$

The X-ray diffraction (XRD) is a non-destructive technique which is used to determine the crystallographic structure, phase and crystallite size of the materials. Figure 4.1 illustrates the basic principle of the XRD.

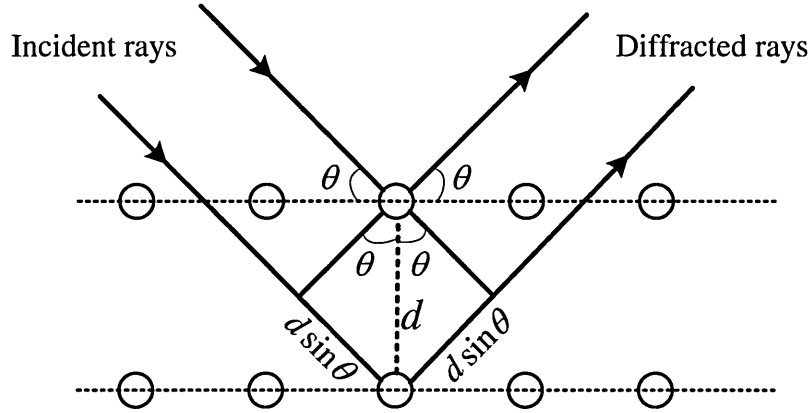


Figure 4.1: The basic principle of X-ray diffraction. The diffracted X-rays exhibit constructive interference when Bragg's law is satisfied.

In XRD analysis, the crystalline sample is exposed to the monochromatic radiation (X-ray) generated by cathode ray tube. The incident ray interact with the sample and produces constructive interference between diffracted rays when conditions satisfy Bragg's law. The Bragg's law state that, the constructive interference occurs when the path difference between two interfering waves is equal to the whole number, (n) of the wavelength (λ). The Bragg's formula is given by Equation (4.2) [2]:

$$n\lambda = 2d \sin \theta \quad (4.2)$$

In this equation, d is the interatomic distance (lattice spacing) and θ is the angle between the incident beam and scattering plane. The characteristic XRD pattern generated in XRD analysis provides useful information about the crystal presented in the sample. When the XRD pattern is compared with the standard reference pattern, the crystalline form can be identified.

In this thesis, the X-ray diffraction (XRD) scans were carried out using Philips PW X'pert diffractometer with Cu-K α monochromator of the wavelength of 1.54 Å at source tension and current of 40 kV and 40 mA respectively.

4.2.2 Energy dispersive X-ray spectroscopy (EDX)

Energy dispersive X-ray spectroscopy (EDX), sometimes called Energy dispersive X-ray analysis (EDXA) is an analytical technique used for the elemental analysis (elemental composition) or chemical characterisation of the materials. This technique is used in conjunction with scanning electron microscopy (SEM). In the EDX analysis, the sample is bombarded by the high energy electron beam. The electron beams collide with the inner shell electrons of atoms and eject them as shown in Figure 4.2. In this process, the electron from higher energy levels (outer shells) falls to the inner shells causing the emission of X-rays with unique amounts of energy [3]. By measuring the amount of energy released during electron beam bombardment, the identity of the atoms can be recognised.

The EDX measurements reported in this thesis were carried out using EDX detector attached to FEI Nova 200 NanoSEM.

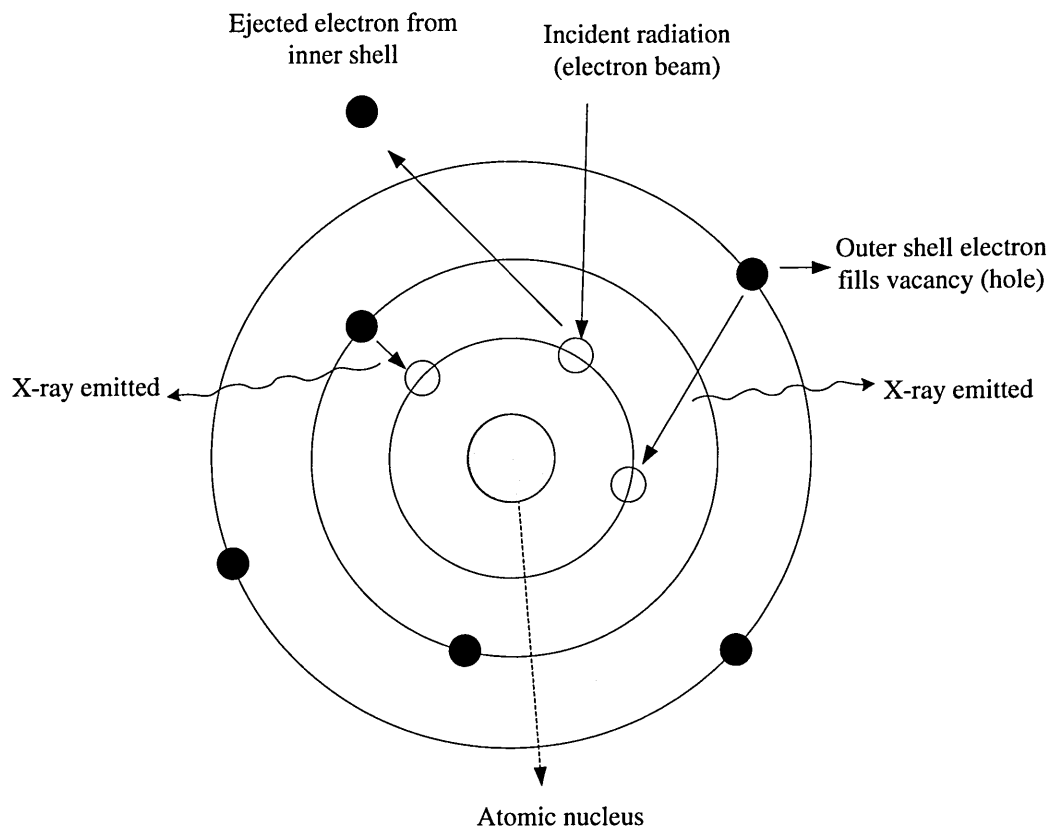


Figure 4.2: Schematic diagram of Energy Dispersive X-ray Spectroscopy (EDX).

4.2.3 X-ray fluorescence (XRF)

X-ray fluorescence (XRF) is a powerful non-destructive analytical technique used to measure the film thickness and composition, and to determine the elemental concentration of the solid materials and liquids. This technique has been used extensively in many industries such as semiconductors, microelectronics, food, agriculture, chemicals etc.

The principle operation of XRF is similar to the EDX method. The main difference between XRF and EDX is that in XRF the incident beam is X-ray beam whereas in EDX the incident beam is an electron beam. In XRF technique, an electron is ejected from inner orbital of the atom when it is irradiated with a high-energy X-ray beam. In this process, an electron from higher energy orbital (outer shell) is transferred to the lower energy level orbitals. In this transition process, the photon is emitted from the atoms which are the characteristic X-ray of the element and is called X-ray

fluorescence. Because the wavelength and energy of the fluorescence radiation is specific for each element, therefore, the fingerprint of each element can be identified.

The relationship between the wavelength λ of a characteristic X-ray photon and atomic number Z of the excited element is given by Moseley's law [5]:

$$\frac{1}{\lambda} = K(Z - s)^2 \quad (4.3)$$

where K and s are constants (s is called shielding constant and its value is close to one).

4.3 Optical spectroscopy techniques

The terms spectroscopy refers to the measurement of the intensity of electromagnetic radiation as a function of wavelength. In spectroscopic techniques, the interaction of light with matter is studied and useful information such as bandgap energy (E_g), defect levels and position of Fermi level can be extracted and analysed. There are various spectroscopic techniques used widely to study thin films. The three spectroscopic techniques used in this thesis include spectrophotometry, Photoluminescence spectroscopy (PL) and Ultraviolet photoelectron spectroscopy (UPS). These techniques are presented and discussed in the following sections.

4.3.1 Spectrophotometry

When a beam of light is incident on a sample (semiconductor), part of the light is absorbed, part is transmitted and the remaining portion is reflected back (scattered). The amount of absorption, transmission and reflection of light depends on the optical properties of the material (semiconductor thin film).

In order to determine the absorbance of a semiconductor material, a beam of light with the initial intensity (I_o) is incident on the sample, the intensity of light decreases exponentially with depth of semiconductor material according to Beer-Lambert Law as shown in Equation (4.4) [6]:

$$I = I_o e^{-\alpha d} \quad (4.4)$$

where I is the intensity of light exiting the sample, α is the absorption coefficient or attenuation coefficient which is usually expressed in units of cm^{-1} , and d is the distance in which light has travelled into the semiconductor. The transmittance (T) is defined as the ratio of the intensity of light exited from sample (I) to the initial intensity (I_o) entering the sample as given by Equation (4.5):

$$T = \frac{I}{I_o} \quad (4.5)$$

The transmittance (T) can also be related to the absorbance (A) according to the Equation (4.6) [6]:

$$A = \log_{10} \left(\frac{I_o}{I} \right) = \log_{10} \left(\frac{1}{T} \right) \quad (4.6)$$

The reflectance of the material can also be calculated from Equation (4.7):

$$R = \frac{(n-1)^2}{(n+1)^2} \quad (4.7)$$

where n is the refractive index of the material used. The absorption coefficient can be related to the transmittance (T) and material thickness (d) according to Equation (4.8):

$$\alpha = -\frac{\ln(T)}{d} \quad (4.8)$$

The absorption coefficient (α) also is related to the energy of incident light ($h\nu$) as well as the energy bandgap of the material according to Tauc's formula. The Tauc's formulas for a direct and indirect energy bandgap semiconductor are shown in Equation (4.9) and (4.10) respectively [7]:

$$(\alpha h\nu)^2 = C(h\nu - E_g) \quad (4.9)$$

$$(\alpha h\nu)^{\frac{1}{2}} = C (h\nu - E_g) \quad (4.10)$$

where C is a constant, E_g is the energy bandgap of the semiconductor material and $h\nu$ is the energy of the incident photon. Also, the absorbance (A), transmittance (T) and reflectance (R) of a material are related by the Equation (4.11):

$$A + T + R = 1 \quad (4.11)$$

Generally, there are two types of spectrophotometers; single beam and double beam setup as shown in Figures 4.3 (a) and 4.3 (b).

In single beam setup, the reference sample (e.g. substrate) is measured first in order to obtain the baseline reading. Afterward, the sample (thin film grown on the substrate) is analysed. If the intensity of light source changes slightly, this can affect the output measurement. For this reason, after a number of measurements, the reference sample should be used again as a baseline for recalibration in order to make sure that the readings are accurate.

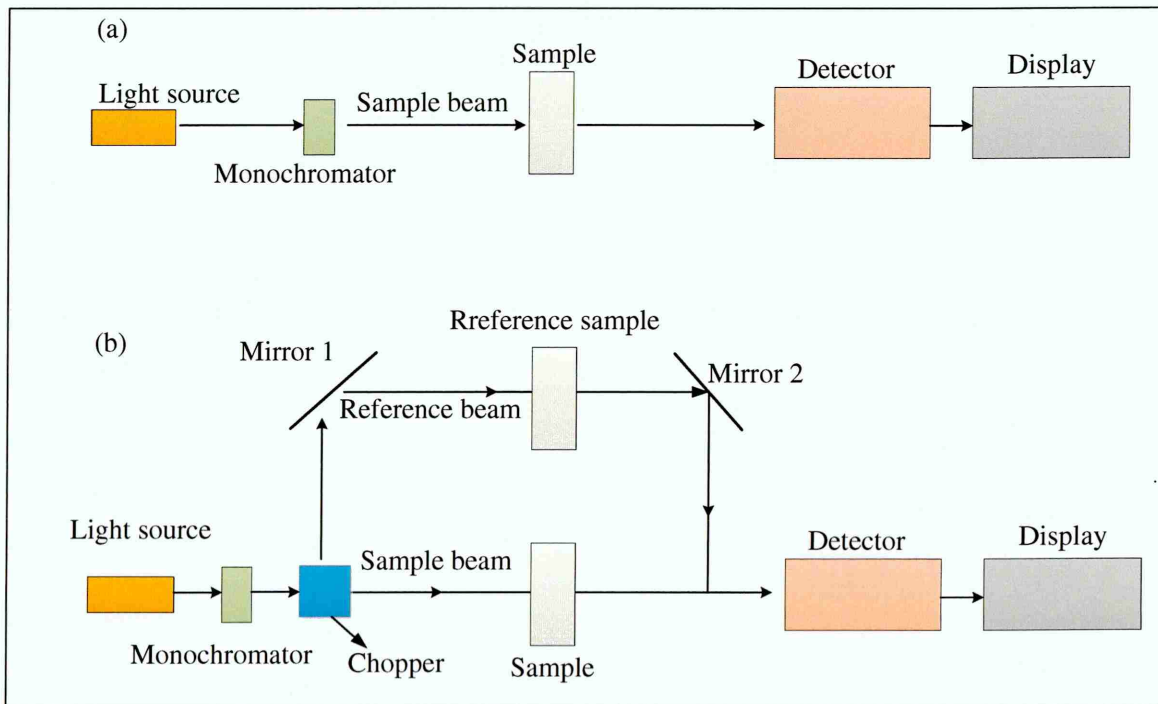


Figure 4.3: Schematic diagrams of (a) single beam and (b) double beam spectrophotometer. Redrawn from [8].

In double beam setup, the light coming from source lamp is split into two light beams. The first beam is directed towards the sample and the second beam is used to measure the reference sample. Since the reference sample is continuously being monitored at the same time and with same light intensity passing through the sample itself, it is no needed to recalibrate the spectrometer repeatedly.

Although the double beam setup gives more accurate results it has some disadvantages. The main disadvantage is that in double beam unit two mirrors are employed. If the surfaces of these mirrors are covered by dust or dirt, it will affect the accuracy of the measurements. Additionally, the mirror replacement always should be done in pairs to make sure that both mirrors give the same results. It should be noted that the single beam setups are cheaper than double beam setup.

All the optical absorption results presented in this thesis were obtained using single beam Cary 50 Scan UV/Vis spectrophotometer with.

4.3.2 Photoluminescence spectroscopy (PL)

Photoluminescence spectroscopy (PL) is a non-destructive technique used to study the electronic structure of the materials. The PL is also a useful technique used to identify the defect level distributions in the bandgap of semiconductor thin films. This technique has been used for many years for material characterisation in solar cell development.

The schematic of the PL process is shown in Figure 4.4 (a) and 4.4 (b). In PL process, a strong light source (monochromatic light or laser) is incident on the sample (semiconductors). The energetic photons which are electromagnetic radiation transfer their energy to the electrons in the valence band (VB) and excite them into higher permissible excited states or directly excite them into conduction band (CB) when the energy of light photons is higher than the bandgap energy of the semiconductor, $h\nu \geq E_g$. This process is also known as photo-excitation. The hot electron produced, gradually comes down to the minimum energy of CB through thermalisation. The excited electrons return back to their equilibrium state either by radiative (emission of light) or non-radiative process. The energy of the emitted light (photoluminescence) depends on the difference between the energy levels of two electron states. When the excited

electrons in the CB directly fall back into the VB (band to band electron transition), the energy of the emitted light corresponds to the energy bandgap (E_g) of semiconductor [9]. Otherwise, the relaxation of the excited electron will be into the defect levels which are located within the energy bandgap of semiconductors. In order to study the fingerprint of defect levels, the intensity of PL spectra is plotted as a function of photon energy ($h\nu$). The higher PL intensity means the high concentration of defect level is present with larger cross-section at that energy state. Also, the broader PL spectra indicate a large number of electron transitions to the defect levels distinguishable in a wide range of energy.

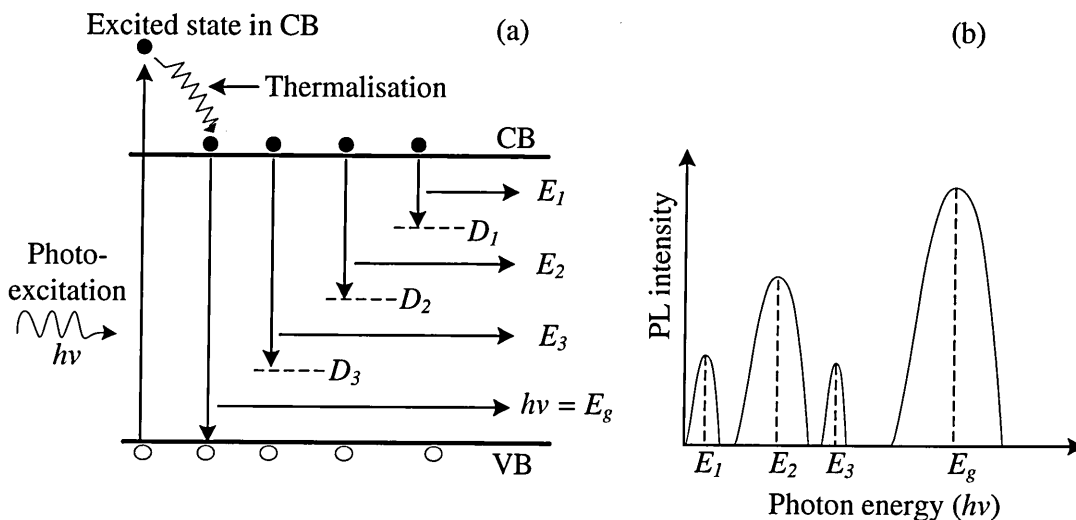


Figure 4.4: Schematic of (a) PL in a semiconductor showing excited electrons in the CB relaxing back into VB and defect levels D_1 , D_2 and D_3 , (b) PL spectra showing the defect energy levels E_1 , E_2 and E_3 as well as the band to band transition (E_g). Redrawn from [9].

4.3.3 Ultraviolet photoelectron spectroscopy (UPS)

In Ultraviolet photoelectron spectroscopy (UPS), the ultraviolet photons are used to study the surface properties of a material. However, this technique is extremely surface sensitive in which even a monolayer of contaminant is sufficient to completely change the signal obtained from the surface of the material [10]. For this reason, this technique requires ultra-high vacuum (UHV) of 10^{-10} mbar in order to avoid the attenuation of emitted photoelectrons. The major strength of UPS technique is that it has

the unique ability to study the electronic structure in the conduction/valence band region. Also, this technique is used in thin film semiconductors to determine the position of the valence band maximum (VB) and Fermi level (FL).

UPS system consists of a light source, electron energy analyser and clean polycrystalline sample in a UHV environment as shown in Figure 4.5 (a). The UPS method relies on the photoelectric effect through which a beam of monochromatic light (photons) is used to eject electrons from valence/conduction band region. Usually, the light sources used for UPS experiment are cathode discharge lamps such as Ne I, He I and He II with the photon energies of 16.86 eV, 22.21 eV and 40.40 eV respectively. These ranges of photon energies are enough to investigate the entire band structure regions of most materials.

When a monochromatic light strike the semiconductor materials, the photoelectrons from the valence band or lower-lying core levels are ejected. The measurement of the kinetic energy of the ejected photoelectrons is called ultraviolet photoelectron spectroscopy. The kinetic energy (KE) of the ejected photoelectron can be measured using Einstein formula as shown in Equation (4.12):

$$KE = h\nu - BE \quad (4.12)$$

where $h\nu$ is the energy of the incident monochromatic light photons and BE is the binding energy or sometimes called ionisation energy of the electrons. In order to analyse UPS data, the intensity of the UPS spectra is plotted as a function of KE of the photoelectrons as shown in Figure 4.5 (b).

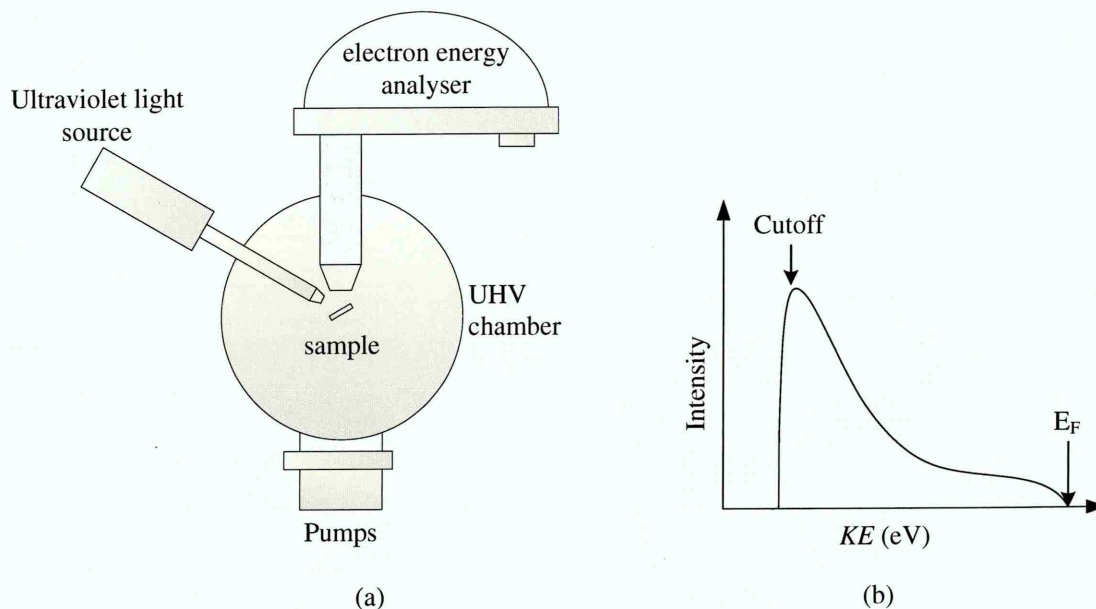


Figure 4.5: (a) Schematic of UPS system and (b) Typical UPS spectra from a metal surface. Redrawn from [11].

4.3.4 Raman spectroscopy

Raman spectroscopy as a non-destructive technique used to identify the molecular fingerprint, crystallinity, strain and stress of the solid-state materials [12]. This technique is based on the inelastic scattering of monochromatic light, generally a laser source. Inelastic scattering means that the frequency of incident photons or monochromatic light changes upon interaction with the materials. In this process, the frequency of the reemitted photons is shifted up or down as compared to the original monochromatic frequency. This process is known as Raman Effect or Raman shift. This shift provides useful information about the vibrational, rotational and other low-frequency transitions in molecules.

In Raman spectroscopy, molecules are deformed and polarised by the electric field of the oscillating electromagnetic radiation. Due to the interaction between the monochromatic light and the sample, molecules start to vibrate. In other words, monochromatic light with frequency ν_o excite molecules and transforms them into oscillating dipoles. In turn, the oscillating dipoles emit light with different frequencies (lower or higher) as compared to the frequency of incident light [13]. The emitted light is detected by a photon detector and then analysed. The resulting data is collected in the form of Raman spectrum which is used as a fingerprint to identify the materials. In this

thesis, all the Raman spectra were recorded by Renishaw's Raman (argon laser with an excitation wavelength of 514 nm) spectrometer.

4.4 Electron beam microscopy techniques

In these techniques, electron beams are used to create images of samples. These techniques are capable of obtaining images with higher resolution and magnification as compared to light microscopes. The two major electron beam microscopy techniques are scanning electron microscopy (SEM) and transmission electron microscopy (TEM) which are presented in the following sections.

4.4.1 Scanning electron microscopy (SEM)

Figure 4.6 shows the main features of a scanning electron microscope (SEM) which includes the electron gun, the anode, the lenses, the scanning coils and objective lenses to manipulate the emitted electrons from the electron gun. There are also three detectors in the SEM system in order to collect all the signals emitted by the sample. These signals are emitted due to the interaction of high energy electron beam with the specimen.

In an SEM experiment, the specimen is placed in a chamber and the pressure is reduced to $\sim(10^{-5}-10^{-7})$ mbar to create vacuum environment [14]. Then, the electron gun which is usually made of a tungsten filament heats up to about 2400°C where it starts emitting electrons. These electrons now are accelerated down the column with the help of the anode. The accelerating potential can be within the range of (1-30) kV depending on the type of materials used for the experiment. The electrons accelerated by the anode are usually scattered. For this reason, the magnetic lenses are used to focus them into a narrow electron beam. These lenses also control the number of electrons reaching the sample. The scanning coils purpose is to deflect the electron in x and y-directions so that the surface of the sample can be scanned. The final focusing of the electron beam is done by the objective lens. Then, the high energy electron beam interacts with the sample and different signals are emitted. These signals are then collected by a relevant detector and used to create an image of the surface.

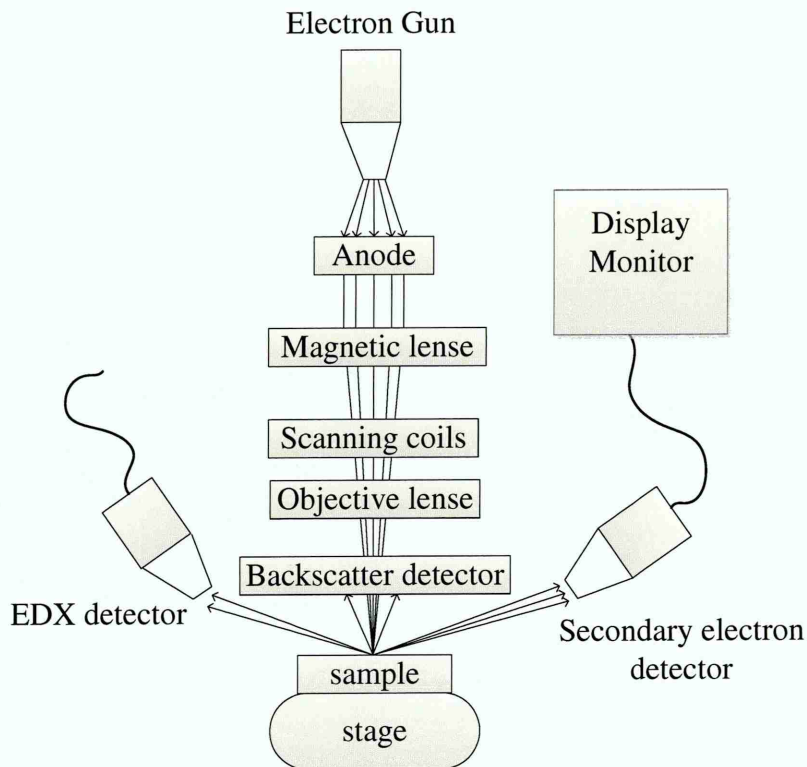


Figure 4.6: Schematic diagram of a scanning electron microscope.

There are basically three types of signals being detected by the electron microscope. These signals are the secondary electrons, the backscattered electrons and characteristic X-rays. These signals are promoted from different depth of the sample depending on their energy and nature. When electrons from primary electron beam interact with the sample, some electrons are ejected from the surface of the sample. These electrons are called secondary electrons. The secondary electrons have very low energies, so they can escape the material from near the surface (5 nm depth) [15]. The secondary electrons are then collected and detected by the positive charge collector and the secondary electron detector respectively. The generated signal is used to create the secondary electron image of the surface.

Also, some of the electrons from the primary electron beam interact with the sample in such a way that they do not lose much energy. These electrons will go deeper into the sample (400 nm depth) and come out in the similar direction. These electrons are called backscattered electrons and are collected by backscatter detector. The generated signals are then used to collect some information about the composition and crystal structure of the sample.

When the primary electron beams have sufficient energy, then they will excite the atoms of the sample and during relaxation process, the characteristics X-rays are generated. These X-rays are then collected (2 μm depth) by the EDX detector which allows measuring the atomic composition of the sample. The SEM is capable of producing an image with a resolution of (1-10) nm and their magnifications can reach 500,000 [16].

The SEM images recorded in this thesis were carried out using FEI Nova 200 NanoSEM.

4.4.2 Transmission electron microscopy (TEM)

The operation principle of the transmission electron microscope (TEM) is similar to light microscope. However, the main difference between TEM and a light microscope is that in TEM technique, an electron beam is used instead of light. Also, TEM and SEM methods are similar in some way. The major differences between TEM and SEM are; (i) in TEM method the energy of electron beam (40-400 kV) is typically higher than those of SEM (1-30 kV), (ii) in TEM technique the prepared samples are ultra-thin (5-10 nm) so that high energy electron beam can easily transmit through it. The TEM system is able to produce the image with a resolution of 0.2 nm at a magnification of 50 million times, required for atomic imaging [17,18]. TEM technique can provide detailed information about the structural quality such as the roughness of interface, lattice defect (e.g. dislocation), crystalline structure, chemical composition and morphology of the thin films. Figure 4.7 shows the schematic diagram of a typical TEM setup.

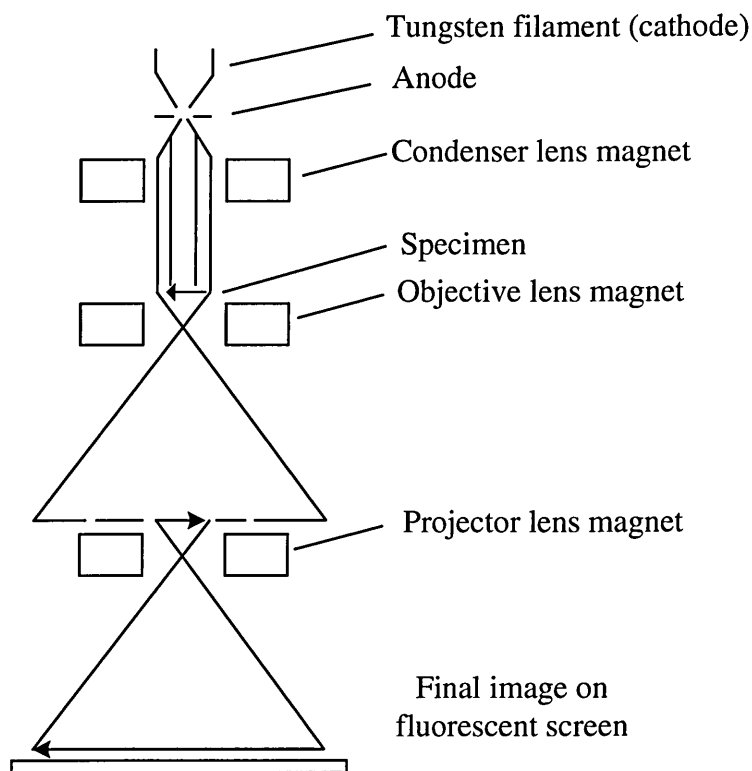


Figure 4.7: Schematic diagram showing main features of a TEM setup.

The TEM technique requires a high vacuum with a pressure of $\sim 10^{-7}$ mbar [19]. In TEM, the electrons are emitted from the electron gun (heated tungsten filament cathode). The electron beam is then accelerated by an anode at high voltage (40-400 kV). The accelerated electrons are then focused by electrostatic and electromagnetic lenses and are directed towards the sample. When the high energy electron beam reaches the sample, part of the beam is transmitted and the other part is scattered. The transmitted electron beam which carries information about the structure of the sample is then magnified by the objective lens of TEM. Then, the image is recorded by projecting the magnified electron image onto a fluorescence screen coated with phosphor. The fluorescence screen is attached to the charge-coupled device (CCD) by means of fibre optic light-guide. Then, the image is detected by the CCD and is displayed on a monitor.

4.4.3 Atomic force microscopy (AFM)

Atomic force microscopy (AFM) is a powerful surface analytical technique used to produce a high-resolution topographic image of the sample. As compared to SEM

and TEM techniques, AFM does not require the vacuum environment. This technique is able to create 3D-image of the surface features and also can magnify the surface of the sample up to 10^8 times [20]. Figure 4.8 shows the schematic of the AFM setup.

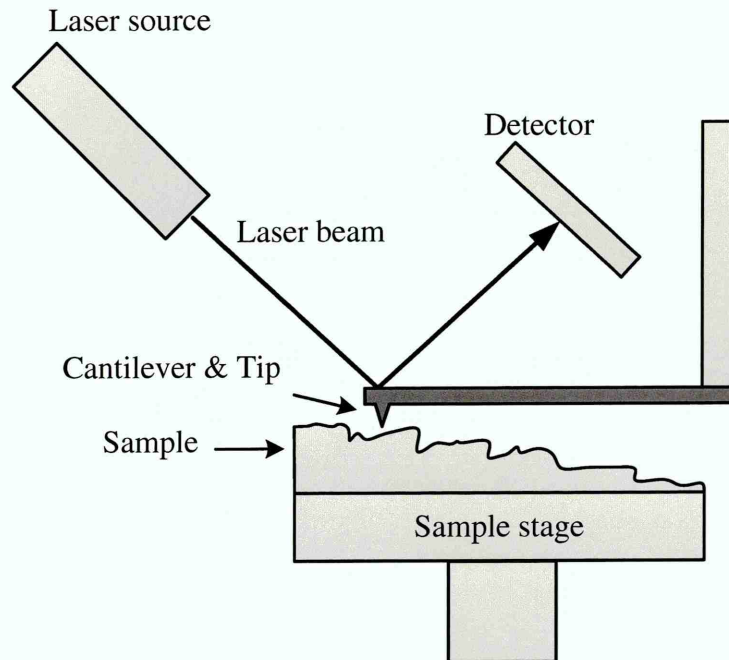


Figure 4.8: Schematic diagram of the AFM setup.

An AFM uses a cantilever (200-600 μm length) with a very sharp tip to scan over the sample surface. The AFM tips are usually made of SiN or etched Si with typical diameter in the range $\sim(15\text{-}25)$ nm and height of $\sim(10\text{-}20)$ μm [21]. The geometrical size and shape of the tips can affect the resolution of the AFM image. As the tip approaches the surface, the close-range attractive forces (Van der Waals force) between the surface and the tip cause the cantilever to bend toward the surface. However, as the cantilever even brought closer to the surface, increasingly repulsive forces (electrostatic forces) cause the cantilever to bend away from the surface. An AFM has a z-scanner which moves the cantilever up and down and x-y scanner which move the sample back and forth underneath the cantilever. Also, it has a position detector which records the bending of the cantilever. The position sensor tracks the laser beam that is reflected from the flat top of the cantilever. Any bending of the cantilever will cause changes in the direction of the reflected beam. The position detector then tracks and records those beam changes.

Using the detection method explained above, an AFM image of the sample is obtained by scanning the cantilever over the region of interest. The raised and lowered features on the sample surface influence the bending of the cantilever measured by the position detector and 2D or 3D-images of the surface can be created.

There are three major methods of AFM image; (i) contact mode, (ii) non-contact mode and (iii) intermediate contact mode (tapping mode) [22].

In contact mode, the cantilever scans across the sample with its tip touching the sample surface. Because the tip is in contact with the surface, a strong repulsive force causes the cantilever to bend as it passes over the surface features. The advantage of this method is the relative simplicity of its technology. However, one disadvantage of this method is that, the sample can be damaged by the gauging action of the sharp tip. Furthermore, while the tip is gauging away at the surface, it also grinds down the tip which reduces the quality of the image. The contact mode is usually used in surface imaging of the rigid materials.

In the non-contact mode, the cantilever oscillates above the surface while it scans but the tip does not touch the surface. A precise high-speed feedback loop is used to keep the cantilever tip from crashing into the surface. This mode retains the tip sharpness and leaving the surface untouched. As the tip approaches the surface, the interaction between the tip and the surface cause the oscillation amplitude of the cantilever to decrease. The feedback loop corrects for these amplitude deviations and constructs an image of the surface topography.

In the tapping mode, the tip is in contact with the surface to provide high resolution and then lifting the tip off the surface to avoid dragging the tip across the surface which produces the best AFM results. In the tapping mode, the cantilever oscillates at much higher amplitude of oscillation when the tip is not in contact with the surface. The bigger oscillation makes the deflection signal large enough for the control circuit and hence an easier control for topographic feedback. The tapping mode is the preferred mode of scanning for soft materials such as polymers and biological samples. [23].

The AFM images presented in this report were obtained from Nanoscope IIIa multimode atomic force microscope (AFM) at Sheffield Hallam University and JSPM-5200 AFM at Kazakhstan (Sokolsky Institute of Organic Catalysis and Electrochemistry, Almaty).

4.5 Electrical characterisation techniques

The performance of the solar cell devices essentially depends on the electrical parameters and electronic properties of the semiconductor thin films. In order to improve the quality of semiconductor thin films and develop solar cell technology, the electrical properties of the semiconductor should be understood. The electrical characterisation techniques can be used to investigate the electrical properties and improve the electronic quality of semiconductor thin films. These characterisation techniques are able to determine electrical parameters such as resistivity, charge carrier mobility, carrier concentration, depletion width, carrier lifetime, deep impurity levels etc. In this section, the common techniques which have been used to determine the electrical parameters and properties of the semiconductor thin films are presented.

4.5.1 Direct current (DC) conductivity measurements

A simple method to determine the electrical conductivity (σ) of the semiconductor thin films is to apply DC voltage to the semiconductor sample. A DC ammeter is used to measure the corresponding DC current flowing through two ohmic contacts fabricated to the semiconductor layer as shown in Figure 4.9 (a).

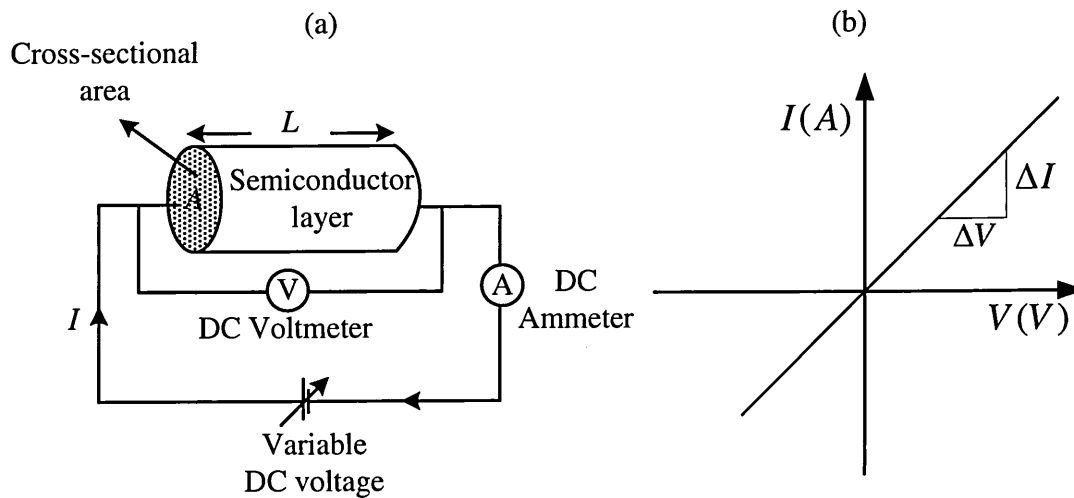


Figure 4.9: (a) Schematic of circuit diagram used to measure DC conductivity of semiconductor thin films, (b) Typical I-V characteristics measured to determine the resistance of the semiconductor thin film using Ohm's law.

The electrical circuit arrangement presented in Figure 4.9 (a) results in the straight line I-V characteristics as shown in Figure 4.9 (b). The slope of straight line is used to determine the resistance, R (Ω) of the semiconductor by applying Ohm's law as shown in Equation (4.13):

$$R = \frac{\Delta V}{\Delta I} \quad (4.13)$$

The electrical resistivity, ρ (Ωcm) is also related to the resistance of the material according to the Equation (4.14):

$$R = \frac{\rho L}{A} \quad (4.14)$$

where L (cm) and A (cm^2) are the thickness and cross-sectional area of the semiconductor thin films respectively. By re-arrangement of Equation (4.14), the electrical resistivity of the semiconductor thin film can be obtained as shown in Equation (4.15) [25]:

$$\rho = \frac{RA}{L} \quad (4.15)$$

The electrical conductivity is the reciprocal of the electrical resistivity according to the Equation (4.16) [25]:

$$\sigma = \frac{1}{\rho} \quad (4.16)$$

4.5.2 Photoelectrochemical (PEC) cell measurements

The photoelectrochemical (PEC) cell measurement is a simple technique used to determine the electrical conductivity types of semiconductor thin films. The PEC cell technique is usually used when a semiconductor layer is grown on a low resistance conducting layer. For example, in some growth techniques such as electrodeposition, a

conducting layer (transparent conducting layer (TCO)) is required to grow semiconductors. The TCO has lower resistance than the semiconductor layer, for this reason, it is not possible to use Hall Effect technique for conductivity measurement. Also, it is extremely difficult to detach the semiconductor thin film from the TCO layer to perform Hall Effect measurements. Therefore, the PEC cell measurement is a suitable alternative method to determine the conductivity types of the thin film semiconductors grown on conducting substrates [26].

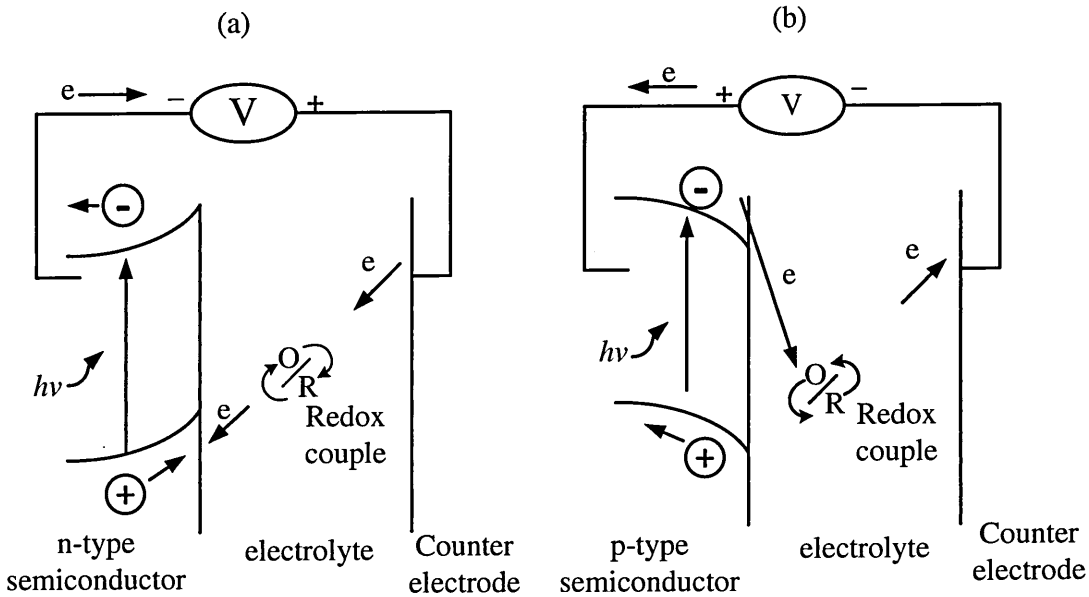


Figure 4.10: Schematic diagrams of PEC cell showing the energy band bending at the interface between (a) n-type semiconductor and (b) p-type semiconductor containing a Redox couple. Redrawn from [27].

The PEC cell method relies on the formation of a solid/liquid junction when a semiconductor is brought into intimate contact with a suitable electrolyte as shown in Figure 4.10 (a) and 4.10 (b). A Schottky barrier is formed at the solid/liquid interface when a semiconductor film is immersed in the electrolyte. This process creates band bending within the semiconductor at the solid/liquid junction. The direction of band bending depends on the conductivity type of the semiconductor. In n-type semiconductors the band bending is upward while in p-type semiconductors, the band bending is downward as shown in Figure 4.10. Then, the voltage across the TCO and the counter electrode are recorded under both dark and illuminated conditions. The

difference between the voltages under dark (V_D) and illuminated (V_L) conditions represent the PEC signal or open circuit voltage of the solid/liquid junction.

The sign of the PEC signal indicates the electrical conductivity type of the semiconductor thin film. The system can be calibrated using a known semiconducting material. The positive and negative PEC signals respectively represent the p-type and n-type electrical conduction. Metals, insulators and intrinsic semiconductors show zero PEC signals due to the very narrow depletion region in the case of metals and very wide depletion region in the case of insulators and intrinsic semiconductors. The magnitude of the PEC signal gives some qualitative information about doping density and strength of the depletion region [26]. Moderately doped semiconductors indicate large PEC signals while a highly doped semiconductors show poor PEC signals [26].

4.5.3 Hall Effect Measurements

Hall Effect is a useful technique to measure the conductivity type, carrier concentration and carrier mobility of semiconducting materials. In Hall Effect experiment, when a magnetic field is applied to a moving charged carriers (electrons or holes), the moving charge carriers are subjected to a force called "Lorentz force" given by [25]:

$$F_{Lorentz} = q (\vec{v} \times \vec{B}) \quad (4.17)$$

where q is a signed quantity indicating charge carrier, v is the particle velocity vector, and B is the magnetic field vector.

The Hall Effect measurement setup is shown in Figure 4.11. A voltage V is applied in the x-direction which creates electric field as shown in Equation (4.18):

$$E_x = \frac{V}{L} \quad (4.18)$$

where L is the length of the semiconductor thin films. If the semiconductor is n-type, the majority charge carriers which are electrons will move opposite to the direction of applied electric field (E_x), from right to left (-x). Therefore, the product of $\vec{v} \times \vec{B}$ will be in the positive y-direction for a magnetic field B directed upward on the page.

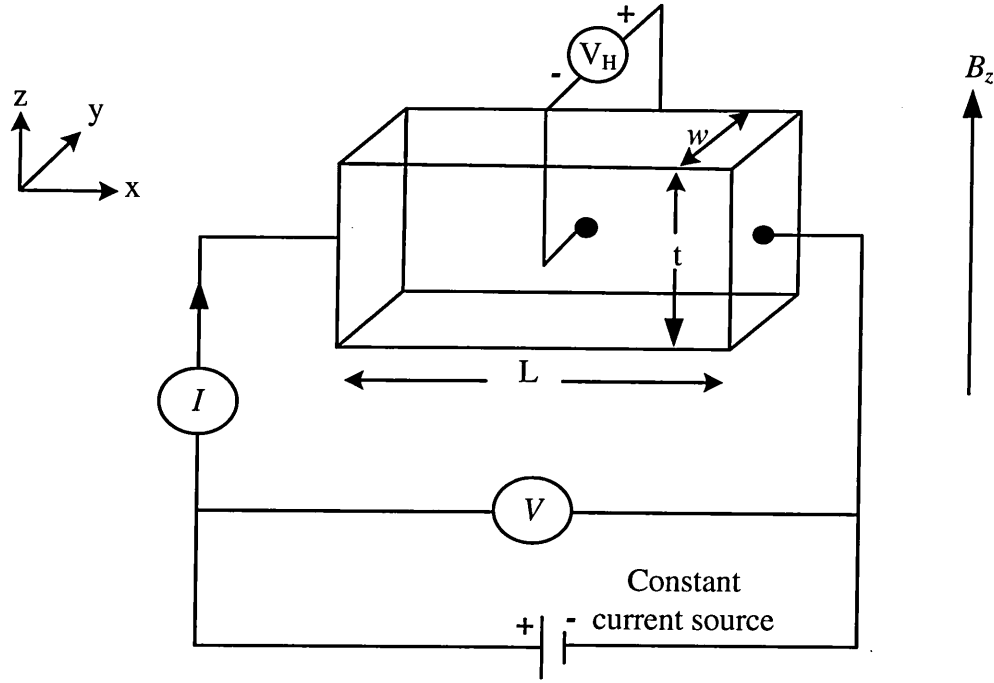


Figure 4.11: The schematic of the Hall Effect measurement setup.

Because the charge carriers are electrons, therefore the actual force will be in the negative y -direction. This force pushes the electrons towards the front edge (toward reader) of the semiconductor and the positive charge moves toward the back edge of the semiconductors. Therefore, the negative and positive charge is accumulated at two edges of semiconductor (front and back), and the electric field will be generated perpendicular to the direction of externally applied electric field E_x and magnetic field B . Eventually, the system reaches steady-state where the electric field force due to the charge accumulation (Hall Field, E_H) balances the force due to the magnetic field (Lorentz force). When the system is at steady-state or equilibrium condition, there will be no net force on the charge carriers. Therefore, a potential difference is created at the front and back edges of the semiconductor which is called Hall voltage (V_H) as shown in Equation (4.19) [25]:

$$V_H = wE_y = wE_H \quad (4.19)$$

where w is the width of the semiconductor film. In the n -type semiconductor, the V_H is negative otherwise, the positive V_H represents a p -type semiconductors. When the system is at steady-state, i.e. when the Lorentz force is equal to the Hall Field,

$$qE_H = qv_d B \rightarrow E_H = v_d B \quad (4.20)$$

Where the $v_d = v_x$ is the carrier drift velocity and is related to current density J by:

$$J = nqv_d \rightarrow v_d = \frac{J}{nq} \quad (\text{n-type semiconductor}) \quad (4.21)$$

$$J = pqv_d \rightarrow v_d = \frac{J}{pq} \quad (\text{p-type semiconductor}) \quad (4.22)$$

By substituting Equations (4.21) and (4.22) into Equation (4.20), one can obtain:

$$E_H = \frac{1}{nq} JB = R_H JB \quad (\text{n-type semiconductor}) \quad (4.23)$$

$$E_H = \frac{1}{pq} JB = R_H JB \quad (\text{p-type semiconductor}) \quad (4.24)$$

where R_H is called the Hall coefficient, also the conductivity is related to the current density J (Acm^{-2}) and electric field E according to Equation (4.25):

$$J = \sigma E = \frac{I}{A} = \sigma \frac{V}{L} \quad (4.25)$$

where I (A) is the current, $A = w.t$ (cm^2) is the area, t is the thickness of semiconductor. Therefore, Equation (4.25) can be rearranged into:

$$I = \left(\frac{\sigma A}{L} \right) V \quad (4.26)$$

by plotting I vs. V in Equation (4.26), the resistance R of the film can be obtained, and since A and L are known, therefore the conductivity of the semiconductor thin film can be calculated. Also, the carrier concentrations (n and p) of the semiconductor can be obtained using Equations (4.19), (4.23) and (4.24) as given by:

$$V_H = \left(\frac{Jw}{nq} \right) B \quad (\text{n-type semiconductor}) \quad (4.27)$$

$$V_H = \left(\frac{Jw}{pq} \right) B \quad (\text{p-type semiconductor}) \quad (4.28)$$

Since the electrical conductivity (σ) and carrier concentrations (n or p) are known, the electron and hole carrier motilities (μ_n and μ_p) can be obtained by using Equations (4.29) and (4.30) [25].

$$\sigma = nq\mu_n \quad (\text{n-type semiconductor}) \quad (4.29)$$

$$\sigma = pq\mu_p \quad (\text{p-type semiconductor}) \quad (4.30)$$

The SI unit of the carrier mobility is $\text{cm}^2\text{V}^{-1}\text{s}^{-1}$. In this thesis, all the Hall Effect measurements were carried out using Van der Pauw Ecopia HMS-3000 System with a magnetic flux density of 0.55 Tesla.

4.6 Conclusions

Various material characterisation techniques have been presented in this chapter. Some of these techniques have been used to study the structural, compositional, morphological, electrical and optical properties of the semiconductors. Other techniques have been used to investigate the electronic structure of semiconductors such as the position of the Fermi level and valence band and defect level distributions in the bandgap of semiconductors. All these techniques have been used to optimise the semiconductor thin films grown in this project for solar cell applications.

4.7 References

- [1] O.H. Seeck and B. Murphy, X-ray diffraction: *Modern Experimental Techniques*, Taylor & Francis Group, LLC, Pan Stanford, (2014) pp.2.
- [2] P. Cerry and A. Duxbury, *Practical Radiotherapy: Physics and Equipment*, Greenwich Medical Media Ltd., London, United Kingdom, (1998) pp.16.
- [3] S.T. Thornton and A. Rex, *Modern Physics for Scientists and Engineers*, 4th edition, Cengage Learning, (2013) pp.165.
- [4] <http://epimtg.blogspot.co.uk/2012/12/energydispersive-x-ray-spectroscopy-edx.html>, Last accessed February (2016).
- [5] http://grundpraktikum.physik.uni-saarland.de/scripts/X-ray_fluorescence_analysis.pdf, Last accessed February (2016).
- [6] H.C. Allen, T. Brauers, and B.J. Finlayson-Pitts, *Journal of Chemical Education*, **74**(12) (1997) 1459-1462.
- [7] B.S. Rao, B.R. Kumar, V. R. Reddy and T.S. Rao, *Chalcogenide Letters*, **8**(3) (2011) 177-185.
- [8] <http://www.slideshare.net/suniu/spectrophotometry-16091660>, Last accessed February (2016).
- [9] I.M. Dharmadasa, O.K. Echendu, F. Fauzi N.A. Abdul-Manaf, H.I. Salim, T. Druffel, R. Dharmadasa and B. Lavery, *J. Mater. Sci: Mater. Electron.*, **26** (2015) 4571-4583.
- [10] D.J. O'Connor, B.A. Sexton, and R.St.C. Smart, *Surface Analysis Method in Materials Science*, 2nd edition, Springer, (2003) pp.337.
- [11] http://www.chem.qmul.ac.uk/surfaces/scc/scat5_3.htm, Last accessed February (2016).
- [12] K.K. Nanda, S.N. Sarangi, S.N. Sahu, S.K. Deb and S.N. Behera, *Physica B*, **262** (1999) 31-39.
- [13] E. Smith and G. Dent, *Modern Raman Spectroscopy A practical Approach*, John-Wiley & Sons Ltd. (2005) pp. 4-5.
- [14] <http://www.mee-inc.com/hamm/scanning-electron-microscopy-sem/>, Last accessed February (2016).
- [15] <http://www.ammrf.org.au/myscope/analysis/eds/xraygeneration/>, Last accessed February (2016).
- [16] <http://alevelnotes.com/Magnification/106?tree=>, Last accessed February (2016).

- [17] G.J. long and F. Grandjean, *Mössbauer Spectroscopy Applied to Magnetism and Materials Science*, Vol. 2, Springer, New York, USA (1996) pp.32.
- [18] http://www.newworldencyclopedia.org/entry/Electron_microscope#cite_note-6, Last accessed February (2016).
- [19] D.B. Williams and C.B.Carter, *Transmission Electron Microscopy: A Textbook for Materials Science*, Springer Science+Business Media, LLC, New York, USA (1996) pp.119.
- [20] <http://whatis.techtarget.com/definition/atomic-force-microscopy-AFM>, Last accessed February (2016).
- [21] <http://www.nanoandmore.com/afm-tips.php>, Last accessed February (2016).
- [22] <http://www.chemistry.uoguelph.ca/educmat/chm729/afm/details.htm>, Last accessed February 2016.
- [23] H. Zhang, Y. Honda, and S. Takeoka, *Langmuir: the ACS journal of surfaces and colloids*, **29**(5) (2013) 1333-1339.
- [24] M. Gaczynska, P.A. Osmulski, *Current Opinion in Colloid & Interface Science*, **13**(5) (2013) 351-367.
- [25] S.M. Sze and K.K. Ng, *Physics of Semiconductor Devices*, 3rd edition, John Wiley & Sons, Inc., New Jersey, USA (2007).
- [26] I.M. Dharmadasa, *Advances in Thin-Film Solar Cells*, Pan Stanford Publishing Pte. Ltd, Boulevard, Singapore, (2012).
- [27] D. Wei and G. Amaratunga, *Int. J. Electrochem. Sci.*, **2** (2007) 897-912.

5.1 Introduction

This chapter discusses the device characterisation techniques used to determine the response of the fabricated solar cells to the optical and electrical excitation. Therefore, device characterisation directly deals with the finished products and also is directly related to the final goal of all research efforts, i.e. to produce efficient solar cells. However, the interpretation of the device measurement is complex due to the large number of optical and electronic effects contributed to relatively featureless results such as current-voltage (I-V) characteristics. So, the challenge of device characterisation lies not only in the measurement of the solar cells but mostly in the analysis and interpretation of data. There are varieties of device characterisation techniques which can be used to characterise the solar cells. The most fundamental device characterisation techniques are current-voltage (I-V), capacitance-voltage (C-V) and spectral response measurement techniques [1,2]. In the I-V technique, the current of the solar cells is measured as a function of applied voltage, illumination intensity, illumination positions and solar cell temperature. However, measurement of the I-V curves under standard condition is of essential importance for the determination and comparison of the opto-electrical energy conversion process. In C-V measurement technique, the capacitance of the solar cell is measured as a function of applied voltage. This technique is very important in the determination of the semiconductor parameters such as doping concentration and conductivity type. The C-V measurement is also useful in improving processes and device performance. The spectral response technique is used to measure the output current per unit incident optical power. This technique has been widely used in solar cells research and development process to test the quality and reproducibility of fabricated solar cells.

5.2 Current-Voltage (I-V) Characterisation

The I-V characterisation measures the important solar cell parameters which give the detailed description of the ability of solar cells in converting sun's energy into electricity. Some important solar cell parameters such as series resistance (R_s), shunt

resistance (R_{sh}), reverse saturation current (I_o), ideality factor (n), barrier height (ϕ_b) and rectification factor (RF) can be obtained from I-V measurement under the dark condition. The major solar cell parameters which indicate the performance of the solar cells can be measured under illumination condition including the open-circuit voltage (V_{oc}), short-circuit current density (J_{sc}), fill factor (FF) and the conversion efficiency (η). The following sections present the I-V characteristics of the solar cell under dark and illuminated condition.

5.2.1 I-V Characteristics under dark conditions

A solar cell under dark condition behaves like an ordinary diode. When diode is ideal, it completely allows the electric current without any loss under forward bias condition and completely blocks the electric current under reverse bias condition as shown in Figures 5.1 (a) and 5.1 (b).

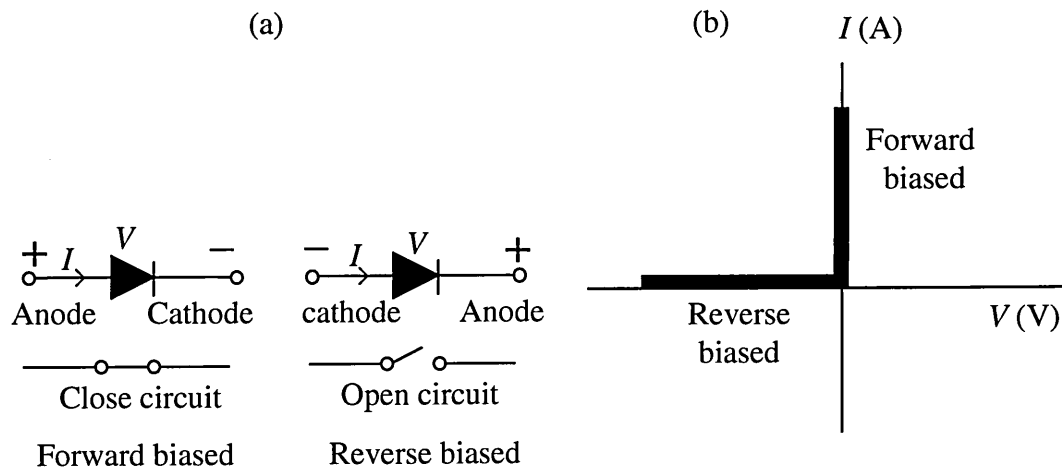


Figure 5.1: (a) The circuit symbol of an ideal diode and (b) the I-V characteristics of an ideal diode under forward and reverse biased conditions.

However, in a non-ideal diode, the effects of series resistance (R_s) and shunt resistance (R_{sh}) are present in its electronic circuits as shown in Figures 5.2 (a) and 5.2 (b):

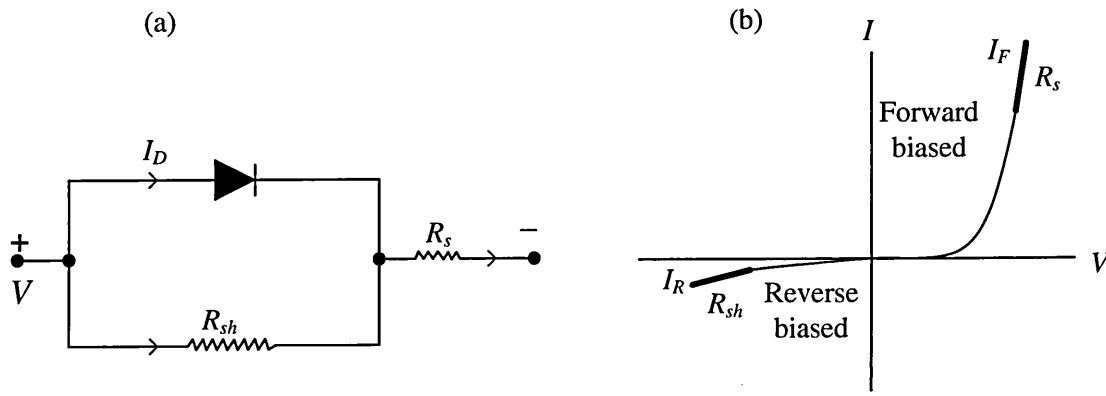


Figure 5.2: (a) The equivalent circuit and (b) the linear-linear I-V characteristics of a practical diode showing the presence of series resistance (R_s) and shunt resistance (R_{sh}).

The I-V characteristics of Schottky type diode under dark condition can be expressed by Equation (5.1) [3].

$$I_D = SA * T^2 \cdot \exp\left(\frac{-e\phi_b}{kT}\right) \left[\exp\left(\frac{eV}{nkT}\right) - 1 \right] \quad (5.1)$$

where

I_D is the dark current

S is the contact area (cm^2)

A^* is the effective Richardson constant for thermionic emission ($\text{Acm}^{-2}\text{K}^{-2}$)

T is the temperature in Kelvin

e is the electronic charge (1.602×10^{-19} C)

ϕ_b is the potential barrier height

k is the Boltzmann constant (1.3806×10^{-23} J K $^{-1}$)

n is the ideality factor of the diode

V is the applied voltage

Equation (5.1) can also be written as:

$$I_D = I_o \left[\exp\left(\frac{eV}{nkT}\right) - 1 \right] \quad (5.2)$$

where

$$I_o = SA * T^2 \cdot \exp\left(\frac{-e\phi_b}{kT}\right) \quad (5.3)$$

I_o represents the reverse saturation current of the diode. When the externally applied voltage is greater than ~ 75 mV ($V \geq 75$ mV), the term $\exp\left(\frac{eV}{nkT}\right)$ in Equation (5.2) become much larger than unity, i.e., $\exp\left(\frac{eV}{nkT}\right) \gg 1$, therefore, Equation (5.2) can be simplified to the following form [3]:

$$I_D = I_o \cdot \exp\left(\frac{eV}{nkT}\right) \quad (5.4)$$

By taking the natural logarithm of Equation (5.4), it can be rearranged as:

$$\ln I_D = \frac{eV}{nkT} + \ln I_o \quad (5.5)$$

Now, converting the Equation (5.5) into base-ten logarithmic form, Equation (5.5) can be re-written as:

$$\log_{10} I_D = \left(\frac{e}{2303nkT}\right) V + \log_{10} I_o \quad (5.6)$$

The plot of $\log_{10} I_D$ versus the applied voltage (V) across the device in Equation (5.6) is useful to obtain a number of solar cell parameters including diode rectification factor (RF), ideality factor (n), reverse saturation current (I_o) and barrier height (ϕ_b). The log-linear plot of $\log_{10} I_D$ versus V is shown in Figure 5.3.

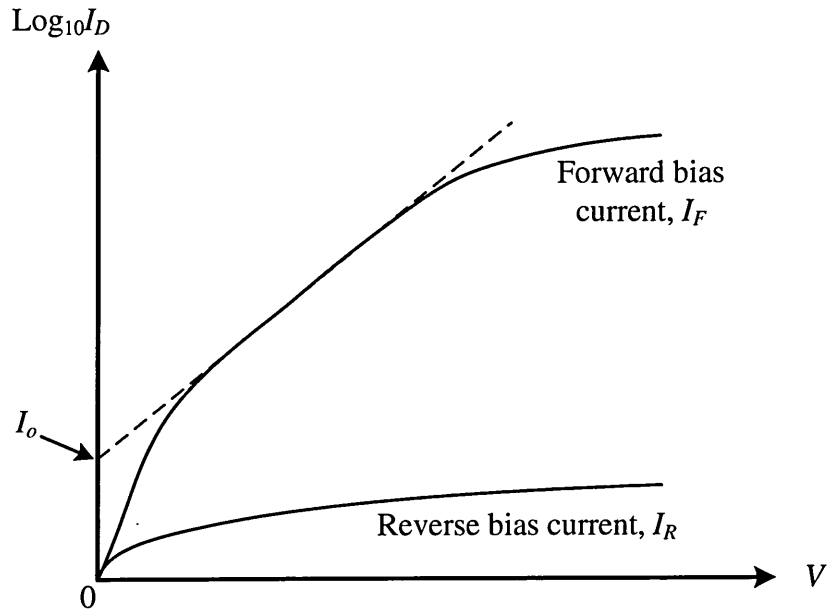


Figure 5.3: Typical Log-linear I-V characteristics of a diode measured under dark condition. For convenience, both forward current (I_F) and reverse current (I_R) are plotted in the same quadrant by changing the sign of the reverse voltages.

The RF of the device can be obtained by dividing the forward current (I_F) by reverse current (I_R) at a given voltage ($V = 1.0$ V) as shown in Equation (5.7) [3]:

$$RF = \left(\frac{I_F}{I_R} \right)_{V=1.0} \quad (5.7)$$

The RF indicates the rectifying quality of a diode, therefore, for an efficient solar cell; a large RF is desirable although the rectification of about three orders of magnitude (10^3) is sufficient to produce good quality device.

Also, in Figure 5.3 by extrapolating straight-line portion in the plot of $\log_{10} I_D$ versus V , the gradient of the straight-line can be obtained. From the gradient, n value can be calculated as shown in Equation (5.8) [3]:

$$Gradient = \left(\frac{e}{2.303nkT} \right) \quad (5.8)$$

The n value provides useful information about the current transport mechanism through the potential barrier. For an ideal diode, the current transport takes place only through thermionic emission over the potential barrier. Therefore, the n value is equal to unity ($n = 1.00$). When full recombination and generation (R&G) centres are present in the depletion region and interface of the device, the current transport will be dominated by R&G process. Therefore, the n value becomes 2.00 [3]. When both mechanisms are present, n takes a value between 1.00 and 2.00. In a device structure, the presence of the large series resistance (R_s) makes the situation even more complicated and n value can become greater than 2.00. When R_s is large, the gradient of the log-linear curve at the high forward-bias region reduces, therefore, the n value increases. Also, the tunnelling effect can increase the low forward bias current through the device which in turn reduces the gradient of the log-linear I-V curve, hence, the n value increases again [3]. It should be noted that, for real devices, the largest gradient of the I-V curve should be used in order to obtain the smallest value of n and more accurate results.

Also, the intersection of the largest gradient with $\log_{10} I_D$ axis provides the more accurate value of I_o . As soon as the I_o value obtained, then, the barrier height (ϕ_b) can be estimated using Equation (5.3).

Also, the R_s and R_{sh} of the device can respectively be estimated from the forward and reverse current portions of the linear-linear I-V curve under dark condition (see Figure 5.2).

5.2.2 I-V Characteristics under illuminated conditions

The most important part of the solar cell research and development is the measurement of the solar cell devices under illumination condition. From this measurement, the important solar cell parameters including open-circuit voltage (V_{oc}), short-circuit current density (J_{sc}), fill factor (FF) and the power conversion efficiency (η) can be obtained.

To begin, an ideal solar cell under illumination is considered first. In the ideal solar cell the $R_s=0$ and $R_{sh}=\infty$, then, one obtains the equivalent circuit of an ideal solar cell under illumination as shown in Figure 5.4.

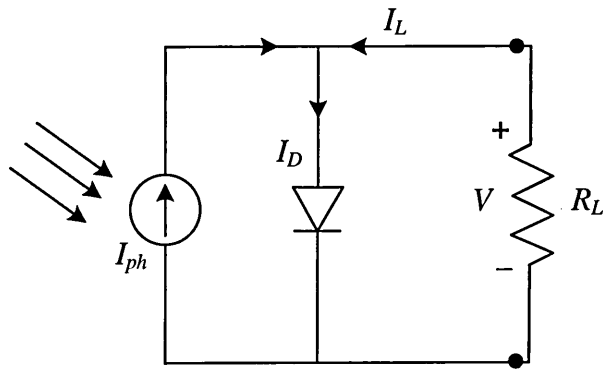


Figure 5.4: Equivalent circuit of an ideal solar cell under illumination condition. Redrawn from [4].

In Figure 5.4, the total current (load current) of the ideal solar cell under illumination is given by Equation (5.9):

$$I_L = I_D - I_{ph} \quad (5.9)$$

where I_L is the load current, I_D is the diode current under the dark condition and I_{ph} is the photogenerated current. It should be noted that the direction of photogenerated current (I_{ph}) is opposite to the direction of diode current (I_D) as shown by minus sign in Equation (5.9). Substituting I_D in Equation (5.2) into Equation (5.9) one obtains:

$$I_L = I_o \left[\exp \left(\frac{eV}{nkT} \right) - 1 \right] - I_{ph} \quad (5.10)$$

when the external circuit is kept open, i.e. when the current through the external circuit is zero, then, $I_L = 0$ and the $V = V_{oc}$. Thus, Equation (5.10) takes the form of Equation (5.11):

$$0 = I_o \left[\exp \left(\frac{eV_{oc}}{nkT} \right) - 1 \right] - I_{ph} \quad (5.11)$$

Substituting I_o in Equation (5.3) into Equation (5.11) and rearrangement of Equation (5.11) gives:

$$SA * T^2 \cdot \exp\left(\frac{-e\phi_b}{kT}\right) \left[\exp\left(\frac{eV_{oc}}{nkT}\right) - 1 \right] = I_{ph} \quad (5.12)$$

Then, the V_{oc} can be obtained by rearrangement of the Equation (5.12) as given by Equation (5.13) [3]. The I_{ph} is same as the short-circuit current (I_{sc}) of the solar cells. The short-circuit current (I_{sc}) per unit area is equal to J_{sc} , as shown in Equation (5.14), therefore:

$$V_{oc} = n \left[\phi_b + \frac{kT}{e} \cdot \ln\left(\frac{J_{sc}}{A * T^2}\right) \right] \quad (5.13)$$

Equation (5.13) shows that the magnitude of V_{oc} depends on the values of n , ϕ_b , J_{sc} and T . From Equation (5.13), it is obvious that a larger V_{oc} can be obtained when n value is high. However, in a real device, the large n values ($n \geq 2.00$) means that the rate of R&G in the device is high [3]. Therefore, J_{sc} and V_{oc} in the device drastically reduce, hence, the device will show poor performance. Also, higher V_{oc} values can be achieved when ϕ_b at the interface is higher. The ϕ_b of the cell can be improved by incorporation of an insulating layer between semiconductor and metal contact (MIS-type interface). Also, V_{oc} can be affected by the temperature of the device. As the temperature decreases, the V_{oc} value increases due to minimisation of the thermal agitation of the charge carriers [3].

The I-V characteristics of a solar cell under dark and illuminated conditions can be obtained by plotting Equations (5.2) and (5.10) together as shown in Figure (5.5). In Figure (5.5) the V_{oc} of the cell can be measured when no current flows through the external circuit and I_{sc} of the cell is a measure of current when no voltage is dropped across the external circuit. In the real device, it is more convenient to use current density J_{sc} (mAcm⁻²) instead of I_{sc} in the measurements. The J_{sc} can be obtained by dividing the I_{sc} by the contact area (S) of the cell given by Equation (5.14):

$$J_{sc} = \frac{I_{sc}}{S} \quad (5.14)$$

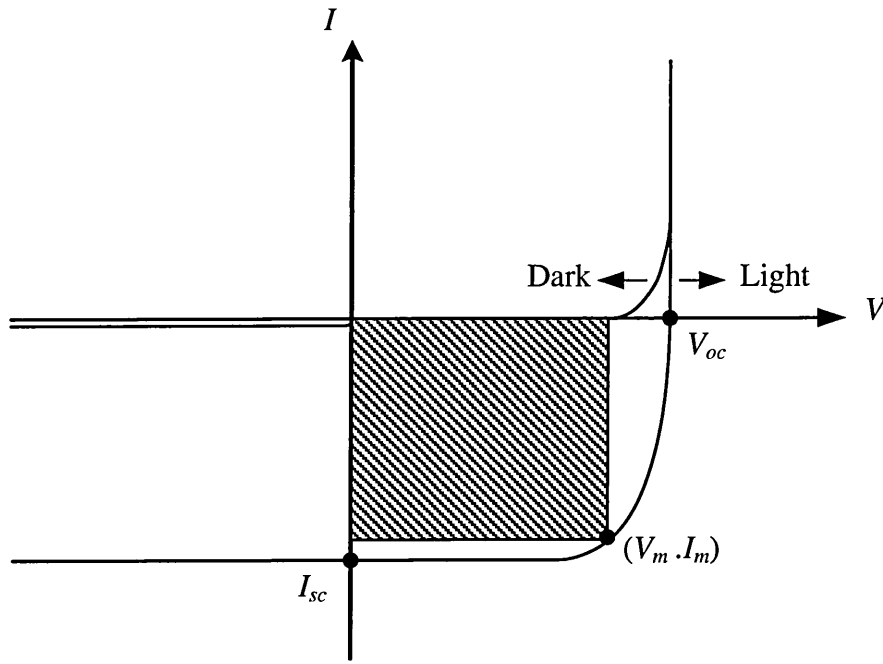


Figure 5.5: I-V characteristics of a solar cell under dark and illuminated conditions. Redrawn from [3].

The FF of the device can be obtained from the ratio of the maximum power of the solar cell to the product of V_{oc} and I_{sc} as shown in Equation (5.15) [3]:

$$FF = \frac{V_m I_m}{V_{oc} I_{sc}} \quad (5.15)$$

where the product of V_m and I_m represent the maximum power of a cell. The FF of a solar cell can be maximised by reducing R_s and increasing R_{sh} in the device. Also, the efficiency of a cell (η) can be defined as [3]:

$$\eta = \frac{\text{Output power}}{\text{Input power}} = \frac{V_m I_m}{P_{in}} = \frac{V_{oc} \cdot I_{sc} \cdot FF}{P_{in}} \quad (5.16)$$

where P_{in} is the power density of the incident light. Because the P_{in} is a solar power incident per unit area the I_{sc} should be replaced by J_{sc} . Therefore, Equation (5.16) can be written as [3]:

$$\eta(\%) = \frac{V_{oc} \cdot J_{sc} \cdot FF}{P_{in}} \times 100\% \quad (5.17)$$

The efficiency of a solar cell is generally measured under the standard illumination condition i.e. AM1.5 with P_{in} value of 1000 Wm^{-2} or 100 mWcm^{-2} .

In a practical solar cell, the effect of R_s and R_{sh} should be considered. The R_s represents the resistive losses due to the movement of current through the bulk of material of solar cells, the resistance between the metal contact and semiconductor and resistance at the front and back metal contact [5, 6]. The R_{sh} is caused by the current leakage across the junction of the solar cell or recombination of photogenerated charge carriers. The current leakages are mainly due to native crystal defects or defects introduced during manufacturing defects or inclusion of impurities in the junction region [7]. The equivalent circuit of a practical solar cell under illuminated condition is shown in Figure 5.6.

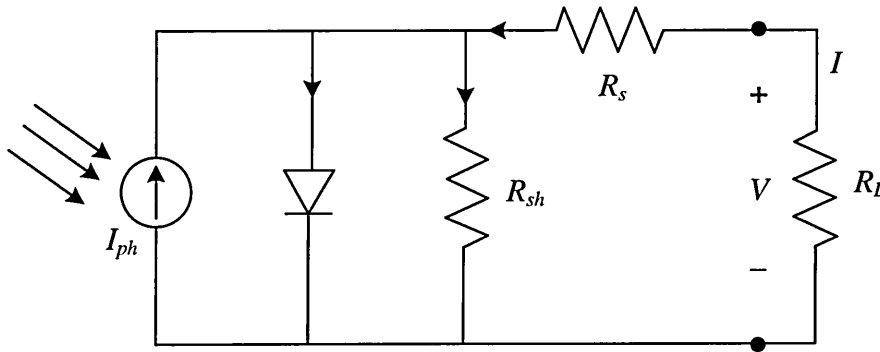


Figure 5.6: Equivalent circuit of a practical solar cell under illuminated condition. Redrawn from [8].

Equation (5.18) shows the general equation used for a practical solar cell under illuminated condition after the addition of R_s and R_{sh} into the Equation (5.10) [9]:

$$I_L = I_o \left[\exp \left(\frac{e(V - IR_s)}{nkT} \right) - 1 \right] + \frac{V - IR_s}{R_{sh}} - I_{ph} \quad (5.18)$$

5.2.3 Capacitance-Voltage characteristics

Capacitance-Voltage (CV) method is a non-destructive measurement technique which has been used widely in industry to determine the doping concentration, potential barrier height, width of the depletion region and the conductivity type of the semiconductor films [1]. In a rectifying junction device, when voltage is applied, the charge variation within the depletion region takes place which yields a voltage dependent capacitance. The capacitance associated with the charge variation in the depletion region is called the junction capacitance. The junction capacitance can be measured using the expression for the parallel plate capacitance with a separation distance of W between the two oppositely charged plates. The junction capacitance, C (in F), of a semiconductor depletion region is given by the Equation (5.19):

$$C = \frac{\epsilon_s A}{W} = \frac{\epsilon_o \epsilon_r A}{W} \quad (5.19)$$

where,

$\epsilon_s = \epsilon_o \epsilon_r$ is the permittivity of semiconductor (Fcm^{-1})

$\epsilon_o = (8.854 \times 10^{-14} \text{ Fcm}^{-1})$ is the permittivity of free space

ϵ_r is the relative permittivity

A is the contact area (cm^2)

W is the width of the depletion layer (cm)

Also capacitance can be expressed by capacitance per unit area (C_A), therefore, Equation (5.19) can be re-written as:

$$C_A = \frac{C}{A} = \frac{\epsilon_s}{W} \quad (5.20)$$

The depletion region width of a semiconductor is given by the Equation (5.21) [1]:

$$W = \sqrt{\frac{2\epsilon_s}{q} \left(\frac{1}{N_A} + \frac{1}{N_D} \right) V_{bi}} \quad (5.21)$$

Where, N_A and N_D are the acceptor and donor concentrations respectively and V_{bi} is the built-in potential. In a one-sided abrupt junction such as $p^+ - n$ junction where $N_A \gg$

N_D , the depletion region width extends more into the n-side of the junction and in the p-n⁺ junction where $N_D \gg N_A$, the depletion region width extends more into the p-side of the junction. Therefore, Equation (5.21) is simplified to Equation (5.22) [1,10]:

$$W = \sqrt{\frac{2\epsilon_s V_{bi}}{qN}} \quad (5.22)$$

Where $N=N_D$ or $N=N_A$ for p⁺-n and p-n⁺ junctions respectively. Equations (5.21) and (5.22) are based on the thermal equilibrium condition where no external applied voltage (V) is applied across the junction. In the presence of externally applied voltage, the total potential across the junction is modified to $(V_{bi} - V)$, where, V has positive value for forward bias and negative value for reverse bias. Therefore, under external applied voltage the depletion region width for one-sided abrupt junction is given by the Equation (5.23):

$$W = \sqrt{\frac{2\epsilon_s (V_{bi} - V)}{qN}} \quad (5.23)$$

The depletion capacitance of the one-sided abrupt junction under externally applied voltage can be obtained by substituting Equation (5.23) into Equation (5.19):

$$C = \frac{\epsilon_s A}{\sqrt{\frac{2\epsilon_s (V_{bi} - V)}{qN}}} = A \sqrt{\frac{q\epsilon_s N}{2(V_{bi} - V)}} \quad (5.24)$$

By rearranging Equation (5.24) and substituting Equation (5.24) into Equation (5.20), the depletion capacitance per unit area can be obtained as given by Equation (5.25) [1]:

$$C_A = \frac{C}{A} = \sqrt{\frac{q\epsilon_s N}{2(V_{bi} - V)}} \quad (5.25)$$

Now, a graph of C_A vs. V using Equation (5.25) under externally applied voltage gives a curve of the form shown in Figure (5.7). The value of C_A at zero bias ($V = 0$) gives the actual depletion capacitance per unit area (C_o) of the junction. From the C_o value in the Figure (5.7), the width of the depletion region can be determined using Equation (5.20).

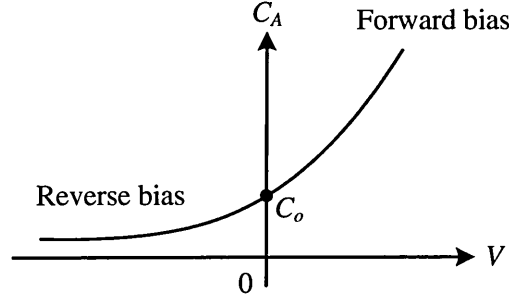


Figure 5.7: Schematic of C_A vs. V characteristics of a typical diode under forward and reverse bias conditions. Note that, the C_o value is used to determine the width of the depletion region at zero bias voltage ($V = 0$).

Now, squaring both sides of the Equation (5.25), yield,

$$C_A^2 = \frac{q\epsilon_s N}{2(V_{bi} - V)} \quad (5.26)$$

taking the reciprocal of both sides of the Equation (5.26), then [1]:

$$\frac{1}{C_A^2} = \frac{2}{q\epsilon_s N}(V_{bi} - V) \quad (5.27)$$

By plotting $1/C^2$ vs. V , in Equation (5.27), the doping concentration (N) and built-in potential (V_{bi}) can be determined. For an ideal diode fabricated in a semiconductor with uniform doping, this should give a straight line as shown in Figure 5.8. The graph $1/C^2$ vs. V is known as Schottky-Mott plot [1]. From the Schottky-Mott plot the doping concentration (N) and built-in potential V_{bi} can be determined. The slope of the Schottky-Mott plot gives the quantity $(2/q\epsilon_s N)$ and the intercept with the V -axis give the built-in potential value, V_{bi} , of the device [11]. It should be noted that, N shows the

resultant uncompensated carrier density in the semiconductor used. When the dominant dopants in the diode material are donors, then, $N = N_D - N_A$ but when the dominant dopants in the diode material are acceptors, then, $N = N_A - N_D$.

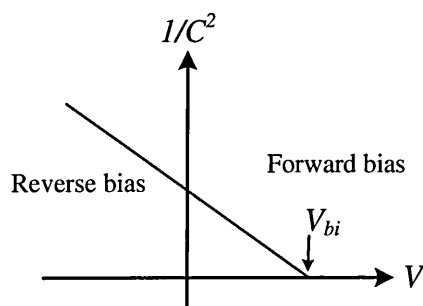


Figure 5.8: A typical shape of a Schottky-Mott plot for an ideal diode.

In the C-V technique, the measurement is usually carried out at high frequencies (1.0-10) MHz due to the presence of defect states (charge traps) in the semiconductors [12,13]. These defects are known to be slow traps, and therefore, at higher frequencies these traps do not respond (are inactive) to fast alternative current (AC) signal [14]. Therefore, more accurate measurement can be obtained at higher frequencies.

5.2.4 Spectral response characterisation

Spectral response (SR) characterisation is an important part of the solar cells research and development process. The data obtained from spectral response can be used to monitor the quality and to assess the performance of the fabricated solar cells. There are three types of spectral response which are used to characterise the solar cells. These include; spectral responsivity (SR), external quantum efficiency (EQE) and internal quantum efficiency (IQE) [15].

Spectral responsivity (SR_{λ}) is defined as the ratio of the photocurrent (I_P) to the incident light power (P) at a given wavelength (λ). In other words, the spectral responsivity is a measure of the effectiveness of the conversion of light power into electrical current. The unit of the R_{λ} is amperes per watt (A/W). The spectral responsivity is given by Equation (5.28):

$$SR_{(\lambda)} = \frac{I_p}{P} \quad (5.28)$$

External quantum efficiency (EQE) also referred to as Incident Photon to Charge Carrier Efficiency (IPCE) is defined as the ratio of the number of charge carriers collected by the solar cell to the number of photons of a given energy incident on the solar cell from outside as given by Equation (5.29) [1]:

$$\begin{aligned} EQE &= \frac{\text{electron / sec}}{\text{photons / sec}} \\ &= \frac{\text{output current / charge of one electron}}{\text{total power of photons / energy of one photon}} \end{aligned} \quad (5.29)$$

The *EQE* can also be given by [16]:

$$EQE(\lambda) = \frac{J(\lambda)}{q\phi(\lambda)} \quad (5.30)$$

where λ is the wavelength of the incident photon, $J(\lambda)$ is the photocurrent at a given wavelength, q is the charge of the electron, $\phi(\lambda)$ is the number of photon per unit area per unit time per unit bandwidth of wavelength. Also, the EQE is related to the spectral responsivity (SR_λ) by [16,17]:

$$EQE(\lambda) = SR_{(\lambda)} \frac{hc}{\lambda q} \approx 1240 \frac{SR_{(\lambda)}}{\lambda} \quad (5.31)$$

where $h = 6.626 \times 10^{-34}$ Js, is the Planck constant, $c = 3 \times 10^8$ ms⁻¹, is the speed of light and $q = 1.602 \times 10^{-19}$ C, is the electron charge. The external quantum efficiency depends on both absorptions of photon and collection of charge carriers. When photons are being absorbed and create electron-hole pairs, these charges must be separated and directed to the external circuit before recombination. The recombination of charge carriers reduces the EQE.

Internal quantum efficiency (IQE) shows the actual number of photons absorbed by the solar cell in order to generate photocurrent. When photons are incident

on the solar cell, some are absorbed, some are reflected back and the remaining part is transmitted through the solar cell. The main difference between EQE and *IQE* is that, in *IQE*, the reflected and transmitted photons should also be considered. The *IQE* can be expressed by the Equation (5.32) which is the modification of Equation (5.31) [16]:

$$IQE(\lambda) = \frac{EQE(\lambda)}{[1-R-T]} = \frac{J(\lambda)}{q\phi(\lambda)[1-R-T]} \quad (5.32)$$

Where R and T represent the fraction of the photons reflected by and transmitted through the solar cell respectively. It should be noted that the *IQE* is always higher than *EQE*. A high *IQE* means that most of the charge carriers created by incident photons are separated and collected by the external circuit.

5.2.5 Conclusions

Different device characterisation techniques including I-V, C-V and spectral response were presented in this chapter. These techniques were used to understand the behaviour of the solar cells under investigation. The I-V characterisation helps to understand the relationship between the current flowing through the device and the applied voltage across the terminals. Also, I-V characterisation helps to evaluate the performance of the solar cell in terms of its efficiency, maximum voltage and current or peak power. The C-V characterisation reveals the voltage dependence of the bulk diode material and provides useful information about depletion region capacitance of the solar cells under different bias conditions and doping profile of the material used. Spectral response characterisation provides the useful information about the solar cell performance at different wavelengths of the solar spectrum. Also, spectral response plays an important role in determining the possible loss mechanisms in the solar cell devices.

5.3 References

- [1] S.M. Sze, K.K. Ng, *Physics of Semiconductor Devices*, John Wiley & Sons, Inc., Hoboken, NJ, USA, (2006).
- [2] D. Abou-Ras, T. Kirchartz, U. Rau, eds., *Advanced Characterization Techniques for Thin Film Solar Cells*, Wiley-VCH Verlag GmbH & Co. KGaA, Weinheim, Germany, (2011).
- [3] I.M. Dharmadasa, *Advances in Thin-Films Solar Cells*, Pan Stanford Publishing Pte. Ltd, Boulevard, Singapore, 2012.
- [4] K.S. Liao, S.D. Yambem, A. Haldar, N.J. Alley, S.A. Curran, *Energies*, **3** (2010) 1212–1250.
- [5] D.K. Schroder, D.L. Meier, *IEEE Trans. Electron Devices*, **ED-31** (1984) 637–647.
- [6] A. Bosio, N. Romeo, S. Mazzamuto, V. Canevari, *Prog. Cryst. Growth Charact. Mater.*, **52** (2006) 247–279.
- [7] A.D. Dhass, E. Natarajan, L. Ponnusamy, *Proc. Int. Conf. Emerg. Trends Electr. Eng. Energy Manag.*, (2012) 382–386.
- [8] D.K. SCHRODER, *Semiconductor Material and Device Characterisation*, 3rd ed., John Wiley & Sons, Inc., New Jersey, USA, 2006.
- [9] B. Qi, J. Wang, *Phys. Chem. Chem. Phys.*, **15** (2013) 8972.
- [10] D. Neaman, *An Introduction to Semiconductor Devices*, McGraw-Hill, Inc., New York, USA, 2006.
- [11] P.E. Bagnoli, A. Nannini, *Solid. State. Electron.*, **30** (1987) 1005–1012.
- [12] J. Szatkowski, E. Płaczek-Popko, B. Bieg, A. Hajdusianek, S. Kuźmiński, *Vacuum*, **46** (1995) 545–546.
- [13] T.L. Chu, S.S. Chu, S.T. Ang, *J. Appl. Phys.*, **58** (1985) 4296–4299.
- [14] S.N. Sarangi, P.K. Adhikari, D. Pandey, S.N. Sahu, *J. Nanoparticle Res.*, **12** (2010) 2277–2286.
- [15] J.S. Hartman, M.A. Lind, *Sol. Cells*, **7** (1982) 147–157.
- [16] C.S. Solanki, *Solar Photovoltaics: Fundamentals, Technologies and Applications*, 3rd ed., PHI Learning Private Limited, Delhi, (2015).
- [17] B. Murali, S.B. Krupanidhi, *Dalt. Trans.*, **43** (2014) 1974–1983.

6.1 Introduction

Cadmium sulphide (CdS) is a group II-VI compound semiconductor with a wide and direct bandgap of 2.42 eV at room temperature (300 K) [1]. This material has been widely used in many applications due to its desirable optoelectronic properties. These applications include semiconductor lasers [2], sensors [3], radiation detectors [4,5], 0 [6], insulated gate thin film transistors [7], photoelectrochemistry applications [8], photoresistors [9] and solar cells [10-13]. In its solar cell applications, polycrystalline n-type CdS thin films with higher bandgap have been used as heterojunction partner with lower bandgap absorber materials. Some examples of the fabricated heterojunction solar cells using CdS as a window or buffer layers are CdS/Cu₂S [14,15], CdS/CuInSe₂ (CIS) [16,17], CdS/Cu(In,Ga)Se₂ (CIGS) [18,19] and CdS/CdTe [20-25]. Thin films of CdS have also been used with single crystalline absorber materials such as Si, GaAs and InP for fabrication of CdS/Si [26], CdS/GaAs [27] and CdS/InP [28] heterojunction solar cells.

A variety of techniques have been used for the growth of polycrystalline CdS thin films. Some examples of these growth techniques are close-space sublimation (CSS) [29], metal organic chemical vapour deposition (MOCVD) [30], vacuum evaporation [31], spray pyrolysis [32], chemical bath deposition (CBD) [33] and electrodeposition [34]. Using these growth techniques, good quality polycrystalline CdS thin films have been grown and then used in solar cell applications. However, most of these growth techniques require expensive and complex equipment. In other growth techniques such as CBD, the production of large Cd-containing waste is a disadvantage. The disposal or recycling of Cd-containing waste after CBD-process introduces extra cost into the production process. In addition, in a production line; it is preferable to use one growth technique for the growth of both CdS and CdTe thin films in order to reduce the production cost. For this reason, continuous growth process such as electrodeposition can be used to grow both CdS and CdTe layers in one production line with reduced manufacturing cost.

In electrodeposition method, thin films can be grown by either aqueous or non-aqueous solutions [35,36]. Some advantages of electrodeposition from aqueous solutions over non-aqueous solutions are; in the aqueous solutions the growth

temperature and the cost of the solvents are lower than the non-aqueous solutions. Also, the aqueous solutions are not flammable and have higher deposition electrolyte conductance as compared to the non-aqueous solutions [37]. For this reason, the electrodeposition of thin films from aqueous solutions has attracted lots of attention due to the lower cost of the deposition process and its simplicity, scalability and manufacturability [23]. It is worth mentioning that in the electrodeposition technique, the doping can be changed by varying the growth voltage, and hence changing the composition of the thin films without adding external impurity dopants. Also high quality and large-area semiconductor materials can be grown using this growth technique [23,38,39].

In the literature, the electrodeposition of CdS thin films has been carried out from acidic and aqueous solutions using 2-electrode and 3-electrode systems. In these reports different sulphur precursors such as sodium thiosulphate ($\text{Na}_2\text{S}_2\text{O}_3$) [40-43], thioacetamide ($\text{C}_2\text{H}_5\text{NS}$) [44] and ammonium thiosulphate ($(\text{NH}_4)_2\text{S}_2\text{O}_3$) [45] have been used. The CdS thin films grown by these precursors were polycrystalline, homogeneous, transparent and showed good adhesion to the underlying transparent conduction oxide (TCO) substrates. However, the major disadvantages of these precursors are the precipitation of elemental S and CdS particles in the solution during the growth which can affect the quality of the deposited thin films. Electrodeposition of the CdS from acidic and aqueous solutions using thiourea ($\text{SC}(\text{NH}_2)_2$) precursor has been able to overcome this disadvantage. The reports are scarce on the cathodic electrodeposition of CdS thin films from thiourea (TU) precursor and used a 3-electrode system [46].

In this work, the electrodeposition of CdS was carried out cathodically using simplified 2-electrode system. The CdS thin films were grown from a combination of TU and $\text{CdCl}_2 \cdot x\text{H}_2\text{O}$ precursors in the acidic and aqueous solutions. The main aim of this research is to establish an electrodeposition method with high stability of the electrolyte, without forming precipitates. Such a process has a huge potential in continuous growth process in an industrial manufacturing line.

6.2 Preparation of ED-CdS deposition system

An aqueous solution, 0.30 M $\text{SC}(\text{NH}_2)_2$ (99.995% purity) serving as sulphur source was made in 800 ml of de-ionised water. Afterwards, 0.20 M $\text{CdCl}_2 \cdot x\text{H}_2\text{O}$ (99.995% purity) serving as the cadmium source was added into the TU solution contained in a 1000

ml plastic beaker. The 1000 ml plastic beaker was placed inside a 2000 ml glass beaker containing de-ionised water to achieve homogeneity in heating the solution. Afterward, the pH of the aqueous solution was adjusted to 2.70 ± 0.02 at room temperature using diluted HCl or NH_4OH . The temperature of the deposition electrolyte was increased to $\sim 85^\circ\text{C}$ using a magnetic stirrer hot-plate. The TEC-7 glass/FTO (fluorine-doped tin oxide) substrates with a sheet resistance of $7 \Omega/\text{square}$ were cut into small pieces with dimensions of $2 \times 2 \text{ cm}^2$. These substrates were cleaned in an ultrasonic bath containing detergent solution for 30 minutes in order to remove any residual particles and contaminants. Afterwards, the glass/FTO substrates were cleaned with organic solvents (methanol and acetone) and subsequently rinsed with de-ionised water. The electrodeposition of CdS thin films were carried out potentiostatically using 2-electrode system. The electrodes used for the electrodeposition of CdS thin films were high purity graphite rods. One electrode serves as the anode while the other electrode serves as the contact for glass/FTO cathode. The graphite rod was attached to the glass/FTO substrate using insulating polytetrafluoroethylene (PTFE) tape. All the reagent grade chemicals and the glass/FTO substrates were purchased from Sigma Aldrich Ltd (UK). Finally, the computerised GillAC potentiostat (ACM instrument) was used to carry out the electrodeposition work.

6.3 Results and discussions

6.3.1 Voltammogram

Cyclic voltammograms were recorded for the acidic and aqueous solution containing a combination of 0.30 M $\text{SC}(\text{NH}_2)_2$ and 0.20 M $\text{CdCl}_2 \cdot x\text{H}_2\text{O}$ in 800 ml of deionised water. The pH of the aqueous solution was adjusted to 2.70 ± 0.02 at room temperature by adding diluted HCl or NH_4OH . The acidic pH was used to prevent the formation of cadmium hydroxide phase and to suppress the homogeneous precipitation of elemental S and CdS particles during the growth [44]. Afterward, the temperature of the aqueous solution was raised to $\sim 85^\circ\text{C}$. Then, cyclic voltammograms were recorded at the cathodic potentials range (0-900) mV with the scan speed of 3 mVs^{-1} and the result is shown in Figure 6.1.

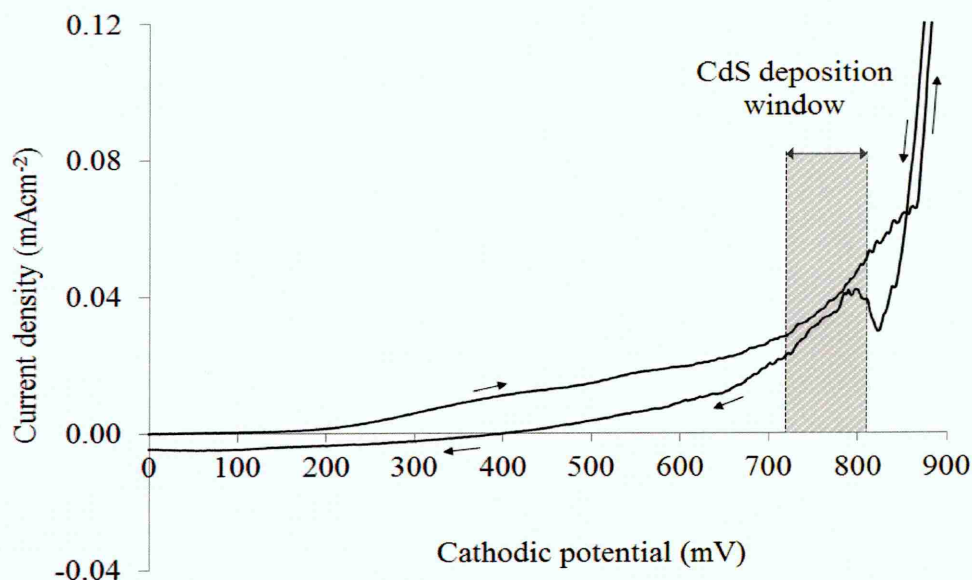
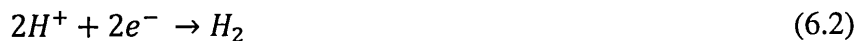


Figure 6.1: A cyclic voltammogram for acidic and aqueous electrolyte containing 0.30 M $\text{SC}(\text{NH}_2)_2$ and 0.20 M $\text{CdCl}_2 \cdot x\text{H}_2\text{O}$ at pH of 2.70 ± 0.02 and temperature of 85°C .

Study on the cyclic voltammograms of acidic and aqueous solution containing $\text{SC}(\text{NH}_2)_2$ and CdCl_2 using 3-electrode system has been reported in the literature [46]. In acidic and aqueous solutions, CdCl_2 provides Cd^{2+} ions and the electrochemical reaction of Cd deposition is as follows:



Reports show that when TU and CdCl_2 are mixed together in acidic and aqueous solutions, most of the Cd^{2+} ions bond to TU and forms Cd^{2+} -TU complexes. This is due to the high tendency of Cd^{2+} ions to coordinate with TU through S atoms [47]. For this reason, the concentration of Cd^{2+} -TU complexes will be much higher than Cd^{2+} ions in the deposition electrolyte. In this case, the deposition of elemental Cd shown in Equation (6.1) can only take place at higher cathodic potentials (in this work more than 820 mV) as shown in Figure 6.1. It should be noted that, the TU is fairly stable in acidic solution but it easily decomposes in alkaline solution. In this case, in acidic and aqueous solution containing Cd^{2+} -TU complexes; none of the constituents, Cd^{2+} or TU, can electrochemically reduce to give CdS but the chemical decomposition of Cd^{2+} -TU complex is promoted under increased pH that is generated by electrochemical reduction of hydrogen and/or oxygen as shown in Equations (6.2) and (6.3):



These reactions raise pH at the vicinity of the electrode (FTO surface) to promote the chemical decomposition of TU. However, in the bulk solution pH remains low. TU undergoes decomposition when pH is raised as shown in Equation (6.4) [48]:



Then H_2S react with Cd^{2+} to form CdS according to the following electrochemical reaction:



In Figure 6.1, the gradual increase in the cathodic current in the range $\sim(150-740)$ mV during the forward scan is due to sulphur deposition and reactions shown in Equations (6.2) and (6.3) which trigger the film growth. Further increase in cathodic current from $\sim(740-820)$ mV results in the CdS layer formation on the FTO surface which agrees with the experimental observations. The sharp increase in the cathodic current at cathodic potential >820 mV is due to the deposition of elemental Cd.

6.3.2 Visual appearance of ED-CdS layers with growth voltage

Figures 6.2 (a) and (b) show the visual appearance of the as-deposited and annealed CdS layers grown at cathodic potential range of 740 to 820 mV. For this experiment, all CdS layers were grown on glass/FTO substrates for 2 hours duration. This growth voltages range was selected from cyclic voltammograms study and experimental observations. The visual appearance can give some qualitative information about the electrodeposited CdS layers.

Results show the light yellowish-green colours for the samples grown at lower growth voltages. The light yellowish-green colour is due to the S-richness of the CdS layers. This is because S (with standard reduction potential $E^{\circ} = -0.14$ V vs. NHE)

deposits first since it has a more positive standard reduction potential than Cd ($E^0 = -0.40$ V vs. NHE) [49]. As the growth voltage increases gradually, more elemental Cd is deposited and therefore layers gradually become darker in colour as shown in Figure 6.2 (a).

From the visual appearance of as-deposited CdS layers, it is obvious that the as-deposited CdS layers require post deposition annealing in order to improve their microstructural and optical properties suitable for device fabrication. After annealing at 400°C for 20 minutes in air, the CdS layers become uniformly orange-yellowish colour as shown in Figure 6.2 (b). The CdS formation is also possible by combining excess un-reacted elemental S and Cd upon heat treatment. CdO formation is also possible by oxidation of elemental Cd due to heat treatment in air. The energy bandgap of CdO is ~ 2.28 eV [50] very close to that of CdS (~ 2.42 eV) and therefore layers become uniformly orange-yellowish colour.

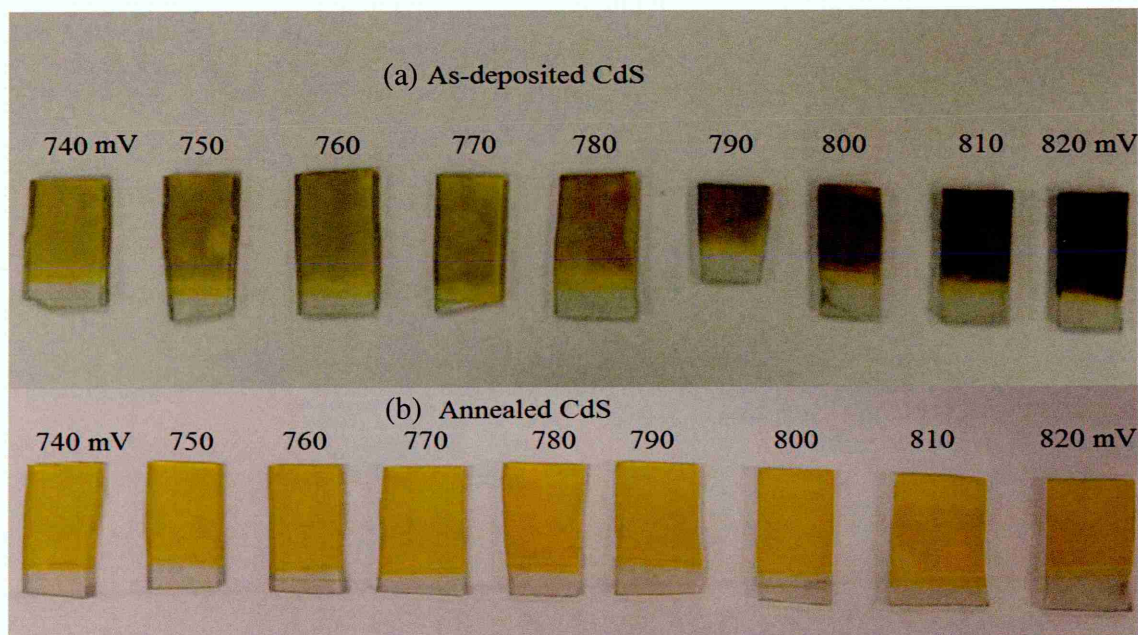


Figure 6.2: Variation of visual appearance as a function of growth voltage for (a) as-deposited and (b) annealed CdS layers.

6.3.3 X-ray diffraction

Figure 6.3 (a) shows the XRD patterns of the as-deposited CdS layers grown on glass/FTO substrates at different cathodic potential range of 740 to 820 mV. This

investigation was carried out in order to find the optimum growth voltage by observing the most intense XRD peaks for the CdS layers. The growth duration for all the as-deposited CdS layers was 2 hours. Among all the CdS samples, the layers grown in the vicinity of 800 mV showed better crystallinity as shown in Figure 6.3 (b).

According to the results presented in Figure 6.3 (a), all CdS layers were polycrystalline with hexagonal crystal structure. Three small XRD peaks observed at 2θ values in the range $(24.88-24.95)^\circ$, $(28.21-28.57)^\circ$ and $(48.01-48.41)^\circ$ represent the diffractions from (100), (101) and (103) hexagonal planes respectively. The preferred orientation peak was observed at 2θ values in the range $(26.53-26.59)^\circ$ representing the diffraction from (002) hexagonal plane which overlaps with a peak from the underlying FTO. For this reason, the analysis were mainly focused on the (101) XRD peak which is the second intense peak next to the (002) peak. In this work, the experimentally observed XRD peaks are in a good agreement with JCPDS file number: 01-080-0006 for the hexagonal CdS.

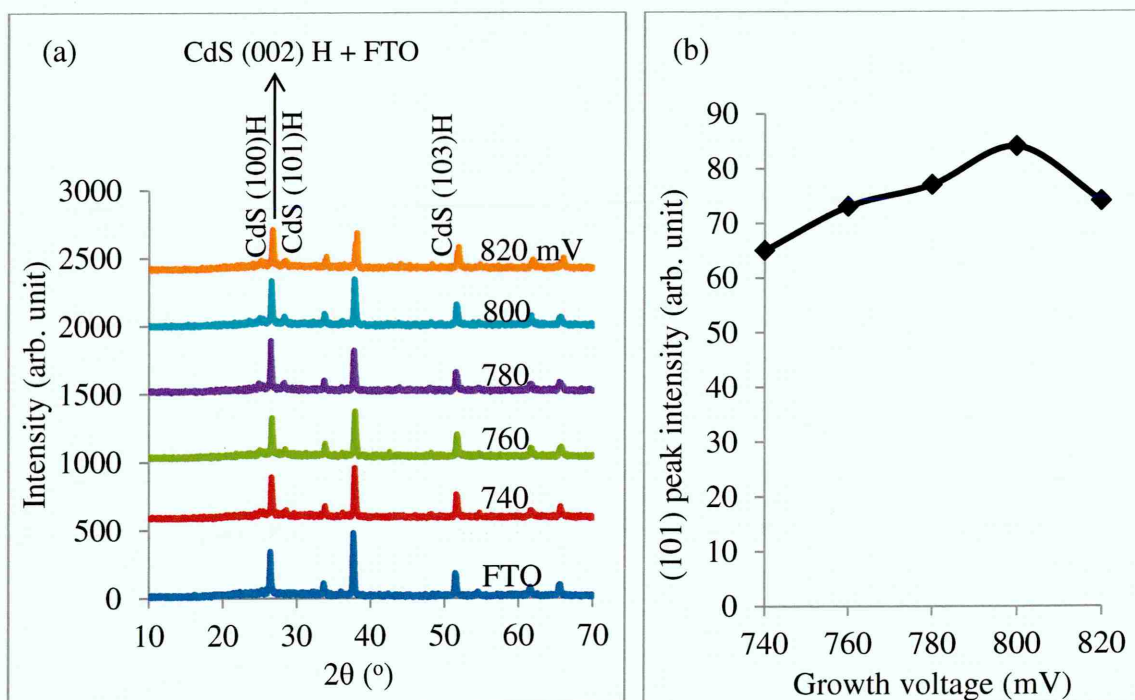


Figure 6.3: (a) XRD patterns of the as-deposited CdS layers grown at the cathodic potentials range (740-820) mV, and (b) the intensity variation of (101) peak as a function of growth voltage.

Similar hexagonal crystal structure has been reported by Yamaguchi *et al* for the electrodeposited CdS layers grown on the ITO substrates from the combination of TU

and CdCl_2 in acidic and aqueous solution [46]. In their reports, the (002) peak is clearly shown to be preferred orientations due to non-overlapping (002) with underlying ITO peaks. Also, hexagonal structure or mixture of hexagonal and cubic crystal structures have been reported for the as-deposited CdS layers grown from different precursors including $\text{C}_2\text{H}_5\text{NS}$ [44], $\text{Na}_2\text{S}_2\text{O}_3$ [40] and $(\text{NH}_4)_2\text{S}_2\text{O}_3$ [45]. In these reports, the hexagonal phases were shown to be more stable than cubic phases at high temperatures for the electrodeposited CdS layers as the cubic phases has completely disappeared after annealing at 400°C for 20 minutes in air.

The optimisation of the growth voltage was narrowed down by growing the CdS layers close to the cathodic potential of 800 mV. For this reason, the CdS layers were grown at the cathodic potentials in the vicinity of 800 mV with 1.0 mV potential step difference while keeping other growth parameters constant. All CdS layers again were grown on glass/FTO substrates for 2 hours. Afterwards, the as-deposited CdS layers were annealed at 400°C for 20 minutes in air and results are shown in Figures 6.4 (a) and (b).

In order to find the best growth voltage for the CdS layers, the intensities of (101) peaks were plotted against the growth voltages for both as-deposited and annealed CdS layers as shown in Figure 6.4 (c). The best crystallinities were observed for the CdS layers deposited at the growth voltage of 797 mV before and after annealing. This growth voltage is related to the stoichiometric point (V_i) where the ratio of Cd/S is close to unity. The lower peak intensities were observed for the layers grown away from the growth voltage of 797 mV due to non-stoichiometric properties (S-richness or Cd-richness) of the deposited layers (see later EDX results for compositions in section 6.3.7). It should be noted that the (101) peak intensities for all CdS layers were improved after annealing as shown in Figure 6.4 (c). This is due to enhancement in crystallinity, grain growth and recrystallisation in the CdS layers after annealing. This shows that for the low temperature solution growth techniques such as electrodeposition and CBD, the post-deposition annealing is an essential step to improve the material quality of the CdS layers.

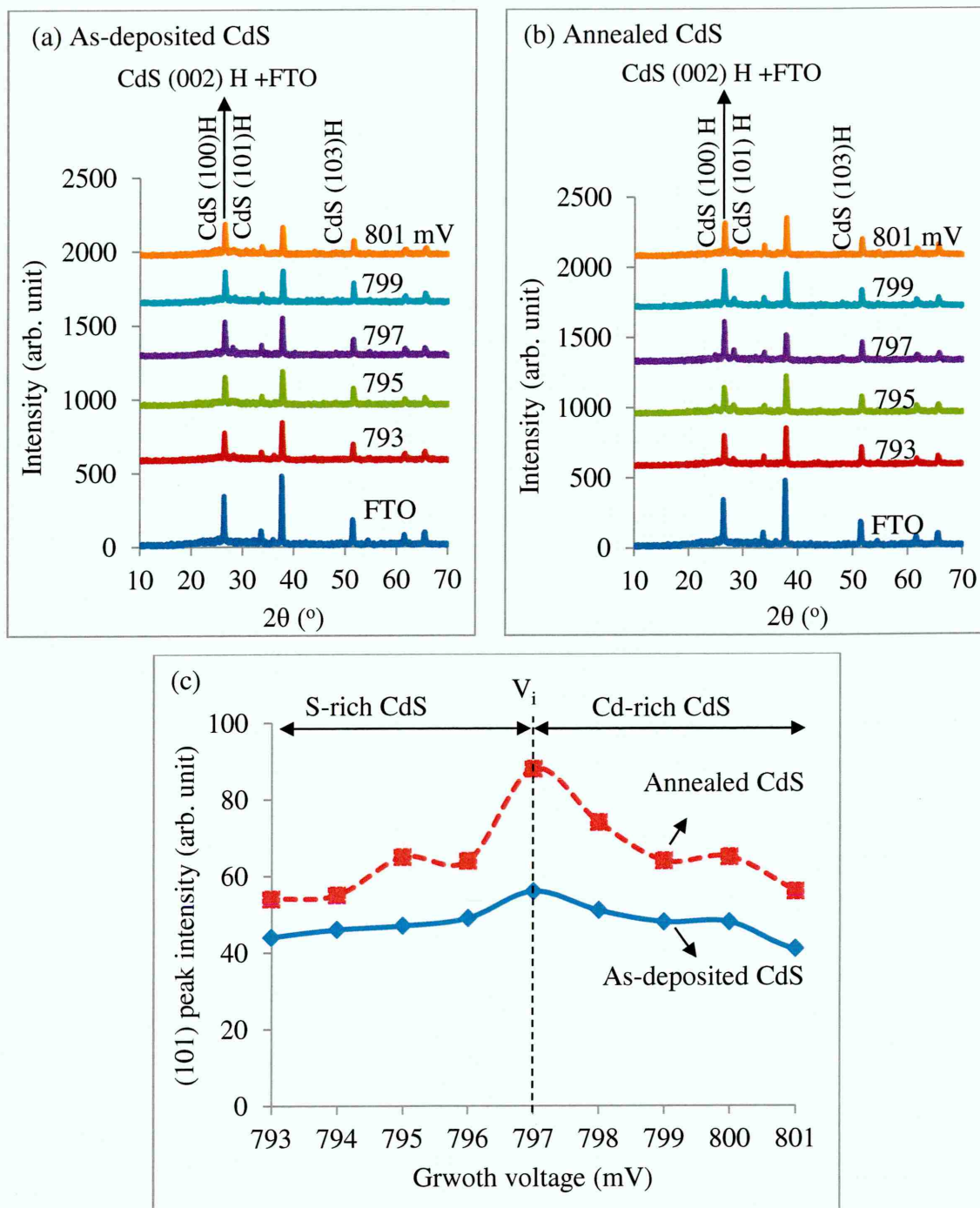


Figure 6.4: The XRD patterns of (a) as-deposited, (b) annealed CdS layers, and (c) the intensity variation of (101) peak as a function of growth voltage for the as-deposited and annealed CdS layers. All CdS layers were grown at growth voltage ranges of 793 to 801 mV for 2 hours duration and then annealed at 400°C for 20 minutes in air.

Table 6.1 shows the variation of the FWHM and the corresponding crystallite sizes as a function of growth voltages for the as-deposited and annealed CdS layers. The

FWHM and crystallite size calculations were based on diffraction from CdS (101) XRD peaks. The crystallite sizes were estimated using the Scherrer's formula as given by [51]:

$$D = \frac{0.94\lambda}{\beta \cos \theta} \quad (6.6)$$

Where, D is the crystallite size in (nm), λ is the X-ray wavelength in (Å), β is the full width at half maximum (FWHM) in degrees and θ is the Bragg angle in degrees. For the as-deposited CdS layers grown at the growth voltage ranges of 793 to 801 mV, the crystallite size values were in the range ~(11-22) nm. After annealing, the crystallite sizes were improved with the values in the range ~(26-33) nm. This is due to the recrystallisation and coalescence of crystallites, reduction in stress/strain and improvement in the structural properties of CdS layers after annealing. It should be noted that, depending on the growth techniques and growth conditions, the crystallite sizes of the CdS thin films can be different. In electrodeposition growth technique, the crystallite sizes can also be different depending on the precursor, growth temperature and pH values used for the growth of thin films [52,40,44,45]. Reports show that, CdS layers grown by high temperature growth techniques produce larger crystallites and larger grains as compared to the low temperature growth techniques such as CBD and electrodeposition [53,54].

Table 6.1: Variation of crystallite size as a function of growth voltage for the as-deposited and annealed CdS layers based on (101) peak.

Growth voltage (mV)	2θ (°)		FWHM (°)		Crystallite size (nm)	
	As-deposited	Annealed	As-deposited	Annealed	As-deposited	Annealed
793	28.44	28.28	0.519	0.259	16	33
794	28.25	28.28	0.779	0.324	11	26
795	28.21	28.32	0.519	0.324	16	26
796	28.27	28.57	0.519	0.324	16	26
797	28.41	28.26	0.389	0.259	22	33

798	28.38	28.26	0.779	0.324	11	26
799	28.49	28.41	0.779	0.259	11	33
800	28.41	28.27	0.779	0.324	11	26
801	28.39	28.26	0.519	0.259	11	33

6.3.3.1 Effect of annealing temperature on the XRD patterns of ED-CdS layers

This experiment was carried out to study the effect of different annealing temperatures on the XRD patterns of the electrodeposited CdS layers. For this reason, CdS layers were grown on glass/FTO substrates at cathodic potential of 797 mV for 2 hours duration. Then, the as-deposited samples were divided into nine parts; the first part remained as as-deposited and remaining eight parts were annealed at different temperatures, ranging from 200 to 550°C. The annealing time for each sample was set to 20 minutes in air. The aim of this experiment was to find the optimum annealing temperature for the CdS layers and results are shown in Figures 6.5 (a) and (b).

Results show that as the annealing temperature increased from 200 to 450°C, the (101) peak intensity were also increased gradually. However, the intensity of the (101) peak were reduced when the annealing temperature exceeds 450°C. These results clearly show that the crystallinity of the CdS layers improves as the temperature increases from 200 to 450°C. Further increase in the annealing temperature (above 450°C), lead to the reduction in the intensity of (100), (101) and (103) peaks. At the annealing temperature of 550°C, the (100) and (101) were reduced drastically (approximately disappeared) which clearly indicates the material losses by sublimation (see SEM images in section 6.3.6.2). In addition, two new peaks appeared at $2\theta = 21.44^\circ$ and $2\theta = 40.99^\circ$ after annealing at temperature of 550°C which is corresponding to the diffraction from CdS₂O₇ (002) and (052) monoclinic planes. These two peaks are in good agreement with JCPDS file number: 01-078-1874 for the monoclinic CdS₂O₇. These observations show that when CdS layers are annealed at high temperature (550°C) in air, the layers oxidised and CdS₂O₇ phase was formed. Depending on the XRD results obtained in this section and optical absorption spectra (see section 6.3.5) and SEM images (see section 6.3.6), the optimum annealing temperature was found to be 400°C for 20 minutes.

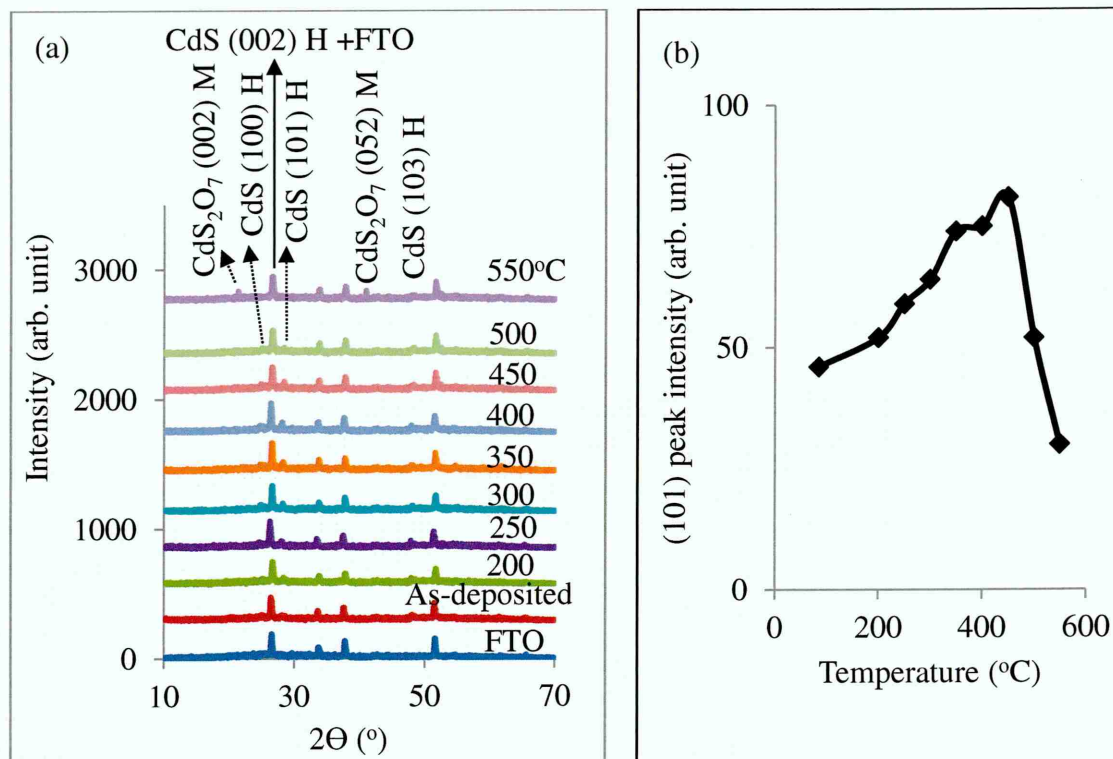


Figure 6.5: (a) Variation of XRD patterns and (b) (101) peak intensity for the as-deposited and annealed CdS layers at different temperature ranges of 250 to 550°C in air. Note that, the CdS layers were grown on glass/FTO substrates at cathodic potential of 797 mV for 2 hours duration. The annealing time for each sample was set to 20 minutes.

6.3.3.2 Effect of annealing time on the XRD patterns of ED-CdS layers

In this experiment, the effects of annealing time on the XRD patterns of the electrodeposited CdS layers were studied. Therefore, the CdS layers were grown on glass/FTO substrates at cathodic potential of 797 mV for 2 hours duration. Then, the CdS layers were divided into seven parts; the first part left as-deposited and the remaining six parts were annealed at 400°C in air for different durations of 5, 10, 15, 20, 25 and 30 minutes, respectively and results are shown in Figures 6.6 (a) and (b).

Results show that as the annealing time increase from 5 to 30 minutes, the intensity of (101) peak intensity also increases gradually. The increase in the (101) peak intensity is due to the recrystallisation, grain growth and improvement of the structural properties of CdS layers after annealing in air. Reports show that annealing in the presence of oxygen promotes the formation of nano crystallites in the CdS thin films. Also, oxygen promotes the recrystallisation and interfusion at CdS/CdTe interface which in turn improves the solar cells performance [55]. In addition, incorporation of

oxygen during the growth or annealing improves the electrical parameters and material characteristics of CdS/CdTe solar cells [56].

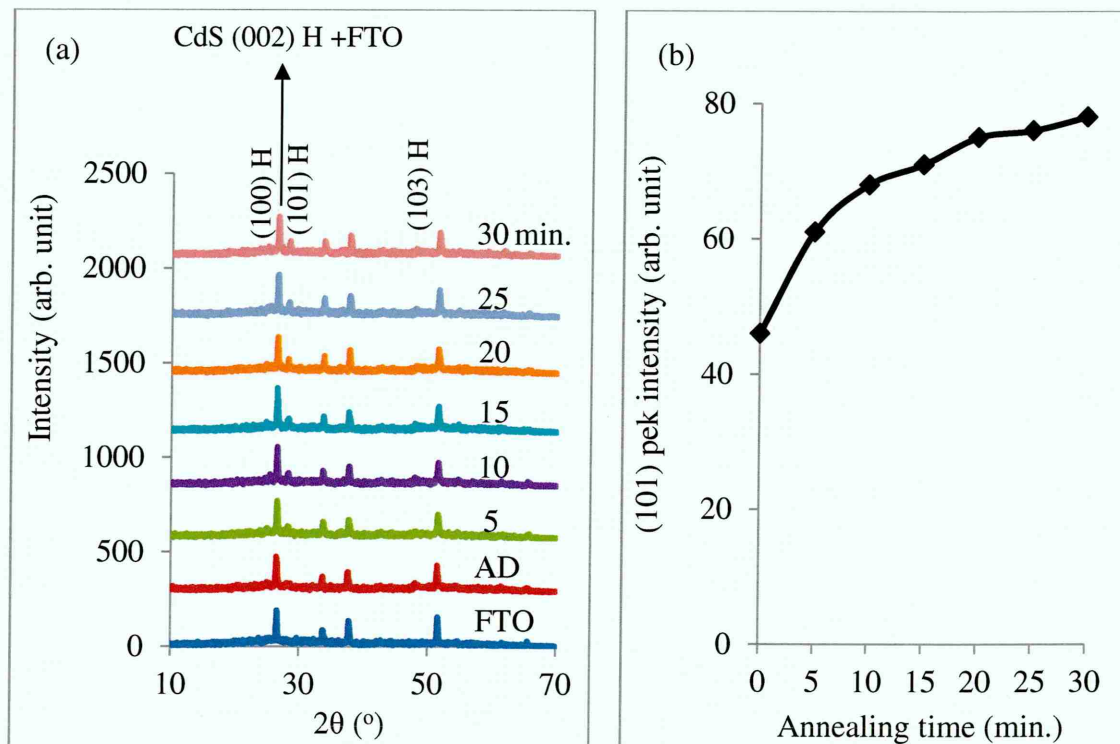


Figure 6.6: (a) Variation of XRD patterns and (b) (101) peak intensity with annealing at 400°C for different durations for the CdS layers. The CdS layers were grown on glass/FTO substrates at cathodic potential of 797 mV for 2 hours duration.

Table 6.2 shows the crystallites sizes for the CdS layers annealed at 400°C for different durations of 5 to 30 minutes in air. The crystallite sizes were estimated using Equation 6.6. Results show that as the annealing time increase from 5 to 30 minutes, the crystallites sizes also increases from ~11 to ~44 nm.

Table 6.2: Variation of the crystallite sizes with annealing time for the CdS layers. All CdS layers were annealed at 400°C in air for different durations of (5-30) minutes.

Annealing time (°C)	2 θ (°)	FWHM (°)	Crystallite size (nm)
As-deposited (0)	28.25	0.779	11
5	28.34	0.324	26
10	28.29	0.259	33
15	28.29	0.259	33
20	28.23	0.259	33
25	28.28	0.227	37
30	28.23	0.194	44

6.3.4 Variation of thickness with growth time for the ED-CdS layers

Thickness measurement is important in thin film solar cells development. The CdS thickness can directly affect the performance of the solar cells. In the device application, CdS thin films are usually used as a window or buffer layers. Reports show that CdS with a thickness of ~100 nm can absorb about 63% of the incident photons with energy greater than the bandgap (E_g) of CdS due to its high absorption coefficient of about 10^4 to 10^5 cm⁻¹ [57, 58]. For this reason, in order to increase the photocurrent in the solar cells, the CdS thickness should be as low as possible ~(50-80) nm [59]. It should be noted that by lowering the thickness of CdS, the possibility of creation of pinholes in the layer also increases. These pinholes create shunting paths within the CdS/CdTe solar cells which will affect the performance of the solar cells. Reducing the thickness of CdS can also adversely affect the open circuit voltage (V_{oc}) and fill factor (FF) of CdS/CdTe solar cells [12]. The ability to grow pinholes-free CdS layers with low thicknesses depends on the growth technique and substrate used.

In this work, the CdS layers thicknesses were measured experimentally using UBM microfocus optical depth profilometer (UBM, Messettechnik GmbH, Ettlingen, Germany). The theoretical thicknesses were estimated using Faraday's law of electrolysis for comparison as shown in Equation 6.7 [60]:

$$T = \frac{JtM}{nF\rho} \quad (6.7)$$

Where T is the thickness of the CdS layer, J is the average deposition current density, M is the molecular weight of the CdS, n is the number of electrons transferred in the reaction for formation of one molecule of CdS ($n = 2$), F is the Faraday's constant and ρ is the density of CdS.

Figure 6.7 shows the variation in CdS thicknesses as a function of growth time. Both theoretical and experimental values show approximately linear increase in film thickness with deposition time. The difference in the theoretically estimated and experimentally measured thickness values is due to the loss of some electronic charges in the electrolyte during electroplating. In this experiment, the error in thickness measurement was about ± 50 nm.

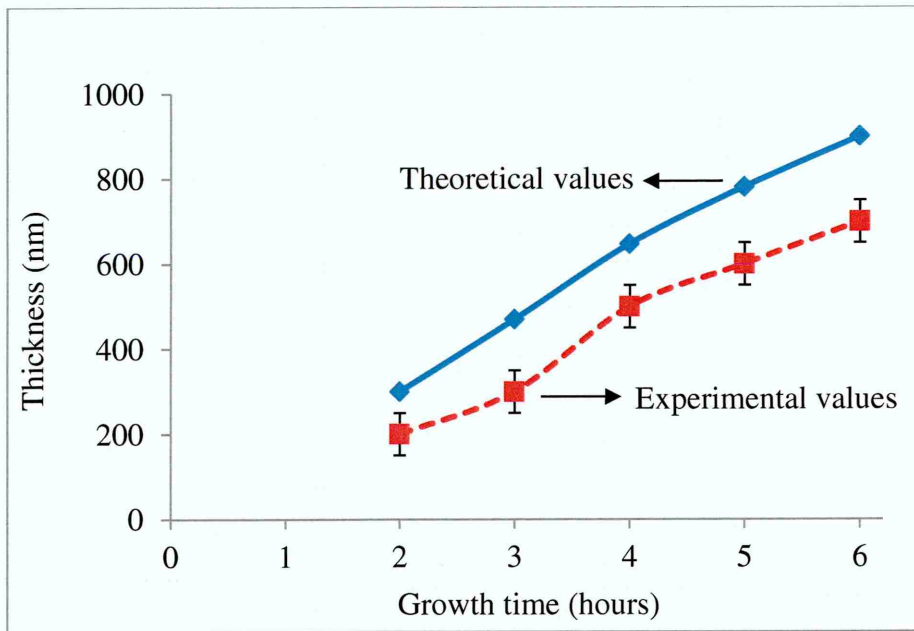


Figure 6.7: Theoretical and experimental thickness variation with growth time for the as-deposited CdS layers grown at cathodic potential of 797 mV.

6.3.5 Optical absorption spectrophotometry

6.3.5.1 Effect of growth voltage on the optical properties of ED-CdS layers

Figures 6.8 (a) and (b) show the $(\alpha h\nu)^2$ vs. photon energy ($h\nu$) for the as-deposited and annealed CdS layers grown at the cathodic potential ranges of 793 to 801 mV, in the vicinity of $V_i = 797$ mV. The CdS layers were grown on glass/FTO substrates for 2 hours duration. Afterwards, CdS samples were cut into two parts; the first part was remained as as-deposited and the second part was annealed at 400°C for 20 minutes in air for comparison. In this work, all direct energy bandgaps were estimated by extrapolating the straight-line to the photon energy axis where the $(\alpha h\nu)^2 = 0$. The aim of this experiment was to study the effect of different growth voltage on the optical properties of the CdS layers.

For the as-deposited CdS layers shown in Figure 6.8 (a), as the growth voltage increases the gradient of the optical absorption edge also increases gradually while the energy bandgaps reduce. The gradual reduction in energy bandgaps is due to the incorporation of more elemental Cd in the CdS layers as the growth voltage increases as shown in Table 6.3 and Figure 6.9. It should be noted that Cd is a metallic element, therefore, incorporation of more elemental Cd in the CdS layers lead to the reduction in energy bandgap. Also, experimental observations show that as the amount of elemental Cd increases in the as-deposited CdS layers, the layers become darker in appearance showing the reduction in energy bandgap.

The estimated energy bandgap values for the as-deposited samples grown at cathodic potential ranges of 793 to 801 mV were in the range (2.53-2.58) eV as shown in Table 6.3. The higher energy bandgap values at lower growth voltages can be due to the S-richness of the layers or nano crystalline nature of the ED-CdS layers. Also, presence of pinholes or gaps in between grains in CdS layers can provide easy path for UV-vis light to pass during optical absorption measurement which can lead to the increase in energy bandgap.

After annealing, as the growth voltage increases gradually the gradient of the optical absorption also increases gradually and reaches its maximum values at 797 mV as shown in Figure 6.8 (b). Above 797 mV, the gradient of optical absorption reduces again. Results show that, after annealing the energy bandgap values of the as-deposited samples were shifted towards the lower energy in the range (2.42-2.48) eV as shown in

Table 6.3. It should be noted that, the lowest energy bandgap value ($E_g = 2.42$ eV) were observed at $V_i = 797$ mV, which coincide with that of the bulk CdS. When the growth voltage deviate from V_i , the energy bandgap increases due to the non-stoichiometric effect, and exposure of gaps between the grains as shown in Figure 6.9. Also, reports show that incorporation of higher amount of oxygen in the CdS during annealing can suppress the Te diffusion from CdTe into the CdS layer. Therefore, the formation of $\text{CdS}_{1-x}\text{Te}_x$ alloy with lower bandgap can be suppressed, and hence, the photo-response in the short wavelength region can be improved [61].

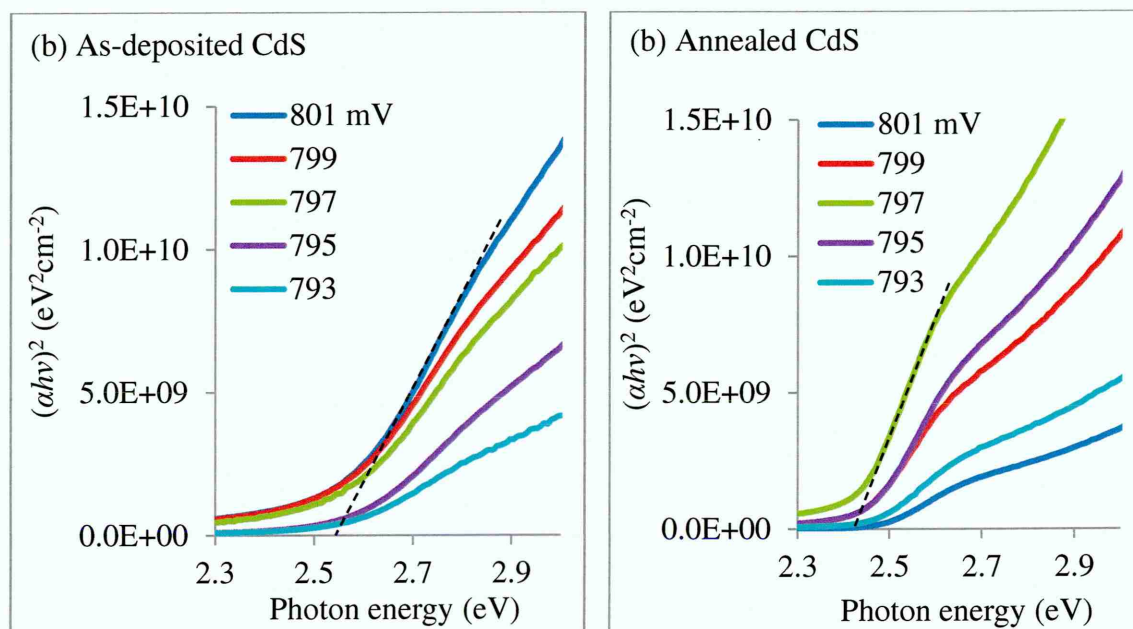
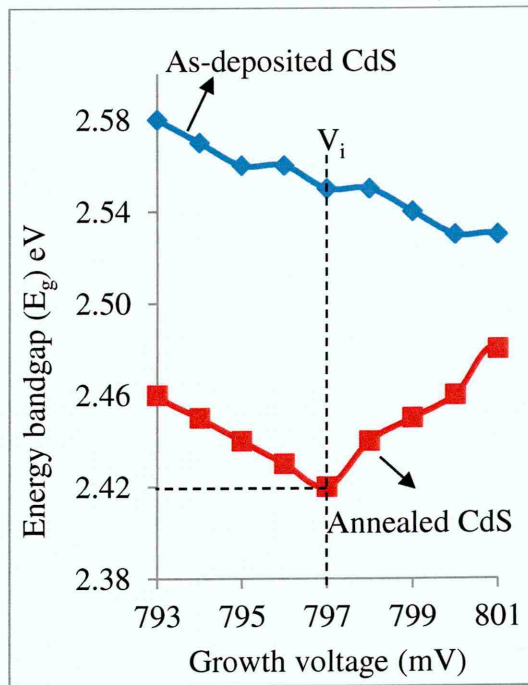


Figure 6.8: Optical absorption spectra of (a) as-deposited and (b) annealed CdS layers at 400°C for 20 minutes in air. The CdS layers were grown on glass/FTO substrates at different cathodic potential range of 793 to 801 mV for 2 hours duration.

Table 6.3 and Figure 6.9: Variation of energy bandgap with growth voltage for the as-deposited and annealed CdS layers at 400°C for 20 minutes in air. The CdS layers were grown on glass/FTO substrates at different cathodic potential ranges of 793 to 801 mV for 2 hours duration.

Growth voltage (mV)	Energy bandgap of CdS ($E_g \pm 0.01$ (eV))	
	As-deposited	Annealed
793	2.58	2.45
794	2.58	2.44
795	2.56	2.45
796	2.55	2.43
797	2.55	2.42
798	2.55	2.45
799	2.54	2.46
800	2.53	2.48
801	2.53	2.46



Figures 6.10 (a) and (b), respectively show the transmittance spectra of the as-deposited and annealed CdS layers grown on glass/FTO substrates at the cathodic potential range of 793 to 801 mV for 2 hours durations. Results show the large scatter in the transmittance spectra of the as-deposited samples as compared to the annealed samples. In the as-deposited samples, as the growth voltage increases transmittance reduces gradually. The gradual reduction in transmittances can be due to the gradual increase in the amount of elemental Cd as the growth voltage increases as shown in Figure 6.10 (a).

Experimental observations show that the transmittance values were in the range of (28-80)% at the wavelength ranges of (530-800) nm for the as-deposited samples. After annealing, the transmittances of the CdS layers were improved and absorption edges became sharper. Also, annealing brought the transmittance spectra closer together and narrow them down to the ranges of (68-89)% within the same wavelength range of (530-800) nm as shown in Figure 6.10 (b). The highest transmittance was observed for the annealed sample grown at stoichiometric growth voltage of $V_i = 797$ mV. When the growth voltage deviates from V_i , the transmittance values show reduction due to non-stoichiometric properties of the layer. The CdS layers with higher transmittance and sharper absorption edges are more suitable for solar cells application.

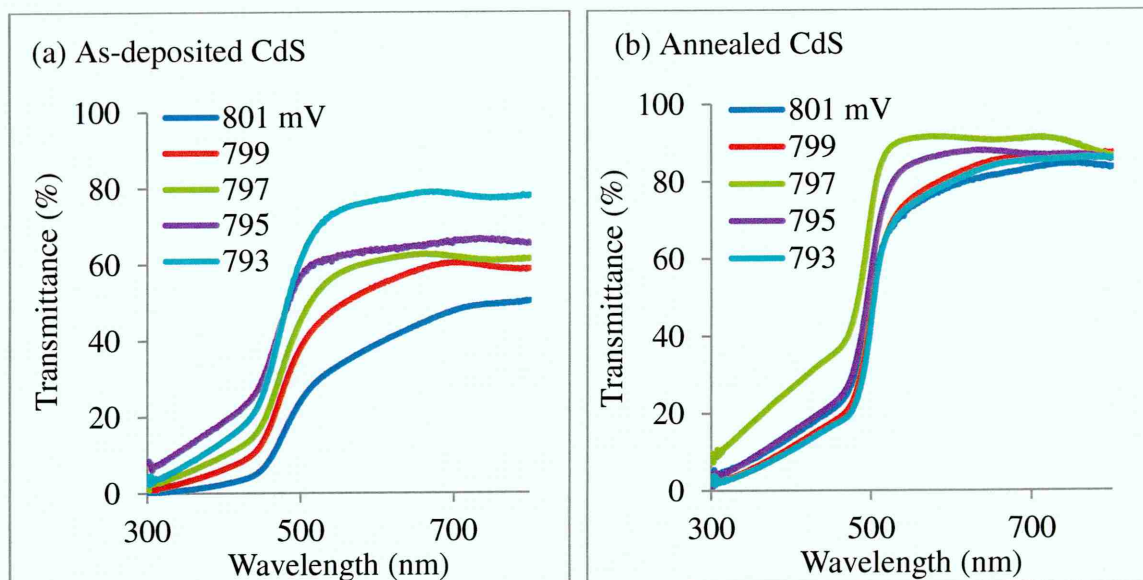


Figure 6.10: Transmittance spectra of (a) as-deposited and (b) annealed CdS layers grown for 2 hours at different cathodic potential range of 793 to 801 mV.

6.3.5.2 Effect of annealing temperature on the optical properties of ED-CdS layers

In this experiment, CdS layers were grown on glass/FTO substrates for 2 hours duration. All CdS layers were grown at cathodic potential of 797 mV and then the samples were divided into nine parts. The first part of the sample was left as as-deposited and the remaining eight parts were annealed at different temperatures in the range of 200 to 550°C, respectively. The annealing time for each sample was set to 20 minutes in air. This experiment was carried out in order to study the effect of different annealing temperatures on the optical properties of CdS layers.

Figures 6.11 (a) and (b), respectively shows the optical absorption and transmittance spectra of the CdS layers annealed at different temperatures in the range of 200 to 550°C. The absorption spectra show that as the temperature increases from 200 to 400°C, the gradient of the optical absorption and transmittance increase as shown in Figures 6.11 (a) and (b). The highest gradient was observed for the layers annealed at 400°C. Also, the energy bandgap values gradually reduce as the temperature increases from 200 to 400°C and reach its minimum value of 2.44 eV at 400°C as shown in Table 6.4. Further increase in the annealing temperature (above 400°C) results in the gradual increase in energy bandgap values and transmittance. The increase in the optical bandgap values and transmittance for the annealing temperatures of more than 400°C

can be related to the appearance of cracks, pinholes and material loss by sublimation of CdS materials (see SEM images in section 6.3.6.2). In this work, these results show that the annealing temperatures of more than 400°C are not suitable for ED-CdS layers. The best annealing temperature for CdS layers is identified as 400°C.

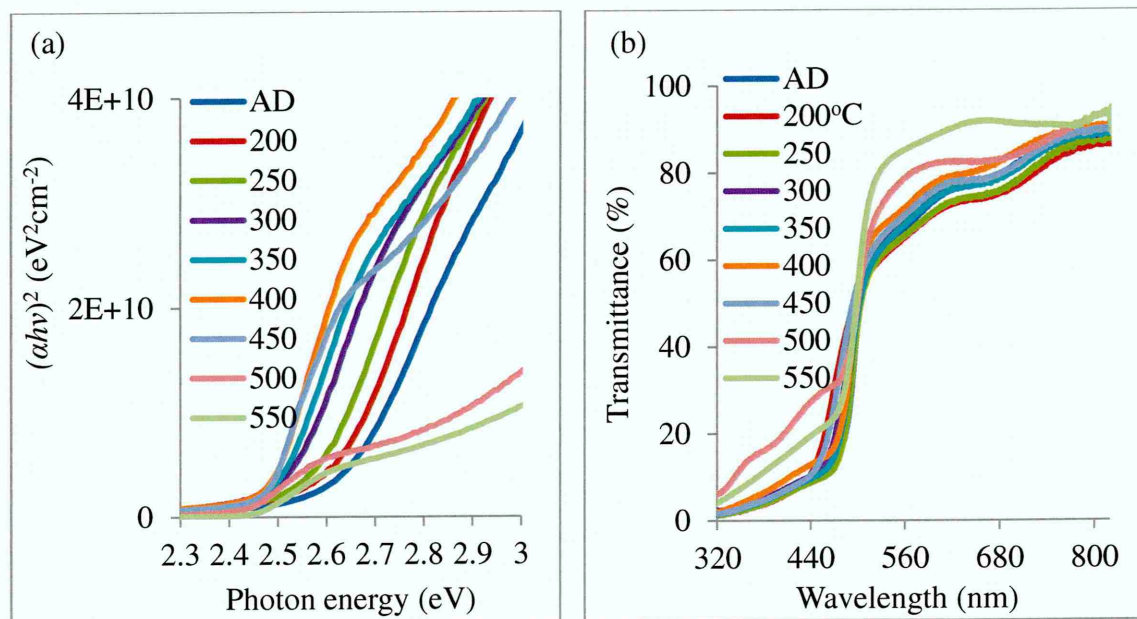


Figure 6.11: (a) Optical absorption and (b) transmittance spectra of CdS layers annealed at temperature range of 200 to 550°C. All CdS layers were grown on glass/FTO substrates at growth voltage of 797 mV for 2 hours duration and annealing time for each sample was set to 20 minutes in air.

Table 6.4: Variation of energy bandgap with annealing temperature for the CdS layers annealed at different temperature range of 200 to 550°C. For each sample the annealing time was set to 20 minutes in air.

Annealing temperature (°C)	As-deposited	200	250	300	350	400	450	500	550
Energy bandgap $E_g \pm 0.01$ (eV)	2.63	2.62	2.58	2.52	2.49	2.44	2.45	2.47	2.48

6.3.5.3 Effect of annealing time on the optical properties of ED-CdS layers

In the previous section, the best annealing temperature was found to be 400°C for CdS layers. In this section, the effect of annealing time on the optical properties of the CdS layers is studied. For this reason, the CdS layers were grown on glass/FTO substrate at cathodic potential of 797 mV for 2 hours duration. Then, the as-deposited sample was cut into seven parts. The first part was left as as-deposited and the remaining six parts were annealed at 400°C in air for different durations of 5 to 30 minutes, respectively. The aim of this experiment was to find the best annealing time at 400°C for the CdS layers.

Figures 6.12 (a) and (b) show the optical absorption and transmittance spectra of the CdS layers annealed at the temperature of 400°C for different durations of 5 to 30 minutes in air. Optical absorption spectra clearly show that as the annealing time increases, the gradient of the optical absorption edge also increases while the energy bandgap values reduce. The energy bandgap value for the as-deposited layers was 2.63 eV. After annealing for 30 minutes, the energy bandgap value was shifted towards the lower energy value of 2.42 eV as shown in Table 6.5. In the as-deposited sample shown in Figure 6.12 (a), the absorption edge was not well-defined. It should be noted that for the annealing time between 5 and 20 minutes, transmittances show improvements as compared to the as-deposited layers. However, for the annealing time of more than 20 minutes, the reduction in the transmittance was observed as shown in Figure 6.12 (b).

These results show that the annealing time for the CdS layers should not exceed 20 minutes. Therefore, based on the experimental observation in this work the best annealing temperature and annealing time for the CdS layers were found to be 400°C for 20 minutes in air.

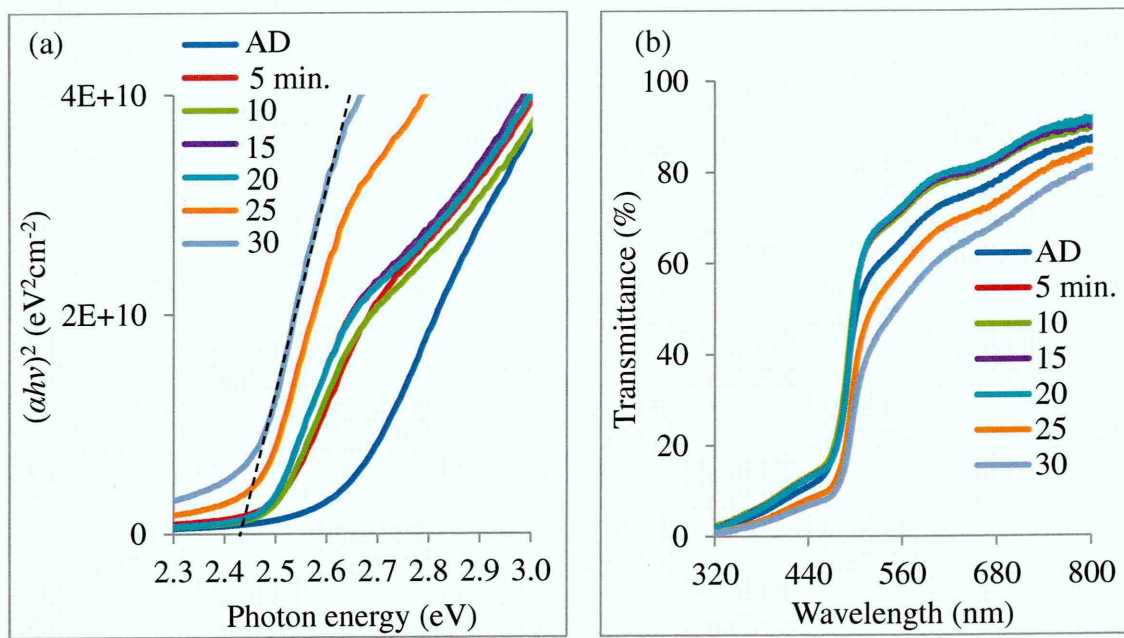


Figure 6.12: (a) Optical absorption and (b) transmittance spectra of CdS thin films annealed at 400°C for different durations of (5-30) minutes in air.

Table 6.5: Variation of the energy bandgap with annealing time for CdS layers. All CdS layers were annealed at 400°C for different durations of 5 to 30 minutes in air.

Annealing time (minutes)	As- deposited	5	10	15	20	25	30
Energy bandgap ± 0.01 (eV)	2.63	2.49	2.46	2.44	2.44	2.43	2.42

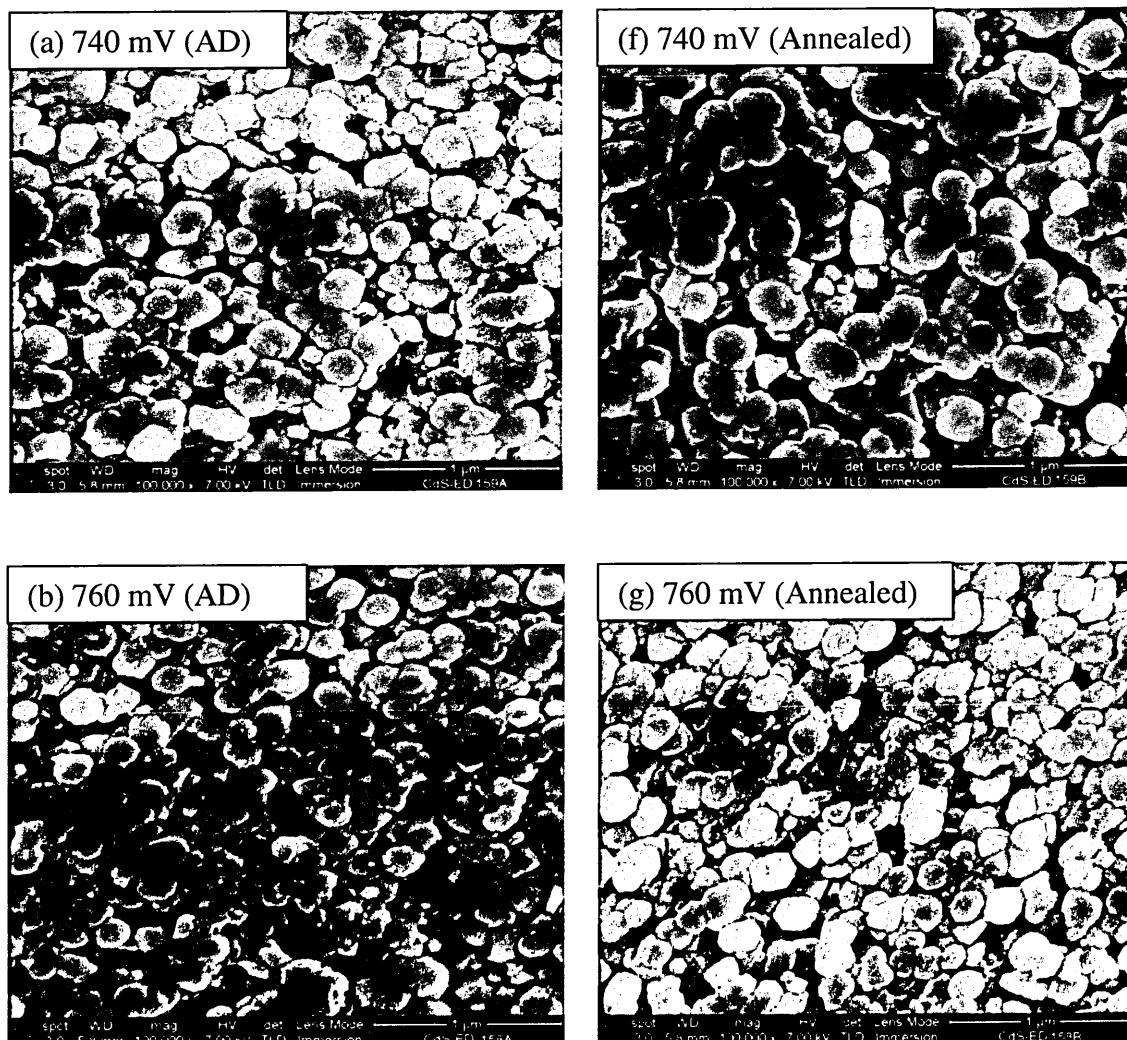
6.3.6 Scanning electron microscopy (SEM)

6.3.6.1 Variation of ED-CdS surface morphology with growth voltage

In this experiment effect of growth voltage on the morphological properties of the CdS layers were studied. Figures 6.13 (a)-(e) and 6.13 (f)-(j), respectively shows the SEM images of the as-deposited and annealed CdS layers grown at different growth voltage range of 740 to 820 mV. All CdS layers were grown on glass/FTO substrates for 2 hours duration and then the as-deposited samples were annealed at 400°C for 20 minutes in air for comparison of SEM images.

SEM images of the as-deposited samples show that as the growth voltage increase from 740 to 780 mV, the grain sizes gradually reduce from ~ 225 to ~ 120 nm as shown in Figures 6.13 (a)-(e). At the growth voltage ranges of 780 to 800 mV, the grain sizes start to increase again reaching approximately to the same values of ~ 225 nm. The SEM images show that the FTO surface was fairly covered with the CdS grains at the growth voltage ranges of 740 to 800 mV. However, small gaps/pinholes were also observed in-between the CdS grains. Further increase in the growth voltage, beyond 800 mV, shows the reduction in grain sizes and produces CdS layers with poor morphology. This can be due to the deposition of more elemental Cd at higher growth voltages.

The same trend was observed for the SEM images of the annealed CdS layers. The only differences was that the grain sizes of the CdS layers slightly increased after annealing as shown in Figure 6.14. In this experiment, samples grown in the vicinity of 800 mV were shown to have better glass/FTO surface coverage with lower number of gaps/pinholes in between the grains before and after annealing.



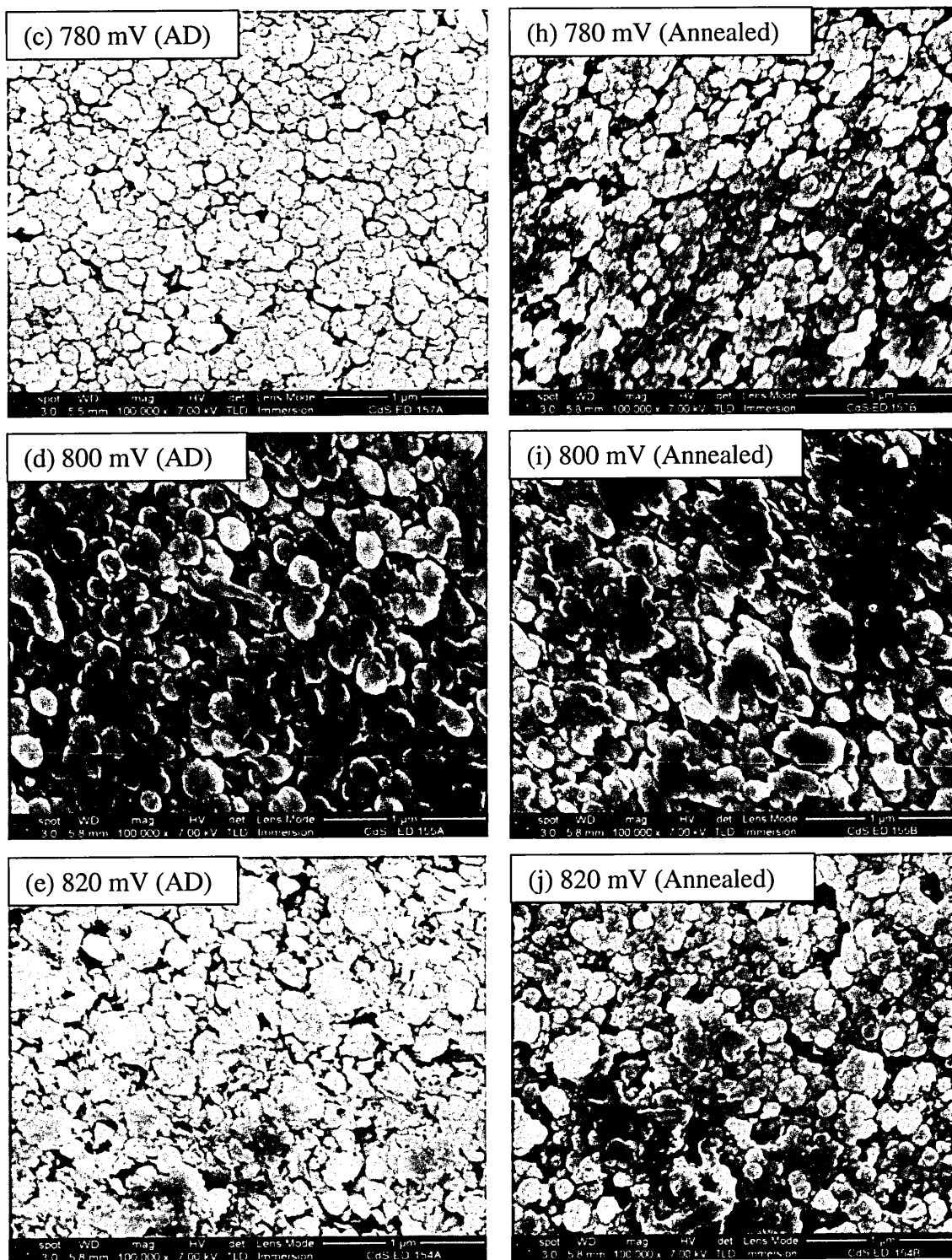


Figure 6.13: SEM images of as-deposited (AD) and annealed CdS layers grown at different growth voltage ranges of 740 to 820 mV for 2 hours duration.

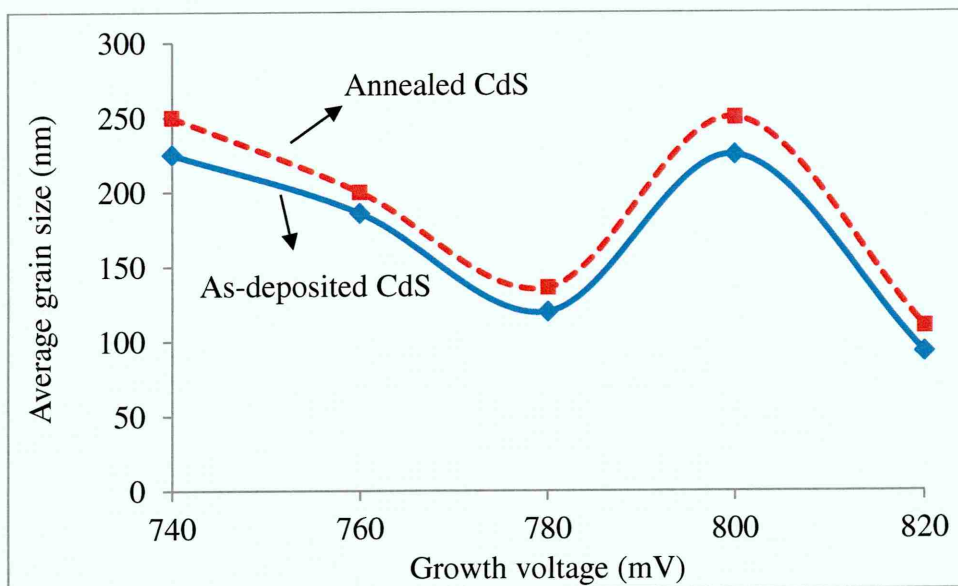


Figure 6.14: Variation of average grain size as a function of growth voltage for the CdS layers. All layers were grown on glass/FTO substrates for 2 hours duration.

Figures 6.15 (a) and (b), respectively show the SEM images of the surface and cross section of the as-deposited CdS thin films grown at optimum growth voltage of 797 mV for 2 hours duration. At the 650,000x magnification, the SEM image of as-deposited CdS layer show that the layers contain nano crystallites in the range of $\sim(11-22)$ nm. The agglomeration of these nano crystallites produces small clusters/grains with the sizes in the range $\sim(60-225)$ nm as shown in Figure 6.15 (a). In this figure, the gaps in-between the grains can be clearly observed. The presence of these gaps can be due to the upward growth nature of the electrodeposition technique and the substrate used. The FTO substrates are known to have rough and spiky surface as shown in Figure 6.15 (b). During electrodeposition, the electric fields at these spikes are higher than those of the valleys. In this case, nucleation starts at these spikes and tends to grow upwards perpendicular to the FTO surface. This will create columnar-like growth for the electrodeposited thin films as seen in Figure 6.15 (a). The columnar growth behaviour has some advantages and disadvantages. The disadvantages of columnar growth are pinholes formation and creation of non-uniformity in the electrodeposited layers. These pinholes are known as shunting paths and should be treated otherwise they will drastically reduce the efficiency of the fabricated thin film solar cells due to short-circuiting of front and back contacts after metallisation. The advantages of the columnar growth are the high crystallinity and high electrical conductivity along the columnar shape grains. In this case it is easier for charge carriers to flow normal to FTO surface

with higher mobility during PV action of CdS/CdTe solar cells with minimized scattering from the grain boundaries [62].

The SEM cross section image of the as-deposited CdS layers with magnification of 200,000x show good CdS grains coverage of the FTO surface. However, the non-uniformity at the surface of the CdS thin films can be due to the high surface roughness of the underlying glass/FTO substrate and also can be due to upward growth nature of the electrodeposited layers. The average thickness of the as-deposited CdS layer estimated from SEM image was ~120 nm. In addition, some voids were observed at FTO/CdS interface. These voids can be originated from the columnar type growth, incomplete cleaning or introduced during the sample preparation for SEM experiment.

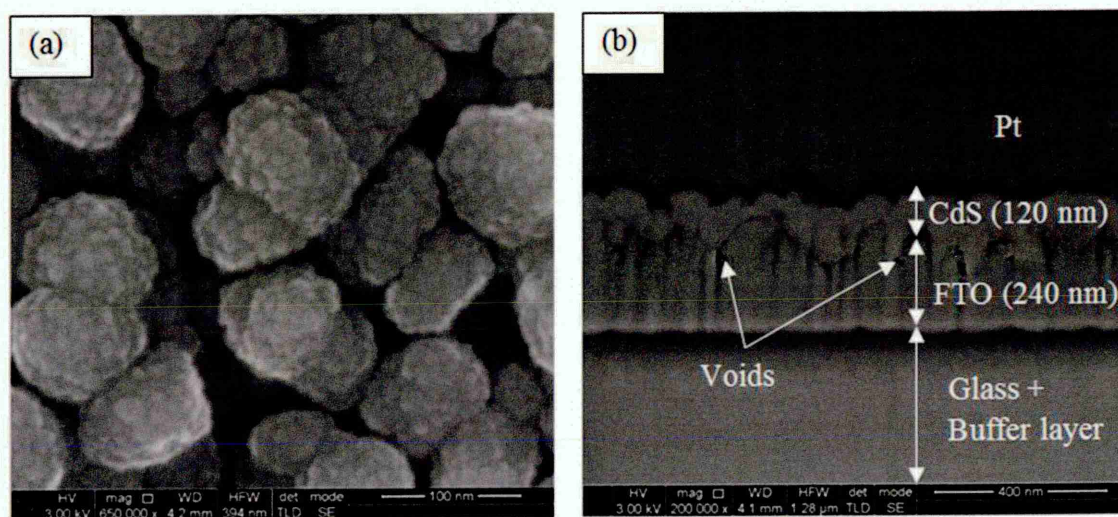


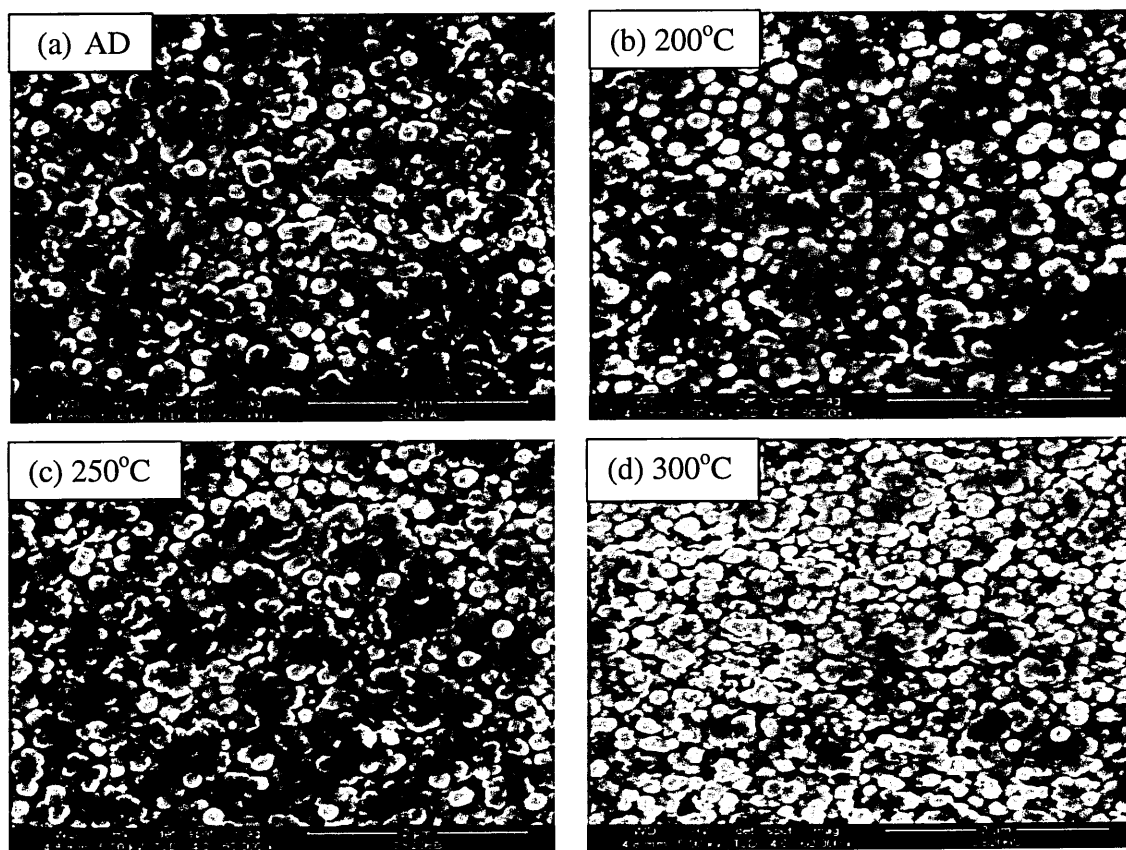
Figure 6.15: Surface and cross section images of the as-deposited CdS layers grown at cathodic potential of 797 mV for 2 hours duration with 650,000x and 200,000x magnification, respectively. The thickness of CdS layer is estimated close to 120 nm.

6.3.6.2 Effect of annealing temperature on the surface morphology of ED-CdS layers

In this experiment, CdS layers were grown at cathodic potential of 797 mV for 2 hours duration. The CdS layers grown on glass/FTO substrate were then divided into nine parts; the first part was left as as-deposited and the remaining parts were annealed at different temperature range of 200 to 550°C for 20 minutes in air. This experiment was carried out in order to study the effect of different annealing temperatures on the morphological properties of the CdS layers and to find the best annealing temperature

for the CdS layers. The SEM images of the as-deposited and annealed CdS layers are shown in Figures 6.16 (a)-(i). In this experiment, the 60,000x magnification was used to image all CdS samples.

The SEM image of the as-deposited sample is shown in Figure 6.16 (a). This image shows a fairly uniform coverage of the FTO surface by CdS grains. The estimated grain sizes obtained from the SEM image of the as-deposited CdS layers were in the range $\sim(60-225)$ nm. After annealing at temperatures between 200 and 450°C, no noticeable changes in the grain sizes of the CdS thin films were observed as shown in Figures 6.16 (a)-(g) and in Figure 6.17. At the annealing temperature of 450°C, cracks were observed in the CdS layers along some grain boundaries. These cracks create discontinuity and shunting paths in the CdS thin films which can results in the short-circuiting effect in the devices as shown in Figure 6.16 (g).



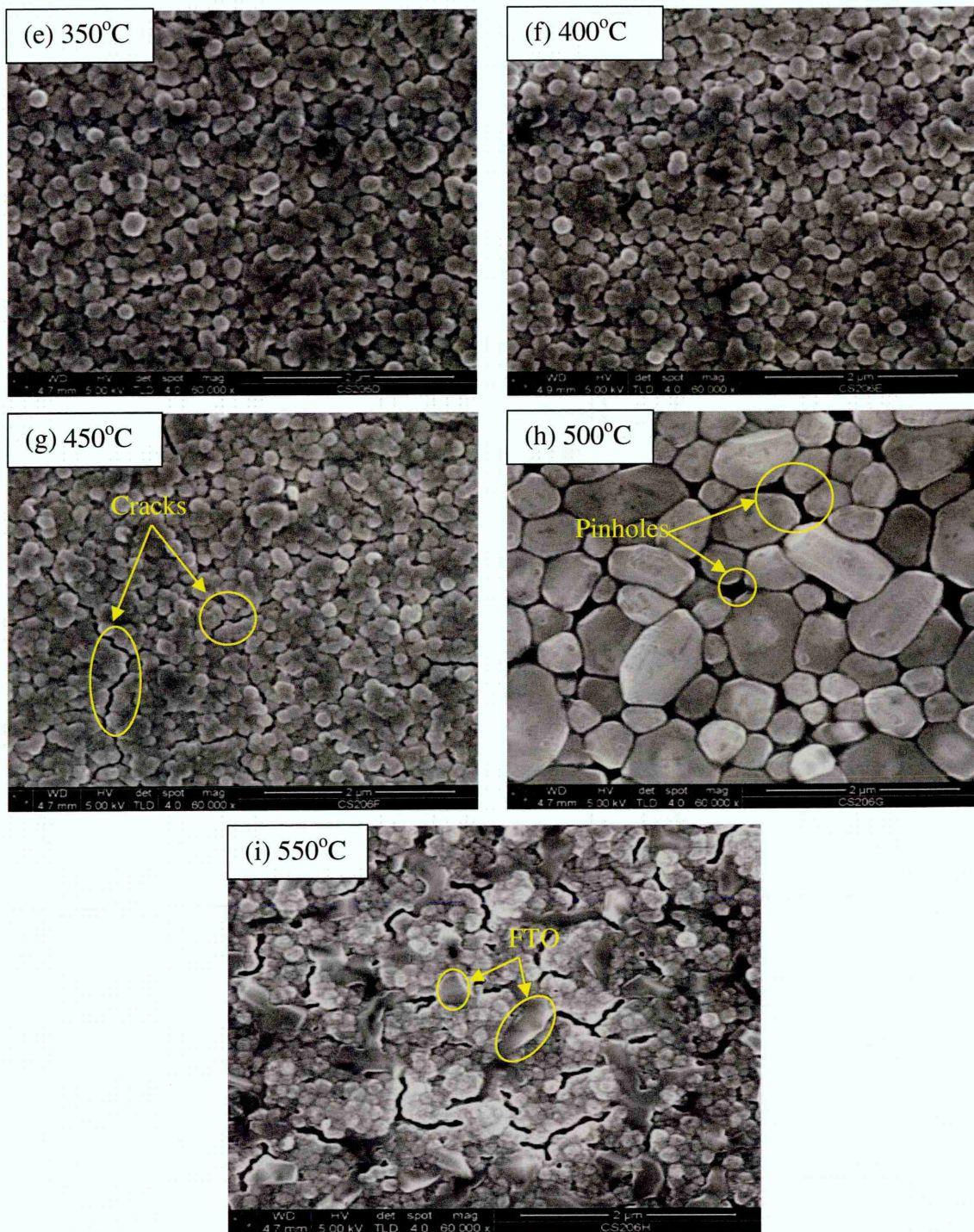


Figure 6.16: SEM images of the as-deposited and annealed ED-CdS layers annealed at different temperatures range from 200 to 550°C for 20 minutes in air. All CdS layers were grown at cathodic potential of 797 mV.

Interesting results were observed for the SEM image of CdS sample annealed at 500°C. At this annealing temperature, the grain sizes were increased up to $\sim 1.1 \mu\text{m}$ as shown in Figures 6.16 (h). However, for the CdS layers annealed at this temperature, large numbers of pinholes were observed. Further increase in the annealing temperature

(above 500°C) results in material loss by sublimation of the CdS material. The exposed FTO surfaces are the evidence of the material sublimation as shown in Figure 6.16 (i). The SEM results observed in this work clearly show that the annealing temperature for CdS layers should not exceed 400°C.

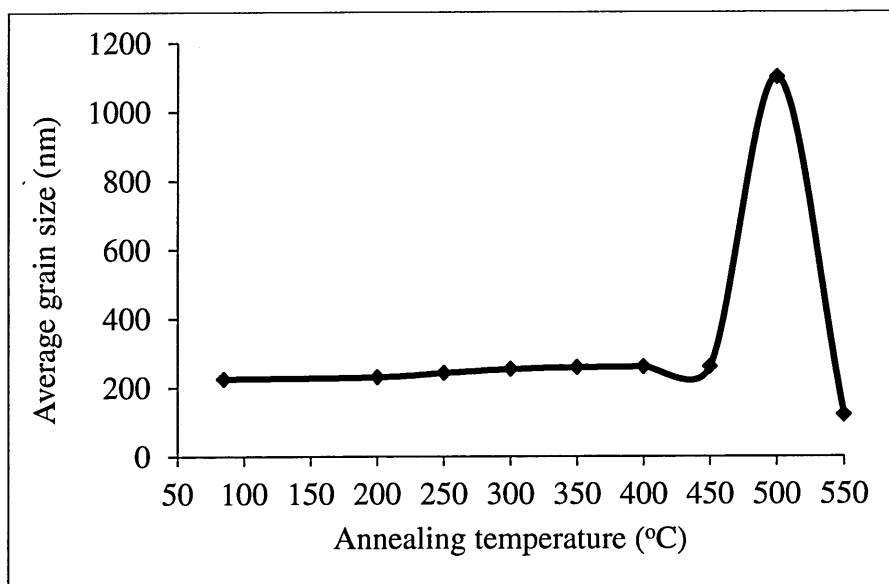


Figure 6.17: Variations of the average grain size with annealing temperature for the CdS layers. All CdS layers were annealed at different temperatures from 200 to 550°C for the same duration of 20 minutes in air.

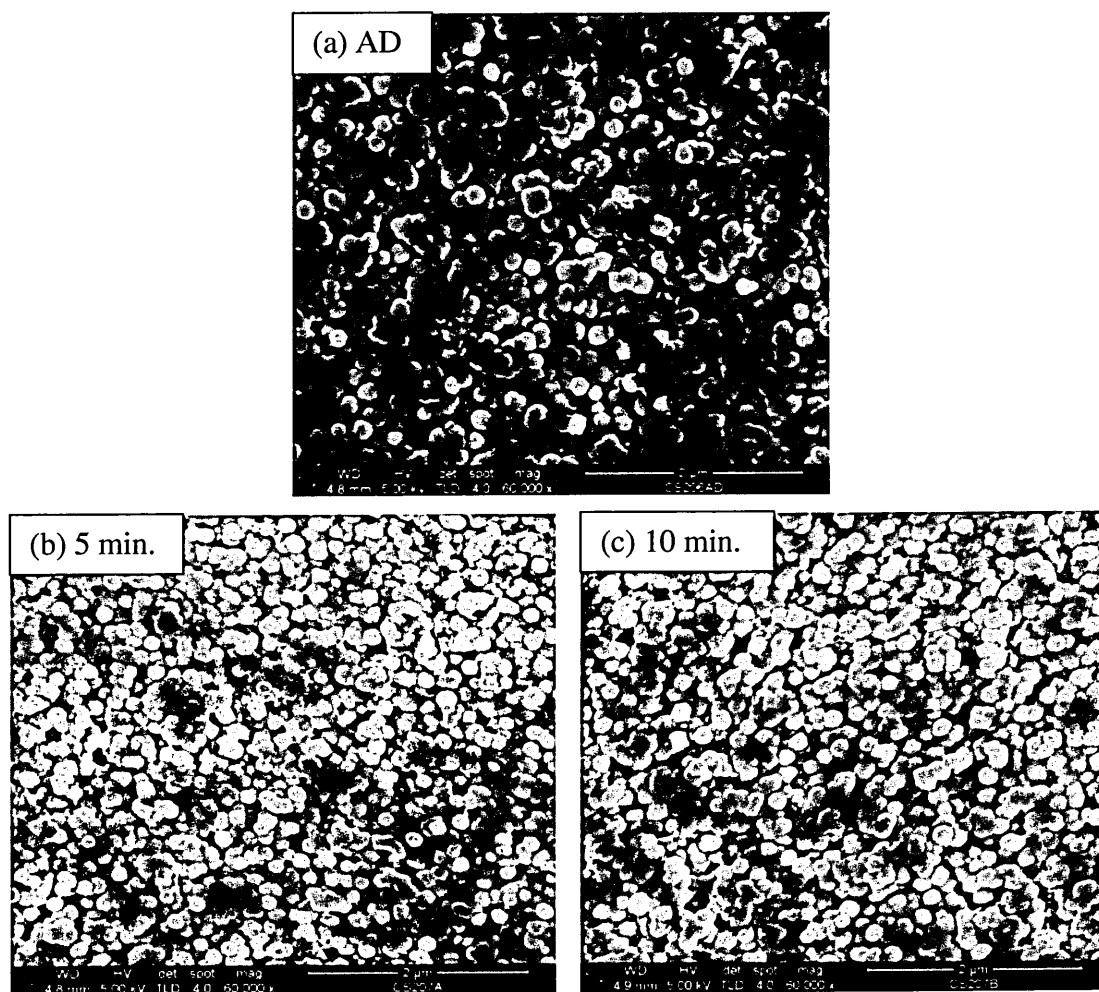
6.3.6.3 Effect of annealing time on the surface morphology of ED-CdS layers

Based on observations from previous section, further experimentation on the effect of annealing time on the surface morphology of the CdS layers were studied. For this work, the CdS layer was grown on glass/FTO substrate at cathodic potential of 797 mV for duration of 2 hours. Then, CdS samples were annealed at the temperature of 400°C for different durations between 5 and 30 minutes in air. Then, the SEM images were compared with the as-deposited sample as shown in Figures 6.18 (a)-(g). In this experiment, the same magnification of 60,000x was used for the CdS layers annealed at 400°C for different durations.

Figure 6.18 (a) shows the SEM image of the as-deposited sample. The estimated grain sizes observed from the SEM image of the as-deposited CdS layers were in the range ~(60-225) nm. When the samples annealed at 400°C for the duration of 5 to 30 minutes, no noticeable change in the grain sizes were observed. The SEM image shows

that when the annealing time exceeds 20 minutes, cracks start to appear in the CdS thin films as shown in Figures 6.18 (f) and (g). The SEM results clearly show that when CdS layers are annealed at temperature of 400°C, the annealing time should not exceed 20 minutes duration.

Based on the experimental observations obtained from XRD, optical absorption and SEM results in this work, the best annealing temperature and annealing time were found to be 400°C for 20 minutes in air.



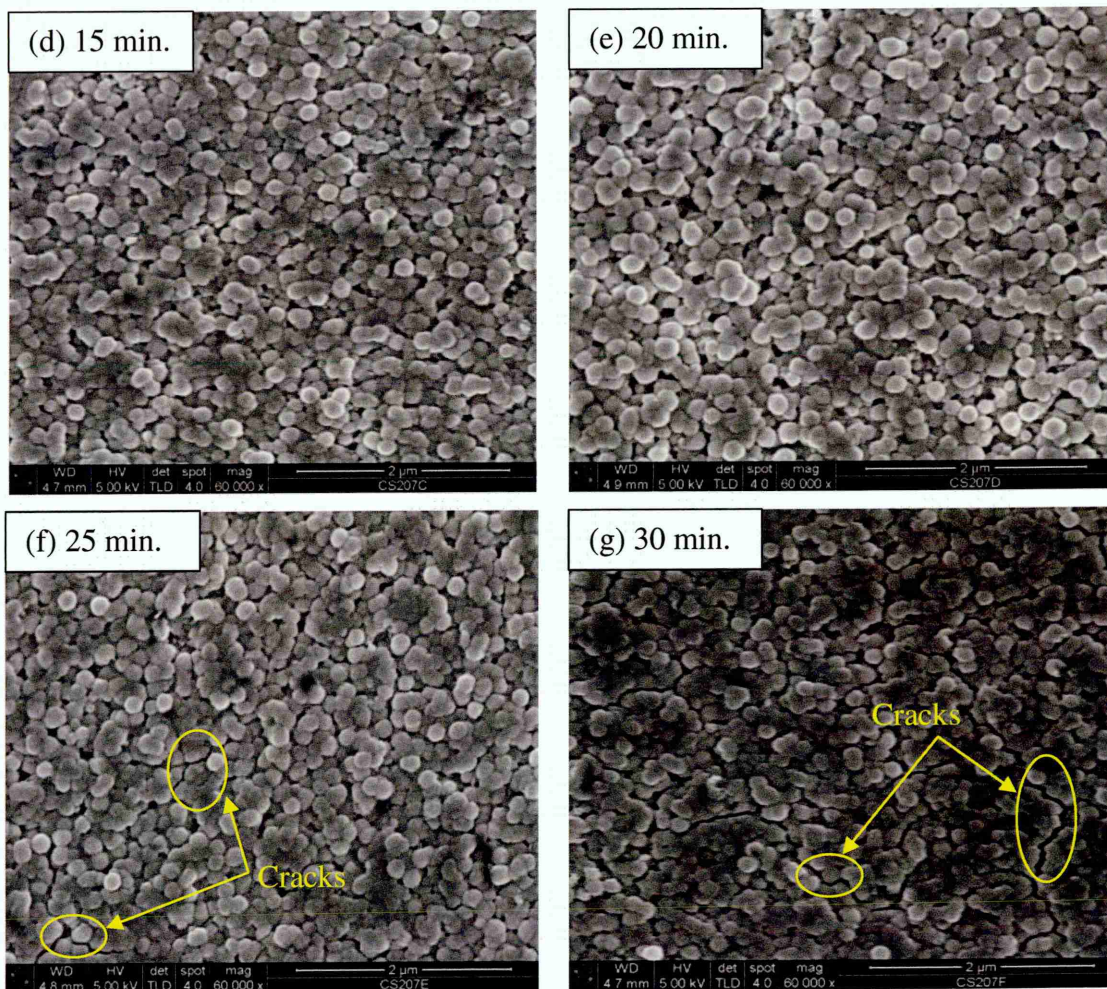


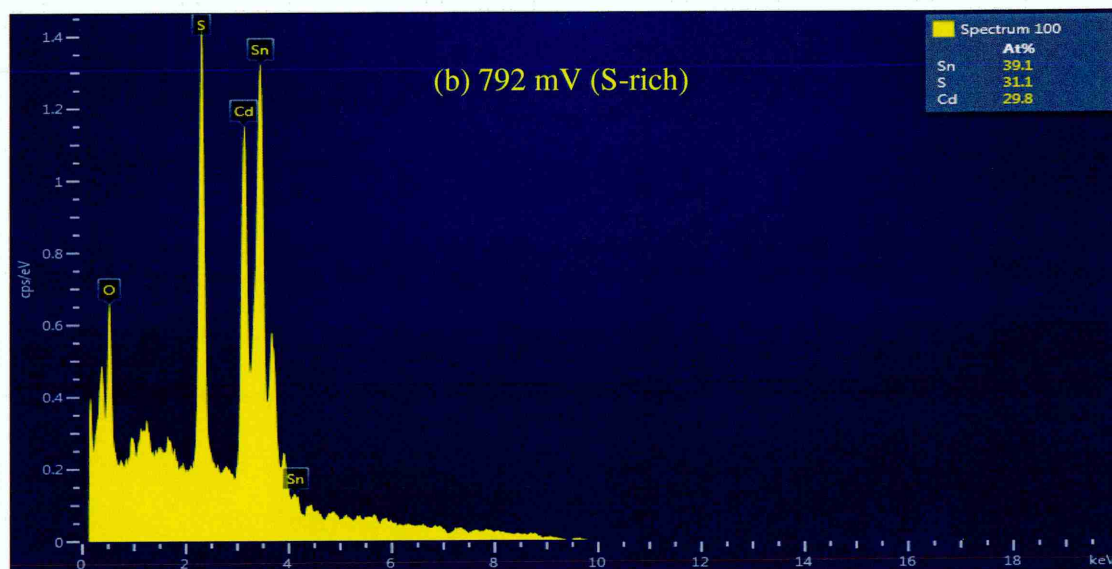
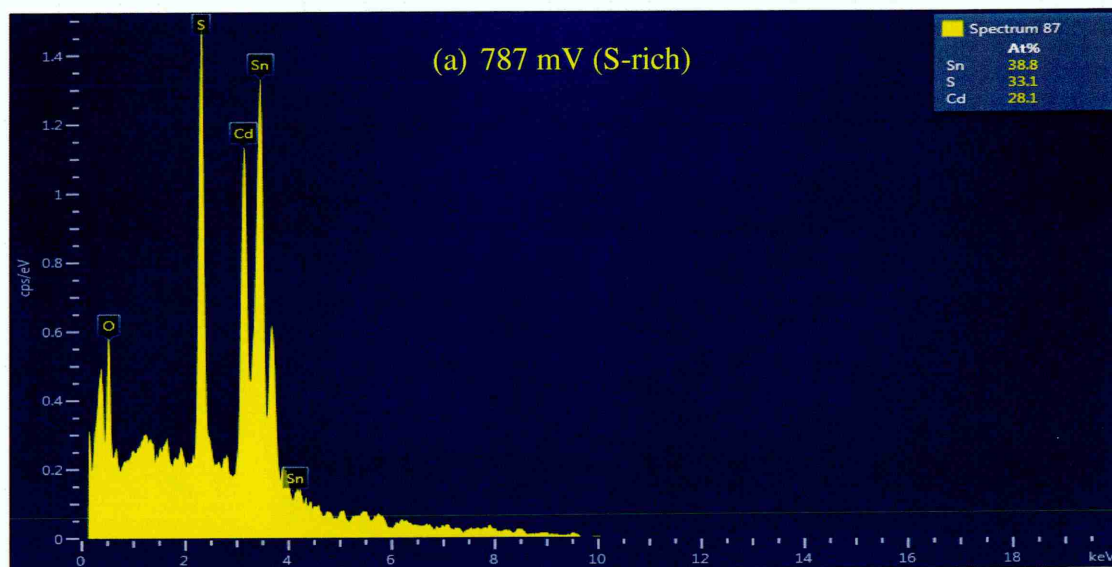
Figure 6.18: SEM images of the as-deposited and annealed CdS layers at temperature of 400°C for different durations of 5 to 30 minutes in air. All CdS layers were grown on glass/FTO substrate at cathodic potential of 797 mV for 2 hours duration.

6.3.7 Energy Dispersive X-ray (EDX) Analysis

The EDX measurements were carried out in order to study the composition and atomic percentage variations of the deposited CdS layers. For this experiment, CdS layers were deposited on glass/FTO substrates for 2 hours duration. The first layer was grown at the stoichiometric growth voltage of 797 mV. The next four layers were grown at 787, 792, 802 and 807 mV respectively close to the stoichiometric growth voltage of 797 mV.

Figures 6.19 (a)-(e), show the EDX spectra of CdS layers grown at the growth voltages of 787, 792, 797, 802 and 807 mV respectively. All the EDX spectra clearly show the presence of Cd and S atoms in the deposited films. The other two peaks, Sn

and O, arise from the underlying glass/FTO substrate. The atomic percentages calculated from EDX measurement are summarised in Table 6.6 and graphically shown in Figure 6.20. The EDX work show that the samples deposited at growth voltages lower than 797 mV are S-rich, whereas samples grown at growth voltages higher than 797 mV are Cd-rich. The samples deposited at the growth voltage of 797 mV were approximately stoichiometric with the Cd/S ratio close to unity as shown in Table 6.6.



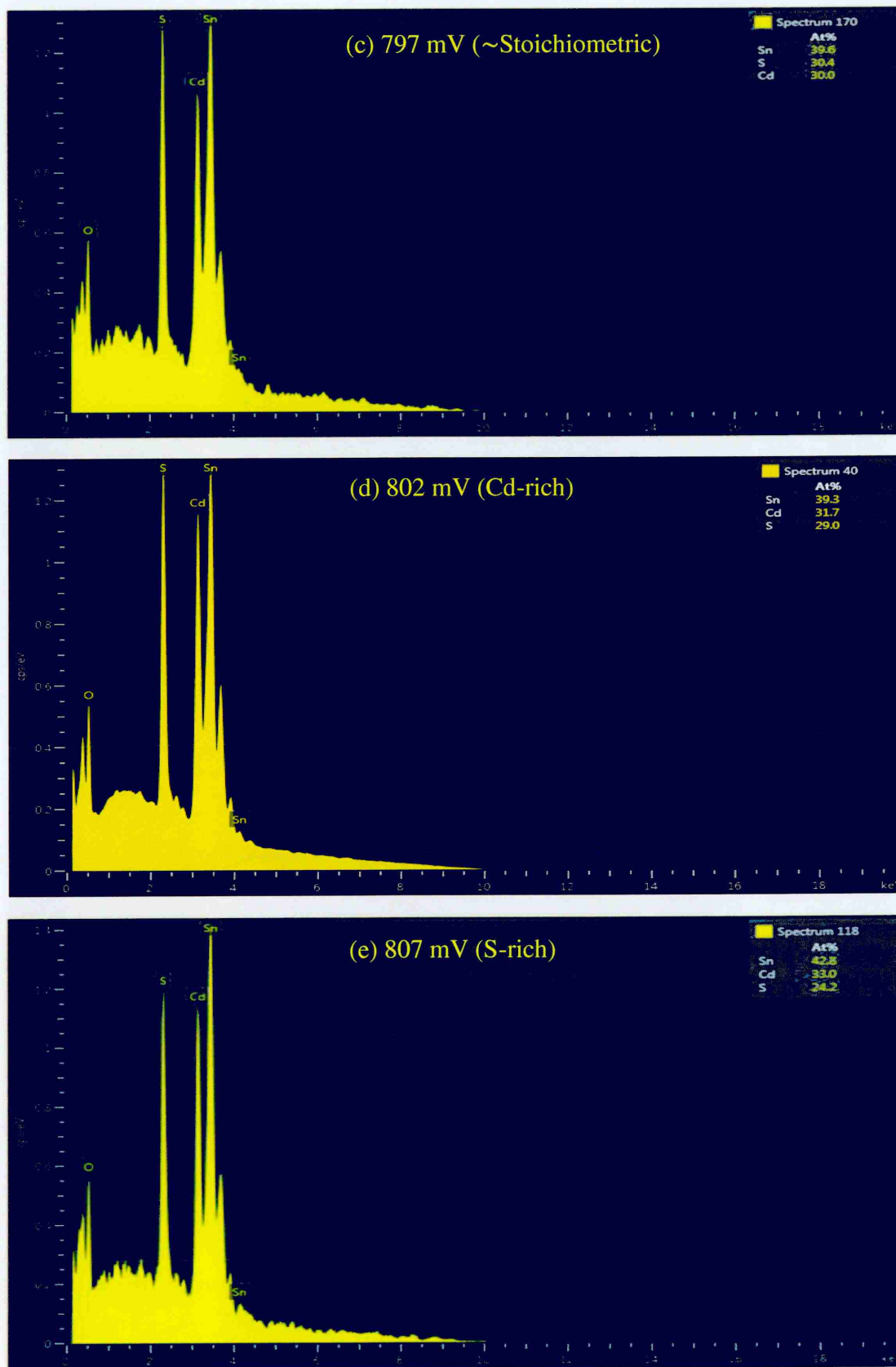


Figure 6.19: EDX spectra of the (a, b) S-rich, (c) Stoichiometric, and (d, e) Cd-rich CdS layers. All as-deposited CdS layers were grown on glass/FTO substrate for 2 hours duration.

Table 6.6: Atomic percentages and Cd/S ratio of the CdS layers grown at 787, 792, 797, 802 and 807 mV respectively. All as-deposited CdS layers were grown on glass/FTO substrates for 2 hours duration.

Growth voltage (mV)	Atomic percentage (at%)			Cd/S ratio	Conditions
	Cd	S	Sn		
787	28.1	33.1	38.8	0.84	S-rich
792	29.8	31.1	39.1	0.95	S-rich
797	30.0	30.4	39.6	0.98	~Stoichiometric
802	31.7	29.0	39.3	1.09	Cd-rich
807	33.0	24.2	42.8	1.36	Cd-rich

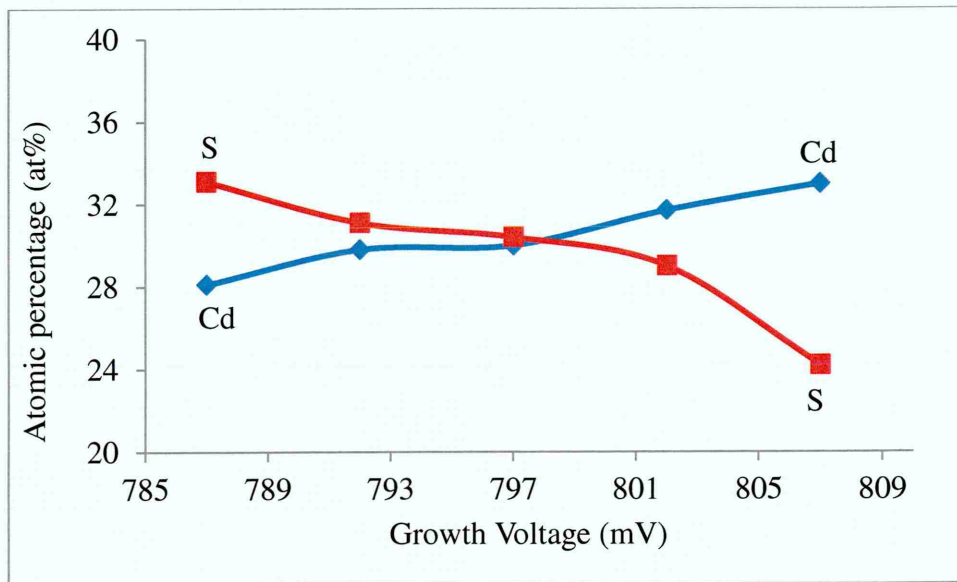


Figure 6.20: Atomic percentage of Cd and S in the CdS layer as determined by EDX. Note the transition of stoichiometry from S-richness to Cd-richness at $V_g = 797$ mV.

6.3.8 Atomic force microscopy (AFM)

For this work CdS samples were grown on glass/FTO substrates at cathodic potential of 797 mV for 2 hours duration. As-deposited CdS layers were divided into two parts; the first part was left as as-deposited and the second part was annealed at 400°C for 20 minutes in air. This experiment was carried out in order to measure the surface grain sizes and also to study surface roughness of CdS layers.

Figures 6.21 (a)-(c) show the 2D and 3D-AFM images of the as-deposited CdS layers. The AFM images of the as-deposited CdS layers show coverage of FTO surface by CdS grains with some gaps in-between the grains. The 2D-AFM image shows that the as-deposited CdS layers contain nano crystallites with the sizes in the range of $\sim(10-25)$ nm as shown in Figure 6.21 (a). These results are in a good agreement with the results obtained from SEM images showed in the previous sections. The non-uniformity at the surface of the as-deposited CdS layers can be observed in the 3D-AFM images CdS thin film shown in Figure 6.21 (b). These non-uniformities are due to high surface roughness of the underlying FTO substrate and upward growth nature of the electrodeposition technique. As explained earlier in the previous section, the electric fields at the spikes are higher than those of the valleys. For this reason, nucleation starts on these spikes and then grows upward normal to the substrate. This columnar or rod-type growth leaves some gaps/pinholes in between the grains as seen in Figure 6.21 (a) and (c).

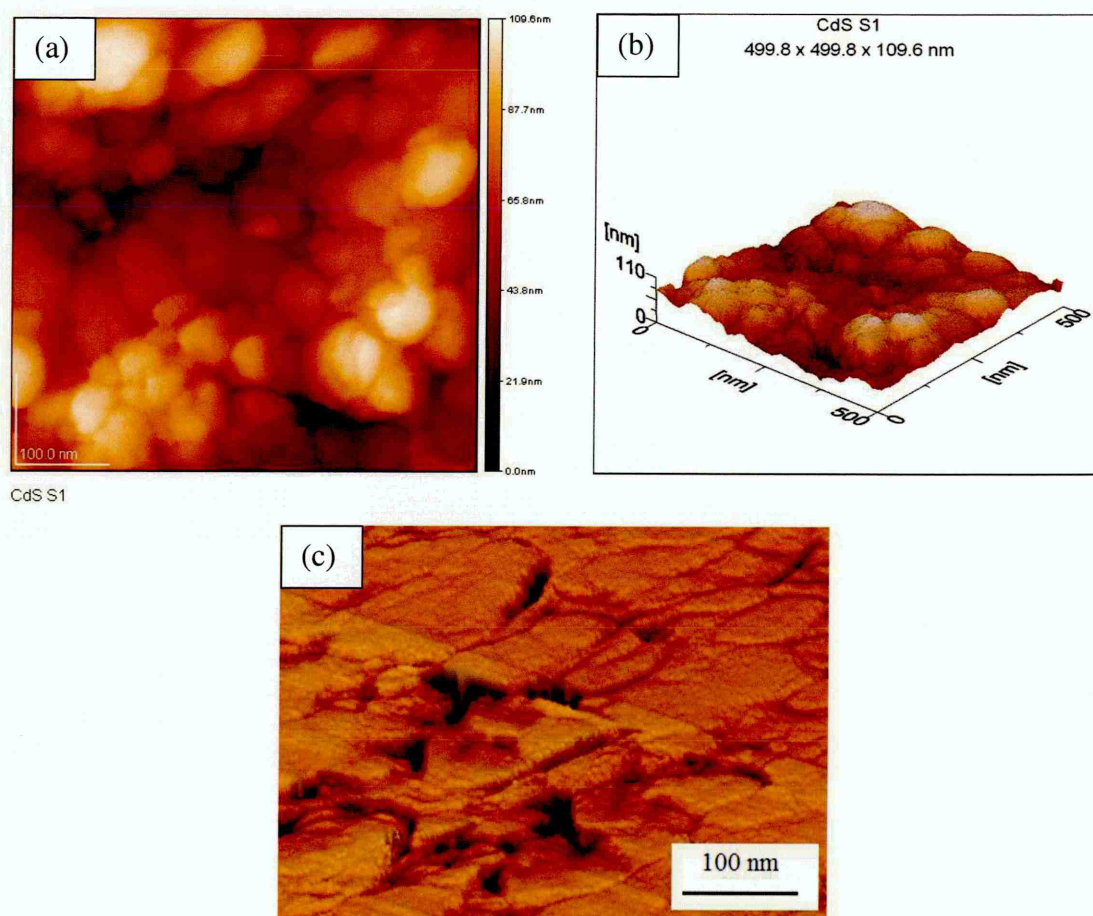


Figure 6.21: 2D and 3D-AFM images of the as-deposited CdS grown on glass/FTO substrates for 2 hours (courtesy: Inst. of Org. Catalysis & Electrochem., Kazakhstan).

Figures 6.22 (a) and (b) show the 2D and 3D-AFM images of the as-deposited and annealed CdS layers with lower magnification as-compared to the previous AFM images. The estimated grain sizes obtained from 2D-AFM of the as-deposited CdS layers were in the range $\sim(60\text{-}230)$ nm as shown in Figure 6.22 (a) which again was in agreement with results obtained from SEM images.

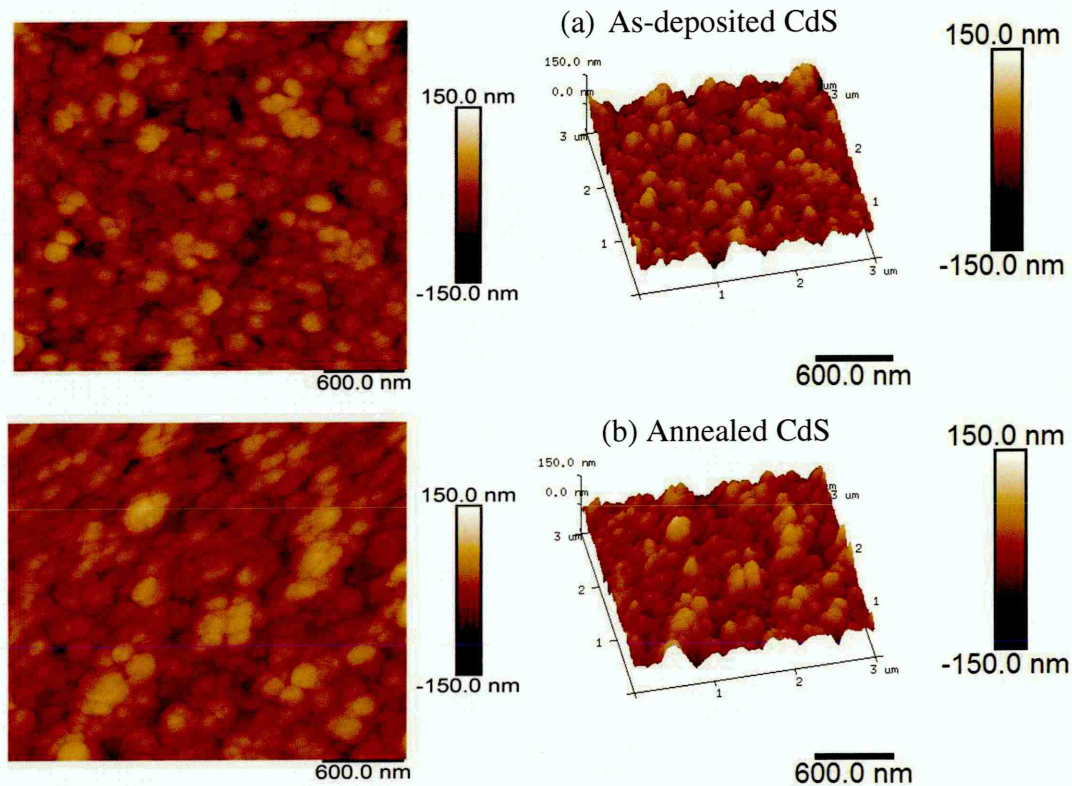


Figure 6.22: 2D-AFM images of the (a) as-deposited and (b) annealed CdS layers grown on glass/FTO substrates for 2 hours [Sheffield Hallam University (SHU)]. The CdS layers were annealed at 400°C for 20 minutes in air.

After annealing, no noticeable change in the grain sizes of the as-deposited sample were observed as shown in Figure 6.22 (b).

The average surface roughness value obtained from 3D-AFM images for the as-deposited CdS layers were in the range ~ 25.7 nm. After annealing, the average surface roughness slightly reduced to ~ 20.8 nm. The surface roughness of the CdS layers depends on the surface roughness of underlying substrate and the growth technique. It is worth mentioning that in the CdS/CdTe thin film solar cells, researchers trying to reduce the thickness of the CdS thin films to improve the photocurrent in the device.

However, as the thickness of the CdS reduces, the surface roughness and the possibility of the creation of pinholes in the layers will also increase. Reports show that the efficiency of the CdS/CdTe solar cells strongly depends on the surface roughness of the CdS thin films [63,64]. CdTe layers will have lower stress and better morphological properties when these layers are deposited on the CdS layers with lower surface roughness. Ohyama *et al* reported that the surface roughness may act as a recombination centres around the depletion region when CdS/CdTe interface is formed and can reduces the efficiency of the solar cells [65]. One strategy used for the reduction of surface roughness is the deposition of bi-layer CdS films (generally used in CBD-CdS growth technique). The first layer is usually deposited at higher temperature with larger grains and second layer is deposited at the lower temperature which composed of smaller grains. The small grains are expected to fill the pinholes which have a positive effect on the open circuit voltage and fill factor of the device. The bi-layer is more compact and more uniform than the single layer CdS thin films which improve the device performance [66].

6.3.9 Raman spectroscopy

In this experiment, CdS layers were grown on glass/FTO substrates at growth voltage of 797 mV for 2 hours duration. Then, the as-deposited layers were divided into two parts; one part remained as it was and another part was annealed at 400°C for 20 minutes in air. Raman study was carried out on the as-deposited and annealed layers and results are shown in Figure 6.23.

In the as-deposited sample, two Raman peaks were observed at 232.1 cm^{-1} and 304.9 cm^{-1} which are related to the TO and 1LO phonon peaks of CdS, respectively. After annealing, the TO phonon peak disappears and the intensity of the 1LO peak increases drastically as compared to the 1LO peak of the as-deposited sample. Also, the second Raman peak appeared at 601.1 cm^{-1} after annealing which is corresponding to the 2LO phonon peak of the CdS. An increase in the intensity of 1LO peak and appearance of the 2LO peak after annealing indicate the improvement in the crystallinity and material quality of the CdS layers. The 1LO and 2LO peaks position for the bulk CdS crystal are 305 cm^{-1} and 610 cm^{-1} , respectively [67]. Obviously, as observed in this work, 1LO and 2LO peaks for the as-deposited and annealed samples

have red shifted as compared to the bulk CdS crystal. The red shift in Raman peaks can arise due to the tensile stress in CdS thin films [68].

In a production line, Raman spectroscopy can be used as a fast and non-destructive method to check the material quality of the deposited thin films as a quality control technique.

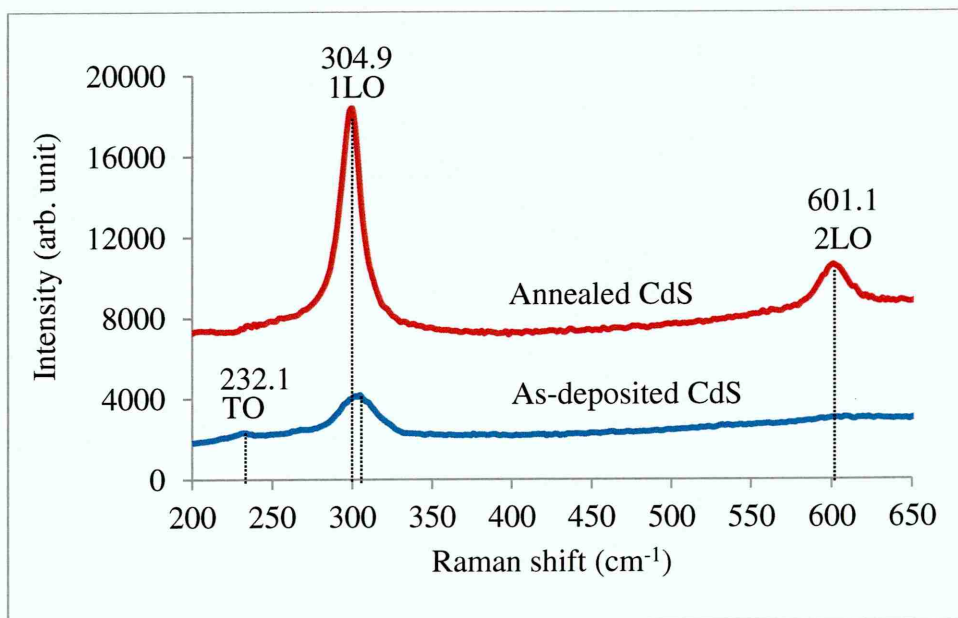


Figure 6.23: Raman spectra of as-deposited and annealed CdS layers grown on glass/FTO substrates. The CdS layers were grown at cathodic potential of 797 mV and annealed at 400°C for 20 minutes in air.

6.3.10 Photoelectrochemical (PEC) cell measurement

The PEC cell measurements were carried out to determine the electrical conductivity type of the CdS layers. For this reason, CdS layers were grown on glass/FTO substrates at different growth voltages range from 793 to 801 mV for 2 hours duration and PEC signals were measured. Then, the as-deposited samples were annealed at 400°C for 20 minutes in air for comparison and the results are shown in Figure 6.24.

For both as-deposited and annealed samples, the negative PEC signals were observed which represents the n-type electrical conductivity. After annealing, the values of negative PEC signal increased as compared to the as-deposited samples. This shows an enhancement in electrical properties and material quality of the CdS layers upon annealing. The n-type conductivity nature of CdS layers arises due to the presence of S

vacancies and Cd interstitials in the crystal lattice of this material. The S vacancies and Cd interstitials are generally known as intrinsic donor defects [69]. CdS layers can also be used for PEC cell calibrations as it is always n-type in electrical conduction.

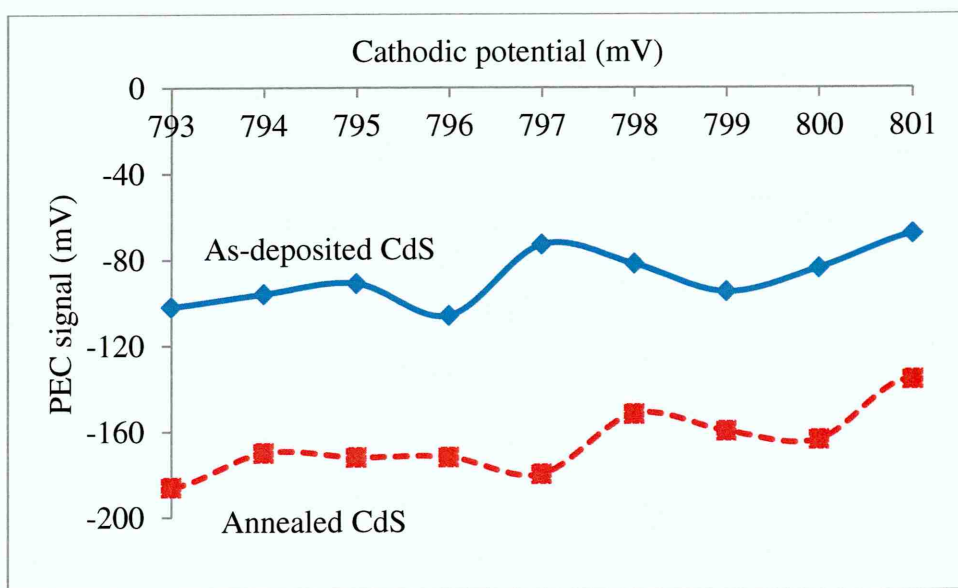


Figure 6.24: The PEC signals of the as-deposited and annealed CdS layers grown at the cathodic potential range of 793 to 801 mV. The CdS layers were annealed at 400°C for 20 minutes in air. All CdS layers were grown on glass/FTO substrates for 2 hours duration.

6.3.11 Electrical resistivity measurements

The electrical resistivity measurements were carried out at room temperature (300 K) for the CdS layers grown on glass/FTO substrates with different thicknesses. Circular indium metal contacts of 2 mm diameter were evaporated on glass/FTO/CdS structures using EDWARDS 306 vacuum coater (metalliser). The pressure of the evaporation chamber during the evaporation of indium metal contacts was 10^{-5} Nm⁻² (Pa). The average resistances of the glass/FTO/CdS/In structures were then measured under dark condition using a computerised I-V system including a Keithley 619 electrometer and a multimeter. Table 6.7 and Figure 6.25 show the variation of CdS resistivity as a function of thickness for the as-deposited and annealed layers at 400°C for 20 minutes in air. In this experiment, all the CdS layers were grown at optimised cathodic potential of 797 mV.

Results show that as the thickness of CdS layers increases the resistivity decreases as shown in Table 6.7 and Figure 6.25. The reduction in resistivity can be attributed to improvement of all properties due to formation of improved crystallites in CdS layers. It should be noted that in CdS thin films, sulphur vacancy and Cd interstitial defects act as electron donor. Therefore, as the thickness of the layers increases, the free electron concentration in the CdS thin film also increases due to increase in the sulphur vacancy and Cd interstitial defects thus leading to the reduction of the resistivity [70]. The other possible reason of reduction in CdS resistivity can be due to the increase in grain size as the thickness increases. It should be noted that as the grain size increases, the grain boundaries reduces. The grain boundaries act as electron traps or scattering centres. Therefore, larger grains mean less scattering centres, and as a result electrons can move easily within the CdS crystal [71].

In this work, annealing of the CdS layers were shown to have lower resistivity than those of the as-deposited layers. The reduction in CdS resistivity indicates an improvement in electrical and structural properties. This can be due to recrystallisation, increase in grain size, carrier concentration and mobility of the free electrons of the CdS thin films and reduction in lattice defect sites after annealing. The resistivity values observed in this work are in agreement with resistivity values reported in the literature [70,45].

Table 6.7: Variation of electrical resistivity with thickness for the as-deposited and annealed CdS layers grown at cathodic potential of 797 mV. The CdS layers were grown on glass/FTO substrates and then annealed at 400°C for 20 minutes in air.

Thickness (nm)	R_{av} (Ω)		Resistivity $\times 10^5$ (Ωcm)	
	As-deposited	Annealed	As-deposited	Annealed
335	525	495	4.92	4.63
393	494	452	3.94	3.61
465	424	385	2.86	2.59
483	291	268	1.89	1.74
500	274	236	1.72	1.48
550	180	145	1.02	0.82

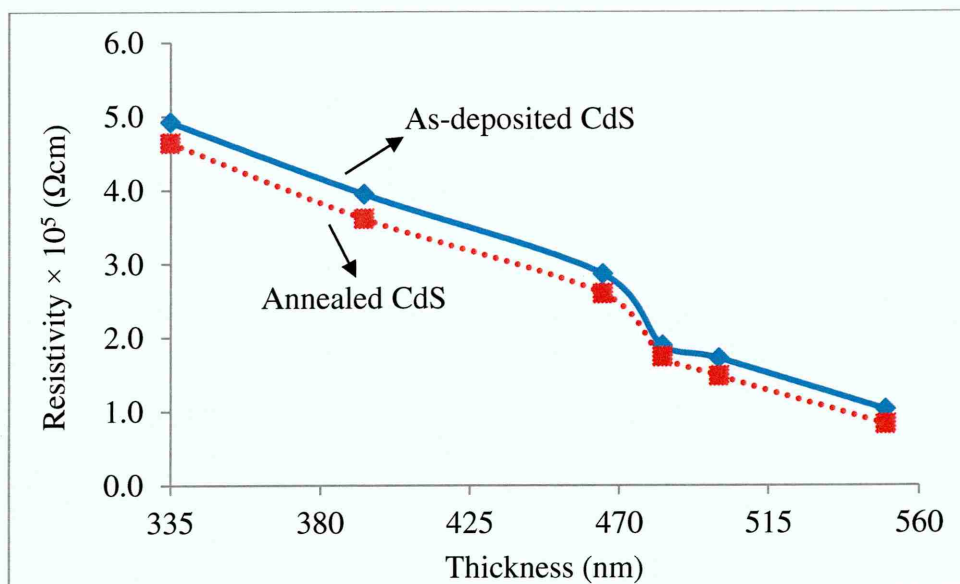


Figure 6.25: Variation of electrical resistivity as a function of thickness for the as-deposited and annealed CdS layers grown at the cathodic potential of 797 mV. The CdS layers were grown on glass/FTO substrates and then annealed at 400°C for 20 minutes in air.

6.4 Conclusions

CdS thin films have been successfully electrodeposited using 2-electrode system. All CdS layers presented in this chapter were deposited at temperature of $\sim 85^\circ\text{C}$ and pH of 2.70 ± 0.02 . The precursors used were aqueous solutions containing 0.30 M $\text{SC}(\text{NH}_2)_2$ and 0.20 M $\text{CdCl}_2 \cdot x\text{H}_2\text{O}$. The deposited CdS thin films showed good adhesion to the glass/FTO substrates. Based on the experimental observations, the best cathodic potential for the deposition of stoichiometric CdS thin films was identified as 797 mV. No visible precipitations of elemental S or CdS particles were observed in the deposition electrolyte showing a stable bath using thiourea precursor during the growth.

From the XRD results, it was found that all the deposited layers were polycrystalline in nature with hexagonal crystal structure and preferentially oriented along (002) plane. Improvements in the crystallinities of the CdS layers were observed after annealing at 400°C for 20 minutes in air. All deposited CdS layers grown at different cathodic potential showed n-type electrical conductivity. Also, optical absorption results showed the bandgap values in the range $\sim (2.42\text{--}2.48)$ eV after annealing.

The EDX spectra show that the layers grown at the growth voltage of 797 mV were approximately stoichiometric. The CdS layers grown below and above the growth voltage of 797 mV were found to be S-rich and Cd-rich respectively.

Observation from SEM and AFM images revealed that the CdS grains contain nano crystallites with the sizes in the range $\sim(11-33)$ nm. Based on the optical absorption and SEM results, the best annealing temperature and annealing time for the CdS layers were identified as 400°C for 20 minutes in air. Results also showed that when annealing temperature exceeds 400°C, the CdS layers will experience degradation, introducing cracks, pinholes and loss of material by evaporation or sublimation.

The electrical resistivity measurements show a reduction in resistivity values as CdS layer thickness increases. The resistivity values were in the range $(0.82-4.92) \times 10^5 \Omega\text{cm}$ for as-deposited and annealed CdS layers.

6.5 References

- [1] T.L. Chu and S.S. Chu, *Solid-State Electronics*, **38**(3) (1995) 533-549.
- [2] E. Sorokin, D. Klimentov, M.P. Frolov, Yu.V. Korostelin, V.I. Kozlovsky, Yu.P. Podmarkov, Ya.K. Skasyrsky, I.T. Sorokina, *Appl. Phys. B.*, **117** (2014) 1009-1014.
- [3] V. Smyntyna, V. Golovanov, S.Kaciulis, G. Mattogno, G.Righini, *Sensors and Actuators B.*, **24-25** (1995) 628-630.
- [4] R.P. Parker, *Phys. Med. Biol.*, **15**(4) (1970) 605-620.
- [5] R. Freriches, *J. Appl. Phys.*, **21** (1950) 312-317.
- [6] R. Zuleeg and R.S. Muller, *Solid-State Electronics*, **7** (1964) 575-582.
- [7] J. Conragan and R.S. Muller, *Solid-State Electronics*, **9**(2) (1966) 182.
- [8] L. Sheeney-Hai-ichia, S. Pogorelova, Y. Gofer and I. Willner, *Advanced Functional Materials*, **4**(5) (2004) 416-424.
- [9] H. Sezen, A.A. Rockett, S. Suzer, *Analatical Chemistry*, **84**(6) (2012) 2990-2994.
- [10] J. Britt and C. Ferekides, *Appl. Phys. Lett.*, **62**(22) (1993) 2851-2852.
- [11] A. Romeo, D.L. Batzner, H. Zogg, A.N. Tiwari, *Thin Solid Films*, **361-362** (2000) 420-425.
- [12] X. Wu, *Sol. Energy*, **77** (2004) 803-814.
- [13] B.M. Basol, *Solar cells*, **23** (1988) 69-88.
- [14] A. Ruthwarf, *Solar cells*, **2** (1980) 115-140.
- [15] M.M. Sayed, L.D. Partain, *Electronics Letters*, **10**(9) (1974) 163-164.
- [16] I.M. Dharmadasa, R.P. Burton, M. Simmonds, *Solar Energy Materials & Solar cells*, **90** (2006) 2191-2200.
- [17] K.W. Boer, *J. Appl. Phys.*, **107** (2010) 023701-023706.
- [18] N.B. Chaure, A.P. Samantilleke, R.P. Burton, J. Young, I.M. Dharmadasa, *Thin Solid Film*, **472** (2005) 212-216.
- [19] P. Jackson, D. Hariskos, E. Lotter, S. Paetel, R. Wuerz, R. Menner, W. Wischmann and M. Powalla, *Prog. Photovolt: Res. Appl.*, **19** (2011) 894-897.
- [20] O.K. Echendu, F. Fauzi, A.R. Weerasinghe and I.M Dharmadasa, *Thin Solid Films*, **556** (2014) 529-534.
- [21] S.K. Das, *Thin Solid Film*, **226** (1993) 259-264.
- [22] H. Matsumoto, K. Kuribayashi, H. Uda, Y. Komatsu, A. Nakano and S. Ikegami, *Solar Cells*, **11** (1984) 367-373.

- [23] A.K. Turner, J.M. Woodcock, M.E. Ozsan, J.G. Summers, J. Barker, S. Binns, K. Buchanan, C. Chai, S. Dennison, R. Hart, D. Johnson, R. Marshall, S. Oktik, M. Patterson, R. Perks, S. Roberts, M. Sadeghi, J. Sherborne, J. Szubert and S. Webster, *Solar Energy Materials*, **23** (1991) 388-393.
- [24] G. Kartopu, V. Barrioz , S.J.C. Irvine, A.J. Clayton, S. Monir, D.A. Lamb, *Thin Solid Films*, **558** (2014) 374-377.
- [25] N.B. Chaure, A.P. Samantilleke, I.M. Dharmadasa, *Solar Energy Materials & Solar Cells*, **77** (2003) 303-317.
- [26] C. Coluzza, M. Garozzo, G. Maletta, D. Margadonna, R. Tomaciello, and P. Migliorato, *Appl. Phys. Lett.*, **37**(6) (1980) 569-572.
- [27] A. Bosacchi, S. Franchi, P. Allegri, V. Avanzini and C. Frigeri, *Materials Chemistry and Physics*, **9** (1983)179-187.
- [28] M. Purica, E. Budianu, E. Rusu, P. Arabadji, *Thin Solid Films*, **511-512** (2006) 468-472.
- [29] N.R. Paudel, C. Xiao, Y. Yan, *J. Mater. Sci: Mater. Electron.*, **25** (2014) 1991-1998.
- [30] R.A Berrigan, N. Maung, S.J.C Irvine, D.J Cole-Hamilton, D. Ellis, *Journal of Crystal Growth*, **195** (1998) 718-724.
- [31] Z. He, G. Zhao, W. Weng, P. Du, Ge. Shen, G. Han, *Vacuum*, **79** (2005) 14-18.
- [32] M.C. Baykul, A. Balcioglu, *Microelectronic Engineering*, **51-52** (2000) 703-713.
- [33] P.K. Nair, M.T.S. Nair, V.M. Garcia, O.L. Arenas, Y. Pena, A. Castillo, I.T. Ayala, O. Gomezdaza, A. Sanchez, J. Campos, H. Hu, R. Suarez, M.E. Rincon, *Solar Energy Materials and Solar Cells*, **52** (1998) 313-344.
- [34] S.J. Lade, M.D. Uplane, C.D. Lokhande, *Materials Chemistry and Physics*, **53** (1998) 239-242.
- [35] S.J. Lade, C.D. Lokhande, *Materials Chemistry and Physics*, **49**(2) (1997) 160-163.
- [36] R.B. Gore, R.K. Pandey and S.R. Kumar, *Applied Surface Science*, **48/49** (1991) 530-534.
- [37] H.J. Gores, J. Barthel, *Naturwissenschaften*, **70**(10) (1983) 495-503.
- [38] I.M. Dharmadasa and J. Haigh, *J. Elechthrochem. Soc.*, **153** (1) (2006) G47-G52.
- [39] I.M. Dharmadasa, *Advances in Thin-Films Solar Cells*, Pan Stanford Publishing Pte. Ltd, Boulevard, Singapore, (2012) 41-42.

- [40] D.G. Diso, G.E. A. Muftah, V. Patel and I.M. Dharmadasa, *Electrochemical Society*, **156**(6) (2010) H647-H651.
- [41] K. Zarebska, M. Skompska, *Electrochimica Acta*, **56** (2011) 5731-5739.
- [42] J. Nishino, S. Chatani, Y. Uotani, Y. Nosaka, *Journal of Electroanalytical Chemistry*, **473** (1999) 217-222.
- [43] G. Sasikala, R. Dhanasekaran, C. Subramanian, *Thin Solid Films*, **302** (1997) 71-76.
- [44] K. Yamaguchi, T. Yoshida, T. Sugiura, and H. Minoura, *J. Phys. Chem. B*, **102** (1998) 9677-9686.
- [45] N.A. Abdul-Manaf, A.R. Weerasinghe, O.K. Echendu, I.M. Dharmadasa, *J. Mater. Sci: Mater. Electron.*, **26** (2015) 2418-2429.
- [46] K. Yamaguchi, P. Mukherjee, T. Yoshida, and H. Minoura, *Chemistry Letters*, **9** (2001) 864-865.
- [47] A.V. Naumov, V.N. Semenov, and E.G. Goncharov, *Inorganic Materials*, **37**(6) (2001) 647-652.
- [48] V.P. Timchenko, A.L. Novozhilov, and O.A. Slepysheva, *Russian Journal of General Chemistry*, **74**(7) (2004) 1046-1050.
- [49] P. Vanysek, *Electrochemical Series Table 1 Alphabetical*, CRC press LLC (2000).
- [50] P.H. Jefferson, S.A. Hatfield, T.D. Veal, P.D.C. King, C.F. McConville, J. Zuniga-Perez and V. Munoz-Sanjose, *Applied Physics Letters*, **92** (2008) 022101.
- [51] A.L. Patterson, *Physical Review*, **56** (1939) 978-982.
- [52] R. Dharmadasa, I.M. Dharmadasa and T. Druffel, *Advanced Engineering Materials*, **16**(11) (2014) 1351-1361.
- [53] A.I. Oliva, R.C. Rodriguez, O.S. Canto, V. Sosa, P. Quintana, J.L. Pena, *Applied Surface Science*, **205** (2003) 56-64.
- [54] H.R. Moutinho, D. Albin, Y. Yan, R.G. Dhere, X. Li, C. Perkins, C.-S. Jiang, B. To, M.M. Al-Jassim, *Thin Solid Films*, **436** (2003) 175-180.
- [55] N.R. Paudel, C.R. Grice, C. Xiao, and Y. Yan, *J. Appl. Phys.*, **116** (2014) 044506.
- [56] N.E. Gorji, *Opt. Quant. Electron.*, **47** (2015) 2445-2453.
- [57] W.J. Danaher, L.E. Lyons and G.C. Morris, *Solar Energy Materials*, **2** (1985) 137-148.
- [58] T.L. Chu, S.S. Chu, *Prog. Photovoltaics: Res. Appl.*, **1** (1993) 31-42.

- [59] A. Bosio, N. Romeo, S. Mazzamuto, V. Canevari, *Progress in Crystal Growth and Characterization of Materials*, **52** (2006) 247-279.
- [60] A.K. Mokhopadhyay, A.K. Chakraborty, A.P. Chatterjee and S.K. Lahiri, *Thin Solid Film*, **209** (1992) 92-96.
- [61] X. Wu, Y. Yan, R.G. Dhere, Y. Zhang, J. Zhou, C. Perkins, and B. To, *Phys. Stat. Sol. (c)*, **1**(4) (2004) 1062-1066.
- [62] I.M. Dharmadasa, P.A. Bingham, O.K. Echendu, H.I. Salim, T. Druffe, R. Dharmadasa, G.U. Sumanasekera, R.R. Dharmadasa, M.B. Dergachëva, K.A. Mit, K.A. Urazov, L. Bowen, M. Walls and A. Abbas, *Coating*, **4** (2014) 380-415.
- [63] M. Tsuji, T. Aramoto, H. Ohyama, T. Hibino, K. Omura, *Journal of Crystal Growth*, **214/215** (2000) 1142-1147.
- [64] A.R. Flores, O. Ares, J.M. Camacho, V. Rejon, J.L. Pena, *Solar Energy*, **86** (2012) 780-785.
- [65] H. Ohyama, T. Aramoto, S. Kumazawa, H. Higuchi, T. Arita, S. Shibutani, T. Nishio, J. Nakajima, M. Tsuji, A. Hanafusa, T. Hibino, K. Omura, and M. Murozono, *26th Photovoltaic Specialists Conference (PVSC)*, Sep. 30-Oct. 3 (1997) Anaheim, CA. pp: 343-346.
- [66] M. Estela Calixto, M. Tufiño-Velázquez, G. Contreras-Puente, O. Vigil-Galán, M. Jiménez-Escamilla, R. Mendoza-Perez, J. Sastré-Hernández, A. Morales-Acevedo. *Thin Solid Films*, **516** (2008) 7004-7007.
- [67] R. Litran, R. Alcantara, E. Blanco, and M. Ramirez-Del-Solar, *J. Sol-Gel. Sci. Technol.*, **8** (1997) 275-283.
- [68] P. Nandakumar, C. Vijayan, M. Rajalakshmi, A.K. Arora, Y.V.G.S. Murti, *Physica E*, **11** (2001) 377-383.
- [69] C. Wu, J. Jie, L. Wang, Y. Yu, Q. Peng, X. Zhang, J. Cai, H. Guo, D. Wu and Y. Jiang, *Nanotechnology*, **21** (2010) 505203 (7pp).
- [70] K.S. Balakrishnan and A.C. Rastogi, *Solar Energy Materials*, **20** (1990) 417-434.
- [71] E. Bertran, J.L. Morenza and J. Esteve, *Thin Solid Film*, **123** (1985) 297-306.

7.1 Introduction

Chemical bath deposition (CBD) is a solution growth technique in which many group I-VI, II-VI, IV-VI and V-VI compound semiconductors can be deposited from a single bath containing metal ions and a source of sulphur or selenium ions at different pH and temperatures [1]. In II-VI compound semiconductors, the CdS layers grown from CBD method are known for their high electronic quality in photovoltaic applications [2]. Also, the CdS thin films have been recognised as the most compatible heterojunction partner with CdTe and CIGS in solar cells application [3]. In the literature, the high efficiency CdTe and CIGS solar cells have been reported using CBD-CdS as a buffer/window layers [4,5]. The CBD growth technique has several advantages such as simplicity, scalability, cost-effectiveness, ability to grow uniform and compact thin films on rough substrates and no requirement for the complex instruments [6]. In addition, CBD is a slow deposition growth technique which simplifies the better orientation of crystallites and produce grains with better crystal structures [7]. This technique is suitable for the growth of semiconductor thin films with thickness in the range (0.02-1.0) μm [8]. Because CBD is a low temperature growth, the post-deposition annealing is required to improve the CdS thin films quality. Usually, for the growth of CBD-CdS layers different cadmium precursors such as cadmium sulphate (CdSO_4) [9], cadmium nitrate ($\text{Cd}(\text{NO}_3)_2$) [10], cadmium chloride (CdCl_2) [11] and cadmium acetate ($\text{Cd}(\text{CH}_3\text{CO}_2)_2$) [12] have been used which serves as the source for Cd ions. In most cases, thiourea ($\text{SC}(\text{NH}_2)_2$) precursor has been used as the source for sulphur ions.

In this work, for the growth of CBD-CdS, cadmium acetate and thiourea precursors were used as the source for Cd and S ions respectively. The aim of this experiment was to study the structural, morphological, optical and electrical properties of the CBD-CdS and compare these results with the ED-CdS presented in chapter 6.

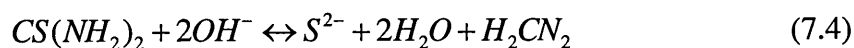
7.2 Preparation of CBD-CdS aqueous solution

For the CBD experiment, a typical bath contained 4×10^{-3} M $\text{Cd}(\text{CH}_3\text{CO}_2)_2 \cdot 2\text{H}_2\text{O}$, 20×10^{-3} M $\text{SC}(\text{NH}_2)_2$, 6×10^{-2} M ammonium acetate ($\text{NH}_4\text{C}_2\text{H}_3\text{O}_2$). All chemicals used

for this experiment were analytical reagent grade with the purity of more than (99.99%) and purchased from the Sigma Aldrich Ltd UK. A 200 ml glass beaker containing 100 ml of deionised water was used for the dissolution of all chemicals. The pH of the aqueous solution was adjusted to 9.10 ± 0.02 using NH_4OH at room temperature. The temperature of the bath was gradually increased to $\sim 80^\circ\text{C}$ using a magnetic stirrer hotplate with moderate and continuous stirring during the deposition. Prior to deposition glass/FTO substrates (TEC 7) were kept in an ultrasonic bath containing detergent solution for 30 minutes. Afterward, glass/FTO substrates were rinsed with deionised water and subsequently cleaned with organic solvents (methanol and acetone) and finally rinsed with deionised water again. During the deposition, the substrates were placed vertically in the bath. The final thicknesses of the films obtained for a deposition time of 20 minutes were ~ 90 nm. The CBD-CdS films were found to be uniform, compact, transparent and well adherent to the glass/FTO substrates.

7.3 Reaction mechanism

The reaction mechanism of the CBD-CdS formation from the combination of cadmium acetate $[\text{Cd}(\text{CH}_3\text{CO}_2)_2 \cdot 2\text{H}_2\text{O}]$, thiourea $[\text{SC}(\text{NH}_2)_2]$, ammonium acetate ($\text{NH}_4\text{C}_2\text{H}_3\text{O}_2$) and ammonium hydroxide (NH_4OH) in the alkaline and aqueous solutions are shown as follows [3]:



NH_4OH serve as complexing agent, thiourea provides S^{2-} , $\text{NH}_4\text{C}_2\text{H}_3\text{O}_2/\text{NH}_4\text{OH}$ serves as buffer. In the CBD-CdS, two reaction mechanisms are taking place. The first mechanism is homogeneous reaction (cluster by cluster) and the second mechanism is heterogeneous reaction (ion by ion) [13,14]. In the homogeneous reaction colloidal particles of CdS grows in the solution which precipitate in the bath and on the substrates.

The results are powdery and non-adherent layers. In the heterogeneous reactions as shown in Equations (7.3), (7.4) and (7.5), the CdS layers grow ion by ion on the substrates and the results are a well-crystallised and well-adherent CdS layers on the substrates. The unfavourable homogenous reactions may be suppressed by reduction of thiourea and cadmium acetate concentrations and increasing ammonium hydroxide and ammonium acetate concentrations at lower temperatures.

7.4 Results and discussions

7.4.1 X-ray diffraction

7.4.1.1 Effect of films thickness on the XRD patterns of CBD-CdS layers

Figure 7.1 (a) shows the XRD patterns of the as-deposited CdS layers grown on glass/FTO substrates with different thicknesses in the range $\sim(90-450)$ nm. Results show that the CBD-CdS were polycrystalline with a mixture of hexagonal, cubic and orthorhombic crystal structures. The small XRD peaks observed at 2θ values in the range $(25.34-25.57)^\circ$ represents the diffraction from orthorhombic (040) plane. The other small XRD peak observed at 2θ values in the range $(54.48-54.58)^\circ$ are corresponding to the diffractions from hexagonal (004) or cubic (222) planes respectively. The preferred orientation peaks were observed at 2θ values in the range $(26.48-26.96)^\circ$ which can be either due to the diffractions from hexagonal (002) or cubic (111) planes. In the literature, the mixtures of cubic and hexagonal phases have been reported for the CBD-CdS layers [3,15,16]. Reports show that the hexagonal phases are more stable than cubic phase at higher temperatures [17,18]. Other investigations on the CdS grown by CBD method also show that the structural transition from cubic to hexagonal phase occurs at annealing temperature of 300°C [19]. Also, the CBD-CdS layers with the hexagonal crystal structure have been reported in the literature [2]. It should be noted that the (002)H/(111)C CdS peaks overlaps with the underlying tetragonal (110) FTO peak (JCPDS No. 41-1445). However, the intensity of the (002)H/(111)C peaks are much higher than the FTO peak when the CdS thicknesses are more than 180 nm. Hence, the effect of FTO peak on the XRD and FWHM of the CdS peak is negligible due to its low intensity. For this reason, in this work, all XRD analysis are based on the diffraction from H(002) or C(111) planes. It is worth mentioning that, unlike the ED-CdS layers which were hexagonal in crystal structures

as shown that, in the previous chapter, the as-deposited CBD-CdS layers were shown to have a mixture of hexagonal and cubic phases. Based on the experimental observations in this work, the XRD peaks were found to be in a good agreement with the JCPDS files number: 00-001-0783, 00-001-0647 and 00-047-1179 for hexagonal, cubic and orthorhombic CdS respectively.

In Figure 7.1 (a), as the thickness of the layers increases, the intensity of orth(040) and H(004)/C(222) peaks increases slightly whereas the (002)H/(111)C preferred orientation peak increased drastically when the thickness of the films are above 180 nm as shown in Figure 7.1 (b). The increase in the peak intensities are due to the increase in crystallite and grain sizes as the film thickness increases.

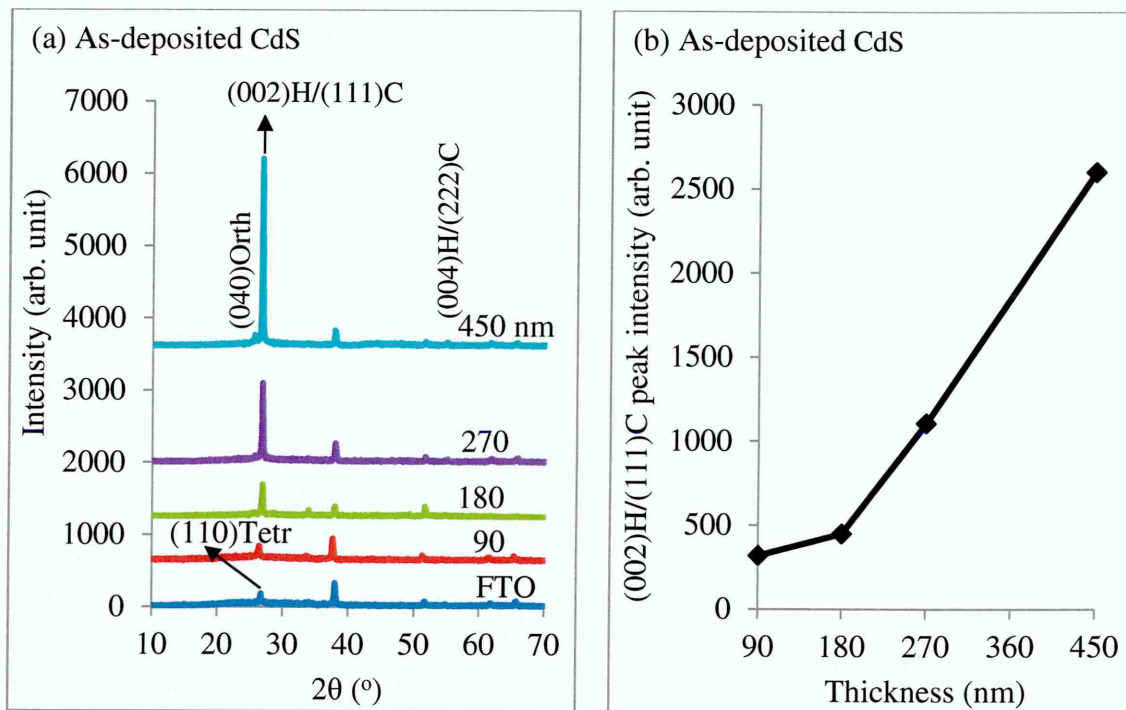


Figure 7.1: Variation of (a) XRD patterns and (b) (002)H/(111)C peak intensities with thickness for as-deposited CBD-CdS layers.

Figure 7.2 shows the XRD patterns of the as-deposited and annealed CdS layers at 400°C for 20 minutes in air with thicknesses of ~450 nm. Results show the improvement in the intensities of all three peaks after annealing.

Table 7.1 shows the variation of the FWHM and the corresponding crystallite sizes for the as-deposited and annealed CdS layers. The crystallite sizes were estimated using Equation (6.6) presented in chapter 6. For the as-deposited CBD-CdS layers, the crystallite sizes were ~11 nm which were the same as the crystallite sizes of the as-

deposited ED-CdS layers shown in chapter 6 (section 6.3.3). After annealing, the crystallite size values of the CBD-CdS layers were increased to ~ 66 nm which are shown to be higher than the crystallite sizes of the annealed ED-CdS layers (~ 33 nm) shown in chapter 6 (section 6.3.3). The difference in crystallite sizes of the ED-CdS and CBD-CdS can be due to the differences in growth techniques and conditions used for the growth.

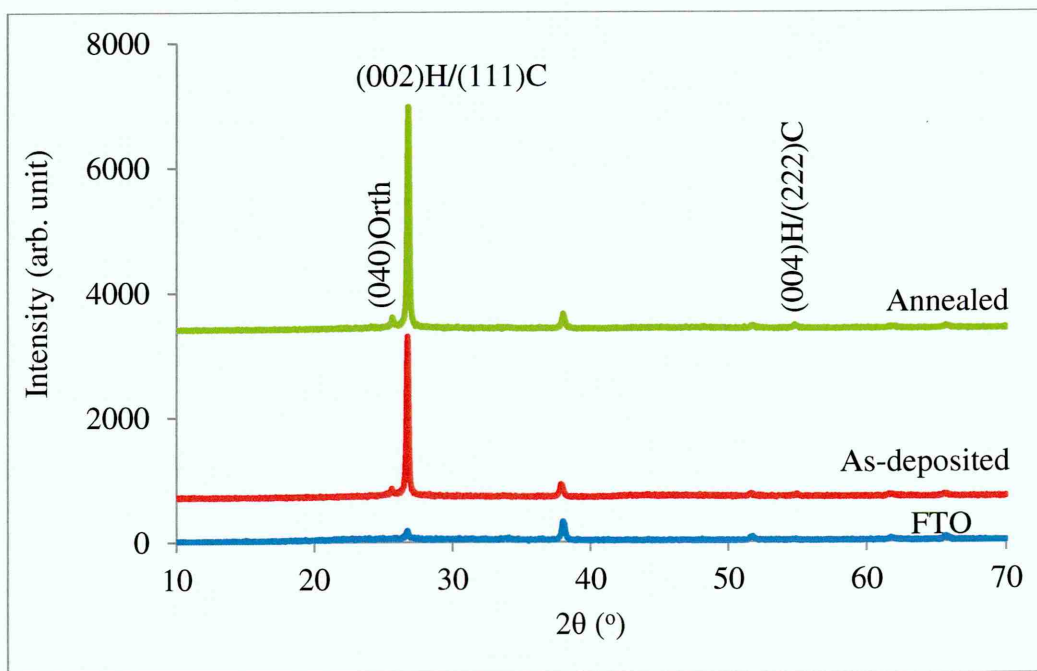


Figure 7.2: The XRD patterns of as-deposited and annealed CBD-CdS layers. The CdS layers were annealed at 400°C for 20 minutes in air.

Table 7.1: Variation of crystallite sizes for the as-deposited and annealed CBD-CdS layers based on (002)H/(111)C peak. The CBD-CdS with thickness of ~ 450 nm was annealed at 400°C for 20 minutes in air.

Thickness (nm)	2θ (°)		FWHM (°)		Crystallite size (nm)	
	As-deposited	Annealed	As-deposited	Annealed	As-deposited	Annealed
450	26.74	26.77	0.779	0.129	11	66

7.4.1.2 Effect of annealing temperature on the XRD patterns of CBD-CdS layers

In this experiment, the effects of different annealing temperatures on the structural properties of the CBD-CdS layers were studied. For this reason, the CdS layers with thickness of ~ 270 nm were deposited on glass/FTO substrates. Afterward, the samples were divided into seven parts; the first part remained as as-deposited and the remaining parts were annealed at different temperatures of 200 to 450°C for 20 minutes in air respectively. In this experiment, the annealing temperatures of 500°C and 550°C have not been used due to the observation of material losses and large number of pinholes in the ED-CdS layers as previously shown in chapter 6 (section 6.3.6.2).

This experiment shows that as the annealing temperature increases from 200 to 400°C, the intensity of (002)H/(111)C peak also increases as shown in Figures 7.3 (a) and (b). Further increase in the annealing temperature from 400 to 450°C, results in the reduction of (002)H/(111)C peak intensity as shown in Figure 7.3 (b).

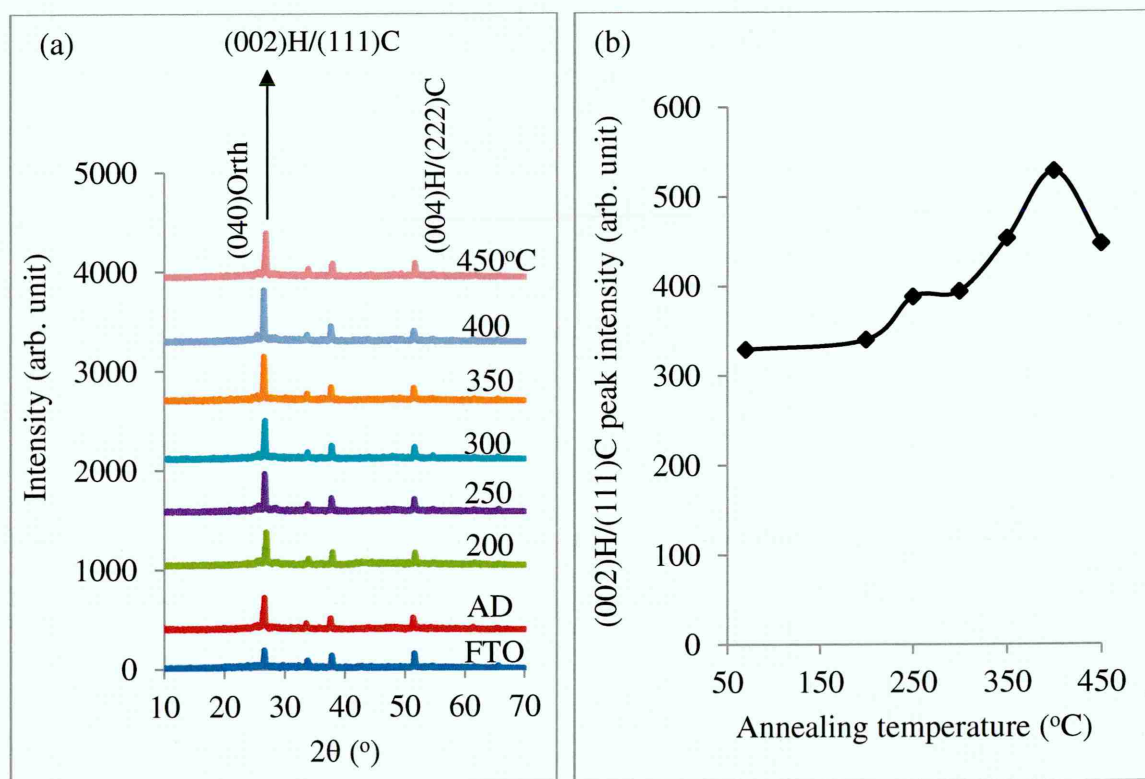


Figure 7.3: Variation of (a) XRD pattern and (b) (002)H/(111)C peak intensity with annealing temperature. All CBD-CdS layers have the same thickness of ~ 270 nm.

Similar trends were observed for the crystallite sizes of the CBD-CdS. The crystallite sizes increased from ~11 nm for the as-deposited layers to ~66 nm after annealing at 400°C for 20 minutes in air. For the annealing temperature of more than 400°C, crystallite sizes start to decrease as shown in Table 7.2. These results clearly show that CBD-CdS should not be annealed at temperature above 400°C which is similar to the annealing condition obtained for ED-CdS layers.

Table 7.2: Variation of the crystallite size with annealing temperature for the CBD-CdS layers. The annealing time for all CdS samples was 20 minutes in air.

Annealing temperature (°C)	2 θ (°)	FWHM (°)	Crystallite size (nm)
As-deposited	26.96	0.779	11
200	26.72	0.227	37
250	26.58	0.227	37
300	26.73	0.194	44
350	26.54	0.194	44
400	26.67	0.129	66
450	26.92	0.194	44

7.4.1.3 Effect of annealing time on the XRD patterns of CBD-CdS layers

This work has been carried out to study the effect of the annealing time on the structural properties of the CBD-CdS layers at temperature of 400°C. Therefore, the CdS layers were grown on glass/FTO substrates with thicknesses of ~270 nm. Afterward, the sample was divided into seven parts; the first part remained as it was and the remaining parts were annealed at 400°C in air for different durations of 5 to 30 minutes.

Results show the gradual increase in the (002)H/(111)C peak intensity for the annealing times between 5 and 20 minutes. Further increase in the annealing time beyond 20 minutes lead to the reduction in the (002)H/(111)C peak intensity. In comparison to the CBD-CdS, in ED-CdS layers the reductions in H(101) peak intensity have not been observed when layers were annealed at 400°C for durations of 25 and 30

minutes as shown in chapter 6 (section 6.3.3.2). This can be due to different crystal orientation of H(101) planes of ED-CdS as compared to the (002)H/(111)C planes of CBD-CdS which can affect the material properties of the films.

Table 7.3 shows the variation of FWHM and crystallite size as a function of annealing time for the CBD-CdS layers. Results show the reduction in FWHM and increase in the crystallite size for the annealing time of 5 to 20 minutes. The crystallite sizes of the as-deposited samples were ~ 11 nm. After annealing for 20 minutes duration, the crystallite sizes gradually were increased and reach to its maximum values of 66 nm. Further increase in annealing time, above 20 minutes, results in the increase in the FWHM and reduction in the crystallite sizes. According to the structural studies in this work, the best annealing temperature and annealing time for CBD-CdS were found to be at 400°C for 20 minutes in air.

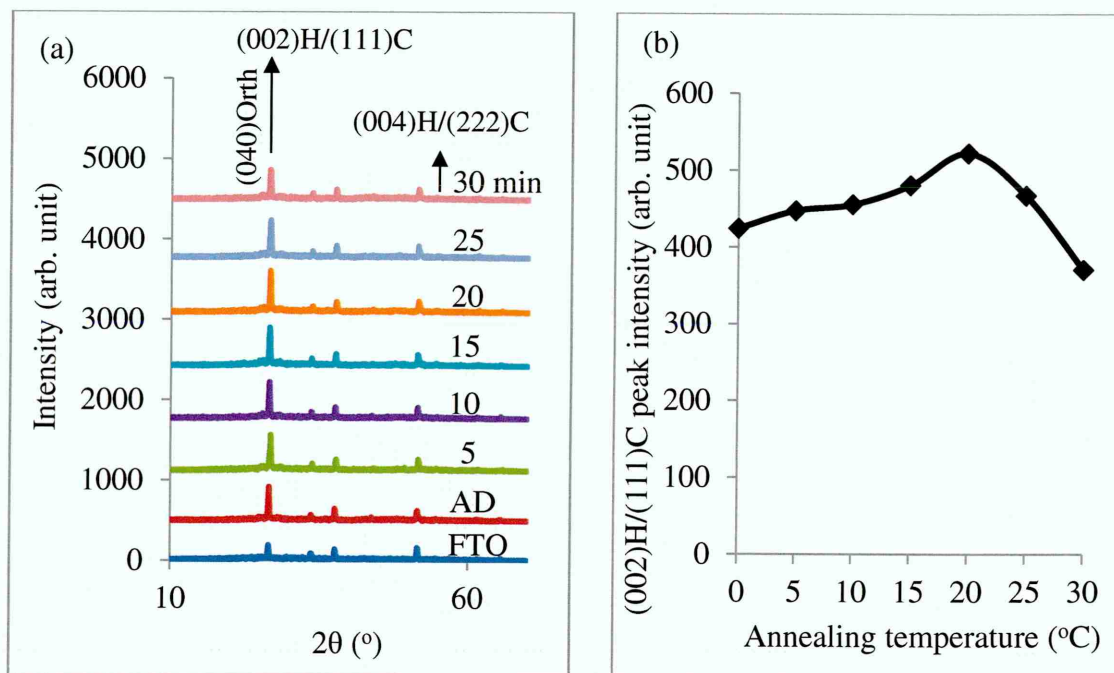


Figure 7.4: (a, b) Variation of (002) peak intensity with annealing time for the CBD-CdS layers. The annealing temperature for all layers was 400°C in air.

Table 7.3: Variation of the crystallite size with annealing time for the CBD-CdS layers. All CdS layers were annealed at 400°C for different durations of 5 to 30 minutes in air.

Annealing time (min.)	2θ ($^{\circ}$)	FWHM ($^{\circ}$)	Crystallite size (nm)
As-deposited	26.96	0.779	11

5	26.72	0.259	32
10	26.67	0.227	37
15	26.65	0.227	37
20	26.64	0.129	66
25	26.66	0.162	52
30	26.74	0.198	44

7.4.2 Optical absorption spectroscopy

7.4.2.1 Effect of film thickness on the optical properties of CBD-CdS layers

In this section, the effect of thickness on the optical absorption and transmittance of the CBD-CdS layers has been studied. For this work, CdS layers with different thicknesses of 90 to 450 nm were grown on glass/FTO substrates. Afterward, CdS layers were annealed at 400°C for 20 minutes in air.

Figures 7.5 (a) and (b) show the optical absorption spectra of the as-deposited and annealed CdS layers. Results show an increase in the gradient of the optical absorption and reduction in energy bandgap values as the thickness increases. For the as-deposited layers, the energy bandgap values were in the range (2.45-2.48) eV. After annealing, the bandgap values shift to the lower energies in the range (2.40-2.41) eV which is close to the bulk bandgap value of CdS crystal (2.42 eV) as shown in Table 7.4. The lowest optical absorptions were observed for the samples having the lowest thickness of 90 nm.

Figures 7.5 (c) and (d) show the transmittance spectra of the as-deposited and annealed layers. Results clearly show the reduction in transmittance as the thickness increases from 90 to 450 nm. In the as-deposited samples, the optical transmittance falls from ~79% to ~31% in the wavelength ranges of 530 to 780 nm when thickness increased from 90 nm to 450 nm. After annealing, improvements in transmittance were observed from ~36% to ~83% due to improvement in the crystallite and grain size of the CdS layers. Also, for the samples with thickness of 90 nm, a clear shift in the absorption edges towards the blue region were observed for both as-deposited and annealed layers as compared to other samples with higher thickness values. Blue

wavelength transmission can also take place due to incomplete coverage or islanding effect. This effect however is not helpful in developing thin film solar cells. The shift in absorption edge toward the blue region increases the blue response and eventually increases the photocurrent in the device. It should be noted that the performance of the CdS/CdTe solar cells strongly depends on the thickness of CdS thin films [20,21]. For this reason, the thickness of CdS layers should be low enough to allow high transmission and uniform to avoid short circuiting effect.

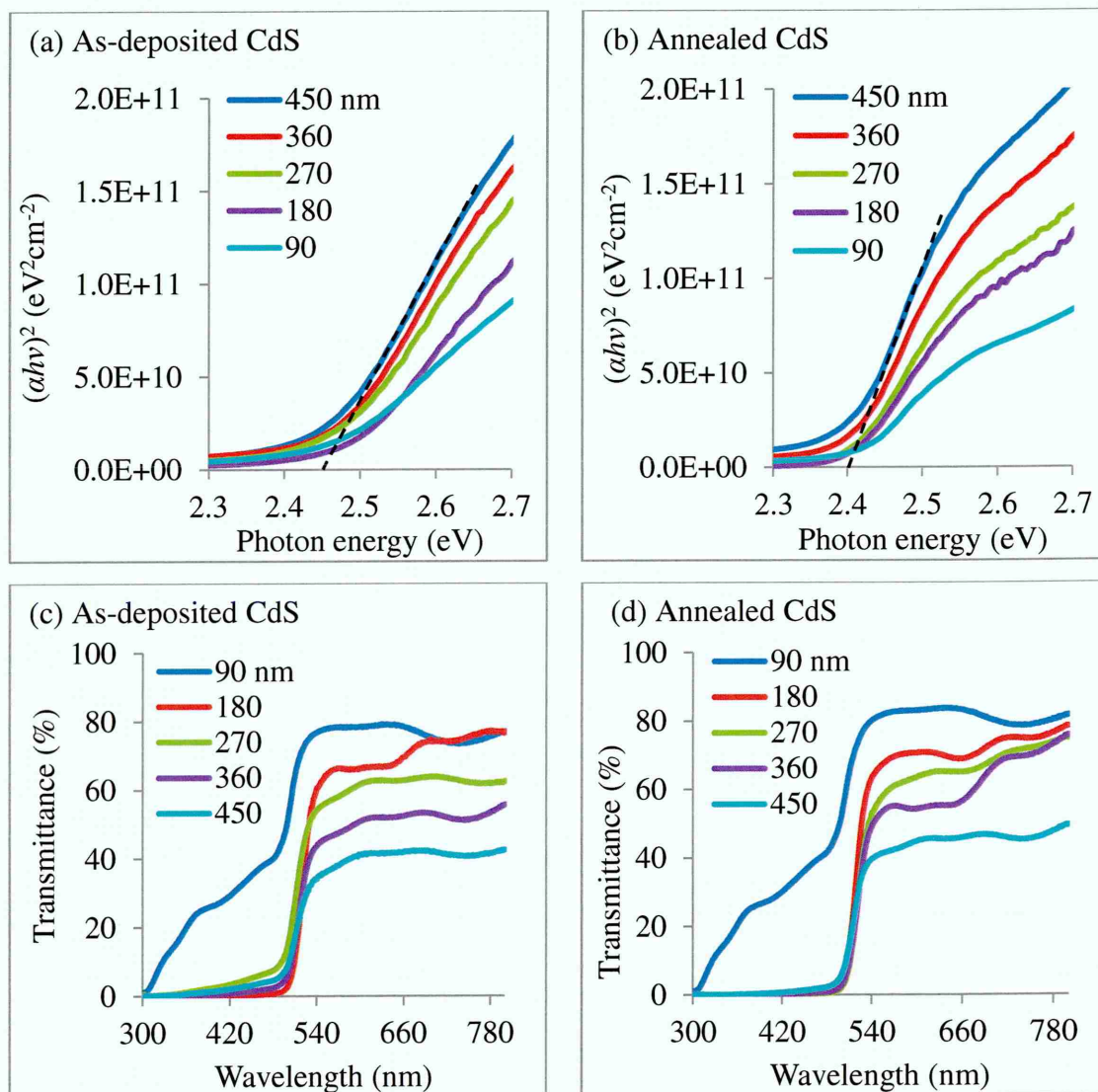


Figure 7.5: (a, b) Variation of optical absorption of different CdS thicknesses as a function of photon energy and (c, d) transmittance spectra of different CdS thicknesses as a function of wavelength for the as-deposited and annealed CBD-CdS layers. The annealing temperature for all CBD-CdS layers was 400°C for 20 minutes in air.

Table 7.4: Variation of energy bandgap with thickness for the as-deposited and annealed CBD-CdS layers. The annealing temperature for all CBD-CdS layers was 400°C for 20 minutes in air.

Thickness (nm)	Energy bandgap ± 0.01 (eV)	
	As-deposited	Annealed
90	2.48	2.41
180	2.46	2.41
270	2.46	2.41
360	2.46	2.40
450	2.45	2.40

7.4.2.2 Effect of annealing temperatures on the optical properties of CBD-CdS layers

In order to study the effect of different annealing temperatures on the optical absorption and transmittance spectra of the CBD-CdS, the layers with the thicknesses of ~90 nm were grown on glass/FTO substrates. Thereafter, the layers were annealed at different temperatures range of 200 to 450°C for the same duration of 20 minutes in air. Finally, results were compared with the as-deposited layers.

Figures 7.6 (a) and (b) show the optical absorption and transmittance spectra of the CdS layers annealed at the temperature ranges of 200 to 450°C for 20 minutes in air. Results show that as the annealing temperature increases from 200 to 450°C, the bandgap decreases gradually and shifts toward lower energy. The energy bandgap values observed for the as-deposited CdS layers were 2.48 eV. After annealing at temperature ranges of 350 to 450°C, the energy bandgap values fall to the same value of 2.42 eV which is the bulk energy bandgap for CdS crystal as shown in Table 7.5. Also, the gradient of the absorption edge increases with increase in annealing temperature. In the transmittance spectra shown in Figure 7.6 (b), as the annealing temperature increases the transmittance increases and reaches its maximum values at annealing temperature of 400°C and reduces again when the annealing temperature exceed 400°C. In addition, the absorption edge in the transmittance spectra shifts toward the blue region as the temperature increases which shows that the absorption loss in the blue

region has been minimised upon annealing. The blue shift in the transmittance spectra improves the photocurrent in the solar cells [22]. In this work, the transmittance of the as-deposited CBD-CdS layers were in the range (60-75)% between the wavelength ranges of 530 and 800 nm. For the samples annealed at temperature of 400°C, the transmittance were in the range (75-85)% for the same wavelengths range of 530 to 800 nm which shows the importance of post-deposition annealing for the improvement of optical properties of the CdS layers. In general, the gradient of the absorption edges in the CBD-CdS layers were higher than the ED-CdS layers before and after annealing (chapter 6-section 6.3.5.2). It should be noted that depending on the thickness of the films, the transmittance can vary in both ED- and CBD-CdS layers. According to the results obtained in this section, the best annealing temperature for the CBD-CdS layers was found to be at 400°C.

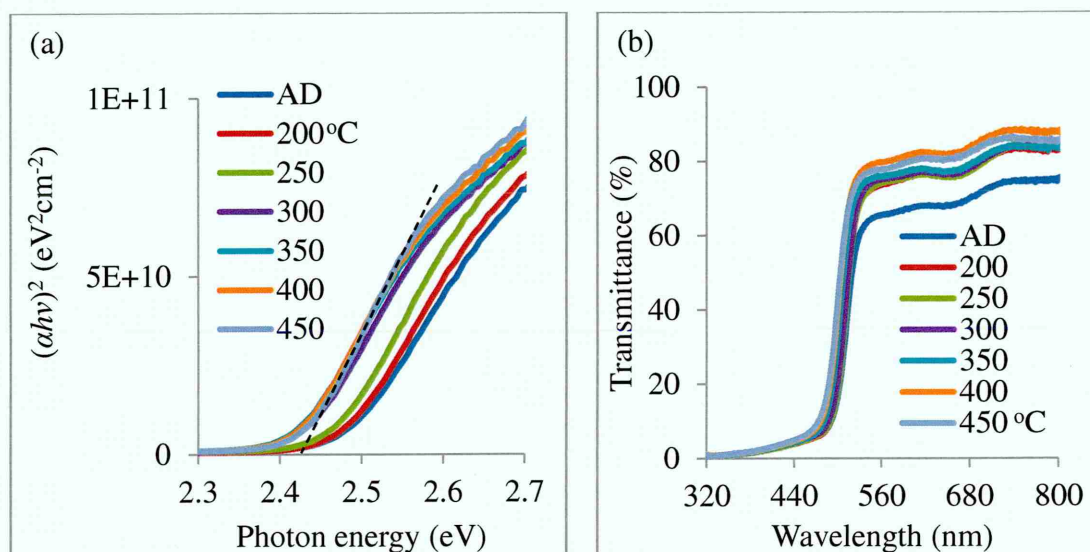


Figure 7.6: (a) Optical absorption and (b) transmittance spectra of CBD-CdS layers annealed at different temperatures (200-450)°C for 20 minutes in air.

Table 7.5: Variation of energy bandgap with annealing temperature for the CBD-CdS layers annealed at different temperatures (200-450)°C for 20 minutes in air.

Annealing temperature (°C)	As-deposited	200	250	300	350	400	450
Energy bandgap ± 0.01 (eV)	2.48	2.47	2.46	2.43	2.42	2.42	2.42

7.4.2.3 Effect of annealing time on the optical properties of CBD-CdS layers

Based on the experimental observation in the previous section, in this section the effect of annealing time on the optical properties of CBD-CdS layers was studied. Because of this, the CdS layers with the thicknesses of ~ 90 nm were grown on glass/FTO substrates. Afterward, the samples were annealed at the same temperature of 400°C for different durations of 5 to 30 minutes in air and results are shown in Figures 7.7 (a) and (b).

In Figure 7.7 (a), when CdS layers were annealed for different duration of 5 to 30 minutes, energy bandgaps were shifted towards the lower energy values. The energy bandgap values shifted from 2.48 eV for the as-deposited layers to the lower energy bandgap values in the range (2.43-2.41) eV after annealing. Also, the gradient of the optical absorption edge increase after annealing. The lower bandgap values were observed for the annealing time of 30 minutes as shown in Table 7.6.

In Figure 7.7 (b), annealing for the different durations of 5 to 25 minutes results in the increase of the transmittance for the CdS layers. The transmittance was approximately the same for the annealing times of 5 to 25 minutes. When the annealing time exceeds 25 minutes, the transmittance reduces again.

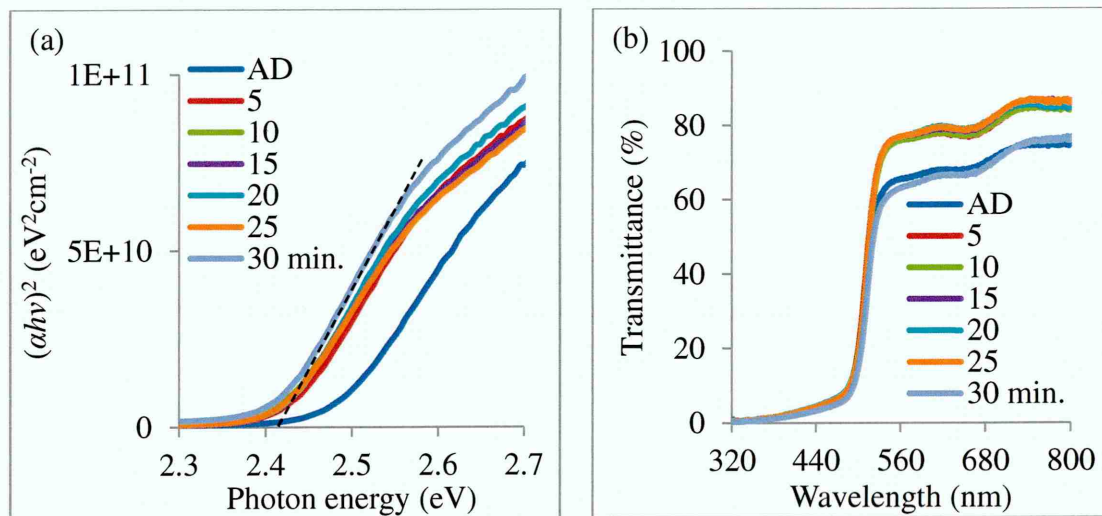


Figure 7.7: (a) Optical absorption and (b) transmittance spectra of CBD-CdS layers annealed at 400°C for different durations of 5 to 30 minutes in air.

Table 7.6: Variation of the energy bandgap as a function of annealing time for the CBD-CdS layers. All CdS layers were annealed at 400°C for different durations of 5 to 30 minutes in air.

Annealing time (min.)	As-deposited	5	10	15	20	25	30
Energy bandgap ± 0.01 (eV)	2.48	2.43	2.42	2.42	2.42	2.42	2.41

Based on the experimental observations obtained from the optical absorption studies for CBD-CdS in this work, the best annealing time and annealing temperature were found to be at 400°C for 20 minutes in air. These results clearly show that both ED- and CBD-CdS layers have the same optimum annealing conditions.

7.4.3 Scanning electron microscopy (SEM)

Figures 7.8 (a) and (b) show the top view and cross section SEM images of the as-deposited CdS layers grown on glass/FTO substrates. The SEM images show a compact and uniform CdS grains coverage of the FTO surface without observing pinholes in between the grains. The grain size values of the as-deposited CBD-CdS layers were in the range (90-200) nm which were slightly lower than the grain size of the as-deposited ED-CdS layers shown in chapter 6 (section 6.3.6). The uniform distribution of the grains in the CBD-CdS thin films can be due to the nature of this growth technique unlike the electrodeposition technique where electric current is required to deposit the thin films. In addition, in CBD-CdS growth technique, the deposition is taking place in an alkaline solutions with pH values in the range $\sim(9.0-13.7)$ [3,7,23] while in ED-CdS the films deposition are taking place in acidic solutions. These differences in growth conditions can affect the morphological properties of the ED- and CBD-CdS layers.

The SEM cross section image of the as-deposited CdS layers with magnification of 120,000x shows that CBD-CdS layer uniformly covers the FTO surface. The average thickness of the as-deposited CdS layer estimated from the SEM cross section was ~ 450 nm. This thickness was obtained from five times growth of CBD-CdS. This

means that in each growth, ~ 90 nm of CBD-CdS layers is deposited on glass/FTO substrates in ~ 20 minutes.

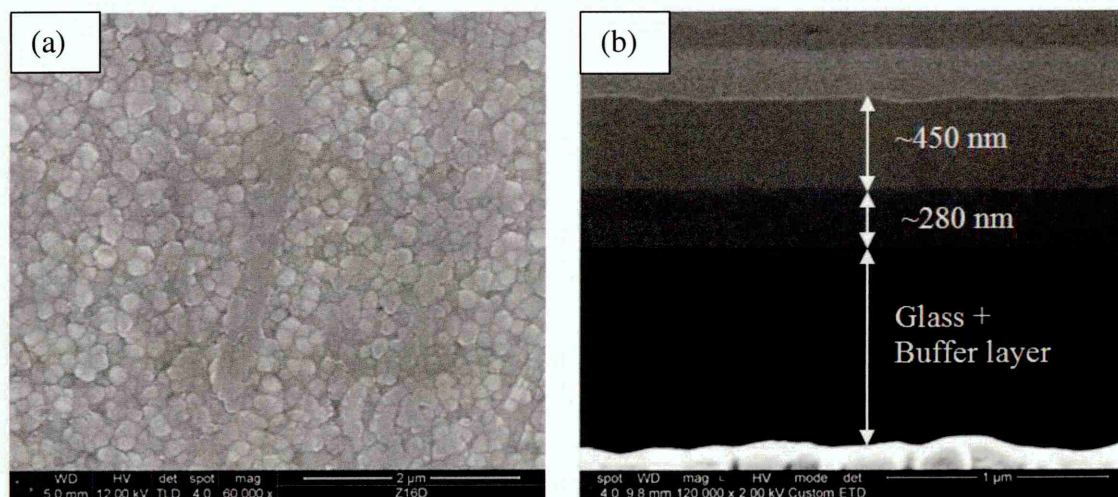


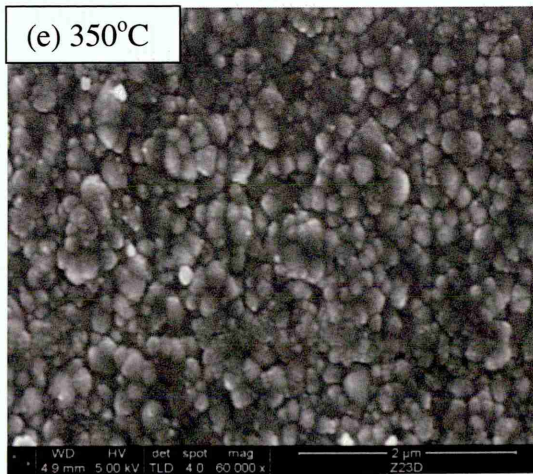
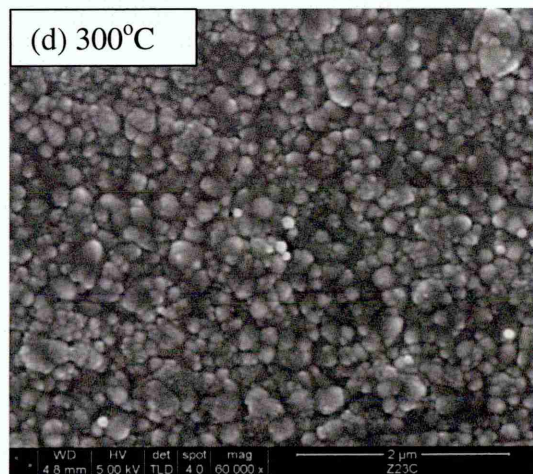
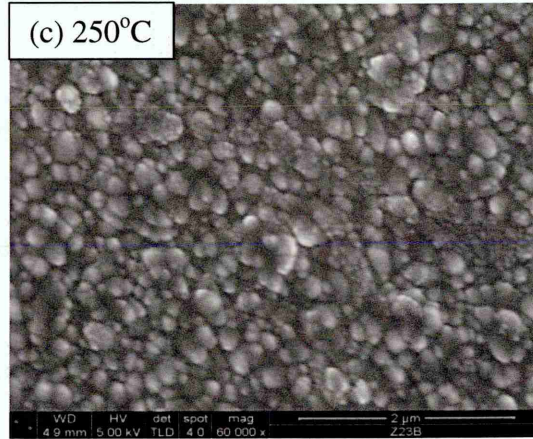
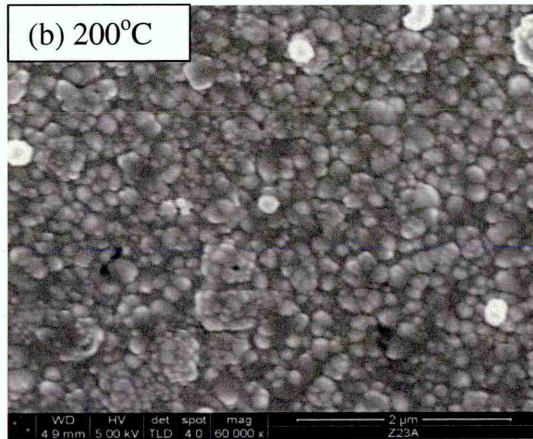
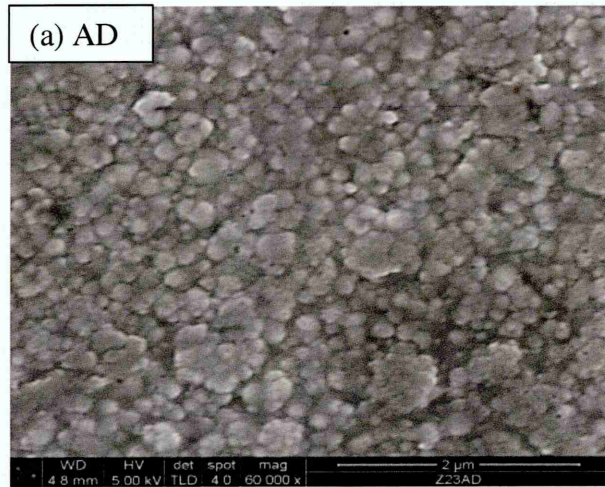
Figure 7.8: (a) Surface and (b) cross section SEM images of the as-deposited CBD-CdS layers with 60,000x and 120,000x magnifications respectively. The thickness of CdS layer is estimated close to 450 nm.

7.4.3.1 Effect of annealing temperature on the surface morphology of CBD-CdS layers

Figures 7.9 (a)-(g) show the SEM images of the as-deposited and annealed CdS layers in the temperature range of 200 to 450°C. All CdS layers were grown on glass/FTO substrates with thickness of 90 nm. This study was carried out in order to investigate the effect of the different annealing temperatures on the surface morphology of the CBD-CdS layers.

For the as-deposited layers, the average grain size values obtained from SEM image were in the range ~ 200 nm. As the annealing temperature increases to 350°C, the average grain sizes increase slightly to ~ 255 nm as shown in Figures 7.9 (a)-(e) and Figure 7.10. When annealing temperature exceeds 350°C, the reduction in the average grain size values were observed. The average grain size values at the annealing temperature of 450°C were ~ 185 nm. However, no cracks and pinholes were observed in the CBD-CdS layers unlike in ED-CdS layers where the cracks have been observed at the same annealing temperature of 450°C. In addition, at annealing temperature of 450°C, some of the grains starts to coalesce together producing larger grains with the size

of ~530 nm which has been circled as shown in Figure 7.9 (g). It should be noted that, for all annealing temperatures of 200 to 450°C, CBD-CdS layers showed a uniform and compact morphology. This uniformity and compactness of the films prevent short circuiting effect in the device and improve the performance of the fabricated solar cells.



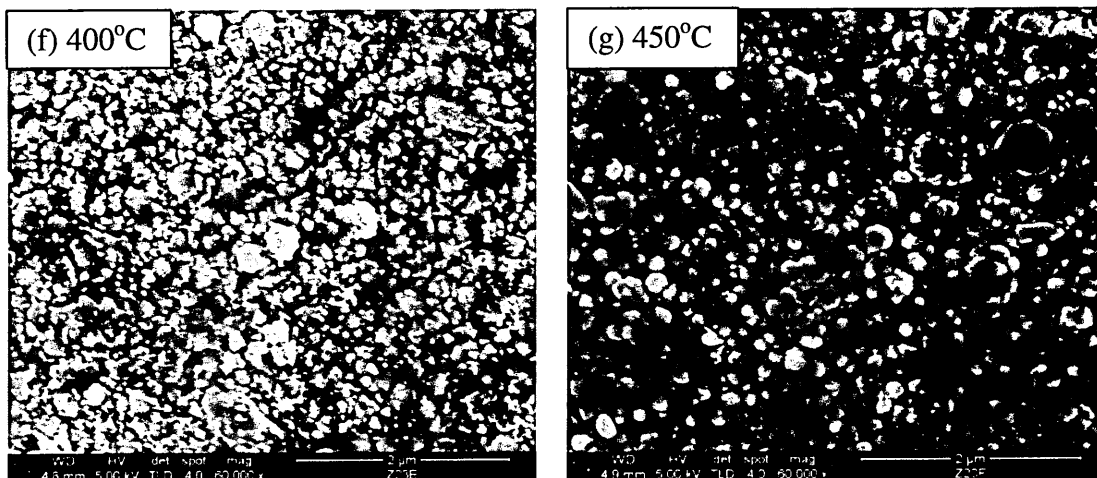


Figure 7.9: SEM images of the as-deposited and annealed CBD-CdS layers at different temperatures in the range (200-450) $^{\circ}$ C. The annealing time for all layers was 20 minutes in air.

From the morphological study, the suitable annealing temperature for CBD-CdS layers were found to be in the range (350-400) $^{\circ}$ C. However, based on the structural and optical study shown in the previous sections, the annealing temperature of 400 $^{\circ}$ C were found to be better than 350 $^{\circ}$ C.

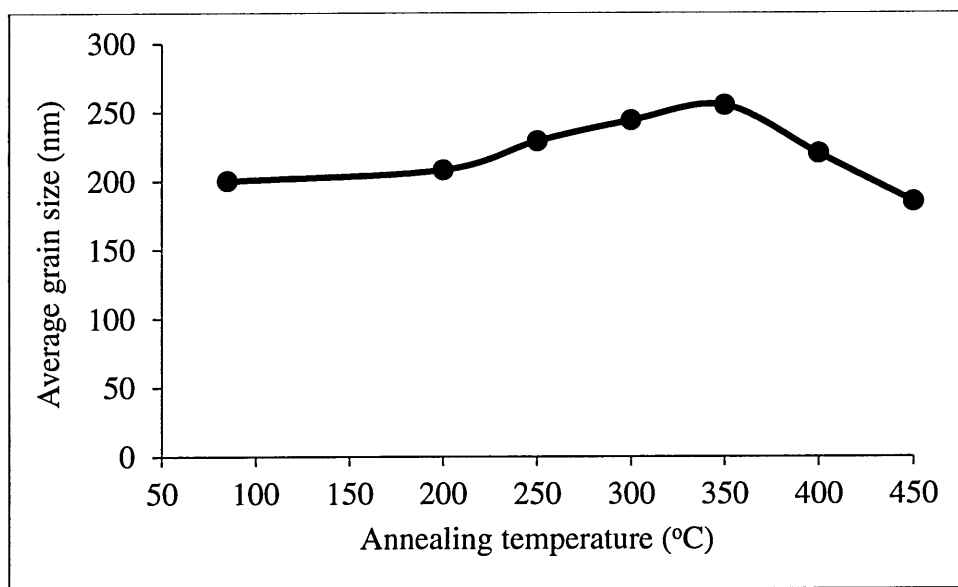
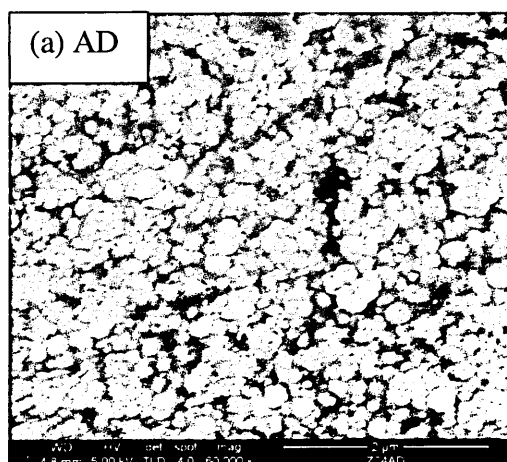


Figure 7.10: Variations of the average grain size with annealing temperature for the CBD-CdS layers. All CdS layers with thickness of \sim 90 nm were annealed at different temperatures in the range of 200 to 450 $^{\circ}$ C for the same duration of 20 minutes in air.

7.4.3.2 Effect of annealing time on the surface morphology of CBD-CdS layers

This experiment was carried out to investigate the effect of different annealing time on the surface morphology of the CBD-CdS layers. For this reason, the CBD-CdS layers with the same thickness of ~ 90 nm were grown on glass/FTO substrates. Afterward, samples were annealed at 400°C for different time durations ranging from 5 to 30 minutes in air. The results are shown in Figures 7.10 (a)-(f).

In the as-deposited sample shown in Figure 7.10 (a), the average grain size values were in the range ~ 200 nm. After 5 minutes annealing, the average grain size values increase slightly to ~ 230 nm. For the annealing time duration of 10 and 15 minutes, the morphologies changed. The grain boundaries become indistinguishable due to the random orientation or recrystallisation as shown in Figures 7.10 (c) and (d). After 20 minutes annealing, the grain boundaries become distinguishable again which can be due to the coalescence of the smaller grains as shown in Figure 7.10 (e). However, the grain size values of the films annealed for duration of 20 minutes were slightly lower than those annealed for 5 minutes duration. The average grain size values obtained for the annealing time of 20 minutes were ~ 180 nm. As the annealing temperature exceeded 20 minutes, the smaller grains gradually start to coalesce together creating larger grains with sizes in the range $\sim (475-720)$ nm which have been circled in Figures 7.10 (f) and (g). In all CBD-CdS layers annealed for different duration between 5 and 30 minutes, the FTO surface were uniformly covered by CdS grains and no pinholes were observed in between the grains.



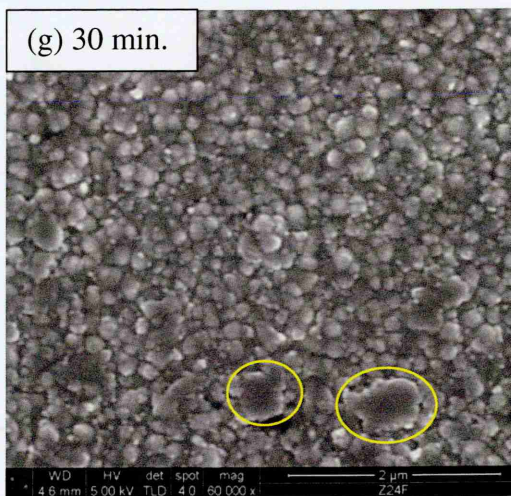
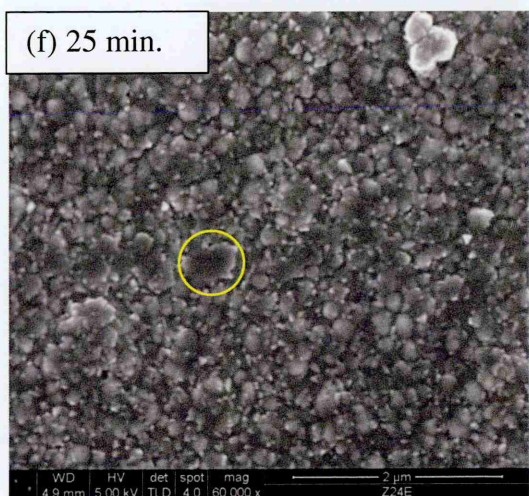
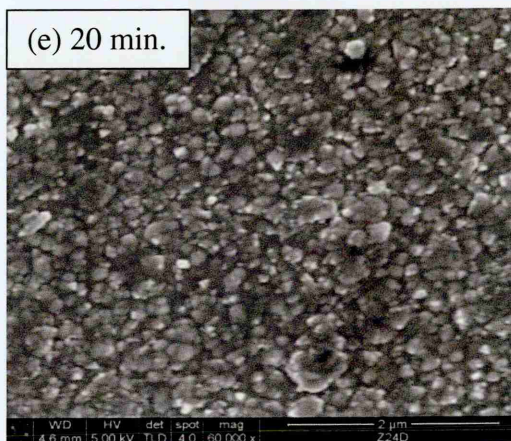
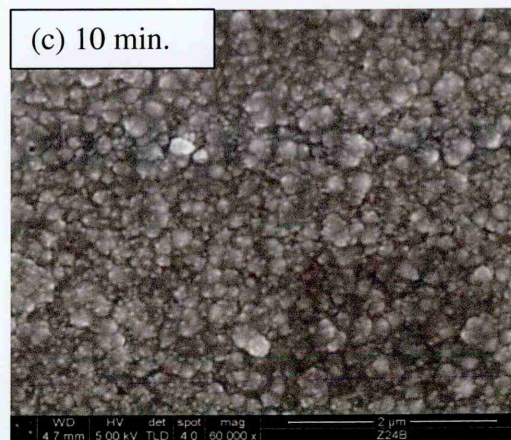
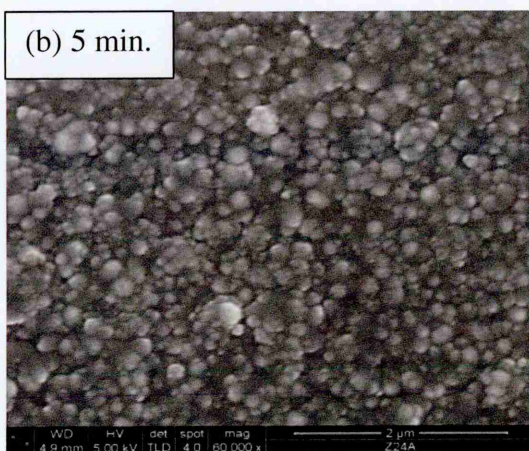


Figure 7.10: SEM images of the as-deposited and annealed CBD-CdS layers annealed at temperature of 400°C for different durations of (5-30) minutes in air.

According to all structural, optical and morphological study presented in this chapter, the best annealing temperature and annealing time for CBD-CdS layer were indicated as 400°C for 20 minutes in air which interestingly were the same annealing conditions observed for the ED-CdS layers.

7.4.4 Energy Dispersive X-ray (EDX) Analysis

For EDX experiment, CBD-CdS layers were deposited on glass/FTO substrates with the thickness of ~ 90 nm. The as-deposited layer was then divided into two parts; the first part remained as as-deposited and the second part was annealed at 400°C for 20 minutes in air. This investigation was carried out to measure the atomic percentage and composition of the as-deposited and annealed CBD-CdS layers.

Figures 7.11 (a) and (b) show the EDX spectra of the as-deposited and annealed CBD-CdS layers. The Cd:S ratio in the as-deposited layer was found to be of the order of 1.04:1 for the layers deposited from the solution containing Cd:S ratio of 1:5. Even though the sulphur concentration in the deposition bath was higher than cadmium, the resulting layers are slightly Cd-rich as shown in Table 7.7. Similar results have been reported by the Ramaiah *et al* [24]. They also grew the CBD-CdS from the solution containing Cd:S ratio of 1:5 and the resulting films were slightly Cd-rich with Cd:S composition ratio of 1:0.93.

After annealing, the Cd:S ratio slightly increased to 1.07:1 as shown in Table 7.7. This can be due to evaporation of some elemental S in the CdS layers. The S loss in the CdS layers can happen due to the higher vapour pressure of elemental S ($\sim 1.30 \times 10^4$ Pa) as compared to the vapour pressure of elemental Cd ($\sim 1.30 \times 10^2$ Pa) at annealing temperature of 400°C [25]. The other two peaks (Sn and O) observed in the EDX spectra originated from the underlying glass/FTO substrate due to the low thickness of the CdS films. The oxygen peak can also originate from the high concentration of O impurities in CBD-CdS layers as compared to CdS layers grown by other techniques [26]. Reports show that the high O concentration in CBD-CdS is likely responsible for better device performance [27]. Also, after annealing in air the O concentration can increase in CBD-CdS layers which in turn have positive effect on the device performance of the CdS/CdTe solar cells. The role of O in CdS is to control/enhance the interdiffusion at CdS/CdTe junction [28].

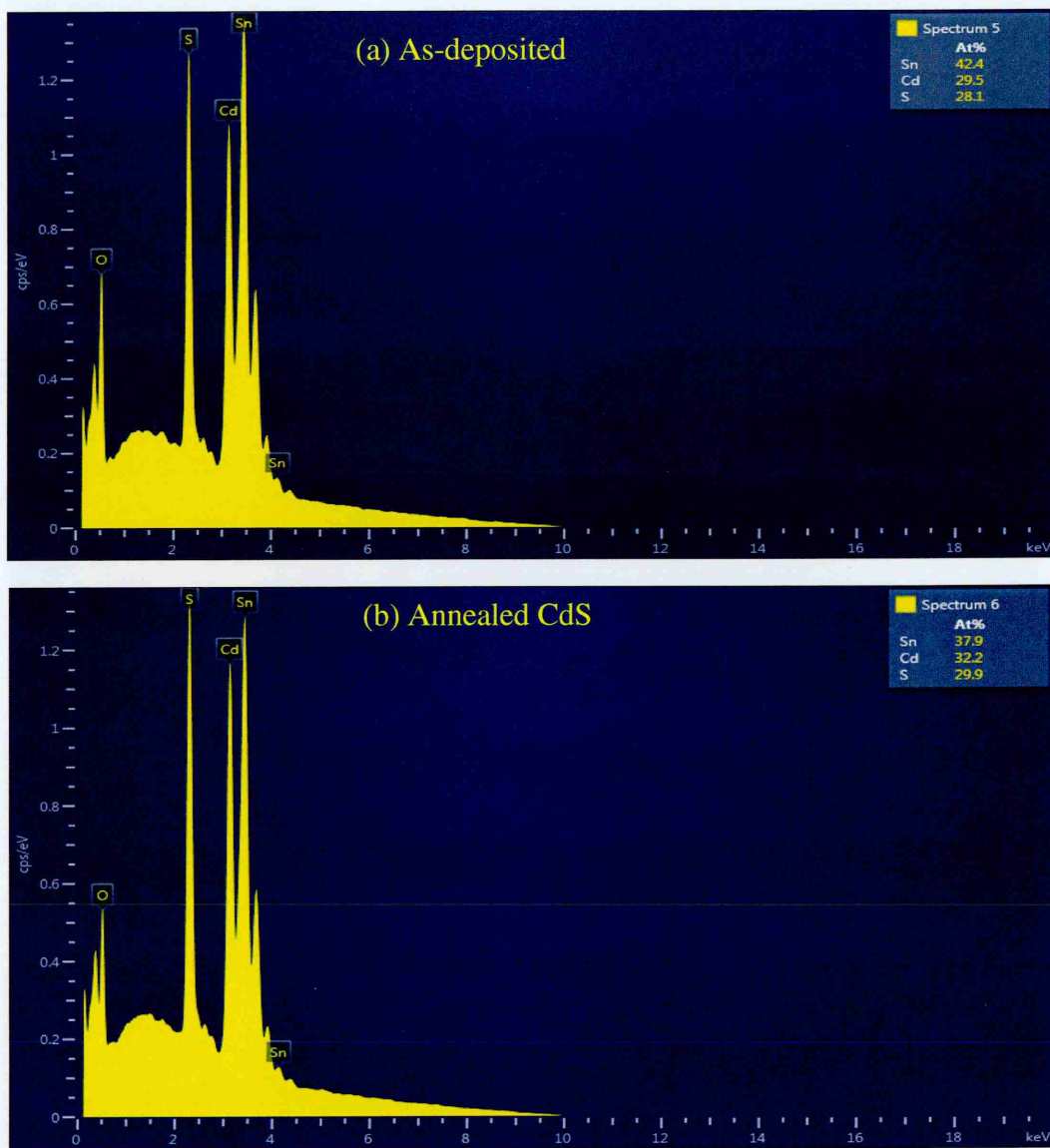


Figure 7.11: EDX spectra of the (a) as-deposited and (b) annealed CBD-CdS layers. The layers were grown on glass/FTO substrate with the thickness of ~ 90 nm and then annealed at 400°C for 20 minutes in air.

Table 7.7: Atomic percentage of the CBD-CdS layers grown on the glass/FTO substrate with the thickness of ~ 90 nm. The temperature and pH of the bath were $\sim 85^{\circ}\text{C}$ and 9.1 ± 0.02 respectively.

Sample	Atomic percentage (at%)			Cd/S ratio	Condition
	Cd	S	Sn		
As-deposited	29.5	28.1	42.4	1.04	Cd-rich
Annealed	32.2	29.9	37.9	1.07	Cd-rich

7.4.5 Raman spectroscopy

For Raman experiments, the CBD-CdS films were grown on glass/FTO substrates with the thickness of ~ 90 nm and result is shown in Figure 7.12. In the Raman spectrum, two Raman peaks were observed at 301.5 cm^{-1} and 604.5 cm^{-1} which corresponds to the 1LO and 2LO phonon peaks of CdS, respectively. The two Raman peaks observed for the as-deposited CdS layer in these experiments are red shifted as compared to the 1LO (305 cm^{-1}) and 2LO (610 cm^{-1}) Raman peaks positions of the bulk CdS crystal [29]. The red shift in Raman peaks are due to the tensile stress in the CdS layers [30]. It should be noted that, in this work, it was not possible to record the Raman peak for the annealed CBD-CdS layers. This was due the high intensity of Raman peak for the annealed samples which go beyond the limitaion of Raman equipment.

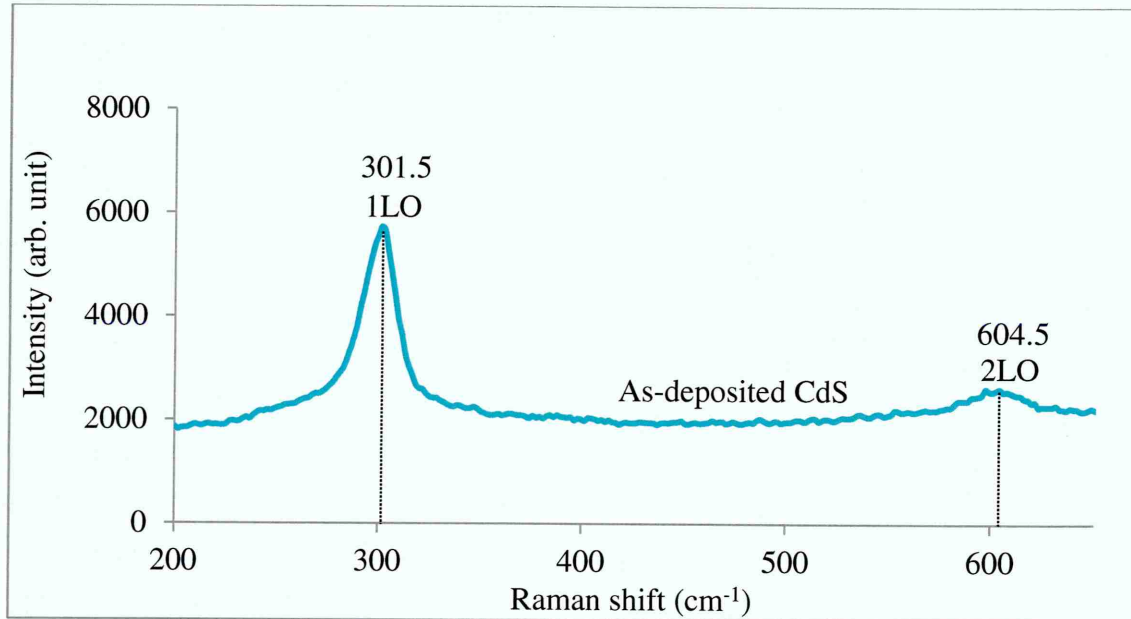


Figure 7.12: Raman spectrum of the as-deposited CBD-CdS layer grown on glass/FTO substrate with the thickness of ~ 90 nm.

7.4.6 Hall Effect measurements

For resistivity measurements, CBD-CdS with thicknesses of ~ 90 to ~ 450 nm layers were grown on the glass substrates. Afterward, these layers were annealed at 400°C for 20 minutes in air for comparison. The resistivity, carrier concentration and

mobility values for the as-deposited and annealed layers were obtained from Hall Effect measurement at room temperature and results are shown in Figures 7.13 and Table 7.8.

For both as-deposited and annealed layers, the resistivity decreases and mobility increases as the thickness increases. The resistivity values of the as-deposited and annealed layers were in the range $(3.07 \times 10^7 - 4.32 \times 10^4)$ and $(4.50 \times 10^5 - 1.60 \times 10^3) \Omega\text{cm}$ respectively. Also, the mobility values for the as-deposited and annealed layers were in the range $(8.7-821.0)$ and $(53.6-950.3) \text{ cm}^2\text{V}^{-1}\text{s}^{-1}$ respectively as shown in Table 7.8. The higher resistivity and lower mobility values in the as-deposited layers might be due to the smaller crystallite sizes, larger number of grain boundaries/scattering centres, dislocations and imperfections of the films [16,31,32]. The reduction in resistivity and increase in mobility values when thickness increases can be due to the grain growth or reduction in the number of grain boundaries/scattering centres. Also, after annealing the resistivity become lower and mobility become higher in values as compared to the as-deposited layers due to the further increase in grain size and sulphur vacancy defects [33]. The resistivity and mobility values of the as-deposited and annealed CBD-CdS layers presented in this work are in agreement with the values reported in the literature [3,23,34,35].

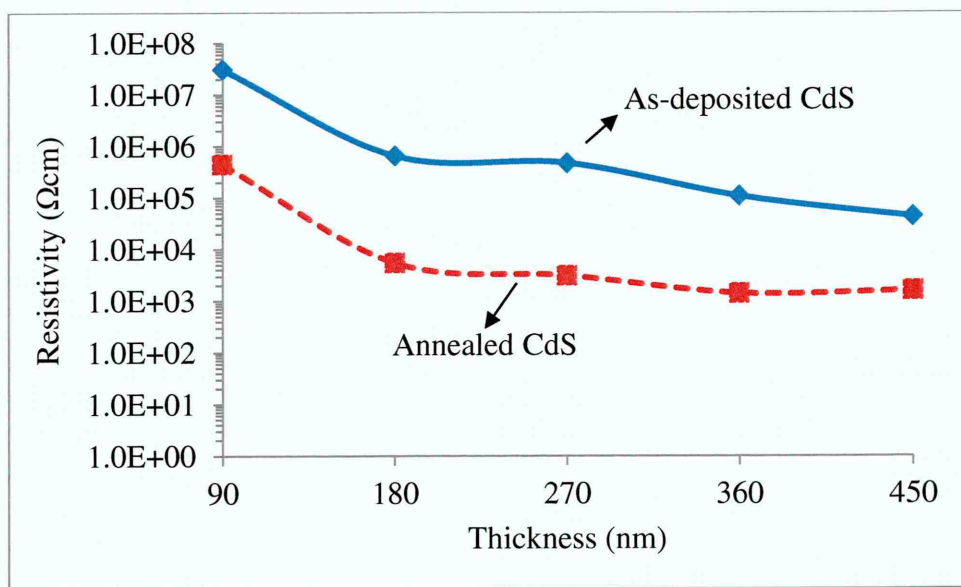


Figure 7.13: Variation of electrical resistivity with thickness for as-deposited and annealed CBD-CdS layers. Resistivity values are in log-scale while thickness values are in linear- scale.

Table 7.8: Hall Effect measurements for as-deposited and annealed CBD-CdS layers with different thicknesses.

Film Thickness (nm)	Carrier concentration (cm ⁻³)		Resistivity (Ωcm)		Mobility (cm ² V ⁻¹ s ⁻¹)	
	As-deposited	Annealed	As-deposited	Annealed	As-deposited	Annealed
90	2.34×10 ¹⁰	2.58×10 ¹¹	3.07×10 ⁷	4.50×10 ⁵	8.7	53.6
180	1.62×10 ¹¹	6.32×10 ¹²	6.49×10 ⁵	5.47×10 ³	59.2	180.3
270	1.98×10 ¹¹	2.86×10 ¹²	4.70×10 ⁵	3.08×10 ³	66.9	705.7
360	1.99×10 ¹¹	6.07×10 ¹²	1.08×10 ⁵	1.41×10 ³	290.0	726.5
450	1.75×10 ¹¹	4.10×10 ¹²	4.32×10 ⁴	1.60×10 ³	821.0	950.3

The carrier concentration of the as-deposited and annealed layers were in the range (2.344×10¹⁰- 1.99×10¹¹) and (2.58×10¹¹- 6.32×10¹²) cm⁻³ respectively. For the thicker CdS layers, the carrier concentration and resistivity obtained in this experimental work are of the same order with values reported by Cha *et al.* [36] for the as-deposited CdS layers. However, the mobility values (2420 cm²V⁻¹s⁻¹) reported by Cha *et al.* is higher than the ones reported in this work. This is likely due to higher thickness range of (1.0-2.0) μm being used by this research group.

7.5 Conclusions

CBD-CdS layers have been successfully deposited on glass/FTO substrates from aqueous solution bath containing 4×10⁻³ M Cd(CH₃CO₂)₂·2H₂O, 20×10⁻³ M SC(NH₂)₂, 6×10⁻² M (NH₄C₂H₃O₂) and NH₄OH at temperature of ~80°C and pH of 9.10±0.02. The deposited CBD-CdS layers show good adhesion to glass/FTO substrates.

XRD results show that the CBD-CdS layers were polycrystalline with mixture of hexagonal and cubic crystal structures and preferentially oriented along (002)H/(111)C planes. The XRD analyses show an increase in crystallite sizes from ~11 nm for the as-deposited layers to maximum values of ~66 nm for the samples annealed at 400°C for 20 minutes in air.

From the optical absorption results, the reductions in the energy bandgap values of the as-deposited layers from 2.48 to 2.45 eV were observed when thickness increased from 90 to 450 nm. The energy bandgap values of the layers approximately fell in the range (2.40-2.42) eV after annealing at different temperature range of 200 to 450°C in air.

The SEM images showed the uniform and compact morphology for both as-deposited and annealed CBD-CdS layers. The average grain sizes estimated from SEM images were ~200 nm for the as-deposited layers. The slight improvement in the average grain sizes were observed after annealing. The estimated average grain size of the annealed layers were in the range ~(208-255) nm for the annealing temperature range of (200-400)°C.

EDX analysis showed that the as-deposited layers were slightly Cd-rich and close to stoichiometry even though the sulphur concentration in the deposition bath was five times higher than cadmium concentration. After annealing, the layers remained Cd-rich and close to stoichiometry.

Observation from Hall Effect measurements showed the reduction in resistivity and increase in the mobility values as the thickness increases from 90 to 450 nm for both as-deposited and annealed layers. Results also showed improvement in mobility and reduction in resistivity values upon annealing at 400°C for 20 minutes in air. The resistivity and mobility values observed for the as-deposited and annealed CdS layers were in the range $(1.60 \times 10^3 - 3.07 \times 10^7) \Omega\text{cm}$ and $(8.7 - 950.3) \text{ cm}^2\text{V}^{-1}\text{s}^{-1}$ respectively. Experimental observation showed that the best annealing conditions for the CBD-CdS layers was at 400°C for 20 minutes in air.

7.6 References

- [1] P.K. Nair, M.T.S. Nair, V.M. Garcia, O.L. Arenas, Y. Pena, A. Castillo, I.T. Ayala, O. Gomezdaza, A. Sanchez, J. Campos, H. Hu, R. Suarez, M.E. Rincon. *Solar Energy Materials and Solar Cells*, **52** (1998) 313-344.
- [2] N.B. Chaure, S. Bordas, A.P. Samantilleke, S.N. Chaure, J. Haigh, I.M. Dharmadasa, *Thin Solid Films*, **437** (2003) 10-17.
- [3] T.L. Chu, S.S. Chu, N. Schultz, C. Wang, and C.Q. Wu, *J. Electrochem. Soc.*, **139**(9) (1992) 2443-2446.
- [4] X. Wu, *Sol. Energy*, **77** (2004) 803–814.
- [5] P. Jackson, D. Hariskos, E. Lotter, S. Paetel, R. Wuerz, R. Menner, W. Wischmann and M. Powalla, *Prog. Photovolt: Res. Appl.*, **19** (2011) 894-897.
- [6] M.A. Martinez, C. Guillen, J. Herrero, *Applied Surface Science*, **136** (1998) 8-16.
- [7] S. Prabahar, M. Dhanam, *Journal of Crystal Growth*, **285** (2005) 41-48.
- [8] A. Arias-Carbajal Readigos, V.M. Garcia, O. Gomezdaza, J. Campos, M.T.S. Nair and P.K. Nair, *Semicond. Sci. Technol.*, **15** (2000) 1022-1029.
- [9] H. Khallaf, I.O. Oladeji, L. Chow, *Thin Solid Films*, **516** (2008) 5967-5973.
- [10] S. Messina, M.T.S Nair and P.K. Nair, *J. Phys. D: Appl. Phys.*, **41** (2008) 095112 (9pp).
- [11] O. Vigil, Y. Rodriguez, O. Zelaya-Angel, C. Vazquez-Lopez, A. Morales-Acevedo, J.G. Vazquez-Luna, *Thin Solid Films*, **322** (1998) 329-333.
- [12] I.O. Oladeji, L. Chow, J.R. Liu, W.K. Chu, A.N.P. Bustamante, C. Fredricksen, A.F. Schulte, *Thin Solid Films*, **359** (2000) 154-159.
- [13] G. Liu, Z. Cheng, R.B. Barat, J. Pan, G.E. Georgiou, K.K. Chin, 37th IEEE Photovoltaic Specialists Conference, (2011) 003750-003753.
- [14] W.J. Danaher, L.E. Lyons, G.C. Morris, *Solar Energy Mater.*, **12** (1985) 137-148.
- [15] S. Chun, Y. Jung, J. Kim, D. Kim, *Journal of Crystal Growth*, **326** (2011) 152--156.
- [16] K.S. Ramaiah, A.K. Bhatnagar, R.D. Pilkington, A.E. Hill, R.D. Tomlinson, *J. Mater. Sci. Mater. Electron.*, **11** (2000) 269-277.
- [17] O. de Melo, L. Hernandez, O. Zelaya-Angel, R. Lozada-Morales and M. Becerril, *Applied Physics Letter*, **65** (1994) 1278-1280.
- [18] C.Y. Yeh, Z.W. Lu, S. Froyen, A. Zunger, *Phys. Rev. B*, **46** (1992) 10086-10097.

- [19] O. Zelaya-Angel, J.J. Alvarado-Gil, R. Lozada-Morales, H. Vargas, and A. Ferreira da Silva, *Applied Physics Letters*, **64** (1994) 291-293.
- [20] J. Han, C. Spanheimer, G. Haindl, G. Fu, V. Krishnakumar, J. Schaffner, C. Fan, K. Zhao, A. Klein, W. Jaegermann, *Solar Energy Materials & Solar Cells*, **95** (2011) 816–820.
- [21] D. H. Rose, F. S. Hasoon, R. G. Dhere, D. S. Albin, R. M. Ribeln, X. S. Li, Y. Mahathongdy, J. A. Gessert and P. Sheldon, *Prog. Photovolt: Research Appl.*, **7** (1999) 7331.
- [22] X. Wu, Y. Yan, R.G. Dhere, Y. Zhang, J. Zhou, C. Perkins, and B. To, *Phys. Stat. Sol. (c)*, **1**(4) (2004) 1062-1066.
- [23] A. Kariper, E. Güneri, F. Göde, C. Gümüş, *Chalcogenide Letters*, **9**(1) (2012) 27-40.
- [24] K.S. Ramaiah, R.D. Pilkington, A.E. Hill, R.D. Tomlinson, A.K. Bhatnagar, *Materials Chemistry and Physics*, **68** (2001) 22-30.
- [25] http://mtm-inc.com/reduce_project_risk/vacuum_compatible_metals_and_alloys/, Last accessed November (2015).
- [26] Y. Yan, M.M. Al-Jassim, *Current Opinion in Solid State and Materials Science*, **16** (2012) 39-44.
- [27] X. Wu, *Sol. Energy*, **77** (2004) 803-814.
- [28] N.R. Paudel, C.R. Grice, C. Xiao, and Y. Yan, *J. Appl. Phys.*, **116** (2014) 044506.
- [29] R. Litran, R. Alcantara, E. Blanco, and M. Ramirez-Del-Solar, *J. Sol-Gel. Sci. Technol.*, **8** (1997) 275-283.
- [30] P. Nandakumar, C. Vijayan, M. Rajalakshmi, A.K. Arora, Y.V.G.S. Murti, *Physica E*, **11** (2001) 377–383.
- [31] E. Bertran, J.L. Morenza and J. Esteve, *Thin Solid Film*, **123** (1985) 297-306.
- [32] H. Metin and R. Esen, *Semicond. Sci. Technol.*, **18** (2003) 647-654.
- [33] K.S. Balakrishnan and A.C. Rastogi, *Solar Energy Materials*, **20** (1990) 417-434.
- [34] K.S. Ramaiah, R.D. Pilkington, A.E. Hill, R.D. Tomlinson , A.K. Bhatnagar, *Material Chemistry and Physics*, **68** (2001) 22-30.
- [35] S.A. Tomas, O. Vigil, J.J. Alvarado-Gil, R. Lozada-Morales, O. Zelaya-Angel and A. Ferreira da Silva, *J. Appt. Phys.*, **78**(4) (1995) 2204-2207.

- [36] D. Cha, S. Kim and N.K. Huang, *Materials Science and Engineering B*, **106** (2004) 63-68.

8.1 Introduction

CdTe is a group II-VI compound semiconductor material with a direct bandgap (E_g) of 1.45 eV and high absorption coefficient of $>10^4 \text{ cm}^{-1}$ at 300 K [1]. About 99% of photons with $E > E_g$ can be absorbed within 2.0 μm of film thickness at standard condition of AM1.5 [2]. These properties make CdTe a suitable semiconductor material for terrestrial photovoltaic solar energy conversion.

The history of CdTe thin films dates back to 1947 when Frerichs synthesise CdTe single crystal by the reaction of Cd and Te vapours in the hydrogen atmosphere and measured their photoconductivity as a new photo-cell and electronic material [3]. Later, Jenny and Bube in 1954 reported that the p-type and n-type CdTe can be obtained by adding foreign impurity dopants to the CdTe single crystal [4]. In 1956, Loferski suggested that CdTe can be used as a suitable semiconductor absorber material for photovoltaic solar energy conversion [1]. Shortly thereafter, Kröger and de Nobel in 1959 showed that n-type and p-type CdTe could also be obtained by varying Cd-Te stoichiometry [5]. In the same year, Rappaport was able to achieve $\sim 2\%$ solar cells efficiency by diffusion of indium into p-type single crystal CdTe by formation a p/n homojunction [6]. Later by 1982, the fabricated solar cell using single crystal CdTe with p/n homojunction structure achieved $>10.5\%$ conversion efficiency [7].

Thereafter, the research moved towards fabrication of heterojunction structure and the first heterojunction solar cell was fabricated in 1963 by Cusano using a p-type Cu_2Te and n-type polycrystalline CdTe to achieve a conversion efficiency of $\sim 6\%$ [8]. However, the fabricated cells show instability due to gradual diffusion of Cu into the n-type CdTe [9]. In 1969, Adirovich *et al* for the first time fabricated the first polycrystalline CdS/CdTe heterojunction with cell efficiency of $>2\%$ [10]. Bonnet and Rabenhorst in 1972, also were able to fabricate CdS/CdTe heterojunction using chemical vapour deposited CdTe and vacuum evaporated CdS with conversion efficiency of $\sim 6\%$ [11]. In 1988, Mitchell *et al* was able to achieve $\sim 10.5\%$ cell conversion efficiency using TO/p-CdTe/C-Ag structure [12]. In their work, CdTe was grown by close-spaced vapour transport (CSVST) method. Five years later, Britt *et al* [13] achieved efficiency of 15.8% using polycrystalline CdS/CdTe solar cell in 1993. In their work, the CdS and CdTe layers were grown by CBD and CSS techniques respectively.

However, the polycrystalline CdS/CdTe solar cells efficiency was stagnated for a decade until 2004 when Wu *et al* [14] came up with efficiency of 16.5%. For another decade, the efficiency was at this value, but during these three years (2013-2015) First Solar Company announced a rapid increase producing a new world record efficiency of 21.5% [15]. It should be noted that, most of the polycrystalline CdTe thin films mentioned above were grown using high temperature vapour phase technique.

Mathers and Turner in 1928 initiated the electrodeposition of CdTe thin films using aqueous acidic solution of CdSO₄, TeO₂ and H₂SO₄ [16]. The electrodeposition of CdTe has been carried out using both alkaline and acidic solutions. They found that alkaline solution produce a poorly adhesive and powdery deposit due to instability of Te at pH>7. For this reason, the acidic bath with pH<7 was used for electrodeposition of CdTe thin films. In addition to that, both cathodic and anodic methods have been tried for electrodeposition of CdTe thin films. The advantage of cathodic deposition over anodic deposition is that, in cathodic deposition stoichiometry of deposited CdTe can be easily controlled.

In electrodeposition technique, the stoichiometry of the semiconductors can be simply changed by varying the deposition potential. At lower cathodic deposition potential, the CdTe layer has excess Te, so it is p-type in electrical conductivity. While at higher cathodic potential, the CdTe layer has excess Cd, therefore the layer is n-type in electrical conductivity. Somewhere in between, the ratio of Cd to Te is 1 to 1, this is known as inversion point where the CdTe layer is intrinsic or i-type [17].

A more systematic work on the cathodic electrodeposition of CdTe was carried out by Panicker *et al* in 1978 [18]. In their work, also acidic aqueous solution containing CdSO₄ and TeO₂ in H₂SO₄ were used at pH of 2.5-3.0. In 1982, Fulop *et al* at Ametek fabricated CdTe/Au Schottky barrier solar cells with conversion efficiency of ~8.7% using electrodeposition technique which was a remarkable achievement [19]. In 1984, Basol in Monosolar was able to increase the efficiency of fabricated solar cell up to ~9.4% using all electrodeposited CdS and CdTe with n-CdS/p-CdTe heterojunction-structure [20].

Later, British Petroleum (BP Solar) company (1984-1999) inherited the electrodeposition technology based on CdTe from Monosolar and proved the reliability, scalability and manufacturability of the simple and low-cost deposition technique. During this time, the electrodeposition technique matured in BP Solar by intensive group work. BP Solar was able to scale up solar panel to 0.94 m² yielding a nearly 11%

efficiency using CdS/CdTe heterojunction structure [21]. BP Solar eventually dropped this work on electrodeposited CdTe in the early 2000s.

Decade after, RSI Company was founded in 2009 by a team of capital equipment veterans based in Silicon Valley, California, USA, to electroplate CdTe thin films. They have developed a method called Rapid Efficient Electroplating on Large-areas (REEL) which speed up the electroplating process and remove the restrictions of electroplating on large-area panels. RSI in 2013 announced new world record for making the large panel with the area of 1.5 m² [22].

Beside RSI, Solopower funders launched new company in 2010 called “Encoresolar” at Silicon Valley in California, USA. Encoresolar is currently electroplating CdTe thin films on a large area panel with dimension of 1.1 m² [23, 24].

Electrodeposition of CdTe thin films can be carried out either by three electrodes or two electrodes system. In three electrodes set-up, electrodeposition cell comprise of working electrode (cathode), counter electrode (anode) and reference electrode while in two electrodes set-up the reference electrode is omitted. There are lots of reports on the electrodeposition of CdTe using three electrodes system [16-21]. The main advantage of the three electrode system is that the cathodic voltage is measured w.r.t the reference electrode, therefore the potential between working and reference electrode can be easily controlled [25,26]. Besides the three electrodes system, two electrode systems also were reported for electrodeposition of CdTe [27-30] and other semiconductor thin films such as CdS [31,32], CdSe [33], InSe [34], ZnTe [35], CIS [36,37] and CIGS [38,39].

The work reported in this thesis is mainly focused on the electrodeposition of n-CdTe thin films using two electrodes system. The first reason of using two electrodes system instead of conventional three electrode system is to eliminate the possible leakage of unwanted group 1A and 1B ions such as K⁺ and Ag⁺ from saturated calomel electrode (SCE) and Ag/AgCl reference electrodes into the electrolyte solution [25]. It should be noted that, the conductivity type of the CdTe thin films critically depends on the parts per billion (ppb) of impurity or dopant level in deposition electrolyte. Dennison reported that, only 5 ppb of Ag⁺ ions and >30 ppb of Cu²⁺ ions has drastically reduced the efficiency of electrodeposited CdTe based solar cells from 11.0 % to 3.6 and 0.7% respectively [40].

The second reason of omitting reference electrode is due to the low operating temperature limit of some reference electrodes such as SCE electrode which is about 60°C [41]. By removing the reference electrode, the growth temperature of aqueous

solution can be increased up to $\sim 85^{\circ}\text{C}$. For obtaining stoichiometric CdTe, higher deposition temperature is required. Generally, depositions at lower temperature produce CdTe thin films with excess Te and poor crystallinity [42]. Higher efficiency CdTe solar cells were reported by Schulmeyer *et al* using CdTe with excess Cd [43].

The third reason of omitting reference electrode is that each reference electrode has its own lifetime and should be replaced when it is not functioning as intended. In this case, the overall cost of the electrodeposition set-up can be reduced by removing the reference electrode, further simplifying the electroplating cell.

Usually, CdTe layers are grown using CdSO_4 as the precursor for Cd ions. This work presents the cathodic electrodeposition of CdTe thin films from acidic and aqueous solution using $\text{Cd}(\text{NO}_3)_2$ as the precursor for Cd ions. The reports are scarce on the electrodeposition of CdTe history, using nitrate precursor [44,45]. Therefore, this report presents a comprehensive work on CdTe layers grown by two electrode system, using nitrate precursor in order to investigate its suitability for use in electronic devices.

8.2 Preparation of CdTe deposition electrolyte

The initial Cd-precursor was prepared by dissolving 1.0 M $\text{Cd}(\text{NO}_3)_2 \cdot 4\text{H}_2\text{O}$ of 99.0% purity in 800 ml of deionized water. Then, the prepared solution was electro-purified by applying a cathodic potential just below the required potential for reduction of Cd^{2+} ions for ~ 100 hours. The initial Te-precursor was prepared by adding 2.0 grams of 99.999% (5N) TeO_2 powder into 250 ml of volumetric flask containing diluted nitric acid (HNO_3) and continuously stirred for 24 hours. Thereafter, about 1 ml of diluted TeO_2 solution was added to 800 ml aqueous solution containing purified 1.0 M $\text{Cd}(\text{NO}_3)_2 \cdot 4\text{H}_2\text{O}$. The pH of the resulting deposition electrolyte was adjusted to 2.00 ± 0.02 using either nitric acid or ammonium hydroxide (NH_4OH) at room temperature. Both $\text{Cd}(\text{NO}_3)_2 \cdot 4\text{H}_2\text{O}$ and TeO_2 used in the deposition electrolyte were purchased from Sigma Aldrich. The substrates used for electro-purification and electrodeposition were TEC-7 glass/FTO (fluorine-doped tin oxide) with sheet resistance of $\sim 7 \Omega/\text{square}$. Prior to electrodeposition, the glass/FTO substrates were cut into small pieces with dimensions of $2 \times 2 \text{ cm}^2$ and washed for 15 minutes in an ultrasonic bath containing soap solution followed by rinsing with deionised water. Subsequently, the glass/FTO substrates were cleaned with methanol and rinsed with deionized water followed by a similar cleaning with acetone and deionized water. The samples were finally dried using

stream of nitrogen gas. An insulating polytetrafluoroethylene (PTFE) tape was used to attach the glass/FTO substrate to a high-purity graphite rod which serves as the working electrode (cathode). Another high-purity graphite rod was used as the counter electrode (anode). The temperature of the electrolyte solution was maintained at $\sim 85^{\circ}\text{C}$ with continuous moderate stirring during deposition using magnetic stirrer. The source of electrical power used for 2-electrode system was a computerised GillAC potentiostat (ACM instruments).

8.3 Results and discussion

8.3.1 Voltammogram

Cyclic voltammograms were recorded for the electrolyte solution containing a combination of about 1 ml of TeO_2 solution and 1.0 M $\text{Cd}(\text{NO}_3)_2 \cdot 4\text{H}_2\text{O}$ in 800 ml of deionised water to study the deposition trends of CdTe. The temperature of the electrolyte was kept at $\sim 85^{\circ}\text{C}$ and the pH value was adjusted to 2.00 ± 0.02 . The reason of using aqueous acidic solution of $\text{pH} = 2.00 \pm 0.02$ and deposition temperature of $\sim 85^{\circ}\text{C}$ was to prevent the formation of cadmium hydroxide precipitates and to increase the deposition rate and crystallinity of CdTe thin films. The cyclic voltammogram was recorded using GillAC computerised potentiostat at cathodic voltage ranges of (0 to 2,000) mV with a scan rate of 3 mVs^{-1} as shown in Figure 8.1.

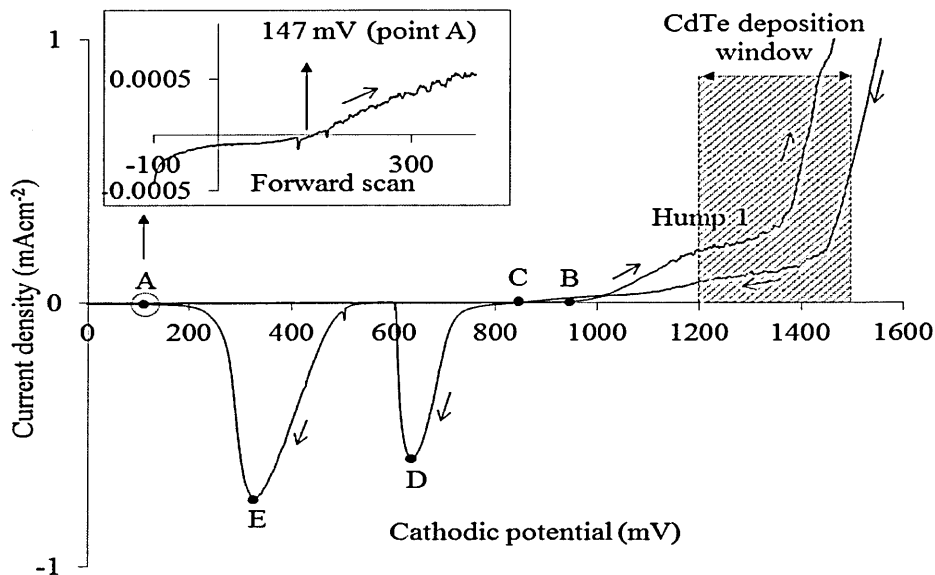


Figure 8.1: A cyclic voltammogram for an aqueous electrolyte containing 1.0 M $\text{Cd}(\text{NO}_3)_2 \cdot 4\text{H}_2\text{O}$ and ~ 1 ml of TeO_2 at $\text{pH} = 2.00 \pm 0.02$ and temperature of 85°C .

In the forward scan, as the cathodic potential is increased, the deposition of Te takes place first because the redox potential for Te is more positive ($E_0 = +0.53$ V vs. NHE) than Cd ($E_0 = -0.40$ V vs. NHE) [16]. The enlargement of point A in Figure 8.1 (inset) shows that Te deposition starts from ~ 147 mV according to the following electrochemical reaction:

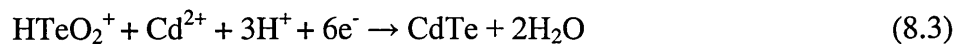


By further increase in cathodic potential at forward scan, the Cd^{2+} ions starts to discharge depositing Cd on the cathode at ~ 920 mV (point B). The discharge rate of Cd^{2+} ions on the cathode surface increases towards higher cathodic potentials and appears as small hump (Hump 1) at ~ 1100 mV. The electrochemical reaction of Cd deposition is given by:



Thus, the co-deposition of CdTe thin film starts at ~ 1100 mV and continues at higher cathodic potentials with the appearance of approximately steady current region between ~ 1200 to ~ 1400 mV. At cathodic potentials > 1400 mV cathodic current

increases rapidly which can be either due to Cd dendrites formation or hydrogen gas evolution process (electrolysis of water). This is possible because the minimum voltage required for electrolysis of water is about 1.23 V [46]. Although the generation of hydrogen gas at the cathode surface can be helpful in passivating defects, it can also reduce the adhesion of CdTe layers to the glass/FTO substrate due to formation of hydrogen bubbles [47]. The overall electrochemical reaction for formation of CdTe thin film between ~1200 to ~1400 mV, can be obtained by the combination of Equations (8.1) and (8.2) as follows:



In the reverse scan, both points C and D, at ~834 and ~633 mV, represents the dissolution of elemental Cd and Cd bonded to the CdTe layer and point E (~327 mV) represents the dissolution of Te from the cathode. In the electrodeposition of CdTe thin films, it is important to maintain the deposition of CdTe thin films close to stoichiometry. For this reason, the concentration of Cd^{2+} ions in the solution should be always much higher than HTeO_2^+ ions due to the higher (more positive) redox potential of Te element as compared to Cd.

8.3.2 X-ray diffraction

8.3.2.1 Optimisation of growth voltage

Figure 8.2 (a) shows the XRD pattern of as-deposited CdTe layers grown at cathodic potential ranges of 1248 to 1258 mV with potential step of 1.0 mV. All CdTe layers were grown on glass/FTO substrate for 2 hours. This experiment was carried out to determine the most intense XRD peak between the cathodic potential ranges of 1248 to 1258 mV which corresponds to stoichiometric CdTe layers with the highest degree of crystallinity. In general, the most intense XRD peaks is expected to appear at the stoichiometry point and the deviation from the stoichiometric point results in less crystallinity due to formation of CdTe layer either with Te-richness or Cd-richness. Furthermore, the presence of two phases in the as-deposited layers reduces the crystalline nature of the CdTe layers.

Results show that, all as-deposited CdTe layers are polycrystalline with cubic crystal structure and strongly oriented along (111) planes. The (111) peak occurs at 2θ values in the range (23.81° - 24.01°). The most intense XRD peak based on diffractions from (111) planes was observed at cathodic potential of 1253 mV as shown in Figure 8.2 (b).

For better identification of all CdTe XRD peaks, the as-deposited CdTe sample grown at cathodic potential of 1253 mV is separately plotted and analysed as shown in Figure 8.3 and Table 8.1. Three XRD peaks observed at 24.01° , 39.53° and 46.75° respectively represent the diffractions from (111), (220) and (311) cubic planes. The observed XRD peaks were found to be in a good agreement with the JCPDS file number: 01-075-2086 for cubic CdTe.

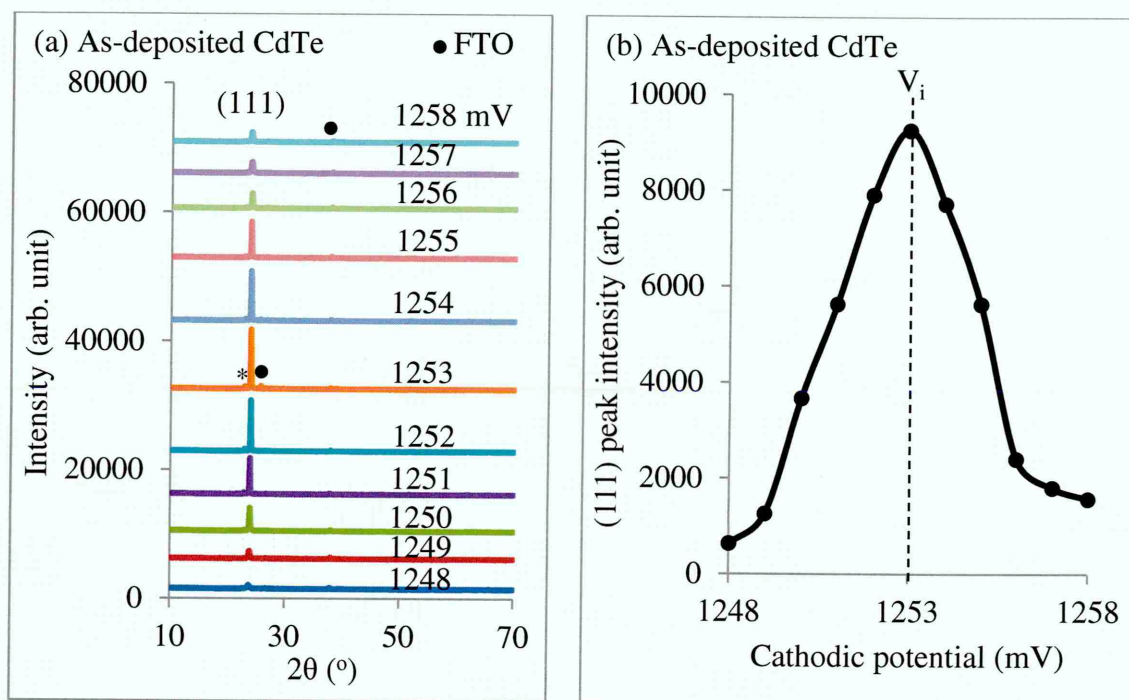


Figure 8.2: (a) the XRD pattern of as-deposited CdTe layers grown at the cathodic potential ranges of 1248 to 1258 mV (b) variation of (111) peak intensity as a function of cathodic potential for the as-deposited CdTe layers grown on glass/FTO substrates for 2 hours each.

In Figure 8.3, there is an indication of mixed phases marked with asterisk (*) which occurs at 2θ in the range (22.55° - 22.99°) and corresponds to Cd_xTeO_y phases. The observation of mixed phase can be due to difference in redox potential of Te and Cd and nature of the deposition techniques. It is known that Te with more positive

redox potential than Cd will deposit first on the FTO surface. In addition, in acidic aqueous solution Te can be easily oxidised and make bonds with Cd atoms to form Cd_xTeO_y . The Cd_xTeO_y can form as a native oxide layer during the growth on the surface or can also be formed on the surface of CdTe layer when annealed in the presence of oxygen or air ambient. The XRD patterns observed for the CdTe grown by electrodeposition techniques are similar and comparable to the XRD pattern of CdTe grown by high temperature CSS growth techniques [48].

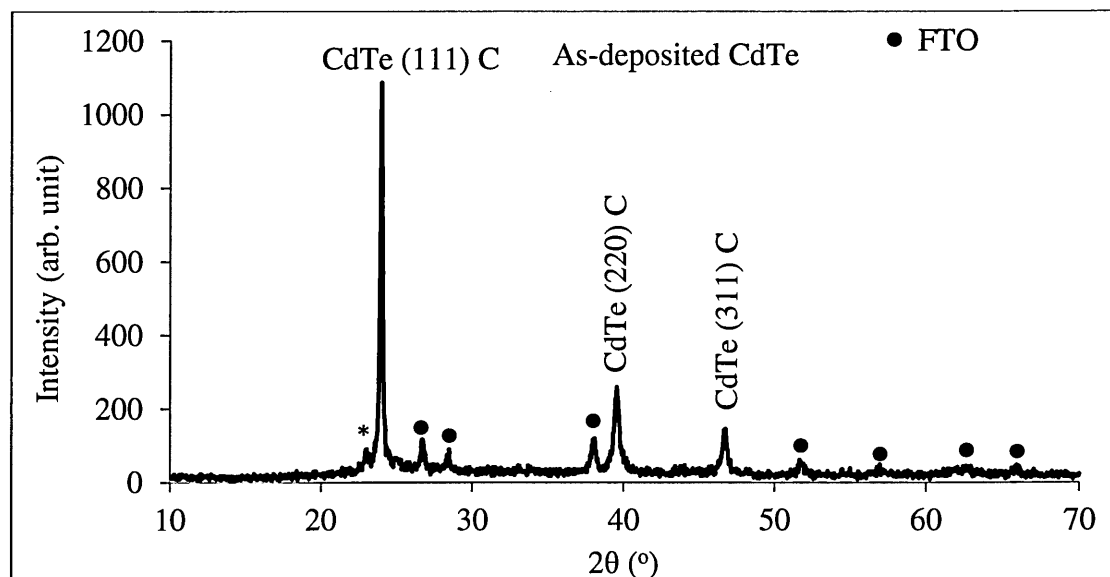


Figure 8.3: The XRD patterns of as-deposited CdTe samples grown at cathodic potential of 1253 mV for 2 hours duration.

Table 8.1: Identification of XRD peaks observed for as-deposited CdTe layers grown at cathodic potential of 1253 mV. The observed XRD peaks match with JCPDS reference file number: 01-075-2086 for cubic CdTe.

Sample	2θ of (111) peak (°)		Lattice spacing D (Å)		(hkl)	Chemical formula/phase
	Observed	Reported	Observed	Reported		
As-deposited	24.01	24.02	3.70	3.70	(111)	CdTe/cubic
	39.53	39.74	2.28	2.26	(220)	CdTe/cubic
	46.75	46.97	1.94	1.93	(311)	CdTe/cubic

Table 8.2 contains the variation of the FWHM and the corresponding crystallite sizes as a function of growth voltages for the as-deposited CdTe samples. The FWHM and crystallite size calculations were based on diffraction from CdTe (111) XRD peaks. The crystallite size was estimated using Equation (6.6) presented in chapter 6.

Results show that the crystallite sizes were in the range of 32 to 65 nm for the as-deposited CdTe layers grown at the cathodic potential ranges of 1248 to 1258 mV. The higher values of crystallite sizes were observed at the cathodic potential ranges of 1250 to 1255 mV close to the stoichiometric growth voltage of 1253 mV. Away from the stoichiometric point the crystallite sizes tend to reduce. The reduction in crystallite size can be due to growth of the CdTe layer with either Cd-richness or Te-richness. The crystallite size calculation shows that the as-deposited CdTe layers grown by electrodeposition technique are nano materials. The as-deposited CdTe layers grown by high temperature growth technique such as CSS were shown to be micro-materials with the grains size in the range of 0.3 to 0.5 μm [49,50]. In this work, the highest value of crystallite size calculated for the as-deposited CdTe layer was about 65 nm and no higher value greater than 65 nm were observed. This seems to be due to the saturation of crystallite size or limitation of the Scherrer's equation used in the measurement and analysis for CdTe samples [51,52].

Table 8.2: Variation of crystallite size as a function of cathodic potential for the as-deposited CdTe layers based on (111) peak.

Cathodic potential (mV)	2 θ of (111) peak ($^{\circ}$)	FWHM of (111) peak ($^{\circ}$)	Crystallite size of (111) peak (nm)
1248	23.81	0.259	32
1249	23.95	0.162	52
1250	23.98	0.129	65
1251	23.95	0.129	65
1252	23.98	0.129	65
1253	24.01	0.129	65
1254	23.98	0.129	65
1255	23.90	0.129	65
1256	23.98	0.194	43
1257	23.95	0.259	32

1258	23.85	0.259	32
------	-------	-------	----

8.3.2.2 Effect of the growth time on the structural properties of CdTe layers

In order to study the effect of growth time on the structural properties of the electrodeposited CdTe layers, XRD measurements were carried out for five samples grown at cathodic potential of 1253 mV for different durations. Each sample layer was divided in to two parts, the first part remains as-deposited and the second part was annealed at 390°C for 10 minutes in air. Figure 8.4 (a) and (b) shows the XRD patterns of the as-deposited and annealed CdTe layers.

In both figures, as the deposition time increases from 2 hours to 6 hours, the intensity of (111) peak increases and reaches its maximum values at 6 hours. The annealed samples show higher (111) peak intensities as compared to the as-deposited samples. This clearly shows the improvement in structural properties of CdTe layer after annealing. The (111) peaks position for the as-deposited and annealed samples respectively occurs at 2θ values in the range $(24.04-24.11)^\circ$ and $(24.02-24.09)^\circ$.

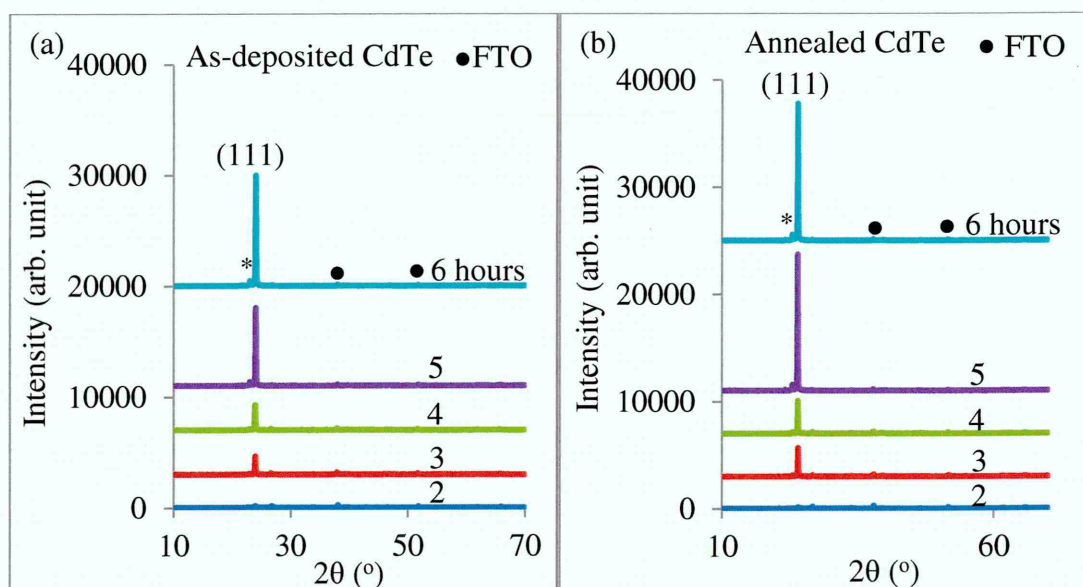


Figure 8.4: The XRD patterns of the (a) as-deposited and (b) annealed CdTe layers grown for different durations of 2 to 6 hours.

The crystallite sizes calculated using Scherrer's equation based on the (111) peak intensity was in the range (37-65) nm for the as-deposited samples as shown in the Table 8.3. At the early stage of growth (2 hours), the crystallite size was small about 37

nm and as the growth time increases (beyond 2 hours), the crystallite size start to increase and reaches their maximum values of about 65 nm. After annealing, all CdTe layers show same the crystallite size value of about 65 nm. It seems the crystallite sizes saturated after annealing due to crystallite size growth and recrystallisation in CdTe thin films. This clearly shows the limitation of application of Scherrer's equation for calculation of crystallite size. Although, the crystals grow larger (see SEM results in section 8.3.5), the Scherrer's equation is not capable of estimating these large values.

The mixed phase Cd_xTeO_y is also observed in all as-deposited and annealed CdTe samples as shown by asterisk (*). This peak is more prominent when the growth duration is >4 hours. Larger growth durations allow oxygen to incorporate on the CdTe layers surface and form a well crystallised phase.

Table 8.3: Effect of growth time on the (111) XRD peak of as-deposited and annealed CdTe layers.

Growth Time (min)	2 θ of (111) peak ($^\circ$)		FWHM of (111) peak ($^\circ$)		Crystallite size of (111) peak (nm)	
	As-deposited	Annealed	As-deposited	Annealed	As-deposited	Annealed
120	24.07	24.09	0.227	0.129	37	65
180	24.04	24.08	0.129	0.129	65	65
240	23.98	24.09	0.162	0.129	52	65
300	24.11	24.02	0.129	0.129	65	65
360	24.09	24.09	0.162	0.129	52	65

Figure 8.5 shows the variation of (111) peak intensity as a function of growth time for both as-deposited and annealed CdTe layers. Observation shows the gradual increase in the peak intensity of both as-deposited and annealed sample when the growth durations are in range of 2 to 4 hours. The peak intensity increases rapidly for the growth duration of >4 hours and reaches their maximum values after 6 hours. In the annealed samples, the peak intensities were approximately the same observed for growth durations between 5 and 6 hours. This observation was made number of times and it simply suggests that the optimum growth time for the CdTe thin films should be in the range of 5 to 6 hours.

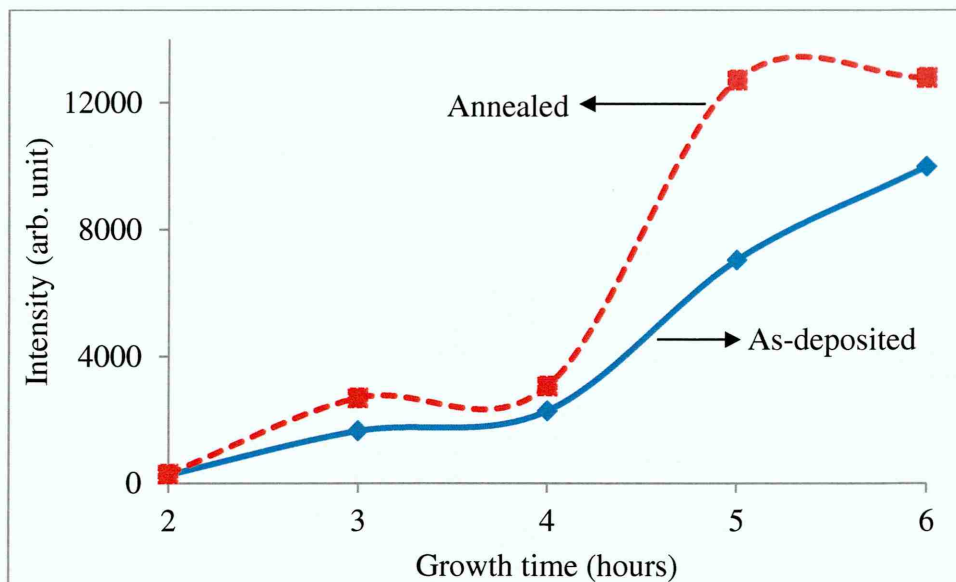


Figure 8.5: Variation of (111) peak intensity with growth time for as-deposited and annealed CdTe layers.

8.3.2.3 Effect of growth time on the thickness of CdTe layers

Figure 8.6 shows the experimental and theoretical thickness variation with growth time for the as-deposited CdTe layer grown at cathodic potential of 1253 mV. The CdTe thickness was experimentally measured using UBM microfocus optical depth profilometer (UBM, Messetechnik GmbH, Ettlingen, Germany) and theoretically estimated using Equation (6.7) presented in chapter 6. It should be noted that, in Equation (6.7), the number of electrons transferred in the reaction for formation of one mole of CdTe is $n = 6$.

Results clearly show that the thickness of CdTe layer increases with the growth time. As shown in Figure 8.6, the variation of thickness as a function of growth time is approximately linear. In this experiment, the error in thickness measurement was about $\pm 0.05 \mu\text{m}$. It should be taken into consideration that the theoretical thicknesses calculated from Faraday's law of electrolysis show higher values than the experimental values. This is because in Faraday's law of electrolysis, all the electronic charges are assumed to have contributed to the deposition of CdTe layers while in real situation, some of the electronic charges actually participated in the electrolysis of water.

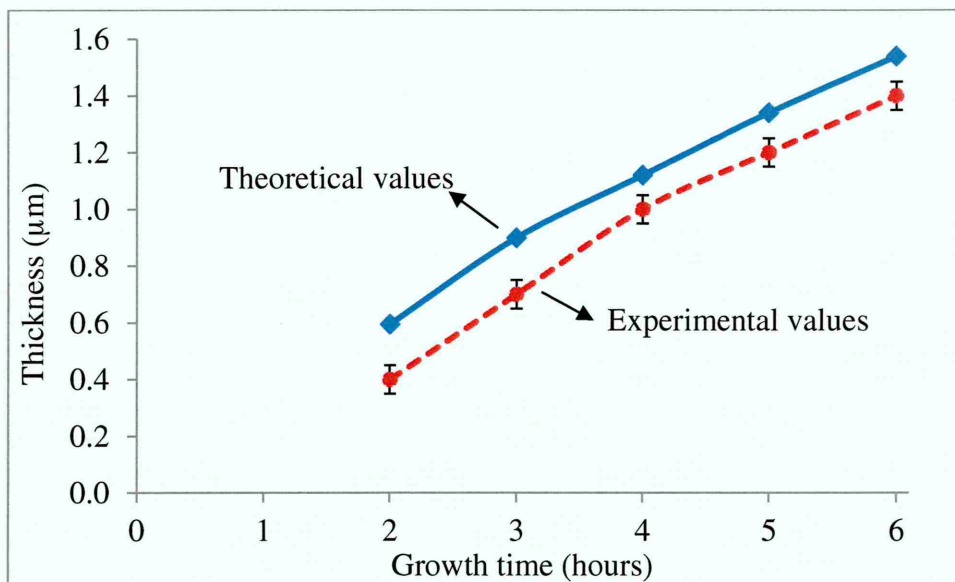


Figure 8.6: Theoretical and experimental thickness variation with growth time for the as-deposited CdTe layers grown at cathodic potential of 1253 mV.

It should be noted that the thickness of the electrodeposited CdTe thin films directly depends on the deposition current density. The current density itself depends on the growth temperature, stirring rate and HTeO_2^+ ions concentration in the aqueous solution. The increase in any of these parameters given above can increase the current density and eventually increase the thickness of the deposited thin films. Reports show that the deposition current density is less dependent on the variation in Cd^{2+} ions concentration in the deposition electrolyte [53]. The experimental observation shows that the deposition current density is more sensitive to the addition of HTeO_2^+ ions into deposition electrolyte. Deposition current density increases drastically when the concentration of HTeO_2^+ ions is high even at low temperature and stirring speed. When the amount of HTeO_2^+ is high in the bath, Te-rich CdTe with a thickness of 2.0 μm can be deposited in a very short time (less than one hour). However, these kinds of layers are not suitable for solar cell devices due to non-stoichiometric properties and Te-richness. The main common issues in the non-stoichiometric layers are the material losses, large number of pin-holes and poor solar cell performance after heat treatment at high temperature ($>385^\circ\text{C}$). From the experience gained in this research, good quality CdTe thin films were electrodeposited when the current density is within the range of $\sim(150-160) \mu\text{Acm}^{-2}$ in the stoichiometric growth voltage range using two electrode system.

In an electrodeposition production line, CdTe with a thickness of 2.0 μm is required to absorb nearly 100% of the incident photons as mentioned earlier. When the deposition current density is $\sim(150-160) \mu\text{Acm}^{-2}$, about 6 hours is required to deposit 2.0 μm thicknesses. This seems to be a long time deposition process in manufacturing process. The effective deposition time can be reduced to $\sim(4-5)$ minutes per 1 m^2 area substrate by using special large electroplating baths which are able to deposit many substrates with areas $\sim(2-3) \text{m}^2$ at the same time [21,36,47,22]. In this case, the deposition time of the electrodeposited CdTe thin films is comparable to the high temperature and high deposition rate growth techniques such as CSS.

8.3.2.4 Effect of CdCl_2 and $\text{CdCl}_2+\text{CdF}_2$ treatments on the XRD patterns of CdTe layer at different temperatures

In this experiment, CdTe layer with a thickness of $\sim 1.5 \mu\text{m}$ was deposited on glass/FTO substrate. Then the deposited layer was divided into three parts. The first part was left as-deposited CdTe. The second part was heat treated with CdCl_2 only and the last part was heat treated with $\text{CdCl}_2+\text{CdF}_2$. Three different heat treatment temperatures of 385, 420 and 450°C for 12 minutes in air were used for this set of experiment and results are shown in Figure 8.7 (a) and (b).

In both figures, the clear difference in the intensity of (111), (220) and (311) can be observed for various conditions. Treatment with CdCl_2 and $\text{CdCl}_2+\text{CdF}_2$ at 385°C clearly improved the intensity of (111) preferred orientation peak as compared to the (111) peak of the as-deposited CdTe sample. The weak intensity of (220) and (311) peaks confirms the preferential growth of (111) peak at 385°C. The improvement in (111) peak intensity is related to recrystallisation and grain growth in the presence of Cl and F [54]. At the temperature of 420°C, structural transition was observed for both CdCl_2 and $\text{CdCl}_2+\text{CdF}_2$ treated samples. The sign of structural transition was the slight reduction in (111) peak intensity and slight increase in (220) and (331) peak intensity as compared to sample heat treated at 385°C.

The structural transition is due to the random orientation or recrystallisation in the CdTe layers, yet the (111) peak intensity remained as the dominant peak in comparison to the other two peaks. A comprehensive study on *in-situ* XRD measurement done by Kim *et al* shows that the structural transition temperature take

place at the temperature of $385 \pm 5^\circ\text{C}$ [55]. The experimental observation reported here was in agreement with the observation made by Kim *et al.*

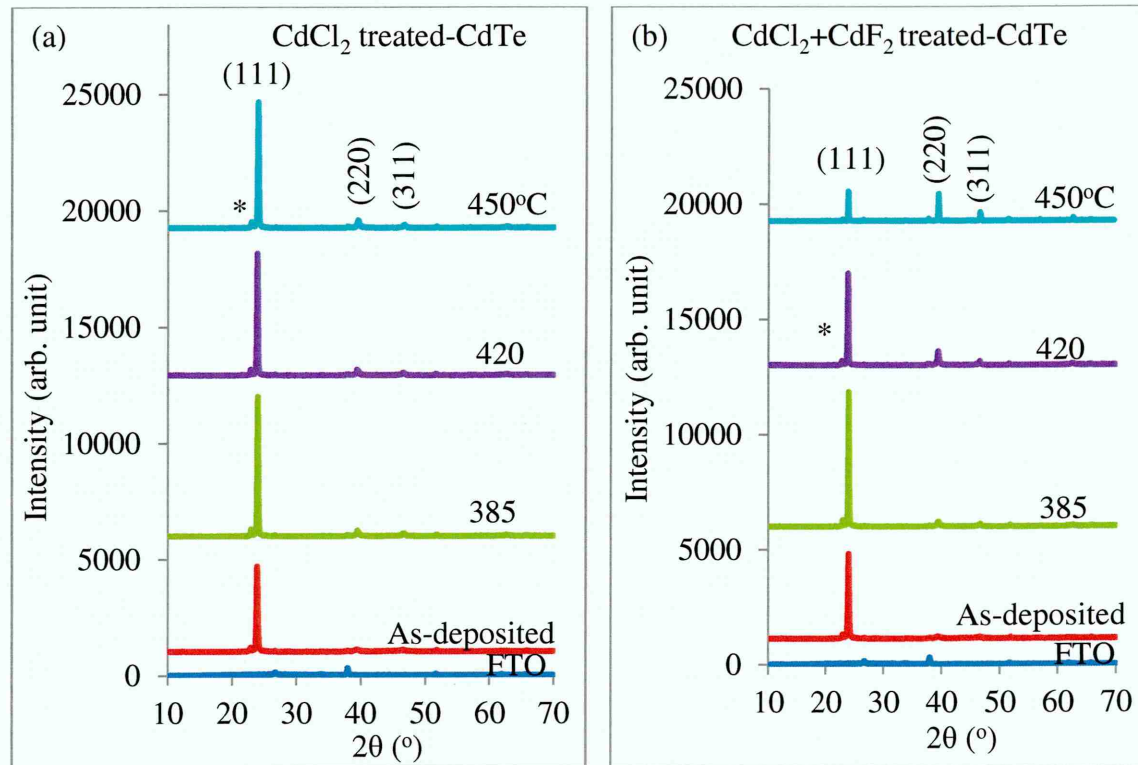


Figure 8.7: The XRD patterns of the (a) CdCl_2 treated and (b) $\text{CdCl}_2+\text{CdF}_2$ treated CdTe layers. Note that the heat treatment was carried out at three different temperatures of 385, 420 and 450°C for 12 minutes in air.

At the temperature of 450°C , (111) peak intensity slightly recovered after CdCl_2 treatment while a sharp collapse was observed after $\text{CdCl}_2+\text{CdF}_2$ treatment. The sharp collapse in (111) peak intensity can be related to the random orientation of the CdTe crystals. When the CdTe crystals are randomly oriented, it is possible that the preferred orientation transfers from (111) plane to other (220) or (311) planes depending on the final orientation of crystals in the CdTe layer. According to the experimental observation in this work, as the temperature increase from 385°C to 450°C , the intensity of the (220) and (311) peaks increases gradually. It should be noted that increase in (220) and (311) peak intensity are more pronounced when CdTe layers was treated with $\text{CdCl}_2+\text{CdF}_2$. Based on the results reported recently in the literature, Dharmadasa *et al* [56] has identified that there are three regions where the structural transition takes place. As shown in Figure 8.8, After the first region, sudden phase transition takes place at the temperature of $385^\circ\text{C} \pm 5^\circ\text{C}$ and after the second region slow transition takes place at

temperature of $385^{\circ}\text{C} < T < 430^{\circ}\text{C}$. In the third region, again the structural transition happens for the temperature of $>430^{\circ}\text{C}$. The first transition has been identified as a sudden change due to melting of grain boundaries while the CdTe crystallites are floating in a liquid phase. Also, Echendu *et al* [57] has recently reported the effect of CdCl_2 and $\text{CdCl}_2+\text{CdF}_2$ treatment on the structural properties of the electrodeposited CdTe layers grown from CdSO_4 precursor. The presence of F enhances these effects and the results presented in this work are in agreement with results obtained from CdSO_4 precursor.

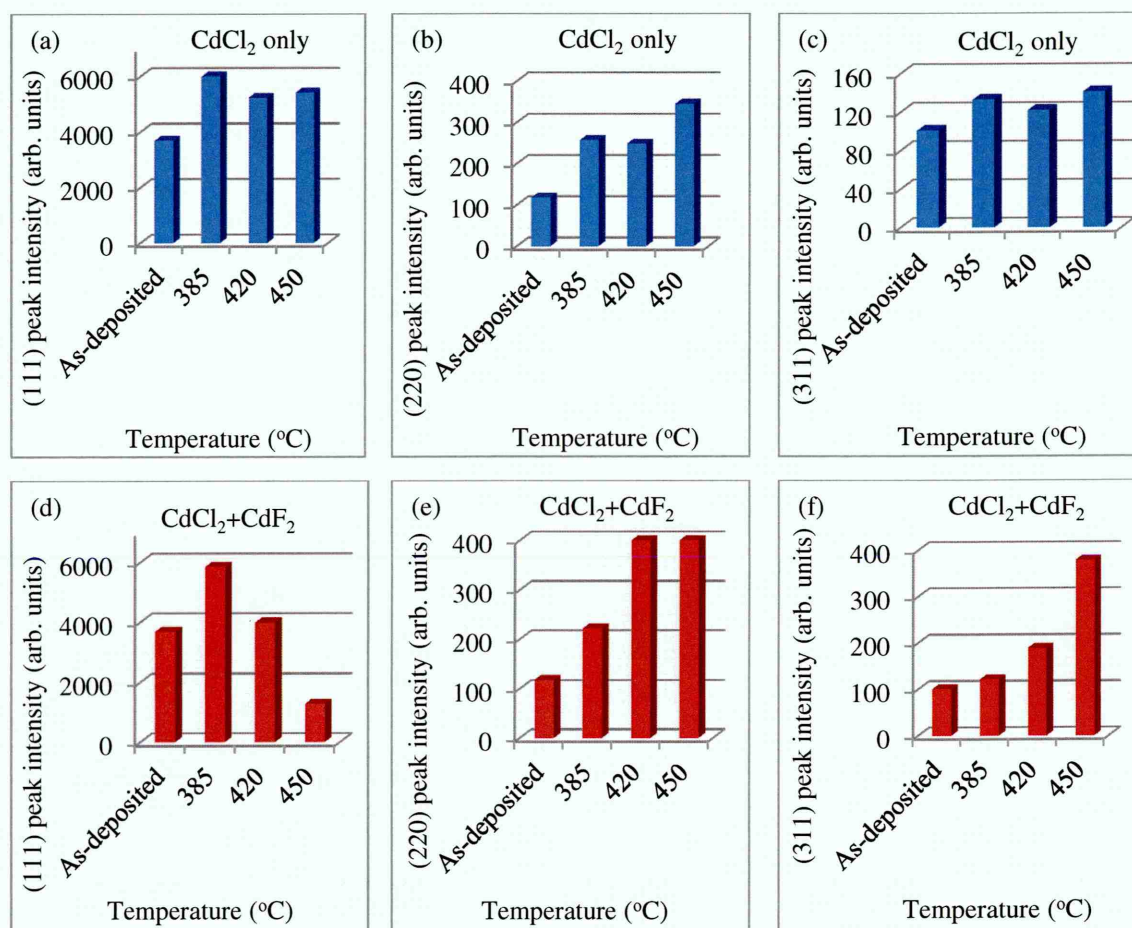


Figure 8.8: Bar charts of the effect of CdCl_2 and $\text{CdCl}_2+\text{CdF}_2$ treatment on the (111), (220) and (311) peak intensity of CdTe layers. The heat treatment was carried out at three different temperatures of 385, 420 and 450°C for 12 minutes in air.

Figures 8.8 (a)-(d) show the summary of results presented in the section 8.3.2.4. These figures clearly show the variation trend of (111), (220) and (311) peak intensity with CdCl_2 and $\text{CdCl}_2+\text{CdF}_2$ treatment at different temperatures. It should also be noted

that these changes do occur due to both the annealing temperature and the annealing period.

8.3.2.5 Effect of CdCl_2 treatment on XRD patterns of Te-rich CdTe layers

In this section effect of CdCl_2 treatment followed by heat treatment on the structural properties of Te-rich CdTe layers were studied. For this reason, Te-rich CdTe layers were grown at cathodic potential of 1233 mV which is 20 mV below the inversion potential of 1253 mV. The CdTe layers were grown on glass/FTO substrate for duration of 2 hours. Afterward, the grown sample was divided into three parts, first part was left as deposited, the second part was annealed at 400°C for 10 minutes in air and the last part was heat treated with CdCl_2 at 400°C for 10 minutes in air and results are presented in Figure 8.9.

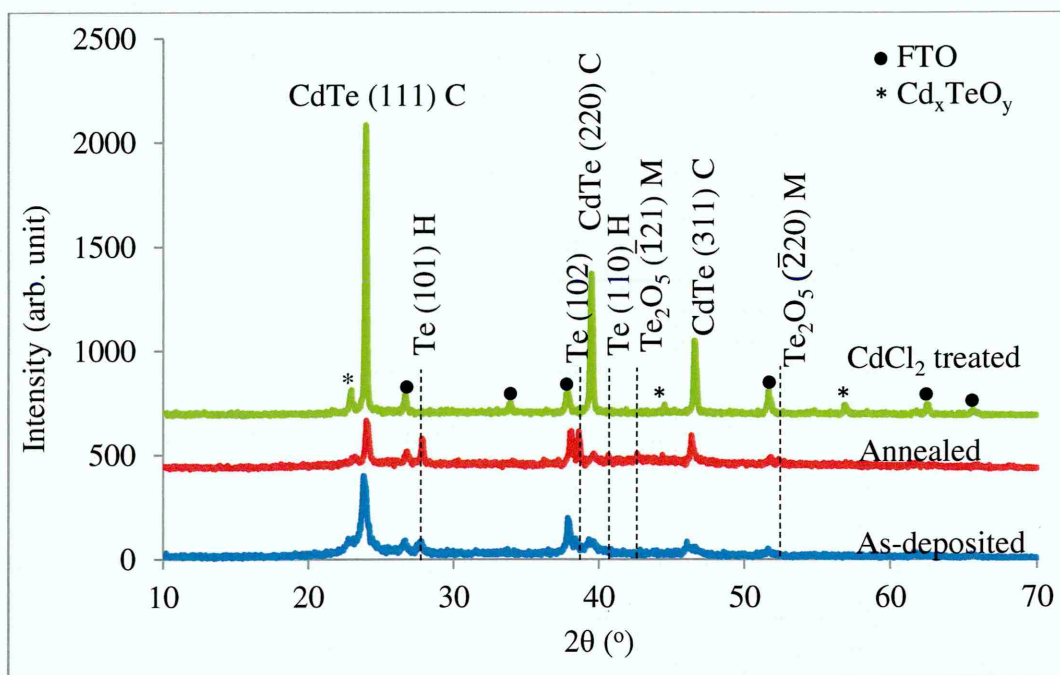


Figure 8.9: Effect of annealing in air and CdCl_2 treatment on XRD patterns of Te-rich CdTe layers.

In the as-deposited CdTe layer with Te-richness, three phases were observed. The first phase belongs to the cubic CdTe (JCPDS No. 01-075-2086) showing the reflections from (111), (220) and (311) crystal planes. The second phase relates to the hexagonal elemental Te (JCPDS No. 00-001-0727) with the reflection from (101), (102)

and (110) crystal planes. The appearance of the third phase which is Cd_xTeO_y can be due to native surface oxide from exposure to oxygen from aqueous solution and air which has been previously explained in section 8.3.2.1. The appearance of three phases in the as-deposited CdTe layer with Te-richness clearly shows that the layer is non-stoichiometric. It should be noted that the non-stoichiometric CdTe layers (Te-rich) are not suitable for solar cells fabrication due to their poor material qualities.

After annealing in air, (111) and (220) peaks intensity was reduced while (331) peak intensity improved slightly due to the random orientation or recrystallisation of the CdTe crystals. In addition, the intensity of Te (101) peak increased showing the improvement of crystallinity of elemental Te after annealing in air. This shows that the post-deposition annealing is an essential step to improve the crystallinity of the thin films. The appearance of Te_2O_5 phases was also expected after annealing. The reason for this oxidation is due diffusion and reaction of oxygen in Te-rich CdTe surface.

Interesting results have been observed when CdTe layers were heat treated with CdCl_2 in air. All the elemental Te and Te_2O_5 XRD peaks disappeared. The intensity of all three main CdTe peaks increased drastically. Reports show that CdCl_2 dissociates the oxide layer on the CdTe surface and Cd in CdCl_2 substitutes the oxygen atoms in Te_2O_5 to form CdTe [58]. This also shows that CdCl_2 treatment removes extra elemental Te and makes the CdTe layer more stoichiometric. The stoichiometric CdTe layers are suitable for fabrication of high efficiency solar cells. This is the reason why CdCl_2 treatment is used in the production of high efficiency solar cells. The CdCl_2 treatment is known as “magic or activation step” because of its significant effect on the device performance which has not yet been fully understood [59]. Observation of additional two peaks of Cd_xTeO_y in the CdCl_2 treated sample can also be related to reaction of oxygen with CdTe surface at 400°C for 10 minutes in air. The formation of thick insulating Cd_xTeO_y layer on the CdTe surface reduces the solar cell efficiency by introducing high series resistance between metal/semiconductor interfaces. However, a very thin layer of insulating Cd_xTeO_y layer can improve the solar cell efficiency by making Metal-Insulator-Semiconductor (MIS) structure [47]. Thick layer of Cd_xTeO_y layer is usually removed by chemical etching prior to metallisation.

8.3.3 Photoelectrochemical (PEC) cell measurements

Figures 8.10 shows the PEC measurement results for the as-deposited, annealed and CdCl_2 treated CdTe layers grown on glass/FTO substrates. The CdTe layers were grown at different cathodic potential ranging from 1248 to 1258 mV for 2 hours duration. The grown CdTe layers were divided into three parts; the first part was for as-deposited, the second and third part was heat treated with and without CdCl_2 at 390°C for 10 minutes in air. This experiment was carried out to identify voltages to grow the Te-rich, stoichiometric and Cd-rich CdTe layers.

Experimental observations reveal two deposition regions for the as-deposited CdTe thin films. The first region shows the Te-rich region starting from 1248 to 1252 mV with positive PEC signals. In this region, because the CdTe layers are rich in Te, and the expected electrical conduction type is p-type as experimentally observed. The values of the positive PEC signals gradually reduce from 1248 mV towards 1252 mV. At the cathodic potential of 1253 mV, zero PEC signal was observed which represents the growth of intrinsic or stoichiometric CdTe layer. The second region shows the Cd-rich region starting from 1254 to 1258 mV with negative PEC signal. Since the CdTe layers are rich in Cd, the expected electrical conduction type is n-type. The value of the negative PEC signals gradually increases from 1254 to 1258 mV due to increase in the Cd in the CdTe layer.

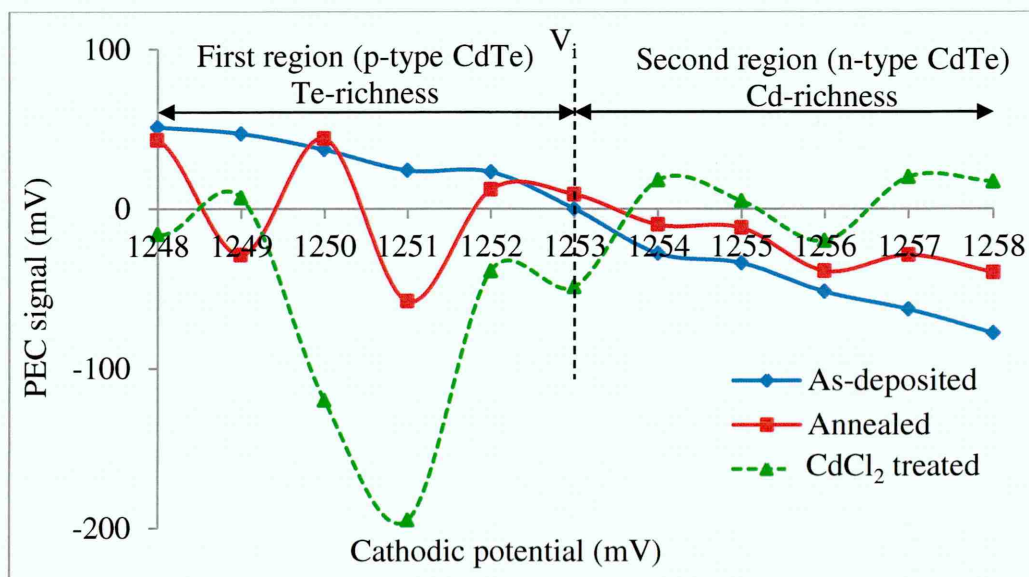


Figure 8.10: The PEC signals of the as-deposited, annealed and CdCl_2 treated CdTe samples grown at different cathodic potentials in the range (1248–1258) mV.

The ability to electrodeposit semiconductor layers of different electrical conductivity type just by the alteration of its growth voltage without addition of external dopants is one of the advantages of electrodeposition technique [60]. Doping in this case is by changing the composition of the semiconductor elements in parts per million (ppm) levels. The results obtained from PEC are in agreement with the XRD results shown in the section 8.3.2.1.

Interesting results was observed when CdTe layers were annealed with and without CdCl₂ treatment on both regions. In the first region when the as-deposited CdTe layers with Te-richness and p-type conductivity was annealed with and without CdCl₂ treatment, the trend shows that the layer moves toward n-type conductivity. Therefore, the Te-vacancy generation must play an important role in this change of doping concentration. In this region, the effect of movement from p-type to n-type conductivity is more pronounced in the CdCl₂ treated sample. When the layers are grown close to the inversion voltage (V_i), the type conversion can go in either direction; n towards p or p towards n depending on the initial and final defects distributions. Interestingly, both type conversions were observed for the i-layer. The i-layer has become p-type after annealing in air and become n-type after heat treatment with CdCl₂.

In the second region when the initial CdTe layers are Cd-rich, and n-type, annealing with and without CdCl₂ treatment changes the doping concentration to make the layers move towards p-type conduction. Therefore, the Cd-vacancy generation must play an important role in this change of doping concentration. Again, the effect of movement from n-type to p-type conductivity is more pronounced after CdCl₂ treatment.

There are lots of reports on the type conversion of CdTe layer from n-type to p-type after annealing with and without CdCl₂ treatment [23, 61-68]. These reports show that CdCl₂ treatment introduces acceptor defects of V_{Cd} , Cl_{Te} and their defect complexes Te_iCl_{Te} and $V_{Cd}Cl_{Te}$ into the CdTe layers which are the main reason of type conversion from n to p. On the contrary, there are also some reports on the type conversion from p to n after heat treatment with and without CdCl₂ [69, 70]. In these reports, the type conversion from p to n was related to the redistribution of donor defects such as Cd_i and V_{Te} after annealing at 400°C in air. In addition, a report shows that the as-deposited n-type CdTe layer still remains n-type even after CdCl₂ treatment [43].

Overall, these results reveal that the change from one conductivity type towards the other depends on the material's initial electrical conduction type, heat-treatment temperature, annealing time and final redistribution of defects in the CdTe layers. One

advantage of PEC measurements is that it shows how Fermi level moves towards p-type or n-type conductivity during annealing with and without CdCl_2 treatment as shown in Figure 8.11 (a) and (b). However, to determine the exact position of the Fermi level using this technique is not possible. The Fermi level movement in both directions, from n towards p and p towards n, shows that the doping density of the CdTe layer is changing after annealing with and without CdCl_2 treatment.

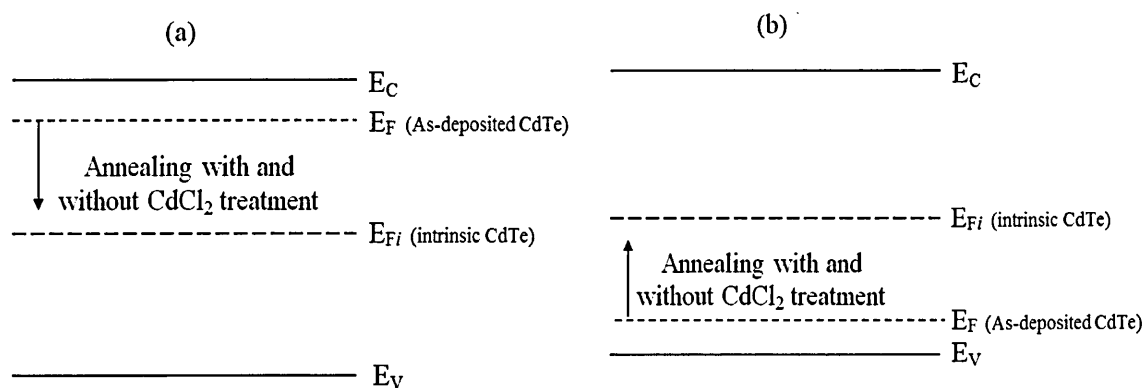


Figure 8.11: The trend of Fermi level movement for CdTe layers from (a) n-type towards p-type conduction and (b) p-type towards n-type conduction after annealing with and without CdCl_2 treatment.

8.3.4 Optical absorption spectrophotometry

8.3.4.1 Effect of growth voltage on the optical properties of CdTe layer

Figure 8.12 (a) - (d) shows the $(\alpha h\nu)^2$ vs. photon energy for eleven CdTe samples grown at the cathodic potential ranges of 1248 to 1258 mV. The CdTe layers were grown on the glass/FTO substrates for two hours and then each sample was divided into two parts. The first part remains as-deposited and second part was annealed at 390°C for 10 minutes in air. This experiment has been carried out to study the effect of different growth voltages on the optical properties of CdTe layers before and after annealing. The as-deposited layers are shown in Figures 8.12 (a) and (b) and annealed samples are shown in Figures 8.12 (c) and (d).

In Figures 8.12 (a) and (b), lower absorption was observed for the samples grown at higher cathodic potential. The estimated energy bandgap for the as-deposited

samples were in the range (1.51-1.54) eV. After annealing, slight improvement in the absorption edge was observed. The absorption edge became sharper and shifts towards lower energy photons as shown in Figures 8.12 (c) and (d). The shift in absorption edge can be attributed to a change in grain size and stoichiometry of the CdTe layers upon annealing. The estimated energy bandgap for the annealed samples were in the range (1.50-1.51) eV. In both as-deposited and annealed samples, the larger scatter in the absorption edge was observed when CdTe samples were grown at higher growth voltage. Among all annealed CdTe layers, sample grown at the cathodic potential of 1253 mV shows the lower bandgap value and sharper absorption edge.

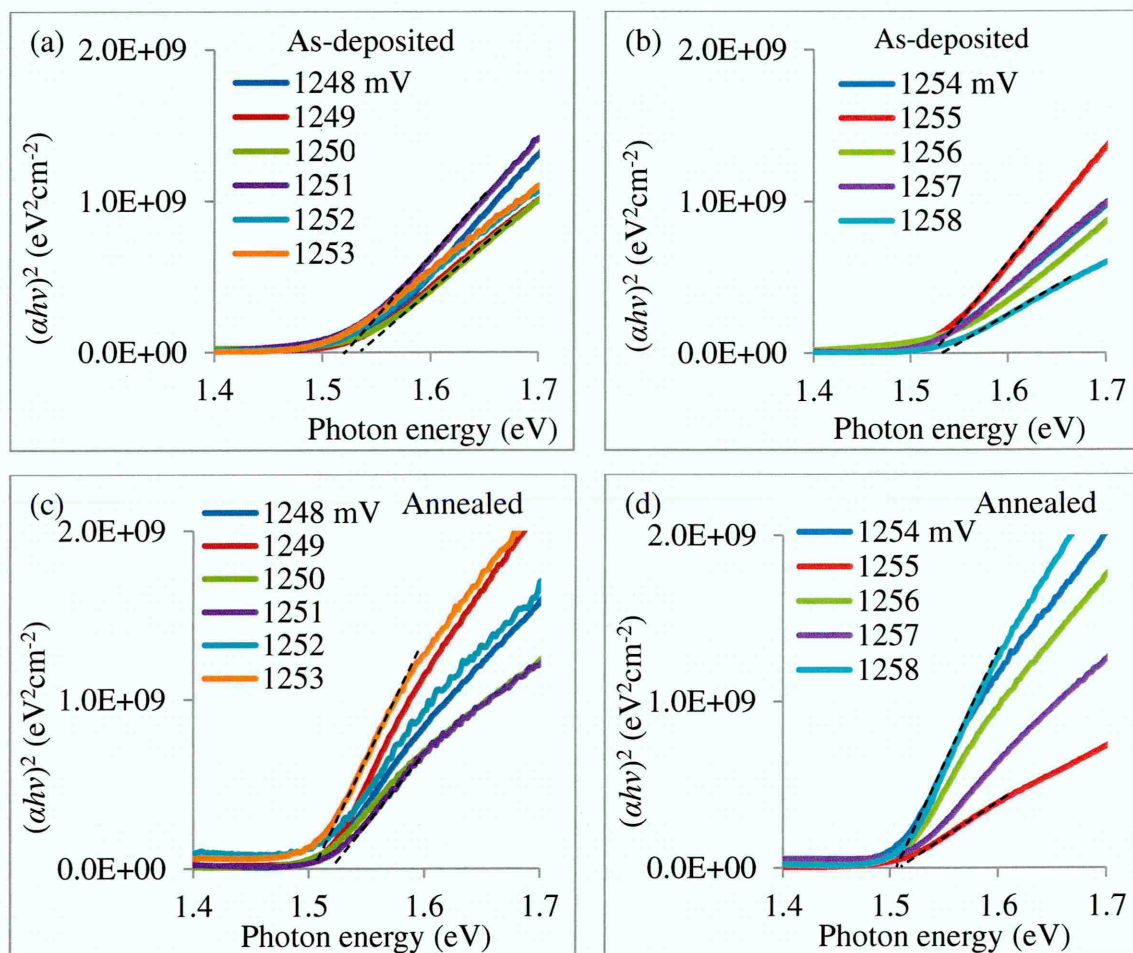
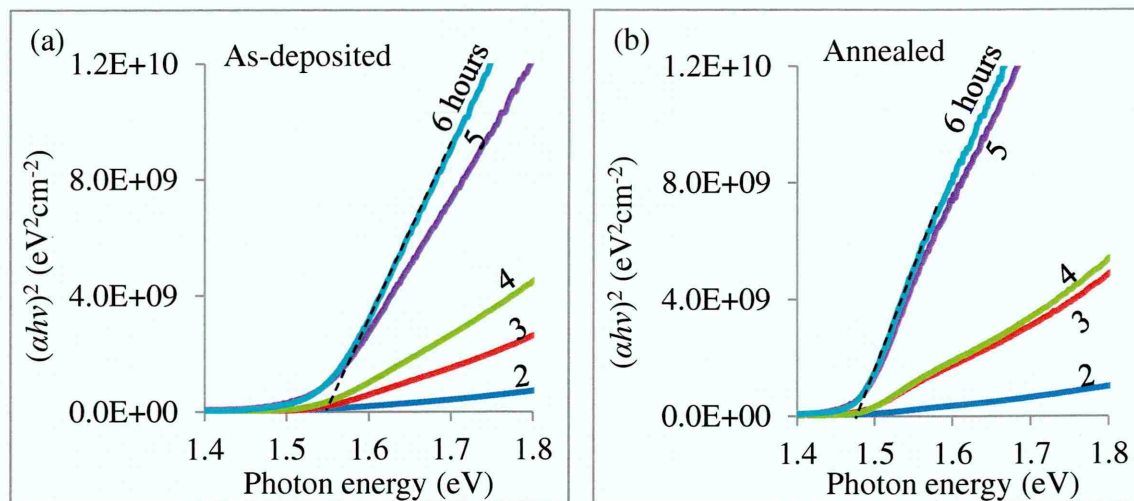


Figure 8.12: Optical absorption spectra of (a, b) as-deposited and (c, d) annealed CdTe samples grown for 2 hours at different cathodic potential range (1248-1258) mV.

8.3.4.2 Effect of the growth time on the optical properties of CdTe layers

In order to study the effect of growth time and thickness on the optical properties of the CdTe layers, five CdTe layers were grown on glass/FTO substrates for different durations between 2 to 6 hours. All CdTe layers were grown at cathodic potential of 1253 mV and each sample were divided into three parts. The first part was left as-deposited; the second and third parts were annealed with and without CdCl₂ treatment at 390°C for 10 minutes in air and results are presented in Figures 8.12 (a)-(c) and Table 8.4.

In all figures, the absorption increases as the growth time increases. The increase in the absorption is due to increase in the thickness of the CdTe layer with growth time. The sharper absorption edge was observed when the thickness of CdTe layer was in the range $\sim 1.5 \mu\text{m}$. The bandgap values for the as-deposited CdTe layers were in the range of (1.54-1.55) eV. After annealing the bandgap slightly improved due to recrystallisation and grain growth. The bandgap values for the annealed samples were in the range of (1.48-1.49) eV as shown in Table 8.4.



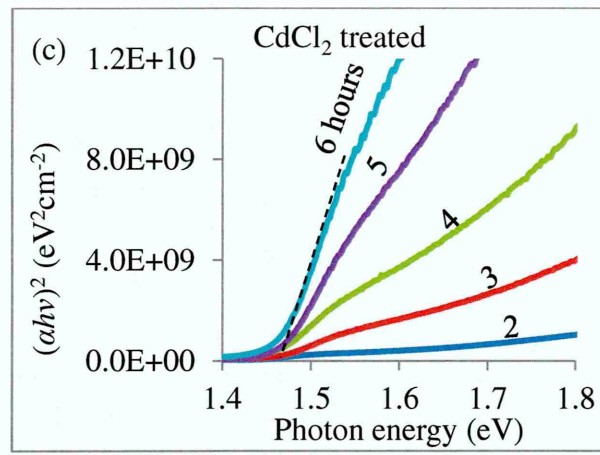


Figure 8.13: Optical absorption spectra of (a) as-deposited, (b) annealed and (c) CdCl₂ treated CdTe samples grown at cathodic potential of 1253 mV for different growth duration.

Interesting results were observed when as-deposited layers were heat treated with CdCl₂ treatment. Optical absorption and the gradient of the absorption edge increase with increasing thickness of the CdTe layers. All bandgap values falls to same value of 1.46 eV as shown in Table 8.4. It was interesting to see the bandgap values of CdTe layers approximately remain unchanged (1.46 eV) within the thicknesses range of ~0.60 to ~1.55 μm after CdCl₂ treatment. The absorption edge becomes sharper as compared to the as-deposited and annealed samples and bandgap shifts towards lower energy close to the bulk band gap value of the CdTe (1.45 eV). This can be related to enhancement in crystallite or grain size of the CdTe layer while removing the pinholes in the material layers. These results reveal that CdCl₂ treatment has a pronounce effect on the bandgap value of CdTe layer, showing reduction in energy bandgap from ~1.54 to ~1.46 eV. Rami *et al* also has reported the reduction in bandgap of electrodeposited CdTe after CdCl₂ treatment [71].

Table 8.4: Variation of bandgap energy as a function of time and thickness for the as-deposited, annealed and CdCl₂ treated CdTe layers grown at cathodic potential of 1253 mV.

Growth time (h)	Thickness (μm)	Bandgap energy ± 0.01 (eV)		
		As-deposited	Annealed	CdCl ₂ treated
2	0.59	1.55	1.49	1.46
3	0.90	1.55	1.49	1.46

4	1.12	1.54	1.48	1.46
5	1.34	1.54	1.48	1.46
6	1.54	1.54	1.48	1.46

8.3.4.3 Effect of temperature on the optical properties of CdCl₂ and CdCl₂+CdF₂ treated CdTe layers

In this experiment, CdTe layer with thickness of ~2.0 μm was grown on the glass/FTO substrate. This layer was grown at cathodic potential of 1253 mV and after deposition the layer was divided into seven parts. The first part was left as-deposited and the next three parts were heat treated with CdCl₂ only at the different temperatures of 385, 420 and 450°C for 12 minutes in air. The last remaining three parts were heat treated with CdCl₂+CdF₂ at different temperatures of 385, 420 and 450°C for 12 minutes in air. The aim of this experiment was to study the effect of different annealing temperature on the optical properties of the electrodeposited CdTe layers in the presence of CdCl₂ and CdCl₂+CdF₂.

Figure 8.14 (a) and (b) respectively show the $(\alpha h\nu)^2$ vs. photon energy for the CdTe layers heat treated with CdCl₂ and CdCl₂+CdF₂ at different temperatures. In both figures, it can be seen that the absorption edge of the as-deposited layer is not very sharp. The bandgap value of the as-deposited layer was 1.51 eV. Slight improvements in absorption edges were observed when CdTe layer were heat treated at temperature of 385°C for both conditions.

Important results were observed when CdTe layers were heat treated at temperatures of 420 and 450°C for both conditions. The absorption edges of the CdTe layers become sharper as compared to the as-deposited layers. In addition, bandgap values clearly shifts towards the lower energy for both conditions. The bandgap values of the CdTe layers heat treated at temperature of 420°C were in the range (1.46-1.48) eV while the ones heat treated at 450°C falls within the bulk bandgap value of 1.45 eV for CdTe.

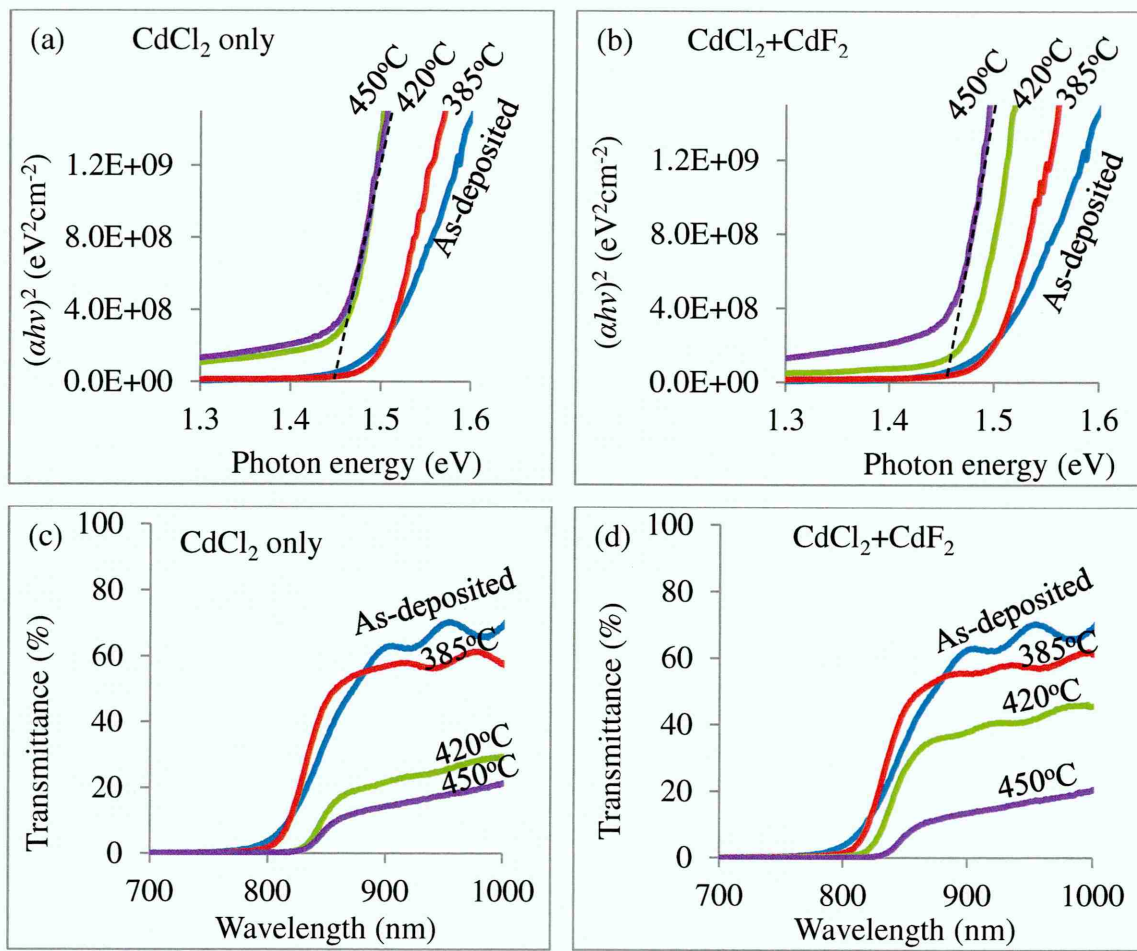


Figure 8.14: Optical absorption and transmittance spectra of (a, c) CdCl_2 treated and (b, d) $\text{CdCl}_2+\text{CdF}_2$ treated CdTe samples with thickness of $\sim 2.0 \mu\text{m}$. The CdTe samples were heat treated at three different temperatures of 385, 420 and 450°C for comparison.

These results clearly show that as the heat treatment temperature increases from 385 to 450°C , the bandgap value reduces and the absorption edge becomes sharper for both CdCl_2 and $\text{CdCl}_2+\text{CdF}_2$ treated samples. When the bandgap of CdTe reduces and absorption edge becomes well-defined, more photon can be absorbed in the layer. This leads to the increase in the number of photo-generated charge carriers in the CdTe thin films and eventually will improve the solar cell performance.

Although the layers heat treated with CdCl_2 and $\text{CdCl}_2+\text{CdF}_2$ approximately shows the same bandgap values for three different heat treatment temperatures, the layer heat treated with $\text{CdCl}_2+\text{CdF}_2$ slightly shows better absorption edge. In this experiment, the best annealing temperature and condition was found to be at 450°C with $\text{CdCl}_2+\text{CdF}_2$.

Figures 8.14 (c) and (d) respectively show the transmittance spectra of the samples heat treated with CdCl_2 and $\text{CdCl}_2+\text{CdF}_2$ at temperatures of 385, 420 and 450°C. The results show that the transmittance decreases as the heat treatment temperature increases for both conditions. In the as-deposited sample, transmittance was in the range (63-70)% in the wavelengths range of (870-1000) nm. For the same wavelengths range, the transmittance of both CdCl_2 and $\text{CdCl}_2+\text{CdF}_2$ treated samples falls to the ranges (56-61)%, (23-46)% and (13-20)% when layers were heat treated at temperature of 385, 420 and 450°C, respectively. From the transmittance spectra, the absorption edge of the as-deposited sample shifts from 810 nm towards the higher wavelengths of 830 nm as temperature increases to 450°C for both conditions. According to these results, the lowest transmittance and maximum shift in absorption towards the higher wavelengths were observed when CdTe layers were heat treated at temperature of 450°C. The lower transmittance means higher absorption in CdTe layer which clearly indicates the enhancement in optical properties of CdTe layer as an absorber material.

8.3.5 Scanning electron microscopy (SEM)

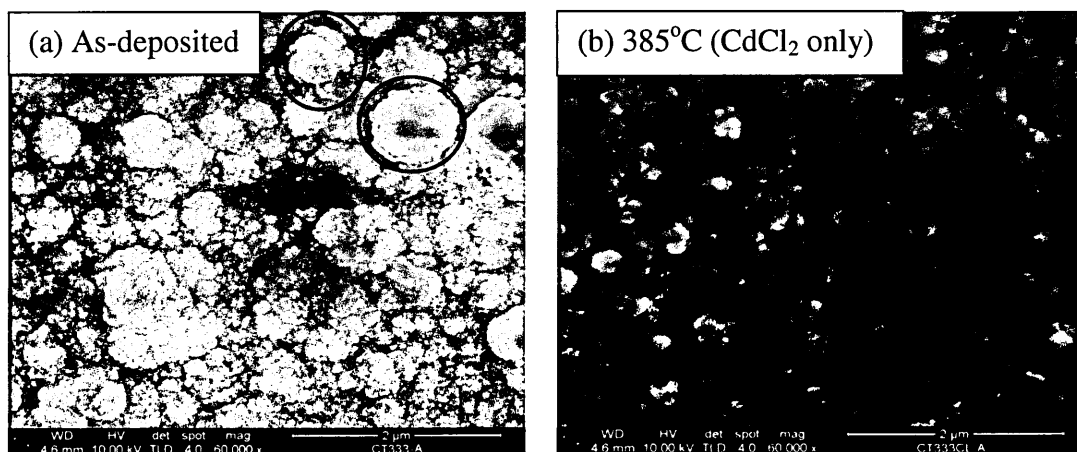
8.3.5.1 Effects of CdCl_2 and $\text{CdCl}_2+\text{CdF}_2$ treatment on the morphological properties of CdTe layers at different temperatures

In this experiment, effects of CdCl_2 and $\text{CdCl}_2+\text{CdF}_2$ treatment at different temperatures on the morphological properties of the CdTe layers were explored. For this reason, CdTe layer with a thickness of $\sim 2.0\ \mu\text{m}$ was grown on the glass/FTO/CdS substrate at cathodic potential of 1253 mV. This sample was then divided into seven parts. The first part was left as-deposited, the next three parts were heat treated with CdCl_2 only and the last remaining three parts were heat treated with $\text{CdCl}_2+\text{CdF}_2$. The heat treatment temperatures used for both CdCl_2 and $\text{CdCl}_2+\text{CdF}_2$ treated samples were 385, 420 and 450°C for 12 minutes in air, respectively. In this experiment, the SEM magnification of 60,000 was used for the as-deposited and heat treated samples at temperatures of 385 and 420°C while 30,000 magnifications was used for the samples heat treated at 450°C.

Figures 8.15 (a)-(d), show the SEM images of the as-deposited, and CdCl_2 treated CdTe layers at temperatures of 385, 420 and 450°C, respectively. The SEM

image of as-deposited samples (Figures 8.15 (a) and 8.16 (a)) show that the layer contains cauliflower-like clusters with a very closely packed morphology without any visible pinholes in the layer. These cauliflower-like clusters were formed as a result of agglomeration of tiny nano crystallites with sizes in the range $\sim(30-65)$ nm. The agglomeration of these tiny crystallites can also lead to the formation of large clusters with sizes up to ~ 750 nm which are circled in Figures 8.15 (a) and 8.16 (a).

When layers were heat treated at temperature of the 385°C with CdCl_2 these tiny crystallites coalesced together and creates small grains with sizes in the range $\sim(250-400)$ nm. As the temperature increases to 420°C , the grain sizes were also increased to $\sim(450-600)$ nm. Clear enhancements in grain sizes with compact grain morphology were observed when CdTe layer was heat treated at 450°C . At this temperature the grain sizes were increased up to $1.5\text{ }\mu\text{m}$ as shown in Figure 8.15 (d). In addition, the grain boundaries at this heat treatment temperature (450°C) can be easily distinguished as compared to the other heat treatment temperatures. There are lots of reports on the effect of CdCl_2 treatment on the morphological properties of CdTe thin films. Most of these reports show grain size enhancement after CdCl_2 treatment due to recrystallisation [59, 72-74, 28]. The grain growth in CdTe after CdCl_2 treatment also reduces the number of grain boundaries. The grain boundaries are known as the scattering centres for charge carriers. Therefore, less grain boundaries means higher charge carriers mobility. Moreover, in the CdS/CdTe solar cells CdCl_2 treatment removes the stress, surface states, abrupt interface and lattice mismatch between CdS and CdTe interface. It also enhances the lifetime of charge carriers and passivates the grain boundaries which lead to the improvement of device performance [75].



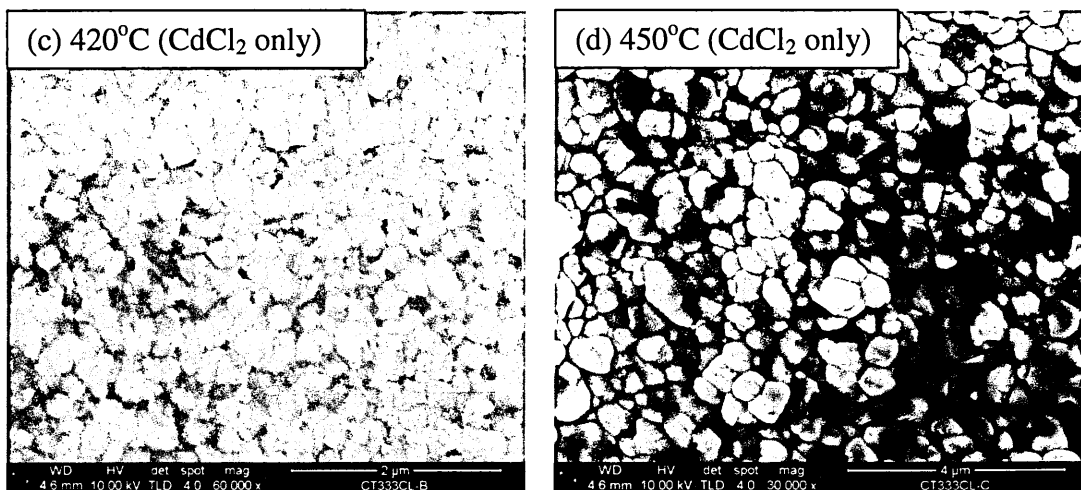


Figure 8.15: SEM images of (a) as-deposited and (b, c, d) CdCl_2 treated CdTe layer at temperature of 385, 420 and 450°C for 12 minutes in air.

In Figures 8.15 (a)-(d), no visible pinholes were observed before and after CdCl_2 treatment. The pinholes in the CdTe are detrimental in solar cell device fabrication due to short-circuiting between two metal contacts.

Figures 8.16 (a)-(d), show the SEM images of the as-deposited, and $\text{CdCl}_2+\text{CdF}_2$ treated CdTe layers at temperatures of 385, 420 and 450°C, respectively. In this case, three different morphologies were observed for three different annealing temperatures. In the sample heat treated at 385°C elongated rice grain-like morphology were observed as shown in Figure 8.16 (b). In this figure the grain boundaries are not distinguishable. This shows that a liquid phase has formed at previously identified [58, 57] transition temperature of $385\pm0.05^\circ\text{C}$ at the grain boundaries. The formation of liquid phase at grain boundaries also has been reported by Hiie [76]. The liquid phase formation is due to lower melting point of the CdTe at grain boundaries as compared to the bulk of CdTe grains. The lower melting point is due to the addition of impurities such as of Cl, F, oxygen and excess Cd into the grain boundaries during CdCl_2 and $\text{CdCl}_2+\text{CdF}_2$ treatment. The presence of these impurities in the CdTe layer can drastically reduce the melting point of stoichiometric CdTe from 1092°C to lower values. However, any deviation from stoichiometry, Cd-richness or Te-richness can also reduce the melting point of the CdTe.

The morphology observed in Figure 8.16 (b) can also be related to structural transition of CdTe layer at $385\pm0.05^\circ\text{C}$ as explained in section 8.3.2.4. Recently, R. Dharmadasa *et al* [77] have used intense pulsed light (IPL) as a rapid thermal processing technique for the heat treatment of the CdTe layer in the presence of CdCl_2 .

In their observation also similar morphology were observed when CdTe layer was IPL treated with energy density of 2157 (100 pulses) Jcm^{-2} which is believed to be equivalent to the transition temperature. At this transition temperature, the CdTe layer begins to lose their (111) preferred orientation due to random orientation of the CdTe crystals which lead to the morphology change in the CdTe layer. The CdCl_2 and CdF_2 are known as fluxing agents for recrystallisation of CdTe layer [78].

When heat treatment temperature increases to 420°C , the grain boundaries become more visible due to coalescence of small crystallites and formation of larger grains as shown in Figure 8.16 (c). The grain sizes observed were larger than the CdCl_2 treated sample annealed at the same temperature. The grain sizes of the $\text{CdCl}_2+\text{CdF}_2$ treated sample were in the range $\sim(0.8-1.5) \mu\text{m}$ at temperature of 420°C . Therefore, the presence of F atoms during heat treatment has drastic effect on structural and morphological changes of CdTe thin films.

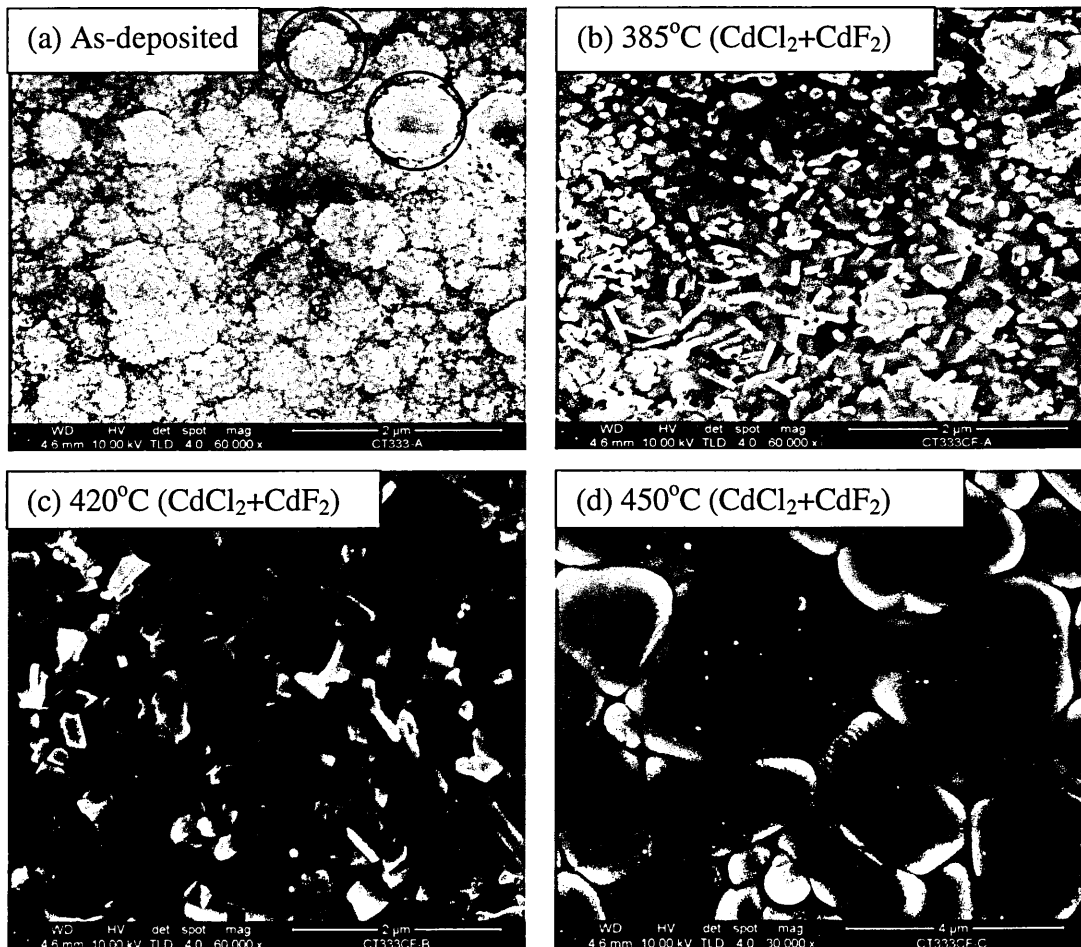


Figure 8.16: SEM images of (a) as-deposited and (b, c, d) $\text{CdCl}_2+\text{CdF}_2$ treated CdTe layer at temperature of 385, 420 and 450°C for 12 minutes in air.

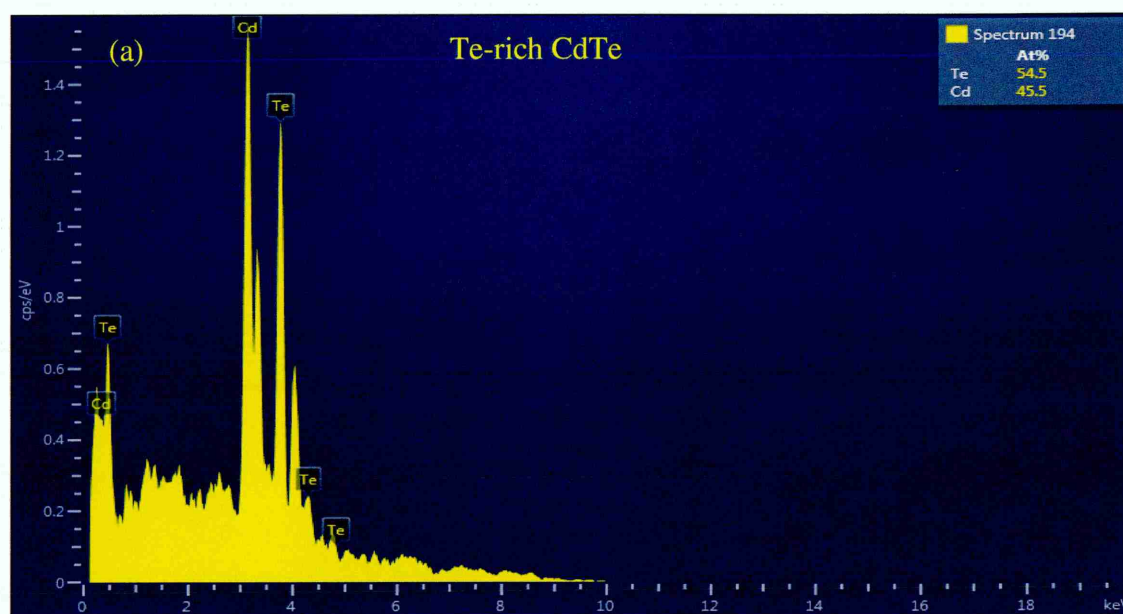
Interesting results were observed when heat treatment temperature was increased to 450°C in the presence of CdCl₂+CdF₂. The grain size increases drastically reaching up to ~8.3 μm and the layer shows a rounded shape grain-like morphology as shown in Figure 8.16 (d). The grain sizes of CdCl₂+CdF₂ treated sample were approximately a few orders of magnitude larger than the grain size of CdCl₂ treated sample at the same temperature of 450°C. These results clearly show that combination of CdCl₂+CdF₂ lead to the formation of larger grain with less number of grain boundaries and scattering centres. Romeo *et al* has also reported the effect CdCl₂ and HCF₂Cl (difluorochloromethane) treatment on the CSS and high vacuum evaporated (HVE)-CdTe layers [79]. In their observations incorporation of fluorine promote the recrystallisation process and lead to the formation of larger grains as compared to CdCl₂ only. Hernandez *et al* also have shown that the larger grains can be obtained when CdTe layer is heat treated with HCF₂Cl in the presence of oxygen [80]. They also show that the both HCF₂Cl and oxygen enhance the recrystallisation process. It should be noted that the higher efficiency CdS/CdTe solar cells have been always reported when the CdS/CdTe layers were heat treated with Cl and combination of Cl and F in the air atmosphere (in the presence of oxygen). Oxygen increase the number of nucleation sites, promote the denser growth, incorporate to form defect complex and helps to yield pinhole free CdTe thin films over the wide range of deposition condition. For these reasons, in this work also CdTe layer were heat treated with CdCl₂ and CdCl₂+CdF₂ in air atmosphere. There are some reports in the literature which shows that the combination of Cl and F yield better solar cells efficiency. Rejon *et al* [81] and Flores *et al* [82] have reported the higher efficiency CdTe based solar cells using the HCF₂Cl in the presence of oxygen. Recently, Echendu *et al* reported that the higher efficiency solar cells were obtained when electroplated CdTe were heat treated with combination of CdCl₂ and CdF₂ in air as compared to CdCl₂ only [83].

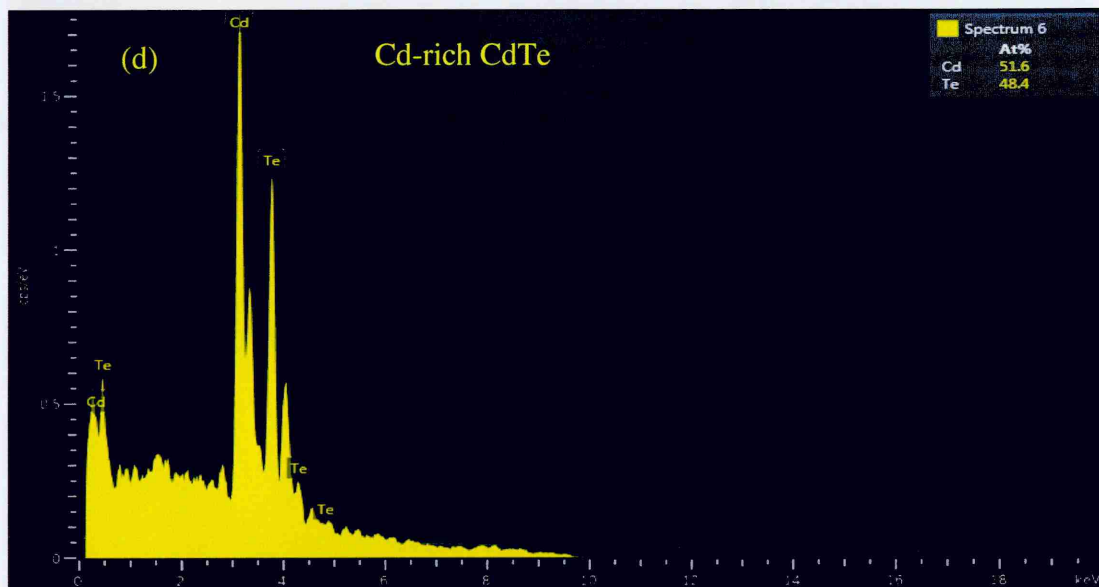
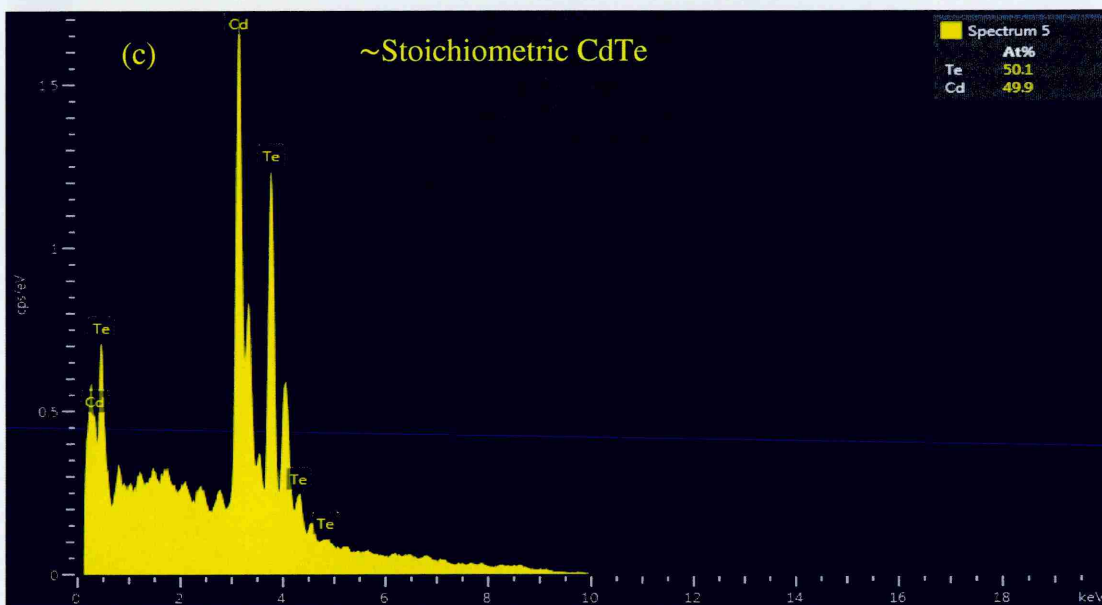
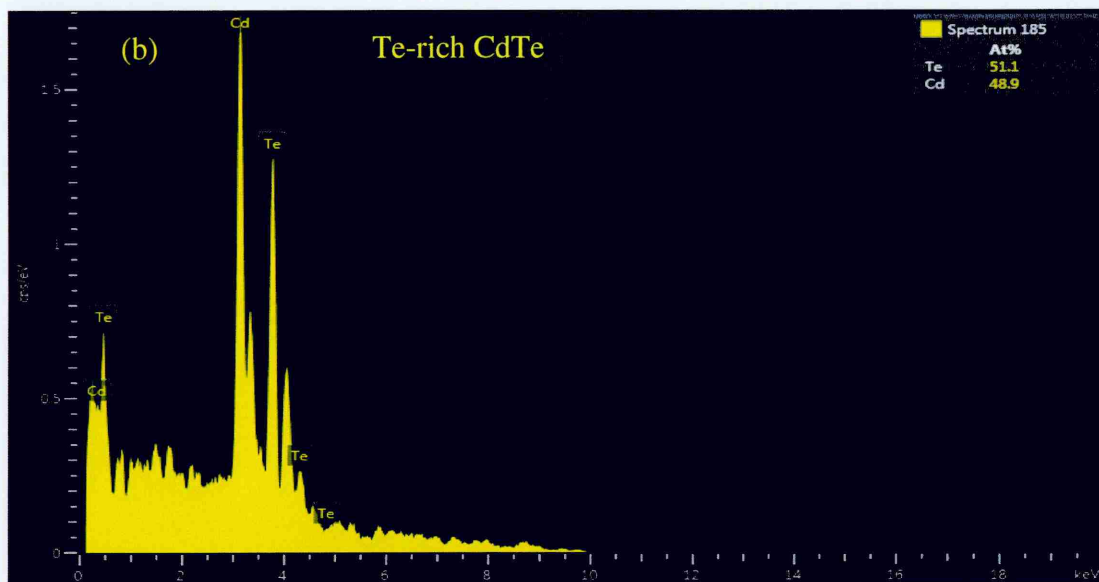
It is worth mentioning that the grain sizes observed in this work are comparable to that of high temperature growth techniques such as CSS. These results shows that even with low temperature growth techniques such as electrodeposition, the high quality CdTe layers can be obtained when these layers are heat treated with CdCl₂ and CdCl₂+CdF₂.

8.3.6 Energy Dispersive X-ray (EDX)

For EDX measurements, CdTe layers were deposited on glass/FTO substrates for 2 hours duration. The first layer was deposited at the growth voltage of 1253 mV (stoichiometric point). The other layers were grown at 5 and 10 mV below and above the growth voltage of the 1253 mV respectively. This experiment was carried out to measure the composition and atomic percentage of the as-deposited CdTe layers grown at different growth voltages.

Figures 8.17 (a)-(e), show the EDX spectra of the Te-rich, stoichiometric and Cd-rich CdTe layers respectively. The spectra indicate the presence of both Cd and Te atoms in these materials. The atomic percentages and Cd/Te ratios of the Te-rich, stoichiometric and Cd-rich CdTe layers are shown in Table 8.5. These results clearly show that the layers deposited at growth voltages below 1253 mV are Te-rich while the layers deposited at growth voltage more than 1253 mV are Cd-rich. The samples grown at the growth voltage of 1253 mV are shown to be approximately stoichiometric with Cd/Te ratio close to one as shown in Table 8.5. The EDX results presented in this section are in agreement with the PEC cell measurements shown in the section 8.3.3.





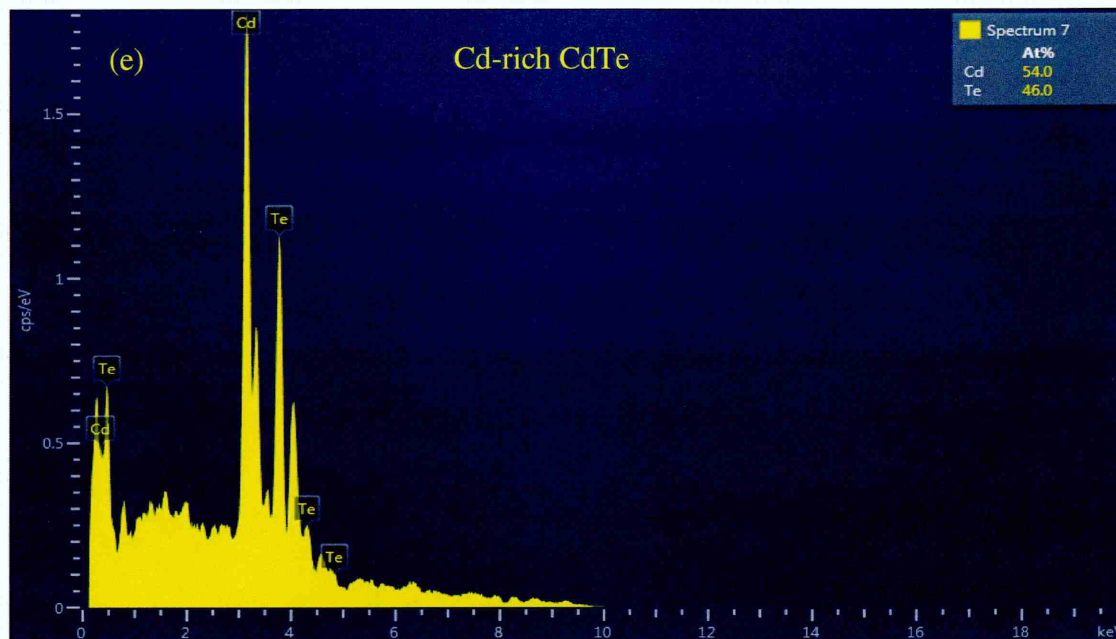


Figure 8.17: EDX spectra of the (a, b) Te-rich CdTe, (c) Stoichiometric CdTe and (d, e) Cd-rich CdTe. All as-deposited CdTe layers were grown on the glass/FTO substrate for 2 hours duration.

Table 8.5: Atomic percentage and Cd/Te ratio of the Te-rich, stoichiometric and Cd-rich CdTe layers. All as-deposited CdTe layers were grown on the glass/FTO substrates for 2 hours duration.

Sample	Atomic percentage (at%)		Cd/Te ratio
	Cd	Te	
Te-rich	45.5	54.5	0.83
Te-rich	48.9	51.1	0.95
Stoichiometric	50.1	49.9	0.99
Cd-rich	51.6	48.4	1.06
Cd-rich	54.0	46.0	1.17

8.3.7 Transmission electron microscopy (TEM)

For TEM study, CdTe layers were grown on glass/FTO/CdS substrates at cathodic potential of 1253 mV. The estimated thickness of as-deposited CdTe layer from TEM image is ~900 nm as shown in Figure 8.18. The TEM image of as-deposited CdTe layer shows the columnar growth during electroplating of these thin films. This

can be due to the low temperature growth nature of electrodeposition technique with tiny crystallite size in the range of $\sim(30-65)$ nm. The columnar or upward growth of the CdTe layer is related to the nature of electrodeposition technique and the substrate used. The FTO substrate is known to have a high surface with spiky surfaces. During the electrodeposition, the electric field at these spikes are higher than those of the valleys. Therefore, nucleation starts at these spikes and CdTe crystallites grow upward normal to the FTO substrate. This can lead to non-uniformity in the CdTe layer which can be seen in Figure 8.18. There are also other reports which show that CdTe favourably tend to grow upward normal to the substrate even in high temperature growth techniques [84, 85, 74].

It should be noted that, the FTO substrates with lower surface roughness are more suitable for CdS/CdTe solar cells fabrication. This is because CdTe grown on substrate with lower surface roughness has low stress and better morphological properties.

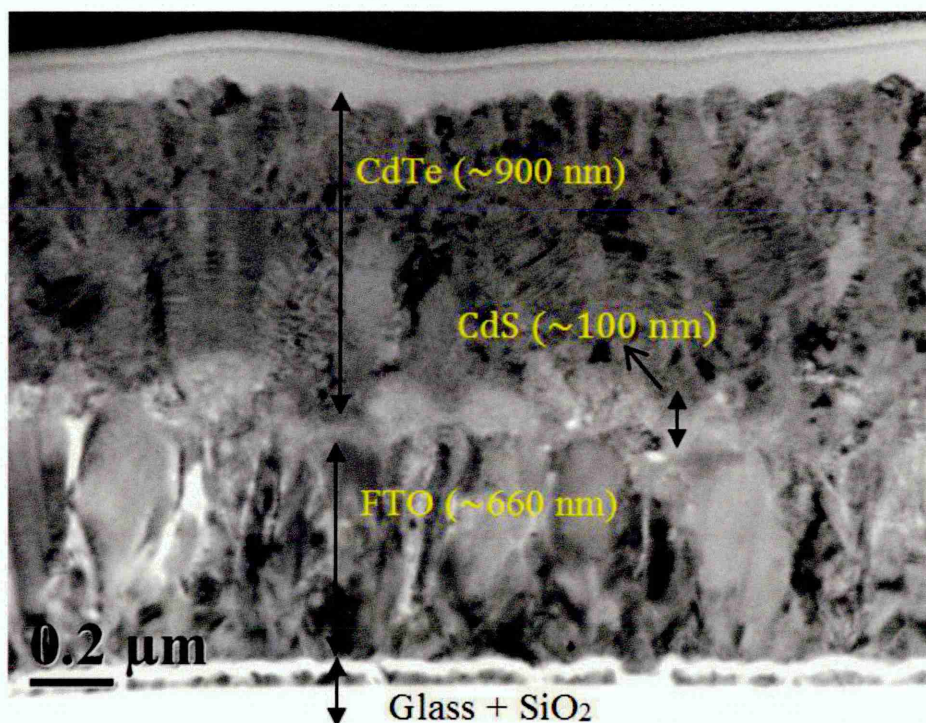


Figure 8.18: The TEM cross section images of the as-deposited CdTe thin film grown on the glass/FTO/CdS substrate. The thicknesses of the CdS and CdTe are estimated close to 100 nm and 900 nm respectively.

8.3.8 Raman spectroscopy

In this experiment, effects of different annealing conditions on the Raman spectroscopy of the Te-rich CdTe layers were studied. For this reason, Te-rich CdTe layer with the same condition mentioned in section 8.3.2.4 was grown on glass/FTO substrate for two hours duration. The sample was then divided into four parts. The first sample remains as-deposited and the second sample was annealed at 400°C for 10 minutes in air. The third and fourth samples were respectively heat treated with CdCl₂ only and CdCl₂+CdF₂ at the same temperature used for the second sample. The Raman results of these four samples are represented in Figure 8.19 for comparison. The aim of this experiment was to see the effect of different annealing conditions on the stoichiometric properties of CdTe layer with Te-richness.

In the as-deposited sample with Te-richness, three Raman peaks were observed. The two Raman peaks observed at 122 and 268 cm⁻¹ correspond to the vibrations from elemental Te, E(Te). The observation of two E(Te) peaks represent the existence of two Te phases in the Te-rich CdTe layer. The Raman peaks observed at ~140 cm⁻¹ is related to the combination of elemental Te and TO (CdTe). Because these two peaks overlap, it has not been used to study the stoichiometry change in CdTe layer in this experiment.

After heat treatment in air, the intensity of two E(Te) Raman peaks slightly increased showing the crystallisation of elemental Te. Interesting results were observed when as-deposited layer was heat treated with CdCl₂ and CdCl₂+CdF₂. The intensity of E(Te) peak at 122 cm⁻¹ has drastically reduced and the other E(Te) peak at 268 cm⁻¹ has been completely removed for both conditions. Additional Raman peak was observed at 155 cm⁻¹ which corresponds to the vibration from LO(CdTe) and indicates the crystallisation of CdTe layer after CdCl₂ and CdCl₂+CdF₂ treatment. These results clearly show that CdCl₂ and CdCl₂+CdF₂ treatment removes excess Te and improve the stoichiometry of CdTe layer. The Raman results in this section also confirm XRD results in section 8.3.2.4. Similar results also have been observed for electrodeposited CdTe layer grown from CdSO₄ and CdCl₂ precursors [86]. In this work, all Raman peaks of CdTe sample after heat treated in air, CdCl₂ treatment and CdCl₂+CdF₂ treatment have shown blue shifts as compared to the Raman peak of as-deposited layers. The blue shift in Raman peaks of CdTe is due to lattice contraction [87].

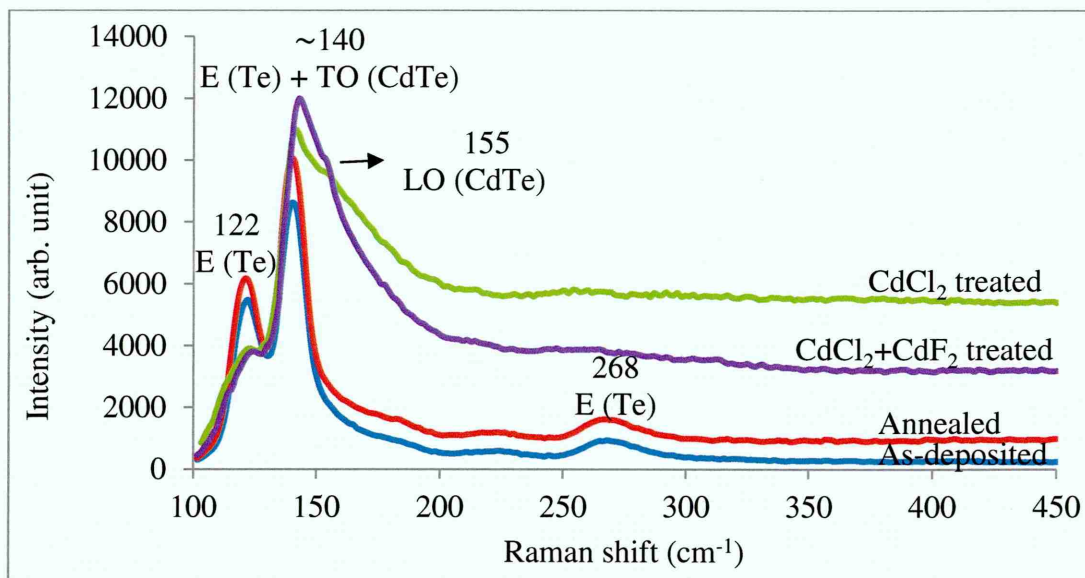


Figure 8.19: Effect of the annealing, CdCl_2 treatment and $\text{CdCl}_2+\text{CdF}_2$ treatment on the Raman spectroscopy of Te-rich CdTe layer.

8.3.9 Ultraviolet photoelectron spectroscopy (UPS)

The UPS experiments were carried out to determine the position of valence band maximum (E_V) and the Fermi level of the CdTe sample at three different conditions. The UPS experiments were carried out by our collaborator at the Conn Centre for Renewable Energy Research at University of Louisville, USA. The measurements were conducted using VG Scientific MultiLab 3000 ultra-high vacuum surface analysis system. The samples were excited with a resonance line He-I ($h\nu = 21.22$ eV) and the base chamber pressure was in the range 10^{-9} Torr. The excited photoelectrons with certain amount of kinetic energy were directed towards the detector using CLAM4 hemispherical electron energy analyser and a differentially-pumped He cold cathode capillary discharge UV lamp. Half of the CdTe samples used for UPS work were covered with a sputtered gold film and the other half was left exposed. By using this method, the Fermi level in Au film and CdTe film was lined up and the Fermi level position can be measured. In this experiment, the Fermi level edge was measured from UPS spectra of the sputtered gold film. The sputtered gold film was connected to the sample stage using silver paste to avoid charging effect.

Figures 8.20 (a), (b) and (c), show the UPS spectra for the area sputtered with gold film. From Figure 8.20 (b), the low kinetic energy cut-off edge indicates the ionisation of electrons from the deepest states in the valence band. Also, the low kinetic

energy cut-off edge shows the maximum distance in which UV light with energy of 21.22 eV has penetrated into the material. In the high kinetic energy end of the UPS spectrum shown in Figure 8.20 (c), the Fermi level edge for gold was determined. The visibility of Fermi level at high kinetic energy end of the UPS spectra is due to the high density of occupied state at and below the Fermi level. The position of fermi level for gold film was obtained from half maximum of the step height as shown in Figure 8.20 (c).

Figures 8.20 (d), (e) and (f) represent the UPS spectra for the CdTe samples. It should be noted that in semiconductors, the Fermi level is located between valence band and conduction band. In some cases, the Fermi level pins very close to the valence band (deep state level). At the deep state level, the densities of states are lower; therefore, in this situation the detection of the Fermi step using UPS spectrum will be possible as shown in Figure 8.20 (f). That is why the Fermi level of CdTe layer was measured from the gold films. In Figure 8.20 (f), two photoionisation edges were observed at high kinetic energy part of UPS spectra which are shown as E_1 and E_2 . In this case, E_1 represents the defect states and E_2 indicates the valence band maximum [88].

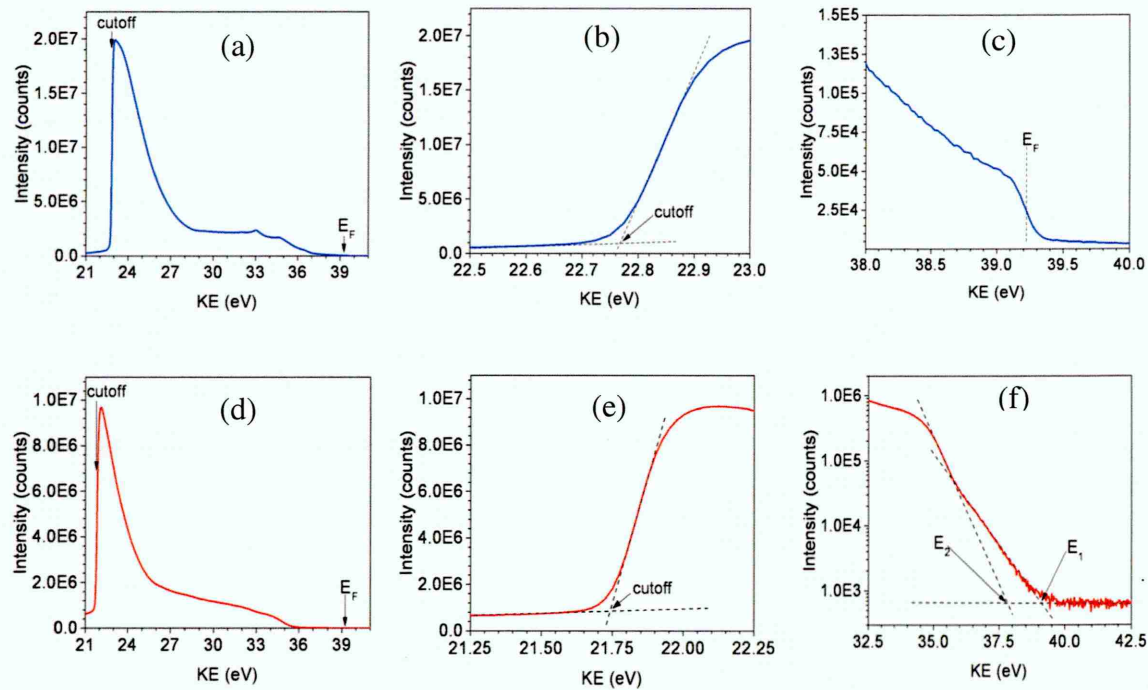


Figure 8.20: Typical UPS spectra obtained for gold film and CdTe layer; (a) UPS spectrum obtained for gold layer, (b) low KE cut-off edge for gold, (c) high KE Fermi

level edge for gold, (d) a typical UPS spectrum obtained for CdTe layer, (e) low KE cut-off for CdTe and (f) high KE cut-off of valence band edge for CdTe.

Table 8.6 shows the summary of the UPS measurements for the as-deposited CdTe sample. The first and second columns respectively represent the high kinetic energy cut-off for the gold and the high-kinetic energy cut-off for the CdTe layer with two different values of E_1 and E_2 as previously shown in Figure 8.20 (f). In order to calculate $E_C - E_F$ (eV), in this experiment, the bandgap of the CdTe film has been taken as 1.44 eV. In order to distinguish between the results, each measurement has been marked differently with different symbols S_1 , S_2 and S_3 . S_1 represents the as-deposited CdTe, S_2 indicates CdTe sample after first CdCl_2 treatment and S_3 shows CdTe sample after second CdCl_2 treatment. According to the results shown in Table 8.6, the Fermi level position for the as-deposited CdTe layer was 0.98 eV below the conduction band minimum. This shows that the as-deposited CdTe is p-type in electrical conduction. Since the as-deposited CdTe layer was grown at the vicinity of the stoichiometric cathodic potential of 1253 mV, it is possible for the material to be n-type or p-type. Therefore, these results are in agreement with the PEC results previously shown in section 8.3.3.

Table 8.6: Summary of several parameters measured by UPS for as-deposited CdTe.

Au E_F cut-off (eV)	CdTe E_F cut-off (eV)		$E_F - E_V$ (eV)		$E_C - E_F$ (eV)		UPS measurement for As-deposited CdTe
39.22	38.85	38.66	0.37	0.56	1.07	0.88	S ₁
			0.46		0.98		

The gradual movement of Fermi level through the bandgap was studied after two steps of CdCl_2 treatment. For this reason, a saturated CdCl_2 solution was prepared. Then this solution was diluted to ~1% using deionised water and sample S_1 was dipped into the solution for five minutes. Thereafter, sample S_1 was allowed to dry and then sample was heat treated at 440°C for 8 minutes in air. The position of Fermi level after the first step of CdCl_2 treatment slightly moves from 0.98 eV to 1.04 eV for sample S_2 as shown in Table 8.7. These results show that the sample still remains p-type after the first step of CdCl_2 treatment.

Table 8.7: Summary of several parameters measured by UPS after the first step of CdCl₂ treatment.

Au E_F cut-off (eV)	CdTe E_F cut-off (eV)		$E_F - E_V$ (eV)		$E_C - E_F$ (eV)		UPS measurement after 1 th CdCl ₂ treatment
39.22	38.83	38.81	0.39	0.41	1.05	1.03	S ₂
			0.40		1.04		

In order to perform the second step of CdCl₂ treatment, same layer was again treated with CdCl₂ in a similar way and heat treated again at 440°C for 16 minutes in air. Interestingly, the Fermi level position for measurement S₃ settled at 0.69 eV below the conduction band minimum as shown in Table 8.8. This clearly shows that sample become n-type in electrical conduction after carrying out the second step of CdCl₂ treatment (S₃). These results once again are in consistency with PEC results presented in section 8.3.3.

Table 8.8: Summary of several parameters measured by UPS after the second step of CdCl₂ treatment.

Au E_F cut-off (eV)	CdTe E_F cut-off (eV)	$E_F - E_V$ (eV)	$E_C - E_F$ (eV)	UPS measurement after 2 nd CdCl ₂ treatment
39.22	38.47	0.75	0.69	S ₃

Table 8.9 and Figure 8.21 show the summary of the results presented in Tables 8.6, 8.7 and 8.8. These results show that how Fermi level position can changes after two steps of CdCl₂ treatment. The Fermi level position also helps to identify the electrical conductivity type of CdTe thin film before and after CdCl₂ treatment. It is very important to know the electrical conductivity type of CdTe layer before fabricating solar cells. This helps to critically analyse the experimental observations and also to draw right conclusions from experimental results. Most of the reports in the literature have shown that after CdCl₂ treatment, the conductivity of CdTe layer changes from n-type to p-type. However, this is not always the case; Schulmeyer *et al* [43] shows that the CSS CdTe after CdCl₂ treatment remains n-type. They have plotted the efficiency of the solar cell as a function of Fermi level position and they observed the highest efficiency solar cells when Fermi level settled above the midgap after CdCl₂ treatment.

Table 8.9: Summary of Fermi level positions of electrodeposited CdTe with respect to the conduction band ($E_C - E_F$) for the as-deposited and CdCl₂ treatment in two steps.

$E_C - E_F$ (eV) For as-deposited CdTe	$E_C - E_F$ (eV) After 1 st CdCl ₂ treatment	$E_C - E_F$ (eV) After 2 nd CdCl ₂ treatment
0.98	1.04	0.69

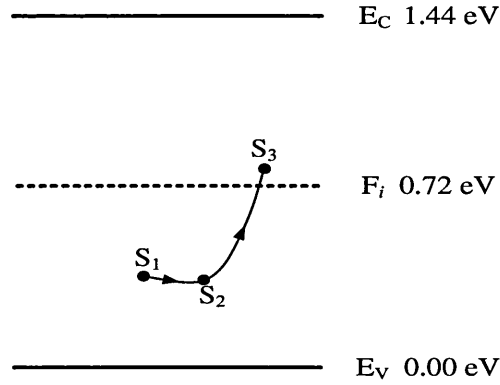


Figure 8.21: The initial Fermi level position for as-deposited CdTe thin film (S₁) and its movement after CdCl₂ treatments (S₂ for step 1 and S₃ for step 2).

In this experiment using the Fermi level position, the electron and hole density can be calculated from Equations (8.4) and (8.5), respectively:

$$n = N_C \exp\left(\frac{-(E_C - E_F)}{kT}\right) \quad (8.4)$$

$$p = N_V \exp\left(\frac{-(E_F - E_V)}{kT}\right) \quad (8.5)$$

Where;

n is the electron density (cm⁻³)

p is the hole density (cm⁻³)

N_C is the effective density of states in the conduction band (7.9×10^{17} cm⁻³)

N_V is the effective density of states in the valence band (1.8×10^{19} cm⁻³)

k is the Boltzmann constant (1.38×10^{-23} JK⁻¹)

T is the temperature (300 K)

The calculated electron and hole densities with respect to the position of Fermi level in the bandgap is shown in Table 8.10. For the p-type samples (S_1 and S_2) Equation (8.5) was used to calculate the hole density while the electron density for n-type sample (S_3) was calculated from Equation (8.4). It should be noted that the right doping density in the CdTe layer is very important and has a direct effect on the performance of the solar cell. Reports show that the high efficiency CdTe solar cells (>10%) were fabricated when the doping density are in the range of $\sim 1.0 \times 10^{14}$ to $\sim 5.0 \times 10^{15} \text{ cm}^{-3}$ [17]. The doping density values shown in Table 8.10 were lower than the optimum doping density range of $\sim (10^{14}-10^{15}) \text{ cm}^{-3}$. In addition to the initial properties of the as-deposited CdTe layer, the external factors which can affect the doping density are the annealing temperature, annealing time and the amount of CdCl_2 used for treatment of the CdTe layers. The process of CdCl_2 treatment is not fully understood yet and further investigations are required to fully understand this process.

Table 8.10: The calculated electron and hole densities with respect to the position of Fermi level in the bandgap.

Fermi level position	Conductivity type	$E_C - E_F$ (eV)	$E_F - E_V$ (eV)	n (cm^{-3})	p (cm^{-3})
S_1	p	0.98	0.46	-	3.36×10^{11}
S_2	p	1.04	0.40	-	3.43×10^{12}
S_3	n	0.69	0.75	2.02×10^6	-

8.3.10 Photoluminescence studies (PL)

The aim of this experiment was to study the effect of CdCl_2 treatment on the defect level distributions in the bandgap of electrodeposited CdTe layers. The experiment was performed with the assistant of our US collaborator University of Louisville, USA. The PL measurements were carried out at temperature of 80 K using Linkam THMS600/720 temperature controlled stage with liquid nitrogen and a Renishaw inVia Raman Microscope. He-Ne laser with a 632 nm ($\sim 1.96 \text{ eV}$) was used as the excitation source. In order to detect the wide range of energy, a charged-coupled device (CCD) camera was combined with a diffraction grating in the system. The PL

measurements were carried out in the energy range of (0.55-1.85) eV below the conduction band in order to observe defect structures in the CdTe bandgap.

For the PL experiment, CdTe was grown on the glass/FTO/CdS substrate and then PL measurement was carried out in three steps. In the first step, PL measurement was carried out on the as-deposited CdTe layer. In the second step, the PL measurement was carried out on the CdTe layer heat treated with ~1% of CdCl₂ at temperature of 440°C for 8 minutes in air. In the final step, the CdTe layer was again heat treated at temperature of 440°C for 16 minutes in air after treating with ~1% of CdCl₂ solution. The PL measurements were repeated again under similar conditions.

Figure 8.22 shows the comparison between the PL spectra of the CdTe layer at three different conditions. In the PL measurements, five peaks were observed in the as-deposited sample. The PL peaks T1-T4 arise from defect levels and their peak maxima respectively appear at 0.66, 0.79, 0.98, and 1.37 eV as shown in Table 8.11. The broad PL peak observed at 1.50 eV is related to the band-to-band electron transition across the CdTe bandgap (E_g). The reason of peak broadening at both side of the E_g is due to the different electron transitions at these energy ranges. The observation of electron transitions with energy ranges higher than E_g can be due to the S-richness of CdS_xTe_(1-x) alloy at CdS/CdTe interface or quantum effect. The quantum effect can increase the bandgap due to the presence of nano crystallites in the as-deposited CdTe layer. The appearance of energy transition at energy ranges lower than E_g can be due to the Te-richness of CdS_xTe_(1-x) alloy and reduction of E_g at CdS/CdTe interface [89] and presence of shallow defects.

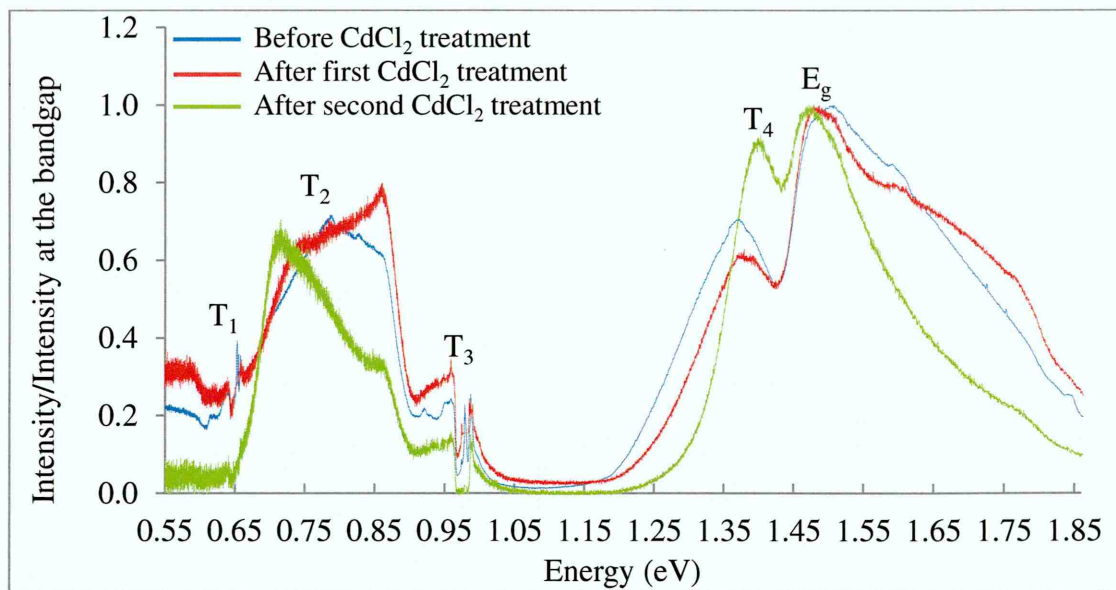


Figure 8.22: Photoluminescence spectra for as-deposited, first CdCl₂ treated and second CdCl₂ treated CdTe layers.

Table 8.11: Details of PL peaks at 80 K for CdTe layers.

Energy (eV)	T ₁ ± 0.02	T ₂ ± 0.15	T ₃ ± 0.03	T ₄ ± 0.08	E _g
CdTe - As deposited	0.66	0.79	0.98	1.37	1.50
CdTe - CdCl ₂ -Step 1	0.66	0.86	0.99	1.38	1.48
CdTe - CdCl ₂ -Step 2	-	0.71	0.99	1.40	1.48

It should be noted that in this work, the disturbance in PL spectra at T₃ is due to the joining of two PL measurements at this energy range. From the Figure 8.22, it can be seen that the distribution of defect level T₂ is much wider than defect levels T₁, T₃ and T₄. This shows that more electrons are captured at T₂ as compared to defect levels T₁, T₃ and T₄. These defect levels are known as charge carriers traps and recombination centres. A trap can only emit or capture one type of charge carrier while at recombination centres, both type of the charge carriers can be captured [90]. The widely distributed defects T₂ are located at the midgap of CdTe. The defects T₂ are known as “killer centres” due to the high possibility for charge carriers to recombine at these defect levels [91]. Reports show that the defect levels T₁ and T₂ are related to the CdTe layer with Te-richness [92].

After first CdCl₂ treatment, the intensity of T₁ and T₄ reduced slightly and slight increase in the intensity of PL peak of T₃ was observed. The intensity and distribution of T₂ and E_g remains approximately the same.

After second CdCl_2 treatment, T_1 completely disappeared and intensity of T_3 peak reduced slightly. In addition, a moderate reduction was also observed in the broadening of peak at T_2 . It is worth mentioning that removal of T_2 defects (killer centres) can drastically improve the performance of solar cells. However, most of the reports show that T_2 defect remains even after CdCl_2 treatment. After second CdCl_2 treatment, the intensity of T_4 increased slightly. Reports show that CdCl_2 treatment in the presence of oxygen enhances and introduces the defect T_4 [54,93,94]. The increase in the PL intensity of T_4 after CdCl_2 treatment is also believed to be due to the formation of $[\text{V}_{\text{cd}}\text{-Cl}]$ complexes during the diffusion of Cl into the CdTe thin films [54]. Another report shows that the T_4 peak was observed from CdTe layer with Cd-rich surface while the same peak has not been observed in CdTe layer with Te-rich surface [91]. In the recent work, Dharmadasa *et al* [95] also has studied the effect of CdCl_2 treatment on the PL spectra of electrodeposited CdTe layers grown from CdSO_4 , CdCl_2 and $\text{Cd}(\text{NO}_3)_2$ precursors and results were compared with CdCl_2 treated PL spectra of Bulk CdTe layer purchased from University Wafer company in USA. In all CdTe layers, similar defects were observed (including results reported in this work) and in all CdTe layers, the intensity of T_4 peak was increased after CdCl_2 treatment which shows that the CdCl_2 treatment enhances or introduces the defect level T_4 . Increase in the intensity of T_4 after CdCl_2 treatment will increase the possibility of Fermi level pinning at this defect level. This will lead to the formation of large Schottky barrier at n-CdTe/metal interface and hence the efficiency of the CdS/CdTe solar cell will be increased.

The second CdCl_2 treatment also increases the intensity of PL peak at E_g as shown in Table 8.12. In addition, the width of the E_g peak reduces and E_g peak position shifts from 1.50 eV to the 1.48 eV. This shows that the band-to-band transition has increased after second CdCl_2 treatment, indicating the reduction of defects in the bandgap.

Table 8.12: Intensity of band-to-band electron transitions (E_g peak) for the as-deposited and CdCl_2 treated CdTe layers.

CdTe (NO_3^-)/2E/C	E_g peak intensity (Photon counts)
As-deposited	5,765
CdCl_2 treated – step 1	11,791
CdCl_2 treated – step 2	30,989

8.4 Conclusions

CdTe thin films have been successfully electrodeposited at $\sim 85^{\circ}\text{C}$ and $\text{pH} = 2.0 \pm 0.02$ in aqueous solution containing 1.0 M $\text{Cd}(\text{NO}_3)_2 \cdot 4\text{H}_2\text{O}$ and ~ 1 ml of dissolved TeO_2 using 2-electrode system. The best crystallinity and stoichiometry for CdTe thin films were observed at cathodic potential of 1253 mV. XRD results show that all deposited CdTe layers have cubic crystal structure and strongly oriented along (111) crystal plane. XRD analyses reveal that the as-deposited CdTe layers contain nano crystallites in the range $\sim (30\text{-}65)$ nm. The improvements in the crystallinity of CdTe layer were observed after annealing in air, CdCl_2 and $\text{CdCl}_2 + \text{CdF}_2$ treatment. The structural changes were observed at three annealing temperatures of 385, 420 and 450°C after CdCl_2 and $\text{CdCl}_2 + \text{CdF}_2$ treatment. The intensity of (111) peak shows variation at different temperatures in the presence of CdCl_2 and $\text{CdCl}_2 + \text{CdF}_2$ treatment. XRD and Raman results show that, CdCl_2 and $\text{CdCl}_2 + \text{CdF}_2$ treatment remove excess Te and improve the stoichiometric properties of the CdTe thin films.

PEC results show that there are two regions of deposition voltage for growing p-type and n-type CdTe layers. The as-deposited CdTe layer was found to be stoichiometric with intrinsic electrical conduction at the cathodic potential of 1253 mV. Deviation from this stoichiometric point towards Te-rich and Cd-rich regions, respectively results in p-type and n-type electrical conductivity. Depending on the initial electrical conductivity type of the CdTe layer, doping concentrations vary from p-type towards n-type, and n-type towards p-type after heat treatment in air and CdCl_2 treatment.

Optical absorption results show that the best annealing temperature was 450°C as compared to the temperatures of 385 and 420°C . After CdCl_2 and $\text{CdCl}_2 + \text{CdF}_2$ treatment at 450°C , absorption edge improves and the bandgap of as-deposited CdTe layers shifts from (1.54-1.55) eV to 1.45 eV which is the bulk bandgap value for CdTe. Results also show the enhancement in absorption edge as the thickness increases.

The EDX spectra show that the layers grown at the growth voltage of 1253 mV were approximately stoichiometric. Below and above this growth voltage, the CdTe layers were found to be Te-rich and Cd-rich respectively.

SEM images show different morphologies for different annealing temperatures of 385, 420 and 450°C after CdCl_2 and $\text{CdCl}_2 + \text{CdF}_2$ treatment. Remarkable increase in CdTe grain sizes were observed when layers were annealed with CdCl_2 and

$\text{CdCl}_2 + \text{CdF}_2$ treatment at temperature of 450°C as compared to other annealing temperatures. SEM results show that, $\text{CdCl}_2 + \text{CdF}_2$ treatment has greater effect on the grain size enlargement of CdTe than CdCl_2 treatment only. The grain sizes of the $\text{CdCl}_2 + \text{CdF}_2$ treated samples ($\sim 8.3 \mu\text{m}$) were several times larger than the grain sizes of the CdCl_2 treated sample ($\sim 1.5 \mu\text{m}$) at annealing temperature of 450°C .

PL results indicate the presence of four electron traps T_1 , T_2 , T_3 and T_4 located within the energy bandgap of CdTe. CdCl_2 treatment reduces the number of electron traps and also reduces the width of the defects distributions in the bandgap. The band-to-band transition (E_g) has also been improved after CdCl_2 treatment. CdCl_2 treatment produces a CdTe layer with less defect levels and hence, it should have positive effect on the device performance.

UPS measurements show that the Fermi level position changes due to the variation in doping concentration of CdTe layer after CdCl_2 treatment. The UPS results also confirm that the conductivity type of the as-deposited p-CdTe thin films moves towards n-type after CdCl_2 treatments which are in agreement with PEC cell measurements.

8.5 References

- [1] J.J. Loferski, *J. Appl. Phys.*, **27** (1956) 777.
- [2] C.S. Ferekides, U. Balasubramanian, R. Mamazza, V. Viswanathan, H. Zhao, and D.L. Morel, *Solar Energy*, **77** (2004) 823–830.
- [3] R. Frerichs, *Phys. Rev.*, **72** (1947) 594-601.
- [4] D. Jenny and R. Bube, *Phys. Rev.*, **96** (1954) 1190-1191.
- [5] F. Krüger and D. de Nobel, *J. Electron.*, **1** (1955) 190-202.
- [6] P. Rappaport, *RCA Rev.*, **20** (1959) 373-397.
- [7] G.C. Solal, D. Lincot and M. Barbe, *Conf. Rec. 4th ECPVSC*, Stersa, Italy, (1982) 621-626.
- [8] D.A. Cusano, *Solid State Electronics*, **6** (1963) 217-232.
- [9] K.B. Dobson, I.V. Fisher, G. Hodes and D. Cahen, *Solar Energy Materials & Solar Cells*, **62** (2000) 295-325.
- [10] E. Adirovich, D.Y.Y. Yugadaev, *Sov. Phys. Semicond.*, **3** (1969) 61–65.
- [11] D. Bonnet, H. Rabenhorst, *Conf. Rec. 9th IEEE Photovoltaic Specialist Conf.*, (1972) 19-132.
- [12] K.W. Mitchell, C. Eberspacher, F. Cohen, J. Avery, G. Duran and W. Buttenberg, *Solar cells*, **23** (1988) 49-57.
- [13] J. Britt and C. Ferekides, *Appl. Phys. Lett.*, **62**(22) (1993) 2851-2852.
- [14] X. Wu, *Sol. Energy*, **77** (2004) 803-814.
- [15] <http://renewables.seenews.com/news/first-solar-hits-21-5-efficiency-with-cdte-pv-cell-462095>, Last accessed September (2015).
- [16] R.K. Pandey, S.N. Sahu and S. Chandra, *Handbook of Semiconductor Electrodeposition*, Marcel Dekker, New York, (1996) pp. 224.
- [17] I.M. Dharmadasa, *Coating*, **4** (2014) 282-307.
- [18] M.P.R Panicker, M. Knaster and F.A. Kröger, *J. Electrochem. Soc.*, **125**(4) (1978) 566-572.
- [19] G. Fulop, M. Doty, P. Meyers, J. Betz and C.H. Liu, *Appl. Phys. Lett.*, **40** (1982) 327-328.
- [20] B.M. Basol, *Journal of Applied Physics*, **55** (1984) 601-603.
- [21] D. Cunningham, M. Rubich and D. Skinner, *Prog. In Photovoltaics: Research and App.*, **10** (2002) 159-168.

- [22] <http://reelsolar.com/news/2013/7/10/rsi-announces-the-worlds-most-powerful-cadmium-telluride-solar-modules>, Last accessed September (2015).
- [23] <http://www.encore-solar.com/technology.html>, Last accessed September (2015).
- [24] <http://guntherportfolio.com/2011/05/what-to-do-for-an-encoresolar/>, Last accessed September (2015).
- [25] M. Lambrechts and W. Sansen, Biosensors: *Microelectrochemical Devices, Sensor series*, IOP Publishing, New York, (1992) pp. 35.
- [26] <http://www.technology.matthey.com/article/52/2/100-106/>, Last accessed September (2015).
- [27] D.G. Diso, Research and development of CdTe based thin film PV solar cells, Doctoral thesis, Sheffield Hallam University, United Kingdom (2011).
<http://shura.shu.ac.uk/4941/>
- [28] O.K. Echendu, F. Fauzi, A.R. Weerasinghe and I.M. Dharmadasa, *Thin Solid Films*, **556** (2014) 529-534.
- [29] H.I. Salim, V. Patel, A. Abbas, J.M. Walls and I.M. Dharmadasa, *J. Mater. Sci: Mater Electron.*, **26** (2015) 3119-3128.
- [30] N.A. Abdul-Manaf, H.I. Salim, M.L. Madugu, O.I. Olusola and I.M. Dharmadasa, *Energies*, **8** (2015) 10883-10903.
- [31] D. G. Diso, G. E. A. Muftah, V. Patel and I.M. Dharmadasa, *J. Electrochem. Soc.*, **157** (6) (2010) H647-H651.
- [32] N.A. Abdul-Manaf, A.R. Weerasinghe, O.K. Echendu and I.M. Dharmadasa, *J. Mater. Sci: Mater Electron.*, **26** (2015) 2418-2429.
- [33] O.I. Olusola, O.K. Echendu and I.M. Dharmadasa, *J. Mater. Sci: Mater. Electron.*, **26**(2) (2015) 1066-1076.
- [34] M.L. Madugu, L. Bowen, O.K. Echendu and I.M. Dharmadasa, *J. Mater. Sci: Mater. Electron.*, **25**(9), 3977-3983.
- [35] F. Fauzi, D.G. Diso, O.K. Echendu, V. Patel, Y. Purandare, R. Burton and I.M. Dharmadasa, *Semiconductor Science and Technology*, **28**(4) (2013) 045005.
- [36] I.M. Dharmadasa, R. P. Burton and M. Simmond, *Sol. Energ. Mat. Sol. Cells*, **90** (2006) 2191-2200.
- [37] A. Bouraiou, M.S. Aida, E. Tomasella, and N. Attaf, *J. Mater. Sci: Mater Electron.*, **44** (2009) 1241-1244.

- [38] I.M. Dharmadasa, N.B. Chaure, O. Islam, J. Wellings, T. Maddock and I. Gee, *Proceedings of the 21st European Photovoltaic Conference*, Dresden, Germany (2006), pp. 1941-1945.
- [39] R.N. Bhattacharya, M.K. Oh and Y. Kim, *Solar Energy Materials & Solar Cells*, **98** (2012) 198-202.
- [40] S. Dennison, *J. Mater. Chem.*, **4**(1) (1994) 41-46.
- [41] <http://www.globalw.com/support/ph-electrode-reference-systems.html>, Last accessed September 2015.
- [42] R.C. Alkire, D.M. Kolb, J. Lipkowski and P.N. Ross, *Advances in Electrochemical Sciences and Engineering; Photoelectrochemical Materials and Energy Conversion Processes: Volume 12*, Wiley.VCH Verlag GmbH & Co, Weinheim Germany, (2010) pp. 10.
- [43] T. Shulmeyer, J. Fritsche, A. Thißen, A. Klein, W. Jaegermann, M. Campo and J. Beier, *Thin Solid Films*, **431-432** (2003) 84-89.
- [44] P.V. Braun, P. Osenar, M. Twardowski, G.N. Tew, S.I. Stupp, *Adv. Funct. Mater.*, **15** (2005) 1745–1750.
- [45] T. Nishio, M. Takahashi, S. Wada, T. Miyauchi, K. Wakita, H. Goto, S. Sato, O. Sakurada, *Electr. Eng. Jpn.*, **164**(3) (2008) 97-102.
- [46] J. Sun, D.K. Zhong, D.R. Gamelin, *Energy Environ. Sci*, **3** (2010) 1252–1261.
- [47] I.M. Dharmadasa, *Advances in Thin-Films Solar Cells*, Pan Stanford Publishing Pte. Ltd, Boulevard, Singapore, (2012) pp.41-42.
- [48] C.S. Ferekides, D. Marinskiy, V. Viswanathan, B. Tetali, V. Palekis, P. Selvaraj and D.L. Morel, *Thin Solid Films*, **361-362** (2000) 520-526.
- [49] A. Romeo, S. Buecheler, M. Giarola, G. Mariotto, A.N. Tiwari, N. Romeo, A. Bosio and S. Mazzamuto, *Thin Solid Films*, **517** (2009) 2132-2135.
- [50] P. Capper, *Narrow-gap II-VI Compounds for Optoelectronic and Electromagnetic Applications*, Chapman & Hall, London (1997) pp. 536.
- [51] A.W. Burton, K. Ong, T. Rea and I.Y. Chen, *Microporous and Mesoporous Materials*, **117** (2009) 75-90.
- [52] D.L. Bish and J.E. Post, *Modern powder diffraction. Reviews in mineralogy, volume 20*, P.H. Ribbe ed. Washington DC, (1989).
- [53] L.E. Lyons, G.C. Morris, D.H. Horton and J.G. Keyes, *J. Electroanal. Chem.*, **168** (1984) 101-116

- [54] S. Mazzamuto, L. Vaillant, A. Bosio, N. Romeo, N. Armani, G. Salviati, *Thin Solid Films*, **516** (2008) 7079-7083.
- [55] M.J. Kim, S. Sohn and S. Lee, *Sol. Energy Mat. Sol. Cells*, **95** (2011) 2295-2301.
- [56] I.M. Dharmadasa, P.A. Bingham, O.K. Echendu, H.I. Salim, T. Druffe, R. Dharmadasa, G.U. Sumanasekera, R.R. Dharmadasa, M.B. Dergacheva, K.A. Mit, K.A. Urazov, L. Bowen, M. Walls and A. Abbas, *Coating*, **4** (2014) 380-415.
- [57] O.K. Echendu and I.M. Dharmadasa, *Materials Chemistry and Physics* **157** (2015) 39-44.
- [58] S.G. Kumar and K.S.R.K. Rao, *Energy Environ. Sci.*, **7** (2014) 45-102.
- [59] J. Fritsche, S. Gunst, E. Golusda, M. C. Lejard, A. Thißen, T. Mayer, A. Klein, R. Wendt, R. Gegenwart, D. Bonnet and W. Jaegermann, *Thin Solid Films*, **387** (2001) 161-164.
- [60] I.M. Dharmadasa and J. Haigh, *J. Electrochem. Soc.*, **153**(1) (2006) G47-G52.
- [61] M. Takahashi, K. Uosaki and H. Kita, *J. Appl. Phys.*, **60**(6) (1986) 2046-2049.
- [62] B.M. Basol, S.S. Ou and O.M. Stafsudd, *J. Appl. Phys.*, **58** (1985) 3809-3813.
- [63] B.M. Basol, *Solar cells*, **23** (1988) 69-88.
- [64] J.M. Woodcock, A.K. Turner, M.E. Ozsan and J.G. Summers, *Photovoltaic specialists Conference 1991, Conference Record of the twenty second IEEE, 7-11 October, 1991, Las Vegas, Nevada, USA, Vol.2, pp. 842-84, http://ieeexplore.ieee.org/xpls/abs_all.jsp?arnumber=169328*.
- [65] A.K. Turner, J.M. woodcock, M.E. Ozsan, J.G. Summers and J. Barker, S. Binns, K. Buchanan, C. Chai, S. Dennison, R. Hart, D. Johnson, R. Marshall, S. Oktik, M. Patterson, R. Perks, S. Roberts, M. Sadeghi, J. Sherborne, J. Szubert and S. Webster, *Solar Energy Materials*, **23** (1991) 388-393.
- [66] C.J. Bridge, P. Dawson, P.D. Buckle and M.E. Ozsan, *Semicond. Sci. Technol.*, **15** (2000) 975 – 979.
- [67] C.J. Bridge, P. Dawson, P.D. Buckle and M.E. Ozsan, *Semicond. Sci. Technol.*, **15** (2000) 975 – 979.
- [68] N.W. Duffy, L.M. Peter, R.L. Wang, D.W. Lane and K.D. Rogers, *Electrochimica Acta*, **45** (2000) 3355-3365.
- [69] V. Valdna, F. Bushmann and E. mellikov, *J. Cryst. Growth*, **161** (1996) 164-167.
- [70] E. Belas, J. France, R. Drill, A.L. Toth, P. Horodysky, P. Moravec and P. Hoschl, *J. Electr. Mayteri.*, **34**(6) (2005) 957-962.

- [71] S. Yang, J. Chou and H. Ueng, *Thin Solid Films*, **518** (2010) 4197 – 4202.
- [72] M. Rami, E. Benamar, M. Fahoume, F. Chraïbi and A. Ennaoui, *M.J. Condensed Matter*, **3**(1) (2000) 66-70.
- [73] J. Quadros, A.L. Pinto, H.R. Moutinho, R.G. Dhere and L.R. Cruz, *J. Matr. Sci.*, **43** (2008) 573-579.
- [74] A. Abbas, G.D. West, J.W. Bowers, P. Isherwood, P.M. Kaminski, B. Maniscalco, P. Rowley, J.M. Walls, K. Barricklow, W.S. Sampath and K.L. Barth, *IEEE Journal of Photovoltaics*, **3**(4) (2013) 1361-1366.
- [75] N. Romeo, A. Bosio, R. Tedeschi, A. Romeo, V. Canevari, *Solar Energy Materials & Solar Cells*, **58** (1999) 209-218.
- [76] J. Hiie, *Thin Solid Film*, **431-432** (2003) 90-93.
- [77] R. Dharmadasa, B.W. Lavery, I.M. Dharmadasa, T. Druffel, *J. Coat. Technol. Res.*, **12**(5) (2015) 835–842.
- [78] B.E. McCandless, K.D. Dobson, *Solar Energy*, **77** (2004) 839–856.
- [79] A. Romeo, S. Buecheler, M. Giarola, G. Mariotto, A.N. Tiwari, N. Romeo, A. Bosio, S. Mazzamuto, *Thin Solid Film*, **517** (2009) 2132-2135.
- [80] E.R. Hernandez, V. Rejon, I. Riech, M. Acosta, J.L. Pena, *Solar Energy*, **107** (2014) 305-313.
- [81] V. Rejon, I. Riech, J.L. Pena, *Solar Energy*, **95** (2013) 319-324.
- [82] A.R. Flores, O. Ares, J.M. Camacho, V. Rejon, J.L. Pena, *Solar Energy*, **86** (2012) 780-785.
- [83] O.K. Echendu and I.M. Dharmadasa, *Materials Chemistry and Physics*, **157** (2015) 39-44.
- [84] A.A. Taylor, J.D. Major, G. Kartopu, D. Lamb, J. Duenow, R.G. Dhere, X. Maeder, S.J.C. Irvine d , K. Durose, B.G. Mendis, *Solar Energy Materials & Solar Cells*, **141** (2015) 341-349.
- [85] B. Siepchen, C. Drost, B. Späth, V. Krishnakumar, H. Richter, M. Harr, S. Bossert, M. Grimm, K. Häfner, T. Modes, O. Zywitzki, H. Morgner, *Thin Solid Films*, **535** (2013) 224-228.
- [86] I.M. Dharmadasa, O.K. Echendu, N.A. Abdul-Manaf, O.I. Olusola, H.I. Salim, M.L. Madugu and A.A. Ojo, Submitted to *Solar Energy Materials & Solar Cells*, (Ref. No.: SOLMAT-D-15-01299).

- [87] S.J. Byrne, S.A. Corr, T.Y. Rakovich, Y. K. Gun'ko, Y.P. Rakovich, J.F. Donegan, S. Mitchell and Y. Volkov, *Journal of Materials Chemistry*, **16** (2006) 2896-2902.
- [88] I.M. Dharmadasa, O.K. Echendu, F. Fauzi, H.I. Salim, N.A. Abdul-Manaf, J.B. Jasinski, A. Sherehiy and G. Sumanasekera, *J. Mater. Sci: Mater Electron.*, (2016) 1-8. (doi: 10.1007/s10854-016-4391-y)
- [89] D.A. Wood, K.D. Rogers, D.W. Lane, J.A. Coath, *J. Phys. Condense. Matter.*, **12** (2000) 4433–4450.
- [90] J. Donecker and I. Rechenberg, *Proceeding of the Seventh International Conference on Defects Recognition and Image Processing in Semiconductors (DRIP IIV)*, IOP Publishing Ltd., 7-10 September, 1997, Templing, Germany, pp. 342.
- [91] K. Zanio, *Semiconductors and Semimetals*, volume 13, Cadmium Telluride, Academic Press, New York, 1978.
- [92] Z. Sobiesierski, I.M. Dharmadasa, R.H. Williams, *Appl. Phys. Lett.*, **53**(26) (1988) 2623–2625.
- [93] P. Fernandez, *J. Optoelectron. Adv. Mater.*, **5**(2) (2003) 369-388.
- [94] M.A. Hernandez-Fenollosa, D.P. Halliday, K. Durose, M.D. Campo, J. Beier, *Thin Solid Films*, **431–432** (2003) 176–180.
- [95] I.M. Dharmadasa, O.K. Echendu, F. Fauzi N.A. Abdul-Manaf, H.I. Salim, T. Druffel, R. Dharmadasa and B. Lavery, *J. Mater. Sci: Mater. Electron.*, **26** (2015) 4571-4583.

9.1 Introduction

This chapter presents the assessment of different solar cells fabricated under different conditions. The main materials used to fabricate the solar cells were ED-CdS, CBD-CdS and ED-CdTe thin films as presented in chapters 6-8. Also, two other layers were incorporated in the solar cell devices including ED-ZnS and ED-ZnTe which have been grown by PhD researchers at Sheffield Hallam University. Using these four materials, solar cells with different device structures were fabricated. These device structures include glass/FTO/n-CdS/n-CdTe/Au, glass/FTO/n-ZnS/n-CdTe/Au and multi-layer graded-bandgap solar cells (glass/FTO/n-CdS/n-CdTe/p-CdTe/Au, glass/FTO/n-CdS/n-CdTe/p-ZnTe/Au, glass/FTO/n-ZnS/n-CdS/n-CdTe/Au). In the literature, the main stream of CdTe-based solar cells are mostly focused on the conventional p-n junction type device structure while in this thesis the main aim is the fabrications of n-n+large Schottky barrier type device structure and multi-layer graded-bandgap solar cells [1].

All devices were processed in three main steps; the first step was the post-deposition annealing with CdCl_2 and $\text{CdCl}_2+\text{CdF}_2$ treatment at different temperatures. The second step was the wet chemical etching of CdTe surfaces using both acidic solutions ($\text{H}_2\text{SO}_4+\text{K}_2\text{Cr}_2\text{O}_7$) and ($\text{NaOH}+\text{Na}_2\text{S}_2\text{O}_3$) alkaline solutions [2,3]. The last step was the evaporation of metal back contact (Au) on the chemically etched CdTe surfaces. The ZnTe layers were used as pin-hole plugging layers between the CdTe and metal (Au) back contact. Afterwards, the fabricated solar cells were assessed using I-V and C-V measurements under dark and illumination conditions. Then, the stability of the fabricated solar cells was measured over a period of time and the device results are presented in this chapter.

9.2 Fabrication of glass/FTO/n-CdS/n-CdTe/Au solar cells

In this work, the CdS layers were grown on glass/FTO substrates using electrodeposition and CBD methods. The electrodeposition of CdS layers was carried out at optimised growth voltage of 797 mV for $\sim(40-60)$ minutes with the estimated thickness of $\sim(90-120)$ nm as shown in chapter 6 (section 6.3.4). The CBD-CdS layers were also grown within 20 minutes with a thickness of ~ 90 nm as presented in chapter

7 (section 7.2). After deposition, the glass/FTO/n-CdS structures were obtained and then the CdS layers were rinsed with deionised water and dried with the stream of nitrogen gas. Afterward, the glass/FTO/n-CdS samples were annealed at 400°C for 20 minutes in air using a carbolite furnace. After annealing, the glass/FTO/n-CdS samples were allowed to cool down gradually. After cooling, the CdS layers were again rinsed with deionised water. Subsequently, the Cd-rich CdTe layers were grown on the CdS layers at growth voltages of more than 1253 mV to produce the glass/FTO/n-CdS/n-CdTe structure. The deposition time for CdTe layers were between 4 and 6 hours with the thickness of $\sim(1.0\text{-}2.0)$ μm .

The next step was the treatment of the CdTe layers with CdCl_2 and $\text{CdCl}_2+\text{CdF}_2$. The CdCl_2 and $\text{CdCl}_2+\text{CdF}_2$ treatments were carried out by dipping of the layers in a saturated solution of CdCl_2 or $\text{CdCl}_2+\text{CdF}_2$ in deionised water. The CdTe layers were then allowed to dry inside a fume cupboard. After drying, the CdCl_2 and $\text{CdCl}_2+\text{CdF}_2$ treated layers were annealed at three different temperatures of 385, 420 and 450°C for the durations of 10 to 12 minutes in air. Then, the annealed layers were allowed to cool down. After cooling, the samples were rinsed with deionised water in order to remove the residual of the CdCl_2 and $\text{CdCl}_2+\text{CdF}_2$ powders on the CdTe layers.

The next step was the wet chemical etching of the CdTe surface using acidic (oxidising) etchant and alkaline (reducing) etchant. The acidic etchant were prepared by adding 0.08 ml of concentrated sulphuric acid (H_2SO_4) and 1.0 g of potassium dichromate ($\text{K}_2\text{Cr}_2\text{O}_7$) into 20 ml of deionised water. The alkaline etchant were separately prepared by adding 0.5 g of sodium hydroxide (NaOH) and 0.5 g of sodium thiosulphate ($\text{Na}_2\text{S}_2\text{O}_3$) into 50 ml of deionised water. The alkaline solution was then heated to $\sim 60^\circ\text{C}$ using a magnetic stirrer hot-plate. The $\text{K}_2\text{Cr}_2\text{O}_7$ and NaOH chemicals were purchased from Sigma Aldrich (UK) while $\text{Na}_2\text{S}_2\text{O}_3$ was purchased from Fischer Scientific, UK.

The etching process starts by dipping the glass/FTO/n-CdS/n-CdTe samples into the acidic etchant for about 5 second. Then, the samples are taken out and rinsed with deionised water. Subsequently, the samples were immersed into the alkaline etchant for about 2 minutes. Afterward, the samples were rinsed with deionised water and dried under the stream of nitrogen gas. The etching process in this research followed the work reported by Dharmadasa [3].

The last process was the evaporation of metal back contact. For this purpose, the etched CdTe samples were placed horizontally on the rectangular masks containing 2

mm or 3 mm diameter circular holes as shown in Figure 9.1 (a). Then, the mask containing the etched CdTe samples was placed in the EDWARDS Auto 306 vacuum coater (metalliser) with an FTM7 Film Thickness Monitor as shown in Figure 9.1 (b). A small piece of gold wire (~4 cm) with the purity of 99.999% (5N) was then cut and placed inside a conical-spiral shape tungsten filament. After closing the evaporation chamber, the evacuation process starts until the chamber pressure reaches 10^{-5} pa (10^{-7} mbar). Then, by passing ~2.0 Ampere of direct current through the tungsten filament, about 100 nm of Au was evaporated on the CdTe samples using thickness monitor controller and shutter.

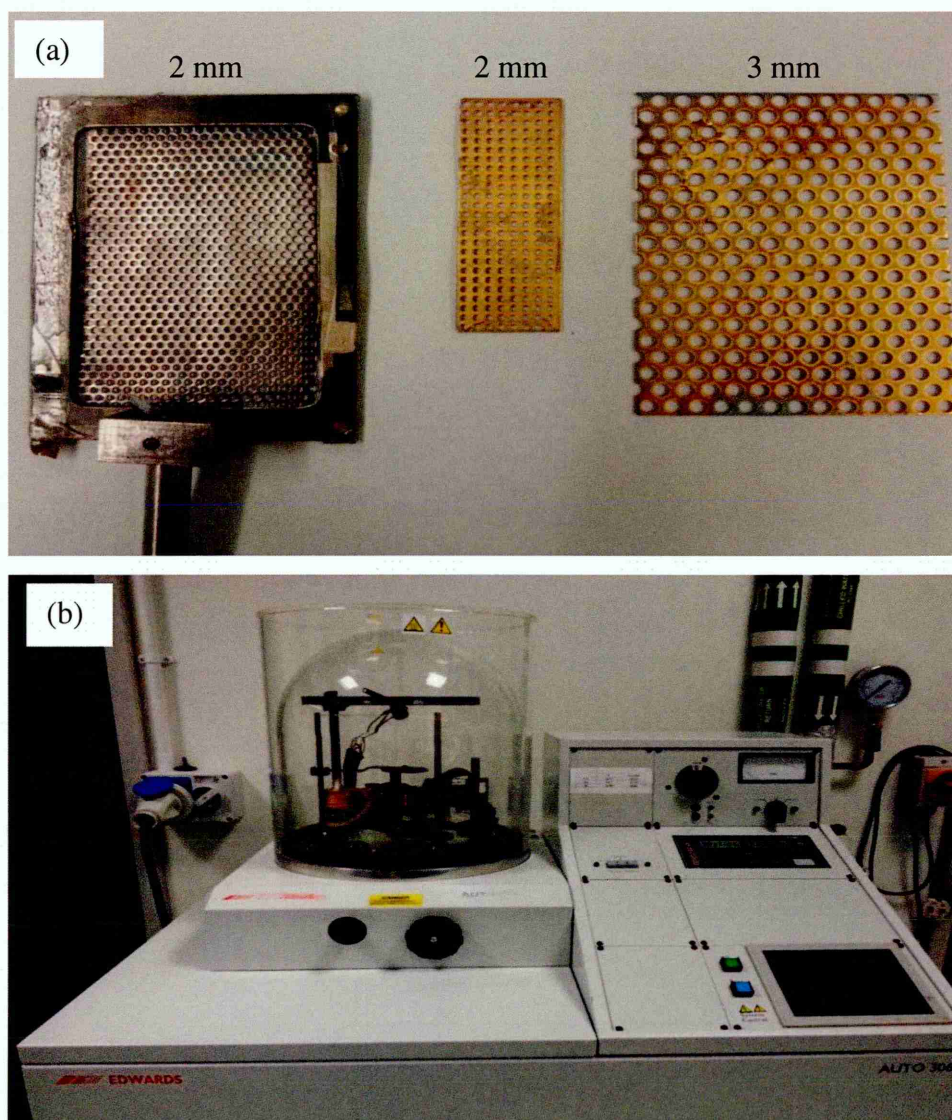


Figure 9.1: (a) The rectangular masks with 2 mm & 3 mm diameter circular holes, (b) EDWARDS Auto 306 vacuum coater (metalliser) used to deposit back metal contacts.

After Au evaporation, the chamber was cooled down for ~30 minutes. Finally, the samples were removed from the evaporation chamber and the completed solar cells were characterized using I-V and C-V measurements. The I-V measurement was carried out by Kiethley 619 Electrometer/multimeter using a solar simulator with light intensity of 1000 Wm^{-2} (AM 1.5) at room temperature. The C-V measurement was carried out using Kiethley 6517A Electrometer/High resistance Meter with Hewlett Packard 4284A (20 Hz to 1.0 MHz) Precision LCR Meter. The results and characterisation of the fabricated solar cells with different device structures are presented in the following sections.

9.2.1 Energy band diagram of glass/FTO/n-CdS/n-CdTe/Au solar cell

Figure 9.2. shows the typical energy band diagram of n-n+Schottky junction for the glass/FTO/n-CdS/n-CdTe/Au solar cell. This new model was proposed in 2002 by Dharmadasa *et al* [1] based on the large body of experimental observations obtained from the work on metal contact to II-VI semiconductors. Dharmadasa [3,4] studied the Schottky barrier formation at n-CdTe/Metal interface and identified that the Fermi level is pinned at five possible discrete defect levels. The experimentally identified defect levels are situated in the energy bandgap (E_g) at $E_1 = 0.40 \pm 0.02$, $E_2 = 0.65 \pm 0.04$, $E_3 = 0.73 \pm 0.02$, $E_4 = 0.96 \pm 0.04$, $E_5 = 1.18 \pm 0.02$ eV below the conduction band minimum as shown in Figure 9.2. The Fermi level pinning can take place at one of the above five defect levels which depends on the history of material, fabrication process such as surface treatment and etching and type of metal contact used. It should be noted that the Fermi level pinning at the n-CdTe/metal interface can create serious problem due to the presence of five different defect levels at the energy bandgap. The implication for instance is that when the n-CdTe/metal junction is created using the same n-CdTe layer and the same metal contact under the same condition, the device can completely show different performance. This is because the Fermi level can pin at one of five defect levels and creates different barrier height leading to different device performance. It should be noted that the high density of these defect states are located at the top surface of CdTe layer with a few 100 Å thickness [1]. For this reason, surface preparation (etching) is used prior to the formation of n-CdTe/metal junction to passivate most of these defect levels. Also, surface etching can help to pin the Fermi level close to the valence band forming larger barrier height with better device performance. When the

Fermi level pins close to valence band at $E_4 = 0.96 \pm 0.04$ eV and $E_5 = 1.18 \pm 0.02$ eV below the conduction band minimum, then the top surface of the CdTe layer can be considered as p-type layer. Also, the incorporation of p-type semiconductor material on the top of CdTe after surface treatment and etching is useful to pin the Fermi level close to the valence band to form larger Schottky barrier height.

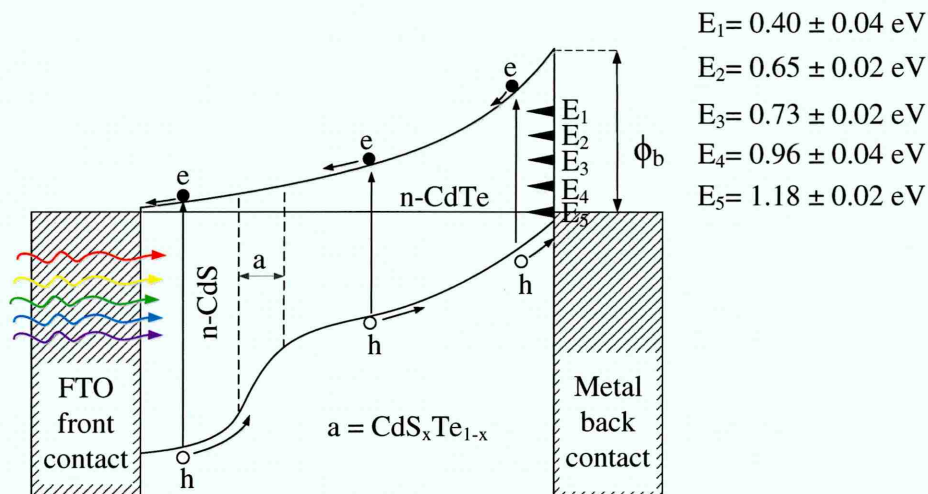


Figure 9.2: The energy band diagram of n-n+Schottky barrier for glass/FTO/n-CdS/n-CdTe/Au solar cells; Redrawn from [1].

As shown in Figure 9.2, the n-CdS was used as heterojunction partner to the n-CdTe absorber layer. It is worth to mention that, better quality CdTe layer can be obtained when the layer is grown on the CdS substrate as compared to the conducting glass substrate. Reports show that the lattice mismatch between CdS and CdTe is about 10% [5]. Despite the large lattice mismatch between CdS and CdTe, still CdS layer is considered as the best heterojunction partner to CdTe [5]. During the CdCl_2 and $\text{CdC}_2 + \text{CdF}_2$ heat treatment the inter-mixing takes place at the CdS/CdTe interface which leads to the formation of ternary alloy, $\text{CdS}_x\text{Te}_{1-x}$ [5-8]. The inter-mixing creates graded-bandgap at the CdS/CdTe interface removing abrupt junction, lattice mismatch and energy spikes at the material boundary which has been marked as region “a” in Figure 9.2. The graded-bandgap helps to effectively harvest the photons at different regions of the solar spectrum in the energy bandgap and also minimise the thermalisation effect in the device [9-11]. In addition, the graded-bandgap solar cells provide the effective collection and acceleration of photo-generated charge carriers towards the front and back contact of the device due to the gradual change in the electric

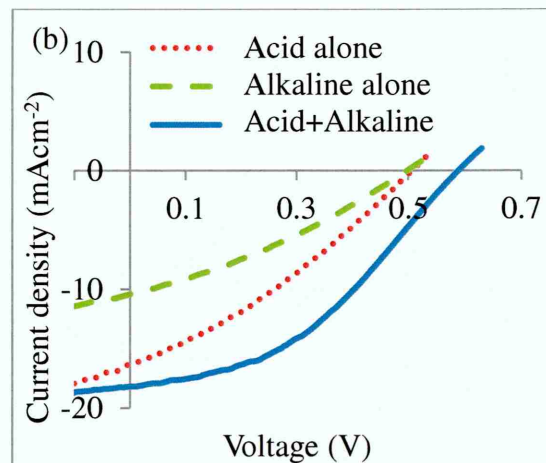
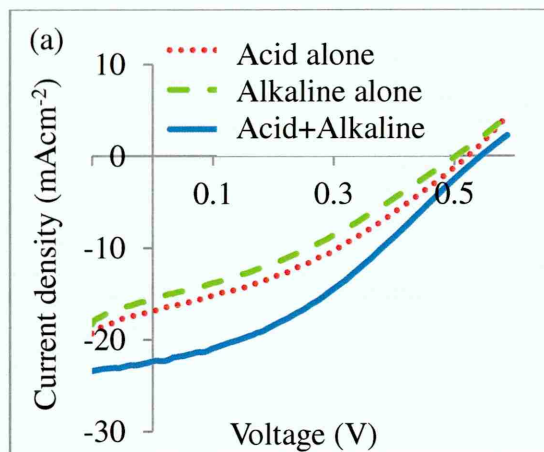
filed across the device length. The collection and acceleration of photo-generated charge carriers can be promoted when the CdS and CdTe layers have the optimum doping densities. The optimum doping density for the CdTe layers can be achieved after CdCl₂ or CdCl₂+CdF₂ heat treatment. For a device with optimum doping concentration, the depletion width is widened and also for a fully depleted device the depletion width spreading across the entire thickness of the device. When all conditions are met, the high efficiency solar cell can be achieved. Based on the energy band diagram shown in Figure 9.2 (new model) the efficiency of ~18.0% was reported in 2003 [12] for a glass/FTO/CBD-CdS/n-CdTe/Au using electrodeposited n-CdTe as absorber material using non-aqueous medium.

9.2.2 Effect of CdTe surface etching on the performance of glass/FTO/n-CdS/n-CdTe/Au solar cells

This study was carried out in order to investigate the effect of acidic alone, alkaline alone and combination of acidic and alkaline etchants on the device performance of the fabricated glass/FTO/n-CdS(CBD)/n-CdTe/Au solar cells. For this reason, the n-CdTe layers with the thickness of ~2.0 µm were grown on glass/FTO/n-CdS(CBD) substrates. Then, the glass/FTO/n-CdS(CBD)/n-CdTe structure was divided into fifteen parts. The first five parts were etched with acidic solution alone. The next five parts was etched with alkaline solution alone. The remaining five parts were etched with acidic solution first followed by alkaline solution as explained in the section 9.2 and results are shown in Table 9.1 and Figures 9.1 (a)-(d). It should be noted that prior to the etching process all CdTe layers were heat treated with CdCl₂ treatment at 385°C for 10 minutes in air. Results show the better device performances for the CdTe layers etched with the combination of acidic and alkaline solutions. The devices etched in acidic solution (oxidising agent) alone or alkaline solution (reducing agent) alone showed lower device performances.

Table 9.1: Summary of device results for glass/FTO/n-CdS(CBD)/n-CdTe/Au solar cells chemically etched with acid alone, alkaline alone and combination of acidic and alkaline solutions.

Sample ID	Etching condition	V_{oc} (mV)	J_{sc} (mAcm ⁻²)	FF	η (%)
CT385A1	Acid alone	555	8.7	0.30	1.4
CT385B1		451	9.7	0.30	1.3
CT385C1		521	16.9	0.35	3.1
CT385D1		528	11.2	0.31	1.8
CT385E1		506	16.3	0.32	2.6
CT385A2	Alkaline alone	552	9.3	0.31	1.6
CT385B2		458	10.2	0.31	1.4
CT385C2		484	15.5	0.33	2.5
CT385D2		452	9.1	0.30	1.2
CT385E2		498	10.4	0.31	1.7
CT385A3	Acid+ Alkaline	598	12.8	0.51	4.0
CT385B3		539	12.1	0.49	3.2
CT385C3		584	22.4	0.47	4.7
CT385D3		614	14.8	0.43	3.8
CT385E3		589	18.1	0.43	4.3



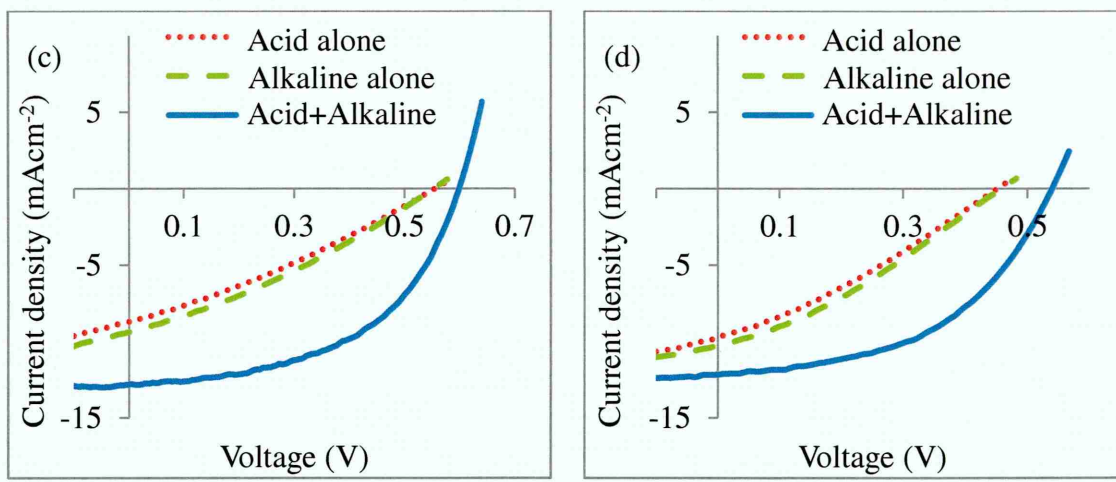


Figure 9.1: The comparison of J-V curves under illumination for glass/FTO/n-CdS(CBD)/n-CdTe/Au solar cells chemically etched with acid alone, alkaline alone and combination of acid and alkaline solutions.

Investigation on the wet chemical etching of the n-CdTe single crystal in the literature show that etching of the CdTe layers in acidic solutions lead to the formation of a Te-rich surface and etching of the CdTe layers in the alkaline or acidic+alkaline solutions lead to the formation of a Cd-rich surface as shown in Figure 9.2 (a,b,c) [3,13]. Also, the PL investigations reported by Sobiesierski *et al* [2] on the chemically etched n-CdTe single crystals showed that when CdTe layers are etched in acidic solutions alone (which leaves Te-rich surface layer), it creates defect levels located at 0.72 eV (300 K). Also, when CdTe are etched with the combination of acidic and alkaline solutions (which leaves Cd-rich surface layer), the 0.72 eV defect levels was completely removed and enhancement in the 0.97 and 1.24 eV defect levels were observed as shown in Figure 9.2 (e). The 0.72 eV defect levels are known as the killer centres (recombination centres) as it located at the middle of the energy bandgap. When Fermi level pins at these defect levels (E_3) it creates lower Schottky barrier height (ϕ_b) and higher ideality factor value, n , therefore, the device performances are lower as shown in Figure 9.2 (d, g). The removal of the midgap defect levels can drastically improve the performance of the solar cell devices. For the Cd-rich surfaces, the larger Schottky barrier height can be formed due to the Fermi level pinning at defect levels E_4 or E_5 close to the valence band, hence the n value will be lower as shown in Figure 9.2 (d, h). In this work, the improvements in all solar cell parameters were observed when CdTe layers are etched with the combination of acidic and alkaline solutions. An increase in

the open circuit voltage (V_{oc}) of the solar cells after acidic+alkaline etching indicates the enhancement in the Schottky barrier height at n-CdTe/Au interface.

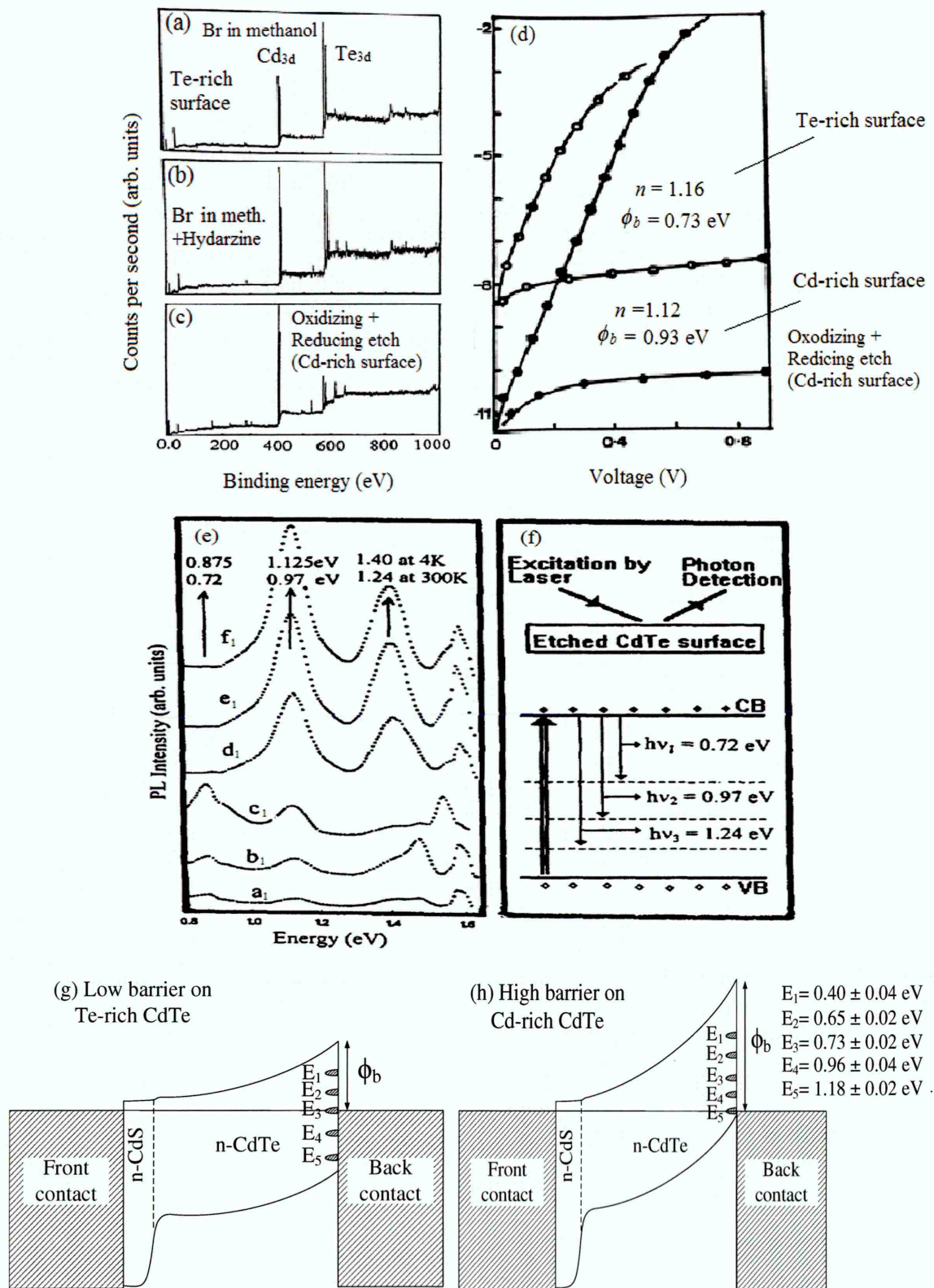


Figure 9.2: X-ray photoelectron spectra (XPS) data for CdTe surfaces etched in (a) 1% Br-methanol, (b) Br-methanol + hydrazine and (c) oxidising + a reducing agent, (d) I-V characteristics of n-CdTe layer with Te-rich and Cd-rich surfaces [Ref. 13], (e) The PL spectra of Te-rich (a_1 , b_1 , c_1) and Cd-rich (d_1 , e_1 , f_1) CdTe surface as a function of photon energy. Note the existence of 0.72 eV defects level for Te-rich and enhancement of 0.97 and 1.24 eV for Cd-rich at room temperature. Possible electron transitions are shown in Figure 9.2 (f) [Ref. 2 and 13]. The comparison of barrier height (g, h), ϕ_b at the n-CdTe/Au interface for Te-rich and Cd-rich layers respectively. Note that in the Te-rich layers, Fermi level pinning position is at the vicinity of midgap whereas for Cd-rich layers Fermi level pins at defect levels close to valence band [Ref. 3 and 14].

The lower device performance observed for the layers etched in acid alone and alkaline alone can also be due to the formation of thick insulating oxide layers (TeO_2 or CdTeO_x) on the CdTe surface [3,15]. The thick oxide layers between CdTe/Au interfaces can drastically increase the series resistance, R_s , hence the device performance reduces.

9.2.3 Effect of CdCl_2 and $\text{CdCl}_2+\text{CdF}_2$ treatment on the performance of the glass/FTO/n-CdS/n-CdTe/Au solar cells at different temperatures

This experiment was carried out in order to study the effect of CdCl_2 and $\text{CdCl}_2+\text{CdF}_2$ treatment on the performance of the glass/FTO/n-CdS/n-CdTe/Au solar cells at three different temperatures of 385, 420 and 450°C respectively. For these experiments both ED and CBD-CdS layers with the thickness of ~90 nm were grown on glass/FTO substrates and then heat treated at 400°C for 20 minutes in air. Afterwards, CdTe layers with the thickness of ~1.10 μm were grown on the glass/FTO/n-CdS (ED) and glass/FTO/n-CdS (CBD) substrates. Then, the glass/FTO/n-CdS (ED)/n-CdTe and glass/FTO/n-CdS (CBD)/n-CdTe samples were separately divided into three sets, where each sets contained four parts. The first, second and last sets were heat treated with CdCl_2 treatment only at 385, 420 and 450°C for 12 minutes in air respectively. The other three sets were heat treated with $\text{CdCl}_2+\text{CdF}_2$ treatment at 385, 420 and 450°C for 12 minutes in air respectively for comparison of device performances and results are shown in Table 9.2 and Figure 9.3 (a)-(d).

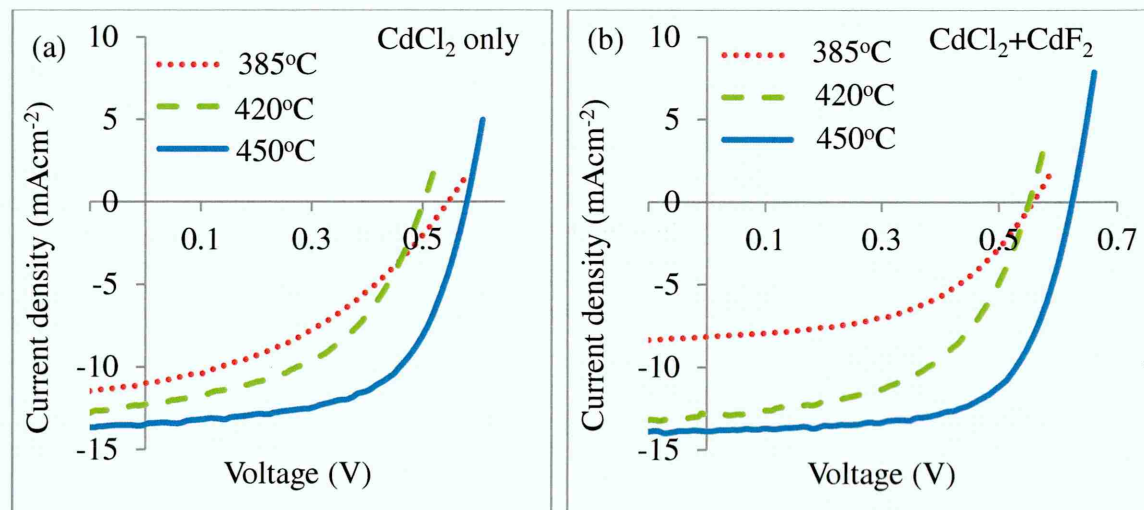
For the CdCl_2 and $\text{CdCl}_2+\text{CdF}_2$ treated samples investigated and presented in this thesis, the better device performances were observed when CdTe layers are heat

treated at the temperature of 450°C as compared to other heat treatment temperatures of 385 and 420°C. This can be due to improvement in structural, optical and morphological properties of the CdTe layers after CdCl₂ and CdCl₂+CdF₂ treatment as previously shown in chapter 8. Also, reports show that CdCl₂ or CdCl₂+CdF₂ treatment drastically improves the device performances due to the promotion of recrystallisation, grain growth, reduction of the grain boundaries (scattering centres), reduction in lattice mismatch as a result of inter-diffusion at the CdS/CdTe interface, increase in the life time of charge carrier and reduction in defect states and Te precipitation within the CdS/CdTe devices [16-21]. It should be noted that, in this work, the device performances of the CdCl₂+CdF₂ treated samples were better than the CdCl₂ treated samples at all heat treatment temperatures of 385, 420 and 450°C as shown in Table 9.2 and Figures 9.3 (a)-(d).

Table 9.2: Summary of device results for glass/FTO/n-CdS/n-CdTe/Au solar cells heat treated with CdCl₂ and CdCl₂+CdF₂ treatment at different temperatures of 385, 420 and 450°C respectively.

385°C for 12 minutes								
Sample ID	CdCl ₂ only				CdCl ₂ +CdF ₂			
	V_{oc} (mV)	J_{sc} (mAcm ⁻²)	FF	η (%)	V_{oc} (mV)	J_{sc} (mAcm ⁻²)	FF	η (%)
CT342A	455	9.7	0.25	1.1	493	8.21	0.34	1.4
CT343A	484	4.3	0.40	0.8	536	9.0	0.35	1.7
CT344A	546	11.0	0.40	2.4	557	8.7	0.54	2.6
CT345A	534	10.7	0.31	1.8	562	14.1	0.38	3.0
420°C for 12 minutes								
Sample ID	CdCl ₂ only				CdCl ₂ +CdF ₂			
	V_{oc} (mV)	J_{sc} (mAcm ⁻²)	FF	η (%)	V_{oc} (mV)	J_{sc} (mAcm ⁻²)	FF	η (%)
CT342B	456	11.7	0.28	1.5	522	11.8	0.31	1.9
CT343B	501	6.4	0.38	1.2	502	11.1	0.30	1.6
CT344B	502	12.2	0.48	3.0	551	12.9	0.53	3.8
CT345B	541	7.8	0.50	2.1	536	8.9	0.56	2.7
450°C for 12 minutes								
Sample ID	CdCl ₂ only				CdCl ₂ +CdF ₂			
	V_{oc} (mV)	J_{sc} (mAcm ⁻²)	FF	η (%)	V_{oc} (mV)	J_{sc} (mAcm ⁻²)	FF	η (%)
CT342C	430	18.0	0.30	1.8	513	11.9	0.36	2.3
CT343C	515	9.5	0.36	1.7	511	13.3	0.34	2.3
CT344C	580	13.4	0.60	4.7	623	13.8	0.65	5.6
CT345C	525	11.6	0.53	3.2	541	15.3	0.48	4.0

Reports show that both Cl and F act as fluxing agent and enhance the recrystallisation process in CdTe [19]. When both CdCl_2 and CdF_2 are used in CdTe treatment process specially at high temperature (450°C in this work), the recrystallisation process further promotes. It seems that CdF_2 act as a catalysts and combination of CdCl_2 and CdF_2 results in the further increase in the CdTe grain sizes as compared to the CdCl_2 treatment alone as previously shown in chapter 8 (section 8.3.5). Romeo *et al* [22] and Hernandez *et al* [23] also reported that the combination of Cl and F in the CdTe heat treatment process further improves the recrystallisation process and result in the formation of larger grains. Larger grains means less grain boundaries or less scattering centres for electrons. Therefore, electrons can move easier through the CdTe crystals, hence mobility of electrons will be higher and device performance will be improved. Zywitzki *et al* [24] has performed the electron beam induced current (EBIC) experiment on CdTe layers and show that before CdCl_2 treatment (activation process) the grain boundaries exhibit no EBIC signal and the main current collection take place at CdTe grain itself. After CdCl_2 treatment, the EBIC signal at the grain boundaries was higher than the CdTe grains itself. This shows that the main current collections take place at the grain boundaries as compared to CdTe grain itself. This is due to the higher diffusion coefficient of Cl or F at the grain boundaries as compared to the CdTe grain itself. McCandless *et al* [25] reported that the diffusion coefficient of Cl at the grain boundaries is five orders of magnitude larger than that of Cl in the bulk CdTe.



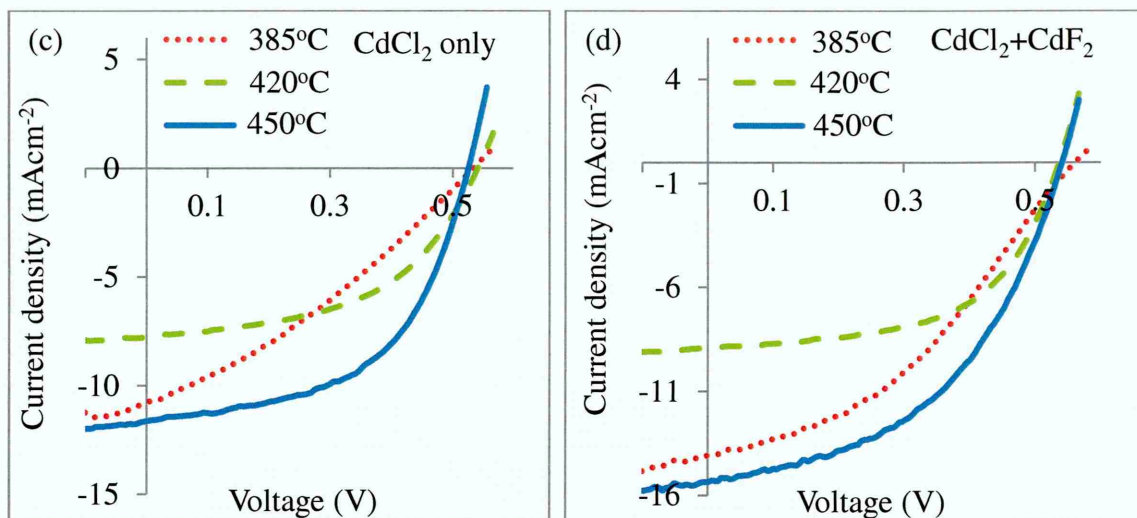


Figure 9.3: The comparison of J-V curves under illumination for glass/FTO/n-CdS/n-CdTe/Au solar cells heat treated with CdCl₂ and CdCl₂+CdF₂ treatment at different temperatures of 385, 420 and 450°C for 12 minutes in air respectively.

This shows that CdCl₂ or CdCl₂+CdF₂ treatment passivates the grain boundaries and the grain boundaries also effectively participate in current collection process. Also, Flores *et al* [26] and Rejon *et al* [27] reported higher solar cells efficiency for the CdTe layers heat treated with both Cl and F in the presence of oxygen. The recent work by Echendu *et al* [28] also shows better device performance for the electrodeposited CdTe layers when layers are heat treated with CdCl₂+CdF₂ at 450°C in air atmosphere as compared to CdCl₂ treatment alone.

The different device performance observed for the samples heat treated with CdCl₂ or CdCl₂+CdF₂ treatment at 385, 420 and 450°C can also be related to the structural transition and morphological change for CdTe layers as previously shown in chapter 8. Based on the experimental observation reported by Kim *et al* [29] using in situ XRD, the sudden structural transition was observed at 385±5°C when CdTe layers are heat treated with CdCl₂ treatment. Also, there are large numbers of experimental observations reported in the literature regarding the XRD and SEM of the CdCl₂ treated CdTe layers including the results presented in this work. Based on these experimental observations, Dharmadasa *et al* [30] has identified that two noticeable structural transitions take place in the CdTe layers when these layers are heat treated with CdCl₂ treatment. The first or sudden structural transition takes place at heat treatment temperature of 385±5°C and the second or slow structural transition takes places at temperatures >430°C as shown in Figure 9.4. It should be noted that in the low

temperature growth techniques such as electrodeposition and sputtering, the cubic CdTe layers are preferentially orientated along (111) plane. The intensity of (220), (311) and (400) are very low as compared to (111) peak at low temperature. When CdTe layers are heat treated with CdCl₂ treatment at low temperature (Region-1), the cell efficiencies are also low as shown in Figure 9.4. As the heat treatment temperature increases gradually, the intensity of the (111) and the efficiency of the solar cells also increases gradually. At the heat treatment temperature of 385±5°C, (111) peak shows the highest intensity which are in agreement with experimental observation in this work. Above this temperature (385±5°C), the grain boundaries melt into a liquid with CdTe grains embedded in the liquid layers. The SEM images of the surface of CdTe layers show that the layers seem to be continuous and pinhole-free due to the formation of liquid phase at the grain boundaries as shown in chapter 8 (section 8.3.5). As soon as the grain boundary melting takes place, the crystallites lose their preferential orientation and therefor, (111) peak collapse and other 3 CdTe peaks increases. During cooling process, this liquid phase crystallises and the CdTe layers show low intensity for (111) peak. Reports also show that the formation of liquid phase takes place at the grain boundaries which facilitate the recrystallisation process [29]. R. Dharmadasa *et al* [31] has also reported the liquid phase formation in the CdCl₂ treated CdTe layers which show that CdTe undergoes sudden structural transition. Hiie's [32] experimental observations also show that the formation of CdTeO₃ phases on the CdTe surface or at the grain boundaries can drastically reduce the Cl diffusion into CdTe crystal during CdCl₂ treatment which can reduce the efficiency of the solar cells.

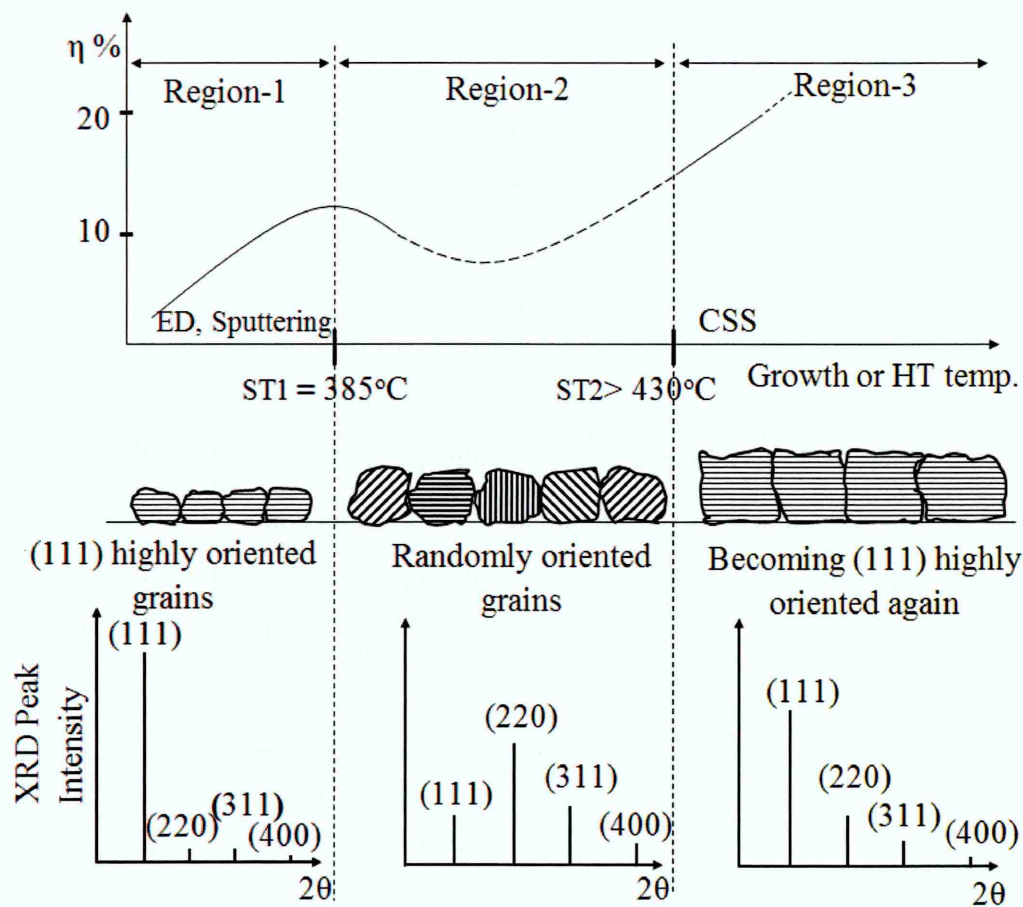


Figure 9.4: Schematic diagrams summarising CdTe grain growth patterns, corresponding XRD patterns and approximate solar cell efficiencies against growth or heat treatment temperature. Note three regions identified with a sudden phase transition at $ST1 = 385^\circ\text{C}$, and a slow phase transition taking place after $ST2 > 430^\circ\text{C}$ [Ref. 30].

When the heat treatment temperature exceed the transition temperature of $385 \pm 5^\circ\text{C}$ as shown in Figure 9.4 (Region 2, $385^\circ\text{C} < T < 430^\circ\text{C}$), the (111) peak intensity collapse due to the random orientation of the grains. As a result of random orientation of the grains, the intensity of the other peaks, (220), (311) and (400) increase. However, the efficiencies of the solar cell devices at the region 2 are lower than region 1.

When the CdTe layers are heat treated with CdCl_2 or $\text{CdCl}_2 + \text{CdF}_2$ treatment at temperatures above 430°C (in this work 450°C), the intensity of the (111) start to increase again. The grain size at this heat treatment temperature of 450°C drastically increases as shown in Figure 9.4 (Region 3). Also, the efficiency of the solar cell devices at the region 3 is higher than Region 1 and Region 2 due to higher heat treatment temperature. The experimental observations for solar cell devices in this work are also in agreement with the experimental observation presented in the Figure 9.4.

These results show that one of the key steps for obtaining better device performance for electrodeposited CdTe layers is the combination of $\text{CdCl}_2 + \text{CdF}_2$ treatment as compared to CdCl_2 treatment alone. The other key step is the treatment of the layers at high temperature (450°C) in air.

9.2.4 Assessment of the fabricated glass/FTO/n-CdS/n-CdTe/Au solar cells using ED-CdS and CBD-CdS layers for comparison

This experiment was carried out in order to compare the device performance of glass/FTO/n-CdS (ED)/n-CdTe/Au and glass/FTO/n-CdS (CBD)/n-CdTe/Au solar cells. For this reason, ED-CdS and CBD-CdS with the thickness of ~ 90 nm were grown on glass/FTO substrates. Then, n-CdTe layers with the thickness of ~ 1.5 μm were grown on the glass/FTO/n-CdS (ED) and glass/FTO/n-CdS (CBD) substrates. Afterward, CdTe layers were heat treated with $\text{CdCl}_2 + \text{CdF}_2$ treatment at 450°C for 12 minutes in air and results are shown in Table 9.3 and Figures 9.5 (a)-(d).

For both glass/FTO/n-CdS(ED)/n-CdTe/Au and glass/FTO/n-CdS(CBD)/n-CdTe/Au solar cells, approximately similar V_{oc} were observed. The current density of some solar cells using CBD-CdS was slightly higher than the ED-CdS layers while in other devices the current densities show very close values as shown in Table 9.3 and Figures 9.5 (a)-(d). The main difference between the solar cells fabricated using ED- and CBD-CdS window layers was in the FF of the devices. The FF and efficiencies of the solar cells fabricated using CBD-CdS layers were higher than those using ED-CdS layers (See Table 9.5). The lower FF observed in the solar cells using ED-CdS as compared to the CBD-CdS layers can be due to presence of pinholes in the ED-CdS layers and nature of electrodeposition growth technique. As previously shown in chapter 6 (section 6.3.6) and chapter 7 (section 7.4.3), in electrodeposition technique the possibility of formation of pinholes in the CdS layers are higher than CBD growth technique due to the upward growth of the CdTe crystallites normal to the glass/FTO substrate. The upward or columnar growth of the CdTe crystallites produces non-uniformity creating pinholes in the ED-CdS layers whereas in CBD growth technique the CdS layers are more uniform, compact and smooth than ED-CdS layers due to absence of the electric field during the growth. The pinholes in the CdS layers create shunting paths and drastically reduce the solar cell efficiency due to the short-circuiting of front and back contacts after metallisation.

Table 9.3: Summary of device results for glass/FTO/n-CdS(ED)/n-CdTe/Au and glass/FTO/n-CdS(CBD)/n-CdTe/Au solar cells for comparison of device performances. All CdTe layers were heat treated with CdCl₂+CdF₂ treatment at 450°C for 12 minutes in air.

Sample ID	glass/FTO/n-CdS(ED)/ED-CdTe				glass/FTO/n-CdS(CBD)/ED-CdTe			
	V_{oc} (mV)	J_{sc} (mAcm ⁻²)	FF	η (%)	V_{oc} (mV)	J_{sc} (mAcm ⁻²)	FF	η (%)
CT275	602	6.3	0.39	1.4	598	13.5	0.57	4.6
CT300	547	11.0	0.39	2.3	554	14.1	0.55	4.3
CT306	580	13.5	0.40	3.2	587	13.9	0.55	4.5
CT307	558	21.2	0.30	3.6	557	24.5	0.47	6.4
CT308	565	14.5	0.40	3.2	567	14.3	0.54	4.4

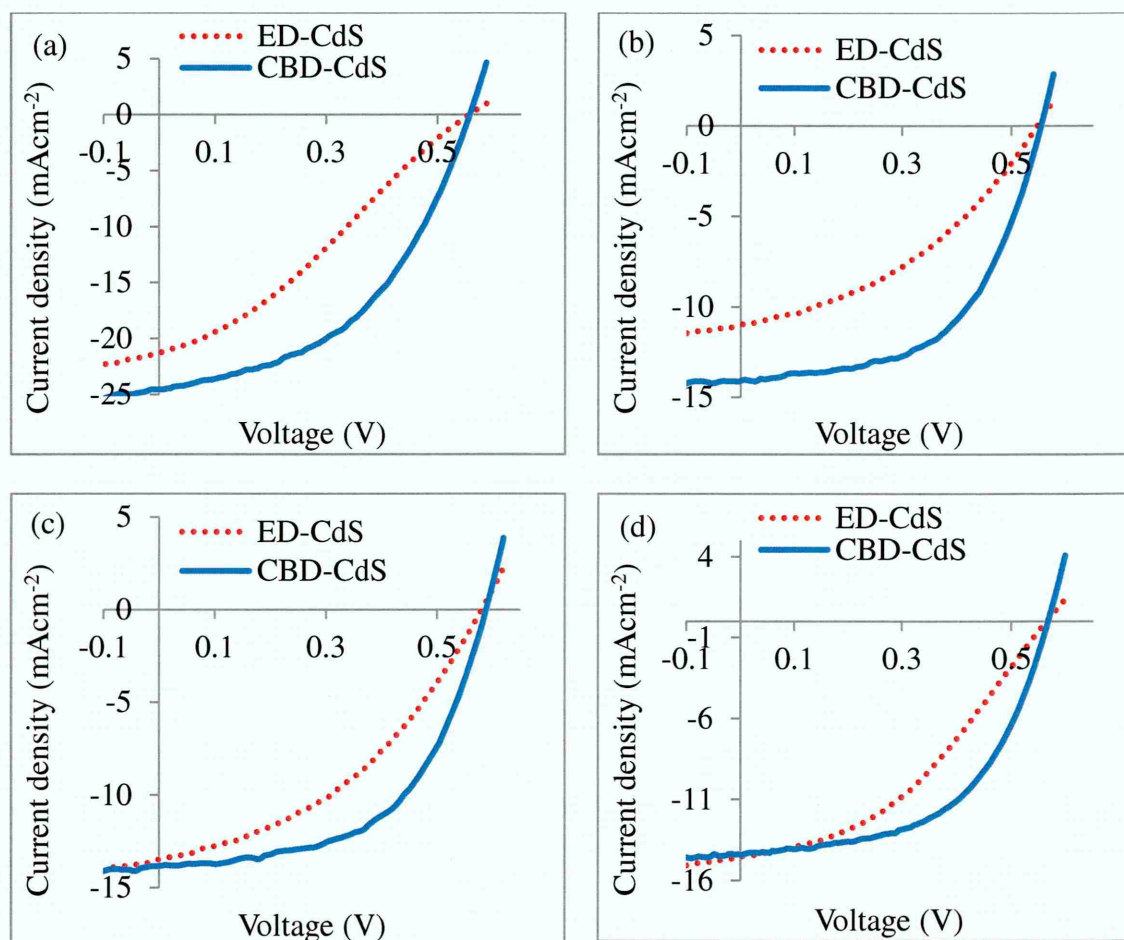


Figure 9.5: The comparison of J-V curves under illumination for glass/FTO/n-CdS (ED)/n-CdTe/Au and glass/FTO/n-CdS (CBD)/n-CdTe/Au solar cells. All CdTe layers were heat treated with CdCl₂+CdF₂ at 450°C for 12 minutes in air.

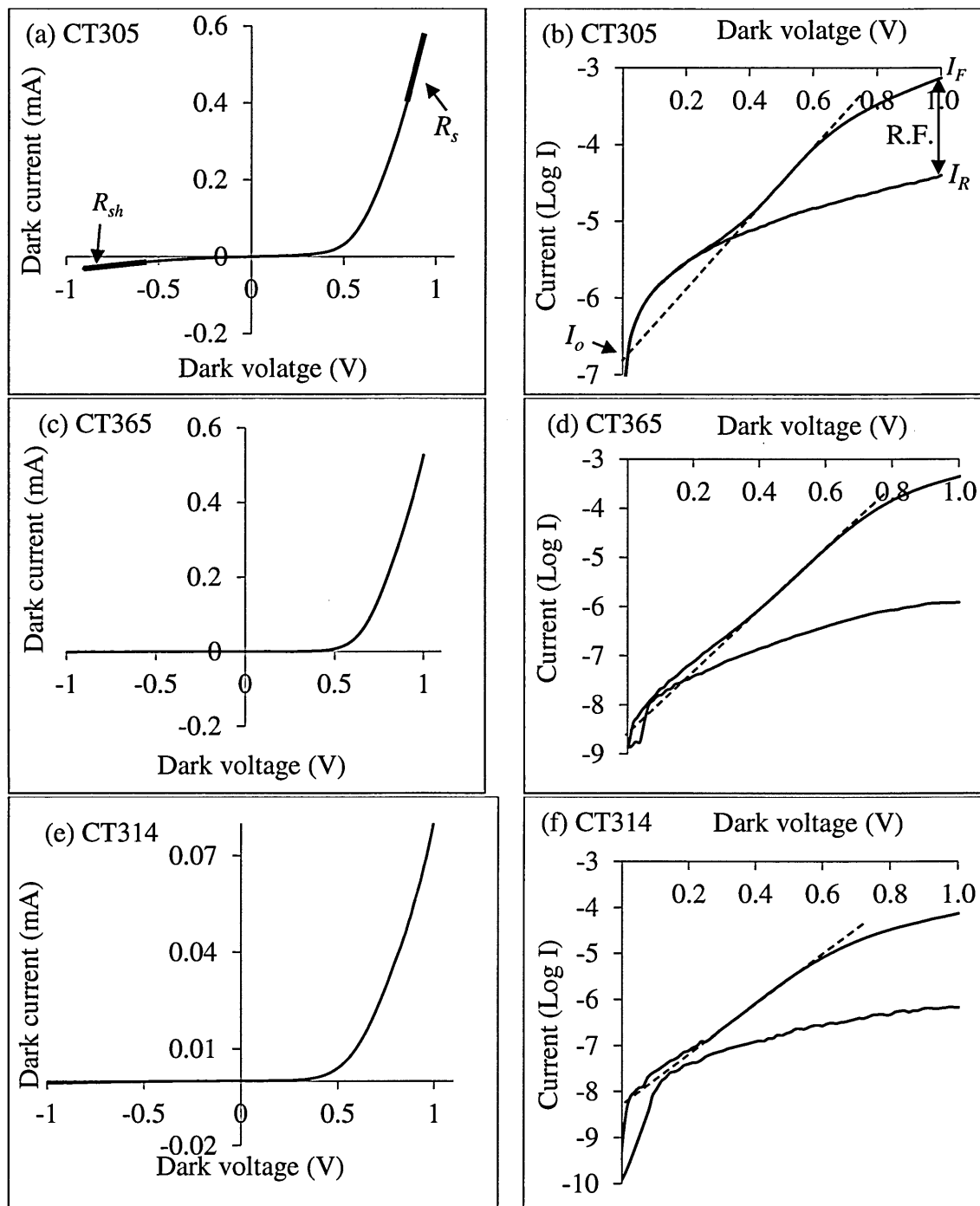
9.2.5 Assessment of glass/FTO/n-CdS/n-CdTe/Au solar cells under dark and illumination conditions

Current-voltage (I-V) measurements under dark condition were carried out in order to determine the series resistance (R_s), shunt resistance (R_{sh}), reverse saturation current (I_o), ideality factor (n), barrier height (ϕ_b) and rectification factor (RF) of the best solar cells fabricated in this work as shown in Figures 9.6 (a)-(j) and Table 9.4.

Figures 9.6 (a, c, e, g and i) show the linear-linear I-V curve of the solar cells measured under dark condition. From these graphs, the R_s and R_{sh} were measured using the forward and reverse part of the I-V curve as shown in Figure 9.6 (a). The R_s and R_{sh} of the best solar cells are shown in Table 9.4. The R_s and R_{sh} of the best cells in this work were in the range (204-3333) Ω and (0.1-5.0) $M\Omega$ respectively. It should be noted that for the high efficiency solar cells, the R_s should be as low as possible and R_{sh} should be as high as possible. The R_s is caused by the bulk resistance of the semiconductor material, the resistance of the electrical contacts and the interconnections. The main impact of the large R_s is to reduce the V_{oc} , FF and the gradient of the log-linear curve at the high forward-bias region, hence, increasing the n value [14,33]. The presences of large R_s in the device mean low solar cells efficiency. Also, significant reduction in solar cells efficiency can be caused by the presence of R_{sh} . The R_{sh} is caused by the current leakage across the junction (recombination of the photo-generated charge carrier before their separation due to the weak junction potential) and manufacturing defects. The low R_{sh} reduces the FF and also leaks off some current which in turn reduces the efficiency of the solar cells [34]. For an ideal diode, the $R_s = 0$ and $R_{sh} = \infty$.

The dark I_o of solar cells were measured by extrapolating the straight line portion of log-linear I-V curve to $V=0$ as shown in Figure 9.6 (b). It should be noted that the more accurate I_o can be provided by interception of the straight line with the highest gradient which can be used to evaluate the smallest value of n [14]. Also, tunnelling through the device increases the low forward-bias current and decreases the gradient of the log-linear I-V curve and, hence increases the n value. The dark I_o values of the best solar cells in this work were extracted from the Figures 9.6 (b, d, f, h and j). The measured dark I_o values were in the range (2.5-200) $\times 10^{-9}$ A. In the high efficiency solar cells the I_o value is lower because of decreased recombination in the depletion region which indicates a healthy junction with reduced defects. The presence of the

defects in the crystal lattice can increase the I_o values because these defects act as trapping or recombination centres which reduce the life time of charge carriers [35].



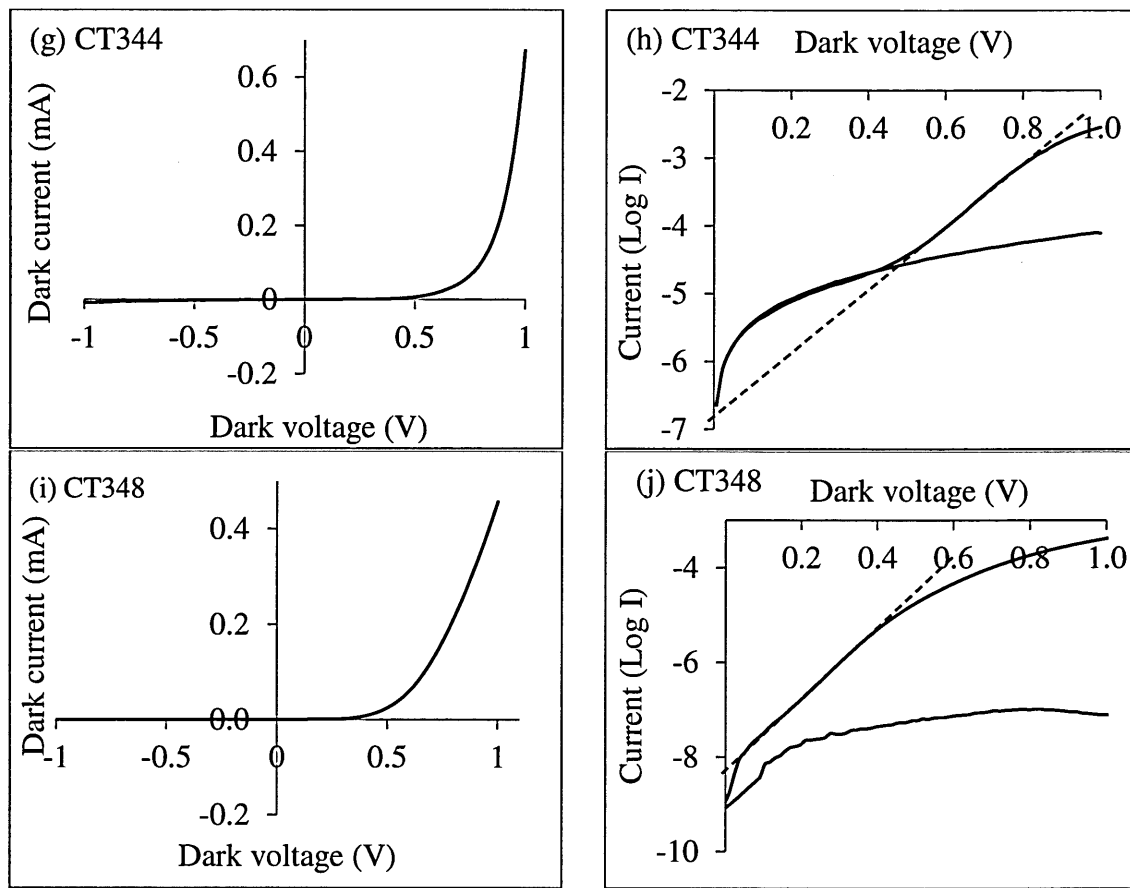


Figure 9.6: The I-V curves of the best glass/FTO/n-CdS/n-CdTe/Au solar cells under dark condition (a, c, e, g and i). Linear-linear I-V in dark and (b, d, f, h and j) Log-linear I-V in dark. The solar cell parameters under dark condition are shown in Table 9.4.

Table 9.4: Summary of solar cell parameters of the best fabricated devices obtained after measurement under dark and illumination conditions.

glass/FTO/n-CdS/n-CdTe/Au					
Cell parameters	Sample ID				
	CT305	CT365	CT314	CT344	CT348
$Dark R_s (\Omega)$	416	555	3333	204	769
$Dark R_{sh} (M\Omega)$	0.1	0.5	1.0	0.5	5.0
$I_o (\times 10^{-9} A)$	200	2.5	4.0	158	4.0
n	3.76	1.71	1.83	3.16	1.36
$\phi_b (eV)$	>0.66	>0.77	>0.76	>0.67	>0.76
RF	$10^{1.3}$	$10^{2.6}$	$10^{2.2}$	$10^{1.9}$	$10^{3.7}$
$V_{oc} (mV)$	564	616	594	623	663
$J_{sc} (mAcm^{-2})$	26.2	23.9	23.4	13.8	15.0
FF	0.48	0.45	0.40	0.65	0.51
$\eta (\%)$	7.1	6.6	5.7	5.6	5.1

The n and ϕ_b values of the solar cells were calculated using Equations (5.9) and (5.3) respectively (see chapter 5). In this work, the solar cell with lower n and I_o values show higher ϕ_b values whereas the solar cell with the higher n and I_o values show lower ϕ_b values as shown in Table 9.4. From the ϕ_b values presented in Table 9.4, it can be seen that the Fermi level pins at defect states >0.77 eV below the conduction band minimum. The observed barrier heights are underestimated due to large n values. The observed values of $\phi_b > 0.77$ eV, can be related to PL spectra presented in chapter 8 (section 8.3.10) which shows the presence of the defect states labelled E4. It should be noted that after CdCl_2 treatment the broadness of defect states E_3 were narrowed down, however, these defect states (E_3) were not completely removed. The PL spectra also show the removal of E_2 after second CdCl_2 treatment as shown in chapter 8 (section 8.3.10). Then it is possible that Fermi level pins at defect states at E4 with the observed ϕ_b values of >0.77 eV as shown in Table 9.4. It should also be noted that the defect states E_2 and E_3 are known as the killer centres or recombination centres and removal of the defect states E_2 and E_3 [Figures 9.2 (g) and 9.2 (h)] can drastically lead to an increase in the efficiency of the solar cells. If defect states E_2 and E_3 are not present, the Fermi level pins at E4 and E5 defect states and higher ϕ_b values can be obtained. The higher ϕ_b means higher V_{oc} and higher efficiency for solar cells. It is worth to mention that, in high efficiency solar cells, n and I_o values are lower and ϕ_b values are higher.

The RF values of the best solar cells in this work were calculated using Equation (5.8) (see chapter 5). The RF of the best solar cells in this work was in the range ($10^{1.3}$ - $10^{3.7}$) as shown in Table 9.4. It should be noted that the solar cell with the efficiency of 7.1% showed low RF $10^{1.3}$ as compared to other cells. This is due to lower CdTe thickness (~ 0.2 μm) of this cell as compared to CdTe thickness in other cells which were in the range $\sim (0.8\text{-}1.1)$ μm . In high efficiency solar cells, a large RF is desirable, although for efficient solar cells, the RF of $\sim 10^3$ is sufficient [14].

Figures 9.7 (a)-(e) show the J-V curves of the best glass/FTO/n-CdS/n-CdTe/Au solar cells under illumination conditions. The important solar cell parameters which can be extracted under illumination condition are V_{oc} , J_{sc} , FF and η . The extracted solar cell parameters from Figures 9.7 (a)-(e) are shown in Table 9.4. It should be noted that in this thesis the highest conversion efficiency achieved was 7.1%. Also, the highest V_{oc} , J_{sc} and FF obtained were 663 mV, 26.2 mAcm^{-2} and 0.65 respectively (as highlighted in Table 9.4).

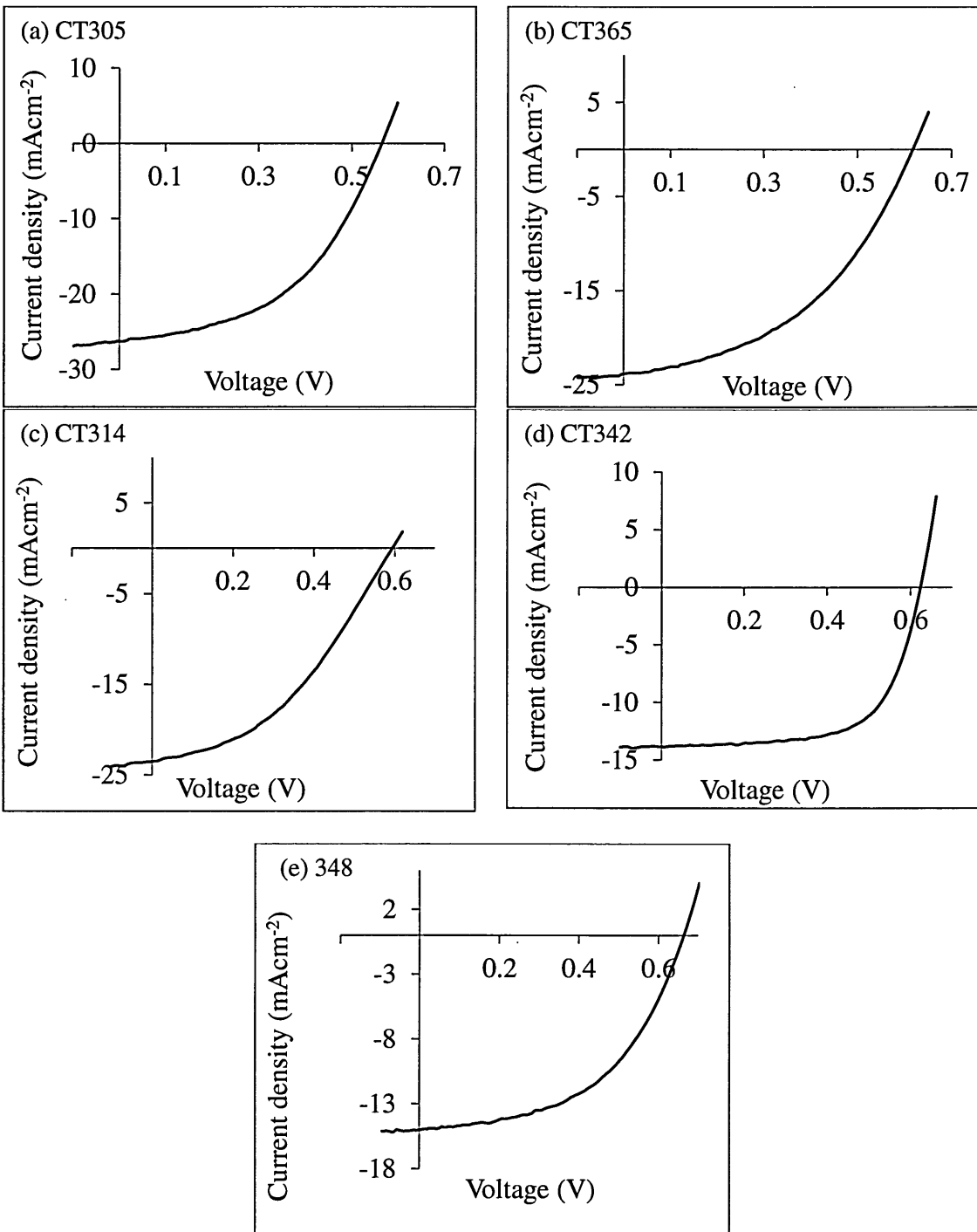


Figure 9.7: The J-V curves of the best glass/FTO/n-CdS/n-CdTe/Au solar cells under illumination conditions. All CdTe layers were heat treated with CdCl₂+CdF₂ at 450°C for 12 minutes in air and the solar cell parameters under illumination are shown in Table 9.4.

9.2.6 The C-V measurements for glass/FTO/n-CdS/n-CdTe/Au solar cells

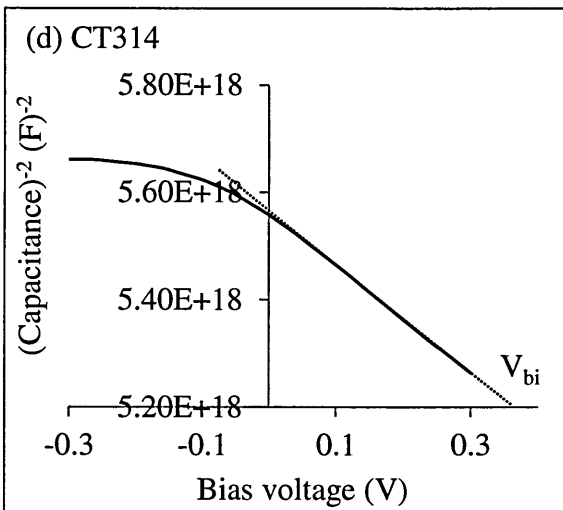
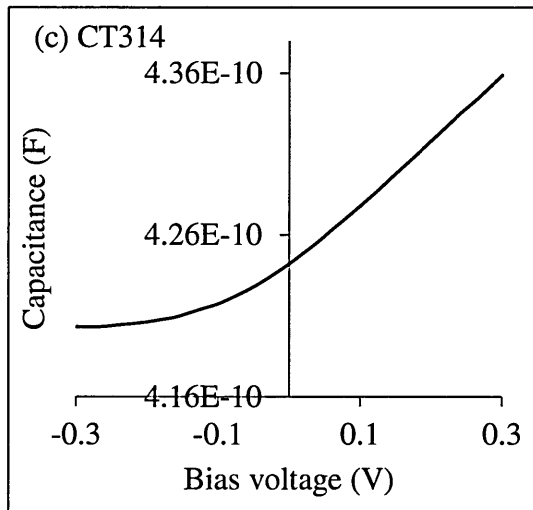
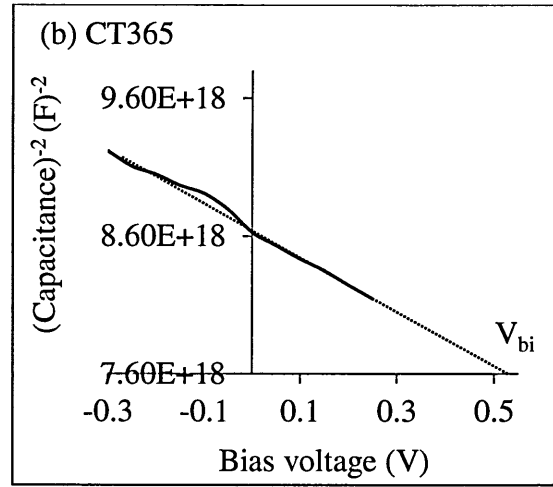
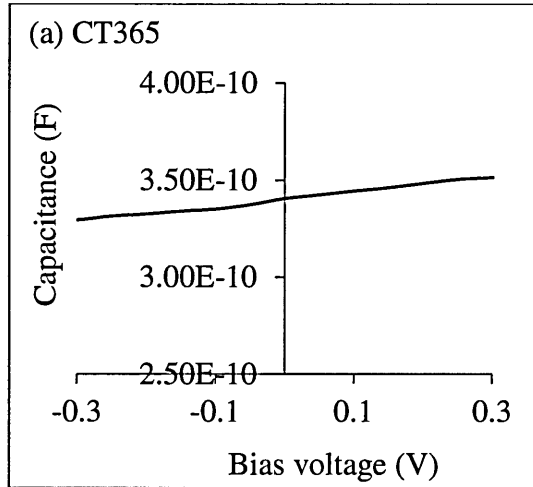
The C-V measurements have been carried out to study the depletion region and also to estimate the doping concentration and built-in voltage (V_{bi}) of the fabricated solar cells.

Figures 9.8 (a, c, e, g) show the typical C-V characteristics of the 6.6, 5.7, 5.6 and 5.1% efficiency device structures of the glass/FTO/n-CdS/n-CdTe/Au solar cells with 2 mm diameter active area (see Table 9.4 in previous section). The C-V measurements were carried out at room temperature and in dark condition using a depletion signal of frequency, 1 MHz at a voltage range of -1.0 to 1.0 V bias. Results show the gradual increase in junction capacitance when the applied voltage changes from reverse bias to forward bias which is due to gradual decrease in the depletion region width, W , as shown in Figures 9.8 (a, c, e, g). In this work, the observed depletion capacitances at zero bias (C_o) for the 6.6, 5.7, 5.6 and 5.1% solar cells were 340, 424, 426 and 314 pF respectively as shown in Table 9.5. Reports show the C_o value of ~ 180 pF at measurement frequency of 1 MHz for the electroplated CdTe based solar cells with the conversion efficiency of $\sim 8.0\%$ [36, 30]. The reported doping concentration of this device was $\sim 10^{15} \text{ cm}^{-3}$ for CdTe film thickness of $\sim 1.65 \mu\text{m}$. Other reports also show the depletion capacitance of ~ 56 pF for a high efficiency electroplated CdTe solar cells with a fully depleted device and thickness of $\sim 2.0 \mu\text{m}$ at measurement frequency of 1 MHz [12]. In this work, the depletion widths were calculated using Equation (9.1) at zero bias ($V=0$) using:

$$W_o = \frac{\epsilon_o \epsilon_r A}{C_o} \quad (9.1)$$

where W_o is the depletion width at zero bias, $\epsilon_o \sim 8.85 \times 10^{-12} \text{ Fm}^{-1}$ is the permittivity of free space, $\epsilon_r \sim 11$ is the relative permittivity of CdTe, $A \sim 0.031 \text{ cm}^2$ is the active device area, and C_o is the junction capacitance at zero bias. In this work, the calculated W_o values were slightly less than the experimentally measured thickness values for CdTe layers as shown in Table 9.5. The calculated W_o values were in the range $\sim (718-922)$ nm and the experimentally measured thickness values were in the range $\sim (800-1100)$ nm. Also, reports show that when CdTe layers are moderately doped, $\sim 10^{15} \text{ cm}^{-3}$, it is possible that the depletion width be equal or greater than the complete device

thickness [14]. When this happens, the device is fully depleted which means depletion region is almost equal to the thickness of the layer. In a fully depleted device, the capacitance is constant in the both reverse and forward bias condition. Therefore, the whole thickness of the layer is photo-active and as soon as the charge carriers are being generated by the incident photons, they will be separated and directed to the front and back contact before their recombination due to the strong built-in electric field.



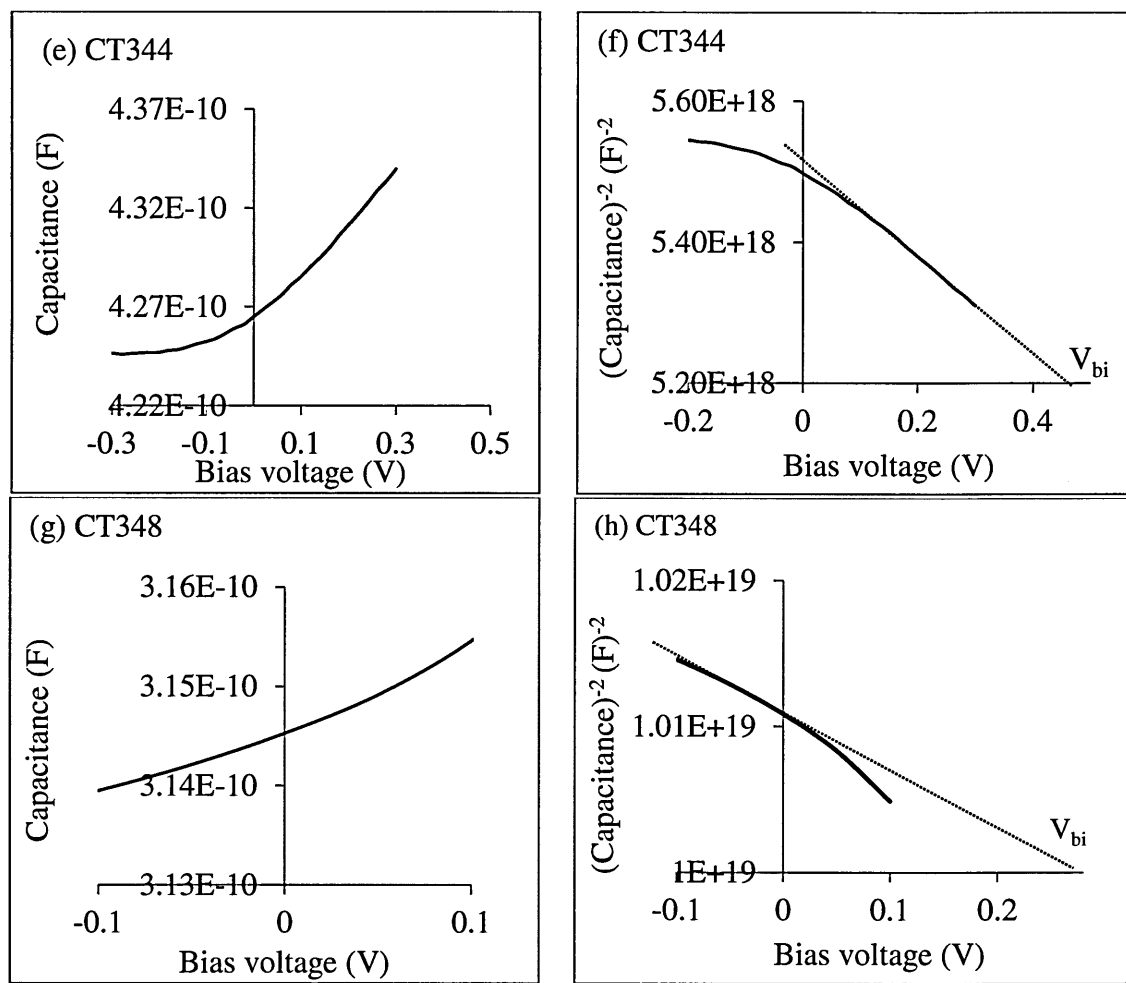


Figure 9.8: Typical C vs. V (a, c, e, g) and $1/C^2$ vs. V graphs (b, d, f, h) of the glass/FTO/n-CdS/n-CdTe/Au solar cells.

Table 9.5: The parameters of the depletion capacitance, depletion width and doping concentration extracted from C vs. V and $1/C^2$ vs. V graphs.

Sample ID	CdTe layer Thickness (nm)	C_o (pF)	W_o (nm)	N_D-N_A (cm ⁻³)	V_{bi} (V)
CT365	1000	340	900	6.50×10^{15}	0.52
CT314	800	424	722	1.30×10^{16}	0.36
CT344	800	426	718	1.88×10^{16}	0.46
CT348	1100	314	972	2.16×10^{16}	0.28

Figures 9.8 (b, d, f, h) show the Mott-Schottky plots of $1/C^2$ vs. V of the best solar cell devices in this work. The non-linear shape of the Mott-Schottky plot indicates

doping levels are non-uniformly distributed in the CdTe layer [37]. Also the non-linearity of the Mott-Schottky plot represents the presence of trap levels in the forbidden band of CdTe [38]. The doping concentration for electrons calculated from Figures 9.8 (b, d, f, h) gave the values ($N_D - N_A$) in the range $\sim 6.50 \times 10^{15}$ to $\sim 1.30 \times 10^{16} \text{ cm}^{-3}$. Reports show that in the high efficiency CdTe based solar cells, the doping concentrations are in the range of $\sim (1.0 \times 10^{14} - 5.0 \times 10^{15}) \text{ cm}^{-3}$ [39-44,30]. It should be noted that in this work, the sample with lower doping concentration of $\sim 6.50 \times 10^{15} \text{ cm}^{-3}$ shows the higher V_{bi} value ($\sim 0.52 \text{ V}$) and higher efficiency (6.6%) as compared to other devices as shown in Figures 9.8 (b, d, f, h). The larger V_{bi} value indicates stronger built-in electric field and higher barrier height, ϕ_b . The strong built-in electric field enhances the separation of the photo-generated charge carriers in the depletion region before their recombination. It should be noted that the C-V method for measuring barrier height is not reliable due to the influence of defects in the depletion region.

9.2.7 Stability of fabricated glass/FTO/n-CdS (CBD)/n-CdTe/Au solar cells

The stability experiment was carried out on the glass/FTO/n-CdS(CBD)/n-CdTe/Au solar cell with the initial efficiency of 6.1%. The cell efficiency for this device was monitored over the period of 45 weeks (7536 hours) and results are presented in Figure 9.9. Results show that the efficiency of the fabricated device gradually increased and reached its maximum value of 7.1% after two weeks (312 hours). Comparing to the initial device fabricated on the first day, device shows $\sim 14\%$ improvement in performance after two weeks. The increase in the cell efficiency is attributed to the gradual diffusion of Au atoms into the CdTe layers which results in the contact improvement between CdTe and Au interface. The major improvements observed were in the J_{sc} and FF of the device as shown in Table 9.6. Also, V_{oc} of the device was slightly improved within this period. The gradual degradation in device performance was observed within the periods of 3 to 45 weeks. The degradation rate was about 2.4% per month. The major degradation was observed in the J_{sc} and FF of the device as compared to V_{oc} as shown in Table 9.6.

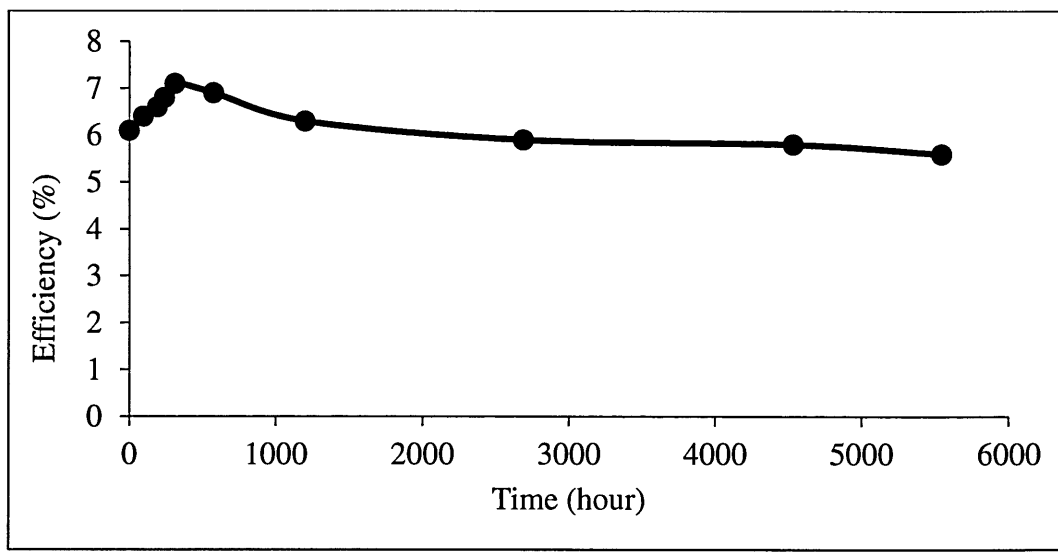


Figure 9.9: The degradation behaviour of the glass/FTO/n-CdS/n-CdTe/Au solar cells over a period of 315 days.

Table 9.6: The device parameters of the glass/FTO/n-CdS/n-CdTe/Au solar cell measured over a period of 315 days.

Time (hours)	V_{oc} (mV)	J_{sc} (mAcm^{-2})	FF	η (%)
24	560	23.6	0.46	6.1
96	560	24.5	0.47	6.4
192	561	25.1	0.47	6.6
240	561	26.0	0.47	6.8
312	564	26.2	0.48	7.1
576	565	26.0	0.47	6.9
1200	564	24.6	0.46	6.3
2928	564	23.3	0.45	5.9
4536	561	23.0	0.45	5.8
5544	561	22.9	0.44	5.6
7536	560	22.6	0.43	5.4

Most of the reports propose that the cells degradation is mainly due to the junction degradation and degradation of the back contact. Mendoza-Perez *et al* [45] has reported that the back contact and semiconductor can deteriorate due to the oxidation in atmospheric conditions which results in the degradation of the device over a period of time. In this work, it is also suggested that the continuous measurement of the solar cells using small probe can create mechanical damage to the back contact after several measurements.

It is worth to mention that the efficiency and long term stability of the CdS/CdTe solar cells strongly depends on the method of deposition and type of the materials used for the back contact. The most commonly investigated metal back contacts used for CdS/CdTe solar cells are Cu/Au [46], Cu/graphite [47], Cu doped ZnTe with Au or Ni [48], Cu/Mo [49] and Au [50].

In p-CdTe (p-n heterojunction junction), small amount of Cu is often used to improve the electrical ohmic contact to CdTe due to p+-doping of CdTe surface. Most of the CdS/CdTe solar cells with Cu-based contact initially show higher efficiencies. However, excess Cu in the p-CdTe back contact enhances the degradation and instability of the CdS/CdTe solar cells. This is because Cu is known to be a strong diffuser [51]. Reports show that Cu can diffuse along the CdTe grain boundaries and across the junction [52]. Therefore, the diffusion of Cu^+ as a p-type dopant into the n-CdS layers can increase the resistivity of the layers due to self-compensation effect [14]. In addition, in n-CdS/p-CdTe junction, diffusion of the Cu from back contact to the front contact can reduce the cell performance mainly due to the degradation of FF as a result of the shunting effects [51]. However, the true mechanism of involvement of Cu in the degradation process is not well understood. In order to obtain long-term stable CdS/CdTe solar cells, the excess Cu should be avoided in back contact. In other word, the thickness of the Cu layer should be very low in the range (2-3) nm.

Also, in n-n+Schottky junction, addition of Cu in the electrical back contact initially improves the device performance. The reason is that, Cu is a p-type dopant and addition of Cu in the electrical back contact helps to pin the Fermi level close to the valence band which lead to the formation of larger potential barrier height at metal/semiconductor junction, therefore, the device performance improves. However, excess Cu (p-type dopant) can diffuses into n-type CdTe and can form a highly resistive CdTe layer due to the self-compensation and eventually results in the instability and degradation of the solar cell devices.

Bosio *et al* [5] has reported that long-term stable CdS/CdTe p-n junction solar cells can be obtained by using $\text{Sb}_2\text{Te}_3/\text{Mo}$ or $\text{As}_2\text{Te}_3/\text{Mo}$ as back contact. Also, in both p-n and n-n+Schottky junctions, incorporation of thin insulating layers (organic insulators) between CdTe and electrical back contact (MIS type electrical contact) minimises the interaction between the metal and semiconductor [14]. In addition, the insulator layer prevents the undesirable chemical reaction from taking place between the inorganic semiconductor and metal back contact and also increases the Schottky barrier

height (ϕ_b) at metal/semiconductor contact. The thin p-ZnTe layer can also be used in n-n+Schottky junctions to increase the Schottky barrier height (ϕ_b) by bringing the Fermi level closer to the valence band and to minimise the interaction between the semiconductor and metal back contact. In p-n junction, the doped p-ZnTe can be doped to improve the ohmic contact and also can be used as electron back diffusion layer between semiconductor and metal contact. All the methods mentioned above can be used to improve the stability and performance of p-n and n-n+Schottky junctions.

9.3 Fabrication of glass/FTO/n-ZnS/n-CdTe/Au solar cells

Figure 9.10 shows the energy band diagram of n-n+Schottky junction for the glass/FTO/n-ZnS/n-CdTe/Au solar cell. The optical bandgap of ZnS is about 3.7 eV [53] higher than 2.42 eV of CdS at 300 K [54]. The higher optical bandgap of ZnS as window layer allow the higher energy photons to reach the CdTe absorber layer for generation of charge carriers as compared to CdS window layer. The reported value of the lattice mismatch between ZnS and CdTe layers is about 16.4 % [55]. The high lattice mismatch creates defects at the interface between ZnS and CdTe and those can affect the performance of the ZnS/CdTe devices. However, the large lattice mismatch can be minimised after heat treatment process. As a result of heat treatment process, the inter-diffusion between ZnS and CdTe layer takes place which lead to the formation of intermediate quaternary compound, $\text{ZnCdS}_x\text{Te}_{1-x}$. The region marked “b” in Figure 9.10 represents the inter-mixing area between the ZnS and CdTe layer after heat treatment process which facilitate the bandgap grading between these two layers.

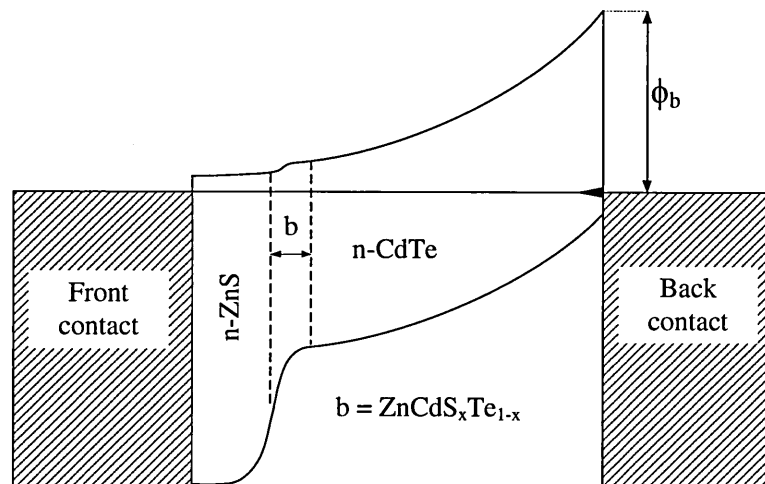


Figure 9.10: Typical energy band diagram of n-n+Schottky barrier model for glass/FTO/n-ZnS/n-CdTe/Au solar cell.

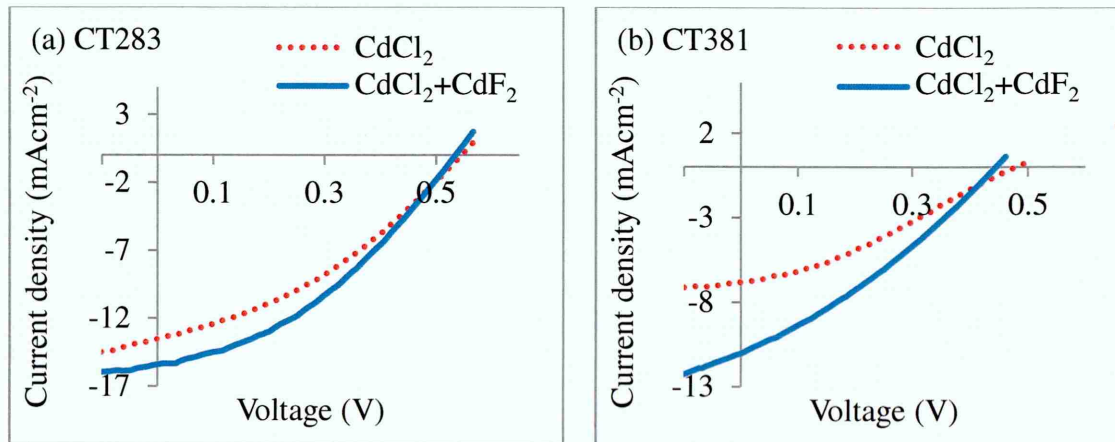
In this work, in order to obtain the glass/FTO/n-ZnS/n-CdTe/Au structure, the n-ZnS layers with the thickness of about 80 nm were grown on glass/FTO substrates to produce the glass/FTO/n-ZnS structure. Thereafter, the ZnS layers were heat treated at 350°C for 10 minutes in air. Then, n-CdTe layers with the thickness of about 1.50 μm were grown on glass/FTO/n-ZnS substrates to obtain the glass/FTO/n-ZnS/n-CdTe structure. The next step was the heat treatment of the CdTe layers with CdCl_2 and $\text{CdCl}_2+\text{CdF}_2$ treatment at 450°C for 12 minutes in air. After etching and metallisation process, the glass/FTO/n-ZnS/n-CdTe/Au structure was obtained. Table 9.7 and Figures 9.11 (a)-(e) show the summary of device results and J-V curves for the glass/FTO/n-ZnS/n-CdTe/Au solar cells. Results show slightly better device performance for the samples heat treated with $\text{CdCl}_2+\text{CdF}_2$ treatment as compared to those heat treated with CdCl_2 treatment alone. Also, Echendu *et al* from Sheffield Hallam University solar energy group have also reported the efficiency of $\sim 12.0\%$ for $\text{CdCl}_2+\text{CdF}_2$ treated glass/FTO/n-ZnS/n-CdTe/Au solar cells at temperature of 450°C [36].

In this work, it was expected that the glass/FTO/n-ZnS/n-CdTe/Au solar cells show better device parameters and performances than the glass/FTO/n-CdS/n-CdTe/Au solar cells (see Table 9.4 and Table 9.7) due to the higher optical bandgap of the ZnS layer as compared to CdS layer. However, the lower device performance of glass/FTO/n-ZnS/n-CdTe/Au devices can be due to the large lattice mismatch between ZnS and CdTe layer and high resistivity of ZnS layer [55, 56] in addition to the processing differences expected in their experimentation.

Table 9.7: Summary of device results for glass/FTO/n-ZnS/n-CdTe/Au solar cells. The CdTe layers were heat treated with CdCl₂ and CdCl₂+CdF₂ treatment at 450°C for 12 minutes in air.

glass/FTO/n-ZnS/n-CdTe/Au								
Sample ID	CdCl ₂ only				CdCl ₂ +CdF ₂			
	V_{oc} (mV)	J_{sc} (mAcm ⁻²)	FF	η (%)	V_{oc} (mV)	J_{sc} (mAcm ⁻²)	FF	η (%)
CT283C	545	13.5	0.35	2.6	535	15.4	0.37	3.1
CT381C	479	6.8	0.31	1.0	444	11.0	0.31	1.5
CT386C	499	5.7	0.36	1.0	521	11.7	0.31	1.9
CT390C	452	9.1	0.30	1.2	474	10.2	0.32	1.5
CT395C	527	7.7	0.33	1.3	542	9.5	0.32	1.6
Sample ID	CdCl ₂ only		CdCl ₂ +CdF ₂		CdCl ₂ +CdF ₂		CdCl ₂ +CdF ₂	
	$R_s \times 10^4$ (Ω)	$R_{sh} \times 10^4$ (Ω)	$R_s \times 10^4$ (Ω)	$R_{sh} \times 10^4$ (Ω)	$R_s \times 10^4$ (Ω)	$R_{sh} \times 10^4$ (Ω)	$R_s \times 10^4$ (Ω)	$R_{sh} \times 10^4$ (Ω)
CT283C	4.41	2.26	3.52	3.15				
CT381C	3.56	3.21	3.44	4.42				
CT386C	8.86	1.34	6.36	1.68				
CT390C	3.73	2.97	3.49	3.06				
CT395C	3.75	1.82	3.62	3.12				

By comparing the R_s and R_{sh} values in Table 9.4 and 9.7, it can be seen that the devices fabricated using ZnS as window layer have higher R_s and lower R_{sh} values than those devices fabricated from the CdS as window layer. In addition, the results presented in Table 9.7 show that the devices heat treated with CdCl₂+CdF₂ treatment show lower R_s and higher R_{sh} values than those devices heat treated with CdCl₂ treatment alone.



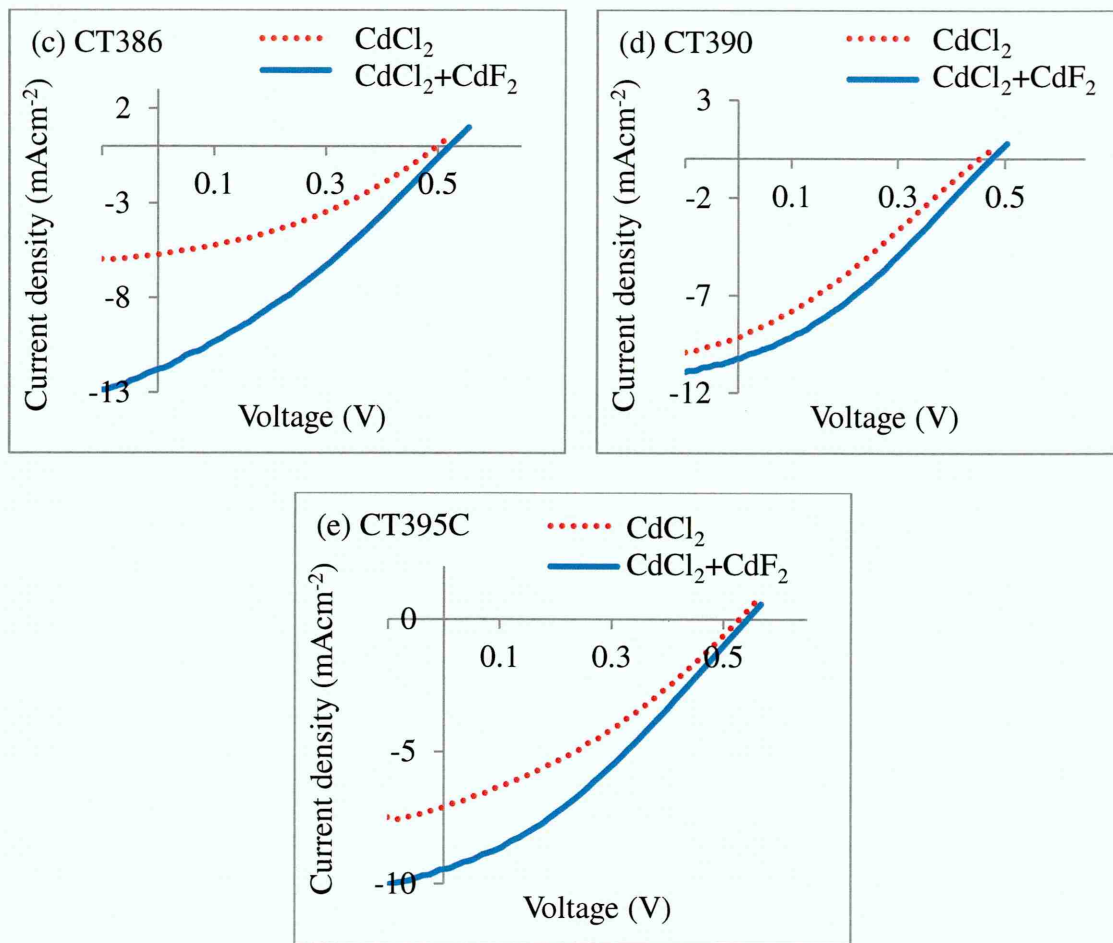


Figure 9.11: The comparison of J-V curves under illumination condition for glass/FTO/n-ZnS/n-CdTe/Au solar cells heat treated with CdCl_2 and $\text{CdCl}_2 + \text{CdF}_2$ treatment at 450°C for 12 minutes in air.

9.4 Fabrication of glass/FTO/n-CdS/n-CdTe/p-ZnTe/Au solar cells

One of the main issues in the device fabrication is the presence of pinholes in CdS/CdTe solar cells. The pinholes provide the shunting paths between the front and metal back contact and can drastically reduce the efficiency of the fabricated solar cells. In order to plug these pinholes, the thin pinhole-plugging layers (PPL) can be deposited on top of the absorber layer (CdTe) prior to metallisation. For this purpose, both organic and inorganic materials have been used as the pinhole-plugging layers. Some examples of the organic materials are polyaniline (PANI) [57-59], pyrrole [60] and cadmium stearate [61,62]. Whereas, the inorganic materials include the CaF_2 , SrF_2 and ZnTe [14]. By incorporating of the thin p-type layers (p-ZnTe) with bandgap larger than that of CdTe, the surface of the CdTe can be protected from reaction with metal contact [14].

Also, the p-ZnTe layer helps to bring the Fermi level close to the valence band and forms the larger potential barrier height (ϕ_{b2}) as shown in Figure 9.12. Therefore, the efficiency and durability of the device improves. Similarly, incorporation of an ultra-thin insulating layer can also be beneficial in decoupling of the CdTe layer from the metal contact by forming MIS type electrical contact. By using MIS contacts, also both lifetime and efficiency of the solar cells can be improved [63].

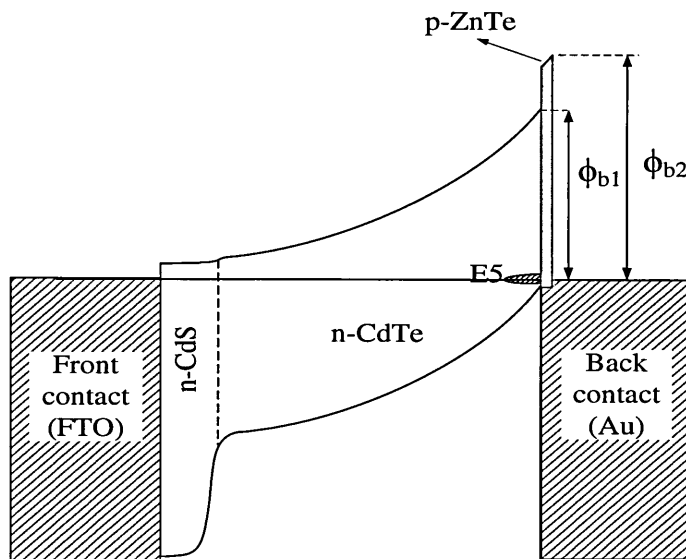


Figure 9.12: Energy band diagram of glass/FTO/n-CdS/n-CdTe/p-ZnTe/Au solar cell. Note the enhancement of barrier height ($\phi_{b2} > \phi_{b1}$) after inclusion of PPL.

The inclusion of the pinhole-plugging layer has been experimentally tested in this work. The first step was the preparation of glass/FTO/n-CdS/n-CdTe structures. The thickness of deposited n-CdS and n-CdTe were 80 nm and 1.50 μm respectively. Then, CdTe layers were heat treated with $\text{CdCl}_2 + \text{CdF}_2$ treatment at 450°C for 12 minutes in air. Subsequently, after etching of the CdTe surface, the p-ZnTe layers with different thicknesses of about 10, 13, 15, 18, 20 nm were grown on glass/FTO/n-CdS/n-CdTe substrates prior to metallisation. The device parameters and corresponding I-V curves of the fabricated glass/FTO/n-CdS/n-CdTe/p-ZnTe/Au solar cells are shown in Table 9.8 and Figures 9.13 (a)-(d). Results show that the incorporation of thick ZnTe layers with the thicknesses above ~ 13 nm has introduced extra series resistance into the device and resulted into poor device performance. When the thickness of ZnTe layer was reduced to ~ 10 nm, the device efficiency was increased from 2.7 to 5.1%. The main improvement was observed in the J_{sc} and FF of the device as shown in Table 9.8.

It should be noted that when the thickness of the ZnTe layer is optimum, all three device parameters improves.

Table 9.8: Results of J-V measurements for glass/FTO/n-CdS/n-CdTe/p-ZnTe/Au solar cells with and without inclusion of p-ZnTe layers as PPL for comparison.

Sample ID	ZnTe Thickness (nm)	Without ZnTe				With ZnTe			
		V_{oc} (mV)	J_{sc} (mAcm ⁻²)	FF	η	V_{oc} (mV)	J_{sc} (mAcm ⁻²)	FF	η (%)
394C1	20	497	7.6	0.39	1.5	446	3.8	0.24	0.4
394C2	18	492	7.2	0.38	1.4	462	4.1	0.31	0.6
394C3	15	497	6.4	0.35	1.1	493	6.0	0.27	0.8
304C1	13	541	13.4	0.32	2.3	572	7.8	0.35	1.6
304C2	10	569	9.4	0.51	2.7	560	16.6	0.54	5.1

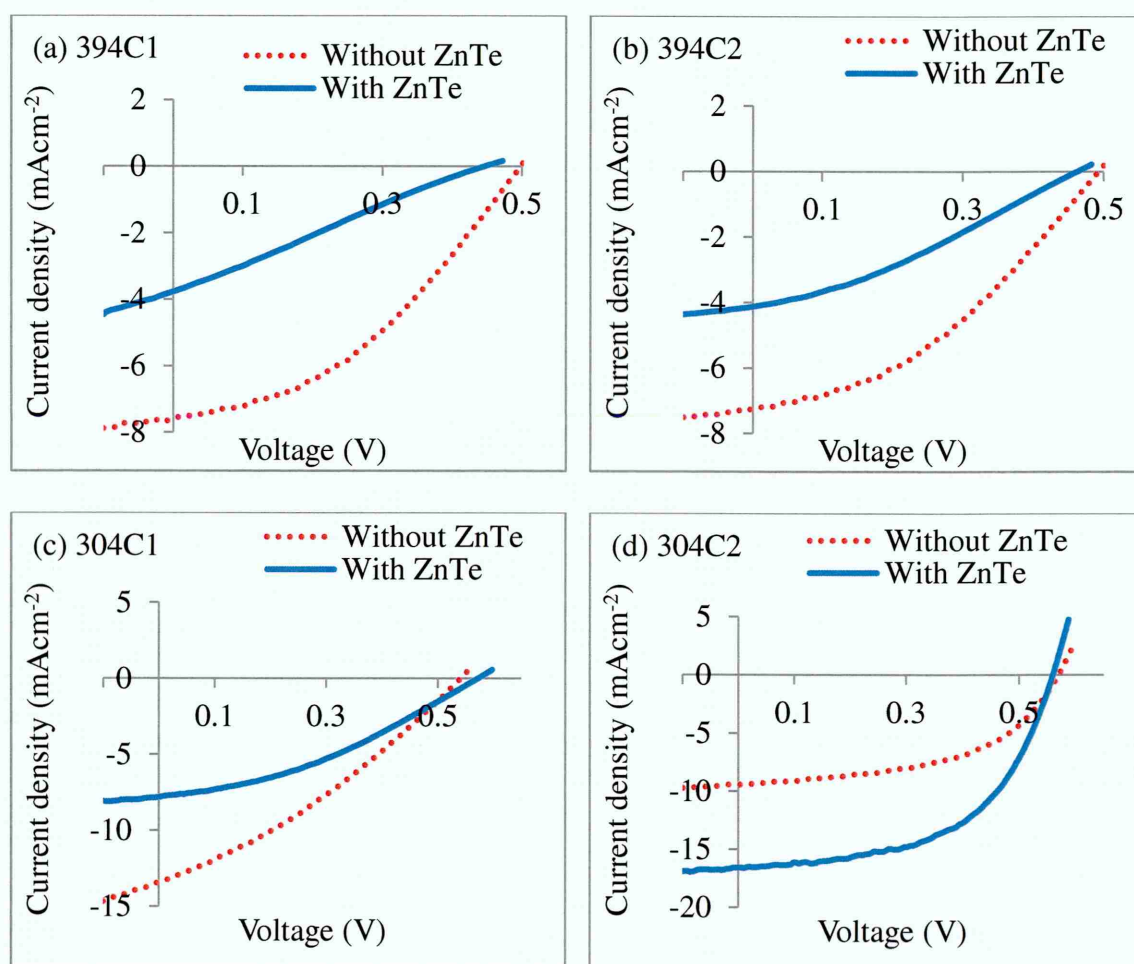


Figure 9.13: The comparison of light J-V curves for glass/FTO/n-CdS/n-CdTe/Au and glass/FTO/n-CdS/n-CdTe/p-ZnTe/Au solar cells.

In solar cells research and development process, most of the attentions have been paid on the simple p-n junctions fabricated by homo- or hetero-structures or p-i-n type devices [4,64-68]. In homo-junction a semiconductor with a single bandgap can only absorb the photons with energy greater or equal to the bandgap of the semiconductor. In the hetero-junction solar cells the absorption range of the photons are extended due to the presence of two different bandgap in the device. However, the effective way of harvesting photons from different parts of the solar spectrum is the multi-layer graded-bandgap structures. These structures consist of semiconductors with different energy bandgaps (E_g) arranged in such a way that the photons with different energies can be efficiently absorbed from different regions of the solar spectrum. With respect to two graded-bandgap device structures shown in Figure 9.14 (a) and (b), both devices start with the window material in the front with the higher energy bandgap of E_{g1} and end up with absorber materials in the back with a lower energy bandgap of E_{g2} [69,70]. The two structures show the gradual reduction in bandgaps from E_{g1} towards E_{g2} . It should be noted that, the structure starts with the p-type window layer in the front is more useful because the higher potential barrier height can be achieved, as shown in Figure 9.14 (b). This can increase the slope available for electron or the internal electric field available for separation of electrons within the device. Also, the directions of movement of the photo-generated charge carriers in two structures are different.

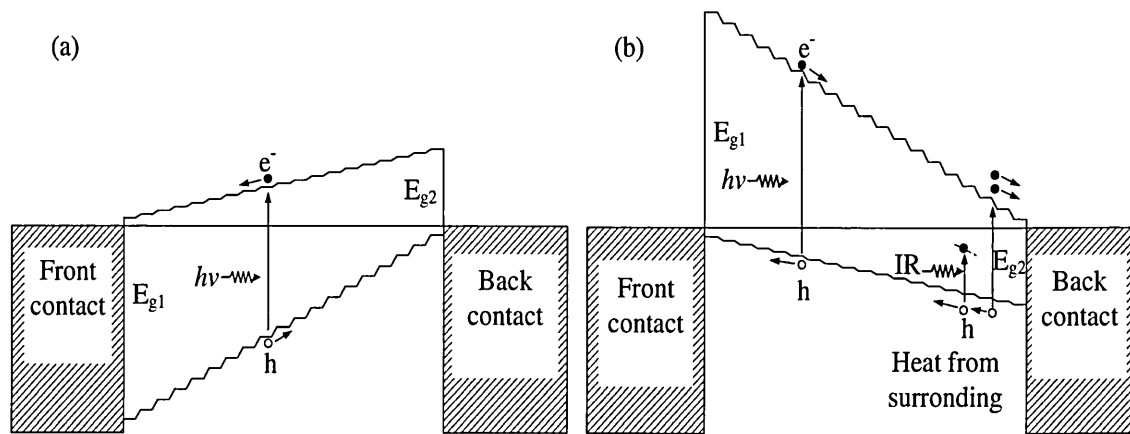


Figure 9.14: Energy band diagrams of the graded-bandgap solar cells with (a) n-type window material and (b) p-type window material. Note that, the higher potential barrier height for electrons can be achieved by using p-type window material. Redrawn from [69].

The main advantage of the graded-bandgap solar cells is that the photons from UV, visible and IR regions of the solar spectrum can be harvested due to the gradual grading of the energy bandgap. Also, the impact ionisation can be effectively incorporated in the graded-bandgap solar cells especially in the structure with p-type window material in the front contact [see Figure. 9.14 (b)]. When the photons with high energies create electron-hole pairs in the device, these charge carriers are separated quickly and accelerated toward the back and front contacts due to the presence of strong built-in electric field in the device. As the electron moves toward the back contact, it gains high kinetic energy across the device and may break the bond by transferring its energy to the electron bonded to atoms located at the rear of the device. This process is called band-to-band impact ionisation. In this case, a photon with high energy can create two electron-hole pairs. Also, the thermalisation effect in this device structure is minimised due to the presence of strong built-in electric field or the large slope of the energy band diagram and absorption of photons in an energy decreasing manner. It should be noted that, most of the semiconductors contain defects in their energy bandgap. Some of these defects are native defects and some can be externally introduced during the fabrication process. The defects can be minimised by optimising growth conditions and processing steps. However, the complete removals of these defects are not possible. In the graded-bandgap solar cells these defects can also be used in harvesting of the photons. The IR radiation or heat from the surroundings does not have enough energy to promote the electrons from valence band to the conduction band but this energy is enough to promote the electron from the valence band to defect levels or from one defect level to another defect level within the bandgap. The created hole by IR radiation will move quickly to the front contact due to the presence of the strong built-in potential and the shape of the energy band diagram as shown in Figure 9.14 (b). Then, relaxation process is not taking place and electron rests for a while in the defect levels. This electron can be promoted to other defect levels close to the conduction band or it can be directly promoted to the conduction band by gaining enough energy from upcoming IR radiation or high kinetic energy electrons generated by solar radiation. This process is known as the impurity PV effect. By combining both impact ionisation and the impurity PV effect processes in the graded-bandgap solar cells, the high current density (J_{sc}) and high efficiency can be achieved.

The graded-bandgap structure shown in Figure 9.14 (b) has been experimentally tested and verified by Dharmadasa *et al* [69] in 2005 using the AlGaAs grown by

MOCVD technique which is the second most researched material after Si. The device structure was p-i-n type AlGaAs graded-band gap solar cells. Within only two growths, device with the conversion efficiency of $\sim 20\%$ was achieved. The solar cells were tested and verified in five laboratories within the UK, Europe and US including NREL. This device showed the V_{oc} of 1175 mV which is the highest V_{oc} reported value for single devices. In their report it has been mentioned that the higher J_{sc} values and higher efficiency for this device is expected when the front contact have the optimum doping density of $\sim 10^{15} \text{ cm}^{-3}$. However, due to the presence of C in the MOCVD reactor it was not possible to obtain the right doping of density $\sim 10^{15} \text{ cm}^{-3}$ in the front contact and other growth techniques such as MBE should be used to achieve this goal. The impurity PV effect also has been verified by observing V_{oc} of 950 mV at complete darkness and IR collection in the responsivity curve [69].

Since the graded-bandgap structure has been tested and verified using expensive material and equipment, the aim of this work is to fabricate the multi-layer graded-bandgap solar cells using the low-cost electrodeposited semiconductor materials. In this thesis, the multi-layer graded-bandgap solar cells were fabricated using n-type window material [n-ZnS (ED) and n-CdS (ED & CBD)] in the front and n-type absorber material (n-CdTe) in the back which follows the energy band diagrams shown in Figures 9.2 and 9.14 (a).

9.5.1 Fabrication of glass/FTO/n-CdS(ED)/n-CdTe/p-CdTe/Au multi-layer graded-bandgap solar cells

Figure 9.15 shows the energy band diagram of glass/FTO/n-CdS(ED)/n-CdTe/p-CdTe solar cells. Also, Table 9.9 and Figures 9.16 (a)-(f) show the summary of the device results and typical J-V curves for the fabricated glass/FTO/n-CdS(ED)/n-CdTe/p-CdTe/Au solar cells. The thickness of the n-CdS, n-CdTe and p-CdTe were 80 nm, 1.5 μm and 200 nm respectively. Prior to etching process, the glass/FTO/n-CdS(ED)/n-CdTe/p-CdTe structures were heat treated with CdCl_2 and $\text{CdCl}_2 + \text{CdF}_2$ treatment at different temperatures of 350, 420 and 450°C for 12 minutes in air. After etching process, the device structures were completed by the evaporation of 100 nm Au with 2 mm diameter active device area on top of the glass/FTO/n-CdS(ED)/n-CdTe/p-CdTe.

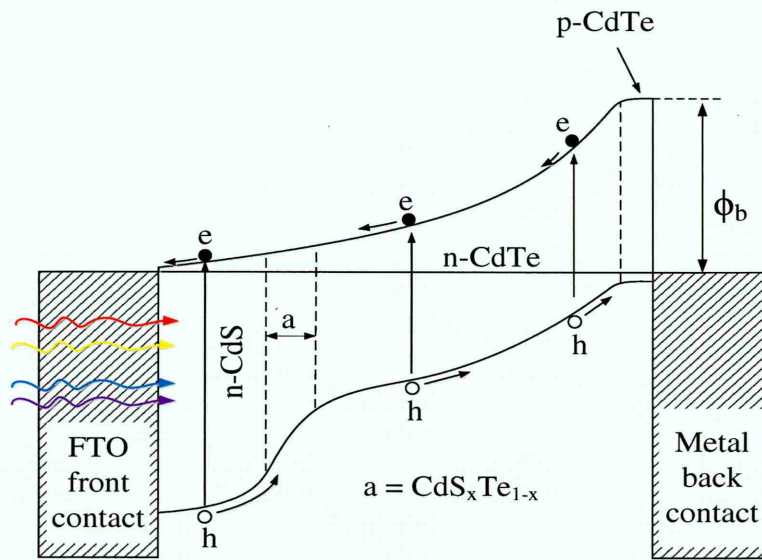


Figure 9.15: The energy band diagram of glass/FTO/n-CdS/n-CdTe/p-CdTe/Au solar cells. Note that the energy diagram is not to scale.

Results show the better device performances for the samples heat treated at high temperature of 450°C with CdCl₂ and CdCl₂+CdF₂ treatment as compared to other heat treatment temperatures as shown in Table 9.9. However, the devices heat treated with CdCl₂+CdF₂ treatment show better device performances than those heat treated with CdCl₂ alone. The observations indicates the low V_{oc} and low FF values in the range $\sim(212-550)$ mV and $\sim(0.26-0.30)$ for these devices respectively. The FF values were almost similar for all heat treatment conditions. The dark I-V curves of the all solar cell devices fabricated in this experiment show approximately ohmic behaviour. In this work, only the dark I-V curve of the samples heat treated with CdCl₂ and CdCl₂+CdF₂ at 450°C are presented [see Figures 9.17(a)-(d)]. Results show the high R_s and low R_{sh} values in the range $\sim(266-390)$ Ω and $\sim(256-431)$ Ω respectively for these devices which can be the main reason for the low FF and V_{oc} of the devices. In the high efficiency solar cells, the reported values for the R_s and R_{sh} are in the range $\sim(1-4)$ Ω and $\sim(2-5)\times 10^3\Omega$ respectively [26,42,65].

Also, for the most of the fabricated devices, high J_{sc} values in the range $\sim(33-58)$ mAcm⁻² were observed as shown in Table 9.9. However, for this set of samples after cells separation, the current density of these devices drop to lower values in the range $\sim(15-26)$ mAcm⁻². This shows that the peripheral collection of charge carriers around the edge of active area has taken place which creates errors in the measurement. The current collection from periphery is more pronounced when the active area of the device

is smaller [71]. Godfrey *et al* [72] has reported that when the active device area of about 0.01 cm^2 the peripheral collection will increase by 80%. This suggests that in order to obtain more accurate measurement, the active device area of the devices should be increased.

The high current densities of 38.5, 36.7 and 31.9 mAcm^{-2} with the cell efficiency of 8.0, 10.1 and 6.5% have also been reported by previous researcher in the Sheffield Hallam University [73-75]. These high current densities have been observed for glass/FTO/n-CdS/n-CdTe/Au solar cells structure using two and three-electrode systems from CdSO_4 and CdCl_2 precursors. In these situations, the high J_{sc} values did not drop indicating the genuine high current arising from some batches of devices.

Table 9.9: Summary of device results for glass/FTO/n-CdS(ED)/n-CdTe/p-CdTe/Au solar cells heat treated with CdCl_2 and $\text{CdCl}_2+\text{CdF}_2$ treatment at different temperatures of 385, 420 and 450°C for 12 minutes in air respectively.

385°C for 12 minutes								
Sample ID	CdCl_2 only				$\text{CdCl}_2 + \text{CdF}_2$			
	V_{oc} (mV)	J_{sc} (mAcm^{-2})	FF	η (%)	V_{oc} (mV)	J_{sc} (mAcm^{-2})	FF	η (%)
CT331A	257	18.8	0.26	1.3	282	20.3	0.27	1.5
CT334A	271	20.5	0.26	1.4	284	25.3	0.26	1.9
CT366A	324	31.7	0.26	2.6	353	36.4	0.26	3.3
CT369A	212	15.9	0.26	0.9	270	18.7	0.26	1.4
420°C for 12 minutes								
Sample ID	CdCl_2 only				$\text{CdCl}_2 + \text{CdF}_2$			
	V_{oc} (mV)	J_{sc} (mAcm^{-2})	FF	η (%)	V_{oc} (mV)	J_{sc} (mAcm^{-2})	FF	η (%)
CT331B	281	22.3	0.27	1.7	293	33.2	0.26	2.6
CT334B	249	15.2	0.27	1.0	314	34.6	0.26	2.9
CT366B	401	29.8	0.27	3.2	448	37.1	0.27	4.5
CT369B	280	31.7	0.26	2.3	306	34.2	0.26	2.7
450°C for 12 minutes								
Sample ID	CdCl_2 only				$\text{CdCl}_2 + \text{CdF}_2$			
	V_{oc} (mV)	J_{sc} (mAcm^{-2})	FF	η (%)	V_{oc} (mV)	J_{sc} (mAcm^{-2})	FF	η (%)
CT331C	306	37.3	0.27	3.2	374	58.3	0.27	6.0
CT334B	318	32.8	0.27	2.8	345	46.3	0.27	4.4
CT366C	522	41.0	0.30	6.4	550	43.6	0.30	7.5
CT369C	285	38.1	0.27	2.9	310	40.1	0.27	3.4

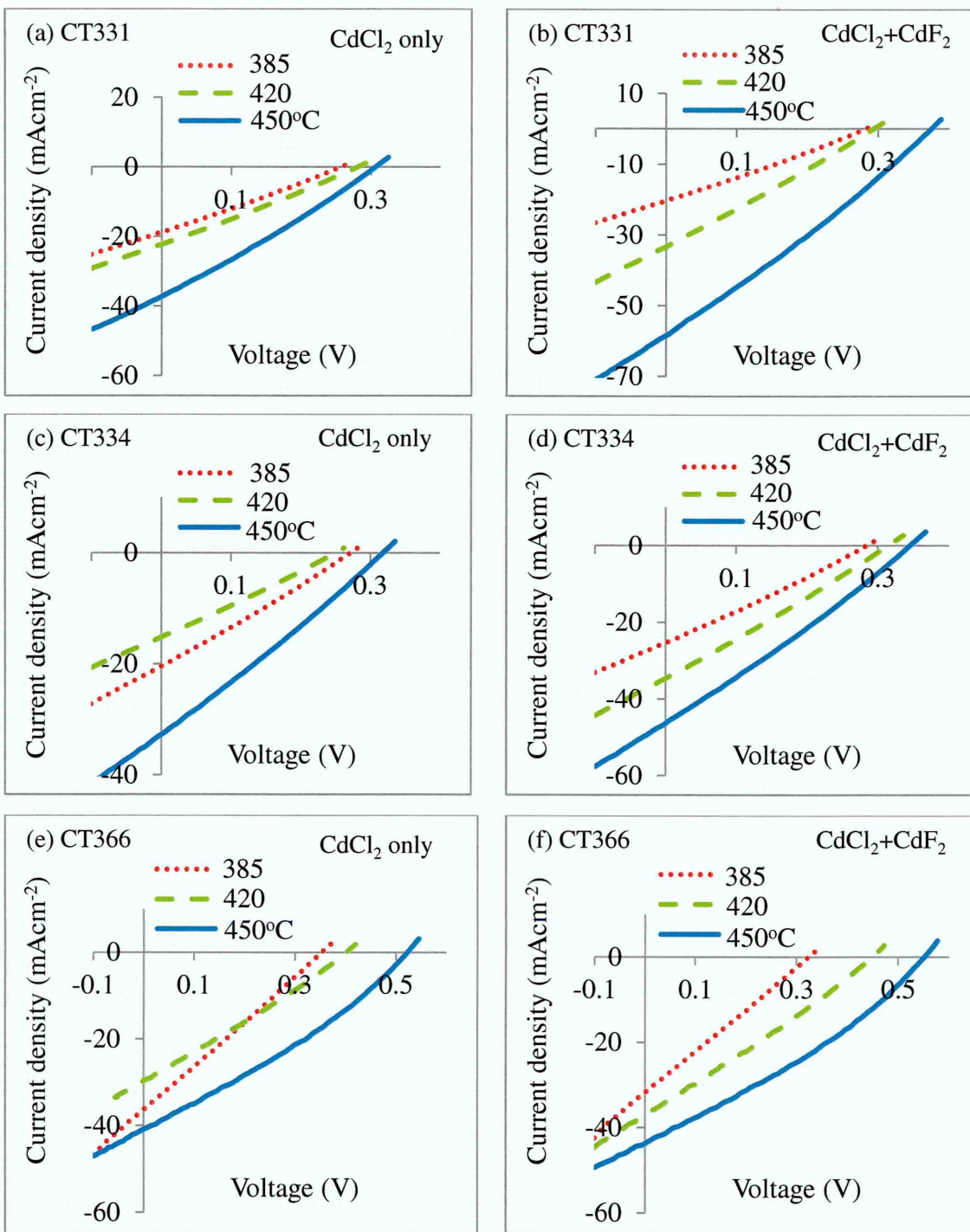


Figure 9.16: Comparison of J-V curves under illumination for glass/FTO/n-CdS(ED)/n-CdTe/p-CdTe/Au solar cells heat treated with CdCl₂ and CdCl₂+CdF₂ at different temperatures of 385, 420 and 450°C respectively.

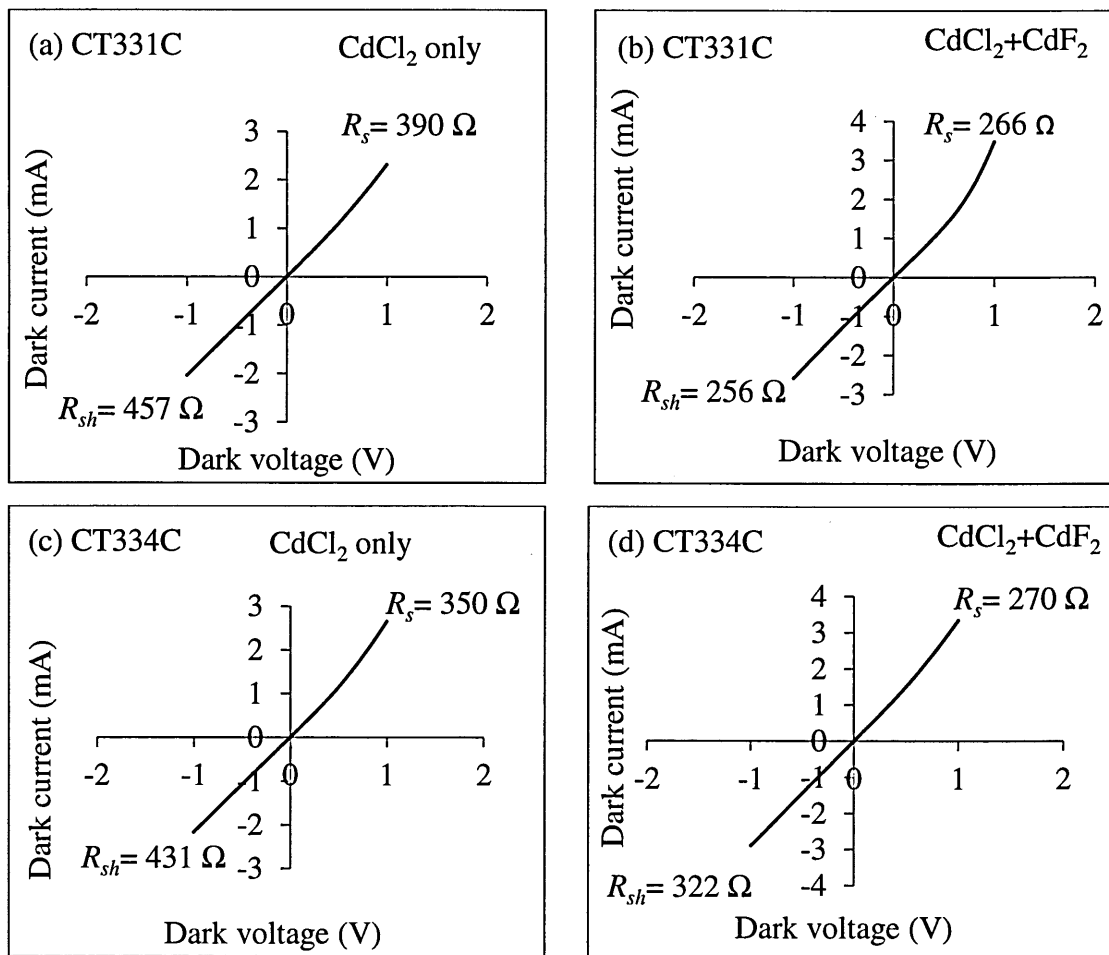


Figure 9.17: Dark I-V curves of the glass/FTO/n-CdS(ED)/n-CdTe/p-CdTe/Au solar cells heat treated with CdCl_2 and $\text{CdCl}_2 + \text{CdF}_2$ at 450°C for 12 minutes in air. Note the high R_s and low R_{sh} for the devices causing low efficiencies.

9.5.2 Fabrication of glass/FTO/n-CdS(CBD)/n-CdTe/p-CdTe/Au multi-layer graded-bandgap solar cells

Based on the experimental observation presented in the previous section, in this section also glass/FTO/n-CdS(CBD)/n-CdTe/p-CdTe/Au solar cells were fabricated. In the previous experiment ED-CdS was used as window material while in this experiment CBD-CdS was incorporated as window material. Also, the thickness of the p-type CdTe was reduced from ~ 200 nm to $\sim (70-80)$ nm between n-CdTe and Au back contact. The energy band diagram of the glass/FTO/n-CdS(CBD)/n-CdTe/p-CdTe/Au solar cells is similar to energy band diagram shown in Figure 9.15.

The summary of device results and related J-V curve of fabricated glass/FTO/n-CdS(CBD)/n-CdTe/p-CdTe/Au solar cells are shown in Table 9.10 and Figures 9.18 (a)-

(f). Results show the improvement in V_{oc} and FF and reduction in J_{sc} values as compared to the results previously shown in Table 9.9. The improvement in V_{oc} and FF are more pronounced when samples are heat treated with both $CdCl_2$ and $CdCl_2+CdF_2$ treatment at higher temperature of $450^\circ C$ for 12 minutes in air. The improvement in V_{oc} values shows the enhancement in the Schottky barrier height and change in the Fermi level pinning position closer to valence band. The improvement in FF can be attributed to the reduction in R_s and increase in R_{sh} values of the devices. The experimental J_{sc} values measured for these devices were in the range $(8.4-23.7) \text{ mAcm}^{-2}$ (see Table 9.9).

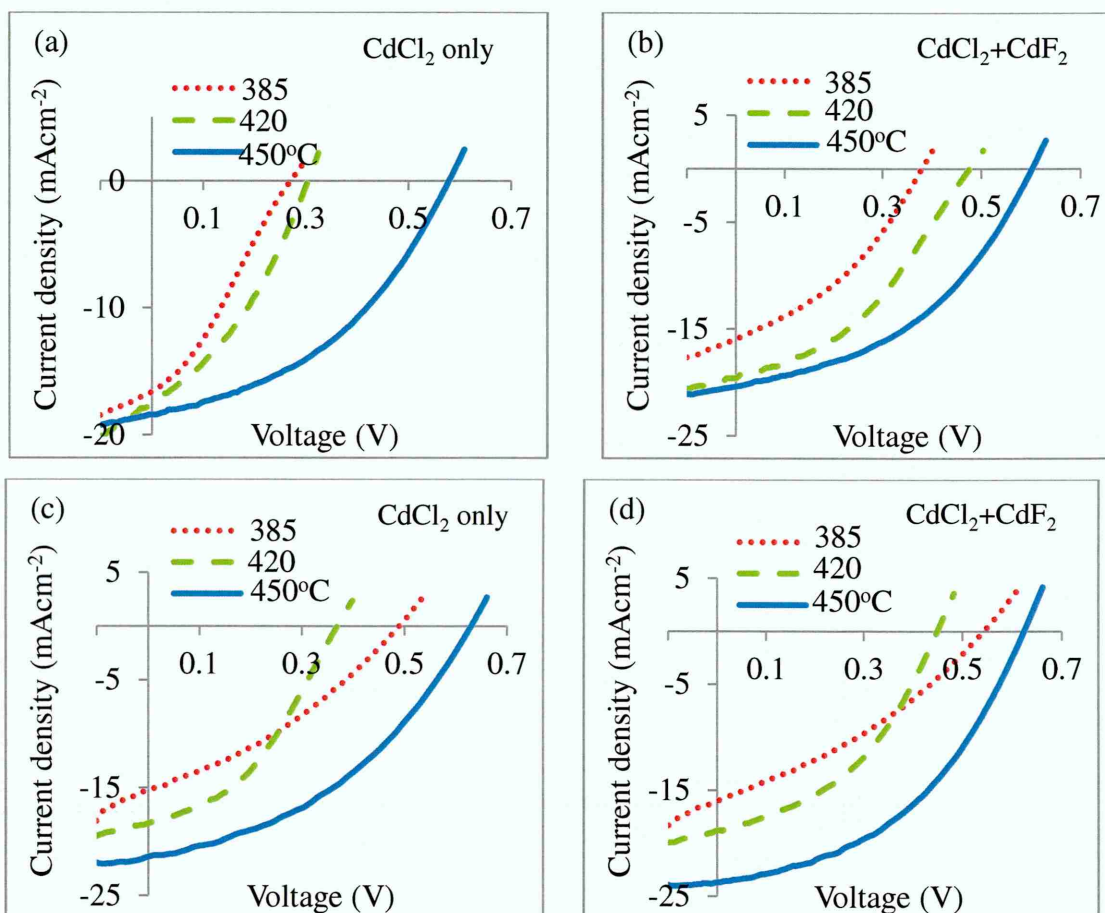
Table 9.10: Summary of device results for glass/FTO/n-CdS(CBD)/n-CdTe/p-CdTe/Au solar cells heat treated with $CdCl_2$ and $CdCl_2+CdF_2$ treatment at different temperatures of 385 , 420 and $450^\circ C$ respectively.

385°C for 12 minutes								
Sample ID	CdCl ₂ only				CdCl ₂ + CdF ₂			
	V_{oc} (mV)	J_{sc} (mAcm ⁻²)	FF	η (%)	V_{oc} (mV)	J_{sc} (mAcm ⁻²)	FF	η (%)
CT364A	272	16.5	0.30	1.3	379	16.0	0.36	2.2
CT365A	489	15.3	0.33	2.5	541	16.0	0.34	2.9
CT370A	537	11.7	0.32	2.0	541	13.3	0.31	2.3
CT373A	460	9.2	0.30	1.3	478	9.6	0.40	1.8
420°C for 12 minutes								
Sample ID	CdCl ₂ only				CdCl ₂ +CdF ₂			
	V_{oc} (mV)	J_{sc} (mAcm ⁻²)	FF	η (%)	V_{oc} (mV)	J_{sc} (mAcm ⁻²)	FF	η (%)
CT364B	305	17.5	0.35	1.9	476	19.5	0.39	3.6
CT365B	369	18.2	0.40	2.7	449	18.9	0.42	3.6
CT370B	522	20.2	0.42	4.5	489	23.7	0.40	4.7
CT373B	474	8.4	0.41	1.6	475	8.7	0.41	1.7
450°C for 12 minutes								
Sample ID	CdCl ₂ only				CdCl ₂ +CdF ₂			
	V_{oc} (mV)	J_{sc} (mAcm ⁻²)	FF	η (%)	V_{oc} (mV)	J_{sc} (mAcm ⁻²)	FF	η (%)
CT364C	578	18.4	0.41	4.4	601	20.3	0.43	5.3
CT365C	629	21.4	0.40	5.5	623	23.6	0.44	6.5
CT370C	550	20.1	0.48	5.3	546	23.4	0.46	5.8
CT373C	500	14.1	0.35	2.5	565	15.8	0.46	4.1

In this work, it has been experimentally observed that when the thickness of p-CdTe layer is more than 100 nm, the devices show ohmic behaviour while for p-CdTe

with the thicknesses less than 100 nm a good rectifying behaviour was observed. These results also show that the incorporation of thinner p-CdTe layer between n-CdTe and Au layers (<100 nm) results in the better device performances than those devices with a thicker (>100 nm) p-CdTe layer before metallisation.

In this experiment, the maximum cell efficiency of 6.5% was observed for the sample heat treated with $\text{CdCl}_2 + \text{CdF}_2$ treatment at 450°C for 12 minutes in air. However, the *FF* of the devices with incorporated (70-80) nm of p-CdTe still were lower than those devices without p-type CdTe as previously shown in Table 9.3 and 9.4. Therefore, more experiments are required to optimise p-CdTe thickness in the glass/FTO/n-CdS/n-CdTe/p-CdTe/Au configuration.



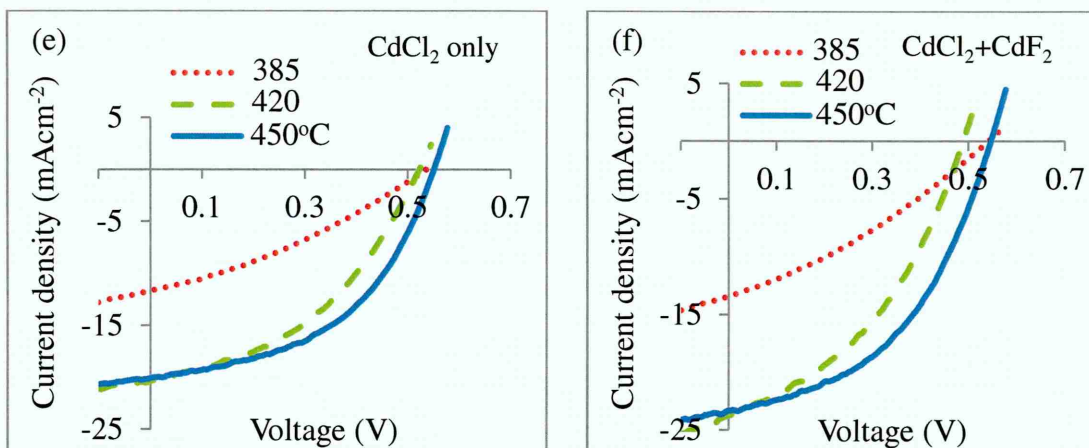


Figure 9.18: The comparison of light J-V curves of glass/FTO/n-CdS(CBD)/n-CdTe/p-CdTe/Au solar cells heat treated with CdCl_2 and $\text{CdCl}_2+\text{CdF}_2$ treatment at different temperatures of 385, 420 and 450°C respectively.

9.6 Fabrication of glass/FTO/n-ZnS/n-CdS(ED)/n-CdTe/Au multi-layer graded-bandgap solar cells

The energy band diagram of the glass/FTO/n-ZnS/n-CdS(ED)/n-CdTe/Au multi-layer graded-bandgap solar cells is shown in Figure 9.19. The ZnS layer with wide energy bandgap of the 3.70 eV was used as the front contact. The wider energy bandgap allow higher energy photons to be harvested in the solar cell device minimising thermalisation. As previously mentioned, the lattice mismatch at ZnS and CdTe interface is large, $\sim 16.4\%$ [55]. Also, the lattice mismatches at ZnS/CdS and CdS/CdTe interfaces are about 6.4% [76] and 10% [5] respectively. For this reason, the CdS layer as an intermediate material has been incorporated between ZnS and CdTe layers. During the heat treatment process, the $\text{Zn}_x\text{Cd}_{1-x}\text{S}$ and $\text{CdS}_x\text{Te}_{1-x}$ alloys form at ZnS/CdS and CdS/CdTe interfaces respectively which have been marked as regions “a” and “b” in Figure 9.19. The formation of these ternary alloys further helps in bandgap grading and also minimises the lattice mismatches and surface states at ZnS/CdS and CdS/CdTe interfaces. Also, the incorporation of CdS layer with the bandgap of 2.42 eV between ZnS and CdTe helps the effective harvesting of the photons from different parts of the solar spectrum. In the energy band diagram shown in Figure 9.19, when all conditions are satisfied the high conversion efficiency can be achieved. The main improvement in the efficiency will be due to the increase in the J_{sc} of the device due to the combination of impact ionisation, impurity PV effect, photon harvesting from UV, visible and near-

IR region of solar spectrum and graded-band gap structure of the device. This device structure is also capable of yielding the external quantum efficiency (EQE) over 100% due to the effects mentioned above [11,77,78].

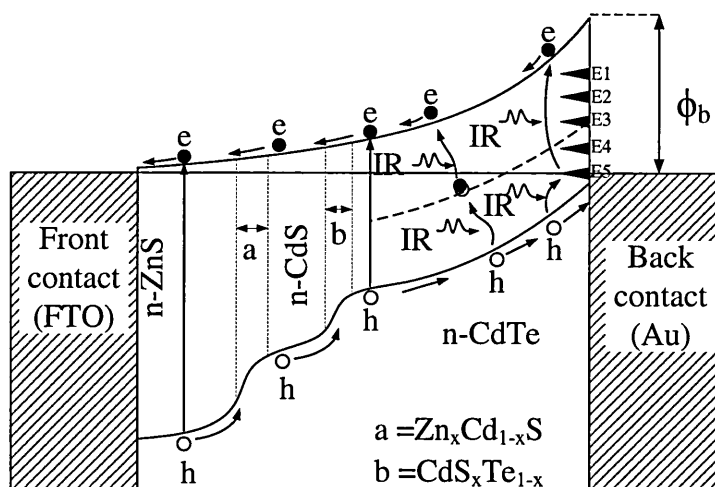


Figure 9.19: Typical energy band diagram of glass/FTO/n-ZnS/n-CdS/n-CdTe/Au multi-layer graded-bandgap solar cells. Redrawn from [1,14].

The preparation for this work starts with the growing of ~ 80 nm of n-ZnS layer on glass/FTO substrates. Then, n-ZnS layers were heat treated at 350°C for 10 minutes in air. Afterwards, ~ 80 nm of ED-CdS layers were grown on glass/FTO/ZnS substrates. The deposited CdS layers were then heat treated at 400°C for 20 minutes in air. Later, n-CdTe layers with the thickness of ~ 1.50 μm were grown on glass/FTO/n-ZnS/n-CdS substrates. The CdTe layers were then heat treated with CdCl_2 and $\text{CdCl}_2 + \text{CdF}_2$ treatment at 450°C for 12 minutes in air. The solar cell devices were then completed by etching and Au metallisation processes. The thickness of the evaporated Au back contact was ~ 100 nm. The summary of the device results is shown in Table 9.11.

Results show the efficiency values in the range of (2.1-3.6)% for glass/FTO/n-ZnS/n-CdS(ED)/n-CdTe/Au solar cells. These efficiency values were higher than those values observed for glass/FTO/ZnS/CdTe/Au solar cells as previously shown in Table 9.7. The lower performance of the glass/FTO/ZnS/CdTe/Au device can be due to the larger lattice mismatch between ZnS and CdTe. Also, these results show that the incorporation of CdS layer between ZnS and CdTe have improved the device performances due to the reduction of lattice mismatches between ZnS and CdTe layers and formation of graded-bandgap structure. It should be noted after inclusion of CdS

layer the main improvements were observed in J_{sc} and FF of the devices. This can be due to higher R_{sh} values of the glass/FTO/n-ZnS/n-CdS(ED)/n-CdTe/Au devices as compared to glass/FTO/n-ZnS/n-CdTe/Au solar cells as shown in Tables 9.11 and 9.7. The higher R_{sh} values after inclusion of CdS layer can also be related to the reduction of the pinholes in the device. The V_{oc} and R_s of both device structures were not shown noticeable differences.

There are reports on the improvement of the solar cell performances after incorporation of CdS layer between ZnS and CdTe layers. Han *et al* [79] has reported the improvement in the conversion efficiency from 9.53% for CdS/CdTe structure to 10.3% for ZnS/CdS/CdTe structure. Liu *et al* [80] has also reported the improvement in the conversion efficiency from 8.6 % to 9.6% using the similar device structure. Their report show the main improvement were in the J_{sc} and FF of the dvice. Echendu *et al* [81] has also reported that the incorporation of ZnS layer as buffer/window material with CdS/CdTe layers results in the improvement in the conversion efficiency from ~8.0% to >10% using all electrodeposited semiconductors.

Table 9.11: Summary of device results for glass/FTO/n-ZnS/n-CdS(ED)/n-CdTe/Au solar cells heat treated with CdCl₂ and CdCl₂+CdF₂ at 450°C for 12 minutes in air.

glass/FTO/n-ZnS/n-CdS(ED)/n-CdTe/Au								
Sample ID	CdCl ₂ only				CdCl ₂ +CdF ₂			
	V_{oc} (mV)	J_{sc} (mAcm ⁻²)	FF	η (%)	V_{oc} (mV)	J_{sc} (mAcm ⁻²)	FF	η (%)
CT387	523	13.0	0.41	2.8	529	14.2	0.42	3.2
CT391	501	14.8	0.46	3.4	543	16.5	0.40	3.6
CT392	474	9.6	0.42	1.9	500	14.1	0.35	2.5
CT396	541	12.8	0.46	3.2	556	14.0	0.43	3.3
CT397	550	8.7	0.44	2.1	568	12.9	0.43	3.2
Sample ID	CdCl ₂ only		CdCl ₂ +CdF ₂		CdCl ₂ +CdF ₂		CdCl ₂ +CdF ₂	
	$R_s \times 10^4$ (Ω)	$R_{sh} \times 10^6$ (Ω)	$R_s \times 10^4$ (Ω)	$R_{sh} \times 10^6$ (Ω)	$R_s \times 10^4$ (Ω)	$R_{sh} \times 10^6$ (Ω)	$R_s \times 10^4$ (Ω)	$R_{sh} \times 10^6$ (Ω)
CT387	5.53	2.23	3.69	2.41				
CT391	3.04	1.02	0.67	5.27				
CT392	7.07	1.45	1.37	1.64				
CT396	1.58	2.06	5.73	2.56				
CT397	4.04	1.89	3.39	4.12				

The glass/FTO/n-CdS/n-CdTe/Au solar cells were successfully fabricated using low-cost electrodeposited CdS and CdTe and CBD-CdS semiconductor materials. The conversion efficiency of 7.1% and 6.6% were obtained using CBD-CdS and ED-CdS layers as window materials respectively. The electrodeposition of the CdS and CdTe layers were carried out using 2-electrode system. Also, the devices fabricated using CBD-CdS layers as window material showed better FF and conversion efficiencies than those devices fabricated using ED-CdS layers. The combination of acidic and alkaline solutions in CdTe surface etching process were found to yields better device performance than those layers etched with acidic or alkaline solutions alone.

The experimental observation showed that when layers are heat treated with the combination of $\text{CdCl}_2 + \text{CdF}_2$ treatment at temperature of 450°C for 12 minutes in air, the device performances further improves as compared to layers heat treated with CdCl_2 treatment alone.

The p-ZnTe layers were used as pinhole plugging layer to improve the Schottky barrier height, device parameters and stability of the glass/FTO/n-CdS/n-CdTe/p-ZnTe/Au solar cells. The positive effect of the inclusion of the p-ZnTe layer was observed when the layer thickness was less than ~ 13 nm.

The inclusion of p-CdTe layer between n-CdTe and Au metal contact were also found to be beneficial in improving the device performance of multi-layer graded-bandgap solar cells with glass/FTO/n-CdS/n-CdTe/p-CdTe/Au structure. Also, it was observed that the thickness of p-CdTe layer should be thin enough (less than 100 nm) in order to see the positive effect in the device performances with rectifying behaviour otherwise it reduces the efficiency due to high R_s and low R_{sh} (with observed ohmic behaviour).

The glass/FTO/n-ZnS/n-CdTe/Au devices fabricated using n-ZnS layer as window material showed low efficiencies due to large lattice mismatch between ZnS and CdTe layers. The device performance improvements were observed when CdS layer were included between ZnS and CdTe layers. The multi-layer garded-band gap solar cell with structure of glass/FTO/n-ZnS/n-CdS/n-CdTe/Au showed better device performances than those devices with glass/FTO/n-ZnS/n-CdTe/Au solar cell structure. The main improvements after inclusion of CdS between ZnS and CdTe layers were

observed in the FF and J_{sc} of the devices due to increase in R_{sh} (reduction of pinholes or leakage paths).

Preliminary results of C-V measurements in this work indicate that the best devices have doping densities of the order of $\sim 6.50 \times 10^{15}$ to $\sim 1.30 \times 10^{16} \text{ cm}^{-3}$.

9.8 References

- [1] I.M. Dharmadasa, A.P. Samantilleke, N.B. Chaure and J. Young, *Semicond. Sci. Technol.*, **17** (2002) 1238-1248.
- [2] Z. Sobiesierski, I.M. Dharmadasa, and R.H. Williams, *Applied Physics Letters* **53** (1988) 2623-2625.
- [3] I.M. Dharmadasa, *Prog. Crystal Growth and Charact.* **36**(4) (1998) 249-290.
- [4] I.M. Dharmadasa, C.J. Blomfield, C.G. Scott, R. Coratger, F. Ajuston and J. Beauvillain, *Solid-State Electronics*, **42**(4) (1998) 595-604.
- [5] A. Bosio, N. Romeo, S. Mazzamuto, and V. Canevari, *Progress in Crystal Growth and Characterization of Materials*, **52** (2006) 247-279.
- [6] G. Gordillo and E. Romeo, *Thin Solid Film*, **484** (2005) 352-357.
- [7] D.W. Lane, *Solar Energy Materials & Solar Cells*, **90** (2006) 1169-1175.
- [8] M.A. Santana-Aranda, M. Malendez-Lira, *Applied Surface Science*, **175-176** (2001) 538-542.
- [9] I.M. Dharmadasa, J.S. Roberts and G. Hill, *Solar Energy Materials & Solar Cells*, **88** (2005) 413-422.
- [10] I.M. Dharmadasa, N.B. Chaure, G.J. Tolan and A.P. samantilleke, *J. Electrochem. Soc.*, **154**(6) (2007) H446-H471.
- [11] I.M. Dharmadasa, A.A. Ojo, H.I. Salim and R. Dharmadasa, *Energies*, **8** (2015) 5440-5458.
- [12] N.B. Chaure, A.P. Samantilleke, I.M. Dharmadasa, *Solar Energy Materials & Solar Cells*, **77** (2003) 303-317.
- [13] I.M. Dharmadasa, J.M. Thornton, and R.H. Williams, *Appl. Phys. Lett.*, **54** (1989) 137-139.
- [14] I.M. Dharmadasa, *Advances in Thin-Films Solar Cells*, Pan Stanford Publishing Pte. Ltd, Boulevard, Singapore, (2012) 15-16.
- [15] I.M. Dharmadasa, O.K. Echendu, F. Fauzi N.A. Abdul-Manaf, H.I. Salim, T. Druffel, R. Dharmadasa and B. Lavery, *J. Mater. Sci: Mater. Electron.*, **26** (2015) 4571-4583.
- [16] N. Romeo, A. Bosio, R. Tedeschi, A. Romeo, V. Canevari, *Solar Energy Materials & Solar Cells*, **58** (1999) 209-218.
- [17] M. Rami, E. Benamar, M. Fahoume, F. Chraibi and A. Ennaoui, *M. J. Condensed Matter*, **3**(1) (2000) 66-70.

- [18] J. Fritsche, S. Gunst, E. Golusda, M. C. Lejard, A. Thißen, T. Mayer, A. Klein, R. Wendt, R. Gegenwart, D. Bonnet and W. Jaegermann, *Thin Solid Films*, **387** (2001) 161-164.
- [19] B.E. McCandless, K.D. Dobson, *Solar Energy*, **77** (2004) 839–856.
- [20] J. Quadros, A.L. Pinto, H.R. Moutinho, R.G. Dhere and L.R. Cruz, *J. Matr. Sci.*, **43** (2008) 573-579.
- [21] A. Abbas, G.D. West, J.W. Bowers, P. Isherwood, P.M. Kaminski, B. Maniscalco, P. Rowley, J.M. Walls, K. Barricklow, W.S. Sampath and K.L. Barth, *IEEE Journal of Photovoltaics*, **3**(4) (2013) 1361-1366.
- [22] A. Romeo, S. Buecheler, M. Giarola, G. Mariotto, A.N. Tiwari, N. Romeo, A. Bosio, S. Mazzamuto, *Thin Solid Film*, **517** (2009) 2132-2135.
- [23] E.R. Hernandez, V. Rejon, I. Riech, M. Acosta, J.L. Pena, *Solar Energy*, **107** (2014) 305-313.
- [24] O. Zywitzki, T. Modes, H. Morgner, C. Metzner, B. Siepchen, B. Spath, C. Drost, V. Krishnakumar, and S. Frauenstein, *Journal of Applied Physics*, **114** (2013) 163518.
- [25] B.E. McCandless, R.W. Birkmire, in: *Proceedings of the 16th European Photovoltaic Solar Energy Conference and Exhibition*, (2000) 349-352.
- [26] A.R. Flores, O. Ares, J.M. Camacho, V. Rejon, J.L. Pena, *Solar Energy*, **86** (2012) 780-785.
- [27] V. Rejon, I. Riech, J.L. Pena, *Solar Energy*, **95** (2013) 319-324.
- [28] O.K. Echendu and I.M. Dharmadasa, *Materials Chemistry and Physics*, **157** (2015) 39-44.
- [29] M.J. Kim, S. Sohn and S. Lee, *Sol. Energy Mat. Sol. Cells*, **95** (2011) 2295-2301.
- [30] I.M. Dharmadasa, P.A. Bingham, O.K. Echendu, H.I. Salim, T. Druffe, R. Dharmadasa, G.U. Sumanasekera, R.R. Dharmadasa, M.B. Dergacheva, K.A. Mit, K.A. Urazov, L. Bowen, M. Walls and A. Abbas, *Coating*, **4** (2014) 380-415.
- [31] R. Dharmadasa, B.W. Lavery, I.M. Dharmadasa, T. Druffel, *J. Coat. Technol. Res.*, **12**(5) (2015) 835–842.
- [32] J. Hiie, *Thin Solid Film*, **431-432** (2003) 90-93.
- [33] <http://www.pveducation.org/pvcdrom/solar-cell-operation/series-resistance>, Last accessed January (2016).

- [34] <http://www.pveducation.org/pvcdrom/solar-cell-operation/shunt-resistance>, Last accessed January (2016).
- [35] A. Rao, S. Krishnan, G. Sanjeev and K. Siddappa, *International Journal of Pure and Applied Physics*, **5**(1) (2009) 55-62.
- [36] O.K. Echendu, F. Fauzi, A.R. Weerasinghe and I.M. Dharmadasa, *Thin Solid Films*, **556** (2014) 529-534.
- [37] C. Bhattacharya and J. Datta, *J. Solid State Electrochem.*, **11** (2007) 215-222.
- [38] O. Almora-Rodriguez, L. Vaillant, and A. Bosio, *Rev. Cub. Fis.*, **31** (2014) 66.
- [39] D.A. Cusano, *Solid-state Electronics*, **6** (1963) 217-232.
- [40] T.L. Chu, S.S. Chu, S.T. Ang, and M.K. Mantravadi, *Solar Cells*, **21** (1987) 73-80.
- [41] J. Baker, S.P. BINNS, D.R. Johnson, R.J. Marshall., S. Oktik, M.E. Ozsan, M.H. Patterson, S.J. Ransome, S. Roberts, M. Sadegh, J. Sherborne, A.K. Turner and J.M. Woodcock, *Int. J. Solar Energy*, **12** (1992) 79-94
- [42] J. Britt and C. Ferekides, *Appl. Phys. Lett.*, **62**(22) (1993) 2851-2852.
- [43] M. Gloeckler, I. Sankin, and Z. Zhao, *IEEE J. Photovolt.*, **3**(4) (2013) 1389-1393.
- [44] B.M. Basol, and B. Mc.Candless, *Journal of Photonics for Energy*, **4** (2014) 040996-1.
- [45] R. Mendoza-Perez, J. S. Hernandez, G. C. Puente and V. Galan, *Solar Energy Materials and Solar Cells*, **93** (2009) 79-84.
- [46] C.S. Ferekides, V. Viswanathan and D.L. Morel, *26th Photovoltaic Solar Energy Conference, Anaheim*, (1997) 423-426.
- [47] T.A. Gessert, P. Sheldon, X. Li, D. Dunlavy, D. Niles, R. Sasala, S. Albright, and B. Zadler, *26th Photovoltaic Specialists Conference, Anaheim, Conference record of the 26th IEEE Publication*, (1997) 419-422.
- [48] J. Tang, D. Mao, T.R. Ohno, V. Kaydanov, J.U. Trefny, *26th Photovoltaic Specialists Conference, Anaheim, Conference record of the 26th IEEE Publication*, (1997) 439-442.
- [49] N. Romeo, A. Bosio, and V. Canevari, *Int. J. Sustainable Energy*, **12**(1-4) (1992) 183-186.
- [50] A. Nimegeers, M. Burgelmann, *J. Appl. Phys.*, **81**(6) (1997) 2881-2886.
- [51] D.L. Bätzner, A. Romeo, H. Zogg, A.N. Tiwari, and R. Wendt, *16th European Photovoltaic Solar Energy Conference, Glasgow*, (2000).

- [52] K.D. Dobson, I. Visoly-Fisher, G. Hodes, and David Cahen, *Solar Energy Materials & Solar Cells*, **62** (2000) 295-325.
- [53] V. Dimitrova, J. Tate, *Thin Solid Films*, **365**(1) (2000) 134-138.
- [54] T.L. Chu and S.S. Chu, *Solid-State Electronics*, **38**(3) (1995) 533-549.
- [55] I.C. Yan, F. Tang, L. Li, H. Li, X. Huang, D. Chen, X. Meng, and J. Ren, *Nanoscale Res. Lett.*, **5** (2010) 189-194.
- [56] J.M. Dona and J. Herrero, *J. Electrochem. Soc.*, **141**(1) (1994) 205-210.
- [57] Y. Roussillon, D.M. Giolando, D. Shvydka, A.D. Compañ and V.G. Karpov, *Applied Physics Letters*, **84** (2004) 616-618.
- [58] M.M. Tessema and D.M. Giolando, *Sol. Energy Materials & Sol. Cells*, **107** (2012) 9-12.
- [59] N.A. Abdul-Manaf, O.K. Echendu, F. Fauzi, L. Bowen and I.M. Dharmadasa, *Journal of Electronic Materials*, **43** (2014) 4003-4010.
- [60] D.K. Koll, A.H. Taha and D.M. Giolando, *Solar Energy Materials & solar cells*, **95** (2011) 1716-1719.
- [61] M.C. Petty, and G.G. Robert, *Electron. Lett.*, **15** (1979) 335-336.
- [62] I.M. Dharmadasa, G.G. Roberts and M.C. Petty, *Electronic Letters*, **16** (1980) 201-202.
- [63] I.M. Dharmadasa, A.P. Samantilleke, J. Young and N.B. Chaure, *Proceeding of the 3rd World Conference on Photovoltaic Energy Conversion*, Osaka, Japan, pp.495-498.
- [64] L. Huang, Y. Zhao, D. Cai, *Materials Letters*, **63** (2009) 2082-2084.
- [65] X. Wu, *Solar Energy*, **77** (2004) 803-804.
- [66] C.S. Ferekides, D. Marinskiy, V. Viswanathan, B. Tetali, V. Palekis, P. Selvaraj, D.L. Morel, *Thin Solid Films*, **361-362** (2000) 520-526.
- [67] P. V. Meyers, *Solar Cells*, **27** (1989) 91-98.
- [68] V. Ramanathan, L.A. Russell, C.H. Liu and P.V. Meyers, *Solar Cells*, **28** (1990) 129-133.
- [69] I.M. Dharmadasa, J.S. Roberts and G. Hills, *Solar Energy Materials & Solar Cells*, **88** (2005) 413-422.
- [70] I.M. Dharmadasa, A.A. Ojo, H.I. Salim and R. Dharmadasa, *Energies*, **8** (2015) 5440-5458.
- [71] R. Singh, G.L. Alapatt and A. Lakhtakia, *IEEE Journal of the Electron Devices Society*, **1**(6) (2013) 129-144.

- [72] R.B. Godfrey and M.A. Green, *Appl. Phys. Lett.*, **31**(10) (1977) 705-707.
- [73] O.K. Echendu, *Thin film solar cells using all-electrodeposited ZnS, CdS and CdTe materials*, (PhD Thesis), Sheffield Hallam University (2014).
- [74] F. Fauzi, *Research and Development of CdS/CdTe solar cells incorporating ZnTe layers*, (PhD Thesis), Sheffield Hallam University (2015).
- [75] N.A. Abdul-Manaf, *Organic/Inorganic Hybrid Solar Cells Based on Electroplated CdTe*, (PhD Thesis), Sheffield Hallam University (2015).
- [76] L.W. Liu, S.Y. Hu, Y. Pan, J.Q. Zhang, Y.S. Feng, and X.H. Zhang, *Beilstein J. Nanotechnol.*, **5** (2014), 919-926.
- [77] N.J.L.K. Davis, M.L. Böhm, M. Tabachnyk, F. Wisnivesky-Rocca-Rivarola, T.C. Jellicoe, C. Ducati, B. Ehrler and N.C. Greenham, *Nature Communications*, **6**(8259) (2015) 1-7.
- [78] D.N. Congreve, J. Lee, N.J. Thompson, E. Hontz, S.R. Yost, P.D. Reuswig, M.E. Bahlke, S. Reineke, T.V. Voorhis, and M.A. Baldo, *SCIENCE*, **340** (2013) 334-337.
- [79] J. Han, G. Fu, V. Krishnakumar, C.Liao, W. Jaegermann and M.P. Besland, *Journal of Physics and Chemistry of Solids*, **74** (2013)1879-1883.
- [80] B. Liu, R. Luo, Q. Liang, Y. Zheng, B. Li, J. Zhang, W. Li, L. Wu and L. Feng, *J. Mater. Sci: Mater. Electron.*, **26** (2015) 9985-9990.
- [81] O.K. Echendu and I.M. Dharmadasa, *Energies*, **8** (2015) 4416-4435.

10.1 Introduction

The solar cells are considered as one of the key technologies towards the sustainable energy resource. This technology can be classified mainly into three generations. The “first generation solar cells” are the oldest and the most commonly used technology. This type of solar cells include crystalline silicon (c-Si) and multi-crystalline silicon (mc-Si) which currently dominates the PV market with 90% of total cells [1]. These types of solar cells have relatively high efficiencies and production cost. The power conversion efficiencies of these types of solar cells are still lower than 31% theoretical Shockley-Queisser limit for single bandgap solar cells. This is because single junction solar cells can only absorb a short range of solar spectrum.

The “second generation solar cells” or thin film solar cells contain solar cells that are about 100 times thinner and larger than Si PV wafer. The power conversion efficiencies of the second generation solar cells are lower than first generation solar cells. However, the second generation solar cells have much more cost effective technology than the first generation solar cells. The second generation solar cells include CdTe, CIGS and a-Si which account for around 5-6% of the PV market and is moving forward [1]. In second generation solar cells, semiconductor material with different bandgaps are utilised to harvest photons in a more efficient way in the solar spectrum. However, the power conversion efficiencies of thin film solar cells are still below the Shockley-Queisser limit. Therefore, further research and developments are required in order to reach and exceed this limit.

The “third generation solar cells” or the next generation solar cells cover a broad range of materials, devices and innovative concepts that are still in experimental stage of research and development. These types of solar cells are promising but not commercially proven yet. The main aim of the next generation solar cells is to overcome the theoretical Shockley-Queisser limit of power conversion efficiency for single bandgap solar cells and also to bring down the production cost [1, 2]. In the following sections some suggested next generation solar cells are presented and discussed.

10.2 Intermediate band (IB) solar cells

In a single junction solar cell with an absorber material of energy bandgap E_g , only photons with the energy higher than energy bandgap $\geq E_g$ are absorbed whereas photons with energy $< E_g$ are transmitted. In order to harvest the sub-bandgap energy photons, a narrow band of states, the intermediate band (IB), is added between the VB and CB of the absorber material. In an IB material, the photon with energy $< E_g$ are absorbed through transitions from the VB to the IB and from the IB to the CB, which together add up to the current produced by photons absorbed through VB to CB transition as shown in Figure 10.1 [3]. The theoretical calculations for a single bandgap show the maximum efficiency of 63% for IB solar cells under concentrated sunlight and 48% under one sun. In these calculations, the temperatures of the sun and earth were assumed to be 6,000 K and 300 K respectively [2,3]. In the IB solar cell, the total optimal bandgap is 1.95 eV which is split to two sub-band gap of ~ 0.71 eV and ~ 1.24 eV. Therefore, the maximum open-circuit photovoltage of IB solar cells is limited to 1.95 V [3].

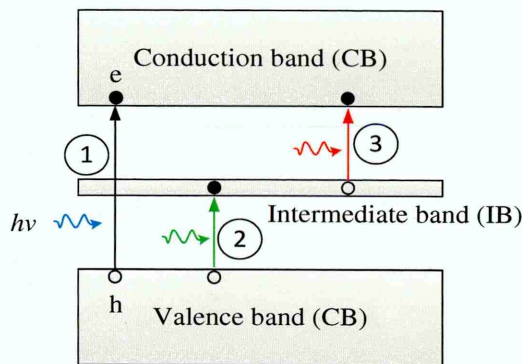


Figure 10.1: Schematic diagram of the intermediate (IB) solar cells. The electron transitions take place from (1) VB to CB, (2) VB to IB, and (3) IB to CB. Note that the recombination process in this diagram is neglected.

The idea of IB solar cell is similar to the impurity PV effect which has been proposed by Wolf in 1960 [4]. It should be noted that the idea of IB solar cells is proposed to increase the efficiency of the solar cells by increasing the photocurrent. However, the efficiency of the IB solar cells have not yet approached those of good single junction solar cells [5]. The possible reason can be due to the fact that IB can act as the recombination centres for photogenerated charge carriers. Therefore, the shape of

the energy band diagram should be engineered in such a way that the existing built-in potential separates the photogenerated charge carrier before their recombination. Most of the theoretical calculation only take into account the positive contribution from low wavelength photons, but increases the detrimental high rates of recombination introduced by the IB. The fact that no practical devices showing high efficiencies with IB have been produced since 1960's show that introduction of IB is not good idea for development of high efficiency devices.

10.3 Quantum dot/quantum well solar cells

The main purpose of incorporation of quantum dots and quantum wells in the solar cells is to enhance the absorption of the sub-bandgap energy photons. This approach is expected to enhance the photocurrent in the device and eventually increase the efficiency of the solar cell [6]. An important property of the quantum dots is that the energy bandgap (E_g) of the quantum dots can be tuned to absorb specific wavelength of the light. This can be done by controlling the size of the quantum dots during synthesis. Also, the E_g of the quantum dots can be tuned by controlling their composition. For example, in CdSSe quantum dot with a typical size of 4.5 nm, by changing the amount of Se in the CdSSe quantum dot the bandgap can be controlled. The smallest amounts of Se in the quantum dot lead to the formation of largest bandgap which can absorb the shortest wavelength of light.

Theoretical calculation shows that the efficiency limit of the quantum dot and quantum well solar cells for a single bandgap junction is about 40% [7,8]. There are many reports on the incorporation of quantum dots and quantum well materials in the first generation and second generation solar cells. In 1996, the efficiency of (9±2)% has been reported by Zachariou *et al* for the InP/In_xGa_{1-x}As multiple quantum well solar cell [9]. Tang *et al* have also achieved 6% efficiency for PbS quantum dots in 2011 [10]. In the same year, Im *et al* have reported the efficiency of 6.5% for perovskite quantum-dot-sensitised solar cell [11]. Also, Tzeng *et al* have reported an efficiency of ~10.9% for In_xGa_{1-x}As multiple quantum dot-well solar cell in 2013 [12]. In 2015, Dutta *et al* have reported the efficiency of 12.9% for hybrid solar cell using nano-crystalline Si quantum dots and Si nano wires [13]. These efficiencies show quantum dot/well solar cells are not yet as efficient as standard types of solar cells. Therefore, lots of investigations are required to bring the efficiency of quantum dot/well solar cells into

the standard level. Reports in the literature also show that there is a contribution from low energy photons, in quantum dots/wells devices. However, overall efficiency becomes less than those of standard reference cells. This clearly indicates that disturbances produced in the host material create more recombination centers to reduce photogenerated currents. To date no high efficiency devices have been produced to exceed reference cells by a considerable amount.

10.4 Solar cells with down conversion

The down conversion is another method which has been proposed and used to harness high-energy photons in the solar cells. This is because the most common loss mechanism in the solar cells is the thermalisation of charge carriers generated by the absorption of high energy photons. The thermalisation of the charge carriers can be prevented by using the down conversion materials. These materials split the higher energy incident photons ($h\nu \geq 2E_g$) into two lower energy photons ($h\nu \geq E_g$) as shown in Figure 10.2. The down conversions materials are (usually rare-earth metal-doped materials) mostly applied on the front side of solar cells and are most suitable for solar cells having smaller energy bandgap.

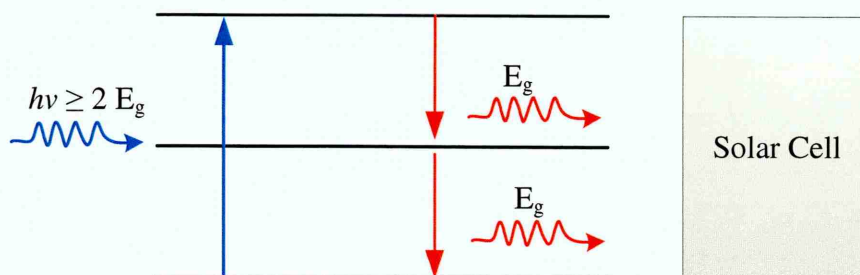


Figure 10.2: Schematic diagram of the down conversion process. The high energy incident photons with energy ($h\nu \geq 2E_g$) are split into two low energy photons ($h\nu \geq E_g$) by the down conversion materials. Redrawn from [14].

The theoretical limiting efficiency of down conversion solar cells as reported in the literature is about 40% for single bandgap solar cells [14,15]. The down conversion materials have been used in many solar cells and most of the reports indicate the slight improvement in the efficiency of the solar cells. In 2006, Liu et al have reported an

increase in the efficiency of the dye-sensitised solar cell from 3.0 to 3.7% using down conversion films [16]. In 2012, Cheng *et al* also reported an improvement in the efficiency of monocrystalline Si from 15.2 to 17.2% using down conversion material [17]. Also, the slight improvement of about 1.8% in the J_{sc} of the CIGS solar cell have been reported by Klampaftis *et al* in 2102 using down conversion films [18]. In 2014, Ross *et al* also reported the 4.3% improvement in J_{sc} of CdS/CdTe module (120 cm × 60 cm dimensions) after incorporation of the thin layer of down conversion material [19]. On the contrary, Shao *et al* have reported 0.07% reduction in the efficiency of the single crystal Si from 16.32 to 16.25% after addition of the down conversion material [20]. These results show that the down conversion materials still have not met the standard performance for industrial purpose. However, investigations are in progress to improve the quality of down conversion films for solar cell applications.

10.5 Solar cells with up-conversion

Unlike the down conversion process, in up-conversion every two or more low energy photons (near infrared) is converted to one high energy photons (blue) using up-conversion materials as shown in Figure 10.3 [14]. The up-conversion materials are more suitable for wide bandgap semiconductors and are usually used at the rear side of the crystalline, thin films and hybrid solar cells to utilise the sub-bandgap photons and reduce the transmission loss [21,22]. Similar to down conversion material, the up-conversion materials consist of rare-earth metal-doped material as well as material doped with transition metals.

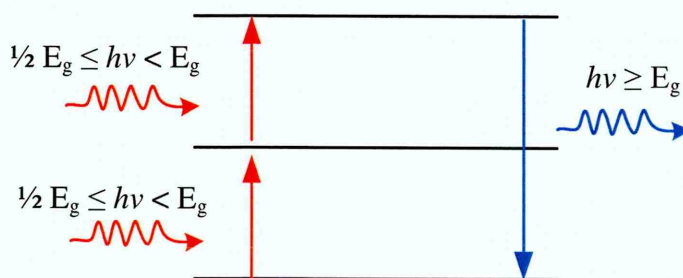


Figure 10.3: Schematic diagram of the up-conversion process. The two low energy photons ($\frac{1}{2} E_g \leq h\nu < E_g$) is converted to a high energy photon ($h\nu \geq E_g$) using up conversion materials. Redrawn from [14].

The efficiency limit of the up-conversion solar cell is about 48% which is higher than ~40% of the down conversion solar cells [21]. Also, the efficiency of the solar cells can be further increased when both down conversion and up conversion films are respectively placed at the front and rear of the solar cells. In 2011, Chen *et al* have reported 1.5-2.7% improvement in the efficiency of single-crystal Si solar cell coated with up-conversion films. The efficiency of bare Si solar cells were in the range (16.23-16.53)% and after addition of the conversion films the efficiency increase were in the range (16.67-16.78)% [23]. Also, Zhang *et al* in 2010 have reported the improvement in J_{sc} and efficiency of the a-Si solar cell from 15.99 to 17.00 mAcm^{-2} and 5.72% to 6.01% using up conversion films [24]. In 2014, Yu *et al* have reported 37% improvement in the efficiency of DSSC by coating the TiO_2 mesoporous layer with the up conversion film [25]. The overall efficiency of this cell was ~10% [25]. These results again show that the incorporation of up-conversion films in the solar cells have just slightly improved the efficiency of the solar cells and still more research on these materials are required to improve the quality of these layers.

10.6 Plasmonic solar cells

In the plasmonic solar cells, the plasmonic effect is used to enhance the absorption and trapping of the longer wavelength photons which are usually transmitted through the solar cells. The plasmonic effect refers to the quantised oscillation of the free electron gas in a metal which have been stimulated by the incident photons. The quanta of the plasma oscillation are called plasmons [26]. In a solar cell usually the plasmonic layer such as gold or silver nanoparticles is coated on the back of the solar cell's absorber material. This layer will trap or scatter back the transmitted long wavelength of the light, hence, enhance the absorption of light in the solar cells. The main aim of the addition of plasmonic layer is to enhance the photocurrent in the solar cells. Lee *et al* in 2014 have reported the improvement in the efficiency of Si solar cell from 9.63 to 12.91% by growing the plasmonic layer of indium-nanoparticles on the patterned TiO_2 matrix [27]. For this device, the major enhancement observed was in the J_{sc} of the solar cells from 23.53 to 30.82 mAcm^{-2} after addition of plasmonic layer. However, another group has reported the reduction in the efficiency of the Si solar cells from 10.7 to 7.3% after incorporation of plasmonic layer [28]. The plasmonic solar cells

similar to the previous mentioned solar cell have not yet been able to increase the efficiency of solar cells in an effective way. Therefore, this type of solar cells requires further investigation in order to reach the standard level.

10.7 Hot-carrier solar cells

In a solar cell, the photons with energies much higher than the bandgap of the absorber material can create charge carriers with high-kinetic energy, called hot-carriers. The hot carriers release their excess energy in the form of phonons into the crystal lattice of the material. This process creates heat in the solar cells and is called the thermalisation. Thermalisation is one major source of efficiency loss in solar cells. The main idea of the hot-carrier solar cells is to collect hot charge carriers before they “cool down” or thermalise to the band edges. One solution to this problem is to slow down the rate of carries cooling to allow hot carries to be collected when they are still at the elevated energies (hot). This process enables higher open-circuit voltage to be achieved which leads to higher efficiency solar cells. The other solution is the extraction or collection of hot-carriers through energy selective contacts [29].

The limiting efficiency of the single band gap hot carrier solar cells is ~66% under one sun illumination and ~85% under maximum concentrated sunlight [29, 30]. It should be noted that the majority of research carried out on hot-carrier solar cells are based on theoretical calculations. The experimental work on the hot carrier solar cells have so far not shown impressive improvement in the cell efficiency [32]. The proposals do not suggest any way to produce selective contacts.

10.8 Tandem solar cells with tunnel junctions

Tandem solar cells are also another class of the third generation solar cells. These types of solar cells are in fact tandem or multijunction solar cells which contain multiple p-n or p-i-n junctions connected together in series through tunnel junctions as shown in Figures 10.4 [33,34]. The multijunction solar cells are generally fabricated using III-V semiconductors with different bandgaps. These tandem devices are arranged in such a way that the device with larger bandgap is deposited in the front of the tandem cell where the light is incident on the device and the device with lower bandgap deposited at the back of the tandem cell. This structure helps to harvest the photons

from different parts of the solar spectrum. The III-V multijunction solar cells have already proven their ability to produce high-efficiency solar cells under concentrated sunlight. In (2013-2014), the Sharp and Fraunhofer Institute for solar energy (ISE) achieved laboratory world record efficiency of 44.4% and 46.0% for triple- and four-junction concentrator solar cells respectively [35]. The maximum module efficiency reported for the triple- and four-junction concentrator solar cells are 35.9 and 38.9% respectively [35]. The efficiency limit of the multijunction solar cells under one sun is about 70% [36]. Also, the limiting efficiency of the infinite number of the junctions under highly concentrated sunlight is 86.8% [37]. As compared to the previous idea proposed for the next generation solar cells, the concentrator solar cells have practically proven their ability and reliability of producing high-efficiency solar cells. The main advantage of the multijunction solar cells is the high open-circuit voltage produced by these kinds of solar cells. However, the major disadvantages of the multijunction concentrator solar cells are that the materials and growth techniques (e.g. MBE and MOCVD) used for their growth and fabrication are expensive. Another disadvantage of this kind of solar cells is that the recombination can take place through tunnel junctions and also current remain constant through to the multiple p-n or p-i-n junctions connected together in series. In this types of tandem cells, the V_{oc} increases due to series connection, but the J_{sc} decreases with the increase of number of junction used.

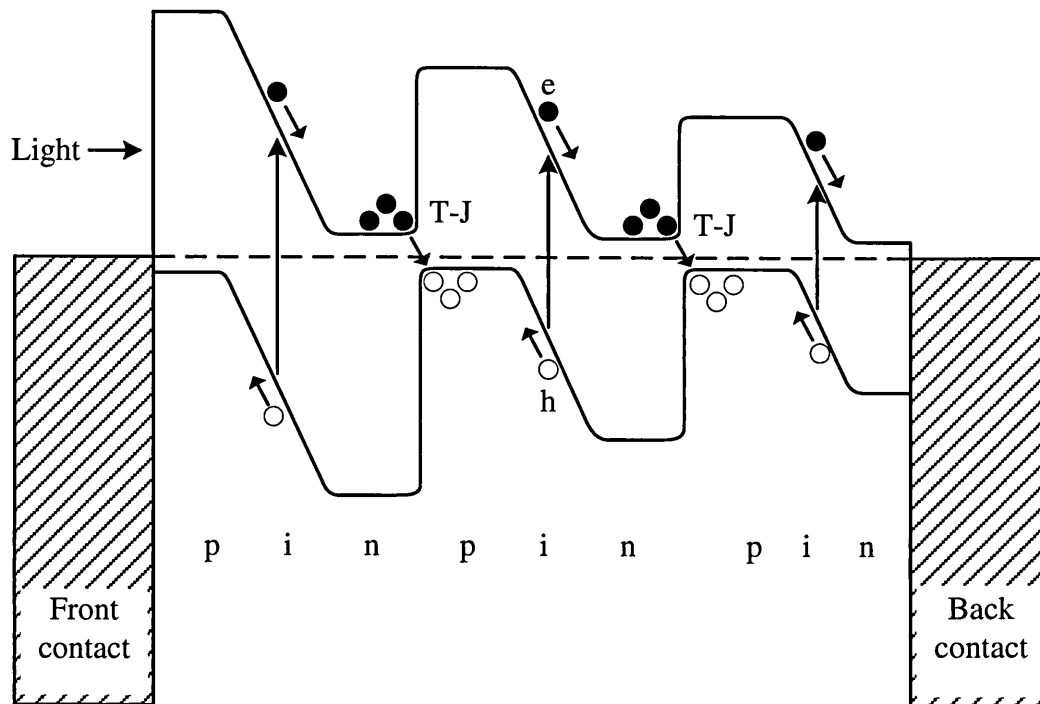


Figure 10.4: Energy band diagram of the three p-i-n junctions connected in series through two tunnel junctions (T-J). Note that, the recombination of photogenerated charge carriers are encouraged at tunnel junctions.

10.9 Organic solar cells (OSCs)

Organic solar cells also represent a promising technology to afford low-cost and large-scale production for the next generation solar cells. The power conversion efficiency of the OSCs has reached up to 8-12% [35,38]. The organic molecules have high optical absorption coefficient ($>10^5 \text{cm}^{-1}$) which makes them suitable for thin film solar cells applications [39]. In OSCs different types of junctions have been fabricated including single layer, bilayer, discrete heterojunction, bulk heterojunction, graded heterojunction and continuous junction. The major challenges to improve the efficiency of the OSCs are; (i) the improvement of the charge carrier transport, (ii) the improvement of the film morphology, (iii) the controlled growth of the heterojunction and blend microstructure, (iv) the development of new electrodes to compete with current electrode such as ITO, and (v) the improvement of the long-term stability of the devices.

10.10 Dye-sensitised solar cells (DSSCs) and Perovskite solar cells (PSCs)

Dye-sensitised solar cells (DSSCs) can also be considered as one of the candidate for the next generation solar cells. This type of solar cells has brought significant improvement in their power conversion efficiencies from 6 to 13% [40,41]. These new hybrid materials hold the promise for low temperature fabrication to considerably reduce manufacturing costs and environmental impact through solution-based scalable roll-to-roll fabrication and short energy payback time. The DSSCs are generally fabricated using cheap and non-toxic components and can also be designed in different colour and transparencies. In order to increase the efficiency of DSSCs, in the last few years a number of new nanostructured photoelectrodes have been proposed to control charge extraction, enhance light harvesting and reduce recombination losses [42]. These nanostructured photoelectrodes include (i) nanoparticles with high surface areas for efficient dye loading, e.g. TiO_2 [40], (ii) one dimensional (1D) nanotubes and nanowires that offer direct electron transport pathways towards the collecting substrate,

e.g. TiO_2 , SnO_2 and ZnO [43,44], (iii) 3D hierarchically ordered photoelectrodes that combine large pores for efficient electrolyte diffusion, large particles for effective light scattering but also small particles needed to achieve high surface areas [45] (iv) 3D template-based techniques that produce highly conductive macroporous scaffolds to produce structures with different length scales for electrolyte diffusion (macro and mesopores) and dye loading (micro and nanopores) [46] and (v) hybrid TiO_2 /graphene nanostructures able to suppress electron recombination in the semiconductor/electrolyte interface [47]. However, the power conversion efficiency of the DSSCs using the nanostructured photoelectrodes are still lower than 13% of the reference DSSCs [48–51].

Perovskite solar cells (PSCs) are also one of the latest and most promising low-cost and highly-efficient next generation solar cells. This type of solar cell has attracted a lot of attention due to the simplicity of their processing at low-temperature. The PSCs are in fact the extension of dye-sensitised solar cells. The true perovskite mineral consist of three atoms (calcium, titanium and oxygen) which are arranged in the form of CaTiO_3 . Today, perovskites refer to any materials that have the similar crystallographic structure of ABX_3 as shown in Figure 10.5. Where A is an organic cation such as methylammonium $(\text{CH}_3\text{NH}_3)^+$ and ethylammonium $(\text{CH}_3\text{CH}_2\text{NH}_3)^+$, B is an inorganic cation such as Pb^{2+} and Sn^{2+} , and X is halogen anions including F^- , Cl^- , Br^- , I^- [52].

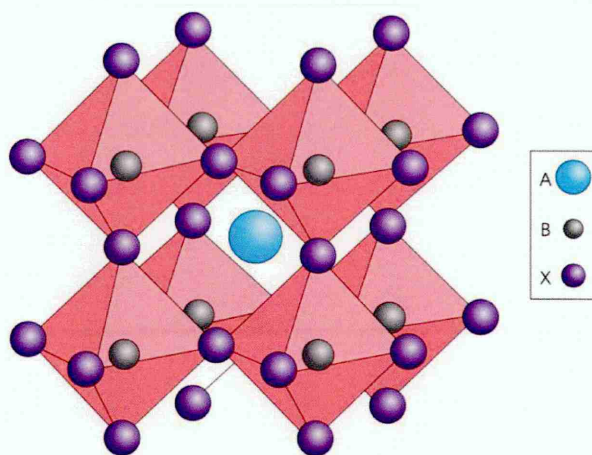


Figure 10.5: Perovskite ABX_3 crystal structure [53].

As compared to other types of solar cell materials, the perovskite solar cells have developed rapidly. The power conversion efficiency of these types of solar cells was increased from 3.8% in 2009 to 20.1% in 2014 which shows that it can be a good candidate for next generation energy devices [54]. The limiting efficiency of the PSCs

as reported by Sha *et al* is about 31% [55]. The main advantages of PSCs are; (i) their relative ease of production, (ii) scalability, (iii) their liquid processing allows for faster manufacturing throughput, (iv) it is easier to achieve high material purity required for manufacturing of solar cells and (v) it can be deposited on flexible substrates [56]. Some disadvantages of PSCs are; (i) insatiability and quick degradation, (ii) they contain toxic and heavy elements such as lead (Pb) in their composition.

10.11 Graded-bandgap solar cells

The graded-bandgap solar cell is another method proposed to increase the efficiency of the solar cells. The graded-bandgap solar cells can be fabricated using one material by alloy with another element or by using different materials (multi-layers) with different bandgaps. In both cases, the prepared materials are arranged in such a way that the bandgap is graded gradually from the front contact towards the back contact as previously discussed in chapter 9 [57–60]. The major advantages of the graded-bandgap structures are; (i) the thermalisation of high-energy charge carriers created by the high-energy blue end photons is minimised due to bandgap grading, (ii) the recombination of photogenerated charge carriers is minimised due to the presence of strong built-in electric field or large slope of the energy band diagram, (iii) the photons can be harvested from different parts of the solar spectrum due to the gradual grading of the energy bandgap, and (iv) the impact ionisation and impurity PV effect is also incorporated in the device as previously discussed in chapter 9. It should be noted that, in the graded-bandgap solar cells, unlike tandem multiple p-n junction solar cells, the multilayer devices are connected together in parallel where the conduction band of one device is connected to the conduction band of the adjacent device as shown in Figure 10.6 [57,58]. With the optimised graded-bandgap structure, extremely high J_{sc} value can be anticipated using this structure and also the EQE over 100% can be achieved as discussed in chapter 9. Also, in multiple p-n junction solar cells, the possibility of the recombination of photogenerated charge carriers through the tunnel junctions is high whereas in the graded-bandgap structure, the recombination process is minimised due to the gradual grading of the energy bandgap and parallel connection of the devices (see Figures 10.4 and 10.6) creating a strong built-in electric field.

There are several reports on the fabrication of the graded-bandgap solar cells using different absorber materials and growth techniques. Wagner *et al* have

experimentally achieved the efficiency values of 14.7% and 17.8% (at 1 sun AM0) for graded-bandgap AlGaAs/GaAs solar cells grown by metalorganic vapour phase epitaxy (MOVPE) technique [61,62]. Dharmadasa *et al* also reported the efficiency values of $\sim 20\%$ in just two attempts for the $\text{Al}_x\text{Ga}_{(1-x)}\text{As}/\text{GaAs}$ graded-band gap solar cells grown by MOCVD method [57,58,63]. It is worth mentioning that this device has produced the highest V_{oc} of ~ 1175 mV reported for a single device under AM1.5 condition in addition to the maximum possible fill factor of ~ 0.85 . Most strikingly, this device structure showed the V_{oc} of ~ 950 mV at complete darkness which indicates the presence of impurity PV effect as previously discussed in chapter 9 [57,58,63]. Also, Contreras *et al* reported the power conversion efficiency of 16.8% for the graded-bandgap solar cell based on CIGS absorber material [64]. Echendu *et al* also reported the efficiency of 10.4% for glass/FTO/ZnS/CdS/CdTe/Au graded-bandgap solar cells using low-cost electroplated materials. It should be noted that all the three layers (ZnS, CdS & CdTe) were grown by scalable electrodeposition technique and this device has showed high J_{sc} value of 40.8 mAcm^{-2} [65].

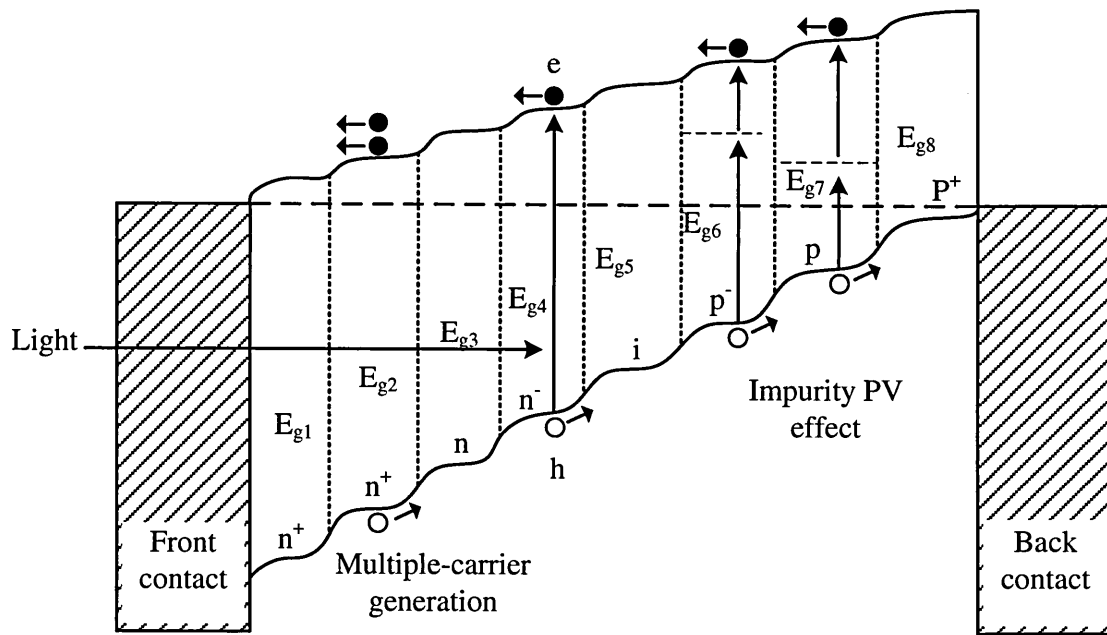


Figure 10.6: An energy band diagram of the multi-layer graded-bandgap solar cells. The number of semiconductor layers included in this structure is eight. Note that, the bandgap of the material gradually reduce ($E_{g1} > E_{g2} > \dots > E_{g7} > E_{g8}$), and conduction type varies from n^+ to p^+ . In this notation, n^+ , n , n^- and i denote heavily n-doped, moderately n-doped, low n-doped and intrinsic semiconducting material. A similar definition applies to p-type materials [66].

The graded-bandgap solar cells have a future prospect for possible applications in next generation solar cells. However, the concentrator solar cells are more expensive to manufacture as compared to the graded-bandgap solar cells due to the expensive materials and growth technique used in their fabrication.

10.12 Conclusions

Various approaches and ideas proposed to increase the efficiency of the solar cells have been briefly reviewed and presented in this chapter. The theoretical calculations of these ideas show that their power conversion efficiencies can exceed the 31% theoretical Shockley-Queisser limit for single bandgap solar cells. However, the experimentally reported efficiencies for these devices so far are still well below the Shockley-Queisser limit. In most of the cases, it has been shown that the efficiency can be increased mainly through enhancement of the photocurrent in these devices. In other words, most of the proposed ideas are based on the harvesting of photons from different parts of the solar spectrum. So far, among all proposed ideas presented in this chapter only two approaches have experimentally shown reasonable efficiency. These two approaches are tandem solar cells and graded-bandgap solar cells. The main difference between these two approaches is that in the concentrated solar cells the efficiency increase is mostly due to increasing in open-circuit voltage while in the graded-bandgap solar cells the efficiency is mainly increased due to increase in the photocurrent. These two techniques at the present appear to be the ones that can deliver the expected results for the next generation solar cells.

- [1] G.W. Crabtree, N.S. Lewis, *Phys. Today*, **60** (2007) 37–42.
- [2] G. Conibeer, *Mater. Today*, **10** (2007) 42–50.
- [3] A. Luque, A. Martí, C. Stanley, *Nat. Photonics*, **6** (2012) 146.
- [4] M. Wolf, *Proc. IRE*, **48** (1960) 1246–1263.
- [5] A. Luque, P.G. Linares, E. Antolín, E. Cánovas, C.D. Farmer, C.R. Stanley, A. Martí, *Appl. Phys. Lett.*, **96** (2010).
- [6] X. Lan, S. Masala, E.H. Sargent, C. Smith, D. Binks, B.J. Beberwyck, Y. Surendranath, a. P. Alivisatos, S. V Kershaw, A.S. Sussha, A.L. Rogach, *Nat. Mater.*, **13** (2014) 233–240.
- [7] K.W.J. Barnham, G. Duggan, *J. Appl. Phys.*, **67** (1990) 3490–3493.
- [8] G.L. Araújo, A. Martí, *Sol. Energy Mater. Sol. Cells*, **33** (1994) 213–240.
- [9] A. Zachariou, K.W.J. Barnham, P. Griffin, J. Nelson, C. Button, M. Hopkinson, M. Pate, J. Epler, in: Conf. Rec. Twenty Fifth IEEE Photovolt. Spec. Conf. - 1996, IEEE, Washington, D.C., USA, 1996, pp. 113–116.
- [10] J. Tang, K.W. Kemp, S. Hoogland, K.S. Jeong, H. Liu, L. Levina, M. Furukawa, X. Wang, R. Debnath, D. Cha, K.W. Chou, A. Fischer, A. Amassian, J.B. Asbury, E.H. Sargent, *Nat. Mater.*, **10** (2011) 765–771.
- [11] J.-H. Im, C.-R. Lee, J.-W. Lee, S.-W. Park, N.-G. Park, *Nanoscale*, **3** (2011) 4088–4093.
- [12] T.E. Tzeng, K.Y. Chuang, T.S. Lay, C.H. Chang, *J. Cryst. Growth*, **378** (2013) 583–586.
- [13] M. Dutta, L. Thirugnanam, P. Van Trinh, N. Fukata, *ACS Nano*, **9** (2015) 6891–6899.
- [14] D. Verma, T.O. Saetre, O. Midtgard, in: 2012 38th IEEE Photovolt. Spec. Conf., IEEE, 2012, pp. 002608–002613.
- [15] T. Trupke, M.A. Green, P. Würfel, *J. Appl. Phys.*, **92** (2002) 1668.
- [16] J. Liu, Q. Yao, Y. Li, *Appl. Phys. Lett.*, **88** (2006) 173119.
- [17] C. Cheng, J. Yang, *IEEE Electron Device Lett.*, **33** (2012) 697–699.
- [18] E. Klampaftis, D. Ross, S. Seyrling, A.N. Tiwari, B.S. Richards, *Sol. Energy Mater. Sol. Cells*, **101** (2012) 62–67.
- [19] D. Ross, D. Alonso-Alvarez, E. Klampaftis, J. Fritsche, M. Bauer, M.G. Debije, R.M. Fifielfield, B.S. Richards, *IEEE J. Photovoltaics*, **4** (2014) 457–464.

- [20] G. Shao, C. Lou, in:, 2012 38th IEEE Photovolt. Spec. Conf., IEEE, 2012, pp. 002596–002600.
- [21] H.-Q. Wang, M. Batentschuk, A. Osvet, L. Pinna, C.J. Brabec, *Adv. Mater.*, **23** (2011) 2675–2680.
- [22] A. Shalav, B.S. Richards, M.A. Green, *Sol. Energy Mater. Sol. Cells*, **91** (2007) 829–842.
- [23] Y.-C. Chen, T.-M. Chen, *J. Rare Earths*, **29** (2011) 723–726.
- [24] X.D. Zhang, X. Jin, D.F. Wang, S.Z. Xiong, X.H. Geng, Y. Zhao, *Phys. Status Solidi C*, **7** (2010) 1128–1131.
- [25] J. Yu, Y. Yang, R. Fan, D. Liu, L. Wei, S. Chen, L. Li, B. Yang, W. Cao, *Inorg. Chem.*, **53** (2014) 8045–8053.
- [26] S.J. Fonash, in:, Light Trapp. Sol. Cell Photo-Detector Devices, Elsevier, 2015, pp. 1–16.
- [27] Y.-Y. Lee, W.-J. Ho, Y.-T. Chen, *Thin Solid Films*, **570** (2014) 194–199.
- [28] P.R. Pudasaini, A.A. Ayon, *Microelectron. Eng.*, **110** (2013) 126–131.
- [29] M.A. Green, G. Conibeer, D. Konig, S. Shrestha, S. Huang, P. Aliberti, L. Treiber, R. Patterson, B.P. Veettil, A. Hsieh, Y. Feng, A. Luque, A. Marti, P.G. Linares, E. Canovas, E. Antolin, D. Fuertes Marron, C. Tablero, E. Hernandez, J.-F. Guillemoles, L. Huang, A. Le Bris, T. Schmidt, R. Clady, M. Tayebjee, in:, 2010 35th IEEE Photovolt. Spec. Conf., IEEE, 2010, pp. 000057–000060.
- [30] R.T. Ross, *J. Appl. Phys.*, **53** (1982) 3813–3818.
- [31] P.J. Reddy, *Solar Power Generation: Technology, New Concepts & Policy*, CRC Press, London, UK, 2012.
- [32] M.C. Hanna, Z. Lu, A.J. Nozik, in:, AIP Conf. Proc., AIP, 1997, pp. 309–316.
- [33] H. Cotal, C. Fetzer, J. Boisvert, G. Kinsey, R. King, P. Hebert, H. Yoon, N. Karam, *Energy Environ. Sci.*, **2** (2009) 174–192.
- [34] J.F. Geisz, D.J. Friedman, J.S. Ward, A. Duda, W.J. Olavarria, T.E. Moriarty, J.T. Kiehl, M.J. Romero, A.G. Norman, K.M. Jones, *Appl. Phys. Lett.*, **93** (2008) 123505.
- [35] M.A. Green, K. Emery, Y. Hishikawa, W. Warta, E.D. Dunlop, *Prog. Photovoltaics Res. Appl.*, **24** (2016) 3–11.
- [36] R.R. King, D. Bhusari, D. Larrabee, X.-Q. Liu, E. Rehder, K. Edmondson, H. Cotal, R.K. Jones, J.H. Ermer, C.M. Fetzer, D.C. Law, N.H. Karam, *Prog. Photovoltaics Res. Appl.*, **20** (2012) 801–815.

- [37] A.S. Brown, M.A. Green, *Phys. E Low-Dimensional Syst. Nanostructures*, **14** (2002) 96–100.
- [38] <http://optics.org/news/4/1/36>, Last accessed March (2016).
- [39] H. Hoppe, N.S. Sariciftci, *J. Mater. Res.*, **19** (2004) 1924–1945.
- [40] N. T  treault, M. Gr  tzel, *Energy Environ. Sci.*, **5** (2012) 8506.
- [41] S. Mathew, A. Yella, P. Gao, R. Humphry-Baker, B.F.E. Curchod, N. Ashari-Astani, I. Tavernelli, U. Rothlisberger, M.K. Nazeeruddin, M. Gr  tzel, *Nat. Chem.*, **6** (2014) 242–247.
- [42] J. Ma  aira, L. Andrade, A. Mendes, *Renew. Sustain. Energy Rev.*, **27** (2013) 334–349.
- [43] A.B.F. Martinson, M.S. G  es, F. Fabregat-Santiago, J. Bisquert, M.J. Pellin, J.T. Hupp, *J. Phys. Chem. A*, **113** (2009) 4015–4021.
- [44] P. Tiwana, P. Docampo, M.B. Johnston, H.J. Snaith, L.M. Herz, *ACS Nano*, **5** (2011) 5158–5166.
- [45] B. Mandlmeier, J.M. Szeifert, D. Fattakhova-Rohlfing, H. Amenitsch, T. Bein, *J. Am. Chem. Soc.*, **133** (2011) 17274–17282.
- [46] N. T  treault,   . Arsenault, L.-P. Heiniger, N. Soheilnia, J. Brillet, T. Moehl, S. Zakeeruddin, G.A. Ozin, M. Gr  tzel, *Nano Lett.*, **11** (2011) 4579–4584.
- [47] N. Yang, J. Zhai, D. Wang, Y. Chen, L. Jiang, *ACS Nano*, **4** (2010) 887–894.
- [48] S. Mathew, A. Yella, P. Gao, R. Humphry-Baker, B.F.E. Curchod, N. Ashari-Astani, I. Tavernelli, U. Rothlisberger, M.K. Nazeeruddin, M. Gr  tzel, *Nat. Chem.*, **6** (2014) 242–247.
- [49] C.-H. Ku, J.-J. Wu, *Appl. Phys. Lett.*, **91** (2007) 093117.
- [50] Y.J. Kim, M.H. Lee, H.J. Kim, G. Lim, Y.S. Choi, N.-G. Park, K. Kim, W.I. Lee, *Adv. Mater.*, **21** (2009) 3668–3673.
- [51] F. Sauvage, D. Chen, P. Comte, F. Huang, L.-P. Heiniger, Y.-B. Cheng, R.A. Caruso, M. Graetzel, *ACS Nano*, **4** (2010) 4420–4425.
- [52] C. Li, X. Lu, W. Ding, L. Feng, Y. Gao, Z. Guo, *Acta Crystallogr. Sect. B Struct. Sci.*, **64** (2008) 702–707.
- [53] M.A. Green, A. Ho-Baillie, H.J. Snaith, *Nat. Photonics*, **8** (2014) 506–514.
- [54] D.-L. Wang, H.-J. Cui, G.-J. Hou, Z.-G. Zhu, Q.-B. Yan, G. Su, *Sci. Rep.*, **6** (2016) 18922.
- [55] W.E.I. Sha, X. Ren, L. Chen, W.C.H. Choy, *Appl. Phys. Lett.*, **106** (2015) 221104.
- [56] B. Susrutha, L. Giribabu, S.P. Singh, *Chem. Commun.*, **51** (2015) 14696–14707.

- [57] I.M. Dharmadasa, J.S. Roberts, G. Hill, *Sol. Energy Mater. Sol. Cells*, **88** (2005) 413–422.
- [58] I.M. Dharmadasa, *Advances in Thin-Films Solar Cells*, Pan Stanford Publishing Pte. Ltd, Boulevard, Singapore, 2012.
- [59] T. Dullweber, G.. Anna, U. Rau, H.. Schock, *Sol. Energy Mater. Sol. Cells*, **67** (2001) 145–150.
- [60] O.K. Echendu, F. Fauzi, A.R. Weerasinghe, I.M. Dharmadasa, *Thin Solid Films*, **556** (2014) 529–534.
- [61] D.K. Wagner, J.R. Shealy, *Appl. Phys. Lett.*, **45** (1984) 162.
- [62] D.K. Wagner, J.R. Shealy, *J. Cryst. Growth*, **68** (1984) 474–476.
- [63] I. Dharmadasa, A. Ojo, H. Salim, R. Dharmadasa, *Energies*, **8** (2015) 5440–5458.
- [64] M. Contreras, J. Tuttle, A. Gabor, A. Tennant, K. Ramanathan, S. Asher, A. Franz, J. Keane, L. Wang, R. Noufi, *Sol. Energy Mater. Sol. Cells*, **41-42** (1996) 231–246.
- [65] O. Echendu, I. Dharmadasa, *Energies*, **8** (2015) 4416–4435.
- [66] I.M. Dharmadasa, *Sol. Energy Mater. Sol. Cells*, **85** (2005) 293–300.

11.1 Conclusions

This thesis has presented the growth and characterisation of some selected semiconductor materials to develop low-cost high efficiency multilayer graded bandgap solar cells based on CdTe absorber material. The semiconductor materials were grown by two different solution growth techniques. The CdS window layers were grown by the chemical bath deposition (CBD) and the electrodeposition (ED) methods using aqueous solutions. The CdTe absorber layers were grown only by electrodeposition technique using 2-electrode system. Also, the electrodeposited ZnTe and ZnS thin films grown by other PhD researchers at SHU were incorporated in the device structures in order to increase the efficiency of solar cells.

The experimental works are presented in chapters 6 to 9. Chapters 6 and 7 are mainly focused on the growth and characterisation of ED-CdS and CBD-CdS window layers and the results are compared with each other. In chapter 8, the growth and characterisation of ED-CdTe absorber layer is presented. In these three chapters, different material characterisation techniques were used to optimise the growth conditions and improve the quality of CdS and CdTe layers. Also, the effects of CdCl₂ and CdCl₂+CdF₂ heat treatment on the CdTe layers were investigated at different annealing temperatures of 385, 420 and 450°C which are presented in chapter 8. It was observed that the larger grains can be obtained when CdTe layers are heat treated with the combination of CdCl₂+CdF₂ treatment at the higher temperature of 450°C as compared to CdCl₂ treatment alone which is key step to obtain higher efficiency solar cells [1–5].

Chapter 9 focused on the fabrication and assessment of the solar cells using n-CdS, n-ZnS, n-CdTe, p-CdTe and p-ZnTe layers. These layers were used to fabricate different device structures including n-n+Schottky heterojunction solar cells and multi-layer graded-bandgap solar cells. Generally, devices heat treated with CdCl₂+CdF₂ treatment at 450°C showed better performances than those devices heat treated with CdCl₂ treatment only. Also in chapter 9, the devices fabricated using CBD-CdS layers as window layer showed better *FF* and conversion efficiencies than those devices fabricated using ED-CdS layers. The lower efficiency of the device fabricated using ED-CdS layers are related to the presence of pinholes in the ED-CdS layer due to the

upward growth nature of the electrodeposition technique. Also, the effect of the p-ZnTe layer as pinhole plugging layer to improve the Schottky barrier height was also presented in this chapter. The results showed that the thickness of the p-ZnTe layer should be thin enough (less than ~13 nm) in order to see the positive effect on the device performances; otherwise, it introduced extra series resistance (R_s) into the device and resulted in the poor device performance. Also, the inclusion of p-CdTe layer between n-CdTe and Au metal contact was also found to be beneficial in improving the device performance of multi-layer graded bandgap solar cells with glass/FTO/n-CdS/n-CdTe/p-CdTe/Au structure. Also, the investigation showed that the thickness of the p-CdTe layer should be thin enough (less than 100 nm) in order to see the positive effect on the device performances with rectifying behaviour, otherwise it reduces the efficiency of solar cell devices due to the high R_s and low R_{sh} (with observed ohmic behaviour). Also, the multi-layer graded-band gap solar cell with the structure of glass/FTO/n-ZnS/n-CdS/n-CdTe/Au showed better device performances than those devices with glass/FTO/n-ZnS/n-CdTe/Au solar cell structure. The main improvements after inclusion of CdS between ZnS and CdTe layers were observed in the FF and J_{sc} of the devices due to increase in R_{sh} (reduction of pinholes or leakage paths). The highest efficiency reported in this thesis is 7.1% for glass/FTO/n-CdS(CBD)/n-CdTe/Au structure whereas the highest V_{oc} , J_{sc} and FF are 663 mV, 26.2 mAcm⁻² and 0.65 respectively.

11.2 Recommendations for future work

The efficiency of the solar cells depends on three solar cell parameters; V_{oc} , J_{sc} and FF of the device. There are various factors which can affect these parameters during the semiconductor growth and fabrication process. In the following section, few suggestions are proposed to improve the efficiency of the solar cells based on electrodeposited CdTe absorber materials.

11.2.1 Preparation of deposition electrolyte using high-purity chemicals

The impurity ions in semiconductors at parts per million (ppm) levels can seriously change the semiconductor properties and also can affect the performance of the solar cell devices [6]. The use of low-purity chemicals can introduce unwanted

impurity ions into the deposition electrolyte as well as the deposited layer during the growth. In this work, the purity of the chemicals used for the deposition of ED-CdS, ED-CdTe and CBD-CdS were $\geq 99.99\%$ ($\geq 4N$). For this reason, when low-purity chemicals are used in electrodeposition technique, the electro-purification process is usually carried out to remove unwanted impurity ions as discussed in chapter 8 [7–12]. It should be noted that, the high-efficiency CdS/CdTe solar cells ($>15\%$) have been fabricated using high purity chemicals (5N and 6N) [13–16]. Therefore, alongside the self-purification process in the electrodeposition technique, it is also better to use high-purity chemicals to reduce the possibility of the addition of detrimental impurity ions into deposition electrolyte.

11.2.2 Effective addition of Te and Cd ions into the deposition electrolyte during the growth

One important factor in the electrodeposition growth technique is the control of ions balance in the deposition electrolyte during the growth. This process can seriously affect the reproducibility of the layers and the subsequent devices fabricated using these layers. This is because, during the deposition process, the ions are gradually depleted in the deposition electrolyte. Therefore, the restoration of the depleted ions is required in order to make sure that the deposited layers have the same quality. In the electrodeposition of CdTe layer, the concentration of Te ions (HTeO_2^+) is always kept much lower than the Cd^{2+} ions because of the more positive redox potential of Te ($E_0 = +0.53$ V vs. NHE) as compared to Cd ($E_0 = -0.40$ V vs. NHE) [17]. For this reason, Te ions are depleted faster than Cd ions. The effective addition and control of the depleted Te ions in the deposition electrolyte was one of the challenges encountered during the course of this research programme. One method used to maintain the Te ions in the deposition electrolyte was the continuous monitoring of the deposition current density during the electrodeposition of the CdTe layer. From the experience gained in this research, good quality of CdTe layers were deposited when the current density was within the range of $\sim(150\text{--}160) \mu\text{Acm}^{-2}$ in the stoichiometric growth voltage range using the 2-electrode system as discussed in chapter 8. When the deposition current density dropped below $\sim(150\text{--}160) \mu\text{Acm}^{-2}$, about 1 ml of diluted TeO_2 was added into the deposition electrolyte to restore the depleted Te ions. It should be noted that, when

deposition current density was higher than $\sim(150-160) \mu\text{Acm}^{-2}$, no TeO_2 was added into the deposition electrolyte.

One method suggested for future work is to use the automated pumping of the Te or Cd ions into the deposition electrolyte during the growth by automated monitoring of deposition current density or ion analyser tools. Another method which can be tried in the future is to use Te rod as the counter electrode (anode). Das and Morris have performed this method in order to inject Te ions into deposition electrolyte from a high-purity (5N) Te rod and have reported the efficiency of 11.5% for electrodeposited CdS/CdTe solar cells [7].

11.2.3 Reducing the resistivity of ED-CdS, CBD-CdS and CdTe layers

One of the factors that affect the efficiency of the fabricated solar cell is the high R_s of the CdS window layer. The high R_s mainly reduce the FF and eventually the efficiency of the solar cells. In this work, the resistivity of the annealed ED-CdS and CBD-CdS were high in the range 10^3 - $10^5 \Omega\text{cm}$; this can be one of the reasons for observing low FF in the fabricated devices. In the literature, researchers have reported the growth of low-resistivity CdS using different methods. De Melo et al have reported a resistivity of $11 \Omega\text{cm}$ for CBD-CdS layer annealed at 350°C in the vacuum environment in the presence of S_2 and $(\text{H}_2 + \text{In})$ [18]. Sanchez *et al* have also reported the growth of low-resistivity CdS layer ($0.1 \Omega\text{cm}$) by the chemical vapour transport (CVT) method using CdCl_2 as a flux [19]. Canevari *et al* obtained the resistivity as low as $2.5 \times 10^{-3} \Omega\text{cm}$ for flash-evaporated CdS layer doped with 1% of indium (In) [20]. As a part of future work, the attempt can be made to reduce the resistivity of the ED-CdS and CBD-CdS by addition of halide ions (F^- , Cl^- , I^-) and group III ions such as In^{2+} and Ga^{+3} into their deposition electrolyte during the growth. The major sources of these ions are CdF_2 , CdCl_2 , CdI_2 , In_2S_3 and GaCl_3 compounds.

Also, another attempt for future works is to make ohmic contacts on the n-CdTe layer to determine the resistivity of the CdTe layer. This is because the attempt was made during the available time of this research programme to make ohmic contacts on n-CdTe layer using In-Ga eutectic as well as In metal which was not successful. Also, attempt will be made to add n-type dopants such as Cl and F into deposition electrolyte to reduce the resistivity of the CdTe layers.

11.2.4 The use of low-resistivity transparent conducting oxide (TCO) layer

Another way of improving the efficiency of the solar cell is to use the low-resistivity glass/transparent conducting oxide (TCO) layer as the front contact. The TCO with higher R_s values will reduce the J_{sc} and FF as well as the efficiency of the solar cells. In this work, the glass/FTO was used as the front contact for the solar cell devices. The FTO can be replaced with lower-resistivity front contacts such as ITO (indium tin oxide). Bosio *et al* have reported the resistivity of $2 \times 10^{-4} \Omega\text{cm}$ and $8 \times 10^{-4} \Omega\text{cm}$ for ITO and FTO respectively [15]. However, due to high-cost and scarcity of indium, ITO is typically more expensive than FTO.

11.2.5 Improvement of the solar cell stability using pinhole plugin layer (PPL) and MIS-type structure

In the electrodeposition technique, the presence of pinholes in the layer can affect the solar cell performance due to short-circuiting effect. These pinholes are formed due to the columnar growth nature of electrodeposition technique as discussed in chapter 8. Therefore, these pinholes should be plugged to prevent short-circuiting of metal back contact with the front contact. In this thesis, the positive effect of the inorganic p-ZnTe layer as the pinhole plugin layer (PPL) was observed. Also, organic polymer layers such as the polyaniline (PANI) can be used as PPL in the future work. These materials have been grown, researched and developed by the PhD researchers at the Sheffield Hallam University solar energy research group using electrodeposition technique [21]. The viability of the PANI has been reported by Tessema *et al* [22]. They used the PANI as the PPL in CdS/CdTe solar cells and reported the efficiency improvement from 1.6% for untreated to 7.1% for treated layer. Apart from plugging the pinholes, incorporation of the organic layer or thin insulating layer can improve the stability and efficiency of the solar cell by creating the MIS-type structure as discussed in chapters 8 and 9. Also, the combination of organic-inorganic material results in the formation of hybrid solar cells as previously discussed in chapter 2.

11.2.6 Multi-layer graded-bandgap solar cells

The fabrication of multi-layer graded bandgap solar cells is one of the approaches being pursued to increase the efficiency of the CdTe-based solar cells as discussed in chapter 9 and 10. In the SHU solar energy research group, different semiconductor layers have been successfully grown by electrodeposition technique. These semiconductor layers include n-CdS, (n & p)-ZnS, n-ZnO, n-CdSe, (n & p)-ZnSe, p-InSe, (n & p)-ZnTe, (p, i, & n)-CdTe, p-CdMnTe and PANI etc [11,21,23–32]. All these layers can be used to develop the high-efficiency graded bandgap solar cells using the low-cost electrodeposition technique in the future.

11.3 References

- [1] A. Romeo, S. Buecheler, M. Giarola, G. Mariotto, A.N. Tiwari, N. Romeo, A. Bosio, S. Mazzamuto, *Thin Solid Films*, **517** (2009) 2132–2135.
- [2] E. Hernández-Rodríguez, V. Rejón, I. Riech, M. Acosta, J.L. Peña, *Sol. Energy*, **107** (2014) 305–313.
- [3] V. Rejón, I. Riech, J.L. Peña, *Sol. Energy*, **95** (2013) 319–34.
- [4] A. Rios-Flores, O. Arés, J.M. Camacho, V. Rejon, J.L. Peña, *Sol. Energy*, **86** (2012) 780–785.
- [5] O.K. Echendu, I.M. Dharmadasa, *Mater. Chem. Phys.*, **157** (2015) 39–44.
- [6] S. Dennison, *J. Mater. Chem.*, **4** (1994) 41.
- [7] S.K. Das, G.C. Morris, *J. Appl. Phys.*, **73** (1993) 782–786.
- [8] G.P. Hernandez, X. Mathew, J.P. Enriquez, N.R. Mathews, P.J. Sebastian, *Sol. Energy Mater. Sol. Cells*, **70** (2001) 269–275.
- [9] X. Mathew, *Semicond. Sci. Technol.*, **18** (2003) 1–6.
- [10] N.A. Abdul-Manaf, H.I. Salim, M.L. Madugu, O.I. Olusola, I.M. Dharmadasa, *Energies*, **8** (2015) 10883–10903.
- [11] H.I. Salim, V. Patel, A. Abbas, J.M. Walls, I.M. Dharmadasa, *J. Mater. Sci. Mater. Electron.*, (2015) 3119–3128.
- [12] A.A. Ojo, I.M. Dharmadasa, *Mater. Res. Innov.*, **19** (2015) 470–476.
- [13] C. Ferekides, J. Britt, *Sol. Energy Mater. Sol. Cells*, **35** (1994) 255–262.
- [14] X. Wu, *Sol. Energy*, **77** (2004) 803–814.
- [15] A. Bosio, N. Romeo, S. Mazzamuto, V. Canevari, *Prog. Cryst. Growth Charact. Mater.*, **52** (2006) 247–279.
- [16] I.M. Dharmadasa, *Advances in Thin-Films Solar Cells*, Pan Stanford Publishing Pte. Ltd, Boulevard, Singapore, (2012).
- [17] R.K. Pandey; S.N. Shau; S. Chandra, *Handbook of Semiconductor Electrodeposition*, M. Dekker, New York, (1996).
- [18] O. de Melo, L. Hernández, O. Zelaya-Angel, R. Lozada-Morales, M. Becerril, E. Vasco, *Appl. Phys. Lett.*, **65** (1994) 1278.
- [19] A. Sanchez, P.J. Sebastian, O. Gomez-Daza, *Semicond. Sci. Technol.*, **10** (1995) 87–90.
- [20] V. Canevari, *J. Vac. Sci. Technol. A Vacuum, Surfaces, Film.*, **2** (1984) 9.
- [21] N.A. Abdul-Manaf, O.K. Echendu, F. Fauzi, L. Bowen, I.M. Dharmadasa, *J.*

- Electron. Mater.*, **43** (2014) 4003–4010.
- [22] M.M. Tessema, D.M. Giolando, *Sol. Energy Mater. Sol. Cells*, **107** (2012) 9–12.
 - [23] A.P. Samantilleke, M.H. Boyle, J. Young, I.M. Dharmadasa, *J. Mater. Sci. Mater. Electron.*, **9** (1998) 289–290.
 - [24] N.B. Chaure, A.P. Samantilleke, I.M. Dharmadasa, *Sol. Energy Mater. Sol. Cells*, **77** (2003) 303–317.
 - [25] I.M. Dharmadasa, A.P. Samantilleke, N.B. Chaure, J. Young, *Semicond. Sci. Technol.*, **17** (2002) 1238–1248.
 - [26] J.S. Wellings, N.B. Chaure, S.N. Heavens, I.M. Dharmadasa, *Thin Solid Films*, **516** (2008) 3893–3898.
 - [27] D.G. Diso, F. Fauzi, O.K. Echendu, a R. Weerasinghe, I.M. Dharmadasa, *J. Phys. Conf. Ser.*, **286** (2011) 012040.
 - [28] D.G. Diso, G.E.A. Muftah, V. Patel, I.M. Dharmadasa, *J. Electrochem. Soc.*, **157** (2010) H647.
 - [29] O.K. Echendu, A.R. Weerasinghe, D.G. Diso, F. Fauzi, I.M. Dharmadasa, *J. Electron. Mater.*, **42** (2013) 692–700.
 - [30] F. Fauzi, D.G. Diso, O.K. Echendu, V. Patel, Y. Purandare, R. Burton, I.M. Dharmadasa, *Semicond. Sci. Technol.*, **28** (2013) 045005.
 - [31] O.I. Olusola, O.K. Echendu, I.M. Dharmadasa, *J. Mater. Sci. Mater. Electron.*, **26** (2014) 1066–1076.
 - [32] M.L. Madugu, L. Bowen, O.K. Echendu, I.M. Dharmadasa, *J. Mater. Sci. Mater. Electron.*, **25** (2014) 3977–3983.